**A Special Issue for**
**International Conference**
**on**
**"Recent Innovation in Science**
**and**
**Workshop on Spectroscopy**
**& its Perspectives"**
**By**
**Physics Department, Municipal Arts & Urban Science**
**College, Mehsana, Gujarat, India**

*UGC Approved online Journal*

# International Journal of Research in Modern Engineering & Emerging Technology (IJRMEET)

## Vol. 5, Sp. Issue 9, September 2017

RAIJMR.COM

**Editor-in-Chief**
**Dr. Nilesh Gajjar**
RET Academy for International Journals of Multidisciplinary Research (RAIJMR)
www.raijmr.com

# International Journal of Research in Modern Engineering and Emerging Technology
# (IJRMEET)

## UGC Approved Online International Peer reviewed, Indexed Journal

NSL/ISSN/INF/2013/467                    Dated: February 28, 2013

President,
Riddhi Education Trust,
Gandhinagar,
Gujarat

Dear Sir/ Madam,

We are happy to inform you that the following serial(s) published by you has been registered and assigned ISSN (Online)

ISSN   2320 – 6586        International Journal of Research in Modern Engineering
and Emerging Technology (IJRMEET)

It is important that the ISSN should be printed on every issue preferably at the right hand top corner of the cover page.

The Indian National Centre will be responsible for monitoring the use of ISSN assigned to Indian Serials and for supplying up to-date data of the same to the International Centre for ISSN, Paris.  For this purpose we request you to send us the forth coming issue of your serial on complimentary basis.

We solicit your co-operation in this regard.

Yours sincerely

*(V.V. Lakshmi)*
(V.V. Lakshmi)
Head
National Science Library

**Please don't forget to send a sample issue of the journal/URL with ISSN printed on it.**

**Contact : Ms. Shobhna Vij**
**e-mail : issn.india@niscair.res.in**
**phone : 011-26516672**

## International Conference on "Recent Innovation in Science and Workshop on Spectroscopy & its Perspectives"

## 15 –16 Sept 2017

### Organized By



**Physics Department**
Municipal Arts & Urban Science College
Mehsana, Gujarat, India

### Collaboration with



**Physics Department**
Sheth M. N. Science College
Patan, Gujarat, India

### Sponsored By



Gujarat Council on Science and Technology

### Supported by



Department of Science & Technology
Government of Gujarat

### Association with

RET International
Academic Publishing
**ISSN: 2320-6586**
**(Online)**



---

### Conference Committee

**President**
Mr. Anilbhai Patel
President, Sardar Vidhyabhavan Trust, Mehsana

**Chief Patron**
Mr. K. K. Patel
M.D., Sardar Vidhyabhavan Trust, Mehsana

**Patron**
Dr. Narottam Sahoo,
Member Secretary & Advisor, GUJCOST.
Dr. D. R. Patel
Principal, Municipal Arts & Urban Science College, Mehsana
Prof. A. N. Swami
Principal, Sheth M. N. Science College, Patan.

**Organizing Secretary**
Dr. V. D. Patel
Head, Physics Department, Municipal Arts & Urban Science College, Mehsana

**Organizing Committee**

Prof. J. M. Kadiya
Prof. S. N. Pandya
Prof. D. K. Patel
Prof. D. I. Patel
Prof. K. C. Mevada
Dr. S. R. Suthar

Physics Department
Municipal Arts & Urban Science College, Mehsana

Prof. M. R. Chaudhary
Dr. P. G. Chaudhary
Prof. M. J. Pindariya
Dr. A. N. Patel
Prof. D. D. Joshi
Dr. K. R. Patel
Prof. N. H. Thakkar
Prof. R. J. Parmar

Physics Department
Sheth M. N. Science College, Patan

**Advisor Committee**
Dr. Rainer Dick, Physics Department, Uni. of Saskatchewan, Canada
Dr. Zhuxi Yang, Department of Physics, Zhejiang University, China.
Dr. CHU, Ching-Chi, National Central University, Taiwan.
Dr. K. S. Parikh, Principal, C. U. Shah Science College, Ahmedabad
Dr. S. C. Dwivedi, Ret. Head, University of Rajasthan, Jaipur
Dr. Manju Arora, National Physical Laboratory, New Delhi.
Dr. A. R. Jani, Director, SICART, V. V. Nagar
Dr. C. G. Limbachiya, Department of Applied Physics, M. S. University.
Dr. A. N. Prajapati, Department of Applied Physics, M. S. University.
Dr. M. K. Thakore, Chemistry Department, Science College, Mehsana
Dr. M. P. Bhrahmbhatt, Chemistry Department, Science College, Patan
Dr. K. G. Patel, Biology Department, Science College, Mehsana
Dr. N. K. Patel, Botany Department, Science College, Patan
Mr. J. H. Barot, Mathematics Department, Science College, Mehsana.
Mr. A. J. Patel, Mathematics Department, Science College, Mehsana
Dr. K. B. Patel, Zoology Department, Science College, Patan
Mr. R. A. Soni, Biotechnology Department, Science College, Mehsana
Dr. R. J. Pathak, Chairman, BOS & Dean, Science Faculty, HNGU, Patan
Dr. J. V. Vora, Head, Chemistry Department, H.N.G.U., Patan
Dr. D. G. Vyas, Head, Physics Department, H.N.G.U., Patan

## Important Date

**Full Paper Submission start Date: 1st July 2017**

**Full Paper Submission End Date: 30th August 2017**

**Notification of Acceptance: within 15 days of submission**

**Registration Dead line: 05th Sept 2017**

**Conference Date: 15-16 Sept 2017**

## Registration & Accommodation

| Registration Type | Registration Fees |
|---|---|
| **Faculty from Institute** | **INR 1250/-** |
| **Faculty from Organizing & Collaborating Institutes** | **INR 500/-** |
| **Students** | **INR 1000/-** |
| **Industry Delegates** | **INR 1500/-** |
| **Foreign Delegates** | **USD 100/-** |

- Accommodation will be provided on first come first bases.
- Listener can register by sending email to **submission.icris@gmail.com**

## Venue & How to Reach

### Venue

Physics Department, Municipal Arts & Urban bank Science College, Nagalpur, Mehsana-Ahmedabad Highway, Mehsana, Gujarat, India, PIN–384002

### How to reach

The nearest airport is Sardar Vallabhbhai Patel International Airport at Ahmedabad (75 Km).
It is also connected by rail to other major cities in India.
There are daily trains to and from Delhi and Mumbai, Bangalore etc.
It is connected by road with major cities of Gujarat like Ahmadabad, Ghandhinagar, Surat, Vadodara, Rajkot etc. via state highways.

---

# CALL FOR PAPERS

The Organizer cordially invites full length research papers from all over the World to participate in the conference. This is the premier forum for the presentation of new advances and research results in the fields of Physical Sciences and Chemical sciences for sustainable development. The main objective of this conference is to bring together faculties, research scholars, students and industrial experts around the globe, to provide a platform to present their research results. This comes in appropriate time to establish an effective channel to exchange new ideas and development activities in the fields of Sciences. This will offer greater opportunity to explore innovative and intelligent concepts and other advanced process in wide range of applications.

All Selected papers will be published in UGC approved international e-Journal having ISSN No.

## Track & Mode of Presentation

**Track - 1: Physical Sciences**
(Suggested field but not limited)
Applied Physics, Crystallography, Theoretical & Computational Physics, Condense matter Physics, Biophysics, Nuclear Physics, Optical Physics, Semiconductors devices and Photonics, Opto-electronics, Nano-science, Thermal science.

**Track - 2: Chemical Sciences**
(Suggested field but not limited)
Inorganic Chemistry, Organic Chemistry, Physical Chemistry, Industrial Chemistry, Bio Chemistry, Medical & Pharmaceutical Chemistry, Material Science,

**Paper Presentation**
Mode of Presentation: Oral and Poster
Oral: Multimedia Presentation of 15 min (Including Q&A)
Poster: 1 meter X 1 meter poster

## Paper Submission

The papers should be sent in Microsoft document format (.doc or .docx) to the submission.icris@gmail.com. Author must mention track and mode of presentation in the subject (i.e. Subject: Submitting manuscript - Physical Science - Oral Presentation)

Download Author Guideline

**Contributor**

- Faculties of Physical Science, Chemical Science.
- Post graduate and Ph. D. Students of Physical Science and Chemical Science.
- Industry Delegates form Concern field

---

## About Conference & Workshop

The International Conference is planned to organize by Physics Departments of Municipal Arts & Urban Science College in collaboration with Physics Department, Sheth M. N. Science College, Patan. The main objective of this conference is to bring together faculties, research scholars, students and industrial experts around the globe, to provide a platform to present their research results. This comes in appropriate time to establish an effective channel to exchange new ideas and development activities in the fields of Sciences. This will offer greater opportunity to explore innovative and intelligent concepts and other advanced process in wide range of applications.

## About Organizing College

Municipal Arts & Urban Science College was established in 1964 and is run by Saradar Vidya Bhavan Trust, Mehsana and affiliated with Hemchandracharya North Gujarat University, Patan. The college has been chosen as CPE by UGC. The green and clean campus is situated in the heart of the city . Institute run UG and PG courses in Arts & Science faculties. Science faculty offered Chemistry, Physics, Mathematics, Botany, Biotechnology courses. The aim of this institute is to spread the spirit of education in the field of intellectual, moral, physical, industrial, commercial, arts, law and agricultural and related activities. Consequently the objective is to start and manage institutions of higher education.

## About Collaborating College

Sheth M. N. Science College was started in 1959 and is managed by North Gujarat Education Society, Mumbai and affiliated with Hemchandracharya North Gujarat University, Patan. The college has been chosen as CPE by UGC. The institute offered Chemistry, Physics, Mathematics, Botany, Zoology courses. College has excellent infrastructure and congenital environment, which provides students a platform to exhibit their potentiality in the field of higher education. The institute boasts of big classrooms, well equipped laboratories, prosperous library, huge sports campus, well designed botanical garden, and highly qualified & well experienced faculty members

# International Journal of Research in Modern Engineering and Emerging Technology
# (IJRMEET)

## VOL. 5, SP. ISSUE 9, SEPTEMBER, 2017

| SR. NO. | CONTENTS | PG. NO. |
|---|---|---|
| 52 | SYNTHESIS AND CHARACTERIZATION OF PURE AND MG DOPED ZNO THIN FILMS AND NANORODS<br>KAUSHAL V. KADIYA | 406-412 |
| 53 | INFRARED SPECTRA OF TERNARY COMPLEXES USING BENZIDINE AND QUINOLINE AS DONORS<br>ASHOK N. PATEL ET AL. | 413-428 |
| 54 | GROWTH CHARACTERIZATION AND STUDIES OF SOME MIXED TARTRATE SINGLE CRYSTAL<br>SANJAY B.KANSARA ET AL. | 429-436 |
| 55 | PREPARATION AND CHARACTERIZATION OF ACTIVATED CARBON PRODUCED FROM AZADIRACHTA INDICA (NEEM LEAF)<br>PARTH JOSHI ET AL. | 437-442 |
| 56 | SYNTHESIS AND CHARACTERISATION OF SOME ACID DYES BASED ON 4, 4'-DIAMINO DIPHENYL AMINE DERIVATIVE AND THEIR APPLICATION ON VARIOUS FIBRES<br>YOGESH S. PATEL ET AL. | 443-451 |
| 57 | A COMPARATIVE STUDY ON PHOTOCATALYTIC ACTIVITY OF ZNO, ZNS AND THEIR COMPOSITE<br>BASANT K. MENARIYA ET AL. | 453-461 |
| 58 | WATER QUALITY STUDY OF GROUNDWATER OF BHABHAR TALUKA (BANASKANTHA DISTRICT, GUJARAT STATE, INDIA)<br>KIRAN V. MEHTA | 462-466 |
| 59 | NOVEL 1,3,4-OXADIAZOLE DERIVATIVES CONTAINING FURAN RING: SYNTHESIS, CHARACTERIZATION, ANTIMICROBIAL ASPECTS<br>DARSHANSINH AJITSINH RAOL ET AL. | 467-476 |
| 60 | STUDY OF THERMODYNAMIC PARAMETERS AND ACTIVATION ENERGY FROM TGA OF SYNTHESIZED NEW TERNARY TRANSITION METAL COMPLEXES<br>DHARA PATEL ET AL. | 477-484 |
| 61 | METHOD DEVELOPMENT AND VALIDATION OF MEBENDAZOLE BY RP HPLC TECHNIQUE<br>AMI PATEL ET AL. | 485-493 |
| 62 | COMPARISON STUDY ABOUT PHYSICO-CHEMICAL ANALYSIS OF GROUND WATER QUALITY OF SELECTED TWO TALUKAS OF MEHSANA DISTRICT. (NORTH GUJARAT).<br>LIMBACHIYA M.C ET AL. | 494-499 |
| 63 | SYNTHESIS, CHARACTERIZATION AND BIOLOGICAL EVALUATION OF SOME AZETIDINONES DERIVATIVES CONTAINING HYDRAZIDE MOEITIES<br>MILANKUMAR ARJUNBHAI SHARDA ET AL. | 500-509 |
| 64 | A STUDY OF SALINITY OF GROUND WATER IN SOME SEMI-ARID TRACTS IN KHERALU TALUKA OF GUJARAT<br>M.R.SOLANKI ET AL. | 510-514 |

# RET ACADEMY FOR INTERNATIONAL JOURNALS OF MULTIDISCIPLINARY RESEARCH (RAIJMR)

Dear Author / Researcher,

I am very thankful to all the Authors and Researcher Scholars on behalf of our RET Academy for International Journals of Multidisciplinary Research **(RAIJMR)** for publishing with us in our Special issue; Vol. 5 Issue 9, Sept. 2017 of **International Journal of Research in Modern Engineering and Emerging Technology (IJRMEET) ISSN: 2320-6589.**

The research work done by the Authors / Research Scholars will prove its high quality for publication of the paper then after it is valid and reliable for publication in our Journal(s). This is the main concern for publication of the paper. Not any type of importance is given to the maintenance charges for publication of the paper.

The prime goal of the academy is to not only to enhance the research work worldwide but also publishes high quality research work on online and International platform. To discover and find out the research problems of education and implementation of their solution on the present scenario of education is the entire aim of all the authors who are publishes their article via this Journal.

I hope and request to all the Authors, Research Scholars, Readers and members of our advisory board that kindly recommend and encourage your colleagues as well as your faculty members for publishing with us.

I am much thankful to all the Dignitaries, Professors, Associate Editors, The Board Members (India & International), Faculty Members, Political Leaders, Social Workers, Supporters, Motivators, Authors, Web developers, Subscriber, Best Complimenters and my Family Members for giving me their fruitful support to release this research work on Wide Area Network via IJRMEET.

Thanks.

**Editor-in-Chief**
 (RAIJMR)
www.raijmr.com
editorraijmr@yahoo.com

# RET ACADEMY FOR INTERNATIONAL JOURNALS OF MULTIDISCIPLINARY RESEARCH (RAIJMR)

## About Us

**RET Academy for International Journals of Multidisciplinary Research (RAIJMR)** is an Intentional academy for International Multidisciplinary Research. Under this title this academy will publish research Journal(s) with different title(s). These all Journal(s) will publish monthly one by one in English language.

The prime aim of the academy is to publish multidisciplinary Journals under the head of RAIJMR and The aim and scope of the Journal is to provide an academic medium and an important reference for the advancement and dissemination of research results that support high-level learning, teaching and research in the fields of Management, Technology, Education, Pharmacy, Humanities, Science, Engineering, Account & Commerce, Social Sciences, Law, etc. The Journal publishes papers, review articles, and short communications dealing with Education, Pharmacy, Management, Engineering, Library Science, Physical Education, Account, Commerce, Arts, Science, Humanities, and Law etc.

RAIJMR would take much care in making your article published without much delay with your kind co-operation. RAIJMR hopes that Researchers, Research scholars, Academician, Industrialists etc. would make use of this research publication for the development of all the discipline. This Academy boasts of hosting four major international Journals under its wings, namely:

(1) **International Journal for Research in Management and Pharmacy (ISSN: 2320-0901)**

(2) **International Journal for Research in Education (ISSN: 2320-091X)**

(3) **International Journal of Research in Modern Engineering and Emerging Technology (ISSN: 2320-6586)**

(4) **International Journal of Research in Humanities and Social Sciences (ISSN: 2320-771X)**

(5) **International Journal of Research in all Subjects in Multi Languages (IJRSML) (ISSN : 2321-2853)**

## Aims and Scopes



# International Journal of Research in in Modern Engineering and Emerging Technology

# (IJRMEET)

IJRMEET "International Journal of Research in Modern Engineering and Emerging Technology" is an online peer reviewed international journal in English published monthly for Scientists, Engineers and Research Scholars involved in Engineering and all other related Engineering Technologies and Science, and related fields to publish high quality and refereed papers monthly under the head of RET Academy for International Journals of Multidisciplinary Research. IJRMEET serves to all practitioners, professionals and clients in the engineering, design and technology sectors. IJRMEET reviews papers within approximately one week of submission and publishes accepted articles on the internet immediately upon receiving the final versions. The aim of IJRMEET is exploring the interface between academic research and practical applications. The entire aim of IJRMEET is to publish peer reviewed researches and review articles fastly without delay in the developing field of engineering science and technology and research science. Manuscripts for publication in IJRMEET are selected through severe peer review to ensure originality, timeliness, relevance, and readability. Original theoretical work and application-based studies, which are contributes to a better understanding of modern engineering, science and technological challenges. The journal publishes research articles and reviews within the whole field of engineering research, and it will continue to provide information on the latest trends and developments in this ever-expanding subjects. The journal also seeks clearly written survey and review articles from experts in the field, to promote insightful understanding of the state-of-the-art and application trends. Original research papers, state-of-the-art reviews and technical notes are invited for publication.

Welcome to Rediffmail × M Inbox - editorraijmr@gm × ✉ (1 unread) - editorraijmr × ✉ Welcome to UGC, New D × ⊕ Welcome to UGC, New D × ⊕ ugc.ac.in/journallist/ugc_ ×

Welcome to Rediffmr — □ ✕

← → C △ ① ugc.ac.in/journallist/ugc_admin_journal_report.aspx?eid=NDcyMDM= ☆ ⬠ ⋮

⠿ Apps □ Digital Gujarat G Google ⧉ RAIJMR ⧬ Dashboard ‹ RAIJMR ✉ Welcome to Rediffma ✦ Facebook ⬛ Mid-Day Meal Y Yahoo ⬓ Google Translate ▥ ISBN free barcode g » □ Other bookmarks

# UGC Journal Details

| | |
|---|---|
| **Name of the Journal :** | International Journal of Research in Modern Engineering and Emerging Technology |
| **ISSN Number :** | 23206586 |
| **e-ISSN Number :** | |
| **Source:** | UNIV |
| **Subject:** | Chemical Engineering(all);Engineering(all) |
| **Publisher:** | RUDRA PUBLICATION |
| **Country of Publication:** | India |
| **Broad Subject Category:** | Science |

Print

|| Home ||

# UGC Approved List of Journals

Home   About Us   Organization   Commission   Universities   Colleges   Publications

You searched for **23206586**

**Total Journals : 1**

Show 25 ▾ entries

Search:

| View | Sl.No. | Journal No | Title | Publisher | ISSN | E-ISSN |
|------|--------|-----------|-------|-----------|------|--------|
| View | 1 | 47203 | International Journal of Research in Modern Engineering and Emerging Technology | RUDRA PUBLICATION | 23206586 | |

Showing 1 to 1 of 1 entries

Previous  1  Next

**For Students**

About NET   UGC NET Online
Ragging Related Circulars
Fake Universities   Educational Loan

**For Faculty**

Honours and Awards   UGC Regulations
Pay Related Orders   M R P

**More**

Notices   Circulars   Tenders   Jobs
UGC ROs   Right to Information Act
Other Higher Education Links

# An Introduction of Arduino and Its Pharmaceutical Application

Joshi Nisarg Chandrakant
Assistant Professor
Ratnamani Science College, Becharaji
nj18716@gmail.com

*Abstract-*

*This paper is representing information about ARDUINO. In This paper we get some information about Arduino like type of Arduino boards, hardware, and software. Arduino has many applications as per example Arduino Satellite (Ardusat), ArduPilot (ArduPilotMega-APM), Lilypad Arduino. Here I explore its Pharmaceutical Application. How to use Arduino in Pharmaceutical field that can be introducing in this paper. The Arduino board can gave a fast processing and easy interfacing. So, the Pharmaceutical Tablets Counting and Monitoring system will established by using Arduino.*

*Index terms-* Arduino, Hardware, Software, Microcontroller based PTCMS

*Introduction-*

Arduino is an open source microcontroller which can be easily programmed, erased and reprogrammed at any instant of time. Introduced in 2005 the Arduino platform was designed to provide an inexpensive and easy way for hobbyists, students and professionals to create devices that interact with their environment using sensors and actuators. Based on simple microcontroller boards, it is an open source computing platform that is used for constructing and programming electronic devices. It is also capable of acting as a mini computer just like other microcontrollers by taking inputs and controlling the outputs for a variety of electronics devices.

The Pharmaceutical Tablets Counting and Monitoring System (PTCMS) is the type of the IR feedback control system. It is one of requirement machine of the tablet medicine factory. It is the Brushed DC motor based controlled by the micro controller control method. The IR sensor is used for the capture of the tablet passing in the key way. Software is developed in C language is using micro-C programming. The LCD module is used to display the counting

number of the tablet by rotary plate. The infrared Sensor is received the IR ray by IR LED. The IR LED generated the IR ray by PWM function of the controller. If the Sensor received the IR ray, the output TTL signal of the sensor is 0. If the sensor not received the IR ray, the output of the sensor is 1. When the tablet is passing through the key way, the tablet is passed between the IR sensors. So the IR ray is block to IR sensor. The controller is captured this state output of IR sensor and display on LCD by character number. This machine is used in many tablet factories in usefully.

### *Types of ARDUINO-*

Arduino boards are available with many different types of built-in modules in it. Boards such as Arduino BT come with a built-in Bluetooth module, for wireless communication. These built-in modules can also be available separately which can then be interfaced (mounted) to it. These modules are known as Shield. Some of the most commonly used Shields are:

- **Arduino Ethernet shield:** It that allows an Arduino board to connect to the internet using the Ethernet library and to read and write an SD card using the SD library.
- **Arduino Wireless shield:** It allows your Arduino board to communicate wirelessly using Zigbee.
- **Arduino Motor Driver Shield:** It allows your Arduino boards to interface with driver of a motor etc.
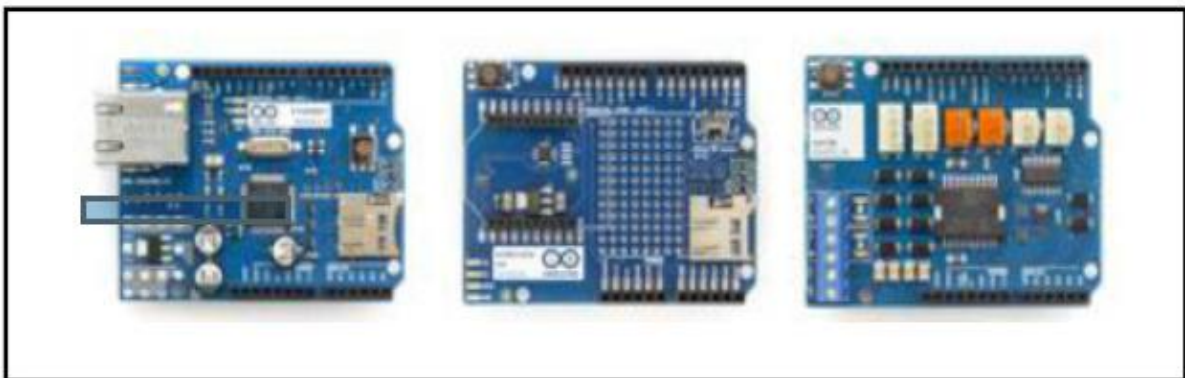


Fig.1. Arduino Shields- Ethernet, Wireless and Motor Driver

Here is a list of the different types of Arduino Boards available along with its microcontroller type, Crystal frequency and availabilities of auto reset facility:

| Arduino Type | Microcontroller | Clock Speed |
|---|---|---|
| Arduino Uno | ATmega328 | 16 MHz with auto-reset |
| Arduino Duemilanove / ATmega328 | ATmega328 | 16 MHz with auto-reset |
| Arduino Nano | ATmega328 | 16 MHz with auto-reset |
| Arduino Mega 2560 or Mega ADK | ATmega2560 | 16 MHz with auto-reset |
| Arduino Leonardo | ATmega32u4 | 16 MHz with auto-reset |
| Arduino Mini w/ ATmega328 | ATmega328 | 16 MHz with auto-reset |
| Arduino Ethernet | Equivalent to Arduino UNO with an Ethernet shield | |
| Arduino Fio. | ATmega328 | 8 MHz with auto-reset |
| Arduino BT w/ ATmega328 | ATmega328 | 16 MHz with auto-reset |
| LilyPad Arduino w/ ATmega328 | ATmega328 | 8 MHz (3.3V) with auto-reset |
| Arduino Pro or Pro Mini | ATmega328 | 16 MHz with auto-reset |
| Arduino NG | ATmega8 | 16 MHz with auto-reset |

Table-1 Types of ARDUINO

*Hardware-*

The Arduino Development Board consists of many components that together make it work. Here are some of those main component blocks that help in its functioning:

- **Microcontroller:** This is the heart of the development board, which works as a mini computer and can receive as well as send information or command to the peripheral devices connected to it. The microcontroller used differs from board to board; it also has its own various specifications.

- **External Power Supply:** This power supply is used to power the Arduino development board with a regulated voltage ranging from 9 – 12 volts.

- **USB plug:** This plug is a very important port in this board. It is used to upload (burn) a program to the microcontroller using a USB cable. It also has a regulated power of 5V which also powers the Arduino board in cases when the External Power Supply is absent.

- **Internal Programmer:** The developed software code can be uploaded to the microcontroller via USB port, without an external programmer.

- **Reset button:** This button is present on the board and can be used to resets the Arduino microcontroller.

- **Analog Pins:** There are some analog input pins ranging from A0 – A7 *(typical)*. These pins are used for the analog input / output. The no. of analog pins also varies from board to board.

➢ **Digital I/O Pins:** There are some digital input pins also ranging from 2 to *16 (typical)*. These pins are used for the digital input / output. The no. of these digital pins also varies from board to board.

➢ **Power and GND Pins:** There are pins on the development board that provide 3.3, 5 volts and ground through them.

*Software-*

The program code written for Arduino is known as a sketch. The software used for developing such sketches for an Arduino is commonly known as the Arduino IDE. This IDE contains the following parts in it:

1) **Text editor:** This is where the simplified code can be written using a simplified version of C++ programming language.

2) **Message area:** It displays error and also gives a feedback on saving and exporting the code.

3) **Text:** The console displays text output by the Arduino environment including complete error messages and other information.

4) **Console Toolbar:** This toolbar contains various buttons like Verify, Upload, New, Open, Save and Serial Monitor. On the bottom right hand corner of the window there displays the Development Board and the Serial Port in use.

*Micro Controller based PTCMS-*

The circuit diagram of the tablet counting machine is composed by five parts. They are key pad, micro controller PIC16F877A, 16×2 LCD and DC motor with relay driver circuit. The key pad is used for data input to PIC and LCD is the display output of the system. The required amount of tablet is type by keypad. The keypad has the digit number 0-9, A, B, C, D and character value *, #. The char * button is used to accept the number of tablets and # button is for clear the numbers of tablet. The digit 0-9 buttons are used for required amount of tablets. The char A-D is non-operation. The welcome screen and amount of tablets is shown in LCD. The PIC controller is start to drive the DC motors (counting and vibration motor) at the button * is pushed. The IR sensor is used for crossing of tablets. If the one tablet is across the IR sensor, the sensor sends the digital data 0 to micro-controller.
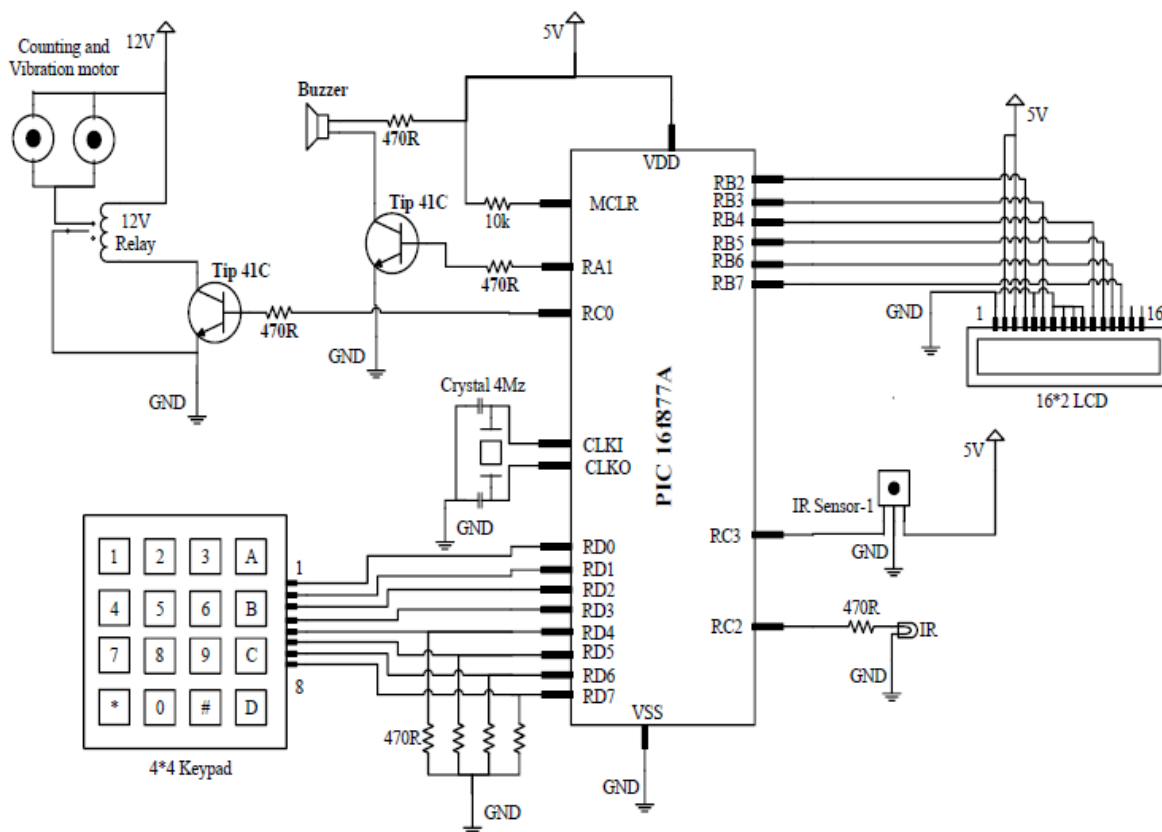
Fig.2. Microcontroller based PTCMS

## Conclusion-

ARDUINO is an open source microcontroller. It can be easily programmed. So it is convenient to generate more than tablets in small time period. And save man power, time and create fully automatic Pharmaceutical Tablets Counting and Monitoring System-PTCMS. The manufacturing and costing of this system is cheap as compare to market available system.

## Acknowledgements-

## References-

[1] ARDUINO.CC, "Arduino – Introduction", 2015 [Online]

Available: http://arduino.cc/en/Guide/Introduction. [Accessed: 25- Feb - 2015].

[2] Arduino.cc, 'Arduino - Products', 2015. [Online].

Available: http://arduino.cc/en/Main/Products. [Accessed: 25- Feb- 2015].

[3] ArduPilot Mega, 'ArduPilot Mega', 2015. [Online].

Available: http://www.ardupilot.co.uk/. [Accessed: 23- Nov- 2015].

[4] Wikipedia, 'ArduSat', 2015. [Online].

Available: http://en.wikipedia.org/wiki/ArduSat. [Accessed: 23- FEB- 2015].

[5] Kickstarter, 'ArduSat - Your Arduino Experiment in Space', 2015. [Online].

Available:https://www.kickstarter.com/projects/575960623/ardusat-your-arduino-experiment-in-space.[Accessed: 23- Feb- 2015].

[6] DIY Space Exploration, 'Ardusat - Your Personal Satellite Built on Arduino', 2013.

Available: http://www.diyspaceexploration.com/ardusat-your-personal-satellite.

[Accessed: 13- Sep- 2015].

[7] A "An Efficiency Analysis of the Kirby Lester KL16df Automatic Tablet and Capsule CountingSystem"(http://thethomsengroup.com/TTGI%20Pages/Articles%20Studies%20&%20Presentations/ThomsenGroup%20KL%20Study%202004.pdf).

Pharmacy Automation. The Thomsen Group Inc. 2004.Retrieved 5 March 2010

[8] A "Labels, patient information leaflets and packaging for medicines" (http://www.mhra.gov.uk/Howweregulate/Medicines/Labelspatientinfomationleafletsandpackaging/index.htm). The Medicines and Healthcare products Regulatory Agency (MHRA). 2010. Retrieved 8 March 2010

[9] A Lagrange F: [Current perspectives on the repackaging and stability of solid oral doses]. AnnPharmFr;2010Nov;68(6):332-58

http://www.sciencedirect.com/science/article/pii/S0003450910001331

[10] Lander, Cyril W. (1993). "8 D.C. Machine Control". Power Electronics (3rd ed.). London: McGraw Hill International UK. ISBN 0-07-707714-8

# Experimental Performance analysis of Evacuated tubes coupled Double basin solar still with pin fin

**Hitesh Panchal**
Assistant Professor, Government Engineering College, Patan, Gujarat, India.
Email :Engineerhitesh2000@gmail.com

**Abstract**
During early morning, lower intensity radiation never passed through glass cover properly, hence the temperature of inner glass cover temperaure remains higher compred with water temperature, hence the distillate ouptut is lower. If preheating of water is carried out then distillate output of the solar still. Hence, the main aim of this resarch work to carry out performance analysis of Evacuated tubes coupled double basin solar still in climate conditions of Patan, Gujarat annually. From the one year research work, it has found 34.3% increment with use of pin fin compared with alone. At last, comparison has been made with other researchers work and it has been found 300% enhancment in distillate output compared with conventional solar still by considering 3 kg average distillate output from conventional solar still.

**Keywords**—Evacuated tubes,distillate output,double basinSolar still, fin

**Introduction:**
A simple way of distilling water is by evaporation and condensation method. In solar still, the water is evaporated using solar energy. In solar still, impure water is taken in a well-insulated air tight basin covered with transparent plastic/glass cover. Practically, solar still is termed as passive solar still. When the cover is exposed to sun, radiation energy is transmitted through transparent cover, falls in the basin, absorbed by the basin absorber plate, converted into heat and transferred to water. The water gets heated up, transfer heat to air inside the still and the air become unsaturated. The water evaporates and makes the air inside still saturated. This air is subjected circulatory motion due to the temperature difference between water surface and cover lower surface. When high temperature air touches the cover, becomes cool and the water present in the air condenses at the lower surface of the cover. This condensed water slides down and is collected using a drain.

The transparent cover receives and transmits radiation into the still. Likewise, the condensation takes place along its lower surface. Also, it should suppress thermal radiation in the atmosphere. Glass is the best material to cover (**Duffie et al. [1]** since it has higher transmittance and less reflectivity. Also glass is opaque to thermal radiation. For higher latitude places, single slope still is preferable, and for northern Chemosphere the still faces south (**Fath et al. [2]**. The inclination of the cover is optimized to collect the accumulated condensate through drain before it drops down to the basin. The condensate mass accumulation depends on solar intensity and condensation rate. They also conducted indoor simulation experiments and found that the production rate is higher for 30° cover inclination. Glass temperature affects the condensation rate at its lower surface. Lower glass surface temperature increases the circulation of air inside the still which enhances convective and evaporative heat transfer between basin water and glass. Also, cooler glass lower surface increases condensation. The glass cover temperature is reduced by continuous flow (**Abu-Hijleh [3]** or intermittent flow (Tiwari and Madhuri, 1985) of raw cooling water on the cover. The cooling water gains latent heat from condensing water and regenerates it in the basin. The

second effect of evaporation and condensation takes place between the covers as shown in. **Bassam A/K Abu-Hijleh et al. [4]** result shows increase in production by 20%. Yousef and **Mousa Abu-Arabi [5]** results also show that, the use of the film-cooling increases the still efficiency up to 20%. Lawrence et al. (1989) had carried out research work on varying mass flow rate of water of upper side of glass cover to see its effect on distillate output and efficiency of solar still. They found that, enhancement of distillate output and efficiency was 9% and 5%, respectively, when the mass flow rate was 1.5 m/s. Wind velocity is also having its effect on the temperature of the glass. At higher wind velocity, due to higher convection heat transfer from the glass to atmosphere the productivity of the still is increasing (**Yousef et al., 2004 and El-Sebaii [6] Tiwari and Rao** [7] theoretically analyzed the effect of water flowing over the glass cover in a single basin still. The result shows the productivity is increased with flowing water over the glass cover. Also, the yield decrease when the water flow rate increases. **Pr. K. Abdenacer and S. Nafila [8]** had conducted lots of experiments on passive and active solar still based on water temperature and efficiency and found that, the active solar still always increased distillate output compared with passive solar still. **Sebaii et al., [9]** had fabricated passive solar still to find the optimum glass cover inclination. They performed studies to see best glass cover inclination during winter and summer. It was found that the optimum glass cover inclination was 33.3° N (Latitude of the place) for both summer and winter. **M.K. Phadatare, S.K**. **Verma, [10]** had evaluated the performance of a solar still with 4 mm plexiglass as a cover material to see the effect on the internal heat transfer coefficient and distillate output by varying the depth of brine. They found that, plexiglass of 4 mm thickness found an enhancement of distillate output by 2 cm brine thickness.

**Karuppusamy [11]** had conducted several experiments on single basin solar still coupled with evacuated tubes in climate conditions of Chennai to see effect of increase in water temperature on distillate output of solar still. He took 0.03 m depth of water inside solar still and tested for one year and found that, the distillate output increased by more than 100% compared with conventional solar still.**Shobha et al.[12]**had conducted simple experiment on single basin solar still coupled with evacuated tubes with help of pipes. They conducted solar still with evacuated tubes to see effect on distillate output. They found 110% increment in distillate output.**Rahul dev and G N Tiwari [13]**had carried out several experiments on single basin solar still coupled with evacuated tubes in climate conditions of New Delhi,India. They also conducted theoretical analysis to see the difference between experimental and theoretical analysis and found good agreement in terms of coefficient of correlation. **J. Xiong et al. [14]**fabricated and tested innovative design of single basin solar still coupled with evacuated tubes. They used stacked tray in the solar still in such a way that the latent heat of condensation can be utilized properly and found increment in distillate output. **Deniz [15]** had conducted research work on single basin solar still with various energy absorbing materials and tested in climate conditions of Oman. He also carried out theoretical analysis and compared with experimental results and found good agreement between them.Patan is a best place for research work on solar energy appliances, due to the higher amount of solar radiations. Hence it is a best place for research work on solar energy applications.**[16-37].**

Literature review exhibited that the solar still is a very important device to convert available brackish water into drinkable water by use of solar energy. Many of the researchers have worked on it for increment in distillate output. For increment in distillate output, evacuated tubes are generally used. But the main problem of loss of latent heat of condensation remains unsolved in solar still when it coupled with evacuated tubes. Hence, in this present research paper, work has done on evacuated tubes coupled double basin solar still for usage of loss of latent heat of condensation. Also, fins have not used by the researchers for increment in surface area. Hence, main aim of this present work is to fabricate evacuated tubes coupled double basin solar still with pin fin for increment in distillate output.

**Experimental set up:**
Fig.1 shows the experimental testing set up made by locally available materials in market of Patan, Gujarat. Fig.2 shows the pin fin used in present experiment. Present experimental set up consists of 1 meter square cross sectional area. It used two glass cover for top and bottom basin. Bottom basin contains attachment of evacuated tubes with help of holes. The main use of direct attachment of evacuated tubes that, the heat loss from the evacuated tubes to pipe is reduced. Upper basin attached with lower basin with help of glass cover. Dimensions of lower and upper basin are 1006 mm *1000 mm *500 mm. The fin size of 3 cm used in present experiment. All the experiments have conducted at clear sky conditions with constant water depth of 0.03 cm during January 2016 to December 2016.
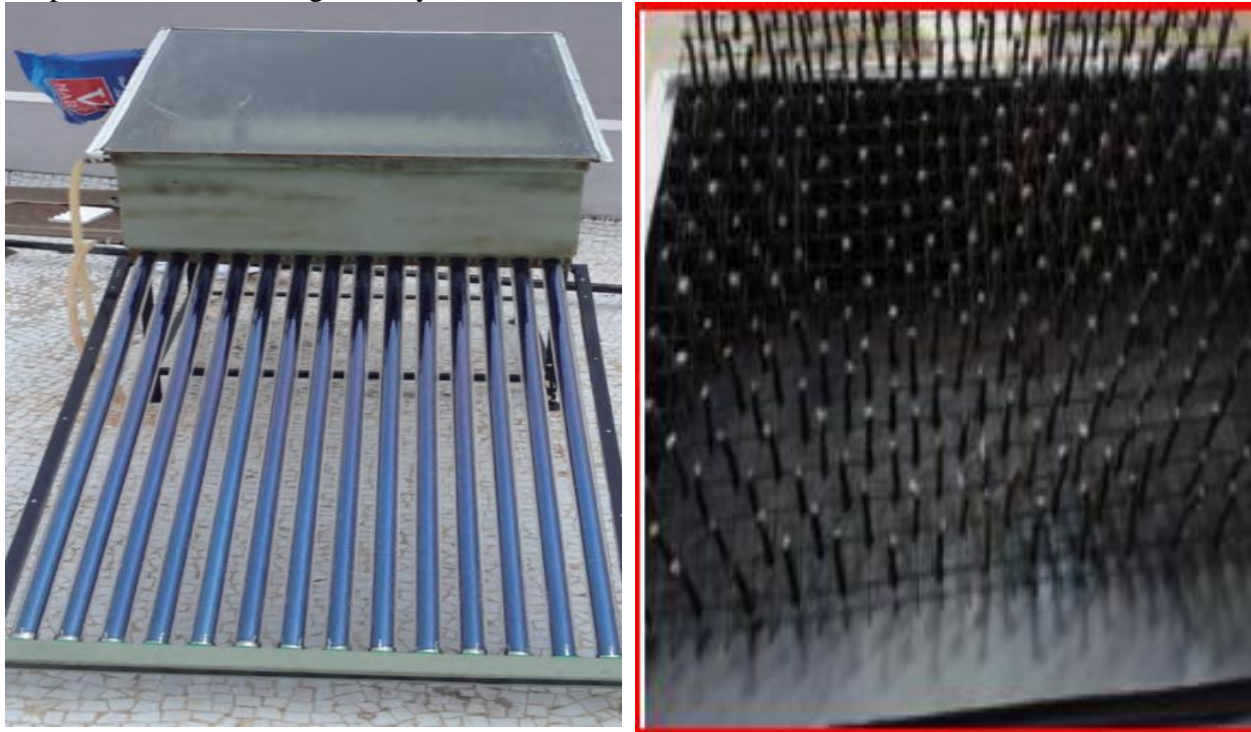


**Fig.1 Experimental set up of double basin solar still with evacuated tubes**



**Fig.2 pin fin arrangement provided in solar still**

**Result and Discussion:**
Generally in all solar energy research work the output depends on amount of solar energy incident on it. Also, the solar radiations increased from morning to noon and then start reducing due to movement of sun towards the south. Fig. 3 shows comparison between the water circulation inside solar still from evacuated tubes. It has found that, the increment in solar intensity increased the radiation incident on evacuated tubes for increment in natural circulation towards the solar still.

Fig. 4 shows that the hourly variations of solar intensity and ambient temperature on 10th May and 10th January. 2015. It exhibits that, solar radiation upsurgestill it influences its supreme value at mid-day, then it fall again. This curve is detected in both summer and winter investigational days. The highest recorded value of solar intensities was 980 and 960 W/m2 and 600 and 620 W/m2 for vacuum tubes and solar still during 10th May and 10th January 2015. The maximum ambient temperature is originateapproximately 36 °C and 24 °C during 10th May and 10th January, 2015
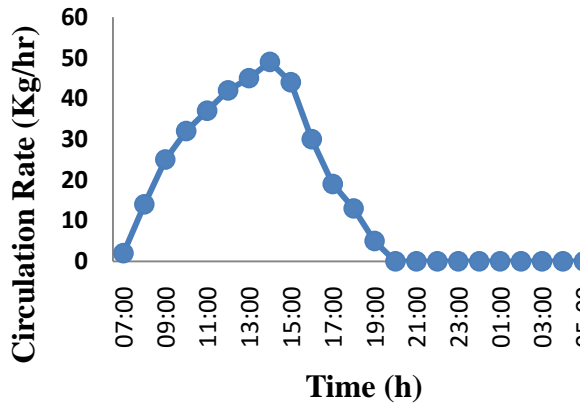
**Fig.3 Hourly circulation of water inside the vacuum tubes**
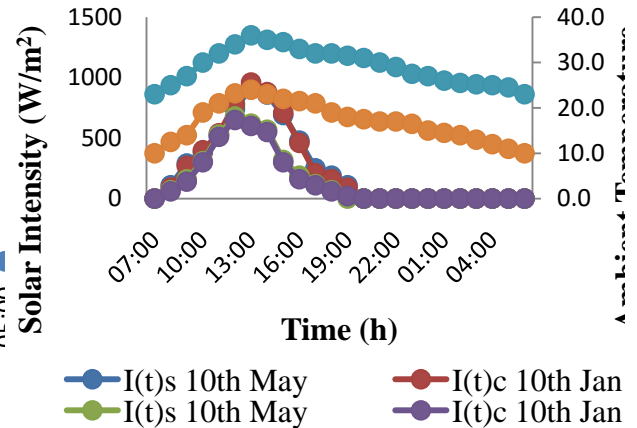


**Fig. 4 Hourly variation of solar intensity and ambient temperature for DBSWVT during summer experimental days**
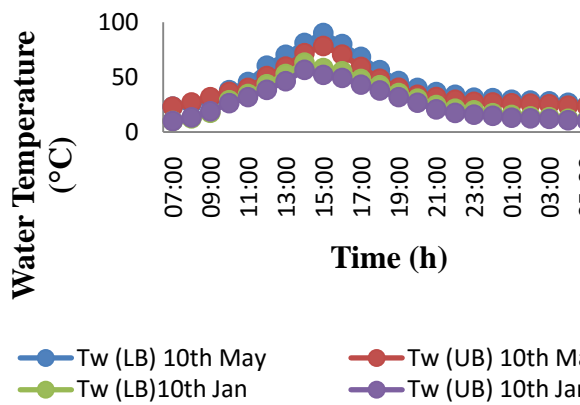


**Fig. 5 Temperature of water in upper and lower basin without use of fins.**
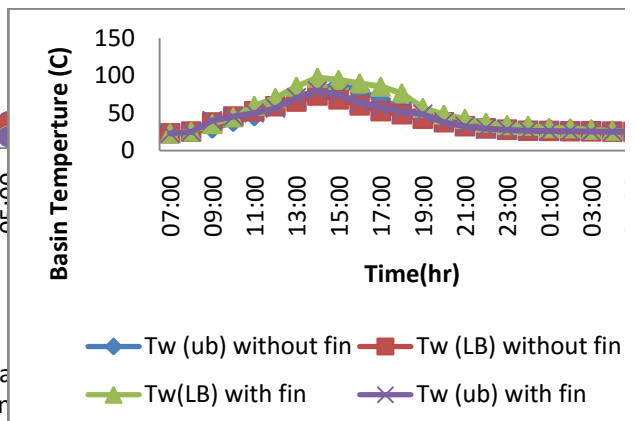


**Fig. 6 Temperature of water in double basin evacuated tubes coupled solar still with and without fins**
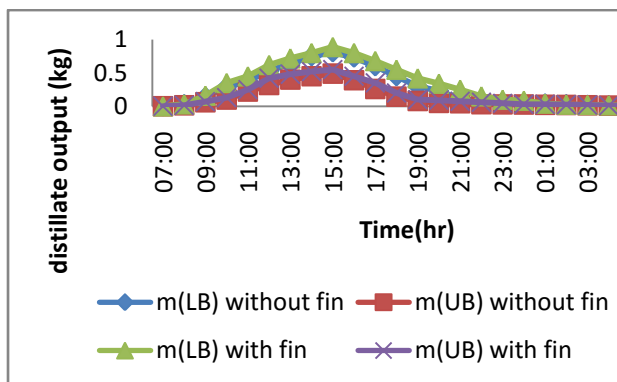


**Fig. 7 Distillate output received from evacuated tubes coupled solar still with and without use of fins**
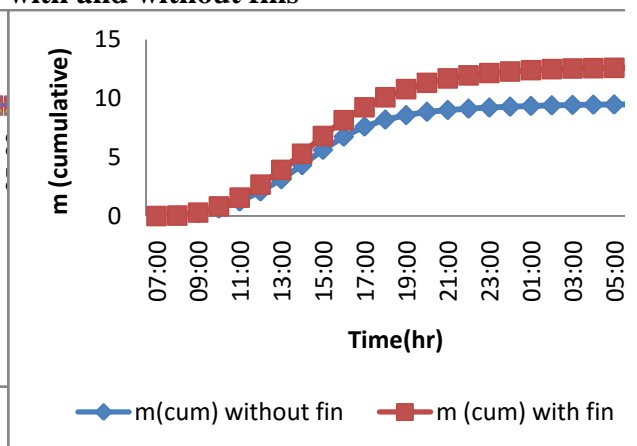


**Fig. 8 cumulative output received from evacuated tubes coupled solar still with and without use of fins**

Fig. 5demonstratesthe difference of water temperatures of lower and upper basin during summer and winter experimental days of 10th May and 10thJanuary, 2015. It is shown that, maximum temperature of water inside the upper and lower basin remains higher during the summer experimental day compared with winter experimental day due to higher solar radiation and ambient temperature of the location. It is also shown that, water temperature increased during the day until it reaches its maximum value at 15:00 pm and then reduced slowly during summer experimental day and winter experimental day found maximum value at 14:00 pm and then reduced drastically compared with summer experimental day. The reason is the volumetric heat capacity of water inside lower and upper basin is responsible for the slow and drastic reduction in water temperature. Water temperature reaches its maximum value was 90.2 °C and 78.4 °C during summer experimental day and 63.2°C and 56.7°C. Climate condition always affects the temperature gained by passive solar still during summer and winter experimental day, hence summer and winter experimental day, maximum temperature achieved at 15:00 pm and 14:00 pm. It is also observed that, the lower basin water temperature remains high throughout the day during summer and winter experimental day, due to augmentation of vacuum tubes. During winter experimental day, temperature is found more than 60 °C during 14:00 pm. Generally, water temperature of passive solar still remains lower during winter, but here lower basin removes excess heat to the upper basin, hence water temperature remains higher during peak hours. It is a main benefit found in this arrangement.

Fin attachment at lower and upper basin found more productive as shown in Fig. 6. Fin has characteristic of having incremeed in heat transfer due to the enhancement of area. Also, they are porous, hence, it does not only increment the water temperature during daytime but also during the off-sunshine hours. Fig. 6, it is clearly shown that the temperature of water reaches to 97 degree celcius and it remains about 90 during two continuous hours.

Fig. 7 signifies the distillate output received by solar still with and without attachment of fins. It is found that the fins enlarged the superficial area of water; hence due to the raise in water temperature, its distillate output was improved. Extreme distillate output received was utpo 0.90 kg during 3 pm. Fins have shown remarkable effect during off-sunshine hours as expected. Attachment of fins increased the distillate output not only for the lower basin but also from the upper basin.Fig. 8 shows cumulative distillate output gained by evacuated tubes coupled solar still with and without use of fins. It has found that, the solar still with fins gained 12.61 kg distillate output and without fins gained 9.5 kg. Hence, the increment of 32.75% distillate output compared with alone solar still. The reason behind increment in distillate output was due to the increment in surface area of water. Fig. 9 shows yearly comparative analysis of solar still with and without use of fins. It has found that, the average distillate output of solar still without use of fins found 9.12 kg and with fins 12.25 kg. Hence, average yearly increment in distillate output of 34.3% found in solar still with use of fins.
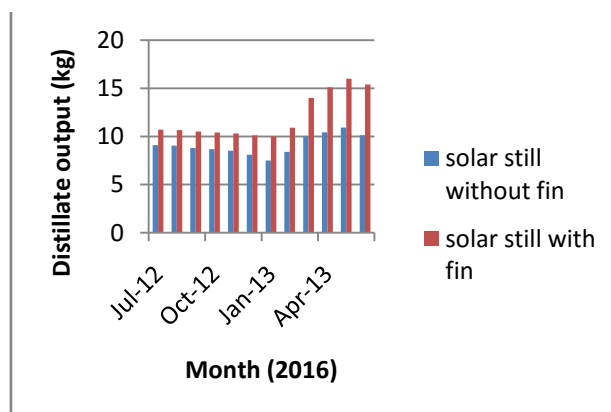


**Fig. 9 comparison of solar still with and without use of fin**

Table 1 shows the comparison of other researchers work with present research. It has found that, the present work found 300% increment in distillate output compared with conventional solar still.

**Table 1: Comparison with other researchers work with present work**

| Sr. No. | Name of Researcher | Type of attachment with passive solar still | Increase in distillate output (%) |
|---|---|---|---|
| 1 | Dev and Tiwari, (2012) | Evacuated tube collector coupled with passive solar still | 32% |
| 2 | SampathkumarKaruppusamy (2012) | Evacuated tube collector with granite gravel | 59.78% |
| 3 | Xiong. et al. (2013) | Multi-effect passive solar still integrated with evacuated tubes and corrugated sheet | 90% |
| 4 | Z. M. Omara et al. (2013) | Evacuated tubes with wick materials | 108% |
| 5 | Present work | Double basin solar still with evacuated tubes and fins | 300% |

**Conclusion:**

From the above research works following points were concluded:

- Evacuated tubes coupled double basin solar still was a better solar still for converting available brackish water into drinkable water by use of solar energy.

- Attachment of fins with coupled double basin solar still found above 30% increment in distillate output compared with without attachment of fin in same still.

- Annual distillate output of evacuated tubes coupled solar still with pin fin found 34.3% increment compared with without fin attachment.

- Evacuated tubes coupled double basin solar still with pin fin found 300% increment in distillate output compared with conventional solar still.

**Acknowledgement:**

**References:**

1. Duffie and Backman.,  Solar Engineering of Thermal Processes, 2[nd]edi,, Wiley Publication, USA, 1985.
2. Fath Hassan E.S., andHosny H.M., Thermal performance of a single-sloped basin still with an inherent built-in additional condenser, Desalination, 142, 19-27, 2005.

3. Bassam A, K., Abu-Hijileh., and Rababa'hHimzeh M., Experimental study of a solar still with sponge cubes in basin', EnergyCoversion and Management , 44. 677-688, 2003.

4. Bassam A, K., Abu-Hijileh., Himzeh M Rababa'h., Experimental analysis of solar still with different materials, Energy Coversion and Management, 33, 1411-1418, 2006.

5. Zurigat, Yousef H., and Abu-Arabi, Mousa K., Modelling and performance analysis of a regenerative solar desalination unit, Applied Thermal Engineering, 24, 1061-1077,2004.

6. Panchal,H,M., Shah P.K., Effect of varying glass cover thickness on performance of solar still : In a winter climate conditions, International Journal of Renewable Energy Research, 1, 212-223, 2014.

7. Zurigat, Yousef H., and Abu Arabi Mpisa K., Modellling and performance analysis of a regenerative desalination unit, Applied Thermal Engineering, 24, 1061–1072, 2004.

8. Bapeshwararao, V.S.V., Singh, U., Tiwari, G.N., Transient analysis of double basin solar still, Energy conversion and Management, 23,83-90,1983.

9. El-Sebaii A.A., Aboul-Enein.s, Ramadan M.R.I, El-Bialy,E., Year-round performance of a modified single-basin solar still with mica plate as a suspended absorber, Energy, 25, 35-49, 2000.

10. Abdenacer, Kaabi Pr., and Nafia, Smakadji., (2007), Impact of temperature difference (water-solar collector) on solar-still global efficiency, Desalination, 209, 298-305,2007.

11. Abderachid Trad., and AbdenacerKaabi., Effect of orientation on the performance of a symmetric solar still with a double effect solar still (comparison study), Desalination, 329, 68–77, 2013.

12. PhadatareM,K., and Verma S.K., Influence of water depth on internal heat and mass transfer in a plastic solar still, Desalination,203, 267–275, 2007.

13. Karuppusamy, Sampthkumar., An Experimental study on single basin solar still augmented with evacuated tubes, Thermal Science, 16, 573-581, 2010.

14. Shobha. B. S., Vilas,Watwe ., Rajesh A. M., Performance Evaluation of A Solar Still Coupled to an Evacuated Tube Collector type Solar Water Heater, International Journal of Innovations in Engineering and Technology, 1, 456-460, 2012.

15. Jianyin, Xiong, Guo Xie, Hongfei Zheng., Experimental and numerical study on a new multi-effect solar still with enhanced condensation surface, Energy Conversion and Management, 73,176–185,2013.

16. Panchal, Hitesh. 2010. "Experimental Analysis of Different Absorber Plates onPerformance of Double Slope Solar Still."International Journal of EngineeringScience and Technology 2 (11): 6626–6629.

17. Panchal, Hitesh. 2011. "Experimental Investigation of Varying ParametersAffecting on Double Slope Single Basin Solar Still." International Journalof Advances in Engineering Sciences 2 (1): 17–21.

18. Panchal, Hitesh. 2016a. "Performance Investigation on Variations of GlassCover Thickness on Solar Still: Experimental and Theoretical Analysis."Technology and Economics of Smart Grids and Sustainable Energy 1(4):1–7.

19. Panchal, Hitesh. 2016b. "Use of Thermal Energy Storage Materials forEnhancement in Distillate Output of Solar Still: A Review." Renewable andSustainable Energy Reviews 61: 86–96.

20. Panchal, Hitesh, Manish Doshi, Prakash Chavda, and RanvirgiriGoswami.2010. "Effect of Cow Dung Cakes Inside Basin on Heat Transfer Coefficientsand

Productivity of Single Basin Single Slope Solar Still." InternationalJournal of Applied Engineering Research, Dindigul 1 (4): 675–690.

21. Panchal, Hitesh, Manish Doshi, KeyursinhThakor, and Anup Patel. 2011."Experimental Investigation on Coupling Evacuated Glass Tube Collectoron Single Slope Single Basin Solar Still Productivity." International Journalof Mechanical Engineering & Technology 1: 1–9.

22. Panchal, Hitesh, and Indra Mohan. 2017. "Various Methods Applied to SolarStill for Enhancement of Distillate Output." Desalination 415: 76–89.

23. Panchal, Hitesh, and Sanjay Patel. 2016. "Effect of Various Parameters on Augmentationof Distillate Output of Solar Still: A Review." Technology andEconomics of Smart Grids and Sustainable Energy 1(4): 1–8.

24. Panchal, Hitesh, Mitesh I. Patel, Bakul Patel, RanvirgiriGoswami, and ManishDoshi. 2011. "A Comparative Analysis of Single Slope Solar Still Coupledwith Flat Plate Collector and Passive Solar Still." IJRRAS 7 (2): 111–116.

25. Panchal, Hitesh, and Patel Sanjay. 2017. "An Extensive Review on DifferentDesign and Climatic Parameters to Increase Distillate Output of Solar Still."Renewable and Sustainable Energy Reviews 69: 750–758.

26. Panchal, Hitesh, and Pravin Shah. 2011a. "Char Performance Analysis of DifferentEnergy Absorbing Plates on Solar Stills." Iranica Journal of Energy &Environment 2 (4): 297–301.

27. Panchal, Hitesh, and Pravin Shah. 2011b. "Modelling and Verification of SingleSlope Solar Still Using ANSYS-CFX." International Journal of Energy andEnvironment 2 (6): 985–998.

28. Panchal, Hitesh, and Pravin Shah. 2012a. "Effect of Varying Glass CoverThickness on Performance of Solar Still: In a Winter Climate Conditions."International Journal of Renewable Energy Research 1 (4): 212–223.

29. Panchal, Hitesh, and Pravin Shah. 2012b. "Investigation on Solar Stills Having Floating Plates."International Journal of Energy and Environment Engineering3 (1): 1–5.

30. Panchal, Hitesh, and Pravin Shah. 2013a. "Experimental and ANSYS CFD SimulationAnalysis of Hemispherical Solar Still." IIRE International Journal ofmRenewable Energy 8 (1): 1–14.

31. Panchal, Hitesh, and Pravin Shah. 2013b. "Modeling and Verification of HemisphericalSolar Still Using ANSYS CFD." International Journal of Energy andEnvironment 4 (3): 427–440.

32. Panchal, Hitesh, and Pravin Shah. 2013c. "Performance Improvement of SolarStills via Experimental Investigation." International Journal of AdvancedDesign and Manufacturing Technology 5 (5): 19–23.

33. Panchal, Hitesh, and Pravin Shah. 2013d. "Performance Analysis of DoubleBasin Solar Still with Evacuated Tubes." Applied Solar Energy 49 (3):174–179.

34. Panchal, Hitesh, and Pravin Shah. 2014a. "Enhancement of Distillate Outputof Double Basin Solar Still With Vacuum Tubes." Frontiers in Energy 8 (1):101–109.

35. Panchal, Hitesh, and Pravin Shah. 2014b. "Enhancement of Upper Basin DistillateOutput by Attachment of Vacuum Tubes with Double-Basin SolarStill." Desalination and Water Treatment 55 (3): 587–595. doi:10.1080/19443994.2014.913997.

36. Panchal, Hitesh, and Pravin Shah. 2014c. "Improvement of Solar Still Productivityby Energy Absorbing Plates." Journal of Renewable Energy andEnvironment 1 (1): 1–7.

37. Panchal, Hitesh, and Pravin Shah. 2014d. "Investigation on PerformanceAnalysis of Novel Design of Vacuum Tube-Assisted Double Basin SolarStill: An Experimental Approach." International Journal of Ambient Energy 37 (3): 220–226. doi:10.1080/01430750.2014.924435.

# Thermal Analysis of Some Metal Chelates of Nickel and Copper

**K P Patel**

R. R. Mehta College of Science & C. L. Parikh College of commerce, Palanpur
kppatelugati@gmail.com

**Abstract**

In the current manuscript a synthesized metal chelates with the combination of ML2 where characterized by author. Metal chelates where manufactured using Nickel and Copper metal with two ligand combination. The Metal chelates where characterized by Thermal Gravitometric Analysis. Broido method is used to analyze the data obtained form thermogram. The thermogravimetric analyses (TGA) of sample have been carried out by using "Perkin Elmer Pyris-1 TGA" in a slow stream of air. Percentage of losses with cause of losses was discussed at the end of manuscript.

**Key Word**

Metal Chelates, TGA, Thermogram, Weight Loss

**Introduction**

The transition metal represents the filling of the atomic d-electron shell, because the transition metals and their alloys typically have high melting temperature and hardness, their economic importance is immense[1-2]. Salen is the abbreviation for a popular chelating ligand used in coordination chemistry and homogeneous catalysis[3-4]. In 1938, T. Tsumaki reported that the cobalt(II) salen reversibly bound O2, and this finding led to intensive research on cobalt complexes salen and related ligands for the storage and transport of oxygen, i.e. synthetic oxygen carriers[5]. For comparative study of thermal behavior of related polymer or simple molecules, each molecule is analyzed by any one or more of these methods of analysis under identical experimental condition. For example TGA is carried out in air and in oxygen free nitrogen[6-8]. From the results of DTA and TGA, it is possible it note the temperature up to which the material does not lose weight. It is also possible to know the temperature at which material starts decomposing[9-11].

**Experiment**

The thermogravimetric analyses (TGA) of sample have been carried out by using "PERKIN ELMER PYRIS 1 TGA" in a slow stream of air. The boat prepared from platinum foil would hold the sample for analysis. It is properly washed and dried. It was suspended on the quartz rod in the TG balance. The powdered sample (about 5 mg) was placed in the boat. The sample in the boat is covered by a quartz tube in which the flow of air was maintained. The weight of sample was noted on TGA balance. The whole assembly was brought down in the furnace. It was ascertained that the boat was hanging on quartz rod. The experiment was started by the heating the system at a constant rate of 10°C/min. Simultaneously change in the weight was recorded automatically with time (temperature). This will reveal percentage weight loss of material s a function of the time and also of temperature. The experiment was stopped at about 650 °C, when there was no further decrease in weight.

**Result and Discussion**

The thermograms were analyzed to obtain information about percentage weight loss at different temperatures. The results of these analyses are presented in Table 1. Selected themograms are shown in Figures 1 and 2.

**Table – 1: Thermogravimetric analysis of Metal Chelates**

| Crystal | % wt loss at temperature | | | |
|---|---|---|---|---|
| | 250 °C | 300 °C | 350 °C | 400 °C |
| ($Cu^{+2}$) Chelates | 6.2 | 7.8 | 16 | 70 |
| ($Ni^{+2}$) Chelates | 2.8 | 5.3 | 24 | 67 |

The brief account of the thermal behavior of samples in air is given below:

- Each crystals degradation in two steps.
- The degradation of all the crystals start in the temperature Range of 200 to 3500C depending upon the natures of crystals.
- The wt. loss amount in this first stage is in between 4.5 to 7 % this may be due to water molecules associated in to the crystals.

- The second stage of decomposition of all crystals is rapid with the loss of mass about 50%. This is due to "in situ" formation of metal oxide during degradation. Which accelerate the rapid degradation of crystals.
- The last stage of digression cause a mass loss of about 80%. This is due to loss molecular fragments of polymers.
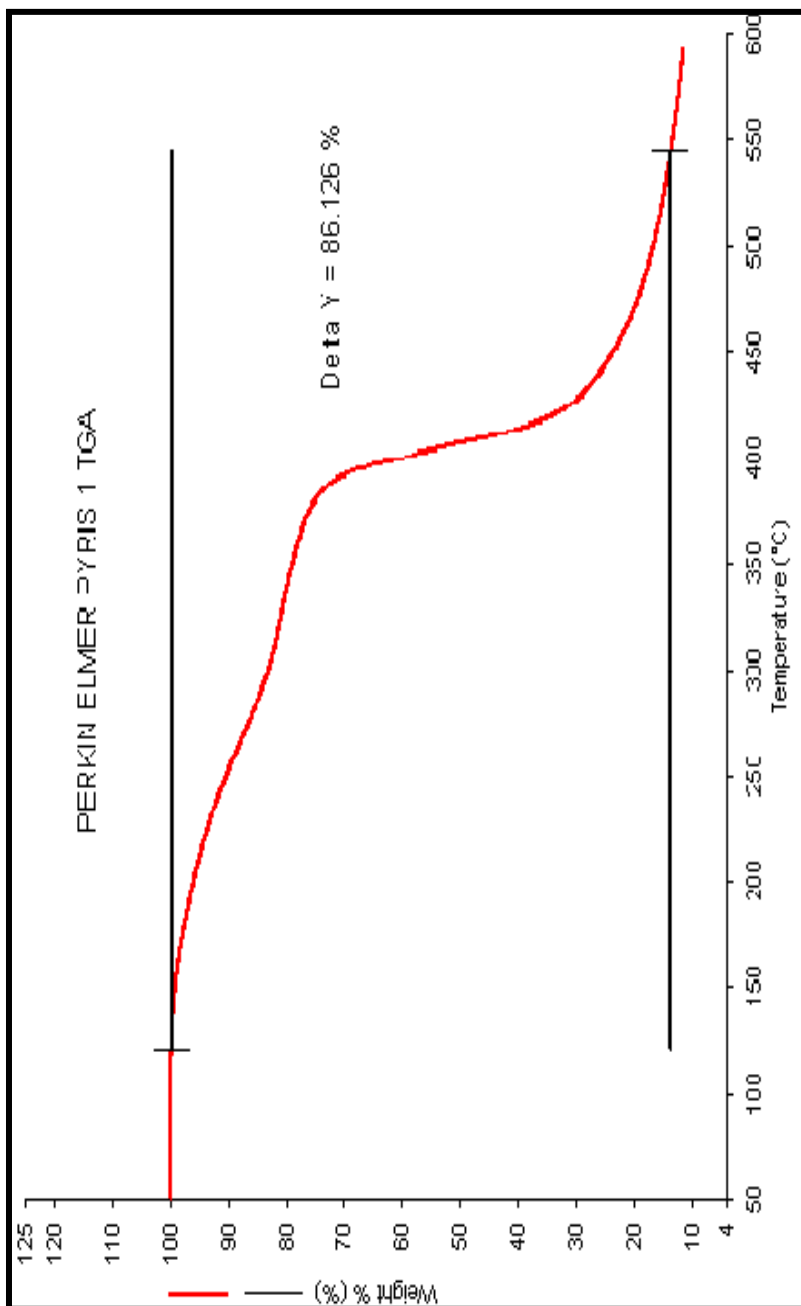


**Figure – 1 TGA Thermogram of Ni(II) Chelates**
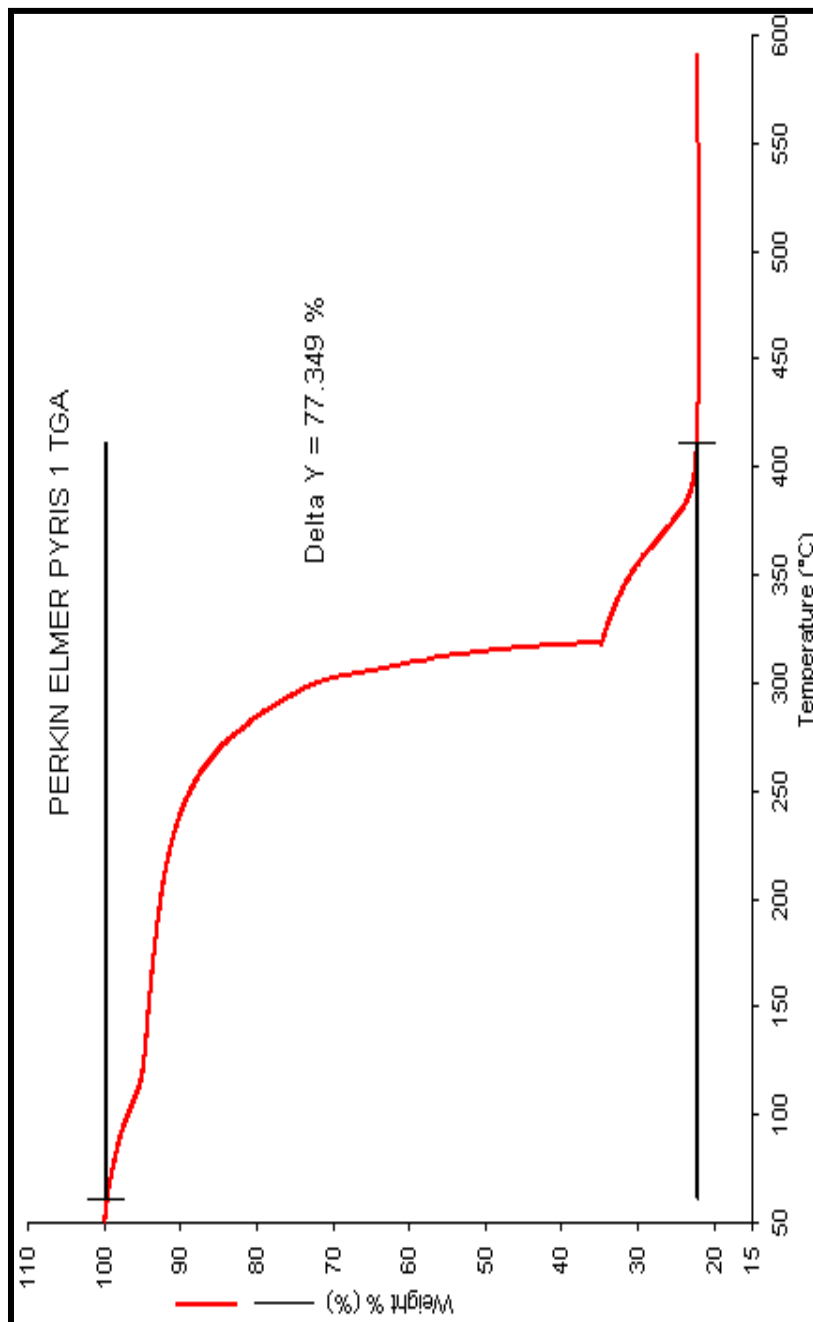
**Figure – 2 TGA Thermogram of Cu(II) Chelates**

**Reference**

1. Jay F. Larrow and Eric N. Jacobsen (2004), "(R,R)-N,N'-Bis(3,5-Di-tert-Butylsalicylidene)-1,2-Cyclohexanediamino Manganese(III) Chloride, A Highly Enantioselective Epoxidation Catalyst", *Org. Synth.*,

2. Zhang, W.; Loebach, J. L.; Wilson, S. R.; Jacobsen, E. N., *J. Am. Chem. Soc.* 1990, *112*, 2801.

3. Irie, R.; Noda, K.; Ito, Y.; Matsumoto, N.; Katsuki, T., *Tetrahedron Lett.* 1990, *31*, 7345.

4. R.M.A. Leith  (Ed.) Preparation and Crystal Growth of Materials with Layered Structures D. Riedel Publication Company, Dordrecht Holland/Boston,  U.S.A. (1977).

5. Tokuichi Tsumaki (1938). "Nebenvalenzringverbindungen. IV. Über einige innerkomplexe Kobaltsalze der Oxyaldimine

6. Charsley, E.L. and Warrington, S.B. Thermal Analysis: Techniques and Application, Royal Society of Chemistry, UK,(1992).

7. Daniels, T.C. Thermal Analysis John Wiley & Sons, NY, (1973).

8. Ferry, J.D. Viscoelastic Properties of Polymers John Wiley & Sons, NY, (1980).

9. Haines, P.J. et al. Thermal Methods of Analysis: Principles, Applications and Problems, Blackie Academic and Professional, England, (1995).

10. Hatakeyama, T. and Quinn, F.X. Thermal Analysis: Fundementals and Applications to Polymer Science, John Wiley & Sons Ltd., England, (1994).

11. Mackenzie, R.C. ed. Differential Thermal Analysis Academic Press, NY, (1970-72)

# Study of GrowthFeaturesand etching on $In_2Se_{3-x}Sb_x$(x= 0.3) Single Crystals

Piyush J. Patel[1,*], Sandip M. Vyas[1], Vimal A. Patel[1], Maunik P. Jani[2] and Girish R. Pandya[3]

[1]Department of Physics, School of Science, Gujarat University, Ahmadabad, Gujarat, India-380009.
[2]Department of Physics, Babaria Institute of Technology, Vagodiya, Vadodara, Gujarat, India
[3]Department of Physics, Faculty of Science, The M.S. University of Baroda, Vadodara-390002, Gujarat, India
*Corresponding author Email: piyush_patel130@yahoo.com;

**Abstract:**

The III-VI compound semiconductors are important for the fabrication of ionizing radiation detectors, solid-state electrodes, and photosensitive heterostructures, solar cell and ionic batteries. In this paper, $In_2Se_{2.7}Sb_{0.3}$ single crystals were grown by the Bridgman method with temperature gradient of 60 °C/cm and the growth velocity 0.35cm/hr. Some interesting features observed on the top free surface of as-grown single crystal were examined under the optical microscope. The study of possible growth mechanism responsible for the appearance of the characteristic growth features is discussed. A new dislocation etchant has been developed by successive trial- error method. The dislocation etchant has been found to give responsible etch-pits on the cleavage surface. Various standard tests for a dislocation etchant have been carried out and the dislocation density calculated by the etch pit count- method and result are reported.

**Keywords**:
Bridgman Method, Shallow Hillock, Parallel Striation, Etching, Scratch Marks and Low Angle Boundary.

**Introduction**

$In_2Se_3$ compound belongs to the group of semiconductor materials with a layered crystal structure. $In_2Se_3$ single crystals can be used for fabrication of ionizing radiation detectors, solid-state electrodes, and photosensitive heterostructures. According to Z.C. Medvedeva, the α-$In_2Se_3$ phase has a hexagonal structure with the unit cell parameters a = 4.0 and c = 19.24 Å[1]. The α- $In_2Se_3$ compound with a layer structure is considered an excellent material applicable to solar cells[2] and the ionic batteries[3] and a number of studies on its electrical and optical properties have been reported[4,5]. It is also known that $In_2Se_3$ single crystals with a stable phase can be grown by introducing impurities during crystal growth [6]. It is well known for pseudo-binary II-VI semiconductors that adjustable band gaps, refractive

indices and lattice parameters, which depend on the relative amounts of chalcogen atoms in the compound, can be obtained. Both factors are important for photovoltaic applications, especially if thin film heterostructures are considered. The need for tailoring band gaps has led us to work in the $In_2$ (Se, Te) $_3$system [7]. Each layer consists of five atomic sheets with atomic structure Se-In-Se-In-Se. These sheets are bound together by strong covalent forces and the Interaction between adjacent layers is much weaker are of Vander Walls type [8]. Indium Selenide ($In_2Se_3$) is one of the important III-VI layered compounds, which has a low density of 2 dangling bonds and is a candidate material for hetero junction formation with a very low density of interface states [9]. The III–VI semiconductors, which crystallize with a layered structure, have been investigated extensively as an example of two-dimensional systems. Indium Selenide ($In_2Se_3$) is a compound semiconductor with a general formula $A_2B_3$ belonging to the hexagonal structure [10]. The ultrahigh-density phase-change memory can be formed by using the difference resistance between various phases of $In_2Se_3$[11, 12]. It also has potential applications in rotary polarisers' optoelectronic device fabrications. Another interesting application of $In_2Se_3$ are solar cells [13] and in phase-change optical recording medium[14].

## Materials and Methods

The Elemental materials Indium, Selenium and Antimony of 99.999 %( 5N) purity, used for the preparation of the alloy. These were weighted to stoichiometric proportion and sealed in a quartz ampoule of0.25 cm in length and 1 cm in diameter under the vacuum of the order of $10^{-5}$ torr. The ampoule containing charges were placed in a horizontal alloy mixing furnace at the temperature 700 $^0$C for 48 hour, during which it was continuously rocked and rotated for proper mixing and reaction. The ingot was then cooled to room temperature over a period of 24 hour. The single crystals of $In_2Se_{2.7}Sb_{0.3}$were grown by the Bridgeman method with the growth velocity was 0.35 cm / hr and freezing interface temperature gradient was 60 $^0$C / cm. Some interesting features on the top free surface of the as grown crystals were observed by using an optical microscope. A new dislocation etchant developed by using AR grade chemicals, as discussed below.

## Result And Discussion

The surface features and etch patterns of the as grown crystals were examined using a optical microscope. The topographical variation is found to be the $In_2Se_{2.7}Sb_{0.3}$ crystal and hence the discussion is generalized for all these crystals. Generally, well developed good quality crystals are found to be orthorhombic in habit. Fig. 1 shows a typical crystal of $In_2Se_{2.7}Sb_{0.3}$. These crystals have well developed (112) faces. It is observed that generally, the opaque crystal.



**Figure 1. Typical crystal photograph of $In_2Se_{2.7}Sb_{0.3}$.**

Most of the orthorhombic crystals have lines running parallel to the major axis and the crystal is easily cleaved along this line, while in case of monoclinic crystal system, cleavage parallel to the basal planes is common[15].

A systematic study of the growth features observed on top free surface of the crystals is discussed in detail. Fig. 2 shows shallow hillock feature observed on top free surface of the all samples.
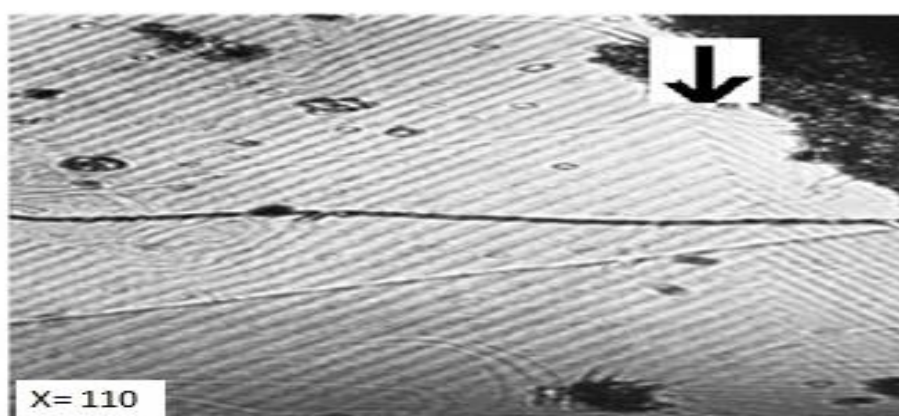


**Figure 2. Shallow hillock observed on the top free surface of $In_2Se_{2.7}Sb_{0.3}$ crystals.**

At the location of the horizontal ridge (denoted by arrows) in fig. 2 a slight bending of the interference fringes can be recognized, and also it shows that the spacing between two steps are uniform or equispaced. From this observation it can be concluded that the burgers vector of the dislocation at the center of the shallow growth spirals must correspond to one unit translation Similar unit lattice height and lower steps on aqueous solution grown crystal have been observed and measured on potash alum[16], $CdI_2$[17] and $NiSO_46H_2O$[18,19]. From above discussion it is indicates the layer growth mechanism is predominant for the formation or growth of crystals.
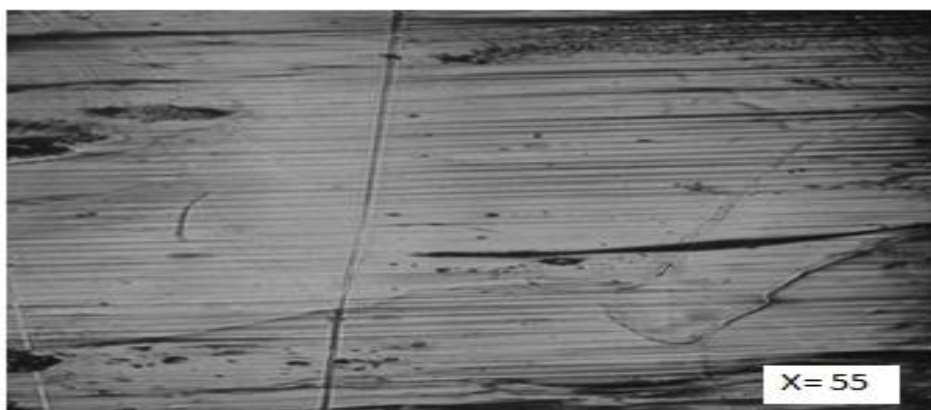


**Figure 3.Parallel Striation observed on the top free surface of $In_2Se_{2.7}Sb_{0.3}$ crystals**.

Striations which are parallel lines are seen on most of the crystals. These striations are growth layers formed on the surface due to periodic incorporation of impurities or variation of microscopic growth rate [20, 21]. Fig. 3 shows the spreading of parallel growth layers are comparatively thick at the top of the surface of the crystal. Parallel Striations to the major axis can be seen which are evidently below the growth patterns. It can be conjectured that the growth pattern has taken place at the final stage of the growth due to a large supply of ions at this stage. Thickness of the growth layer increases when the concentration of the reactants is high.

Desai C. F. have been reported in his Ph. D. Work, the striated morphology of the as-grown crystal surface can be assigned to transient thermal currents set up by temperature instabilities which are in turn usually caused by gradients, radial as well as longitudinal [22]. The striations on a surface normal to the growth axis should then be specifically associated with the radial gradients. Ideally, there should not be any radial temperature gradient. Nevertheless, this cannot usually be eliminated because, apart from the furnace characteristics, the ampoule and material together produce such gradients owing to the vast

difference in their thermal conductivities. Such features were observed in all the crystals grown by the Bridgman technique.
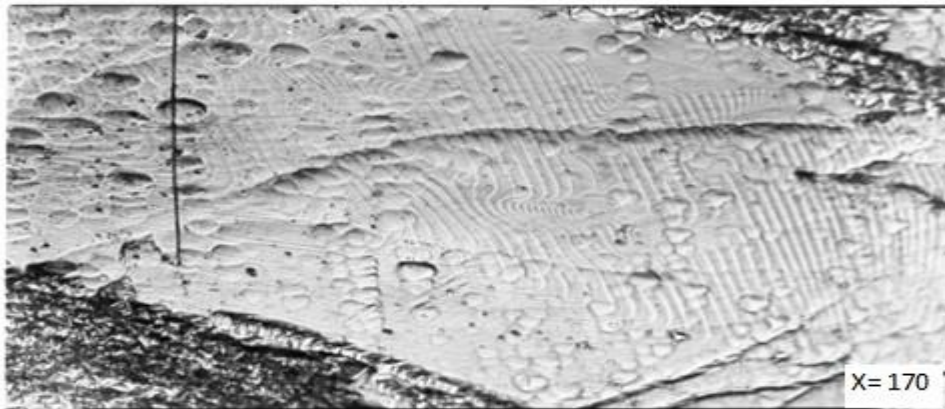


**Figure 4.Very low step train on {110} observed on the top free surface of $In_2Se_{2.7}Sb_{0.3}$ crystals.**

The Bridgman grown crystals were cleaved and the cleavage plane was almost parallel to the growth axis, except for few cleavage lines, which may be due to the stress introduced during the act of cleaving, the planes were seen to be free of any structures which may resemble striations.

Also non – bunched steps with very low steps heights, as shown in fig. 4 were commonly observed. The height of these steps equal about 10-20 Å as was estimated by comparison of their contrasts on the phase contrast micrograph with the contrast of steps of well-known height on {111} and {100} potash alum [23].

Observation of very low steps on {110} layer is extremely difficult, even more than on the {100} and {111} faces because of the high anisotropy of the band within a growth layer of {110}. The {110} faces do not only contain the strong PBC $\langle\bar{1}1$, but also the weaker PBC

$\langle 00$. Such anisotropy, due to the occurrence of some weak lateral bond in the growth layer

of the {110}face lead to a lowering of the edge free energy of a two- dimensional nucleus, this promoting two- dimensional nucleation as was shown by Monte Carlo Simulation [24]. So, due to an enhanced probability of nucleation growth at somewhat higher super saturations, which may occur for a short time during the removal of crystal from the solution, the original step pattern may be no longer visible by optical microscopy because of interference of this step pattern by two- dimensional nuclei.This may occur as a result of body phenomena.

The perfection of the grown crystals in terms of dislocation content was estimated by the using dislocation etchant developed by the present authors after numerous trials. The characteristics of the etchant are shown below.

ETCHANT PROPORTIONS: 5 part of saturated solution of Tartaric acid + 4 part of $HNO_3$ (70% AR) + 1.1 part of Distilled water.

This mixture is capable of producing well defined triangular etchpits. The etching time is 12 second to yield the etch pits. Fig. 5 shows the etch pits, etchant to be capable of revealing dislocations intersecting the cleavage plane.
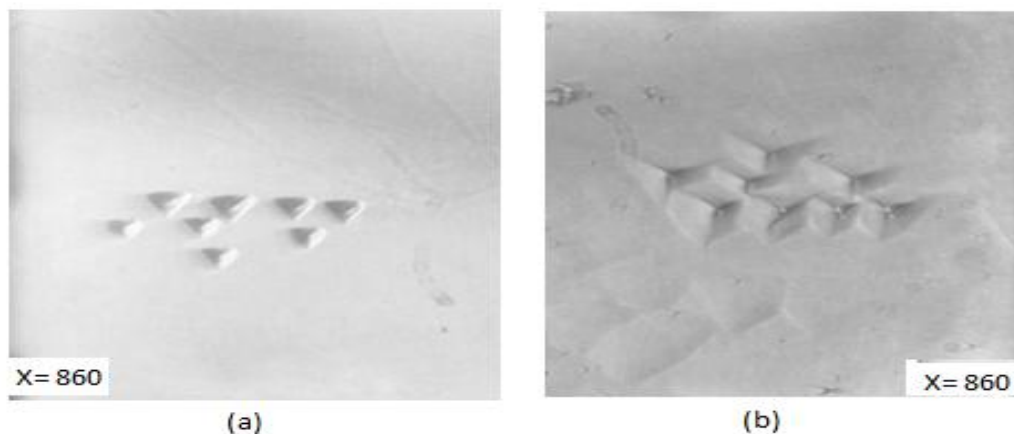


**Figure 5.Increasing etching observed on the top free surface of $In_2Se_{2.7}Sb_{0.3}$ crystals.**

The test of successive etching is based on the fact that a dislocation line cannot terminate within the crystal. Fig.5 show the etch patterns obtained on the same region on the same cleavage surface etched for 10 and 15 seconds, respectively. It can be seen that the pits have to some extent increased in size with the etching time, whereas their number has remained the same, indicating thereby that the pits are at the sites of emergence of dislocation.
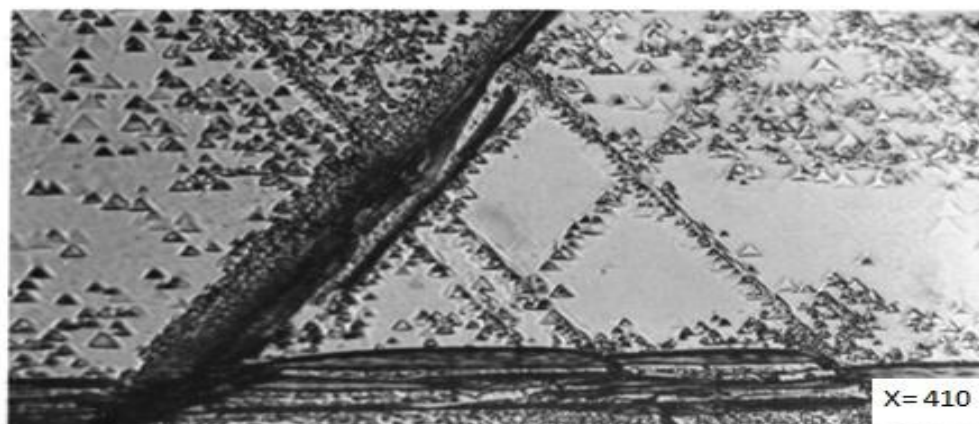


**Figure 6.SCRECH MARK observed on the top free surface of $In_2Se_{2.7}Sb_{0.3}$ crystals.**

Fig. 6 shows the etch pattern obtained around a scratch produced on the surface. The increased density and rearrangement of the etch-pits along the slip traces near the scratch show that the etchant is capable of revealing fresh dislocations also.
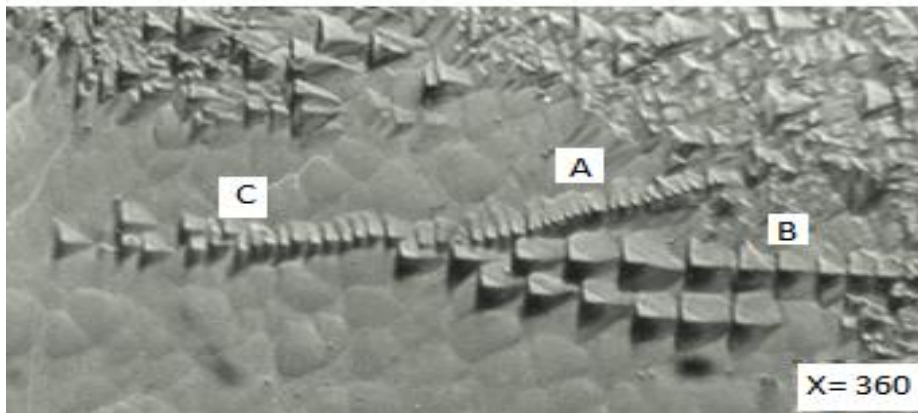


**Figure 7.Low Angle Boundary observed on the top free surface of In$_2$Se$_{2.7}$Sb$_{0.3}$ crystals.**

Fig. 7 shows the rows of etch pits originating from point are clearly visible. In the upper part of the photograph, scattered etch pits are seen and the rows of etchpits may be due to the deformation introduced during the act of cleavage. The distribution of etch pits and low angle boundary obtained after etching the specimen by the etchant[25]. There are seen distinct rows of closely spaced etch pits as well as branching of rows. These rows resemble the low angle boundaries commonly observed in metallic and intermetallic crystals [25-31]. Three rows of dislocations meeting at a point are known as triaxial boundaries. A model based on minimum free energy [32] for dislocation tilt boundary gives the relation

$$nA = nB + nC \qquad \ldots\ldots\ldots\ldots\ldots (1).$$

Where, nA,nB and nC are average density of pits along A, B and C branches, respectively. This relation is satisfied with A, B and C designations indicated on the photograph in the figure above.

**CONCLUSION**

Shallow hillock, observed on the top free surface of as grown crystal which represents the layer growth mechanism is predominant during the crystal growth.
An etchant develop by the author is capable of revels the freshly new dislocations intersecting the cleavage plane of the crystal.

**REFERENCES**

1. Medvedeva, Z.C. Nauka, Moscow, 1968 (in Russian).
2. Herrero, J.;Ortega, J. Solar Energy Mater. 1987, 16, 477.
3. Whittingan,M. S. Solid State Chem. 1978, 12, 41.
4. Julien,C.; Chery, A.; Siapkas, D. Phys. Stat. Sol. (a) 1990, 118, 553.
5. Soeda,J. Ye,; Nakamura, S. Y.; Nittono, O. Jpn. J. Appl. Phys. 1998, 37 , 4264.
6. Katty, A.; Castro, C. A.; Odile, J. P.; Soled S.; Wold,A.J. Solid State Chem. 1978, 24, 107.
7. Sebastian, P.J.; Sivaramakrishnan, V. J. Appl. Phys. 1989, 65, 237.
8. Julien, C.; Eddrief, M. Materials Science and Engineering B, 1992, 13, 247.
9. Mccany, J. V.; Murray, R. V. J. Phy. C 1977, 10, 1211.
10. Parlak, M.; Ercelebi, C.; Gunal,I.; Salaeva Z.; Allkhverdiev,K. Thin Solid Films 1995, 258, 86.
11. Gibson, G. A.; Chaiken,A.; Nauka, K.; Yang,C. C.; Davidson, R.; Holden,A.; Bicknell, R.; Yeh,B. S.; Chen,J.; Liao, H.; Subramanian,S.;Schut,D.;Jasinski J.;Lilliental-Weber, Z. Appl. Phys. Lett. 2005, 86, 051902.
12. Lee, H.; Kang, D. H.; Tran, L., Mater. Sci. & Eng. B 2005, 119, 196.
13. Contreras,M.; Gabor,A.; Tennant, A.; Asher,S.; Noufi,R. J Mo Solar Cell Prog. Photovoltaics 1994, 2, 287.
14. Nishida, T.; Terao, M.; Miyauchi,Y.; Horigome,S.; Kaku, T.; Ohta,N. Appl. Phys. Lett. 1987, 50, 667.
15. J. D. Dana., The System of Mineralogy, John Wiley and Sons, New York, 1951, 2, 208.
16. Van Enckevort,W. J. P.; Bennema, P.; Van der Linden,W. H. Z. Phy. Chemi (Neue-Folge) 1981, 124, 171.
17. Okaya, Y. Acta Crystal. 1965, 19, 879.
18. Van Enckevort, W. J. P.; Klapper, H. J. Crystal Growth,1987, 80, 91.

19. Bennema,P.; Van der Eerden,J.; Van Enckevort,W.J.P.; Vander Hock, B.; Tsukamoto,K.Phys. Stat. Solidi (a) 1979, 55, 403.

20. Authier, A. J. Cryst. Growth, 1977, 42, 612.

21. Kitamura, K.; Komatsu, H. Krist. and Tech., 1978, 13, 811.

22. C. F. Desai,Ph.D. Thesis; The M. S. University(Vadodara, Gujarat, India,1980)

23. Van Enckevort, W. J. P.; Bennema, P.; Van der Linden,W. H. Z. Phy. Chemi 1981, 124, 171.

24. Van der Eerden, J. P.; Van Leeuwen,C.; Bennema, P.; Vander Kruk, W. L.; Veltman,B. P. Th. J. Appl. Phys. 1977, 48, 2124.

25. Yim, Y. M.;Dismukes,J. P. J. Phys. Chem. Solid, suppl,1967, 187, 187.

26. Bhatt, V.P.; Pandya, G.R. J. Phys. "C" Solid State Physics, 1973, 6, 36.

27. Sagar, A.; Faust, J.W.J. Appl. Phys., 1967, 2S, 482..

28. Sagar, A.; Faust, J.W.Phys. Lett., 1966, 23, 406..

29. Amelinckx, S.Phil. Mag., 1956, 1, 269.

30. Brown, D.M.;Heymann, F.K.J. Appl. Phys., 1964, 35, 1947.

31. Jani, T.M.; Pandya, G.R.; Desai, C. F.J. Cryst. Res. And Technol., 1993, 28, K40.

32. Wemick, J.H.;Hobstetter, J.N.; Lovell, L.C.;Worsi, D.J. Appl. Phys.1958, 29, 1101.

# Ultrasonic and Volumetric Study in the Solutions of Alkanols with Aqueous Ethylene Glycol

**Chintu J Patel**
Research Scholar

**Vibha Sharma**
Faculty

Faculty of Science
Pacific Academic of Higher education and Research University
Udaipur
Chintupatel551@gmail.com

## Abstract

In the current paper the Ultrasonic and volumetric study of some solutions were performed by authors. In the current manuscript Comparison of ultrasonic velocities densities and viscosity of pure liquids with the corresponding literature values at 308.15 K for different solutions were studied and presented their experimental results. In the same time Variation of ultrasonic velocity in the mixtures of methanol, ethanol and 1- propanol with aqueous ethylene glycol was calculated and graphical data were obtained. Deviation in ultrasonic velocity, deviation in isentropic compressibility, excess intermolecular free length, excess acoustic impedance, with mole fraction of methanol, ethanol and 1- propanol in aqueous ethylene glycol solution at T = 308.15 K were calculated.

## Key Word

Ultrasonic, Ultrasonic Velocity, Deviation in ultrasonic velocity, deviation in isentropic compressibility, excess intermolecular free length, excess acoustic impedance

## Introduction

The properties of liquid mixtures and solutions can be altered continuously within a reasonable range by varying the concentration till an optimum value of some desired parameter is attained. The pure liquids lack such flexibility[1]. The study of properties of liquid mixtures and solutions finds direct application in chemical, biochemical and medical industry[2]. Speed of sound, itself, is highly sensitive to the structure and interactions present in liquid systems as it is fundamentally related to the binding forces between the constituents of the medium[3-5]. The measurement of speed of sound in liquids enables determination of some useful acoustic and thermodynamic parameters that are found to be very sensitive to molecular interactions[6].

Hence such measurements are useful to study the nature and strength of molecular interactions in liquid mixtures[7]. Water and alcohol mixtures show unique maxima and minima in their thermodynamic and acoustic properties at low alcohol concentrations[8]. The formation of such maxima/minima in some aqueous solutions of electrolytes and in non-aqueous solutions is also reported in literature[9].

**Experiment**

The chemicals used in the present study are ethylene glycol (mass fraction purity 0.99), methanol (mass fraction purity 0.99), ethanol (mass fraction purity 0.99) (Changshu Yangyuan Chemicals-China make) and 1-propanol (mass fraction purity 0.99) (G.R Grade, obtained from LOBA Chemicals, Mumbai, INDIA). These were further purified by standard methods. The solutions of aqueous ethylene glycol of 0.3 m and 0.9 m are prepared using triply distilled deionised water. These solutions, in turn, are used to prepare liquid mixtures with methanol, ethanol and 1-propanol so that its entire range of composition is covered. All the mixtures have been prepared in the specially designed glass bottles with air tight stoppers and adequate precautions have been taken to minimize evaporations losses. The weighing of solutions has been made using a METTER TOLEDO (Switzerland make) ABB5-S/FACT digital balance with an accuracy of 0.01mg. The ultrasonic velocities, densities and viscosities are measured at 308.15 K for the pure liquids used in this investigation and are compiled in Table 6.A.1 together with the literature data available.

**Table 1: Comparison of ultrasonic velocities ($u$), densities ($\rho$) and viscosity ($n$) of pure liquids with the corresponding literature values at 308.15 K**

| Liquid | $\frac{u}{m} \cdot s^{-1}$ | | $\frac{\rho}{kg} \cdot m^{-3}$ | | $\frac{n}{10^{-3}N} \cdot s \cdot m^{-2}$ | |
|---|---|---|---|---|---|---|
| | Expt. | Lit. | Expt. | Lit. | Expt. | Lit. |
| Water | 1520.22 | 1519.36 | 994.06 | 994.1 | 0.7190 | 0.7210 |
| Ethylene glycol | 1632.32 | 1632.10 | 1105.85 | 1103.10 | 10.4894 | 10.9680 |
| Methanol | 1072.65 | 1072.40 | 776.63 | 776.70 | 0.4786 | 0.4780 |
| Ethanol | 1115.10 | 1111.00 | 776.49 | 776.41 | 0.8840 | 0.8930 |
| 1-propanol | 1175.60 | 1175.10 | 791.41 | 791.40 | 1.4152 | 1.4172 |

**Result and Discussion**

The variation of ultrasonic velocity $(u)$ at two different molalities of aqueous ethylene glycol with mole fraction of methanol/ethanol/1-propanol is shown in Figures 6.A.1.a, 6.A.1.b and 6.A.1.c respectively. The ultrasonic velocity increases in the $0 < x < 0.15$ mole fraction of alkanol and it is found to decrease beyond 0.15 mole fraction of alkanol. The ultrasonic velocity shows a maximum value at about 0.15 m mole fraction of methanol/ethanol/1-propanol for 0.3 m and 0.9 m aqueous solutions of ethylene glycol. Water and ethylene glycol are both associated liquids, through the formation of hydrogen bonding. When ethylene glycol is added to water, association between ethylene glycol and water molecules takes place through hydrogen bonding which is shown in schema I. This leads to the increase of open structures in the solution as diol acts as a structure maker.

**Table 2: Calculated properties of mole fraction of methanol (x) in aqueous ethylene glycol solution at T = 308.15 K**

| X | Volume fraction of methanol | $\dfrac{\Delta u}{m.s^{-1}}$ | $\dfrac{\Delta k_s}{10^{-10}Pa^{-1}}$ | $\dfrac{L_f^E}{10^{-10}m}$ | $\dfrac{Z^E}{10^6 kg}.m^{-2}.s^{-1}$ |
|---|---|---|---|---|---|
| **0.3 m aqueous ethylene glycol** | | | | | |
| 0.0000 | 0.0000 | 0.0000 | 0.0000 | 0.0000 | 0.0000 |
| 0.0987 | 0.0981 | 69.32 | -0.7406 | -0.0296 | 0.0670 |
| 0.1968 | 0.1937 | 124.27 | -1.4004 | -0.0558 | 0.1249 |
| 0.3009 | 0.2937 | 166.15 | -1.9896 | -0.0784 | 0.1669 |
| 0.3915 | 0.3803 | 199.59 | -2.4663 | -0.0966 | 0.1967 |
| 0.4944 | 0.4774 | 200.68 | -2.7687 | -0.1061 | 0.1980 |
| 0.5947 | 0.5707 | 185.88 | -2.9005 | -0.1091 | 0.1871 |
| 0.7001 | 0.6713 | 154.25 | -2.7953 | -0.1022 | 0.1564 |
| 0.7963 | 0.7652 | 130.64 | -2.6003 | -0.0933 | 0.1330 |
| 0.8932 | 0.8744 | 67.19 | -1.6557 | -0.0555 | 0.0637 |
| 1.0000 | 1.0000 | 0.0000 | 0.0000 | 0.0000 | 0.0000 |
| **0.9 m aqueous ethylene glycol** | | | | | |
| 0.0000 | 0.0000 | 0.0000 | 0.0000 | 0.0000 | 0.0000 |
| 0.0986 | 0.0978 | 66.21 | -0.7285 | -0.0290 | 0.0668 |
| 0.1937 | 0.1905 | 122.68 | -1.3816 | -0.0551 | 0.1247 |
| 0.2965 | 0.2885 | 165.73 | -1.9781 | -0.0785 | 0.1708 |
| 0.3956 | 0.3816 | 202.40 | -2.5076 | -0.0992 | 0.2086 |
| 0.4939 | 0.4741 | 205.42 | -2.8117 | -0.1091 | 0.2103 |
| 0.5969 | 0.5717 | 188.64 | -2.9358 | -0.1108 | 0.1910 |
| 0.6972 | 0.6672 | 168.59 | -2.9326 | -0.1083 | 0.1705 |
| 0.7957 | 0.7634 | 140.71 | -2.7214 | -0.0984 | 0.1425 |
| 0.8934 | 0.8765 | 63.85 | -1.6140 | -0.0535 | 0.0585 |
| 1.0000 | 1.0000 | 0.0000 | 0.0000 | 0.0000 | 0.0000 |

**Table 6.A.3 Calculated properties of mole fraction of ethanol $(x)$ in aqueous ethylene glycol solution at T = 308.15 K**

| X | Volume fraction of ethanol | $\dfrac{\Delta u}{m.\,s^{-1}}$ | $\dfrac{\Delta k_s}{10^{-10}Pa^{-1}}$ | $\dfrac{L_f^E}{10^{-10}m}$ | $\dfrac{Z^E}{10^6 kg}.\,m^{-2}.\,s^{-1}$ |
| --- | --- | --- | --- | --- | --- |
| **0.3 m aqueous ethylene glycol** | | | | | |
| 0.0000 | 0.0000 | 0.0000 | 0.0000 | 0.0000 | 0.0000 |
| 0.0579 | 0.0576 | 62.97 | -0.5059 | -0.0219 | 0.0564 |
| 0.1485 | 0.1456 | 139.49 | -1.1839 | -0.0512 | 0.1329 |
| 0.2275 | 0.2216 | 171.74 | -1.5783 | -0.0667 | 0.1597 |
| 0.3038 | 0.2931 | 165.85 | -1.7650 | -0.0723 | 0.1565 |
| 0.4045 | 0.3884 | 152.14 | -1.9199 | -0.0757 | 0.1397 |
| 0.5094 | 0.4893 | 138.43 | -2.0143 | -0.0766 | 0.1203 |
| 0.6114 | 0.5869 | 113.52 | -1.9505 | -0.0720 | 0.0982 |
| 0.7413 | 0.7132 | 98.13 | -1.8745 | -0.0681 | 0.0872 |
| 0.8611 | 0.8434 | 40.48 | -1.0662 | -0.0358 | 0.0311 |
| 1.0000 | 1.0000 | 0.0000 | 0.0000 | 0.0000 | 0.0000 |
| **0.9 m aqueous ethylene glycol** | | | | | |
| 0.0000 | 0.0000 | 0.0000 | 0.0000 | 0.0000 | 0.0000 |
| 0.0703 | 0.0696 | 77.13 | -0.6220 | -0.0272 | 0.0741 |
| 0.1447 | 0.1420 | 132.13 | -1.1278 | -0.0485 | 0.1254 |
| 0.2265 | 0.2202 | 166.62 | -1.5468 | -0.0653 | 0.1569 |
| 0.3562 | 0.3395 | 181.83 | -2.0024 | -0.0827 | 0.1813 |
| 0.4675 | 0.4429 | 158.21 | -2.1139 | -0.0842 | 0.1577 |
| 0.5585 | 0.5264 | 139.95 | -2.1104 | -0.0824 | 0.1345 |
| 0.6578 | 0.6243 | 119.20 | -2.0762 | -0.0786 | 0.1162 |
| 0.7845 | 0.7500 | 91.16 | -1.8284 | -0.0676 | 0.0902 |
| 0.8593 | 0.8397 | 33.95 | -1.0017 | -0.0337 | 0.0272 |
| 1.0000 | 1.0000 | 0.0000 | 0.0000 | 0.0000 | 0.0000 |

**Table 6.A.4 Calculated properties of mole fraction of 1-propanol $(x)$ in aqueous ethylene glycol solution at T = 308.15 K**

| X | Volume raction of methanol | $\dfrac{\Delta u}{m.\,s^{-1}}$ | $\dfrac{\Delta k_s}{10^{-10}Pa^{-1}}$ | $\dfrac{L_f^E}{10^{-10}m}$ | $\dfrac{Z^E}{10^6 kg}.\,m^{-2}.\,s^{-1}$ |
| --- | --- | --- | --- | --- | --- |
| **0.3 m aqueous ethylene glycol** | | | | | |
| 0.0000 | 0.0000 | 0.0000 | 0.0000 | 0.0000 | 0.0000 |
| 0.0548 | 0.0545 | 71.30 | -0.4835 | -0.0222 | 0.0617 |
| 0.1167 | 0.1150 | 100.97 | -0.7649 | -0.0339 | 0.0862 |
| 0.1886 | 0.1852 | 71.22 | -0.7197 | -0.0287 | 0.0467 |
| 0.2606 | 0.2553 | 61.98 | -0.7607 | -0.0285 | 0.0297 |
| 0.3448 | 0.3373 | 45.64 | -0.7440 | -0.0258 | 0.0087 |
| 0.4456 | 0.4371 | 26.14 | -0.6583 | -0.0204 | -0.0157 |
| 0.5471 | 0.5387 | -5.31 | -0.3874 | -0.0083 | -0.0457 |
| 0.6934 | 0.6860 | -17.58 | -0.1577 | -0.0001 | -0.0539 |
| 0.8179 | 0.8106 | -2.19 | -0.2662 | -0.0062 | -0.0231 |
| 1.0000 | 1.0000 | 0.0000 | 0.0000 | 0.0000 | 0.0000 |

| 0.9 m aqueous ethylene glycol | | | | | |
|--------|--------|--------|---------|---------|---------|
| 0.0000 | 0.0000 | 0.0000 | 0.0000 | 0.0000 | 0.0000 |
| 0.0561 | 0.0556 | 69.29 | -0.4755 | -0.0218 | 0.0621 |
| 0.1159 | 0.1142 | 92.07 | -0.7117 | -0.0312 | 0.0773 |
| 0.1842 | 0.1805 | 74.47 | -0.7388 | -0.0298 | 0.0520 |
| 0.2956 | 0.2875 | 61.15 | -0.8278 | -0.0310 | 0.0333 |
| 0.3565 | 0.3474 | 47.39 | -0.8569 | -0.0308 | 0.0297 |
| 0.4427 | 0.4327 | 31.87 | -0.7330 | -0.0237 | -0.0083 |
| 0.5687 | 0.5592 | -15.11 | -0.3947 | -0.0085 | -0.0401 |
| 0.7086 | 0.7000 | -22.02 | -0.2642 | -0.0043 | -0.0360 |
| 0.8276 | 0.8209 | -1.76 | -0.2745 | -0.0064 | -0.0233 |
| 1.0000 | 1.0000 | 0.0000 | 0.0000 | 0.0000 | 0.0000 |
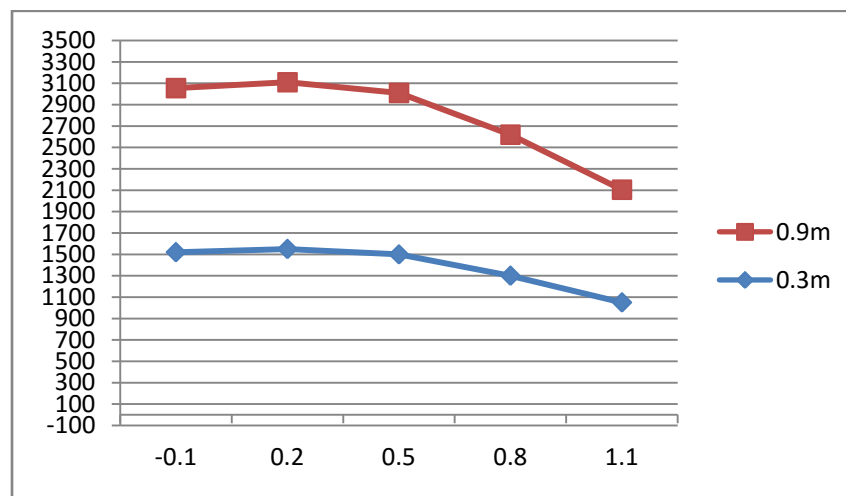


**Fig. 1: Variation of ultrasonic velocity ($u$) in the mixtures of methanol with aqueous ethylene glycol**
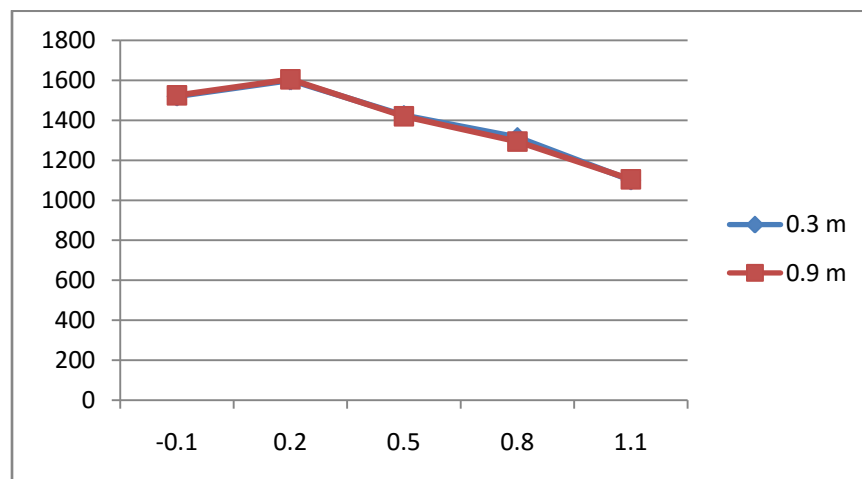


**Fig. 2: Variation of ultrasonic velocity ($u$) in the mixtures of ethanol with aqueous ethylene glycol**
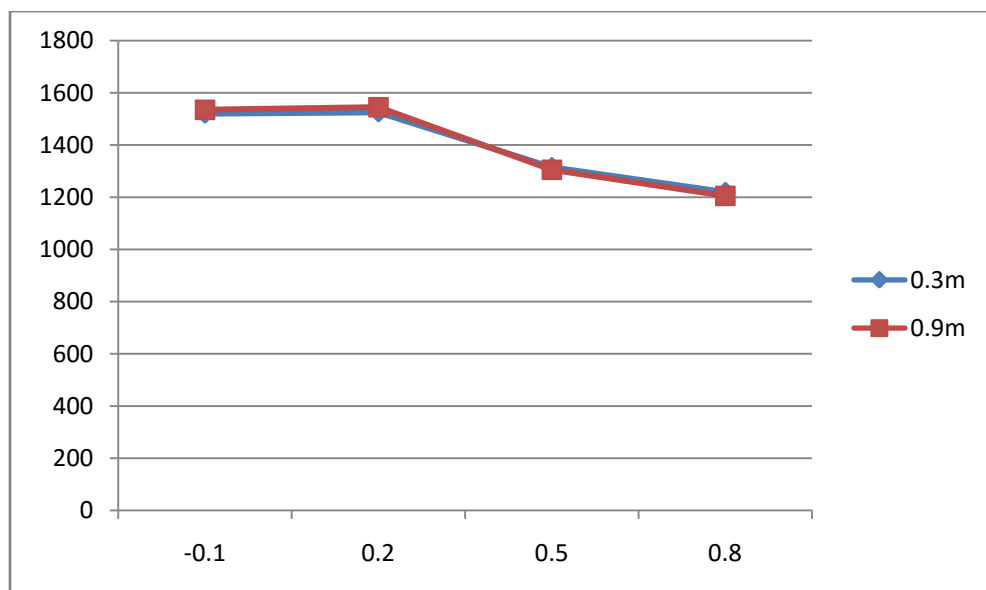
**Fig. 3: Variation of ultrasonic velocity ($u$) in the mixtures of 1- propanol with aqueous ethylene glycol**

Representation of inter molecular interactions in (a) water (b) alcohols (c) ethylene glycol (d) between water and ethylene glycol molecules. The maximum value in ultrasonic velocity is observed in the low concentration region of alkanols added to the aqueous ethylene glycol. The origin of maximum in the low concentration region of alkanol is due to long-range order in water giving rise to hydrogen bonded structure. Such a structure possesses many cavities and these cavities can accommodate solute such as alkanol molecules. This is further supported by the observed large differences in the molar volume between the components of the solution. As alkanol is added to the aqueous ethylene glycol, alkanol molecules go on occupying the cavities created in the aqueous ethylene glycol structure. This gives rise to a denser packing of molecules resulting in the increase of ultrasonic velocity of solutions. This process continues until all the cavities are filled with solute molecules. Further addition of alkanol, leads to gradually for the formation of unassociated monomer structures in the solution and at the same time there are some alkanol molecules which disrupts the hydrogen bonding existing between the water + ethylene glycol molecules resulting in unassociated ethylene glycol molecules in the solution.

Thus, the structure of solution becomes more and more loosely packed by increasing the concentration of alkanol molecules. As a result, the ultrasonic velocity in the solution decreases.

This might be the possible reason to explain the ultrasonic velocity behaviour in the present investigated solutions. The deviation in ultrasonic velocity $(\Delta u)$, deviation in isentropic compressibility $(\Delta k_s)$, excess inter molecular free length $(L_f^E)$ and excess acoustic impedance $(Z^E)$ have been calculated from the experimental results of ultrasonic velocity $(u)$ and density $(\rho)$ and the data for the above properties are listed in Table 2, .3 and 4 for methanol, ethanol and 1-propanol with aqueous ethylene glycol solution respectively. The variation of deviation in ultrasonic velocity $(\Delta u)$ and deviation in isentropic compressibility $(\Delta k_s)$ with mole fraction of methanol/ethanol/1-propanol is shown in Figures 6.1, 6.2 and 6.3 respectively. The sign and magnitude of $\Delta u \ and \ , \Delta k_s$ played an important role to describe the molecular rearrangement and is resulted to the existence of molecular interactions among the component molecules in the solutions.

**Reference**

1.  B Garcia, R Alcalde, J M Leal and J S Matos, J. Chem. Soc., Faraday Trans. 93, 1115 (1997)

2.  K S Pitzer, Thermodynamics, 3rd. Ed. (McGraw-Hill Book Co., NY, 1995)

3.  G Douheret, M I Davis, I J Fjallanger and H Hoiland, J. Chem. Soc., Faraday Trans. 93, 1943 (1997)

4.  K Tamura, T Sonoda and S Murakami, J. Solution Chem. 28, 777 (1999)

5.  A Ali, A K Nain and M Kamil, Thermochim. Acta 274, 209 (1996)

6.  A Ali, S Hyder and A K Nain, Acoustics Lett. 21, 77 (1998); J. Mol. Liq. 79, 89 (1999); Indian J. Phys. B74, 63 (2000)

7.  B Jacobson, Acta Chem. Scand. 5, 1214 (1951); 6, 1485 (1952); J. Chem. Phys. 20, 927 (1952)

8.  W Van Dael and E Vangeel, Proc. Ist Internat. Conf. on calorimetry thermodynamics, Warsaw (1969)

9.  J A Riddick, W B Bunger and T K Sakano, Techniques in chemistry, vol. VII, Organic solvents, 4th edn. (John Wiley, New York, 1986)

# Mobile Controlled Robot Without Microcontroller

**Patel Virendrakumar N.**
School of Science, Physics Department, Gujarat University Navrangpura, Ahmedabad
virendrapatel95@gmail.com

**Abstract**
In this project, we present the controlling of a Robot using DTMF technique Therobot is controlled by a mobile phone that calls the other mobile phone attached to the robot. During the call, if any button is pressed, the tone corresponding to the button pressed is heard at the other end. This tone is called "Dual Tone Multi Frequency tone (DTMF) Using DTMF code direction of motion of the robot can be controlled by mobile phone. The above system can be used for military purpose as bomb detector and as "spy robot" and for surveillance

**Introduction**
DTMF is the acronym for Dual tone Multi frequency. Robotic vehicle based on DTMF technology is explained in this article. Here is a circuit that operates the robot without using a microcontroller. This circuit consists of simple ICs. When a key is pressed from our mobile, it generates a tone combination of two frequencies from our keypad. In the two frequencies, one is high frequency and another one is low frequency. This frequency can be decoded by the decoder IC into binary sequence.

**DTMF BASED ROBOTIC vehicle circuit principle**
DTMF based robotic vehicle circuit consists of DTMF decoder IC, driver IC l293D IC and motors. DTMF decoder IC used is IC CM8870. It has 18 pins. Tone from DTMF encoder is given to the DTMF decoder IC. The decoder IC internally, consists of operational amplifier whose output is given to pre-filters to separate low and high frequencies. Then it is passed to code detector circuit and it decodes the incoming tone into 4bits of binary data. This data at the output is directly given to the driver IC to drive the two motors. These motors rotate according to the decoded output.

If the button pressed from mobile is '1', it gives a decoded output of '0001'. Thus, motor connected to the first two pins will get 0 volts and second motor will have 5 volts to one pin and 0 volts to another pin. Thus, second motor starts rotating and first motor is off. So, robot moves in one direction either to left or right. If the robot is to rotate forward or backward then the binary value should be either '0101' or '1010'. These values indicate that two motors rotate in the same direction i.e. either forward or backward. The following table gives the low frequency, high frequency and binary output value of each button pressed in the keypad.

| Button | Low DTMF frequency (Hz) | High DTMF frequency (Hz) | Binary coded output | | | |
|--------|------|------|----|----|----|----|
| | | | Q1 | Q2 | Q3 | Q4 |
| 1 | 697 | 1209 | 0 | 0 | 0 | 1 |
| 2 | 697 | 1336 | 0 | 0 | 1 | 0 |
| 3 | 697 | 1477 | 0 | 0 | 1 | 1 |
| 4 | 770 | 1209 | 0 | 1 | 0 | 0 |
| 5 | 770 | 1336 | 0 | 1 | 0 | 1 |
| 6 | 770 | 1477 | 0 | 1 | 1 | 0 |
| 7 | 852 | 1209 | 0 | 1 | 1 | 1 |
| 8 | 852 | 1336 | 1 | 0 | 0 | 0 |
| 9 | 852 | 1477 | 1 | 0 | 0 | 1 |
| 0 | 941 | 1336 | 1 | 0 | 1 | 0 |
| * | 941 | 1209 | 1 | 0 | 1 | 1 |
| # | 941 | 1477 | 1 | 1 | 0 | 0 |

**Figure 1 - DTMF**

**BLOCK DIAGRAM**
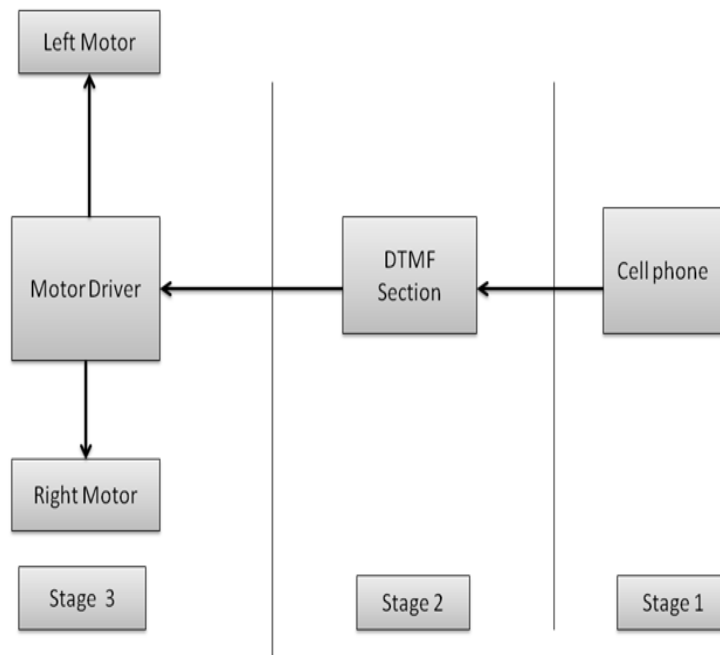


**Figure – 2 DTFM block Diagram**

**CIRCUIT DIAGRAM**
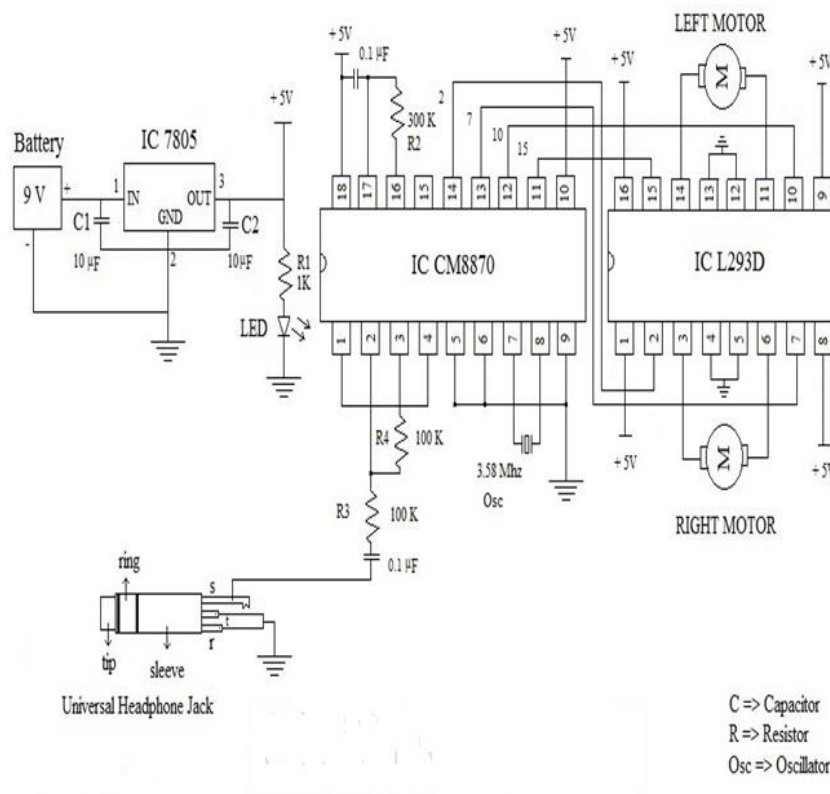


**Step by Step Instructions.**

**1)  Power Supply**
- Take the breadboard and connect the battery holder in horizontal position.
- Insert the positive and negative wire of battery snap in holder.

- Attach IC 7805 (Voltage Regulator), and place one 10 µF capacitor in IN & GND connection of IC 7805 and other in GND & OUT connection.
- Take the positive supply from the battery holder via breadboard wire and place it in IN of IC 7805, and connect its negative supply in the last row of the breadboard.
- Place the GND of IC 7805 in the last row of the breadboard, and transfer its OUT to the first row of the breadboard.
- Because of these connections, +5V power is obtained in the first row of the breadboard.
- To check the power flow path, an LED is given a positive supply via 1K Resistor.

## 2) IC CM8870 Connections
- Connect $1^{st}$ & $4^{th}$ pin of CM8870 (DTMF Receiver) together.
- Pick one 100K resistor and place one side of it in $2^{nd}$ pin and other side to the 0.1 µf capacitor.
- Pick another 100K resistor and connect $3^{rd}$ and $2^{nd}$ pin.
- Provide GND connection to $5^{th}$, $6^{th}$, and $9^{th}$ pins.
- Couple $7^{th}$ and $8^{th}$ pins with 3.58 MHz Oscillator.
- Provide +5V supply to $10^{th}$ and $18^{th}$ pins.
- Take one 300K resistor, and place one side of it to 16th pin and other to 0.1 µf capacitor from 17th pin.
- Connect 0.1 µf capacitor to the $18^{th}$ pin.

## 3) IC L293D connections
- Insert IC L293D (Motor Controller) in the breadboard.
- Supply +5V power to $1^{st}$, $8^{th}$, $9^{th}$, and $16^{th}$ pins.
- Provide ground connection to $4^{th}$, $5^{th}$, $12^{th}$ and $13^{th}$ pins.
- Attach $2^{nd}$, $7^{th}$, $10^{th}$, and $15^{th}$ pins of L293D to $14^{th}$, $13^{th}$, $12^{th}$, and $11^{th}$ pins of IC CM8870 respectively.

## 4) 12V DC motor connections
- Take the wire of Right Motor and insert it in $3^{rd}$ and $6^{th}$ pins of IC L293D.
- Also, place the wire of Left Motor in $11^{th}$ and $14^{th}$ pins of IC L293D.

## 5) Universal Headphone Jack Connection
- Connect the sleeve to the output of 0.1 µf capacitor ($2^{nd}$ pin) in the IC CM8870.
- Provide GND connection to the tip and ring.

## Working
After completing the construction, connect the circuit with 9V battery. Also, connect the universal headphone jack to its respective cell phone with incoming facility. Activate auto-answer mode in the cell phone before connecting it to the circuit, and enable keypad tones in the cell phone that you use to make calls. Now, your robot is ready to operate wirelessly with GSM facility once you make a call to the cell phone connected to the robot. By pressing the number keypads in your cell phone, you will be able to move the robot in various directions.It is made possible with the help of Dual Tone Multi Frequency receiver (IC CM8870), in which the sleeve connection of the robot cell phone is connected to the IC CM8870. The tone received from your cell phone to the robot cell phone will be converted into binary form, and suitable output is provided by the IC CM8870 to IC L293D.For example, if you press no. 9 in your cell phone, then the robot will move forward (as per this circuit).

**Output**

| Input given on your cell phone | The output obtained from the robot |
|---|---|
| 1 | Front Right |
| 2 | Reverse Left |
| 3 | Stop |
| 4 | Reverse Right |
| 5 | 360 degree rotation (Right) |
| 6 | Reverse |
| 7 | Reverse Right |
| 8 | Front Left |
| 9 | Forward |
| 0 | 360 degree rotation (Left) |

**Hardware Module**
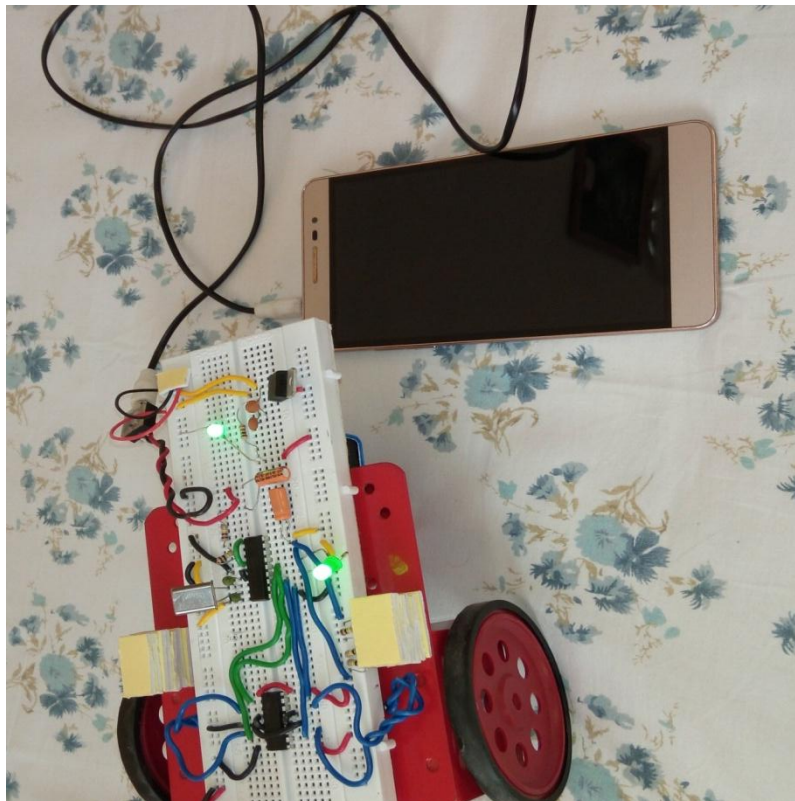


**Acknowledgements**

**Application**
[1] Industrial application
[2] With camera, can be used in surveillances system

**References**

[1] www.roboticsbible.com
[2] www.engineersgarage.com

# A study on the peak Dst and peak negative Bz relationship during intense geomagnetic

**Nirav H Thakkar , D.D.Joshi**

Sheth M N Science College, Patan

niravvv28@gmail.com

**Abstract**

This paper is a study of the relationship between the geomagnetic storm index Dst and the southward component, Bs, of the interplanetary magnetic field (IMF) driver. This study was performed during observational period (2011-2013), for which 64 intense geomagnetic storms (Dst 85 nT) were analyzed. After taking into account the propagation time between the L1 point and Earth (1 h) and the magnetosphere/ring current response-time to solar wind forcing (1 h), it was determined that the average delay between the peak Bs and the peak Dst values is 2 h. It was also observed that the Bs value at peak Dst is 75% of the peak Bs value in the entire event. When these results are analyzed in terms of the interplanetary electric field, associated with Bz, some interesting additional studies are indicated, for which some simple results, of practical space weather forecasting use, are anticipated.

**Keywords—** Dst Index,Bs component,Bz component,IMF

## Introduction

For the association of geomagnetic storm intensity and the interplanetary magnetic field driver, it is usually assumed that the peak value of the storm, as measured by the storm index Dst, is attained after the southward component of the interplanetary magnetic field, Bz, has also reached a peak value[1-2]. However, since there has not been done as yet a quantitative study of this assumed relationship, in this paper we try to perform such a study for the ACE observational period of 1997– 2002, during which 64 intense magnetic storms (Dst < 85 nT) were identified, as described in the following section[3-5]. We believe that this study is important not only as a forecast tool in space weather applications, but also for a better physical understanding of solar wind magnetosphere interaction and ring current dynamics during intense storms[6].

**Methodology Analysis**

The 1 hour Dst geomagnetic index was used in this work to characterize the geomagnetic storm development and it was obtained from the World Data Center for Geomagnetism, Lasco-SOHO CME Catalog. One-hour data of the interplanetary magnetic field Bz component and Dst index were obtained from Lasco-SOHO CME Catalog. The period selected for our analysis is observational period from January2011 –December 2013, for which the Dst index was available in its final form when this work was performed. We have selected intense geomagnetic storms that reached, at least, a Dst peak of 85 nT. Considering this criterion, and also selecting storms with multiple, but well separated, peaks corresponding to different energy injection events were obtained.
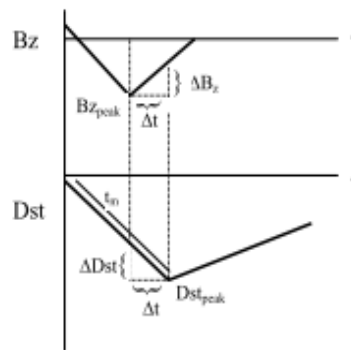


**Figure 1. Scheme of Bz and Dst profiles during intense magnetic storms.**

Figure 1 shows a scheme illustrating how the analysis was done. Figure 1 shows idealized Bz and Dst profiles as a function of time (t). The Dst and Bs(Bz) peaks are identified by the labels Dst peak and Bs peak. The storm main phase duration is indicated by the thinner line and by the tm label. Two dotted vertical lines passing through the Dst and Bz peaks are shown, and the corresponding values of Dst and Bz in their intersection with the curves are determined. The Bz and Dst variations were calculated as the ratio between their peak values and the values in those intersections (the variations are shown as DDst and DBz in Figure 1). The delay time between Dst and Bz peaks is also determined and is indicated by Dt in Figure 1. This procedure was performed for each storm. For each geomagnetic storm, the hourly values were provided by CDAW Data Center by NASA.This value was corrected in two hours, i.e., the Dst curve was displaced two hours backwards in time, in order to take into account the propagation time, of about 1h.

## Results
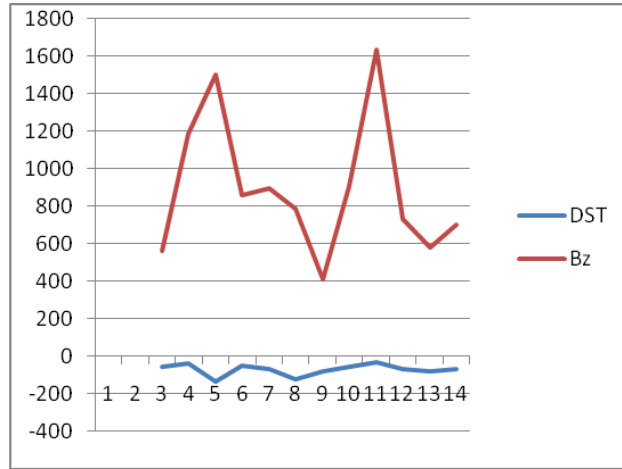


**Figure 2**
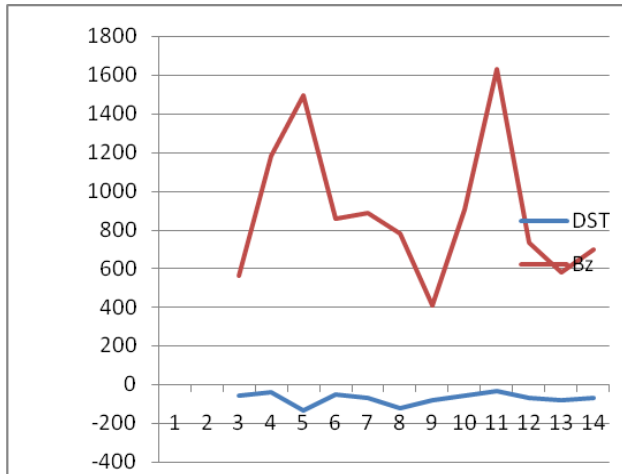


**Figure 3**
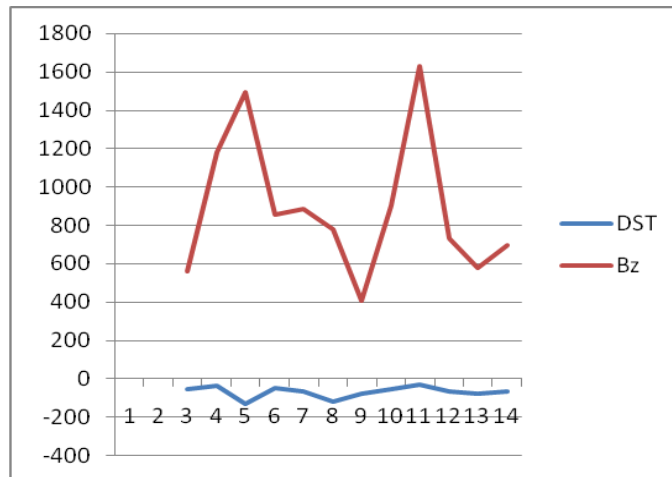


**Figure 4**

Figures 2 and 3 and 4 show examples of geomagnetic storms studied in this work. Both Figures 2 and 3 present the hourly averages of Bz and Dst. The position of peak Dst is marked by a vertical line, whereas the duration of the main phase before this peak is indicated by a horizontal bar. The peak values of Dst and Bz are also indicated by labels.  In Figure 2, the storm during January-December  2011 is shown. This was a typical 'simple', one-step magnetic storm. Thus the Dt between these peaks was of 1 hour in this storm. Dst peak reached 201 nT and Bz peak 23.9 nT. The IMF Bz varied rapidly and reached a peak in a few hours, giving a Bz variation. The Dst index responded slowly and its relative variation. In Figure 3, the storm during January-December  2012 is shown. This was a typical 'simple', one-step magnetic storm. Thus the Dt between these peaks was of 1 hour in this storm. Dst peak reached 201 nT and Bz peak 23.9 nT. The IMF Bz varied rapidly and reached a peak in a few hours, giving a Bz variation. The Dst index responded slowly and its relative variation In Figure 4, the storm during January-December  2013 is shown. This was a typical 'simple', one-step magnetic storm. Thus the Dt between these peaks was of 1 hour in this storm. Dst peak reached 201 nT and Bz peak 23.9 nT. The IMF Bz varied rapidly and reached a peak in a few hours, giving a Bz variation. The Dst index responded slowly and its relative variation

| Table 1.  Average Storm Parameters Storms (2011-2013) | |
|---|---|
| **Parameter** | **Average ± Standard Deviation** |
| Dst peak | 134.6 ± 55.8 nT |
| Bz in the Dst peak | 11.9 ± 7.1 nT |
| Bz peak | 15.6 ± 6.6 nT |
| Dst in the Bz peak | 112.5 ± 58.6 nT |

 Table 1 shows the average and standard deviation parameters for the  storms studied. The values are the Dst peak (Dstpeak), the Bz value during the time of Dst peak (Bz0 ), the Bz peak (Bzpeak), the Dst value during the time of Bz peak (Dst0 ).  We can see that the average delay between the Bz and Dst peaks is around 2 hours. As the main phase duration is around 10 hours, the ratio between these two periods is 0.2. The relative Bz and Dst variations are 0.75 and 0.82. This means that the Bz value at peak Dst is 75%, on average, of the minimum Bz value, while the Dst value at peak Bz is, in average, 82% of the Dst peak.

Above figures show the distribution of the number of storms (left axis; percentage of storms on the right axis) as a function of the delay Dt between the Bz-Dst peaks. It is seen that most of the storms have a delay between 0 – 4 hours (more than 70% of the storms), while Table 1 gave an average of 2 hours. Scheme of Bz and Dst profiles during intense magnetic storms. The peak values of Bz and Dst are indicated by Bzpeak and Dstpeak, the main phase duration by tm, the delay between the Dst-Bz peaks by Dt and the relative variations by DDst and DBz.

Figure 2  Geomagnetic storm during January-December 2011. The Bz and Dst hourly averages are shown. The Dst peak is indicated by a line. This was a typical 'simple', one-step, magnetic storm. Figure 3. Geomagnetic storm during January-December 2012. The Bz and Dst hourly averages are shown. The Dst peak is indicated by a line. This was a typical complex, double-step, magnetic storm.

Table 1. Average Storm Parameters for  Storms (2011 – 2012) Parameter Average ± Standard Deviation Dst peak $134.6 \pm 55.8$ nT Bz in the Dst peak $11.9 \pm 7.1$ nT Bz peak $15.6 \pm 6.6$ nT Dst in the Bz peak $112.5 \pm 58.6$ nT

## Discussion and Conclusions

The main result of the present study indicates that the average delay between the peak Dst value of an intense magnetic storm and the corresponding peak of the driving Bs value is about two hours. Since the average duration of the main phase intervals of the studied storms is 10 hours, this two-hour delay represents 20% of the average main phase duration. Thus, for storm-forecasting purposes, one can expect that the peak of the storm's intensity, as measured by the Dst index, will occur about two hours after the driving Bs component of the IMF has reached its peak value.  It was also found that the Bs value at the time when Dst reaches its peak is, on average, 75% of the peak Bs value, whereas the Dst value at the time when Bs reaches its peak is, on average, 82% of the peak Dst value. These two percentages are somewhat similar. The result shown by Figure 4, that peak Dst occurs with a delay between 0 and 4 hours (with an average of 2 hours) after Bs has reached its peak, may suggest a physical response time of the ring current to the solar wind driver at the peak interval of an intense magnetic storm. This information would be of interest for modeling efforts of the ring

current dynamics and studies of loss processes near the peak of the storm. We should note that delay times between Dst and Bs at other moments of the storm evolution may take different and usually larger time lags [e.g., Gonzalez et al., 1994]. The corresponding result that the Bs value at the time of peak Dst is, on average, 75% of the peak Bs value, could suggest that the storm continues growing for a time interval of about 2 hours, even though Bs is already decreasing in magnitude. Again, this time lag can be associated to the loss processes that need such a time constant to overcome the energy input associated to Bs at this phase (near maximum) of the storm evolution. The two-hour delay can also be used in studies of storms for which one knows the peak Dst value but, for the corresponding solar wind driver, one does not have a measured value of peak Bs, only a modeled value from indirect observations and also one does not know the time at which to select the peak Bs value. This was the case of a recent study of the historical super intense storm of September 2, 1859, for which Tsurutani et al. [2003] assumed a direct and simultaneous time association for the occurrence of the Bs and Dst peaks. In order to do a more complete study of this issue, a more detailed treatment of the data would be necessary, for different levels of Dst domains, since each event is different, both in the shape of the Ey structure as well as in its duration. This type of study is outside the scope of the present letter. To our knowledge, the main results addressed in this letter have not been treated in magnetic storm models, probably because models usually tend to predict specific events, while we have done a more statistical study. Thus, we would like to suggest that coming models, whenever possible, tend to use the information provided by our results.

## Acknowledgments

## References

1. Akasofu, S.-I. (1981), Energy coupling between the solar wind and the magnetosphere, Space Sci. Rev., 28, 121 – 190.

2. Burton, R. K., R. L. McPherron, and C. T. Russell (1975), Empirical relationship between interplanetary conditions and Dst, J. Geophys. Res., 80, 4204 – 4214.

3. Gonzalez, W. D., J. A. Joselyn, Y. Kamide, H. W. Kroehl, G. Rostoker, B. T. Tsurutani, and V. Vasyliunas (1994), What is a geomagnetic storm?, J. Geophys. Res., 99, 5771 – 5792.

4. Kamide, Y., et al. (1998), Current understanding of magnetic storms: Storm-substorm relationships, J. Geophys. Res., 103, 17,705 – 17,728.

5. Tsurutani, B. T., and W. D. Gonzalez (1997), The interplanetary causes of magnetic storm, in Magnetic Storms, Geophys. Monogr. Ser., vol. 98, edited by B. T. Tsurutani et al., p. 77, AGU, Washington, D. C.

6. Tsurutani, B. T., W. D. Gonzalez, G. S. Lakhina, and S. Alex (2003), The extreme magnetic storm of 1 – 2 September, 1859, J. Geophys. Res., 108(A7), 1268, doi:10.1029/2
002JA009504.

# Thermodynamic and Transport Properties of Aliphatic Alcohols with Aqueous Ethylene Glycol

## Chintu J Patel*, Sonam Brahmbhatt#, Vibha Sharma*

*Pacific Academic of Higher education and Research University, Udaipur
#Sarvajanik Science College, Mehsana
chintupatel551@gmail.com

## Abstract

In the current paper the Thermodynamic and Transport Properties of Aliphatic Alcohols with Aqueous Ethylene Glycol were performed by authors. The variation of density ($\rho$) and viscosity (n) data with mole fraction of methanol/ethanol/1-propanol in aqueous ethylene glycol solution is calculated at 308.15 K and presented their experimental results. The experimental values of density and viscosity have been used to calculate the deviation/excess properties like, excess molar volume, deviation in viscosity, excess enthalpy and excess Gibb's free energy of activation of viscous flow.

## Key Word

Thermodynamic, Transport Properties, Enthalpy, Gibb's free energy of activation

## Introduction

Thermodynamic properties of sodium liquid and vapor that have been assessed include: enthalpy, heat capacity at constant pressure, heat capacity at constant volume, vapor pressure, boiling point, enthalpy of vaporization, density, thermal expansion, adiabatic and isothermal compressibility, speed of sound, critical parameters, and surface tension. Transport properties of liquid sodium that have been assessed include: viscosity and thermal conductivity[1]. Transport and thermodynamic properties of a sintered pellet of the newly discovered MgB2 superconductor have been measured to determine the characteristic critical magnetic fields and critical current densities[2]. The ability to obtain reliable thermodynamic and transport properties from a simulation depends both on the quality of the force field and on the use of a proper simulation method. Properties such as densities and heat capacities may be obtained readily using standard techniques. With more effort and advanced simulation methods, solid–liquid and vapor–liquid phase equilibria may also be determined. Transport properties can also be computed, but the

notoriously slow dynamics of many ionic liquid systems means that great care must be taken to ensure that the simulations are accurate[3-5]. Fourteen estimation methods for mixture thermal and transport properties have been compared with each other and with over 1400 experimental data points to facilitate the choice of methods best suited to this application. A statistical analysis of the data (including expected accuracy) is presented and recommendations are made for practical use[6-8].

## Experiment

The chemicals used in the present study are ethylene glycol (mass fraction purity 0.99), methanol (mass fraction purity 0.99), ethanol (mass fraction purity 0.99) (Changshu Yangyuan Chemicals-China make) and 1-propanol (mass fraction purity 0.99) (G.R Grade, obtained from LOBA Chemicals, Mumbai, INDIA). These were further purified by standard methods. The solutions of aqueous ethylene glycol of 0.3 m and 0.9 m are prepared using triply distilled deionised water. These solutions, in turn, are used to prepare liquid mixtures with methanol, ethanol and 1-propanol so that its entire range of composition is covered. All the mixtures have been prepared in the specially designed glass bottles with air tight stoppers and adequate precautions have been taken to minimize evaporations losses. The weighing of solutions has been made using a METTER TOLEDO (Switzerland make) ABB5-S/FACT digital balance with an accuracy of 0.01mg. The ultrasonic velocities, densities and viscosities are measured at 308.15 K for the pure liquids used in this investigation and are compiled in Table 6.A.1 together with the literature data available.

## Result and Discussion

The variation of ultrasonic velocity ($u$) at two different molalities of aqueous ethylene glycol with mole fraction of methanol/ethanol/1-propanol is shown in Figures 6.A.1.a, 6.A.1.b and 6.A.1.c respectively. The ultrasonic velocity increases in the $0 < x < 0.15$ mole fraction of alkanol and it is found to decrease beyond 0.15 mole fraction of alkanol. The ultrasonic velocity shows a maximum value at about 0.15 m mole fraction of methanol/ethanol/1-propanol for 0.3 m and 0.9 m aqueous solutions of ethylene glycol. Water and ethylene glycol are both associated liquids, through the formation of hydrogen bonding. When ethylene glycol is added to water, association between ethylene glycol and water molecules takes place through hydrogen bonding

which is shown in schema I. This leads to the increase of open structures in the solution as diol acts as a structure maker.

**Table 1 Calculated properties of excess molar volume,, deviation in viscosities,, excess enthalpy, and excess Gibb's free energy of activation of viscous flow, with mole fraction of methanol in aqueous ethylene glycol solution at T = 308.15 K**

| mole fraction of methanol | $\dfrac{V_m^E}{10^{-5}m^3} \cdot mol^{-1}$ | $\dfrac{\Delta n}{10^{-3}} N.S.M^{-2}$ | $\dfrac{H^E}{J} \cdot mol^{-1}$ | $\dfrac{\Delta G^{*E}}{kJ} \cdot mol^{-1}$ |
|---|---|---|---|---|
| : 0.3 m aqueous ethylene glycol | | | | |
| 0.0000 | 0.0000 | 0.0000 | 0.0000 | 0.0000 |
| 0.0987 | -0.0241 | 0.1484 | 2885.92 | 0.4855 |
| 0.1968 | -0.0639 | 0.2506 | 4633.85 | 0.7867 |
| 0.3009 | -0.0969 | 0.4342 | 8440.01 | 1.2755 |
| 0.3915 | -0.1156 | 0.4394 | 8296.03 | 1.3218 |
| 0.4944 | -0.1396 | 0.4384 | 8560.21 | 1.3548 |
| 0.5947 | -0.1649 | 0.4445 | 9288.12 | 1.4015 |
| 0.7001 | -0.1684 | 0.4379 | 10197.74 | 1.4311 |
| 0.7963 | -0.1603 | 0.4302 | 11019.46 | 1.4586 |
| 0.8932 | -0.0864 | 0.1198 | 3126.52 | 0.5158 |
| 1.0000 | 0.0000 | 0.0000 | 0.0000 | 0.0000 |
| : 0.9 m aqueous ethylene glycol | | | | |
| 0.0000 | 0.0000 | 0.0000 | 0.0000 | 0.0000 |
| 0.0986 | -0.0321 | 0.1747 | 3414.56 | 0.5270 |
| 0.1937 | -0.0666 | 0.2865 | 5309.62 | 0.8407 |
| 0.2965 | -0.1086 | 0.4464 | 8434.89 | 1.2471 |
| 0.3956 | -0.1430 | 0.4631 | 8510.54 | 1.3223 |
| 0.4939 | -0.1630 | 0.4935 | 9528.62 | 1.4370 |
| 0.5969 | -0.1721 | 0.5128 | 10791.65 | 1.5364 |
| 0.6972 | -0.1759 | 0.5285 | 12139.76 | 1.6292 |
| 0.7957 | -0.1666 | 0.5080 | 12876.90 | 1.6422 |
| 0.8934 | -0.0777 | 0.1207 | 3320.64 | 0.5305 |
| 1.0000 | 0.0000 | 0.0000 | 0.0000 | 0.0000 |

**Table 2 Calculated properties of excess molar volume, deviation in viscosities, excess enthalpy, and excess Gibb's free energy of activation of viscous flow, with mole fraction of ethanol in aqueous ethylene glycol solution at T = 308.15 K**

| mole fraction of ethanol | $\dfrac{V_m^E}{10^{-5}m^3}.mol^{-1}$ | $\Delta n/10^{-3}N.s.m^{-2}$ | $H^E/J.mol^{-1}$ | $\dfrac{\Delta G^{*E}}{kJ}.mol^{-1}$ |
| --- | --- | --- | --- | --- |
| **0.3 m aqueous ethylene glycol** | | | | |
| 0.0000 | 0.0000 | 0.0000 | 0.0000 | 0.0000 |
| 0.0579 | -0.0226 | 0.1467 | 2724.47 | 0.4563 |
| 0.1485 | -0.0829 | 0.2974 | 4759.92 | 0.8231 |
| 0.2275 | -0.1161 | 0.5235 | 8791.25 | 1.2962 |
| 0.3038 | -0.1620 | 0.5649 | 9483.17 | 1.3455 |
| 0.4045 | -0.1911 | 0.5919 | 10126.44 | 1.3702 |
| 0.5094 | -0.1965 | 0.6243 | 11056.27 | 1.4110 |
| 0.6114 | -0.2076 | 0.6824 | 12815.26 | 1.4864 |
| 0.7413 | -0.2064 | 0.6320 | 12353.69 | 1.3697 |
| 0.8611 | -0.1162 | 0.1681 | 3216.98 | 0.4277 |
| 1.0000 | 0.0000 | 0.0000 | 0.0000 | 0.0000 |
| **0.9 m aqueous ethylene glycol** | | | | |
| 0.0000 | 0.0000 | 0.0000 | 0.0000 | 0.0000 |
| 0.0703 | -0.0405 | 0.1836 | 3127.29 | 0.5113 |
| 0.1447 | -0.0807 | 0.2990 | 4646.11 | 0.7765 |
| 0.2265 | -0.1238 | 0.5155 | 8331.90 | 1.2097 |
| 0.3562 | -0.2194 | 0.5827 | 8992.89 | 1.2825 |
| 0.4675 | -0.2580 | 0.6323 | 10286.36 | 1.3466 |
| 0.5585 | -0.2922 | 0.7174 | 12503.67 | 1.4657 |
| 0.6578 | -0.2687 | 0.7099 | 12891.17 | 1.4554 |
| 0.7845 | -0.2429 | 0.5963 | 11604.95 | 1.2576 |
| 0.8593 | -0.1294 | 0.1702 | 3362.19 | 0.4201 |
| 1.0000 | 0.0000 | 0.0000 | 0.0000 | 0.0000 |

**Table 3 Calculated properties of excess molar volume, deviation in viscosities, excess enthalpy and excess Gibb's free energy of activation of viscous flow, with mole fraction of 1-propanol in aqueous ethylene glycol solution at T = 308.15 K**

| mole fraction of 1-propanol | $\dfrac{V_m^E}{10^{-5}m^3}.mol^{-1}$ | $\dfrac{\Delta n}{10^{-3}N.s.m^{-2}}$ | $H^E/J.mol^{-1}$ | $\dfrac{\Delta G^{*E}}{kJ}.mol^{-1}$ |
| --- | --- | --- | --- | --- |
| **0.3 m aqueous ethylene glycol** | | | | |
| 0.0000 | 0.0000 | 0.0000 | 0.0000 | 0.0000 |
| 0.0548 | -0.0266 | 0.1528 | 2791.39 | 0.5071 |
| 0.1167 | -0.0652 | 0.2890 | 5198.57 | 0.8600 |
| 0.1886 | -0.0852 | 0.4295 | 8396.16 | 1.1614 |

| | | | | |
|--------|---------|--------|----------|--------|
| 0.2606 | -0.1005 | 0.5445 | 10624.29 | 1.3600 |
| 0.3448 | -0.1149 | 0.6830 | 13313.32 | 1.5517 |
| 0.4456 | -0.1075 | 0.6495 | 12905.27 | 1.4507 |
| 0.5471 | -0.0921 | 0.5314 | 11258.27 | 1.2118 |
| 0.6934 | -0.0697 | 0.3833 | 8646.65 | 0.8806 |
| 0.8179 | -0.0616 | 0.2269 | 4817.02 | 0.5271 |
| 1.0000 | 0.0000 | 0.0000 | 0.0000 | 0.0000 |
| **0.9 m aqueous ethylene glycol** | | | | |
| 0.0000 | 0.0000 | 0.0000 | 0.0000 | 0.0000 |
| 0.0561 | -0.0344 | 0.1931 | 3498.10 | 0.5666 |
| 0.1159 | -0.0661 | 0.3613 | 6524.07 | 0.9546 |
| 0.1842 | -0.0934 | 0.5648 | 10568.19 | 1.3318 |
| 0.2956 | -0.1384 | 0.6722 | 12391.38 | 1.4664 |
| 0.3565 | -0.1353 | 0.7013 | 12701.41 | 1.4918 |
| 0.4427 | -0.1269 | 0.6490 | 12354.28 | 1.3803 |
| 0.5687 | -0.1009 | 0.5185 | 10552.19 | 1.1264 |
| 0.7086 | -0.0797 | 0.4086 | 8447.68 | 0.8738 |
| 0.8276 | -0.0566 | 0.3144 | 6543.48 | 0.6458 |
| 1.0000 | 0.0000 | 0.0000 | 0.0000 | 0.0000 |

**Table 4 Coefficients $A_i$ of Redlich-Kister type polynomial equation and the corresponding standard deviations ($\sigma$) of all the systems at T = 308.15 K**

| | $A_0$ | $A_1$ | $A_2$ | $A_3$ | $A_4$ | $\sigma$ |
|---|-------|-------|-------|-------|-------|----------|
| **methanol with 0.3 m aqueous ethylene glycol** | | | | | | |
| $\frac{V_m^E}{10^{-5}m^3}.mol^{-1}$ | -0.5610 | 0.4486 | -0.6893 | -0.1101 | 0.9883 | 0.0042 |
| $\Delta n/10^{-3}N.s.m^{-2}$ | 1.7428 | -0.4118 | 2.9995 | 0.4028 | -5.4932 | 0.0435 |
| $\frac{\Delta G^{*E}}{kJ}.mol^{-1}$ | 5.3574 | -2.0166 | 9.6915 | 1.2598 | -15.1140 | 0.1274 |
| **methanol with 0.9 m aqueous ethylene glycol** | | | | | | |
| $\frac{V_m^E}{10^{-5}m^3}.mol^{-1}$ | -0.6435 | 0.4315 | -0.4800 | -0.1062 | 0.8575 | 0.0086 |
| $\Delta n/10^{-3}N.s.m^{-2}$ | 1.9222 | -1.0235 | 3.8448 | 1.6406 | -6.8399 | 0.0457 |
| $\frac{\Delta G^{*E}}{kJ}.mol^{-1}$ | 5.5943 | -3.7065 | 11.8674 | 4.2720 | -18.1980 | 0.1306 |

**ethanol with 0.3 m aqueous ethylene glycol**

| | | | | | | |
|---|---|---|---|---|---|---|
| $\dfrac{V_m^E}{10^{-5}m^3}.mol^{-1}$ | -0.7982 | 0.3354 | -0.6555 | -0.1272 | 1.2166 | 0.0080 |
| $\Delta n$ $/10^{-3}N.s.m^{-2}$ | 2.5069 | -1.4024 | 4.1477 | 4.3499 | -9.3069 | 0.0355 |
| $\dfrac{\Delta G^{*E}}{kJ}.mol^{-1}$ | 5.6534 | -2.2050 | 8.9452 | 9.1388 | -17.1540 | 0.0770 |

**ethanol with 0.9 m aqueous ethylene glycol**

| | | | | | | |
|---|---|---|---|---|---|---|
| $\dfrac{V_m^E}{10^{-5}m^3}.mol^{-1}$ | -1.0891 | 0.6539 | -0.0065 | -0.5462 | 0.6521 | 0.0152 |
| $\Delta n$ $/10^{-3}N.s.m^{-2}$ | 2.6165 | -1.8110 | 4.3198 | 4.9521 | -9.6441 | 0.0474 |
| $\dfrac{\Delta G^{*E}}{kJ}.mol^{-1}$ | 5.4698 | -2.9427 | 9.7249 | 9.7113 | -18.138 | 0.0981 |

**1-propanol with 0.3 m aqueous ethylene glycol**

| | | | | | | |
|---|---|---|---|---|---|---|
| $\dfrac{V_m^E}{10^{-5}m^3}.mol^{-1}$ | -0.4010 | -0.3188 | -0.1032 | 0.4935 | -0.2832 | 0.0033 |
| $\Delta n$ $/10^{-3}N.s.m^{-2}$ | 2.4412 | 1.8690 | -1.1454 | -2.0887 | 1.5341 | 0.0235 |
| $\dfrac{\Delta G^{*E}}{kJ}.mol^{-1}$ | 5.4532 | 4.0268 | -0.6783 | -1.8843 | 3.2200 | 0.0384 |

**1-propanol with 0.9 m aqueous ethylene glycol**

| | | | | | | |
|---|---|---|---|---|---|---|
| $\dfrac{V_m^E}{10^{-5}m^3}.mol^{-1}$ | -0.4709 | -0.3980 | -0.2195 | 0.4635 | 0.1582 | 0.0045 |
| $\Delta n$ $/10^{-3}N.s.m^{-2}$ | 2.3689 | 1.9725 | 1.7280 | -2.0017 | -0.9256 | 0.0122 |
| $\dfrac{\Delta G^{*E}}{kJ}.mol^{-1}$ | 5.0758 | 3.8484 | 3.7201 | -1.3646 | -0.0143 | 0.0229 |

The variation of density ($\rho$) and viscosity ($n$) data with mole fraction of methanol/ethanol/1-propanol in aqueous ethylene glycol solution is calculated respectively. The ñ decreases linearly in all the systems studied where as ç increases considerably up to certain mole fraction beyond

that it decreases slowly with increase in the mole fraction in all the liquid solutions. This non monotonic behaviour can be explained in terms of molecular interactions exists in the present systems.

The experimental values of density and viscosity have been used to calculate the deviation/excess properties like, excess molar volume ($V_m^E$), deviation in viscosity ($\Delta n$), excess enthalpy ($H^E$) and excess Gibb's free energy of activation of viscous flow ($\Delta G^{*E}$). The data obtained for these properties are presented in Tables 1, 2 and 3 for the solutions of methanol/ethanol/1-propanol in the aqueous ethylene glycol solution respectively.

The deviation/excess values are fitted to Redlich-Kister type polynomial equation 3.16 and the corresponding standard deviations, ó are computed using the equation 3.17. The Redlich-Kister coefficients Ai and the standard deviations of all the solutions are presented in Table 4.

## Reference

1. Fink, J. K., and L. Leibowitz. Thermodynamic and transport properties of sodium liquid and vapor. No. ANL/RE--95/2. Argonne National Lab., IL (United States), 1995.

2. Lemmon, Eric W., Marcia L. Huber, and Mark O. McLinden. "NIST reference fluid thermodynamic and transport properties–REFPROP." (2002).

3. Maginn, Edward J. "Atomistic simulation of the thermodynamic and transport properties of ionic liquids." Accounts of chemical research 40.11 (2007): 1200-1207.

4. Mikityuk, Konstantin. "Heat transfer to liquid metal: review of data and correlations for tube bundles." Nuclear Engineering and Design 239.4 (2009): 680-687.

5. Shpil'rain, E. E., et al. "Dynamic and kinematic viscosity of liquid alkali metals." Handbook of thermodynamic and transport properties of alkali metals. 1985.

6. Todd, B., and J. B. Young. "Thermodynamic and transport properties of gases for use in solid oxide fuel cell modelling." Journal of power Sources 110.1 (2002): 186-200.

7. Suwanwarangkul, R., et al. "Performance comparison of Fick's, dusty-gas and Stefan–Maxwell models to predict the concentration overpotential of a SOFC anode." Journal of Power Sources 122.1 (2003): 9-18.

8. Nam, Jin Hyun, and Dong Hyup Jeon. "A comprehensive micro-scale model for transport and reaction in intermediate temperature solid oxide fuel cells." Electrochimica Acta 51.17 (2006): 3446-3460.

# Infrared spectra of ternary complexes using benzidine and quinoline as donors

Ashok N. Patel[1*],  G. K. Solanki[2,], Ajay T. Oza[2]

[1]Sheth M.N. Science College, Hemchandracharya North Gujarat University, Patan-384 265, Gujarat, India

[2]Department of Physics, Sardar Patel University, Vallabh Vidyanagar- 388 120, Gujarat, India

[*]Correspondence: patelashok_patan@yahoo.co.in

**Abstract:** The charge transfer complexes of ternary type are prepared using benzidine and quinoline as donor molecules and studied with FTIR spectroscopy. Direct interband transitions are found around 0.22 eV except TCNE complex. The lower absorption edge is found to be of indirect type. TCNQ and chloranil complexes show half- power beta density and DDQ and TCNE complexes show triangular distributions. Only iodine complex shows Gaussian distribution. The low frequency background absorption is Gaussian distributed in TCNQ, chloranil and iodine complexes. Only TCNE complex shows a square power beta density. Iodine complex has highest conductivity with a range of free-carrier absorption.

**Keywords:** Infrared, ternary complexes, beta density, Gaussian distribution, nature of transition

**Introduction**

The earlier studies on ternary organic CT complexes included doped $(TMTSF)_2$ $ClO_4$, alkyl-ammonium donors with TCNQ-iodine, pyrene-TCNQ-ferrocene, substituted anthraquinone complexes and others [1-6]. $(TMPD)_{1.5}$ –KI-$I_2$ and $(TMPD)_{1.5}$ –HI-$I_2$ can be also considered as ternary systems [7]. There are two types of ternary systems. (1) one-donor and two-acceptor based systems which include, K-$(BEDT-TTF)_2$ $Cu[(CN)_2]NX$ where X=Cl, Br, I, $(C_1-TET-TTF)(FeBr_4)_{1-x}$ $Fecl_4)_x$ etc. [8-15] some of which were organic superconductors. (2) Two-donors and one acceptor based systems including $\alpha$-$(BEDT-TTF)_2MHg(SCN)_4$ where M=K,$NH_4$, $\alpha$-$(BEDT-TTF)_2RbZn(SCN)_4$ and $\beta$-$(CH_3)_4AS[Pd(dmit)_2]$ [16-23],  some of which were also superconducting. Ternary charge transfer complexes and radical-ion salts

possess unique physical properties which are absent in binary (bimolecular) complexes. These properties include two-band transport, incommensurate to commensurate transition, alloy properties, cooperative and competitive binding, more than two oscillator models or three absorption envelopes, complex-salt character, superconduction and electron-exciton interactions. In the present work, we report CT complexes of benzidine-quinoline-$(TCNQ)_2$, benzidine-quinoline-$(TCNE)_2$, benzidine-quinoline-$(chloranil)_2$, benzidine-quinoline-$(DDQ)_2$ and benzidine-quinoline-$(I_2)_2$ all in 1:1:2 molecular weight proportions.

**Experimental**

The donor benzidine was grinded with acceptors like TCNQ(7,7,8,8-tetra-cyano-p-quinodimethane), TCNE(N,N,N′,N′-tetracyano-p-ethylene), chloranil (2,3,5,6-tetrachloro-p-benzoquinone), DDQ(2,3-dichloro-5,6-dicyano-p-benzoquinone) and iodine in 1:2 molecular weight proportions. The liquid donor quinoline was added with the help of micropipette in a few drops needed in molecular weight proportions to form 1: 1:2 ternary complexes. The infrared spectra were recorded using a standard Perkin-Elmer spectra-photometer on the KBr-based semi-transparent pellets of all the five ternary complexes.

**Results and discussion**

The first is the infrared spectrum of benzidine-quinoline-$(TCNQ)_2$ which is shown here (Figure 1a). This spectrum can be divided in to three parts according to background absorption governed by electronic absorption. The first range is the 1700-3600 $cm^{-1}$ where a very broad half-power beta density distribution is observed given by

$$\alpha = \alpha_0 E^{*1/2}(1-E^*)^{1/2} \qquad (1)$$

where $E^* = (E-a)/b$ is the reduced, dimensionless energy variable.

But difference in the spectrum between this and that of benzidine-pyridine-$(TCNQ)_2$ reported recently is in the splitting of the above distribution at 2317 $cm^{-1}$ by a dispersion shape of $\varepsilon_1(\omega)$ the real part of dielectric constant. Because of this splitting the distribution becomes asymmetric below 2317 $cm^{-1}$. The second range 1700-2170 $cm^{-1}$ correspond more to a transition across the usual band gap around 1700 $cm^{-1}$, rather than being a part of beta density. This splitting and asymmetry arise from stronger interaction between quinoline and TCNQ than pyridine-TCNQ interaction. The third part is below 1700 $cm^{-1}$ down to 500 $cm^{-1}$. This range consists of a very broad symmetric Gaussian band around 1100 $cm^{-1}$. There are no

two envelopes below 1700 cm$^{-1}$. This also is a consequence of strong interaction between quinoline and TCNQ.

The second spectrum is that of benzidine-quinoline-(DDQ)$_2$ (Figure 1b). Here too, the spectrums can be divided in three main parts. The first range is above 1800 cm$^{-1}$ where a very large triangular distribution centered around 3082 cm$^{-1}$ is observed. This is a consequence of screening of interaction between benzidine and DDQ by quinoline. In this range, spectrum significantly differs from that of TCNQ complex. This arises from asymmetric nature of DDQ molecule leading to more electronic molecular polarizability. It can not be attributed to the halogen end- group interacting with donor because iodine complex shows different features in this range.

The triangular distribution can be attributed to the nesting of Fermi surface, i.e. scattering of q=2k$_F$ electrons by phonons, which remains imperfect as revealed by an symmetric distribution. Then comes the second range which contains an interband electronic transition.

The third range is below 1800 cm$^{-1}$ down to 400 cm$^{-1}$. The background absorption is a monotonic function rather than a Gaussian distribution, the later found in the TCNQ complex. The absorption decreases as the frequency (or energy) decreases. The absorption is minimum at or below 0.05eV (400 cm$^{-1}$). Thus in the both ranges spectrum differs for DDQ complex from that of the TCNQ complex. Benzidine-DDQ interaction is stronger than benzidine-TCNQ interaction. Benzidine is enable to screen strongly in the DDQ complex. There is a steep rise in transmission above 1560 cm$^{-1}$ towards the high frequency side. The absorption is minimum near 1750 cm$^{-1}$ and there is a long band-tailing towards low frequency side. This may be related with imperfect nesting leading to this feature [24]. The real part of optical conductivity $\sigma_1$ ($\omega$) and the imaginary part of dielectric constant $\varepsilon_2$ ($\omega$) are related. If we look at the high-frequency behaviour, it is a broad dispersion shape between 3600 cm$^{-1}$ and 1750 cm$^{-1}$. The constant high frequency background above 3600 cm$^{-1}$ is extrapolated and considered to be zero level, the curve in 1750 – 3600 cm$^{-1}$ is cut to give a dispersion shape governed by $\varepsilon_1$ ($\omega$). There is anomalous dispersion in this range. It is a fluctuation in absorption around zero level and if we apply lever rule, there is no net absorption. The integration (area under the band) is almost zero in this range.

The second range of absorption below 1400 cm$^{-1}$ mainly consists of absorption across a very small band gap (E$_g$<0.05 eV). These transitions coupled two bands through a Gaussian distribution in the TCNQ salts. The transitions are hindered in TCNQ complex while the

transitions occur without being screened in the DDQ complex. In both of TCNQ and DDQ complexes, the lowest-lying envelope around 750 cm$^{-1}$ is not observed because it merges in the mid-IR envelope.

The third spectrum is that of benzidine-quinoline-(chloranil)$_2$ (Figure 2a). In this case, three envelopes are observed because of lack of delocalization due to screening effect. Benzidine-chloranil binary complex is weaker in interaction than benzidine-DDQ binary complex. As a result, the interaction is screened by quinoline molecules. The highest-lying half power beta density envelope is somewhat similar to the one found in the TCNQ complex but somewhat asymmetric rather than symmetric with more absorption on high-frequency side. This is between 1800 cm$^{-1}$ and 3600 cm$^{-1}$. The mid-IR envelope between 1000 cm$^{-1}$ and 1800 cm$^{-1}$ is also a flat beta density peak following a half-power law as given by equation 1. In this case, sharp bands are neglected and either background is considered or inflexion points of the spikes are joined. The lowest lying Gaussian-shaped envelope around 750 cm$^{-1}$ is clearly seen. Thus the spectrum is similar to that of benzidine-pyridine-(chloranil)$_2$.

The next is the IR spectrum of benzidine-quinoline-(TCNE)$_2$ (Figure 2b). The interaction is stronger than in the chloranil complex. The high-frequency envelop above 1800 cm$^{-1}$ is a triangular envelope associated with imperfect nesting as observed in the DDQ complex. This similarity reveals that this special spectral feature arises out of molecular polarizability of TCNE. TCNE does not contain aromatic ring as in TCNQ but contains C=C bridge. The four cyano-groups are more flexible and rotatable in three-dimensions leading to orientational polarizability. These rotations are hindered by the charge cloud of aromatic ring in TCNQ.

The mid-IR envelope between 950cm$^{-1}$ and 1800 cm$^{-1}$ is highly asymmetric with low-frequency tailing as compared to the envelope of chloranil complex. The lowest-lying envelope between 400 cm$^{-1}$ and 900 cm$^{-1}$ shows with square power beta density asymmetric distribution compared to that in the case of chloranil complex.

Thus there are two triangular distributions around 3000 cm$^{-}$ and 1400 cm$^{-1}$. The one at higher frequency is due to nesting of Fermi surface and the other at lower frequency is due to triangular interband gap connected with slant band edges in internal electric field. The later is related with tunneling of charge carriers.

The last spectrum of benzidine-quinoline-(iodine)$_2$ is also shown (Figure 2c). This spectrum is similar to its pyridine analog above 1700 cm$^{-1}$. The range below 1700 cm$^{-1}$ consists of a large number of absorption bands but leaving a scope for the background absorption which

increases as the frequency decreases. This may correspond to a negative band gap as in semi-metals or free-carrier absorption above a very small band gap lying in far-infrared range. Also there is a possibility of a transition to an impurity level [25].

There is almost a semicircular distribution related with either isotropically disordered and positively charged quinoline molecules or disordered molecular iodine in this ternary complex. There is a small range of free carrier absorption between 1400 cm$^{-1}$ and 1600 cm$^{-1}$. This is realized by increase in absorption with an increase in wavelength of EM waves.

The beta density distribution is the fitted for the TCNQ complex having the highest-frequency envelope of this type. The plot of F/(1-k*)$^{1/2}$ vs k*$^{1/2}$ where F=$\alpha$-$\alpha_0$ and K$^*$=(K-a)/b is a straight line indicating half-power beta density based on Bernoulli trials (Figure 3a). The broad lower frequency envelope is fitted a Gaussian distribution (Figure 3b) described by

$$A = A_0 \exp\left(\frac{\left(K - K_0\right)^2}{2M_2}\right) \quad (2)$$

where $A_0$ is the maximum absorption, $K_0$ is the central wave-number and $M_2$ is the second moment of the distribution. This last parameter is related with the full-width at half-maximum W according to

$$M_2 = \frac{W^2}{8\ln 2} \quad (3)$$

W is in turn related with electron-phonon coupling constant. Strong electron-intermolecular vibration coupling in TCNQ complex leads to very broad Gaussian band spanning more than half-IR-range and leads to a merging of central envelope and lowest-lying envelope associated with rocking and wagging vibrations. The part of the profile lying above the 2170 cm$^{-1}$ split, is fitted for a nature of transition. This transition is found to be allowed direct type (Figure 3 c), not involving any phonon.

Next is the analysis of spectrum of benzidine-quinoline-(DDQ)$_2$. The analysis indicates that the higher transition across the gap of about 0.2 eV is forbidden direct and the lower transition across the gap of nearly 0.05 eV is indirect and forbidden type. The lower band gap can be assigned to the quinoline- DDQ interaction because it is not found in the spectrum of binary benzidine-DDQ system. This analysis is shown (Figure 4a and 4b)

These graphs reveal direct exciton band around 0.25 eV and involvement of phonon of energy 0.01 eV, in the cases of a forbidden direct transition and forbidden indirect transition,

respectively. In the later case the break between phonon absorption and phonon emission is found at 0.15 eV.

Similar analysis of the nature of transition for the chloranil complex is also carried out (Figure 5a) having indirect exciton. An allowed direct transition is evident. The high-frequency and mid-IR envelopes are both beta distribution with half-power beta densities (Figure 5b and 5c). The lowest-frequency envelope is analyzed to be Gaussian curve (Figure 5d).

Thus there is an allowed direct transition with a break due to indirect exciton at 0.245 eV and exciton threshold at 0.225 eV. The Gaussian envelope has maximum absorption , central wavenumber and full-width at half maximum (FWHM) as noted in Table 2.

More strongly interacting TCNE-based ternary complex shows two band gaps of 0.2 eV and 0.1 eV with corresponding forbidden indirect and allowed indirect transitions, respectively (Figure 6a and b). Thus TCNE complexes are small band gap semiconductor-phonon

The higher edge at 0.21 eV shows a break in $(\alpha h\nu)^{1/3}$ Vs $h\nu$ (eV) transition involving a phonon of energy of 0.02 eV. The TCNE complex also shows a square power beta density in the IR spectrum around 700 cm$^{-1}$. The analysis of the last spectrum of benzidine-quinoline-(iodine)$_2$ complex reveals an allowed direct transition (Figure 7a) and two Gaussian envelopes (Figure 7b and 7c).

The plot of allowed direct transition shows a direct exciton of energy of 0.24 eV. There are two Gaussians whose parameters are tabulated in table 2. The analysis of free-carrier absorption is made by plotting $\log\alpha$ Vs $\log\lambda$ giving a slope of 2-5 which corresponding to scattering of charge carriers by phonons.

Details of upper and lower absorption edges and both absorption envelopes are summarized (Table 1)


## Conclusion

The three out of five ternary complexes based on TCNQ, DDQ and iodine show unusual spectral features which are making use of benzidine-quinoline combination. The TCNQ complex shows merging of two lower envelopes with unusually broad Gaussian band DDQ complex shows two triangular distributions related with imperfect nesting and the second due to one Franz-Keldy effect. TCNE and chloranil show three envelopes related with three band

model. Iodine complex seems to be having highest conductivity because of negative band gap or free-carrier absorption.

**References**:

[1]  C. Coulon, S. Flandrois, P. Delhaes, C. Hauw, P. Dupis, Phys. Rev. B, 1981, 23, 2850.

[2]  C. Coulon, P. Delhaes, J. Amiell, J. P. Monceau, L. M. Fabre, L. Giral, J. Physique (France), 1982, 43, 1721.

[3]  Andre Barraud, Pierre Lasieur, Annie Ruaudel-Teixier, Michel Van Devyer, Thin Solid Filam, 1995, 134, 195.

[4]  M. G. Abd El Wahed, S. Aaly, H. A. Hammad, S. M. Metwally,  J. Phys. Chem. Solids, 1974, 55, 31.

[5]  K. Kudo, M. Nagqoka, S. Kuniyoshi, H. Tanaka, Synthetic Metals**,** 1995, 71, 2059.

[6]  Jeong-Woo Choi, Gun-Yung Jung, Se Young Oh, Won Hong Lee, Dong Myung Shin, Thin Solid Films**,** 1996, 284-285, 876.

[7]  A.T. Oza, Solid State Commun., 1989, 71, 1005.

[8]  J. Wosnitza, H. Elsinger, J. Hagel, S. Wanka, D. Schweizer, Synthetic Metals, 2001, 120, 705.

[9]  J. J. McGuire, T. Room, A. Pronin, T. Timusk, J. A. Sch-Wieter, M. E. Kelly, M. A. Kini, Phys. Rev. B**,** 2001, 64, 094503.

[10]  S. Kamiya, Y. Shimojo, M. A. Tanatar, T. Ishiguro, H. Yamohi, G. Saito, Phys. Rev. B, 2002, 65, 13410.

[11]  K. D. Truong, S. Jandl, M. Poirier, Synthetic Metals, 2002, 130, 229.

[12]  Akane Sato, Hiroki Ahutsu, Kazuya Saito, Michio Sorai, Synthetic Metals, 2001, 120, 1035.

[13]  A. Paoneli, A. Girlando,  A. Fortuneli, Phys. Rev. B, 2001, 64, 054509.

[14]  M. A. Tanatar, S. Kagoshima, T. Ishiguro, H. Ito, V. S. Yefanov, V. A. Bonderenko, N. D. Kushah, E. B. Yagubskii, Phys. Rev. B, 2000, 62, 15561.

[15]  M. Enomoto, A. Miyazaki, T. Enoki, Synthetic Metals, 2001, 121, 1800.

[16]  D. Andres, M.V. Kartsovnite, W. Biberacher, H. Weiss, E. Balthes, H. Muler, N. Kulshch, Phys. Rev. B, 2001, 64, 161104.

[17]   N. Harrison, C.H. Mielke, A.D. Christianion, J.S. Brooks, M. Tokumoto, Phys. Rev. Letters, 2001, 86, 1586.

[18]   N. Harrison, L. Balicas, J.S. Brooks, M. Tokumoto, Phys. Rev. B, 2000, 62, 14212.

[19]   M. Maesato, Y. Kaga, R. Kondo,  S. Kagoshima, Phys. Rev. B.,  2001, 64, 155104.

[20]   M. Maesato, Y. Kaga, R. Kondo, H. Hirai, S. Kagoshima, Synthetic Metals, 2001, 120, 941.

[21]   Y. Shimajo, T. Ishiguro, H. Yamochi, G. Saito, Synthetic Metals, 2001, 120, 751.

[22]   N. L. Wang, H. Mori,  S. Tanaka, J. Dong, B.P. Claymany,  J. Phys. Condens. Matter, 2001, 13, 5463.

[23]   Reizo Kato, Naoya Tajima, Masafumi Tamura,  Jun-Ichi Yamaura, Phys. Rev. B, 2002, 66, 020508.

[24]   Balazs Dora, Kazumi Maki, Attila Virosztek, Phys. Rev. B, 2002, 266, 15116.

[25]   J.I. Pankove; Optical processes in semiconductors, Eglewood Cliffs, Prentice – Hall Inc., New Jercy, 1971.

**Table 1.** **Infrared absorption edges for the ternary complexes based on benzidine quinoline combination.**

| Name of the complex | Upper edge | | | Lower edge | | |
|---|---|---|---|---|---|---|
| | Absorption function | Type of transition | Band gap $E_g$ (eV) | Absorption function | Type of transition | Band gap $E_g$ (eV) |
| Benzidine-quinoline-$(TCNQ)_2$ | $\alpha h\nu = A(h\nu - E_g)^{1/2}$ | Allowed direct | 0.22 | — | — | — |
| Benzidine-quinoline-$(DDQ)_2$ | $\alpha h\nu = A(h\nu - E_g)^{3/2}$ Direct exciton 0.25 eV $E_p = 0.01$ | Forbidden direct | 0.18 | $\alpha h\nu = A(h\nu - E_g)^{3}$ Phonon $E_p = 0.01$ eV | Forbidden indirect | 0.006 |
| Benzidine-quinoline-$(chloranil)_2$ | $\alpha h\nu = A(h\nu - E_g)^{1/2}$ Indirect exciton 0.23eV | Allowed direct | 0.22 | — | — | — |
| Benzidine-quinoline-$(TCNE)_2$ | $\alpha h\nu = A(h\nu - E_g)^{3}$ Phonon 0.02 eV | Forbidden indirect | 0.21 | $\alpha h\nu = A(h\nu - E_g)^{2}$ | Allowed indirect | 0.11 |
| Benzidine-quinoline-$(I_2)_2$ | $\alpha h\nu = A(h\nu - E_g)^{1/2}$ Direct exciton 0.16 eV | Allowed direct | 0.21 | — | — | — |

**Table 2. Types and parameters of electronic absorption envelopes in the spectra of ternary complexes based on benzidine-quinoline combination.**

| Name of the complex | First envelope | | | Second envelope | | |
|---|---|---|---|---|---|---|
| | $K_o$ (cm$^{-1}$) | $\delta K$ (cm$^{-1}$) | $\alpha_m$ % | $K_o$ (cm$^{-1}$) | $\delta K$ (cm$^{-1}$) | $\alpha_m$ % |
| Benzidine-quinoline-(TCNQ)$_2$ | 2800 (Half power-Beta density) And NT-1 | 1300 | 30% | 1100 (Gaussian distribution) NT-2 | 1050 | 35% |
| Benzidine-quinoline-(DDQ)$_2$ | 3200 (Triangular distribution) | 1100 | 50% | NT-1 and 2 | | |
| Benzidine-quinoline-(chloranil)$_2$ | 2800 (Half-power beta density) 1400 (Half power beta density) | 1700 800 | 20% 16% | 770 (Gaussian distribution) | 600 | 16% |
| Benzidine-quinoline-(TCNE)$_2$ | 3200 (Triangular distribution) 1450 (TD) | 1200 500 | 65% 60 | SPBD 650 | 250 | 35 |
| -Benzidine-quinoline-(Iodine)$_2$ | 2800 (Gaussian distributions) Or CD | 1700 | 25% | 850 (Gaussian distribution) | 800 | 20% |

**Figure 1.** Infrared spectra of
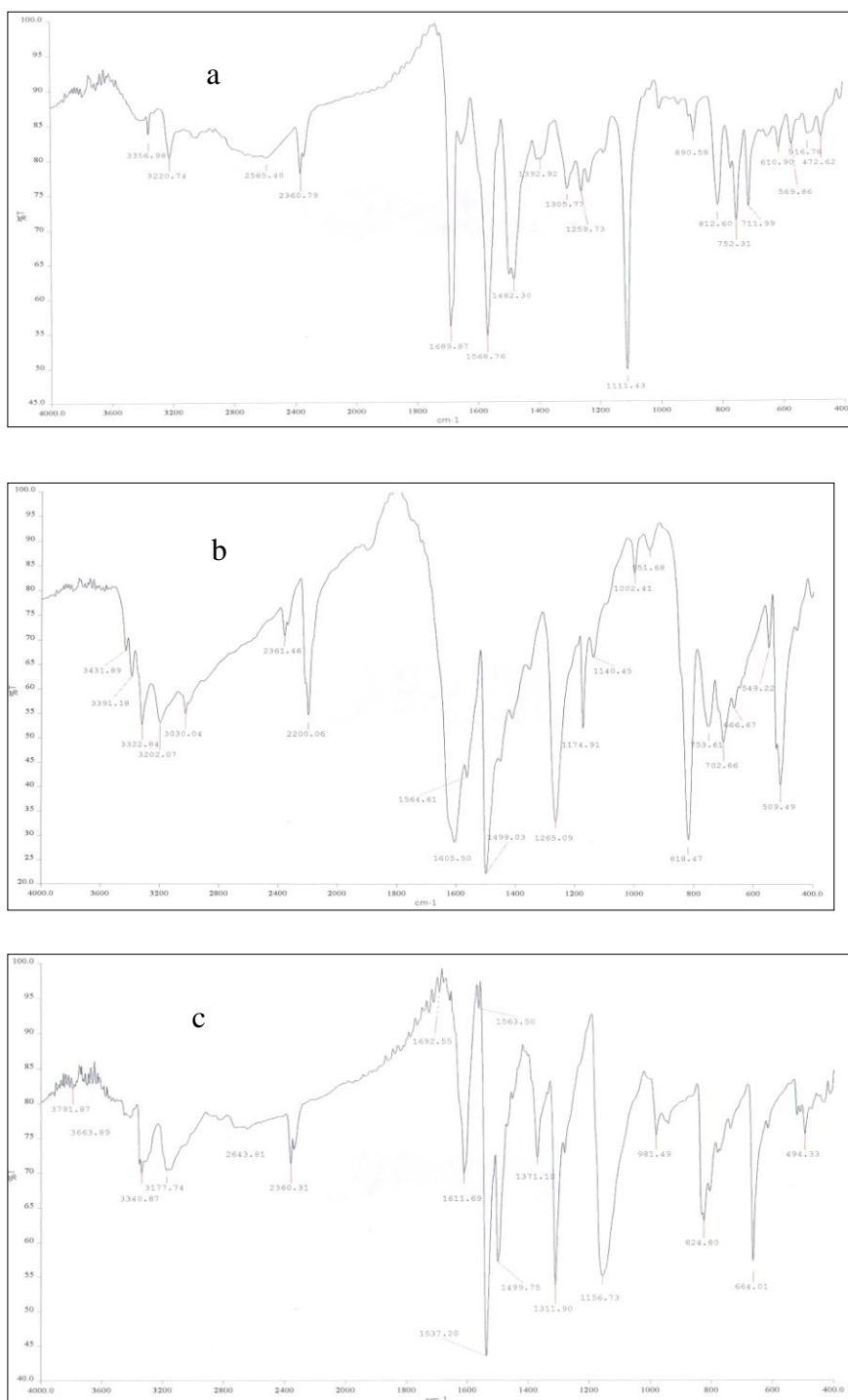
    (a)    benzidine-quinoline-$(TCNQ)_2$ and

    (b)    benzidine-quinoline-$(DDQ)_2$.

**Figure 2.**      Infrared spectra of

(a) benzidine-quinoline-(chloranil)$_2$

(b) benzidine-quinoline-(TCNE)$_2$ and

(c) benzidine-quinoline-(iodine)$_2$.

Benzidine-Quinoline-(TCNQ)$_2$
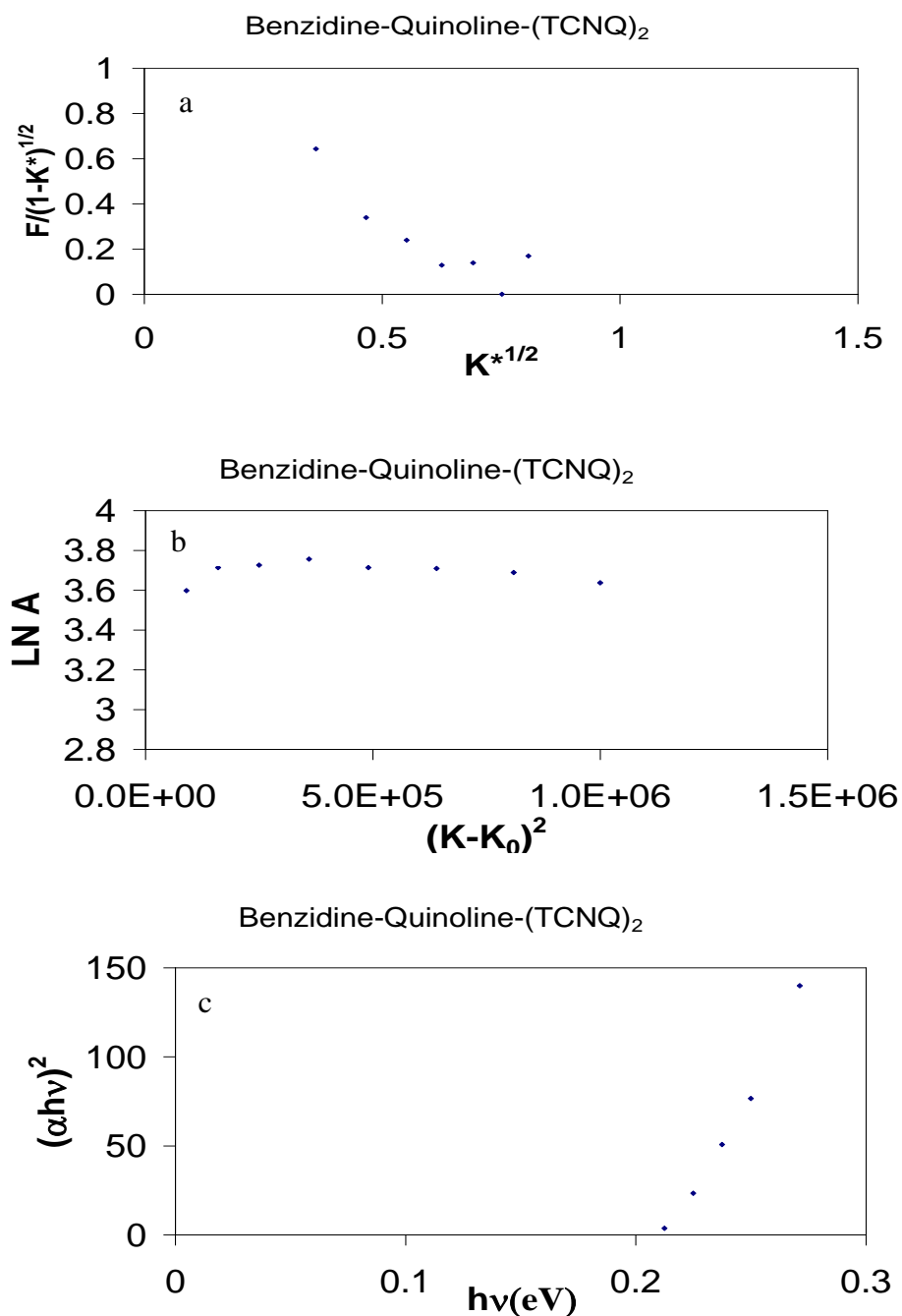
**Figure 3.**　　　(a) Beta density fit

(b)Gaussian fit and

(c) Nature of transition above 0.2 eV gap

– all of the TCNQ complex.
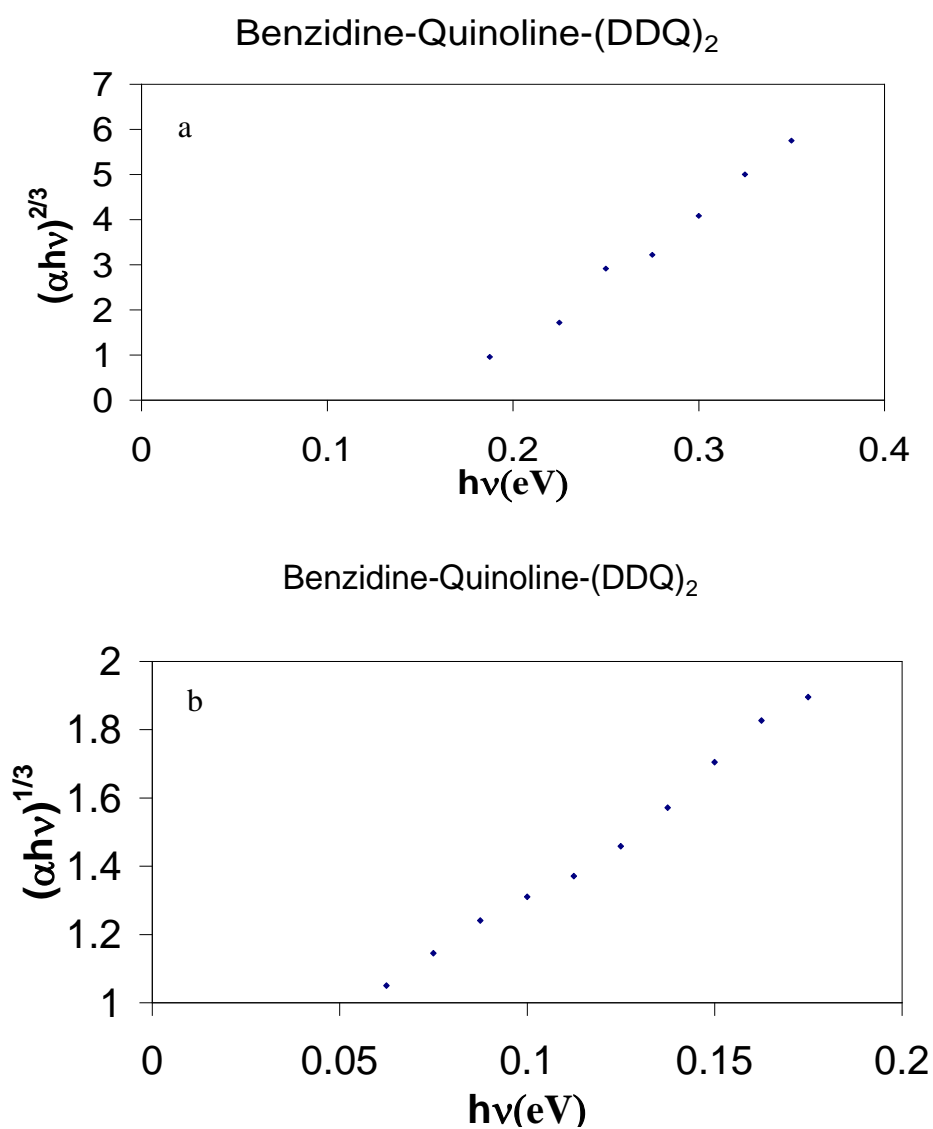
**Figure 4.** (a) Nature of transition above 0.2 eV gap and

(b) nature of transition above 0.05 eV gap.

**Figure 5.** (a) Nature of transition above 0.225 eV gap with indirect exciton
(b) beta density peak
(c) second beta density peak and
(a) Gaussian band analysis.
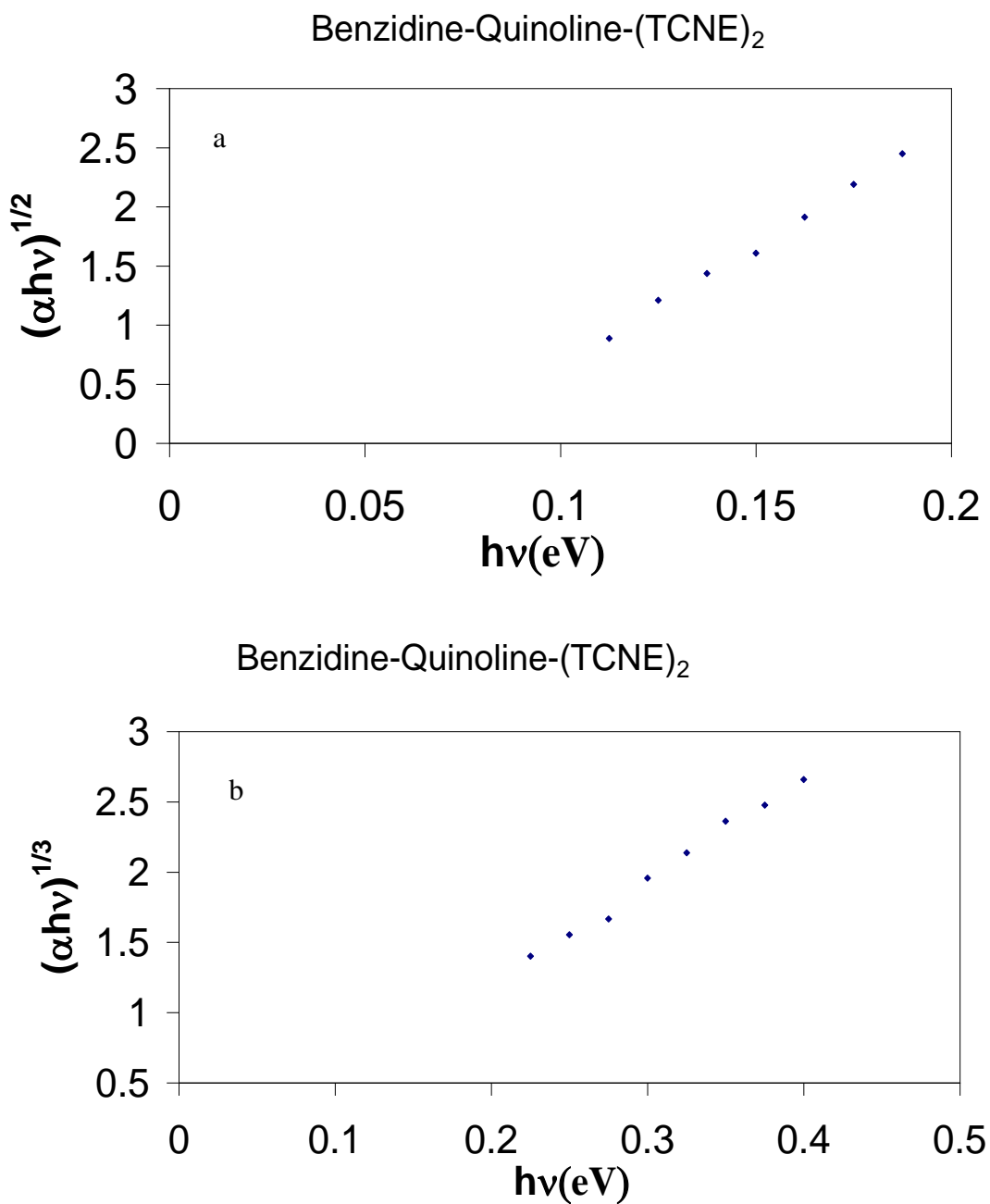
**Figure 6.**  (a) nature of transition above 0.1 eV gap and
(b) nature of transition above 0.2 eV gap.
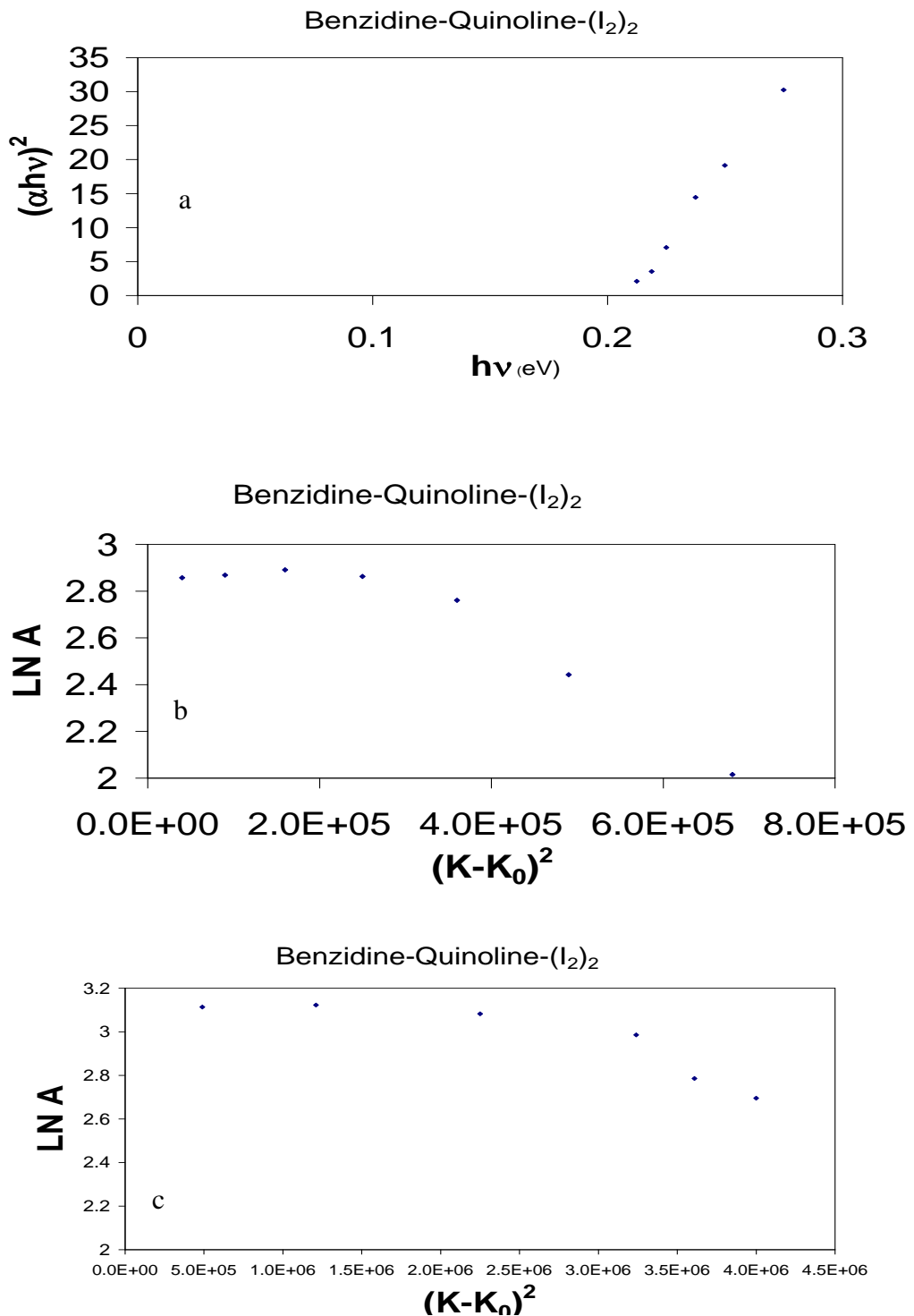
**Figure 7.**  (a) Nature of transition above 0.21 eV gap

(b) The first Gaussian peak and

(c) The second Gaussian peak.

# Elastic Properties of Titanium-based $Ti_{44}Zr_{20}V_{36}$ bulk metallic glass

## P.G. Chaudhari[1], S.G. Khambholja[2] and B.Y.Thakore[3]

[1]Department of Physics, Sheth M. N. Science College, Patan-384265, Gujarat, India

[2]Department of Science & Humanities, B & B Institute of Technology, Vallabh Vidyanagar-388120, Gujarat, India

[3]Department of Physics, Sardar Patel University, Vallabh Vidyanagar-388120, Gujarat, India

[1]email: *chaudhariprakruti@yahoo.com*

[2]email: *physik.shyam@gmail.com*

[3]email:*brijmohanthakore@rediffmail.com*

**Abstract:** Using Hubbard-Beeby approach and our newly proposed model potential, phonon modes and elastic properties of titanium-based $Ti_{44}Zr_{20}V_{36}$ BMG are evaluated. Five different forms of the local field correlation functions viz. Hartree (H), Taylor (T), Ichimaru and Utsumi (IU), Farid et al (F) and Sarkar Sen et al (S) are used to investigate the influence of the screening effects on vibrational dynamics of $Ti_{44}Zr_{20}V_{36}$ bulk metallic glass. The results for bulk modulus B, modulus of rigidity G, Poisson's ratio $\xi$, Young modulus Y propagation velocity of elastic waves and dispersion curves are studied. The theoretical computations are found to be in good agreement with the available experimental results.

**Keywords:** Phonon frequencies, elastic constant, model potential

**PACS:** 81.05 Kf; 63.50. Lm; 62.20.dq

## Introduction

Recent progress in 2-phase alloys with a glassy matrix phase that exhibits large glass-forming ability (GFA)[1,2] in ductile-phase–reinforced bulk metallic glass(BMG) composites has demonstrated that with proper design and microstructure, control enhanced toughness and tensile ductility can be achieved. Mechanical, magnetic, elastic properties, thermo plastic behavior and bond properties of material are one of key issues for both scientific significance and practical application in condensed matter physics [3, 6].

For the commercialization of these new alloys (in present case, Zr-based composites) reducing the cost and density of composites is beneficial. Low density components with high toughness and strength could be particularly useful in aerospace and aeronautics industry as replacements for some crystalline titanium alloy hardware. Ti-based BMG composites are competitive with conventional titanium alloys for some structural applications where high strength and toughness are necessity. The elastic properties of metallic glass can be roughly predicted to guide the selection of alloying elements for developing Ti-based bulk metallic glass (BMG) with larger glass forming ability (GFA). In present paper, focus is given on the $Ti_{44}Zr_{20}V_{36}$ bulk metallic glass (BMG) and the computation is carried out for phonon dispersion curve, bulk modulus B, modulus of rigidity G, Poisson's ratio $\xi$ and Young modulus Y [6-9].

Our new model potential represented as the combination of linear and quadratic terms modulated by repulsive exponential damping factor, which tends to cancel Coulomb potential, inside the core. While outside the core, it has the Coulombian tail. It becomes zero at r = 0 and smoothness of the bare-ion potential due to exponential term results in to faster convergence in r-space. In addition this bare-ion potential is continuous at the core separation. Potential parameter is estimated through nearest neighbor distance. This form has feature of a Columbic term outside the core and varying cancellation due to a repulsive and an attractive contribution to the potential within the core. It is assumed that the potential within the core should neither be zero nor constant but it should very as a function of r. Thus the model potential has the novel feature of representing varying cancellation of potential within the core over and above its continuity and weak nature.

The newly bare-ion model potential used in the present investigations, in r-space, is of the form [10].

$$W(r) = \frac{-Ze^2e^*}{r_c}\left[\frac{2r}{r_c} - \frac{r^2}{r_c^2}\right]e^{\frac{-r}{r_c}} \qquad ; r \le r_c$$

$$= \frac{-Ze^2}{r} \qquad\qquad ; r \ge r_c \qquad (1)$$

It may be noted that the above form of the potential contains only single parameter $r_c$ and is calculated formula, is given in Ref.[5].

$$r_c = \left[\frac{0.51 \cdot r_s}{Z^{1/3}}\right] \qquad (2)$$

Here, Z, $\Omega$, q, e, $r_s$ are the valency, atomic volume, wave vector, charge of electron and the parameter of the potential respectively.

Five different forms of the local field correlation functions viz. Hartree (H) [11], Taylor (T) [12], Ichimaru and Utsumi (IU) [13], Farid et al (F) [14] and Sarkar Sen et al (S) [15] are employed for investigation of relative effect of local field correction function on phonon dispersion curve (PDC) and elastic properties of $Ti_{44}Zr_{20}V_{36}$ Bulk metallic glass.

## Theory

For bulk metallic glass, effective interaction pair potential is written as following.

$$V_{eff}(r) = \left(\frac{Z_{eff}^2 e^2}{r}\right) + \frac{\Omega_{eff}}{\pi}\int F_{eff}(q)\left[\frac{\sin(qr)}{qr}\right]q^2 dq \qquad (3)$$

Here $Z_{eff}$ and $\Omega_{eff}$ are the effective valance and atomic volume of present system respectively.

The theoretical calculation of the elastic properties of BMGs is based on the pair potential between ions. 1st term is the direct columbic interaction between ions, which is repulsive and 2nd term represents the indirect columbic interaction between ions via electron cloud, which cause the attractive interaction. $F_{eff}(q)$ determines the long range behavior of inter atomic forces is also known as volume energy term.

The energy wave number characteristics appearing in the equation (3) is written as below [6,7].

$$F_{eff}(q) = \frac{-\Omega_{eff}}{16\pi}\left|V_b^{eff}(q)\right|^2 \frac{(\varepsilon_H^{eff}(q)-1)}{(\varepsilon_H^{eff}(q)-1)(1-f_{eff}(q))} \qquad (4)$$

Here, $V_b^{eff}(q)$ is the effective bare ion potential in q space , $\epsilon_H^{eff}(q)$ is the Hartree dielectric response function. $f_{eff}(q)$ is the local field correction function to incorporate the exchange and correlation effects. The pair correlation function g(r), is computed theoretically from the effective pair potential as,

$$g\,(\,r\,) = \quad \exp\!\left(\frac{-V_{eff}}{k_B\,T}\right) - 1 \tag{5}$$

Here, $k_B$ is the Boltzmann' constant and T is the absolute temperature.

According to Hubbard and Beeby approach [7], the longitudinal and transverse phonon frequencies are given by following equations (6) and (7), respectively.

$$\omega_L^2(q) = \omega_E^2\left[1 - \frac{3\sin(q\sigma)}{q\sigma} - \frac{6\cos(q\sigma)}{(q\sigma)^2} + \frac{6\sin(q\sigma)}{(q\sigma)^3}\right] \tag{6}$$

$$\omega_T^2(q) = \omega_E^2\left[1 - \frac{3\cos(q\sigma)}{(q\sigma)^2} + \frac{6\sin(q\sigma)}{(q\sigma)^3}\right] \tag{7}$$

$\omega_E$ represents the maximum phonon frequency and is given as,

$$\omega_E = \frac{4\pi n_{eff}}{3\,M_{eff}}\int_0^\infty g(r)r^2 V_{eff}''(r)dr \tag{8}$$

$$V_{eff}''(r) = \frac{4Z^2}{r^3} + \frac{\Omega_{eff}}{\pi^2}\int_0^\infty F(q)\left[\frac{2\sin(qr)}{qr^3} - \frac{2\cos(qr)}{r^2} - \frac{q\sin(qr)}{r}\right]dq \tag{9}$$

Here, $\rho$, $M_{eff}$, $\Omega_{eff}$ and f(q) are the number density, atomic mass, atomic volume and energy wave number characteristic, respectively. Sound velocities are calculated from long-wavelength limit of phonon dispersion curve, where phonon frequencies are linear.

Various elastic properties are then determined by the longitudinal and transverse phonon frequencies. The bulk modulus B, Poisson's ratio $\xi$, modulus of rigidity G, Young modulus Y and Debye temperature $\theta_D$ are calculated using the expression below[8,9],

$$B = \rho\left(v_l^2 - \frac{4}{3}v_t^2\right) \tag{10}$$

$$G = \rho v_t^2 \tag{11}$$

$$\xi = \frac{1-2(v_t^2/v_l^2)}{2-2(v_t^2/v_l^2)} \tag{12}$$

$$Y = 2G\,(\,\xi + 1\,) \tag{13}$$

$$\theta_D = \frac{h}{k_B}\left[\left(\frac{9\rho}{4\pi}\right)^{1/3}\left(\frac{1}{v_l^3} + \frac{2}{v_t^3}\right)^{-1/3}\right] \tag{14}$$

Where $\rho$ is the isotropic density of the solid, h is Planck's constant and $k_B$ is the Boltzmann constant.

## Results and Discussions

### Table 1. Input Parameter and constant

| BMG | $Z_{eff}$ | $\Omega_{eff}$ (au)$^3$ | $rc^{eff}$ (au) | $M_{eff}$ (amu) |
|---|---|---|---|---|
| $Ti_{44}Zr_{20}V_{36}$ | 2.76 | 117.52 | 1.986 | 57.436 |

Table 1 shows the input parameters and constants required for the present study. The newly proposed bare-ion model potential is used along with different local field correction functions for the first time to generate pair potential for the $Ti_{44}Zr_{20}V_{36}$ , a tough and low densities titanium-based bulk metallic glass system.
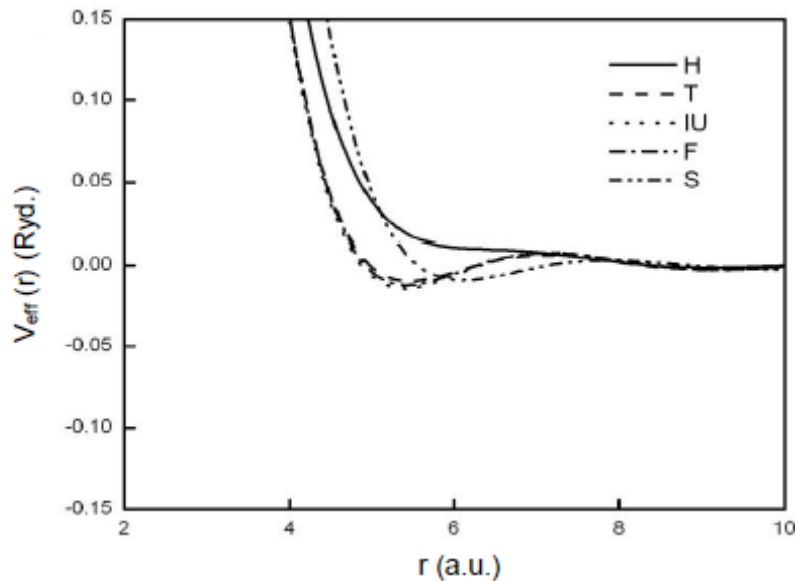


**Figure:1**. Effective pair potential in $Ti_{44}Zr_{20}V_{36}$ bulk metallic glass using model potential.

The study reveals the general trends of the pair potential in all cases, suggesting that position of the first minima is greatly affected by the type of screening used. The steep pair potential is in accordance with the hardness of glassy system.
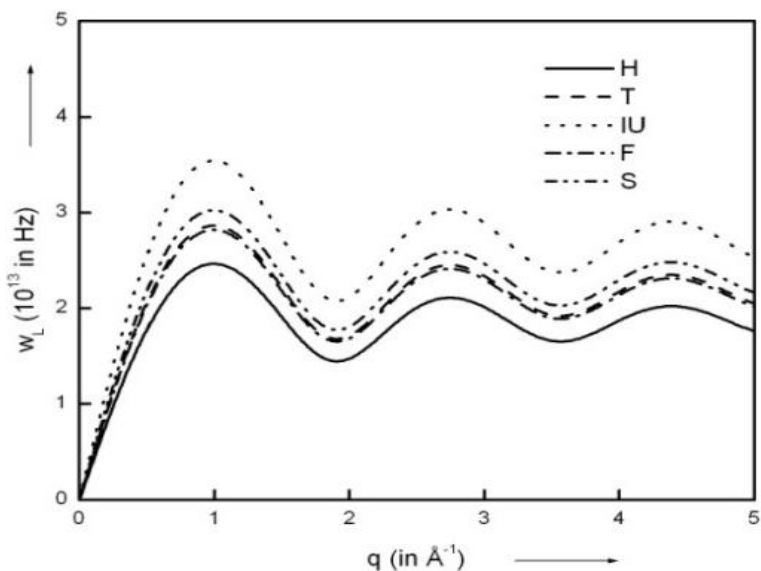
**Figure:2**. Longitudinal phonon modes of $Ti_{44}Zr_{20}V_{36}$ bulk metallic glass.
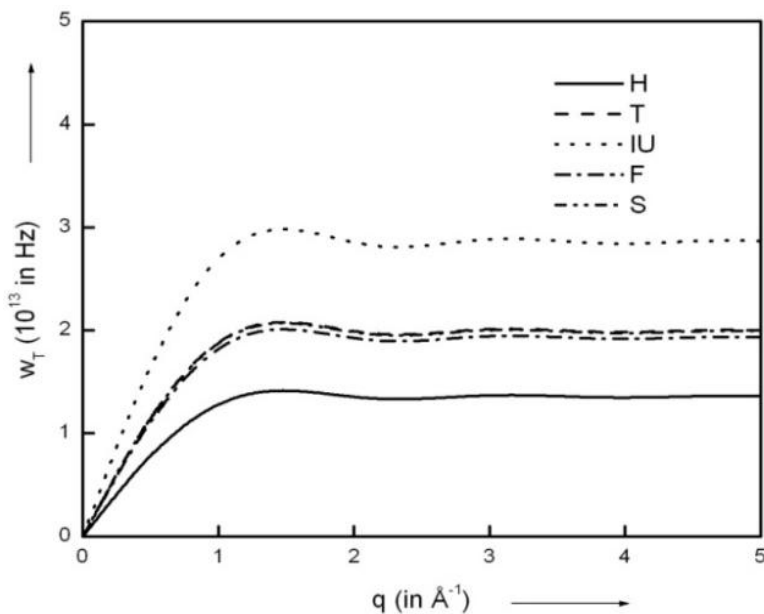


**Figure:3**. Transverses phonon modes of $Ti_{44}Zr_{20}V_{36}$ bulk metallic glass.

The computed of the PDC generated using HB scheme along with five different screening functions are shown in figures 2 and 3 for the $Ti_{44}Zr_{20}V_{36}$ From figure 2 and 3, it is observed that the inclusion of local field correction function raises the phonon frequencies in both longitudinal

as well as transverse branches. The first minimum in the longitudinal branch of $Ti_{44}Zr_{20}V_{36}$ BMG falls at $q \approx 1.97 - 1.98 \, Å^{-1}$. The related magnitude of first peak of PDC increases but position of first peak obtained through IU screening function is at higher q value T, F and SS screening functions give moderate values of phonon frequency. Phonons of transverse branch are undergoing large thermal modulation due to anharmonicity of lattice vibrations in this branch.

### Table 2. Elastic properties of $Ti_{44}Zr_{20}V_{36}$ BMG

| Properties | H [11] | T[12] | IU[13] | F[14] | S[15] | Expt.[17] |
|---|---|---|---|---|---|---|
| $\upsilon_l(10^5 cm/s)$ | 4.02 | 4.15 | 4.11 | 4.05 | 4.20 | - |
| $\upsilon_t(10^5 cm/s)$ | 2.32 | 2.39 | 2.38 | 2.34 | 2.43 | - |
| $B_T$ (GPa) | 107.30 | 114.30 | 112.20 | 108.70 | 117.20 | 113.4 |
| G (GPa) | 24.77 | 26.39 | 25.89 | 26.08 | 27.04 | 36.7 |
| $\Xi$ | 0.25 | 0.25 | 0.25 | 0.25 | 0.25 | 0.35 |
| Y (GPa) | 61.93 | 65.96 | 64.73 | 62.70 | 67.61 | 98.8 |
| $\theta_D$ (K) | 241.33 | 249.07 | 246.73 | 242.83 | 252.16 | - |

Listed in table 2 are presently computed elastic properties for the $Ti_{44}Zr_{20}V_{36}$ along with other data [17]. Table 2 shows that the calculated value of bulk modulus using T and IU screening functions are very close to one another and close to experiment values, whereas the calculated bulk modulus using other screening functions show little more deviation from experimental results. Calculated values of modulus of rigidity and Young's modulus show higher deviation from experimental results. This deviation can be justified as following. In the HB approach, the Poisson's ratio is calculated in terms of ratio of sound velocity. Since, this ratio of sound velocity remains constant, the calculated Poisson's ratio also remains constant i.e. 0.25 and hence the calculated values of modulus of rigidity and Young modulus are underestimated as observed by Khambholja et al [18-20]. For the complete analysis, q dependent sound velocities are to be obtained.

## Conclusion

In the present paper, phonon dispersion curves and elastic constants of bulk metallic glass $Ti_{44}Zr_{20}V_{36}$ are obtained using theoretical approach of Hubbard and Beeby. The calculated values of bulk modulus are in good agreement with the experimental results and hence justify the use of newly proposed model potential in conjunction with HB approach.

## References:

1. Hofmann DC,*et al*Designing metallic glass matrix composites with high toughness and tensile ductility. *Nature* 451,2008;1085-1089.

2. DC Hofmann, A Suh J-Y,Wiest, W L Johnson New processing possibilities for highly toughned metallic glass matrix composites with tensile ductility. *Scripta Matter* 59, 2008,684-687.

3. A L Geer 1995 *Science* 267, 1947.

4. W H Wang, C Dong and C H Shek *Mater.Sci.Eng*.R 2004, 44, 45.

5. Q K Jiang, G Q Zhang, L Yang , X D Wang , K Saksl, H Franz , R Wunderlich , H Fecht and J Z Jiang *Acta Mater***.** 55 , 2007, 4409.

6. W H Wang J.*Appl.Phys*.99**,** 2006, 093506.

7. J Hubbard and J L Beeby J.*Phys*. C 2**,** 1969,556.

8. BY Thakore, PN Gajjar and AR Jani *Bull.Mat.Sci.*23**,** 2000, 5.

9. BY Thakore, H Dabhi, M Joshi and AR Jani *Phys. Scr*.7, 2009.0250007.

10. P B Thakore, PN Gajjar and AR Jani *Communication* in Phys.14**,** 2004,15.

11. WA Harrison *Phys. Stat.Sol*.(6) 181, 1969, 1036.

12. R Taylor *J. Phys.F* 8, 1981,1699.

13. S Ichimaru and K Utsumi *Phys. Rev*. B 24**,** 1981, 3220.

14. B Farid, V Heine, G E Engel and I S Robertson *Phys. Rev*. 48,1993,11602.

15. A Sarkar, D S Sen and H D Roy *Mod. Phys. Lett***.** 12, 1998, 639.

16. P H Suthar, PN Gajjar, BY Thkore and AR Jani J.Phys.: Conf.Ser. 423,2013,012030.

17. C Douglas. Hofmann PNAS 105, 2008, 20136.

18. S.G. Khambholja, A.L. Ladva and B.Y. Thakore AIP Conference Proceedings 1728, 2016, 020202

19. S.G. Khambholja, B.Y. Thakore, N.K. Bhatt, P.N. Gajjar and A.R. Jani, Crystalline & Non Crystalline Materials, 384-9, 2014, 83

20. S.G. Khambholja, B.Y. Thakore and A.Jani, Adv Mat Research, 1141, 2016, 162

# THEORETICAL STUDY OF ELECTRICALRESISTIVITY($\rho$)

# OF SOME LIQUID ALKALI ELEMENTS

Mayank H. Jani[1]and A. M. Vora[2]
[1]Department of Physics, Kalol Institute of Technology and Research Centre,
Kalol 382721, Gujarat, India
[2]Department of Physics, University School of Sciences,
Gujarat University, Ahmedabad 380009, Gujarat, India

## Abstract

A universal model potential of Fiolhais*et al.*is used to investigate the electrical resistivity($\rho$) of someliquid metallic elementswith Ziman's theoretical model. Five different types of local field correction functions are used to study the effect of the exchange and correlation on the aforementionedproperties. The generalized mean spherical approximation (GMSA) method is adopted for computing the structure factor of liquid metals. The presently computed results are found in comparable one with other such available data wherever exists in the literature either theoretical or experimental.

## 1. Introduction

In the present study, we have investigated the electrical resistivity (ρ) of some alkali elements with the help of pseudopotential formalism. A universal model potential of Fiolhais[1, 2] used to describe the electron-ion interaction in these systems is of the form:

$$V(r) = -\frac{Z}{R}\left\{\frac{1}{x}\left[1 - (1 + \beta x)e^{-\alpha x}\right] - Ae^{-x}\right\} \tag{1}$$

The Fourier transform of the model potential is given as,

$$V(q) = \frac{4\pi Ze^2 R^2}{\Omega_O}\left[\frac{-1}{(qR)^2} + \frac{1}{\left[(qR)^2 + \alpha^2\right]} + \frac{2\alpha\beta}{\left[(qR)^2 + \alpha^2\right]^2} + \frac{2A}{\left[(qR)^2 + 1\right]^2}\right] \tag{2}$$

Where,

$x = r/R$, $R$ being a core decay length, and with $\alpha > 0$.

An analyticity condition at $r = 0$ determines $A$ and $\beta$ in terms of $\alpha$.

$\beta = \dfrac{\alpha^3 - 2\alpha}{4(\alpha^2 - 1)}$ and

$$A = \frac{1}{2}\alpha^2 - \alpha\beta$$

(3)

Other details of this potential are described intheir respective papers [1, 2].

During the last several years there has been an increasing interest in the properties of non-crystalline conductors such as liquid metals and liquid metallic alloys. Such a liquid exhibits metallic as well as fluid-like behaviour and hence can help to make a link between the theory of the liquid states and the theory of the electronic states in metals. And hence the study of electrical transport properties of liquid metals and their alloys remain one of the favourite quantities either experimentally or theoretically [3-26].

The Ziman's [6, 7] nearly free electron (NFE) theory has been fairly successful in describing the quantitative behaviour of the electrical properties of simple liquid metals. This is because in these metals the mean free path is about the one hundred times the interatomic distance and the weak scattering picture should be valid. Even for the heavy polyvalent metals where the mean free path is only about two interatomic distances, the NFE model can yield results, which are reasonable in agreement with the experiments. In the present computation of electrical resistivity ($\rho$) of binary mixture, the most recent local field correction functions due to Hartree (H) [28], Taylor (T) [29], Ichimaru-Utsumi (IU) [30], Farid*et al.* (F) [31] and Sarkar *et al.* (S) [32] are employed to investigate the influence of exchange and correlation effects.The generalized mean spherical approximation (GMSA) method [27] is adopted for computing the structure factor of liquid alkali metals in the present computation.

## 2. Computational Methodology

The Faber's [6] approach of investigating electrical resistivity of liquid metals assumes the model of a gas of conduction electrons which interact with and are scattered by irregularly placed metal ions. Assuming the free-electron distribution, an expression for the electrical resistivity of liquid metal in terms of the average of the product of the structure factor and pseudopotential matrix element is written as [3-26]

$$\rho = \frac{3\pi m^2}{4e^2\hbar^3 n k_F^6}\int_0^\infty S(q)|V(q)|^2 q^3 \, dq \, \theta(2k_F - q).$$

(2)

Where $n$ the electron density is related to Fermi wave number and $\theta$ is the unit step function that cuts of the $q$-integration at $2k_F$ corresponding to a perfectly sharp Fermi surface, S(q) the structure factor and V(q) the screened ion pseudopotential form factor. Here, we have used generalized mean spherical approximation (GMSA) formulations [27] to generate the structure factor of the metallic elements.

## 3. Results and Discussion

The input parameters and constants used in the present computations are written in Table 1.

| Metals | Z | Ω (a.u.) | T (K) | η | α | r |
| --- | --- | --- | --- | --- | --- | --- |
| Li | 1 | 142.47 | 453 | 0.46 | 3.549 | 0.361 |
| Na | 1 | 254.25 | 378 | 0.46 | 3.075 | 0.528 |
| K | 1 | 480.24 | 343 | 0.46 | 2.807 | 0.745 |
| Rb | 1 | 588.98 | 313 | 0.43 | 2.748 | 0.824 |
| Cs | 1 | 743.53 | 323 | 0.43 | 2.692 | 0.92 |

The presently computed results of electrical resistivity ($\rho$) of liquid alkali metals are narrated in Table 2 with available experimental [4, 6, 18, 19, 22] or theoretical [4-6, 15-23] data whenever exists in the literature.

**Table 2** :Electrical Resistivity ( $\rho$ )(in μΩ-cm) of Liquid Alkali Metals.

| Metals | Present results | | | | | Expt. [4, 6, 18, 19, 22] | Others [4-6, 15-23] |
| --- | --- | --- | --- | --- | --- | --- | --- |
| | H | T | IU | F | S | | |
| Li | 6.58 | 11.10 | 12.03 | 12.17 | 9.18 | 24.7 | 4.58, 5.48, 7, 7.3, 13.76, 18.91, 20.95, 21.15, 23.2, 23.8, 24.7, 24.86, 25, 26.80 |
| Na | 8.52 | 15.63 | 17.14 | 17.38 | 12.58 | 9.6 | 5.3, 7.9, 8.44, 9.48, 9.82, 10.11, 10.25, 10.38, 13.58, 13.91, 15.8, 16.3, 18.50, 17.24, 37.7 |
| K | 11.15 | 22.82 | 25.31 | 25.75 | 17.58 | 13 | 11.1, 11.48, 11.61, 13.31, 13.60, 13.67, 14.06, 14.87, 15.38, 18.29, 18.5, 19.6, 20.27, 26.11, |
| Rb | 14.75 | 31.14 | 34.67 | 35.29 | 23.71 | 22.5 | 10, 14.70, 18.62, 19.8, 20.8, 20.97, 22, 23.09, 23.38, 23.55, 23.62, 26.85, 26.67, 30.66, 36.74 |
| Cs | 16.24 | 35.96 | 40.17 | 40.98 | 26.81 | 36 | 10, 13.8, 14.9, 15.44, 19.81, 20.71, 22.73, 31.29, 31.47, 32.25, 34.67, 39.73, 45.86, 50.44, 54.9, 62.71 |

It is also noticed from Table 2 that, the present results of the electrical resistivity ( $\rho$ ) of the liquid alkali metals are found in qualitative agreement with the experimental or theoretical findings. Also, it is noted that, among the five employed local filed correction functions, the local field correction function due to H (without exchange and correlation) gives the minimum numerical value of the electrical resistivity, while the local field correction function due to F gives the maximum value. In comparison with the presently computed results of the electrical resistivity ( $\rho$ ) from static H-function, the percentile influences for Li, Na, K, Rb and Cs liquid metals of T, IU, F and S-functions are of the order of 23.93%-93.44%, 38.77%-104.72%, 42.11%-147.29%, 44.77%-152.24% and 14.69%-65.05%, respectively.

The effect of local field correction functions plays an important role in the computation of electrical properties of the liquid metals. The local field correction functions due to IU, F and S are able to generate consistent results regarding the electrical properties of the liquid metals of the different groups of the periodic table as those obtained from more commonly employed

H- and T-local field correction functions. Thus, the use of these more promising local field correction functions is established successfully.

## 4. Conclusions

Lastly we conclude that, the present computations not only confirmsthe applicability of universal model potential of Fiolhais*et al.* for study of the aforesaid properties but it also establishes the use of more prominent dielectric functions.

## References

[1]     C. Fiolhais, J. P. Perdew, S.Q. Armster, J. M. MacLaren, and M. Brajczewska, Phy. Rev. B**51**, 14001 (1995)

[2]     C. Fiolhais, J. P. Perdew, S.Q. Armster, J. M. MacLaren, and M. Brajczewska, Phy. Rev. B**51**, 20 (1995)

[3]     P. L. Rossiter, *The electrical resistivity of metal and alloys*(Cambridge University Press, London, 1987).

[4]     Y. Waseda, *The structure of non-crystalline materials liquid and amorphous solids*(McGraw-Hill, New York, 1980).

[5]     M. Shimoji, *Liquid metals*(Academic Press, London, 1977).

[6]     T. E. Faber, *An Introduction to the theory of liquid metals* (Cambridge University Press, London, 1972).

[7]     J.M.Ziman, Phil. Mag. **6**, 1013 (1961).

[8]     T. Khajil, Phys. Chem.  Liq. **37**, 773 (1999).

[9]     O. Dreieach, R. Evans, H.J. Guntherodt, H.U. Kunz, J. Phys. **F2**, 709 (1972).

[10]    R. Evans, D. A. Greenwood, P. Lloyd, Phys. Lett. **A35**, 57 (1971).

[11]    A. M. Vora, M. H. Patel, B. Y. Thakore, P. N. Gajjar, A. R. Jani, Solid State Phys. **45**, 427 (2002).

[12]    Aditya M. Vora, Russian Phys. J. **49**, 834 (2006).

[13]    Aditya M. Vora, J. Optoelec. Adv. Mater. **1**, 227 (2007).

[14]    Aditya M. Vora, Phys. Chem. Liq. **46**, 442(2008)

[15]    J. K. Baria, Brazilian J. Phys. **34**, 1185 (2004).

[16]    J. K. Baria, Physica B**337**, 245 (2003).

[17]    S. Korkmaz, S. D. Korkmaz, Comp. Mater. Sci. **37**, 618 (2006).

[18]  A. R. Jani, H. K. Patel, P. N. Gajjar, G. Sajeevkumar, *Disordered materials (Structure and Properties)*, Eds. S. K. Srivastava, INDIAS Publications (Wiley Eastern Limited, New Delhi, 1993)

[19]  T. M. K. Kahjil, M. Tomak, Phys. Stat. Sol (b) **134**, 321(1986).

[20]  F. Daver, T.M. A. Khajil, M. Tomak, Phys. Stat. Sol. (b)**138**, 373 (1986).

[21]  W. Geertsma, D. Gonzalez, L. H. Gonzalez, Brazilian J.Phys. **33**, 406 (2003).

[22]  H. S. Schnyders, J. B. Van Zytveld, J. Phys :Conden. Matter **8**, 10875 (1996).

[23]  G. Bose, H. C. Gupta, B. B. Tripathi, J. Phys. Chem. Solids **35**, 595 (1774).

[24]  C. R. Leavens, A. H. Macdonald, R. Taylor, A. Ferraz, N. H. March, Phys. Chem. Liq. **11**, 115 (1981).

[25]  J. S. Ononiwu, Phys. Stat. Sol. (b) **177**, 413 (1993).

[26]  J. Gorecki, J. Popielawski, J. Phys. F: Met. Phys. **13**, 2107 (1983).

[27]  E. Waisman, Mol. Phys. **25**, 45 (1973).

[28]  W. A. Harrison*, Elementary Electronic Structure*(World Scientific, Singapore, 1999).

[29]  R. Taylor, J. Phys. F: Metal Phys. **8**, 1699 (1978).

[30]  S. Ichimaru, K. Utsumi, Phys. Rev. **B24**, 7385 (1981).

[31]  B. Farid, V. Heine, G. E. Engel, I. J. Robertson, Phys. Rev. **B48**, 11602 (1993).

[32]  A. Sarkar, D. S. Sen, S. Haldar, D. Roy, Mod. Phys. Lett. **B12**, 639 (1998).

# Coupling of the Solar Photosphere and the Corona

*Jitesh M Rami **Chetan M Patel, ***C A Patel, #D K patel
*Gokul Science College, Sidhpur, **Anjana Science College, Palanpur
***Pramukh Swami Science College, Kadi
#Municipal Arts & Urban Science College, Mehsana
jr17792@gmail.com

**Abstract**
The atmosphere of the sun is characterized by a complex interplay of competing physical processes, convection, radiation, conduction and magnetic field. Beside this dominating scale there is a more or less smooth distribution of spatial scales, both towards smaller and larger scales making the sun essentially a multi-scale object. Convection and overheating give the photosphere its face but also act as drivers for the layers above namely the chromospheres and the corona. The magnetic field configuration effectively couples the photosphere far instant in the form of loops that are anchored in the convection zone and continue through the atmosphere up into the chromospheres and corona. The magnetic field is also an important structuring agent for the small, granulation size scale, although shock waves also play an important role-especially in the inter network atmosphere where mostly weak field prevail. The magnitude of the flare depends on the accumulation and storage of magnetic flux, while release of this magnetic field energy depends on other plasma triggering mechanisms. These mechanisms may be gradient, deviation and/or variation in sunspot rotation angle as shown earlier by Jain et al., (2011). Based on recent result from observation and numerical simultaneous, I attempt to study that corona is heated up by the induction of magnetic flux energy from the photosphere.

**Key Word**
Convection, Radiation, Conduction, magnetic field, Photosphere, Chromospheres, Corona, Flare, Plasma triggering, Gradient, Sunspot Rotation Angle

**Introduction**
The Sun lies at the heart of the solar system, where it is by far the largest object. It holds 99.8 percent of the solar system's mass and is roughly 109 times the diameter of the Earth about one million Earths could fit inside the sun. The sun has three different layers that define its internal structure: core, radiative zone, and convective zone[1-2]. The core is the source of all the Sun's energy. Fortunately for life on earth, the Sun's energy output is just about constant so we do not see much change in its brightness or the heat it gives off. The Sun's core has a very high temperature, more than 15 million degrees Kelvin, and the material in the core is very tightly packed or dense[3-4]. It is a combination of these two properties that creates an environment just right for nuclear reactions to occur. Once energy is produced in the core of the Sun, it needs a way to travel from the solar center to the outer regions[5-7]. The physical transport of energy from its production site to the surrounding regions can be done in a number of ways. However,

for a star like the Sun, the most efficient means of transferring energy near the core is by radiation. Once out of the radiation zone the energy, originally produced in the core, requires a new transport mechanism to continue its journey to the surface[8]. Above the convective zone of the solar interior is the solar atmosphere. As said above, this is made up of three main layers, the photosphere, the chromospheres and the corona and there exists a region sandwiched between chromospheres and corona, named as transition region. The photosphere is the lowest of the three layers of the atmosphere. It is the optical `surface' of the sun, but it isn't actually a solid surface, it is a shallow shell of gas about 400km deep. The outermost layer of the Sun is called the corona. It gets its name from the crown like appearance evident during a total solar eclipse. The corona stretches far out into space and, in fact, particles from the corona reach the earth's orbit[9-10]. The continuously changing dark regions on the surface of the sun is called SunSpots. An area with a strong magnetic field is called Actve Region Solar flare and CME's blast forth from AR.Solar flares are huge explosion on the Sun. Solar flares are understood to be one of the most hazardous events occurring in the atmosphere of the Sun. Typically $10^{32}$ ergs of energy is released in 1000 s from a solar flare. It has been widely established that this gigantic energy comes from the magnetic flux evolving at sub-photospheric level and being transferred to corona. The random motion of magnetic flux tubes which transfer the energy from photosphere to corona for storage, which later release in the form of flare emission, can be studied through observing the magnetic field of the active region (AR)[11-12].

**Instruments**
In this paper, I probe photospheric magnetic-field observations by Heliospheric Magnetic Imager(HMI; Scherrer et. al., 2012) onboard Solar Dynamic Observatory (SDO; Pesnell et. al., 2012).

**Instrument used for emission from photosphere**
Measuring the magnetic field in the photosphere has a long tradition (Hale 1908). Photospheric magnetic field, optical intensity, and sunspot evolutions are some of the major areas of observations of this part of solar atmosphere. Magnetic non-potential fields are the source of various physical processes occurring in the flux tubes, coronal holes, and energetic flare etc. Therefore, measurement of magnetic field of the solar photospheric disk is of fundamental importance. HMI observes the full solar disk at 6173 A˚ with a spatial resolution of 1 arc-second. It consists of a refracting telescope, a polarization selector, an image stabilization system, a narrow band tunable filter and two 4096×4096 pixels CCD cameras with mechanical shutters and control electronics. Images are obtained in a sequence of tuning and polarizations at a 4-second cadence for each camera. One camera is dedicated to a 45s Doppler and line-of-sight magnetic field component while the other to 90s vector magnetograms. All of the images are processed at the HMI/AIA Joint Science Operations Center and archived for science use from where we have obtained the observations of LOS magnetogram employed for investigation in this thesis. **Table 1** shows the key parameters of HMI/SDO.

**Table 1 Key Parameters of HMI/SDO**

| S. N. | Property | SDO/HMI |
|-------|----------|---------|
| 1 | Central wavelength | 6173.3 ± 0.1 A˚ |
| 2 | Filter bandwidth | 76 mA |
| 3 | Field of view | ~2000 arc sec |
| 4 | Angular resolution | ~1.5 arc sec |
| 5 | Spatial resolution | 0.50 ± 0.01 arc sec |
| 6 | Cadence | 45s |

**Instrument used for emission from corona**

The mean temperature of the solar corona is about 2 MK, which however exceeds 10 MK during solar flares. The quiet corona emits UV, EUV and soft X-ray waveband but during solar flare, the emission is originated mainly in EUV, X-Ray and Radio waveband due to high-temperature nature of the emission. The study of processes of energy release in solar flares has been made employing X-ray observations from Solar X-ray Spectrometer (SOXS) and Reuven Ramaty High Energy Solar Spectroscopic Imager (RHESSI) missions.The SOXS and RHESSI observations have been used for the spatial,spectral and temporal evolution of X-ray sources. In this section, I describethe instruments employed for observing emission from corona. We use the X-ray observations provided by Geostationary Operational En-vironmental Satellites (GOES) for the investigation of temporal evolution of flare. GOES has been developed for National Oceanic and Atmospheric Administration (NOAA) by the National Aeronautics and Space Administration(NASA). It measures solar radiation in the X-ray and EUV region and the in-situ magnetic field and energetic particle environment at geosynchronous orbit, providing real-time data to the NOAA Space Weather Prediction Center (SWPC). GOES satellites provide un-interrupted observations of the Sun and therefore extensively used for temporal evolution studies in solar flare X-ray emission. The Space Environment Monitor (SEM) subsystem onboard GOES consists of four instruments: An energetic particles sensor (EPS), high energy proton and alpha detector (HEPAD), X-ray sensor (XRS) and two redundant three-axis magnetometers. HEPAD monitors the incident flux density of protons, alpha particles, and electrons over an extensive range of energy levels.XRS monitors the X-ray emission from the solar atmosphere. Two redundant three-axis magnetometers operate one at a time to monitor earths geomagnetic field strength in the vicinity of the spacecraft. The SEM instruments are capable of ground command-selectable, in-flight calibration for monitoringon-orbit performance and ensuring proper operation.

**Observation**

In following **Table - 2** ,we enlist the characteristics of the time duration selected for investigation ofstatistically independent relationship between photospheric magnetic flux and coronal X-ray flux. We also list the number of flares as a function of importanceclass for the selected duration.

**Table – 2 List of the observation duration for the study of photospheric magnetic flux and coronal X-ray flux**

| S. N. | Duration | AR Nos. | No. of Flares(Class) |
|---|---|---|---|
| 1 | November 2011 | NOAA 11339 | C(32)-M(8)-X(1) |
| 2 | March 2012 | NOAA 11429 | C(38)-M(12)-X(3) |
| 3 | May 2012 | NOAA 11476 | C(78)-M(7)-X(0) |

The photospheric full-disc magnetic field observations are regularly obtainedfrom HMI /SDO instrument. HMI provides full-disk magnetograms at wavelength 6173Å with spatial resolution of 0.5 per pixel and temporal cadence of 45 s. However, for this analysis, we have selected only that active region which was associated with the respective flare. The magnetic flux for each polarity is then estimated using above relation in the units ofGauss/cm$^2$ (Mx). For these eventsthe Coronal X-ray flux is taken from the observations provided by full-diskX-ray sensors on-board the Geostationary Operational Environmental Satellites (GOES) operated by NOAA since 1974. GOES X-ray flux 2 s cadencedata is available from the URL *http://goes.ngdx.noaa.gov/data/avg*whichis also processed through SolarSoft package as describe above in **chapter 3**. These observations are then averaged to 4 hours time period in order to achieve the same time cadence asthat of photospheric magnetic field observations.Finally, this time averagedcoronal X-ray flux is averaged over 4-hours to obtain 6 values in each day.The standard deviation is termed as the uncertainty in this dataset as well asoccurred due to averaging.

**Table – 3 (March- 2012) Active Region NOAA11429**

| Date/Time | Magnetic flux (Mx) | X-Ray flux (Watt/m$^2$) |
|---|---|---|
| 04/03/2012 00:00 | 1.30E+26 | 5.65E-07 |
| 04/03/2012 04:00 | 1.43E+26 | 7.13E-07 |
| 04/03/2012 08:00 | 2.46E+26 | 5.77E-06 |
| 04/03/2012 12:00 | 6.26E+26 | 4.80E-06 |
| 04/03/2012 16:00 | 6.88E+26 | 1.33E-06 |
| 04/03/2012 20:00 | 5.21E+26 | 1.05E-06 |
| 05/03/2012 00:00 | 1.92E+26 | 9.45E-06 |
| 05/03/2012 04:00 | 3.74E+26 | 2.99E-05 |
| 05/03/2012 08:00 | 4.89E+26 | 1.69E-06 |
| 05/03/2012 12:00 | 3.98E+26 | 1.72E-06 |
| 05/03/2012 12:00 | 4.10E+26 | 2.85E-06 |
| 05/03/2012 20:00 | 2.77E+26 | 1.79E-06 |
| 06/03/2012 00:00 | 2.03E+26 | 2.76E-06 |
| 06/03/2012 04:00 | 2.02E+26 | 2.31E-06 |
| 06/03/2012 08:00 | 2.10E+26 | 1.37E-06 |

| 06/03/2012 12:00 | 2.28E+26 | 3.10E-06 |
|---|---|---|
| 06/03/2012 16:00 | 2.46E+26 | 1.19E-06 |
| 06/03/2012 20:00 | 2.76E+26 | 3.75E-06 |
| 07/03/2012 00:00 | 2.67E+26 | 9.34E-05 |
| 07/03/2012 04:00 | 2.77E+26 | 4.05E-06 |
| 07/03/2012 08:00 | 2.54E+26 | 1.32E-06 |
| 07/03/2012 12:00 | 2.11E+26 | 1.26E-06 |
| 07/03/2012 16:00 | 1.95E+26 | 1.37E-06 |
| 07/03/2012 20:00 | 1.83E+26 | 8.38E-07 |
| 08/03/2012 00:00 | 2.19E+26 | 9.79E-07 |
| 08/03/2012 04:00 | 1.99E+26 | 8.63E-07 |
| 08/03/2012 08:00 | 1.89E+26 | 6.64E-07 |
| 08/03/2012 12:00 | 1.66E+26 | 8.53E-07 |
| 08/03/2012 16:00 | 1.46E+26 | 9.17E-07 |
| 08/03/2012 20:00 | 1.34E+26 | 7.75E-07 |
| 09/03/2012 00:00 | 1.55E+26 | 6.66E-06 |
| 09/03/2012 04:00 | 1.35E+26 | 1.16E-05 |
| 09/03/2012 08:00 | 1.23E+26 | 1.31E-06 |
| 09/03/2012 12:00 | 1.26E+26 | 1.14E-06 |
| 09/03/2012 16:00 | 1.38E+26 | 1.19E-06 |
| 09/03/2012 20:00 | 1.46E+26 | 3.03E-06 |
| 10/03/2012 00:00 | 1.53E+26 | 1.96E-06 |
| 10/03/2012 04:00 | 1.55E+26 | 7.02E-07 |
| 10/03/2012 08:00 | 1.62E+26 | 1.56E-06 |
| 10/03/2012 12:00 | 1.62E+26 | 2.68E-05 |
| 10/03/2012 16:00 | 1.43E+26 | 4.36E-06 |
| 10/03/2012 20:00 | 1.23E+26 | 1.81E-06 |
| 11/03/2012 00:00 | 1.33E+26 | 1.07E-06 |
| 11/03/2012 04:00 | 1.26E+26 | 4.98E-07 |
| 11/03/2012 08:00 | 1.08E+26 | 6.41E-07 |
| 11/03/2012 12:00 | 1.02E+26 | 5.48E-07 |
| 11/03/2012 16:00 | 1.00E+26 | 5.85E-07 |

**Table- 4  (May-2012) Active Region NOAA11476**

| 06/05/2012 00:00 | 1.08E+26 | 1.27E-06 |
|---|---|---|
| 06/05/2012 04:00 | 4.33E+25 | 9.17E-07 |
| 06/05/2012 08:00 | 7.30E+25 | 6.05E-07 |
| 06/05/2012 12:00 | 1.27E+26 | 6.87E-07 |
| 06/05/2012 16:00 | 1.27E+26 | 1.72E-06 |
| 06/05/2012 20:00 | 1.46E+26 | 1.06E-06 |

| | | |
|---|---|---|
| 07/05/2012 00:00 | 1.48E+26 | 1.60E-07 |
| 07/05/2012 04:00 | 1.54E+26 | 1.09E-06 |
| 07/05/2012 08:00 | 1.54E+26 | 8.91E-07 |
| 07/05/2012 12:00 | 1.22E+26 | 3.87E-06 |
| 07/05/2012 16:00 | 1.02E+26 | 8.93E-07 |
| 07/05/2012 20:00 | 1.13E+26 | 5.28E-07 |
| 08/05/2012 00:00 | 1.60E+26 | 4.22E-07 |
| 08/05/2012 04:00 | 1.43E+26 | 4.04E-07 |
| 08/05/2012 08:00 | 1.32E+26 | 7.85E-07 |
| 08/05/2012 12:00 | 1.27E+26 | 1.06E-06 |
| 08/05/2012 16:00 | 1.32E+26 | 4.71E-07 |
| 08/05/2012 20:00 | 1.39E+26 | 3.49E-07 |
| 09/05/2012 00:00 | 1.70E+26 | 3.52E-07 |
| 09/05/2012 04:00 | 1.38E+26 | 4.20E-07 |
| 09/05/2012 08:00 | 1.28E+26 | 5.70E-07 |
| 09/05/2012 12:00 | 1.12E+26 | 3.00E-06 |
| 09/05/2012 16:00 | 1.23E+26 | 6.99E-07 |
| 09/05/2012 20:00 | 1.28E+26 | 2.55E-06 |
| 10/05/2012 00:00 | 1.35E+26 | 7.07E-07 |
| 10/05/2012 00:00 | 1.35E+26 | 4.11E-06 |
| 10/05/2012 00:00 | 1.31E+26 | 6.85E-07 |
| 10/05/2012 00:00 | 1.41E+26 | 1.48E-06 |
| 10/05/2012 00:00 | 1.42E+26 | 1.05E-06 |
| 10/05/2012 00:00 | 1.40E+26 | 2.03E-06 |
| 11/05/2012 00:00 | 1.26E+26 | 7.46E-07 |
| 11/05/2012 00:00 | 1.18E+26 | 8.76E-07 |
| 11/05/2012 00:00 | 1.27E+26 | 1.12E-06 |
| 11/05/2012 00:00 | 1.21E+26 | 1.13E-06 |
| 11/05/2012 00:00 | 1.17E+26 | 1.14E-06 |
| 11/05/2012 00:00 | 1.33E+26 | 1.83E-06 |
| 12/05/2012 00:00 | 1.22E+26 | 3.03E-06 |
| 12/05/2012 00:00 | 1.16E+26 | 5.85E-07 |
| 12/05/2012 00:00 | 1.16E+26 | 4.72E-07 |
| 12/05/2012 00:00 | 1.14E+26 | 4.77E-07 |
| 12/05/2012 00:00 | 1.06E+26 | 5.35E-07 |
| 12/05/2012 00:00 | 1.08E+26 | 4.17E-07 |
| 13/05/2012 00:00 | 1.06E+26 | 5.39E-07 |
| 13/05/2012 00:00 | 1.06E+26 | 9.27E-07 |
| 13/05/2012 00:00 | 1.02E+26 | 1.02E-06 |
| 13/05/2012 00:00 | 1.03E+26 | 4.78E-07 |
| 13/05/2012 00:00 | 1.03E+26 | 4.42E-07 |
| 13/05/2012 00:00 | 1.06E+26 | 4.84E-07 |

**Table – 5 (Nov-2011) Active Region NOAA11339**

| Date | Flux (Mx) | Flux (Watt/m$^2$) |
|---|---|---|
| 04/11/2011 00:00 | 3.24E+26 | 4.15E-06 |
| 04/11/2011 04:00 | 3.29E+26 | 2.45E-06 |
| 04/11/2011 08:00 | 3.42E+26 | 1.01E-06 |
| 04/11/2011 12:00 | 4.55E+26 | 9.15E-07 |
| 04/11/2011 16:00 | 4.93E+26 | 1.24E-06 |
| 04/11/2011 20:00 | 3.88E+26 | 2.20E-06 |
| 05/11/2011 00:00 | 3.57E+26 | 7.18E-06 |
| 05/11/2011 04:00 | 3.74E+26 | 3.20E-06 |
| 05/11/2011 08:00 | 3.60E+26 | 2.55E-06 |
| 05/11/2011 12:00 | 3.69E+26 | 1.50E-06 |
| 05/11/2011 16:00 | 3.73E+26 | 1.08E-06 |
| 05/11/2011 20:00 | 3.45E+26 | 3.08E-06 |
| 06/11/2011 00:00 | 2.54E+26 | 3.00E-06 |
| 06/11/2011 04:00 | 2.59E+26 | 2.05E-06 |
| 06/11/2011 08:00 | 2.49E+26 | 1.49E-06 |
| 06/11/2011 12:00 | 2.28E+26 | 1.43E-06 |
| 06/11/2011 16:00 | 2.18E+26 | 9.35E-07 |
| 06/11/2011 20:00 | 2.09E+26 | 8.46E-07 |
| 07/11/2011 00:00 | 2.77E+26 | 1.07E+06 |
| 07/11/2011 04:00 | 2.83E+26 | 1.26E-06 |
| 07/11/2011 08:00 | 2.90E+26 | 8.15E-07 |
| 07/11/2011 12:00 | 2.82E+26 | 1.03E-06 |
| 07/11/2011 16:00 | 2.36E+26 | 7.88E-07 |
| 07/11/2011 20:00 | 2.05E+26 | 1.35E-06 |
| 08/11/2011 00:00 | 1.75E+26 | 1.02E-06 |
| 08/11/2011 04:00 | 1.64E+26 | 9.15E-07 |
| 08/11/2011 08:00 | 1.72E+26 | 1.17E-06 |
| 08/11/2011 12:00 | 1.72E+26 | 7.42E-07 |
| 08/11/2011 16:00 | 1.53E+26 | 7.57E-07 |
| 08/11/2011 20:00 | 1.44E+26 | 7.67E-07 |
| 09/11/2011 00:00 | 1.46E+26 | 1.15E-06 |
| 09/11/2011 04:00 | 1.54E+26 | 7.25E-07 |
| 09/11/2011 08:00 | 1.73E+26 | 6.95E-07 |
| 09/11/2011 12:00 | 1.77E+26 | 3.88E-06 |
| 09/11/2011 16:00 | 1.77E+26 | 1.00E-06 |
| 09/11/2011 20:00 | 1.87E+26 | 7.45E-07 |
| 10/11/2011 00:00 | 1.74E+26 | 8.07E-07 |
| 10/11/2011 04:00 | 1.80E+26 | 9.73E-07 |
| 10/11/2011 08:00 | 1.89E+26 | 9.02E-07 |
| 10/11/2011 12:00 | 1.86E+26 | 1.04E-06 |
| 10/11/2011 16:00 | 1.69E+26 | 1.79E-06 |
| 10/11/2011 20:00 | 1.71E+26 | 7.48E-07 |
| 11/11/2011 00:00 | 1.88E+26 | 7.96E-07 |
| 11/11/2011 04:00 | 1.95E+26 | 1.65E-06 |
| 11/11/2011 08:00 | 2.19E+26 | 1.16E-06 |
| 11/11/2011 12:00 | 2.37E+26 | 1.02E-06 |

| 11/11/2011 16:00 | 2.36E+26 | 2.17E-06 |
| 11/11/2011 20:00 | 2.28E+26 | 8.70E-07 |

## Result and Conclusion

After doing all the procedure mentioned earlier the following results were obtained.
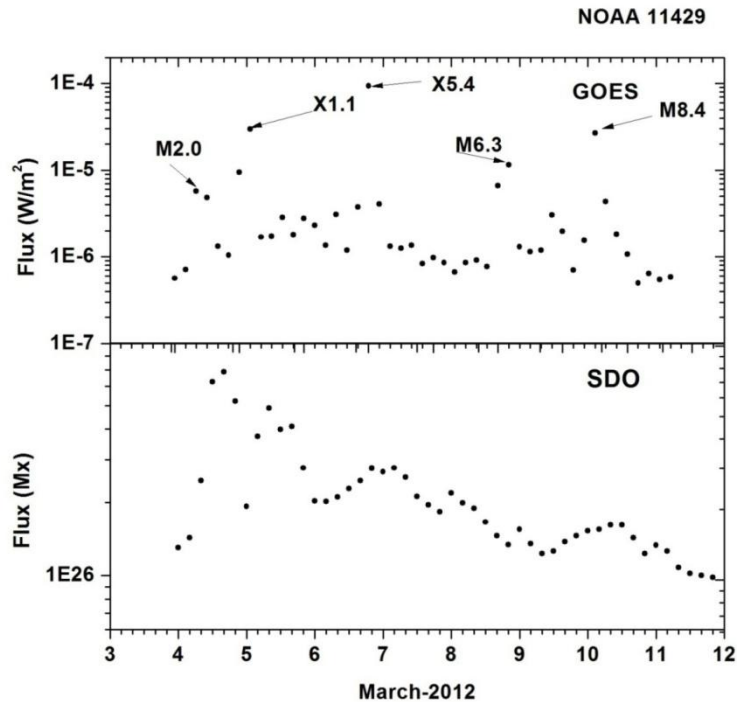


**Figure - 1 magnetic flux and x-ray flux for an active region (NOAA 11429) with during the 04-March-2012 to 11-March-2012.**
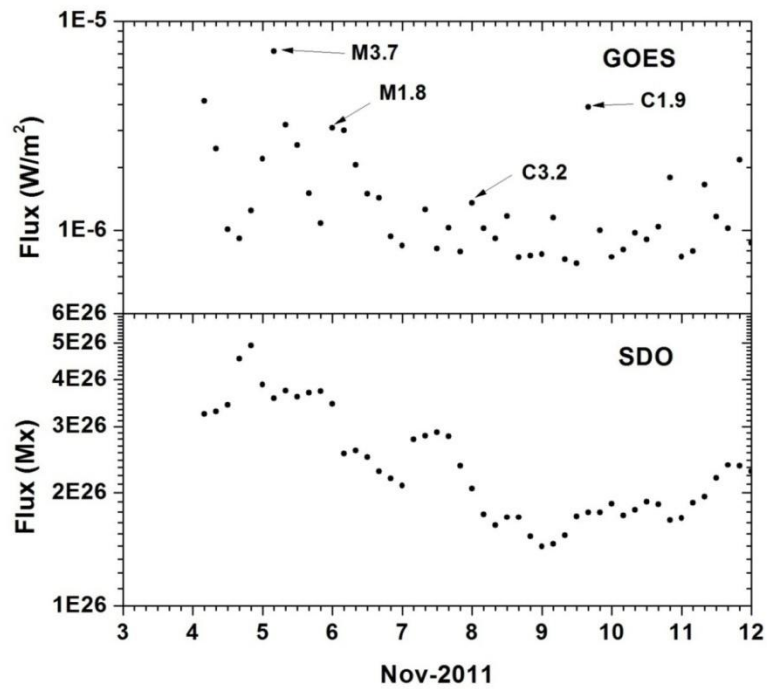
**Figure - 2 magnetic flux and x-ray flux for an active region (NOAA 11339) with during the 04-Nov-2011 to 11-Nov-2011**.
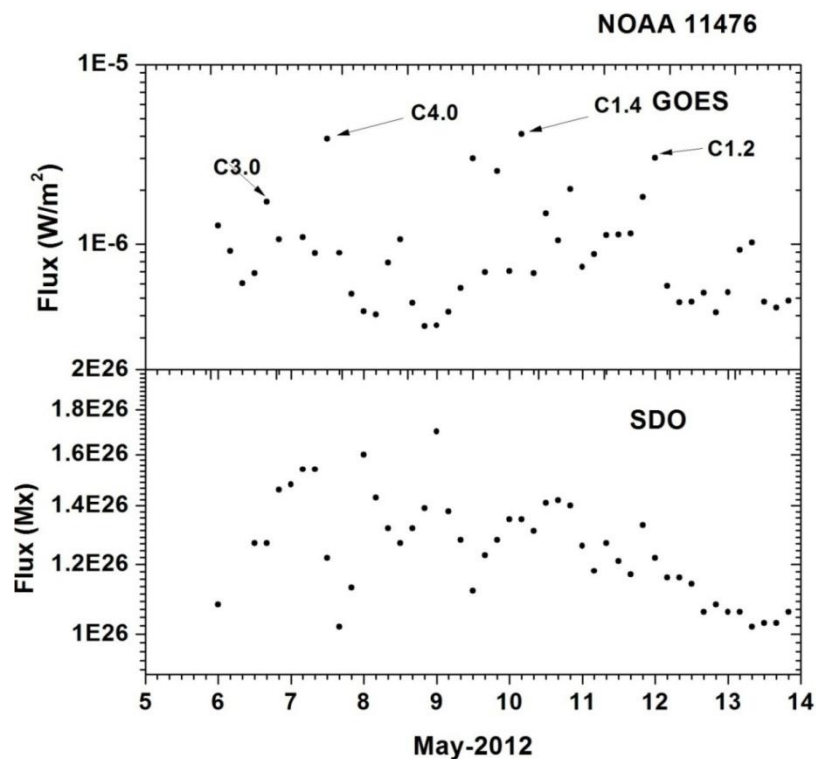
**Figure - 3 magnetic flux and x-ray flux for an active region (NOAA 11476) with during the 06-May-2012 to 13-May-2012**

We found that, in the photosphere whenever magnetic flux enhances then within we found that next few hour flare activity start. The magnitude of the flare depends on the accumulation and storage of magnetic flux, while release of this magnetic field energy depends on other plasma triggering mechanisms. These mechanisms may be gradient, deviation and/or variation in sunspot rotation angle as shown earlier by Jain et al., (2011). Result of study of three active region (AR) show that corona is heated up by the induction of magnetic flux energy from the photosphere

**Reference**

1. Aschwanden, M. J., 2005, Physics of the Solar Corona. An Introduction with Problems and Solutions (2nd edition)
2. Bhatnagar, A. and Livingston, W., 2005, Fundamentals of solar astronomy
3. Jain, R., Awasthi, A. K., Chandel, B., Bharti, L., Hanaoka, Y., and Kiplinger, A.L., 2011, *Solar Phys.* **271**
4. G. E. Hale, 1908, *Astrophys. J.*, **28**, 315
5. Hollweg, J. V., 1985, *Chromospheric Diagnostics and Modelling*, pp 235–251 9
6. Heyvaerts, J. and Norman, C., 2001, *Astronomical and Astrophysical Transactions* **20**, 295

7. Phillips, K. J. H., Feldman, U., and Landi, E., 2008, Cambridge University Press **5** Pesnell, W. D., Thompson, B. J., and Chamberlin, P. C., 2012, *Solar Phy.,* **275**

8. Scherrer, P. H., Schou, J., Bush, R. I., Kosovichev, A. G., Bogart, R. S.,Hoeksema, J. T., Liu, Y., Duvall, T. L., Zhao, J., Title, A. M., Schrijver,

9. C. J., Tarbell, T. D., and Tomczyk, S., 2012, *Solar Phys.* **275**

10. Svestka, Z., 1976, Solar Flares

11. Withbroe, G. L. and Noyes, R. W., 1977, *Annual Rev. in Astron. & Astrophys.***15**, 363

12. Wikstol, O., Judge, P. G., and Hansteen, V. H., 1997, *Astrophys. J.* **483**, 972

# "Effect of concentration of TEA and annealing temperature on band gap of ZnO: A review"

**Vipul J. Shukla[a], Dr.Amitkumar J.Patel[b]**

[a]*Gujarat Technological University, Chandkheda, Ahmedabad –382424 Gujarat*

[b]*Goverment Engineering college, Godhara –389001 Gujarat*

*Email – vipuljshukla317@gmail.com*

## Abstract

The nanocrystalline Zinc Oxide (ZnO) thin films were prepared on glass substrates by chemical bath deposition (CBD) method utilizing aqueous solutions of zinc chloride. Zinc oxide is classified a semiconductor in group II-VI, whose covalence is on the limit amongst ionic and covalent semiconductors. A wide energy band (3.37 eV), high bond energy (60 meV) and high thermal and mechanical stability at room temperature. Different chemical and physical deposition techniques have been connected to create ZnO thin films. Most cases, high temperature and special atmosphere are fundamental. Be that as it may, the chemical bath deposition (CBD) technique speaks to a basic and viable method for deposition. Basically, CBD processes involve preparing ZnO nanoparticles seed layer on special substrate. This review summarizes the main chemical routes used in the chemical bath deposition synthesis of undopedZnO thin films. This paper includes review about effect of complexing agent e.g. TEA and annealing temperature on band gap.

**Keywords**: Zinc oxide, chemical bath deposition, TEA,band gap, annealing temperature.

## Introduction

In recent years, there is a great interest in production of transparent conducting oxide (TCO) and transparent oxide semiconductorsfor the development of photonic devices and transparentconducting electrodes (TCE) for solar cells. As of late, there is an incredible enthusiasm for generation of transparent conducting oxide (TCO) and transparent oxide semiconductors for the improvement of photonic gadgets and transparent conducting electrodes (TCE) for solar cells. Zinc oxide has pulled in critical consideration as a material for ultraviolet (UV) light-producers, varistors, straightforward high power hard transparent high power electronics ware, surface acoustic wave gadgets, piezoelectric transducers and gas sensors and furthermore as a window material for presentations and solar cells. zinc oxide is a hopeful host for solid state blue to UV optoelectronics, including lasers. The applications

incorporate high thickness information stockpiling frameworks, strong state lighting, secure correspondences and bio detection. Zinc oxide, with its remarkable physical and chemical properties, for example, high substance solidness, high electrochemical coupling coefficient, expansive scope of radiation retention and high photostability, is a multifunctional material [1,2]. In materials science, zinc oxide is delegated a semiconductor in gathering II-VI, whose covalence is on the limit amongst ionic and covalent semiconductors. A broad energy band (3.37 eV), high bond energy (60 meV) and high thermal and mechanical dependability at room temperature make it appealing for potential use in electronics, optoelectronics and laser innovation [3,4]. The piezo-and pyroelectric properties of ZnO imply that it can be utilized as a sensor, converter, vitality generator and photocatalyst in hydrogen creation [5,6]. In light of its hardness, unbending nature and piezoelectric consistent it is an imperative material in the ceramics industry, while its low danger, biocompatibility and biodegradability make it a material of enthusiasm for biomedicine and in expert environmental frameworks [7–9]. With respect to preparation method ofZnO nanostructures, there are an amount of techniques used to synthesizeZnO nanostructures. metal-organic chemical vapor deposition (MOCVD) [10], pulsed laser deposition [11], magnetron sputtering method [12], chemical bath deposition (CBD), electrochemically deposited ZnO thin films and so on. CBD has been connected all the more extensively in light of the fact that it is a straightforward technique in watery arrangement and developed in low temperature. Likewise, CBD have another remarkable attributes, such as the simplicity of operation, the low cost, and so forth [13]. Chemical bath deposition is generally utilized for the deposition of different metal chalcogenide thin films. It creates great stores on suitable substrates by the controlled precipitation of the compound from the solution. The technique offers many points of interest over other well-knownvapour phase synthetic routes. It might enable us to effectively control the growth factors, for example, film thickness, deposition rate and nature of crystallites by varying the solution pH, temperature and bath concentration [14]. It doesn't require high voltage equipment, works at room temperature, and thus it is economical. The main necessity for this deposition route is an aqueous solution comprising of a couple of regular chemicals and a substrate for the film to be kept. It frequently experiences an absence of reproducibility in examination with other compound procedures; be that as it may, by the best possible and cautious streamlining of the development parameters, one can accomplish sensible reproducibility. Another favorable position of the CBD technique over other strategy is that the film can be kept at various shapes and size of substrates. In this paper, thin films of ZnO have been deposited on silica

glass substrate using chemical bath method. The band gap and the effect of annealing temperature on band gap have also been investigated. In this paper, we report that decreasing in concentration of TEA, band gap increases.

**Experimental Procedure**

CBD method has been ended up being a decent approach for synthesis of ZnO thin film with the utilization of ZnO seeds in the types of thin films. The substrate is imperative for the development of thin filmslattice and thermal mismatching between it and the film since it generally prompts the development of stress in the deposited film.

The ZnO thin films were prepared by chemical bath technique at room temperature. The reaction bath is composed of $ZnCl_2$, NaOH and TEA (triethanolamine) used as complexing agent. Concentration of $ZnCl_2$ (0.04 M) and of NaOH (0.08 M) were utilized as a part of this technique. Tri ethanolamine was used either directly or as aqueous solution with varying concentration of TEA to ZnOthin films were developed on glass substrate. Before utilize, these glass slides were absorbed aquaregia, a mixture of concentrated HCl and $HNO_3$ in the proportion of 3:1. They were removed after 24 h and washed thoroughly in cold detergent solution, rinsed in distilled water and dribble dried in air. The properly degreased and cleaned substrate surface has the advantage of producing highly adhesive and uniform film. The substrate was immersed vertically at the focal point of response shower in such a way it ought not touch the walls of the beaker [15].Now utilizing same precursori.e.zincchloride(0.1 M) and instead of other complexingagent,small drops of ammonia were added and stirred continuously using a magnetic stirrer to obtain optimum pH of 9.4. For this deposition 70 ml solution of zinc chloride aqueous ammonia were put in 100 ml beaker and the substrates whose surface had been prepared under standard conditions were vertically suspended in the beaker and the solution was constantly stirred using magnetic stirrer in a water bath of constant temperature of $70^{o}$C.The deposition time was 70 minutes. After 70 minutes the substrate with kept thin films were removed, washed with distilled water and left to dry. The as-stored ZnO thin films were additionally tempered at $200^{o}$C and $300^{o}$C in a furnace.The absorbance of the film was also measuredusing UV mini Schmadzu UV-VIS spectrophotometer in thewavelength range 300-1100 nm [18].

**Results and Discussions**

In direct Used of TEA (sample 219) the colour of the film was white but when we decrease the concentration of TEA in aqueous solution the whiteness of the deposition film decreases and become almost transparent and their band gap also increases. In sample 219 (3 ml of direct solution of TEA) we obtain band gap as 2.59 eV [17] and transmittance between 30 and 40%. In sample 311 we used 10 ml of 1 mol aqueous solution of TEA, we obtain band gap as 2.92 eV and transmittance between 40 and 50%. In sample 339 and 328 we used 8 ml of 0.1 and 8 ml of 0.01molarity aqueous solution of TEA, we obtain band gap between 3.37 and 3.57 eV and transmittance between 60 and 80%. We obtain different result when we used aqueous solution of TEA.

In direct Used of TEA (sample 219) the colour of the film was white yet when we decrease the concentration of TEA in aqueous solution the whiteness of the affidavit film decrease and turn out to be practically transparent and their band gap also increases. In sample 219 (3 ml of direct solution of TEA) we get band gap as 2.59 eV [17] and transmittance between of 30 and 40%. In sample 311 we utilized 10 ml of 1 molaqueous solution of TEA, we get band gap as 2.92 eV and transmittance in the vicinity of 40 and half. In sample 339 and 328 we utilized 8 ml of 0.1 and 8 ml of 0.01molarity aqueous solution of TEA, we acquire band crevice in the vicinity of 3.37 and 3.57 eV and transmittance in the vicinity of 60 and 80%. We get distinctive outcome when we utilized aqueous solution of TEA.For different sample 219,311,339 and 328,the band gap are 2.59 eV, 2.92 eV, 3.37 eV and 3.57 eV respectively.

**Optical Band Gap**

The band gap can be determined from the Stern (1963) relation

$A\upsilon = k(h\upsilon - E_g)^{n/2}$

The band gap of the metallic oxide was dictated by plotting $(\alpha h\nu)^2$ as a component of $h\nu$, and extrapolating the straight segment of the bend to $(\alpha h\nu)^2 = 0$ as appeared in Fig.1. The value obtained for the optical band gap is 3.37 and 3.57 eVof 339 and 328 sample.
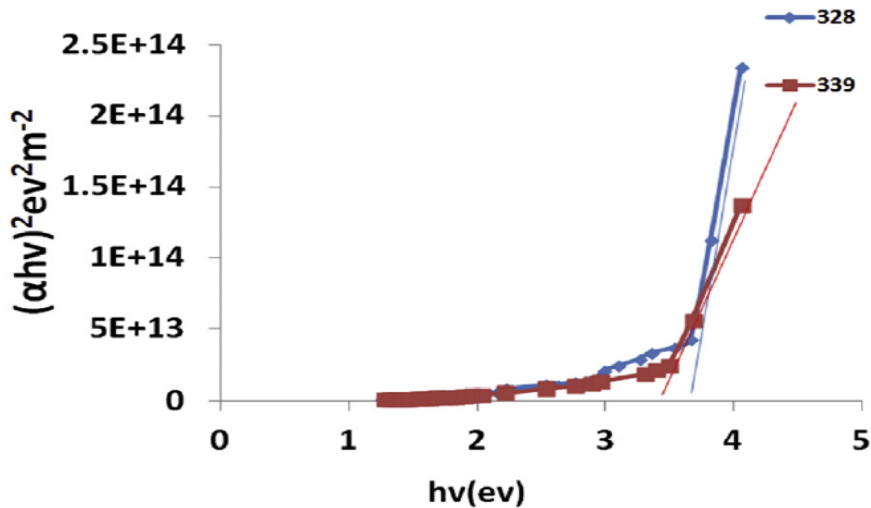
Figure1. Plots of $(\alpha h\upsilon)^2$ ev$^2$ m$^{-2}$against h$\upsilon$(ev).[15]

A plot of against the photon energy hυ gives a curve as shown in Figure 2 and extrapolation of the linear portionof the curve to the axis gives the band gap Eg .The band gaps Eg for as-deposied, annealed at 200 $^{o}$C and 300 $^{o}$C are respectively 2.72, 2.66 and 2.60 eV. The band gapestimation of 2.72 for as-deposited thin film is practically identical to the band gap value acquired by Eya et al (2005). There is a red shift in the band gap estimations of the as-deposited2.72 eV, annealed at 200$^{o}$C of 2.66 eV and 300$^{o}$C of 2.60 eV. This is likewise in concurrence with the works of Elilarassi and Chandrasekaran (2010) and Lv et al, 2011] who
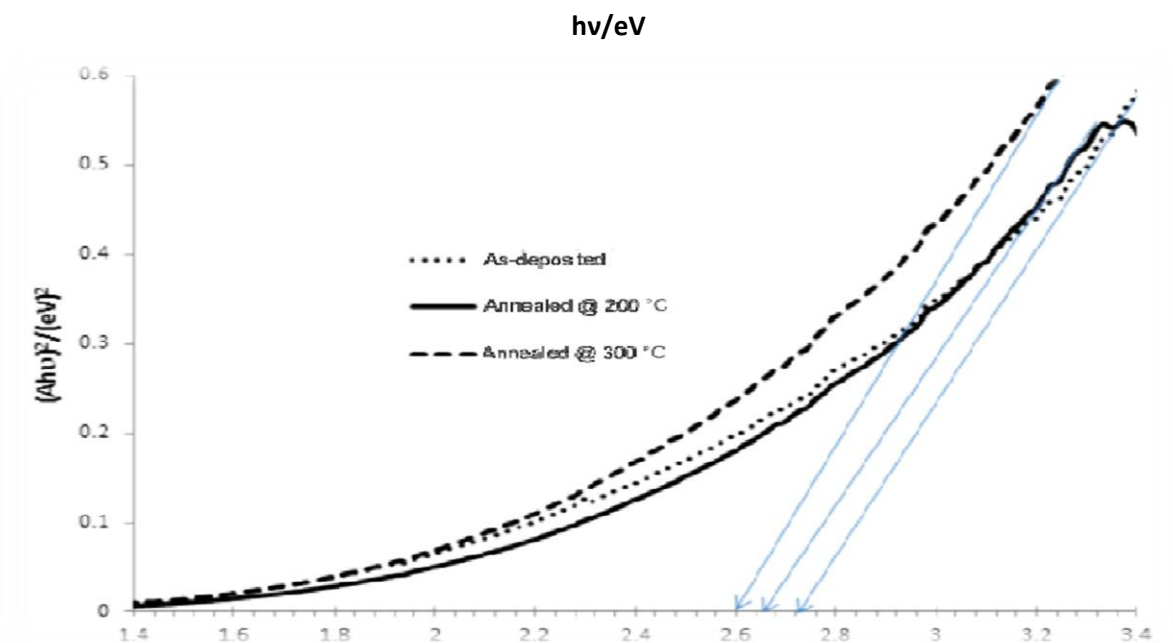
additionally watched a lessening in band gap of ZnO as the annealing temperature was incresed. This may be because of a change in the crystallinity of the ZnO thin film

Figure 2: A graph of $(Ah\upsilon)^2$ versus $h\upsilon$ of ZnO thin film for as-deposited, annealed at 200 °Cand 300°C [16]

## Conclusions

ZnOfilms have been effectively arranged by CBD technique utilizing $ZnCl_2$ and NaOHwith TEA as complexing agent. The band gap of the film is 3.57 eV. The ZnO thin films could be successfully synthesized through the simple chemical bath techniques. The chemical bath deposition technique was effectively used to manufacture ZnO thin films on zinc plates.Structural, optical and morphological reviews were done. The crystallite size and band gap energy were found to rely on upon the bath temperature. The band gap decreased as the crystallite measure increased. The bath temperature was found to impact the development of ZnO crystallites: at temperatures over 50 °C, great crystalline film was produced. The pH range 9.5–10.5 was observed to be the most appropriate for CBD development of ZnO. The utilization of zinc as the substrate is helpful for smooth adsorption of zinc ions on the surface and it brings about a fantastic coating. With the expansion of the annealing temperature, the carrier concentration decreased and the resistivity increased thus band gap is decreased. A decrease in the band gap was seen after expanding the bath temperature and size of the crystallites.

## References

[1]Segets, D.; Gradl, J.; Taylor, R.K.; Vassilev, V.; Peukert, W. Analysis Of Optical Absorbance Spectra For The Determination Of ZnO Nanoparticle Size Distribution, Solubility, And Surface Energy. *AcsNano*2009, *3*, 1703–1710.

[2] Lou, X. Development OfZnO Series Ceramic Semiconductor Gas Sensors. *J. Sens. Trans. Technol.* 1991, *3*, 1–5.

[3] Bacaksiz, E.; Parlak, M.; Tomakin, M.; Özcelik, A.; Karakiz, M.; Altunbas, M. The Effect Of Zinc Nitrate, Zinc Acetate And Zinc Chloride Precursors On Investigation Of Structural And Optical Properties Of ZnO Thin Films. *J. Alloy. Compd.* 2008, *466*, 447–450.

[4] Wang, J.; Cao, J.; Fang, B.; Lu, P.; Deng, S.; Wang, H. Synthesis And Characterization Of Multipod, Flower-Like, And Shuttle-Like ZnO Frameworks In Ionic Liquids. *Mater. Lett.* 2005, *59*, 1405–1408.

[5] Wang, Z.L. Splendid One-Dimensional Nanostructures Of Zinc Oxide: A New Nanomaterial Family For Nanotechnology. *AcsNano*2008, *2*, 1987–1992.

[6] Chaari, M.; Matoussi, A. Electrical Conduction And Dielectric Studies Of ZnO Pellets. *Phys. B Condens. Matter* 2012, *407*, 3441–3447.

[7] Özgür, Ü.; Alivov, Y.I.; Liu, C.; Teke, A.; Reshchikov, M.A.; Doğan, S.; Avrutin, V.; Cho, S.J.; Morkoç, H. A Comprehensive Review OfZnO Materials And Devices. *J. Appl. Phys.* 2005, *98*, Doi:10.1063/1.1992666.

[8] Bhattacharyya, S.; Gedanken, A. A Template-Free, Sonochemical Route To Porous ZnONano-Disks. *MicroporousMesoporous Mater.* 2007, *110*, 553–559.

[9] Ludi, B.; Niederberger, M. Zinc Oxide Nanoparticles: Chemical Mechanism And Classical And Non-Classical Crystallization. *Dalton Trans*. 2013, *42*, 12554–12568.

[10] J. Y. Park, D. J. Lee, B. T. Lee, J. H. Moon, S. S. Kim, *Journal Of Crystal Growth*, 2005, 276, 165.

[11] Y. Sun, G.M. Fuge, M. N. R. Ashfold, *Chem. Phys. Lett.*, 2004, 396, 21.

[12] K. B. Sundaram, A. Khan, *Thin Solid Films*, 1997, 295, 87.

[13] G. Z. Jia, N. Wang, L. Gong, X. N. Fei, *Chalcogenide Letters*, 2009, 6, 463.

[14] Sankapal B.R., Sartale S.D., Lokhande C.D., Ennaoui A., Sol. Energy Mater. Solar Cells, 2004, 83, 447.

[15] P.B. Taunk , R. Das, D.P. Bisen, R.K. Tamrakar, NootanRathor., Synthesis And Optical Properties Of Chemical Bath Deposited ZnO Thin Film, Karbala International Journal Of Modern Science, 2015, XX , 1-7

[16] Nkrumah, F.K. Ampong, B. Kwakye-Awuah, R.K. Nkum, F. Boakye, Synthesis And Characterization Of ZnO Thin Films Deposited By Chemical Bath Technique,International Journal Of Research In Engineering And Technology, 2013, 2 ,12, 809-812

[17]PengZhiwei, Dai Guozhang, Chen Peng, Zhang Qinglin,WanQiang, ZouBingsuo, Synthesis, Characterization And Optical Properties Of Star-Like ZnO Nanostructures, Mater. Lett., 2010, 64, 890.

[18] A.K. Singh, V. Viswanath, V.C. Janu, Synthesis, Effect Of Capping Agents, Structural, Optical And Photoluminescence Properties Of ZnO Nanoparticles, J. Luminescence, 2009, 129, 874-878.

# Asphericity in the Fermi surface of some alkaline earth metals

P. H. Suthar[*], B. Y. Thakore[+] and P. N. Gajjar[++]

[*]Department of Physics, C. U. Shah Science College, Ahmedabad 380 014,

[+]Department of Physics, Sardar Patel University, Vallabh Vidyanagar 388 120,

[++]Department of Physics, School of Sciences, Gujarat University, Ahmedabad 380 009

[*]E-mail: sutharpunit@rediffmail.com

## Abstract

The theoretical observed shape of the Fermi surface (FS) as a probe to examine the applicability, validity and comparing of our well establish two different pseudopotentials for computing actual physical quantities to characterize metallic properties is used, the present paper first time reports a calculation of the shape of the shape of the FS of alkaline earth metals along (Ca (FCC), Sr (FCC), Ba (BCC)) three principal directions [1 0 0], [1 1 0] and [1 1 1] based on a local model potential. The effect of four different forms of dielectric functions on asphericity in the FS, confirms the general correctness of the empirical form factor employed in the investigation.

**Keyword:** Fermi Surface, alkaline earth metals, Asphericity, Pseudopotential

## Introduction

As known as the alkaline earth metals can be considered as simple metals regarding their electronic structure and from the experimental and theoretical point of view, few properties have been determine to the date because of this metals have the high chemical reactivity and to the gas adsorption ability that further increase with temperature [1-5]. These difficulties have induced a low interest for technological purpose and a disinterested for the theoretical work. So that theoretical point of view first time we have study the Fermi surface (FS) of an alkaline earth metals show a small but departure from a free electronic sphere and the study of its asphericity thus provides a delicates test of band theory predictions. Several electronic properties of metals are determined from variation in the shape of the Fermi surface. The recent success of such investigation pertaining to the Fermi surface[1-27] of fcc (Ca and Sr) and bcc (Ba) alkaline earth metals has motivated us to study of distortion in the Fermi surface of metals to confirms the wide applicability of pseudopotential theory. The sharp and more complicated than those of alkaline

earth metals. In the present paper asphericity in the Fermi surface of Ca, Sr and Ba is calculated and compared using our well establish two different model potentials [28, 29].

In the present we focus our attention to the detailed theoretical investigation on the as asphericity in the Fermi surface in the alkaline earth metals using two different model potentials [28,29] along with local field correction function due to Hartree(H) [2], Taylor(T) [30], Ichimaru and Ustumi (IU) [31] , Farid et al (F) [32], Sarkar et al (S) [33] and Hubbard and Sham (HS) [34-35].

**Theory and method of computation**

The Fermi surface of Fermi-energy EF in wave-number space and is defined by

$$\varepsilon(k) = E_F \tag{1}$$

The Fermi surface (FS) provides us all the electron states that can play any part in the ordinary transport properties of the metal and for binary alloys. For a metal at absolute zero temperature, all the states inside the Fermi Surface are filled while those outside are empty. Thus the FS in a mathematical construction related to the dynamical properties of the conduction electrons in a metal. In a free electron gas the FS is a sphere.

It is a well-establish fact that the Fermi Surface of a real metal shows a small but definite departure from the perfectly spherical shape of the free electron gas. The asphericity of the FS provides us a sensitive test of certain results derived from electronic energy bands. Several electronic properties of metals are determined from variation in the shape of the FS.

The distortion in the spherical shape of the free electronic Fermi surface is the case of metals and binary alloys may be given by the expression [1-5].

$$\boldsymbol{k}_F = \boldsymbol{k}_F^0 \left[ 1 + \Delta\left(\theta_{kq}\right) \right] \tag{2}$$

Here, $\Delta\left(\theta_{kq}\right)$ is the dilation to the free electron Fermi wave number, $k_F^0$ and $\theta_{kq}$ are the angle between direction k and reciprocal lattice vector q. The Fermi energy $E_F$ on the basis of perturbation approach up to the second order may be written as [5-7]

$$E_F = \frac{\hbar^2}{2m}\left(k_F^0\right)^2 - \sum_{qpair} C(q) Vs^2(q) \tag{3}$$

Where $V_s^2(q)$ is the screened ion pseudopotential from factor is given in Suthar et al [28, 29]. The function C(q) is given as [5-7]

**108** Online International, Refereed, Impact factor & Indexed Monthly Journal
RET Academy for International Journals of Multidisciplinary Research (RAIJMR)
www.raijmr.com

$$C(q) = \frac{m}{2\hbar^2 k_F^0 q} \ln \left| \frac{2k_F^0 + q}{2k_F^0 - q} \right| \tag{4}$$

This function is estimated from the conclusion that the distortion should not alter the volume element enclosed by the Fermi surface.

The expression representing the distortion in the Fermi surface shape, after neglecting higher power of $\Delta(\theta_{kq})$ is given as [5-7]

$$\Delta K = \frac{\Delta k_F}{k_F} = \sum_{q-pair} \frac{V_s^2(q)}{E_F^0} \left[ \frac{1}{\frac{\hbar^2}{2m} q^2 - 4E_F^0 \cos^2 \theta_{kq}} - C(q) \right] \tag{5}$$

Here $E_F^0$ is the free electron Fermi energy. Another method for computing the distortion in the FS has been suggested by Wallace [36]. Both the methods are found to give similar results.

The quantities X, Y and δ are most frequently used in the study of radial distortion of the Fermi surface of alkaline earth elements, which are represented by [27]

$$X = (\Delta k_{100} - \Delta k_{111}) \times 10^4 \tag{6}$$

$$Y = (\Delta k_{110} - \Delta k_{111}) \times 10^4 \tag{7}$$

$$\delta = (\Delta k_{110} - \Delta k_{100}) \times 10^4 \tag{8}$$

**Results and Discussion**

Table-1: Input parameters and Constants.

| Metals | Z | $\Omega_0$ (a.u) | $r_c$ (a.u) | |
|--------|---|------------------|-------------|---|
| | | | Model-1 | Model-2 |
| Ca | 2 | 293.492 | 1.3639 | 1.0453 |
| Sr | 2 | 380.442 | 1.4871 | 1.1398 |
| Ba | 2 | 428.515 | 1.5113 | 1.1583 |

Table-1 shows the Input parameters and constants use in the present computation. The Ca, Sr (d-shell) and Ba (d-shell) alkaline-earth metals can be considered as a simple in regard of the electronic aspect, they are certainly the less studied elements among the metals. So that here first time the asphericity in the Fermi surface of FCC Ca, Sr and BCC Ba metals along with [100], [110] and [111] directions has been evaluated. Fig. 1, 2 and 3 shows the computed asphericity in

the Fermi surface of Ca, Sr and Ba along three principal symmetry directions and it is observed that the present graphs show the almost same in nature computed using Model-1[28] and Model-2[29] pseudopotentials. Table 2, 3 and 4 give the numerical values of the Fermi surface distortion at the points of high symmetry.
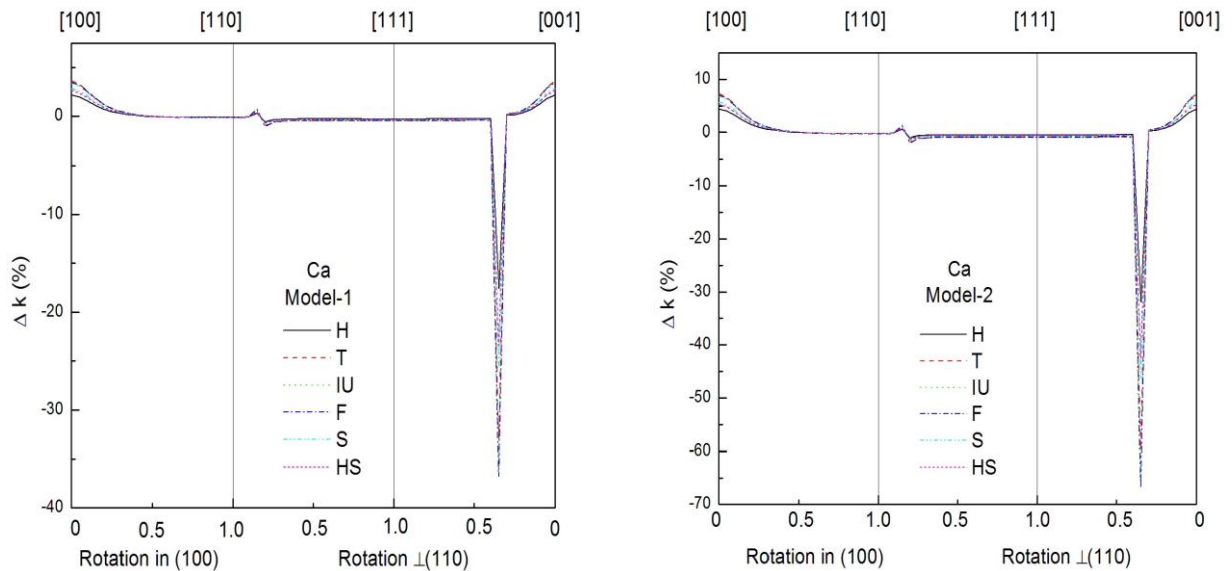


Fig. 1: Asphericity in the Fermi surface for Ca using Model-1[28] and Model-2[29] potential.
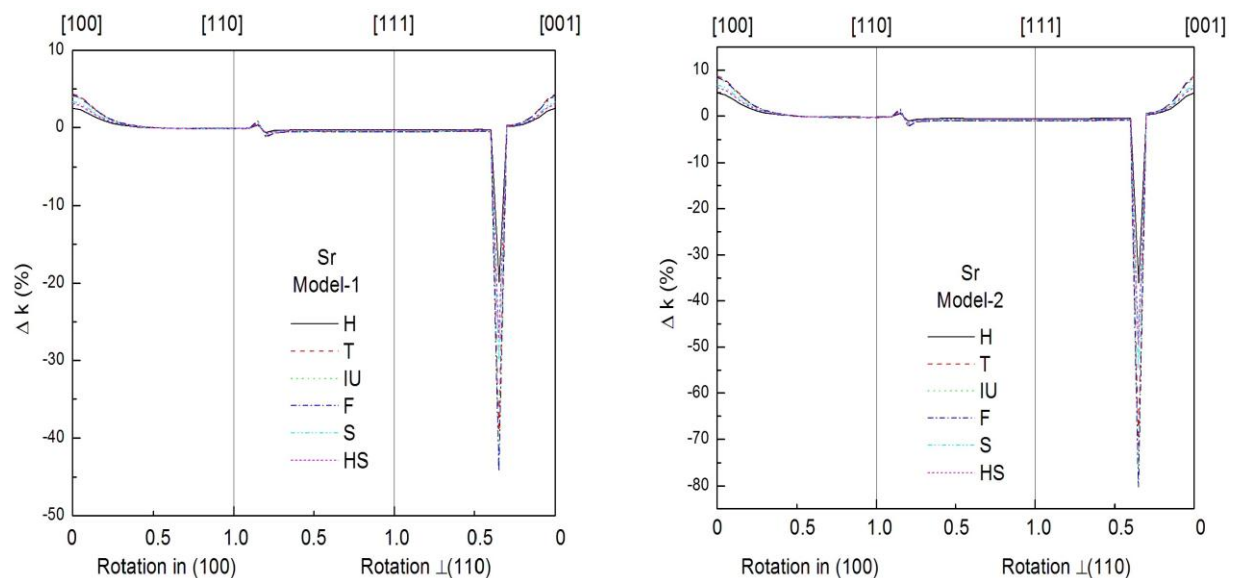


Fig. 2: Asphericity in the Fermi surface for Sr using Model-1[28] and Model-2[29] potential.
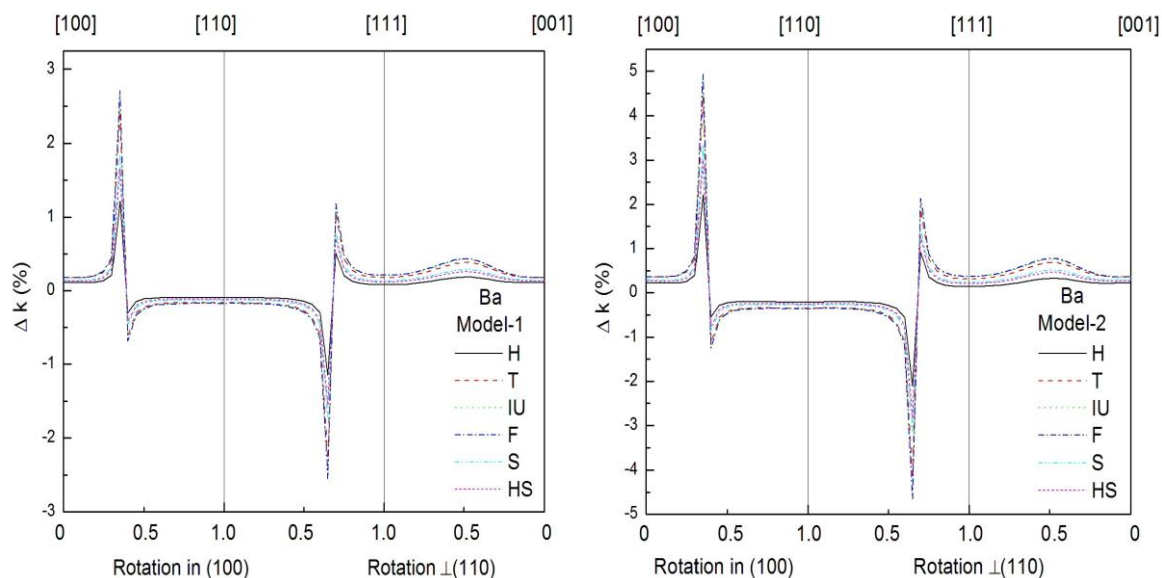
Fig. 3: Asphericity in the Fermi surface for Ba using Model-1[28] and Model-2[29] potential.

The variation in the present results of $\Delta k(\%)$ in going from [1 0 0] to [1 1 0] and [0 0 1] (via [1 1 1]), due to various local filed correction functions can be judged from the Fig. 1, 2 and 3 the results obtained with Model-1 and Model-2 along with IU, F, S and HS dielectric functions are falling between those obtained with H and the T dielectric functions. It is also observed that present results computed using Model-1 and Model-2 along with IU and F screening almost overlaps each other. Compared from Fig. 1 to the Hartree dielectric function [2] the variation in the present finding in the Fermi surface for FCC Ca due to Taylor [31] function is about 64.20% along [1 0 0], 47.61% along [1 1 0] and 67.02% along [1 1 1] for Model-1. Those variations in the Fermi surface for Model-2 are about 64.28% along [100], 51.84% along [110] and 66.55% [1 1 1]. Similarly we can found for the Fermi surface from Fig. 2 for FCC Sr due to T function is about 71.72% along [1 0 0], 54.67% along [1 1 0] and 74.25% along [1 1 1] for Model-1[28]. Those variations in the Fermi surface for Model-2[29] are about 71.70% along [1 0 0], 59.08% along [1 1 0] and 74.22% along [1 1 1]. From Fig 3 to the Hartree dielectric functions the variation in the Fermi surface for BCC Ba due to 63.06% along [1 0 0], 72.31% along [1 1 0] and 158% along [1 1 1] for Model-1, variation in the Fermi surface for Model-2 are about 60.50% [1 0 0], 65.12%[1 1 0] and 119.12% along [1 1 1]. From Table-2, 3 and Table-4 it is observed that the Outcome of results computed using the Model-2[29] potential is almost double the

values than those obtained using Model-1[28] potential along with all screening function. Here the core radius plays a very important role in predicting various properties using the local pseudopotentials.

**Table-2:** Radial distribution of the Fermi Surface of Ca (in %)

| LFCF | Model | $\Delta k_{100}$ | $\Delta k_{110}$ | $\Delta k_{111}$ | X | Y | δ |
|------|-------|--------|--------|--------|--------|--------|--------|
| H | M-1 | 2.2104 | -0.1046 | -0.2732 | 2.4836 | 0.1686 | -2.3150 |
| | M-2 | 4.4188 | -0.2170 | -0.5424 | 4.9612 | 0.3254 | -4.6358 |
| T | M-1 | 3.6295 | -0.1544 | -0.4563 | 4.0858 | 0.3019 | -3.7839 |
| | M-2 | 7.2584 | -0.3295 | -0.9034 | 8.1618 | 0.5739 | -7.5879 |
| IU | M-1 | 3.3961 | -0.1175 | -0.4373 | 3.8334 | 0.3198 | -3.5136 |
| | M-2 | 6.7913 | -0.2601 | -0.8642 | 7.6555 | 0.6041 | -7.0514 |
| F | M-1 | 3.5111 | -0.1249 | -0.4509 | 3.9620 | 0.3260 | -3.6360 |
| | M-2 | 7.0215 | -0.2751 | -0.8912 | 7.9127 | 0.6161 | -7.2966 |
| S | M-1 | 2.8654 | -0.1235 | -0.3593 | 3.2247 | 0.2358 | -2.9889 |
| | M-2 | 5.7296 | -0.2618 | -0.7120 | 6.4416 | 0.4502 | -5.9914 |
| HS | M-1 | 2.6433 | -0.1142 | -0.3312 | 2.9745 | 0.2170 | -2.7575 |
| | M-2 | 5.2851 | -0.2415 | -0.6565 | 5.9416 | 0.4150 | -5.5266 |
| Other | -- | -- | -- | -- | -- | -- | -- |

**Table-3:** Radial distribution of the Fermi Surface of Sr (in %)

| LFCF | Model | $\Delta k_{100}$ | $\Delta k_{110}$ | $\Delta k_{111}$ | X | Y | δ |
|------|-------|--------|--------|--------|--------|--------|--------|
| H | M-1 | 2.5357 | -0.1220 | -0.3125 | 2.8482 | 0.1905 | -2.6577 |
| | M-2 | 5.0708 | -0.2522 | -0.6211 | 5.6919 | 0.3689 | -5.323 |
| T | M-1 | 4.3544 | -0.1887 | -0.5461 | 4.9005 | 0.3574 | -4.5431 |
| | M-2 | 8.7111 | -0.4012 | -1.0821 | 9.7932 | 0.6809 | -9.1123 |
| IU | M-1 | 4.0470 | -0.1408 | -0.5210 | 4.568 | 0.3802 | -4.1878 |
| | M-2 | 8.0958 | -0.3108 | -1.0301 | 9.1259 | 0.7193 | -8.4066 |
| F | M-1 | 4.2043 | -0.1508 | -0.5395 | 4.7438 | 0.3887 | -4.3551 |
| | M-2 | 8.4108 | -0.3314 | -1.0669 | 9.4777 | 0.7355 | -8.7422 |
| S | M-1 | 3.3838 | -0.1479 | -0.4235 | 3.8073 | 0.2756 | -3.5317 |
| | M-2 | 6.7686 | -0.3128 | -0.8397 | 7.6083 | 0.5269 | -7.0814 |
| HS | M-1 | 3.0872 | -0.1349 | -0.3862 | 3.4734 | 0.2513 | -3.2221 |
| | M-2 | 6.1742 | -0.2845 | -0.7660 | 2.8482 | 0.1905 | -2.6577 |
| Other | -- | -- | -- | -- | -- | -- | -- |

**Table-4:** Radial distribution of the Fermi Surface of Ba (in %)

| LFCF | Model | $\Delta k_{100}$ | $\Delta k_{110}$ | $\Delta k_{111}$ | X | Y | δ |
|------|-------|---------|---------|---------|--------|---------|---------|
| H | M-1 | 0.1083 | -0.0975 | 0.0802 | 0.0281 | -0.1777 | -0.2058 |
| H | M-2 | 0.2289 | -0.2127 | 0.1438 | 0.0851 | -0.3565 | -0.4416 |
| T | M-1 | 0.1766 | -0.1680 | 0.1774 | -0.0008 | -0.3454 | -0.3446 |
| T | M-2 | 0.3674 | -0.3512 | 0.3156 | 0.0518 | -0.6668 | -0.7186 |
| IU | M-1 | 0.1698 | -0.1714 | 0.2035 | -0.0337 | -0.3749 | -0.3412 |
| IU | M-2 | 0.3478 | -0.3511 | 0.3053 | 0.0425 | -0.6564 | -0.6989 |
| F | M-1 | 0.1750 | -0.1758 | 0.2076 | -0.0326 | -0.3834 | -0.3508 |
| F | M-2 | 0.3591 | -0.3604 | 0.3723 | -0.0132 | -0.7327 | -0.7195 |
| S | M-1 | 0.1397 | -0.1314 | 0.1310 | 0.0087 | -0.2624 | -0.2711 |
| S | M-2 | 0.2918 | -0.2778 | 0.2340 | 0.0578 | -0.5118 | -0.5696 |
| HS | M-1 | 0.1261 | -0.1208 | 0.1166 | 0.0095 | -0.2374 | -0.2469 |
| HS | M-2 | 0.2701 | -0.2570 | 0.2088 | 0.0281 | -0.1777 | -0.2058 |
| Other | -- | -- | -- | -- | -- | -- | -- |

The quantities X, Y and δ are calculated using the equation 6-8 and calculated values are displayed in tables along with the available results. X represent the asphericity (%) at [1 0 0] point relative to [1 1 1]. For the first time we have made here in detail about the asphericity in the Fermi surface of Ca, Sr and Ba along the [1 0 0], [1 1 0] and [1 1 1] directions. This can be used as a test for the present local pseudopotentials and other various pseudo-potentials which have been well established so far. The present approximation for the Fermi surface distortion of alkaline earth metals might give additional information regarding the trends in the Fermi surface distortion of the fcc and bcc metals which may be lead to definite relation between the radial distortion of a nearly spherical surface and the Fourier components of the effective lattice potential. In the absence of other data and experimental values for present alkaline earth metals we do not offer any concrete remark at the present, but this results obtained will surely serve as a good data for further comparison.

## Conclusion

Finally it is concluded that for the alkaline earth metals, Ca, Sr and Ba the Fermi surface distortion is extremely sensitive to the choice of the screening function and it is found from the present computation that FSD in the Ca, Sr and Ba metals are very similar in nature. Due to lack

of other information and experimental data we do not put any concrete remarks on Fermi surface of the alkaline earth metals. The different forms of the local field corrections influence heavily the asphericity in the Fermi surface in all the three regions considered in the present work. This is also satisfies the self consistency conditions in the compressibility sum rule and the short range correlation.

**Acknowledged**

**References**

[1]     A. P. Cracknell and K. C. Wong, The Fermi surface, (its concepts, determination and use in the phys of metals) Cladendon press Oxford (1973).

[2]     W. A. Harrison, Pseudopotential in the theory of metals W. A. Benjamin, Inc. (1996).

[3]     C. Kittle, Introduction to Solid State Physics,John Wiley and Son, New York (1971).

[4]     R. Ahuja, S. Auluck J. M. Wills, O. Eriksson, P. Soderlind, and B. Johansson, Phys. Rev B,1994, 50, 18 003.

[5]     P. N. Gajjar, B. Y. Thakore and A. R. Jani, Solid Stat. Commu.1996, 100, 785.

[6]     P. N. Gajjar, B. Y. Thakore, J. S. Luhar and A. R.Jani, Ind. J. Pure & Appl. Phys., 1995 33, 309

[7]     M. H. Patel, A. M. Vora, P. N. Gajjar and A. R. Jani, Commun. Theor, Phys.,2002, 38, 365.

[8]     G. Jacucci and R Taylor, J. Phys. F: Metal Phys., 1981, 11, 787.

[9]     F. S. Ham, Phys. Rev., 1962, 128, 2524.

[10]    D. Shohenberg, P.J. Stiles, Proc. Roy. Soc. London, 1964, 281, 62.

[11]    M. J. G. Lee,Phys. Rev. B,1971, 4, 673

[12]    M. J. G. Lee and V. Heine, Phys. Rev. B, 1971, 5, 3839.

[13]    K. O. Okumara and I.M. Templeton,Phil. Mag., 1962, **7**, 1239.

[14]    J. R. Anderson and A. V. Gold, Phys. Rev. A, 1965,  139, 1459.

[15]    T. Schneider and E. Stoll,Phys, Kondens Materie, 1966, 5, 364.

[16]    L. Dagens, F. Perrot,Phys. Rev. B, 1973, 8, 1281.

[17]    M. Matasura,Phys. Lett. A, 1974,  50, 131.

[18]    Shin-Ichi T. Inoue, S. Asano, and J. Yamasta,J. Phys. Soc. Jpn.1971, 30, 1546.

[19]    W. Y. Ching,  and J. Callaway, Phys. Rev. B, 1973,  9, 5115.

[20]    M. Matasura, C. H.  Wo and S. Wang, J. Phys. F, 1975, 5, 1849.

[21]    D. Jennison,Phys. Rev. B, 1974, 16, 5147.

[22]    H. Bross and G. Bohn, Z. Phys. B, 1975, 20, 261.

[23]    K. N. Khanna and P. K. Sharma, Phys. Stat. Sol (b), 1978, 88, 809.

[24]    K. N. Khanna and P. L. Srivasta, Phys. Stat. Sol (b), 1979, 94, K 169.

[25]    S. S. Rajput, R. Prasad, R. M. Singru, W. Trifishauser, A. Eckert G. Kogel, S. Kaprazyk and A. Bansil, J. Phys,: Condens Matter, 1993, 5, 6149.

[26]    H. K. Patel, PhD. thesis, Sardar Patel University,(Vallabh Vidyanagar, India, 1991).

[27]    M. H. Patel, PhD. thesis, Sardar Patel University,( Vallabh Vidyanagar, India 2002).

[28]    P H Suthar, International conference on condensed matter, 30-31 Oct. 2015,Bikaner, India, ( AIP Conference Proceeding,USA, 2016) 020599.

[29]    P. H. Suthar, B. Y. Thakore, P. N. Gajjar, communication in Physics,2014, 24,135

[30]    R. Taylor, J. Phys .F, 1981,  8, 1699.

[31]    S. Ichimaru and K. Utsumi, Phys.  Rev. B **24** 3220 (1981).

[32]    B. Farid, V. Heine, G E Engel, I J Robertson, Phys. Rev. B,1993, **48** , 11602.

[33]    A Sarkar, D S Sen, H D Roy, Mod. Phys. lett., 1998, **12,** 639.

[34]    J. Hubbard,  Proc. Roy. Soc. London A, 1957,  243**,** 336.

[35]    L. J. Sham, Proc. Roy. Soc. London A, 1965,  283**,** 33 1965.

[36]    D. C. Wallace, Thermodynamics of crystals, New York: John Wiley and Sons, 1972.

# Dielectric Properties of Ammonium Dihydrogen Phosphate (ADP)

Vimal Patel[1], S. M. Vyas[2], Piyush Patel[3], Himanshu Pavagadhi[4]

[1,2,3,4] Department of Physics, School of Sciences, Gujarat University, Ahmedabad-380009.

Mail id: [1]vimalpatel082013@gmail.com

[2]s_m_vyas_gu@hotmail.com

## Abstract

Non linear optical phenomenon in material plays a major role in the opto electro technologies. Ammonium dihydrogen phosphate (ADP) is an excellent inorganic nonlinear optical material which is used in various instrument applications. In the present work, Pure ADP powder is used for the characterization at room temperature by the complex relative dielectric function $\varepsilon^*(\omega) = \varepsilon' - j\varepsilon''$ of mixture of ADP with water in molar fraction have been measured using precision LCR meter in the frequency range 20Hz to 2MHz. The dielectric properties of the liquid samples are represented in terms of complex relative dielectric function $\varepsilon^*(\omega)$, conductivity $\sigma^*(\omega)$, Refractive Index, Density as well as permeability $(\varepsilon_\alpha)$.

## Key Words

NLO, Complex relative dielectric function, conductivity, aqueous solution.

## Introduction

Ammonium dihydrogen phosphate (ADP) and potassium dihydrogen phosphate (KDP) is a nonlinear optical material. Potassium dihydrogen phosphate ($KH_2PO_4$) and several other isomorphous salts i.e. potassium dihydrogen arsenate ($KH_2ASO_4$), ammonium dihydrogen phosphate ($NH_4H_2PO_4$), and ammonium dihydrogen arsenate ($NH_4H_2ASO_4$) exhibited phase changes at low temperatures [1]. The group of phosphates isomorphous with the tetragonal form of $NH_4H_2PO_4$ (ADP) and $NH_4H_zAsO_4$ (ADA) provides an opportunity to examine a structure layout with various combinations of the cationic and anionic groups. In crystal engineering, the success of controlling various properties of NLO in molecular engineering from the last few years has prompted better initiative as well as photonic devices have found more importance because of their capability of carrying information, large storage and high processing capacity, low cost, etc. All these devices require single crystals or fibres with nonlinear optical (NLO) properties. This crystal is widely used for electro-optical

applications such as Q- switch for Nd: YAG, Nd: YLF, Ti-sapphire lasers and for acoustic-optical applications and it is widely used as the second, third and fourth harmonic generator of Nd: YAG and Nd: YLF lasers. Single crystals of ADP are used for frequency doubling and tripling of laser system [2-4]. As a representative hydrogen-bonded material, ADP has also attracted towards relationship between crystal structure and their properties extensive attention in the investigation of hydrogen bonding behaviors in crystal [5–8]. ADP has been the subject of a wide variety of investigations compares to last few years. Acceptable studies have been done on the growth and properties of pure ADP and doped ADP [9-11]. ADP belongs to tetragonal crystal structure and ADP has unit cell parameters of a = b = 7.510 Å and c = 7.564 Å [12-14]. The demand for high quality large KDP and ADP single crystals increases due to their application as frequency conversion crystal in inertial confinement fusion [15-16]. In this paper we have study the dielectric spectroscopy of binary mixture of ADP crystal and pure water. In present there is a large interest on the molecular interaction in the liquid materials, it will provides information to make a comparative dielectric study of the liquid samples ADP-water mixtures in the frequency range 20Hz to 2MHz and result will be accurately measured dielectric constant and other evaluated dielectric parameter at constant temperature. The dielectric properties of material are represented in terms of intensive quantities i.e. complex relative dielectric function $\varepsilon^*(\omega)$, conductivity $\sigma^*(\omega)$.

## Materials & Preparation:

ADP materials were of AR grade and the crystal growth process was carried out in aqueous solution. The calculated amount of ADP was dissolved in double dissolved water. According to molar fraction the amount of ADP is dissolve in the double distilled water in the range of 0.1 to 0.8 different molar fractions. This solution is used for the study of dielectric spectroscopy over the frequency range 20Hz to 2MHz.

## Result and Discussion

The complex dielectric function $\varepsilon^*(\omega)$ of liquid samples were determined by using precision LCR meter with four terminal liquid dielectric test fixture used for measurement of capacitance and resistance in the frequency range 20Hz to 2MHz. The capacitance and parallel resistance of the dielectric liquid test fixture without samples and with samples were measured to compensate for a short. The test fixture correction coefficient was also considered to cancel the effect of stray capacitance during the calculation of the complex

relative dielectric function $\varepsilon^*(\omega)$. The complex relative dielectric function contains two terms in which first term gives the dielectric constant and it is an important property of the dielectric materials. The term dielectric constant depends on the frequency of the chemical structure imperfection of the material, alternating field, temperature and pressure [17]. This part is basically used for the study of frequency dependence of dielectric constant and dielectric loss of the liquid samples with different molar fraction of the ADP sample at room temperature.

$$\varepsilon^*(\omega) = \varepsilon' - j\varepsilon'' = \alpha \left[ \frac{C_P}{C_0} - j \frac{1}{\omega C_0 R_P} \right] \qquad (1)$$

Where $C_O$=Capacitance of air, $C_P$=parallel capacitance with sample, $R_P$=Parallel resistance with sample, $\omega=2\pi f$ and is the angular frequency, $\alpha$=correction coefficient of the cell, all measurements were made at room temperature.
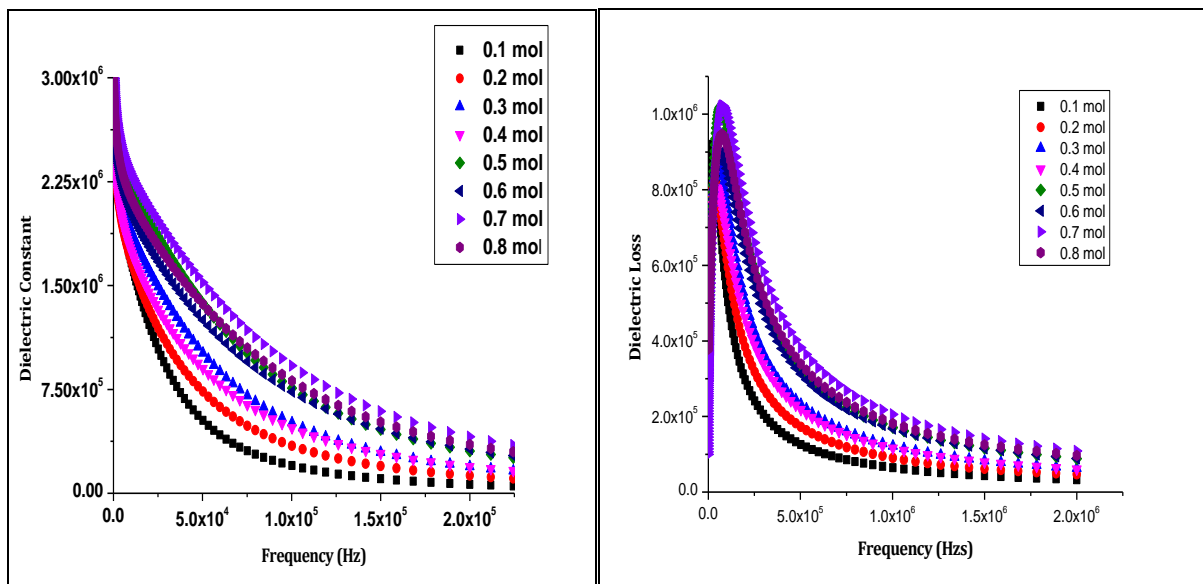


Figure 1 (a): Dielectric Constant of liquid of ADP and Figure 1(b): Dielectric Loss of Liquid of ADP.

The $\varepsilon^*(\omega)=\varepsilon'-j\varepsilon''$ is a important quantity with the condition that in the experiment the electric field is an independent variable and the charge is the dependent one. Considering the charge as the independent variable, the dielectric constant is shown in figure 1, all mixtures samples decreases as the frequency increasing from 20Hz to 2MHz. from the figure, dielectric constant of different molar fraction of ADP in water over a entire frequency range is high in the low frequency region and decreases gradually with the increases the frequency. This effect of high dielectric constant at low frequency is due to various polarizations and high

value at low frequency is responsible due to electrode polarization and ionic conduction. Figure 1 (a) show that as the frequency increases value of dielectric constant decreases because of as the frequency increases the vibration of molecules increases result decreases in dielectric constant. Figure 2 (b) shows the spectra of dielectric loss with different molar fraction and the peak at low frequencies in dielectric loss spectra which is used to separate the bulk material properties depending on electrode polarization and relaxation frequency. During this electrode polarization, ions are absorbed on the electrode surfaces in the alternating electric field which involves the charging and discharging of the ions on the electrode surface [18-19].

**Conductivity**

Real part $\sigma'$ and the imaginary part $\sigma''$ are two part of the complex conductivity $\sigma^*(\omega)$ and its values can be obtained from the equation 2. Where $\varepsilon_0$ (8.854 x $10^{-11}$ F·m$^{-1}$) is free space dielectric constant.

$$\sigma = \sigma' - j\sigma'' = \omega\varepsilon_0\varepsilon'' - j\omega\varepsilon_0\varepsilon'' \tag{2}$$
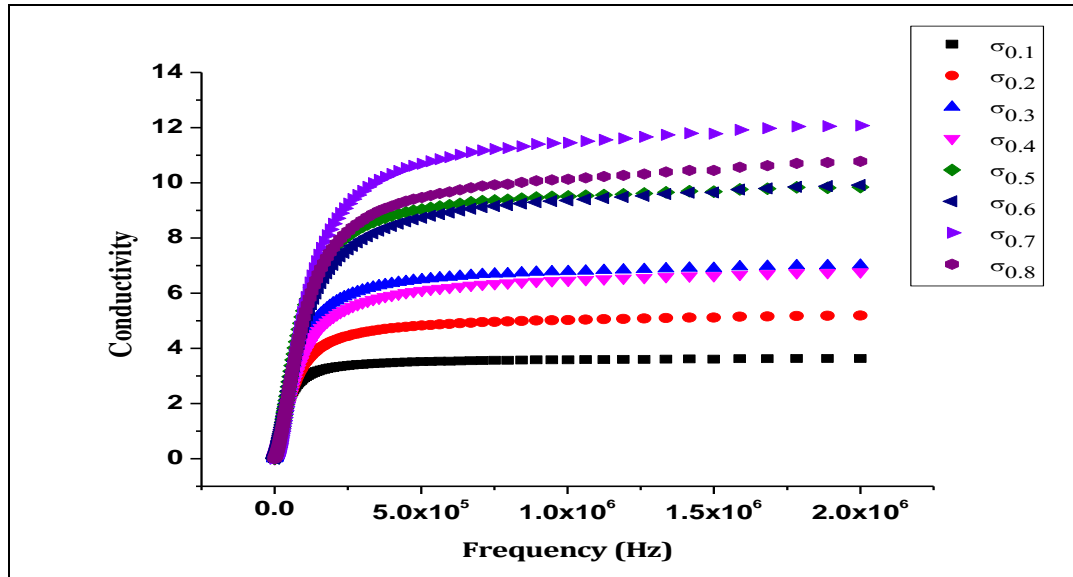


**Figure 3: Real part of conductivity as a function of frequency.**

Figure 3 shows the $\sigma'$ spectra of the liquid mixture of ADP. This figure shows the linearly increment upto certain limit in ionic conductivity at low frequency region and this is due to the increment of number of mobile charge carrier as the molar fraction of the liquid

increases. Spectra show high conductivity at low frequency and as the frequency increases it become almost saturation.

**Refractive Index**

The Abbe refractometer is a classic optical instrument which is used to measure the refractive index of liquids. In order to measure the index, A filtered white light source is used. At the yellow sodium D line of 589 nm. The refractive index (η) can be calculated using the equation (3).

$$\eta = \frac{c}{v} \tag{3}$$

**Table 1 : various parameter obtain from the experimental data.**

| Molar Weight(%) | Refractive Index | $\varepsilon_\alpha$ | Density $(Kg/m^3)$ |
|---|---|---|---|
| 0.1 | 1.339 | 1.793 | 1.76 |
| 0.2 | 1.348 | 1.817 | 1.80 |
| 0.3 | 1.354 | 1.834 | 1.84 |
| 0.4 | 1.367 | 1.870 | 1.87 |
| 0.5 | 1.374 | 1.887 | 1.91 |
| 0.6 | 1.382 | 1.910 | 1.93 |
| 0.7 | 1.389 | 1.930 | 1.96 |
| 0.8 | 1.397 | 1.951 | 1.99 |

From the Table 1 we can say that the refractive indices of liquid mixtures are increases as the molar concentration of mixture increases this is because of as the number of ions increases, refraction of light also increases. Permeability ($\varepsilon_\alpha$) can be calculated as the square of refractive index which is shown in table 1 and increases as the molar fraction of mixtures increases. pycnometer is used to measure the density of liquid mixtures. Density also increases as the molar fraction increases. All the measurements were carried out at room temperature.

**Conclusion**

This paper gives experimental data for complex relative dielectric function, conductivity, Refractive index and $\varepsilon_\alpha$ of the mixtures with different molar concentration. Dieletric constant is high at low frequency but as the frequency increases then it decreases and Dielectric Loss

decreases as the frequency and as molar fraction increases, Conductivity shows increases linearly as the frequency increases after certain frequencies it becomes constant values. This analysis shown various dielectric and electric quantity behavior in spectra confirms that this behavior is governed by the change in molar fraction liquids materials of the ADP and it is basically used to study the intermolecular of the liquid mixture.

## Acknowledgement

## References

1. Georg Busch, "Neue Seignette Elektrika," Helv. Phys. Acta, 1938, 11, No. 3.
2. N. Zaitseva, L.Carman, "Progress in Crystal Growth and Characterization", 2001, vol. 43, no. 1.6.
3. S. M. Klimentov, S. V Garnov, A. S. Epifanov, A. A Manenkov, "Proceedings of SPIE" 1994, vol 342, pp-2145.
4. R. Ramirez, J. A Gonzala, "Solid state communications", 1990, vol. 75, pp 482.
5. D. Xue, S. Zhang, "Physica", 1999, vol B 262. pp 78.
6. D. Xue, H. Ratajczak, "J. Mol. Struct.", 2005, vol 716, pp 207.
7. D. Xue, S. Zhang, "Chem. Phys. Lett.", 1999, vol 301, vol 449.
8. D. Xue, S. Zhang, "J. Phys. Chem. Solids", 1996, vol. 57, pp 1321.
9. K. Sethuraman, R. R. Babu, R. Gopalakrishnan and P. Ramasamy, "Unidirectional Growth of(1 1 0) Ammo- nium Dihydrogen Orthophosphate Single Crystal by Sankaranarayanan Ramasamy Method," Journal of Crystal Growth, 2006, Vol. 294, No. 2, pp. 349-352.
10. S. Nagalingam, S. Vasudevan and P. Ramasamy, "Effect of Impurities on the Nucleation of ADP from Aqueous Solution," Crystal Research and Technology, 1981, Vol. 16, No. 6, pp.647-650.
11. R. Ramesh and C. Mahadevan, "Nucleation Studies in Supersaturated Aqueous Solutions of $(NH_4)H_2PO_4$ Doped with $(NH_4)_2C_2O_4 \cdot H_2O$," Bulletin of Materials Science, 1998, Vol. 21, No. 4, pp. 287-290.
12. M. E. Lines and A. M. Glass, "Principles and Applica- tions of Ferroelectrics and Related Materials," Clarendon Press, Oxford, 1977.
13. N. P. Rajesh, K. Meera, K. Srinivasan, S. Ragavan and P. Ramasamy, "Effect of EDTA on the Metastable Zone width of ADP," Journal of Crystal Growth, 2003,Vol. 213, No. 3- 4, pp. 389-394.

14. K. Srinivasan, P. Ramasamy, A. Cantoni and G. Bocelli, "Mixed Crystals of NH$_4$H$_2$PO$_4$-KH$_2$PO$_4$: Compositional Dependence of Morphology, Microhardness and Optical Transmittance," Materials Science and Engineering: B, 1998, Vol. 52, No. 2-3, pp. 129-133.

15. X. Sun, X. Xu, Z. Gao, Y. Fu, S. Wang, H. Zeng, and Y. Li, J. Cryst. Growth, 2000, vol. 217, pp. 404.

16. N. Zaitseva, L. Carman, and I. Smolsky, J. Cryst. Growth 241, 363 (2002).

17. Kao K. C., "Dielectric Phenomena in Solids," Elsevier Academic Press, London, 2004, pp. 54.

18. R. J. Sangwa, S. Sankhla, "Dielectric dispersion study of coexisting phases of aqueous polymeric solution: Poly(vinyl alcohol)+ Poly (vinyl pyrrolidone) two-phases system," j. polymer Science, 2007, vol. 48, no. 9, pp. 2737-2744.

19. N. Shinyashiki, S. Yagihara, I. Arita and S. Mashimo, "Dynamic Study on Dynamic of Water in Polymer Matrix Studied by a Microwave Dielectric Measurement," Journal of Physical Chemistry B, 1998, vol. 102, no. 17, pp. 3249-3251.

# Crystal Growth and Etching of $In_X Bi_{(2-x)}Se_3$ ( X = 0.05) single crystal

Himanshu Pavagadhi [a], S.M.Vyas [a], Vimal Patel [a], Jaydev Patel [a], M.P.Jani [b], G.R.Pandya [c].

[a] Department of Physics, School of Science, Gujarat University, Ahmedabad, Gujarat, India.
[b] Neotech B.Sc college , Vadodara,  Gujarat, India.
[c] Department of Physics,  MSU Baroda, Gujarat, India

Email: pavagadhihimanshu@yahoo.co.in

## Abstract

$In_X Bi_{(2-x)}Se_3$ crystals were grown by Bridgman method at a growth velocity of 0.5cm/h with temperature gradient of $65^0$ C/cm in our laboratory. For the structural information about the $In_X Bi_{(2-X)}Se_3$ crystals have been carried by the XRD pattern and composition of material can be studied by EDAX pattern and using SEM observed crystalline structure. The Parallel striations perpendicular to the ingot axis are observed on the top free surfaces of crystals using an optical microscope. A new dislocation etchant based on nitric acid has been found to give reproducible etch-pitting on the cleavage surface which reveals the freshly dislocations on the sites. Standard tests for a dislocation etchant have been carried out and results are reported.

## Introduction

$Bi_2Se_3$ is a narrow band gap material which has hexagonal structure and it is useful application in the field of thermoelectric devices as solid state coolers or generators [1–3]. Both n- and p-type $Bi_2Se_3$ Single crystals grown by the Bridgman technique is used to make excellent Hall Effect magnetometers .it can be work in magnetic fields to at least 10 Tesla and over a wide range of temperature [4]. The thermoelectric figure of merit is high [5] for $Bi_2Se_3$ and $Bi_2Te_3$ material. So these materials are useful for thermoelectric energy conversion. The band gap is very narrow, so it can be used for infrared radiation detectors [6]. The low temperature peaks found in the Seebeck coefficients in Bi2Se3, materials that have strong spin orbit coupling and nearby Dirac points [7-10], suggests that these characteristics may be related. In addition, processing of the microstructure of n- and p-type $Bi_2Se_3$ to reduce the thermal conductivity to the < 1 WK-1 m-1. $Bi_2Se_3$, $Bi_2Te_3$, and $Sb_2Te_3$ are used as 3D topological insulators [11-12]. Many physical phenomena are predicted to emerge in low dimensional nanostructures of $Bi_2Se_3$. [13], ultra-thin $Bi_2Se_3$ down to a few

($\leq 5$) nanometers is expected to exhibit topologically non-trivial edge. Recently, preparation of $Bi_2Se_3$ nanostructured materials via wet chemical methods has attracted increasing attention due to low cost and convenient. Qiu et al [14]. Therefore studies on various properties of $Bi_2Se_3$ are interesting for both basic and applied research. If we crystallize under proper controlled conditions $Bi_2Se_3$ can easily cleavable.

## Experimental Details

The stoichiometric amount of In, Bi, and Se each of 5N (99.999%) purity were weighed accurately up to $10\mu$ gms using a semi micro balance. They were sealed in quartz tube under a pressure of $10^{-4}$ Pa. then the tube was kept horizontal in an alloy mixing furnace at a temperature of about 775 °C for 48 hr. during which the ampoule was continuously rocked and rotated for proper mixing and reaction Then the ingot was cooled to room temperature over a period of 24 hr at a rate of 20 $^0$C/hr. Single crystal $In_X Bi_{(2-X)}Se_3$. Grown by Bridgman method with a temperature gradient of 65 $^0$C/cm and a growth rate of 0.5 cm/hr. The top free surfaces of the as grown crystal were observed under the optical microscope to exhibit the growth feature. A crystal was cut at the cleavage plane and used for SEM characterization. Powder X-ray diffractograms for compounds were analyzed by using Powder X software for the confirmation of crystal structure and determination of lattice parameters. The compositions of all the elements present in the grown crystals are determined by energy dispersive analysis of X-rays (EDAX).The degree of homogeneity was determine by etching studies. For the study of crystal defect of $In_X Bi_{(2-X)}Se_3$ crystal, After numerous trial, the etchant concentration is 2.5 ml Nitric acid (70% Ar grade) + 10 ml Tartaric acid + 2 ml Water is found to be good to well define etch pits on a clear background of the sample and the etching time taken was 10 seconds.

## Result & Discussion

Occurrence of parallel striations seems to be a very common phenomenon as far as the crystal growth of metals, semiconductors, alloys and solid solutions is concerned. For example STEWART et al. [15], MULLER and WILHELM [16], YIM [17], as well UEDA [18] have reported such striations on crystals of InSb, BiSb, Ge, etc crystlals. The striations were explained in terms of variations in speed of solidification resulting due to thermal fluctuations during crystal growth. The present paper deals with crystallographic study of the parallel striations and associated characteristic features observed on the top free surface. The

microphotograph in figure typical transverse striations, were found to form an array of parallel rectilinear lines.
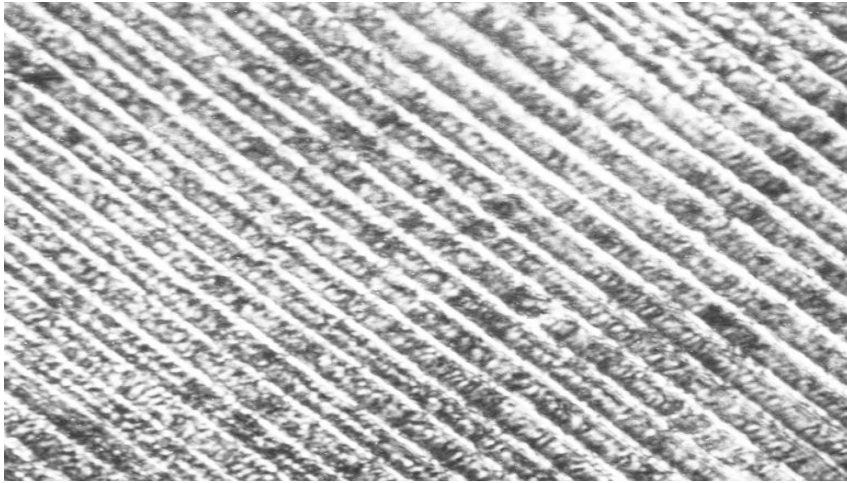


Figure - 1: Parallel Striations observed on freshly cleaved as- grown crystal of $In_X Bi_{(2-X)}Se_3$.

The height of these steps equals about 10-20 $A^0$. As was estimated by comparison of their contrasts on the phase contrast micrographs with the contrast of steps of well known heights on {111} and {100} potash alum [19].

Figure 2 indicate that the $In_X Bi_{(2-X)}Se_3$. As- grown crystals are crystalline and show that the number of cleavage line is very less so that the perfection of the crystal is more and also indicates the layer growth mechanism in In: $Bi_2Se_3$ single crystal is predominant.
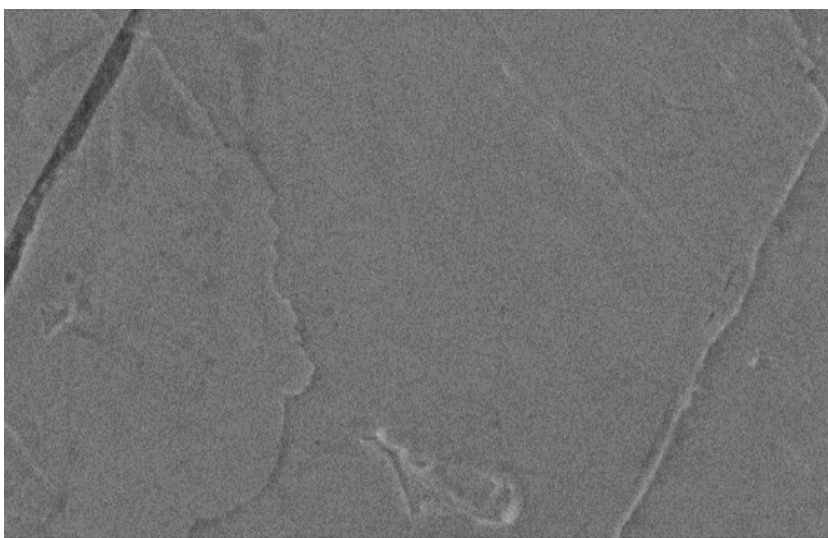


Figure -2: SEM Image of Crystal $In_X Bi_{(2-X)}Se_3$.

Fig.3 shows the compositions of all the elements present in the grown crystals are determined by energy dispersive analysis of X-rays (EDAX). However composition estimated in terms of wt percentage In = 0.05 %, Bi= 36.52 % Se= 63.43 %.
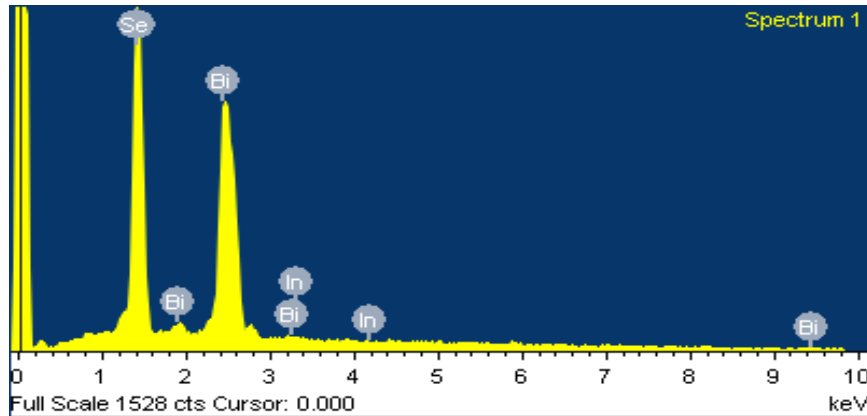


Figure -3 : EDAX of Crystal $In_X Bi_{(2-X)}Se_3$.

Fig.4 shows a typical diffraction pattern recorded with as grown $In_X Bi_{(2-X)}Se_3$ single crystal. There are well resolved peaks with high intensity as well as relatively small intensity. The structural parameters has been calculated from these data and the obtained values of lattice parameters are a = 7.535, b = 11.659, c = 3.386 and α = 92.82, ß = 101.17, γ =100.92. The crystal structure is Triclinic Lattice which is found to match with JCPDS data.
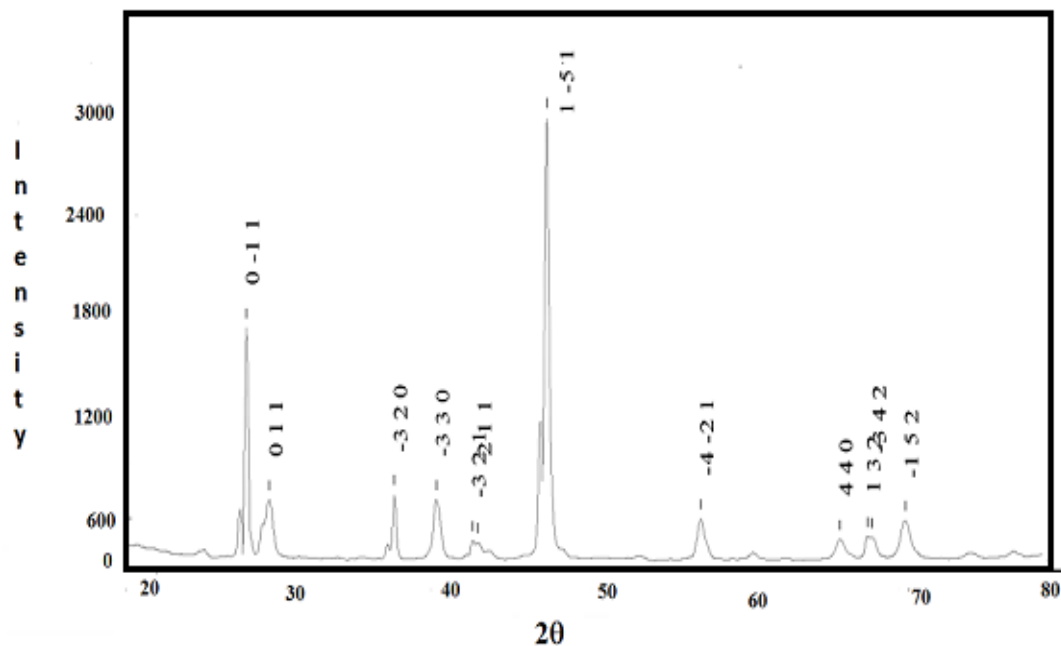


Fig.- 4 : X-Ray Diffraction Pattern of $In_X Bi_{(2-X)}Se_3$.

For the study of crystal defect in $In_X Bi_{(2-X)}Se_3$. Crystal, after numerous trials, the etchant concentration is 2.5 ml Nitric acid (70% Ar grade) + 10 ml Tartaric acid + 2 ml Water. This mixture is capable of producing well defined triangular etchpits. The etching time taken is 10 seconds.
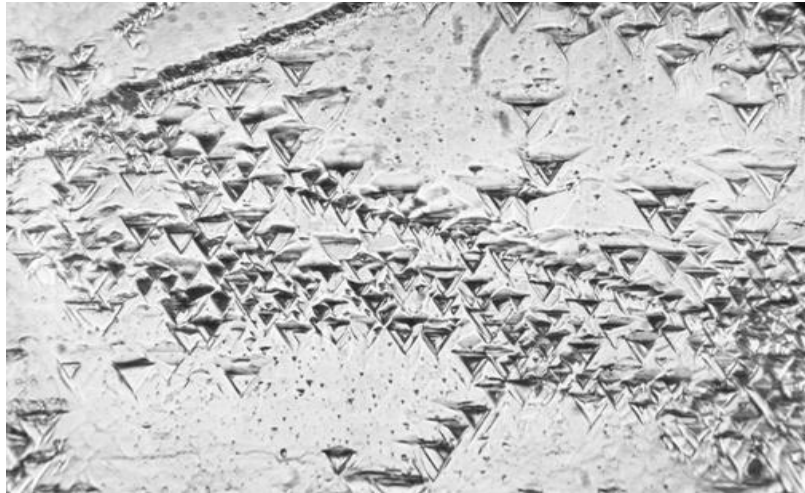


Figure - 5: Etching photograph of Crystal $In_X Bi_{(2-X)}Se_3$.

The indices of the planes of the etch pits are determined stereographically. The edges of the triangular etch pits are in < 110> direction and there planes of point bottomed etch pits developed on etching are parallel to {111} sleep planes. Further a specimen was pin-indented on its cleavage plane and subsequently etched. Rosettes of etch pits around the indentation mark were observed as an etching result indicating that the etchant can reveal freshly introduced dislocations as well. The fact discussed above indicates that the newly developed etchant by the authors is a good dislocation etchant. The average dislocation density of the crystals as measured by the etch-pit count method was found to be $6.2 * 10^{-4}$ cm $^{-2}$ on an average.

**Conclusion:**

Parallel striation observed on top free surface of the as grown crystals and from The SEM characterization of these crystals indicates the layer growth mechanism is predominant. X-ray diffractograms of $In_X Bi_{(2-X)}Se_3$ are indexed indicate the triclinic structure with lattice parameters are a = 7.535,  b = 11.659,  c = 3.386 and  α = 92.82,  ß = 101.17,  γ =100.92 its cleaved along (1 1 1) plane. From the EDAX characterization, the percentage of $In_X Bi_{(2-X)}Se_3$. Components in the crystal which are In = 0.05 %, Bi= 36.52 % Se= 63.43 %. An etchant

developed by the author is capable of revealing dislocations intersecting the cleaveage plan of the material.

## Acknowledgment

## References

1. S. Augustine and E. Mathai,Mater. Res. Bull.,36,(2001),

2. U. Birkholz,Amorphe und Polykristalline Halblein( Springer, Berlin, 1984).

3. D.M.Rowe,CRC Handbook of thermoelectrics(Chemical rubber, Boca Raton, FL.1995).

4. J.A.Woollan, I.L.Spail, "property of crystal Bi2Se3 and its use as a Hall effect Magnetometer " NASA" Technical Note Tn D 7057 , Nov 1972.

5. Champness, C. H.; Muir, W. B.; and Chiang, P. T.: Thermoelectric Properties of n-Type BigTeg-BigSeg Alloys. Can. J. Physics, vol. 45, no. 11, Nov. 1967, pp -3611-3626.

6. Harman, T. C.: The Physics of Semimetals and Narrow Band-Gap Semiconductors.

7. L. Fu and C.L. Kane, Phys. Rev. B 76 045302 (2007).

8. S. Murakami, New J. Phys. 9 356 (2007).

9. Y. Xia, L. Wray, D. Qian, D. Hsieh, A. Pal, H. Lin, A. Bansil, D. Grauer, Y. S. Hor, R. J. Cava, and M.Z. Hasan, arXiv:0812.2078 (2008).

10. Haijun Zhang, Chao-Xing Liu, Xiao-Liang Qi, Xi Dai, Zhong Fang, Shou-Cheng Zhang, arXiv: 0812.1622 (2008).

11. Hsieh, D.; Qian, D.; Wray, L.; Xia, Y.; Hor, Y. S.; Cava, R. J.; Hasan, M. Z. Nature 2008, 452, pp- 970-974.

12. Chen, Y. L.; Analytis, J. G.; Chu, J.; Liu, Z. K.; Mo, S.; Qi, X. L.; Zhang, H. J.; Lu, D. H.; Dai, X.; Fang, Z.;Zhang, S. C.; Fisher, I. R.; Hussain, Z.; Shen, Z. Science 2009, 325, pp- 178-181.

13. Liu, C.; Zhang, H.; Yan, B.; Qi, X.; Frauenheim, T.; Dai, X.; Fang, Z.; Zhang, S. Phys. Rev. B 2010, 81, 041307.

14. Qiu XF, Zhu JJ, Pu L, Shi Y, Zheng YD, Chen HY. Sizecontrollable sonochemical synthesis of thermoelectric material of Bi2Se3 nanocrystals. Inorg Chem Commun 2004; 7: pp-319-21.

15. STEWART.M.T. et al. ;phys.Rev.83 (1951), pp- 657.

16. MULLER.A.,WILHELM.W. :Natureforsch. (germany) 19a (1964), pp- 254.

17. YIM.W.M. : Trans. AIME 236 (1966), pp- 474.

18.  UEDA.H. : j.Phys. Soc. Japan 16 (1956), pp- 61.

19.  Fang lang Hsu : J. Chin Inst. Eng> Taiwan : 12, (1989), pp-755.

# Study of Tin Selenide Nanoparticles Prepared by Two Different Methods

**R.J.Parmar[1], V. R.Solanki[2], R. J.Pathak[2], M. D.Parmar[3], K.D.Patel[4]**

[1*]*Department of Physics, Sheth M.N. Science College, Patan, Gujarat, India*
[2]*R.R. Mehta College of Science& C.L. Parikh College of Commerce, Palanpur, Gujarat, India*
[3]*M.N. Science College, Visnagar, Gujarat, India*
[4]*Physics Department, S.P. University, V.V. Nagar, Anand, Gujarat, India*

*Corresponding author e-mail:rushiparmar8786@gmail.com*

## Abstract

In present paper structural properties of SnSe nanoparticles prepared by two different methods is reported. It is one of the promising materials from its applications. SnSe powder has been prepared by using two methods, first chemical precipitation method and second one is Chemical Bath method in deionized water. The prepared samples were investigated for structural characterization by XRD. The X-ray diffraction studies of the particles show the polycrystalline nature with orthorhombic crystal structure. Micro- structural parameters such as crystalline size, dislocation density and microstrain were calculated with respect to different method.

**Key words:**SnSe nanoparticles, aqueous solution method, Chemical Bath Method, X-Ray Diffraction.

## INTRODUCTION

Tin Selenide (SnSe), a member of group IV-VI semiconductors is one of the promising materials from its applications. Tin Selenide (SnSe) is an exciting semiconductor compounds that are broadly used as holographic recording systems, optical and optoelectronic materials in infrared electronic and memory switching devices and in photoelectrical cells [1-4].Lots of investigators have been involved in the study of nanocrystals because of their special properties like electric, optoelectric and magnetic [5, 6].SnSe nanoparticles were synthesized by several methods like solid – state reaction, state metathesis, Bridgman method, self – propagating high temperature synthesis, brush plating technique [7-11]. These methods have some limitations like the requirement of a special device and high temperature. Recently, solution routes, such as hydrothermal, solvothermal, and organ metallic precursor methods have been developed for the Synthesis of SnSe [12-14].In this reported work we have used two methods chemical precipitation method and chemical bath method, it' svery easy technique and it does not require any special sophisticated equipment. It is a time-consuming process, which facilitates a better

orientation of the crystallites with an improved grain structure, depending on the deposition situation. Present paper reports the preparation and structural study of the tin selenide powder obtained by different chemical route.

## EXPERIMENTAL DETAILS:
### (1) Chemical Precipitation Method:

For the growth of SnSe nanoparticles all the chemicals were of AR grade with 99.99% purity from Lobal Chemie. Tin chloride and selenium oxide used as precursors of $Sn^{+2}$ and $Se^{-2}$ ions in the reaction system. The $SnCl_2$ and $SeO_2$ solutions were mixed for 30 minutes using a magnetic stirrer by drop wise and as a result precipitations of SnSe were obtained in a solution. This precipitation is separated by filtering method. Finally separated SnSe nanoparticles were washed by water and ethanol several times and kept at 100°c for one hour for obtaining dry powder of SnSe nanoparticles.

### (2) Chemical Bath Method

Tin chloride and Sodium selenosulphate used as precursors of $Sn^{+2}$ and $Se^{-2}$ ions in the reaction system. For Sodium selenosulphate, 9.48gm of sodium sulfite in 120 ml water was refluxed with 2.36gm of selenium for almost 8 hour. It was sealed and kept overnight. It was then filtered to obtain clear solution. It is recommended to make small volume of selenosulphate stock solution to be used within 3-4 day.

Sodium hydroxide (1M) solution in deionized water. This solution is used to maintain alkaline media of PH at about 12.2. In a 100ml beaker 0.95gm of tin chloride in 10ml water is placed and sodium hydroxide is added drop wise to obtain an alkaline media of PH 12.2. Then 10ml of sodium selenosulphate solution is introduced into the beaker for the time of 1hours in the bath. Then filtration and finally dried in hot bath, from the residue solution. This solid phase (Powder) consist of SnSeNanocrystals.
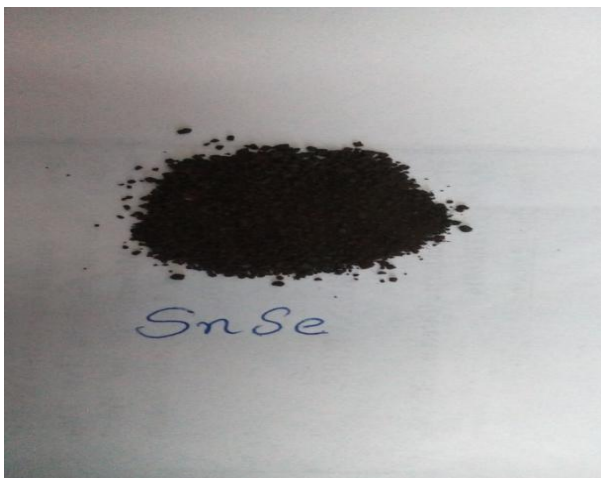


Figure 1.Photograph of synthesized SnSe nanoparticles From Chemical Bath Method
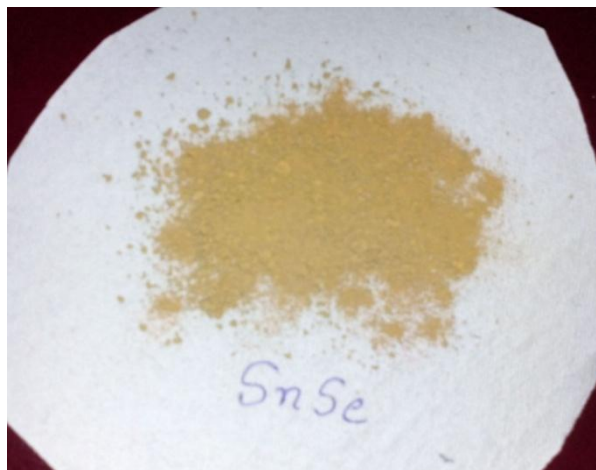


Figure 2.Photograph of synthesized SnSe nanoparticles From Chemical Precipitation Method

## RESULTS AND DISCUSSION:
## XRD: (Chemical Precipitation Method)

The X-Ray diffraction pattern exhibit peaks at 26.86°, 37.33° and 50.76° corresponding to the (210), (401) and (221) planes. All these peaks correspond to the orthorhombic phase. The lattice parameter value a, b and c have been calculated and are found to be a = 11.50Å, b = 4.15Å and c = 4.44Å which are in good agreement with other research papers [6, 12, 15].
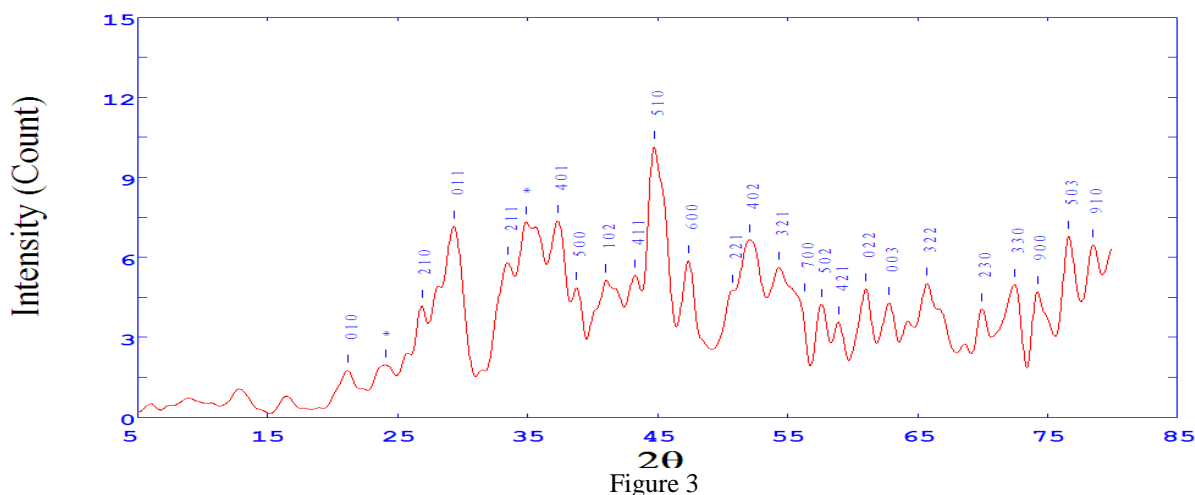


Figure 3
XRD Pattern of prepared SnSe nanoparticles From Chemical Precipitation Method

## XRD: (Chemical Bath Method)

The X-Ray diffraction pattern exhibit peaks at 23.56°,29.77° and 51.80° corresponding to the (300), (111) and (402) planes. All these peaks correspond to the orthorhombic phase. The lattice parameter value a, b and c have been calculated and are found to be a=11.42Å, b=4.19Å and c=4.46Å which are in good agreement with other research papers [2, 4, 8].
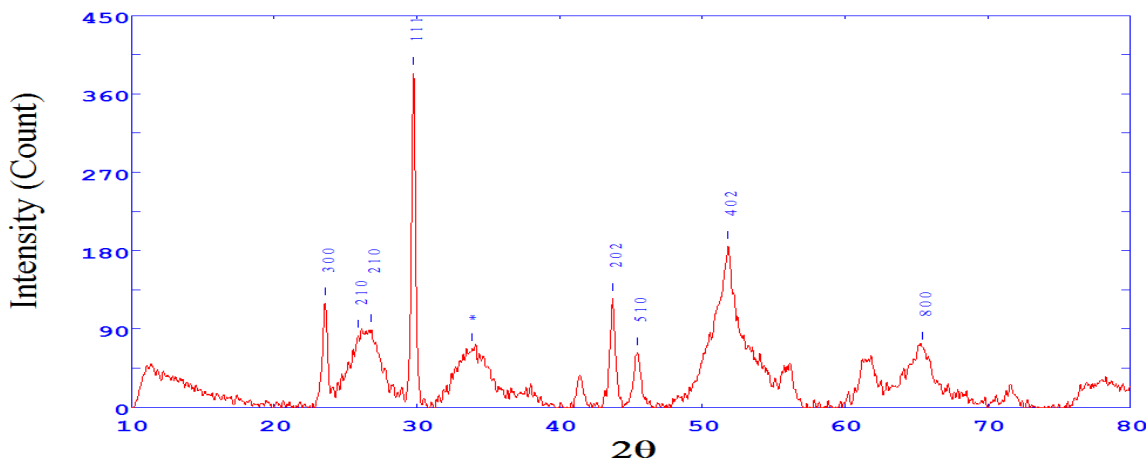


Figure 4
XRD Pattern of prepared SnSe nanoparticles From Chemical Bath Method

The average size of particles has been obtained from the X-ray diffraction pattern using the Scherrer's formula[15].

$$D = \frac{K\lambda}{\beta \cos\theta}$$

Where D is the grain size, K is a constant taken to be 0.94, wavelength of X-ray (1.5406Å), $\beta$ is the full width half maximum (FWHM), $\theta$ is the diffraction angle. The obtained average crystalline size SnSenanoparticles from Chemical Precipitation Methodis9.88 nm.&Chemical Bath Method is2.63nm.

Using crystalline size values, the dislocation density ($\delta$), defined as the length of dislocation lines per unit volume of the crystal was calculated using Willianson and Smallman's formula.[16]

$$\delta = 1/D^2$$

The obtained values of the dislocation density ($\delta$) from Chemical Precipitation Methodis 0.0102 (Lin·nm$^{-2}$) &Chemical Bath Method is 0.1445 (Lin·nm$^{-2}$). This clearly indicates that increasing the crystalline size and reducing the dislocation density making it a potential candidate for optoelectronic devices.

The micro strain can be obtained by using the relation

$$\varepsilon = \frac{\beta \cos\theta}{4}$$

**Table:1**Structural parameter of SnSe Nanoparticles from Chemical Precipitation Method.

| Plane (hkl) | Inter planar spacing, d (nm) | FWHM (degrees) | Crystalline size D (nm) | Dislocation density $\delta$ (Lines/m$^2$) | Micro strain $\varepsilon$ |
|---|---|---|---|---|---|
| (210) | 3.3160 | 0.9500 | 2.3817 | 0.1766 | 0.1520 |

**Table:2**Structuralparameter of SnSe Nanoparticles from Chemical Bath Method.

| Plane (hkl) | Inter planar spacing, d (nm) | FWHM (degrees) | Crystalline size D (nm) | Dislocation density $\delta$ (Lines/m$^2$) | Micro strain $\varepsilon$ |
|---|---|---|---|---|---|
| (210) | 3.3207 | 1.6200 | 1.3546 | 0.5494 | 0.2673 |

## CONCLUSION

In this study, two different chemical routes for Tin selenide have been described. The Chemical Bath method is time consuming and took too much time to compare Chemical Precipitation method. From Chemical bath method we find black SnSe nanoparticles and from Chemical precipitation method particles are saffron color. The SnSe Nanoparticles from Chemical Bath Method had smaller crystalline size (~ 2 nm) as compared to the one prepared from Chemical Precipitation Method(~ 9 nm). The crystalline sizes were examined by XRD. The X-ray diffraction studies of the Nanoparticles show the polycrystalline nature with orthorhombic crystal structure.

## REFERENCES

[1] N. R. Mathews, 2011, Electrodeposited tin selenide thin films for photovoltaic applications, Solar Energy, In press.

[2] J. F. Suyver, R. Bakker, A. Meijerink, J. J. Kelly, Phys. Stat. Sol. (b), 224, pp. 307-312, (2001).

[3] D. L. Kelin, R. Roth, A. K. L. Lim, A. P. Alivisatos, P. L. McEuen, Nature, 389, pp. 699-701, (1997).

[4] K. R. Murali, V. Swaminathan, D. C. Trivedi, 81, pp. 113-118, (2004).

[5] Zulkarnain Zainal, Saravanan Nagalingam, Anuarkassim, Mohd Zobir Hussein, Wan Mahmood Mat Yunus, Solar Energy Materials & Solar Cells, 81, pp. 261-268, (2004).

[6] K. Zweibel, Solar Energy Mater. Solar Cells, 63, pp. 375-386, (2000).

[7].L. Seligson and J. Arnold, J. Amer. Chem. Soc., 115, 8214-8220 (1993)

[8]. Bhatt V.P., Giresan K. and Pandya G.R., J. Crystal Growth, 96, 649-651 (1989)

[9]. Yi H. and Moore J.J., J. Mater. Sci., 25, 1159-1168 (1990)

[10]. Parkin I.P., Chem. Soc. Rev., 25, 199-207 (1996)

[11]. Subramanian B., Sanjeeviraja C. and Jayachandran M., J. Crystal Growth, 234, 421-426 (2002)

[12]. Wang W., Geng Y., Qian Y., Wang C. and Liu X., Mater. Res. Bull., 34, 403-406 (1999)

[13]. B. Li, Y. Xie, J. Huang and Y. Qian, Inorg. Chem., 39, 2061-2064 (2000)

[14]. G. Henshaw, I .Parkin and G. Shaw, J. Chem. Soc. Chem. Commun., 10, 1095-1096 (1996) 20

[15].ZiaulRaza Khan, M. Zulfequar, Mohd. Shahid Khan, Chalcogenide Letters, 7, 431-438 (2010).

[16]. G.K. Williamson and R. E. Smallman, 1956, III. Dislocation Densities in some annealed and cold-worked metals from measurements on the X-ray Debye- Scherrer spectrum, Philos. Mag., 1(1), 3445.

# Effect of Deposition Temperature on Structural Properties of Chemically Deposited SnSe Thin Films

**V. R.Solanki[1], R.J.Parmar[2], R. J.Pathak[1], M. D.Parmar[3], K.D.Patel[4]**

[1]R.R.Mehta College of Science & C. L. Parikh College of Commerce, Palanpur, Gujarat, India
[2]Department of Physics, Sheth M. N. Science College, Patan, Gujarat, India
[3]M.N. Science College, Visnagar, Gujarat, India
[4]Physics Department, S.P. University, V.V. Nagar, Anand, Gujarat, India

Corresponding author e-mail:vijaysolanki019@yahoo.in

## Abstract

Recently there has been a large amount of interest on the preparation and characterization of semiconducting materials, mainly SnSe due to its potential applications in various fields. Tin Selenide (SnSe) is an important IV-VI semiconductor material. Tin Selenide (SnSe) thin films have been prepared successfully using chemical bath deposition method with different temperature in deionizer water. The prepared samples were investigated for structural characterization by XRD. The X-ray diffraction studies of the films show the polycrystalline nature with orthorhombic crystal structure. Micro structural parameters such as crystalline size, dislocation density and micro strain were calculated.

**Key words:** SnSe thin films, Chemical Bath Deposition method, XRD.

## INTRODUCTION

Recently the search for thin film materials for solar energy conversion and other related applications have been identified. Metalchalcogenide materials have shown somewhat better performance when compared to others. Along with the important binary semiconductors of IV-VI group, the chalcogenides formed with Sn, especially SnSe have attracted considerable attention in recent years. SnSe has an orthorhombic crystal structure and studied in the form of both single crystals and thin films. It's having paying attention budding interest owing their significant unique properties. SnSe thin films have been used as light emitting diodes or laser diodes, memory switching devices, and infrared production and detention [1-6].

For the deposition of thin films of SnSe, various methods like spray pyrolysis, electro-deposition, chemical vapor deposition, magnetron sputtering, successive ionic layer adsorption and reaction (SILAR), vacuum evaporation, brush plating, microwave assisted chemical deposition and chemical bath deposition (CBD) have been employed [7-15]. Among these methods CBD is relatively simple, more rapid and inexpensive method suitable for deposition on large substrates irrespective of the shape and morphology of substrates nearly at room temperature. Present paper

reports the preparation and morphological study of the tin selenide thin films obtained by chemical bath deposition method with different temperature.

## EXPERIMENTAL DETAILS:
## Chemical Bath Deposition Method:

In this method all the chemicals used were of AR grade. (99.99% purity,Alpha essar).Tin chloride and Sodium seleno sulphate used as precursors of $sn^{+2}$ and $se^{-2}$ ions in the reaction system. To prepare the stock Sodium seleno sulphate solution, 9.48gm of sodium sulfite in 120 ml water was refluxed with 2.36gm of selenium for almost 8 hours. The mixture remained under constant stirring throughout the reflux process seleno sulphate is produced according to the following reaction.

$$Na_2SO_3 + Se \rightarrow Na_2SeSO_3$$
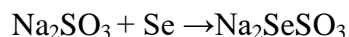
Unreacted selenium is filtered off and seleno sulphate solution is placed in air tight bottle. It is recommended to make small volume of seleno sulphate stock solution to be used within 3-4 days.

Sodium hydroxide (1M) solution in deionized water is used to maintain alkaline media of PH at about 12.03. In a 100ml beaker 0.95gm of tin chloride in 10ml water is placed and sodium hydroxide is added drop wise to obtain an alkaline media of PH 12.03. Then 10ml of sodium selenosulphate solution is introduced into the beaker and substrates are mounted vertically in the bath. The film growth was carried out at 40ºC&50ºC. A dark brown precipitate gradually fills the bath and turns black after 20 min. During deposition period the beaker was kept undisturbed for a time period of 1 hour. We got two films for different temperature.



*Fig. 1 Experimental set up for CBD*



*Fig. 2 Water Bath for CBD*

## RESULTS AND DISCUSSION
## XRD:

The X-Ray diffraction pattern of SnSe nanoparticles prepared by chemical bath deposition method with different temperature is shown in figure 3. The X-Ray diffraction pattern for at 40ºC temperature shows 20 to 90.49 $2\theta$ values and it gives total 127 experimental peaks. Total 91 matching lines are found. The X-Ray diffraction pattern for at 50ºC temperature shows 20 to 90.49 $2\theta$ values and it gives total 66 experimental peaks. Total 55 matching lines are found. The X-Ray diffraction pattern for both patterns confirms orthorhombic structure. For both graphs the lattice parameter values a, b and c have been calculated and are found to be a=11.38Å, b=4.18Å and c=4.42Å which are in good agreement with other reported paper [6, 8, 16].
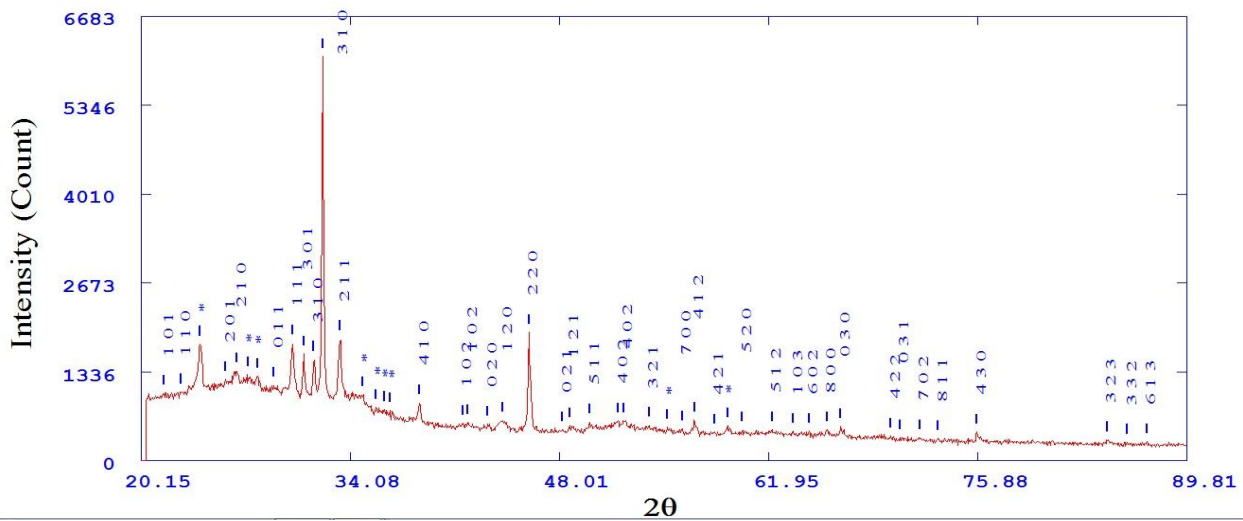


*Fig. 3 SnSe thin films XRD pattern* for at 40ºC temperature.
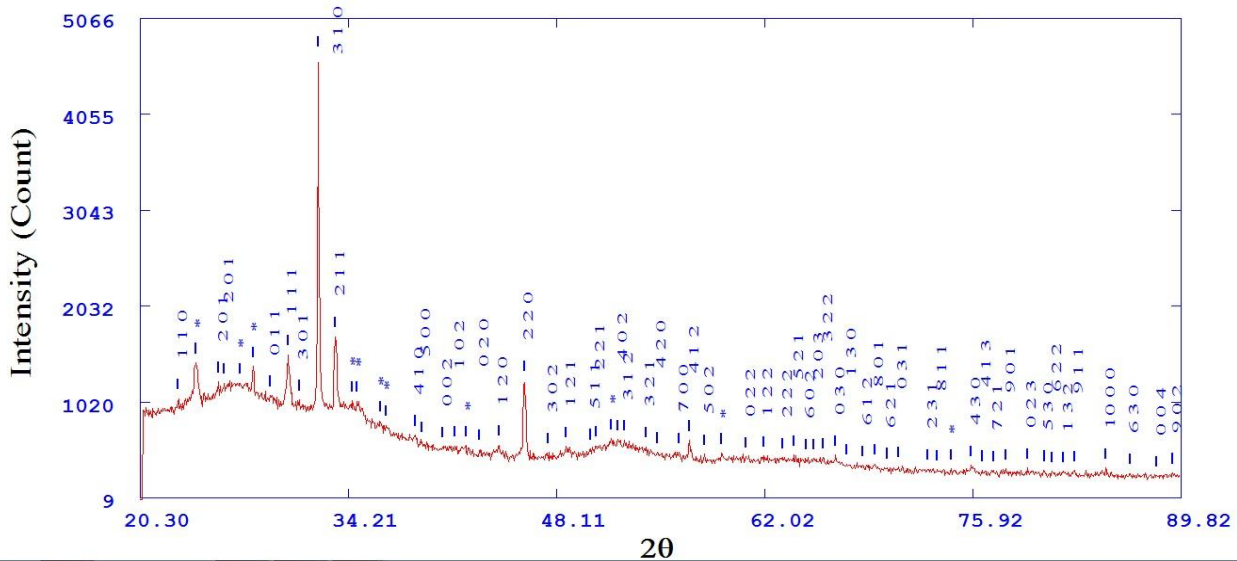


Fig. 4SnSethinfilms *XRD pattern* for at 50ºC temperature.

The average crystalline sizes or grain sizes were estimated from the X-ray diffraction pattern using the Scherrer's formula [16].

$$D = \frac{K\lambda}{\beta\cos\theta}$$

Where D is the grain size, K is a constant taken to be 0.94, wavelength of X-ray (1.5406Å), is the full width half maximum (FWHM), is the diffraction angle. The obtained average crystalline size for 40ºC temperature is 5.98 nm&for 50ºC temperature is 4.60nm.

Using Crystalline size values, the dislocation density ($\delta$), defined as the length of dislocation lines per unit volume of the crystal was calculated using Willianson and Smallman's formula [17].

$$\delta = 1/D^2$$

This clearly indicates that increasing the crystalline size and reducing the dislocation density making it a potential candidate for optoelectronic devices.

The microstrain can be using the relation

$$\varepsilon = \frac{\beta\cos\theta}{4}$$

**Table:1** Structural Parameters of SnSe Thin Films Prepared at 40ºC Temperature.

| Plane (hkl) | Inter planar spacing, d (nm) | FWHM (degrees) | Crystalline size D (nm) | Dislocation density (Lines/m | Micro strain |
|---|---|---|---|---|---|
| 310 | 2.8241 | 0.3019 | 4.8932 | 0.04176 | 0.0739 |
| 220 | 1.9728 | 0.4529 | 7.0780 | 0.0199 | 0.0511 |

**Table: 2**Structural Parameters of SnSe Thin Films Prepared at 50ºC Temperature.

| Plane (hkl) | Inter planar spacing, d (nm) | FWHM (degrees) | Crystalline size D (nm) | Dislocation density (Lines/m | Micro strain |
|---|---|---|---|---|---|
| 310 | 2.7788 | 0.4529 | 3.4504 | 0.0839 | 0.1049 |
| 220 | 1.9736 | 0.4529 | 5.7530 | 0.0302 | 0.0629 |

## CONCLUSION

SnSe thin films were prepared by chemical bath deposition methods at 40ºC & 50ºC temperature. The SnSe thin film prepared at 50ºCtemperature had smaller crystalline size (~ 4.60 nm) as compared to the one prepared at 40ºCtemperature (~ 5.98 nm). The crystalline sizes were examined by XRD. The X-ray diffraction studies of the films show the polycrystalline nature with orthorhombic crystal structure.

## REFERENCES

[1] N. R. Mathews, 2011, Electrodeposited tin selenide thin films for photovoltaic applications, Solar Energy, In press.

[2] J. F. Suyver, R. Bakker, A. Meijerink, J. J. Kelly, Phys. Stat. Sol. (b), 224, pp. 307-312, (2001).

[3] D. L. Kelin, R. Roth, A. K. L. Lim, A. P. Alivisatos, P. L. McEuen, Nature, 389, pp. 699-701, (1997).

[4] K. R. Murali, V. Swaminathan, D. C. Trivedi, 81, pp. 113-118, (2004).

[5] Zulkarnain Zainal, Saravanan Nagalingam, Anuarkassim, Mohd Zobir Hussein, Wan Mahmood Mat Yunus, Solar Energy Materials & Solar Cells, 81, pp. 261-268, (2004).

[6] K. Zweibel, Solar Energy Mater. Solar Cells, 63, pp. 375-386, (2000).

[7] Z. Zainal, N. Saravanan, K. Anuar, M. Z. Hussein and W. M. M. Yunus, 2004, Chemical bath deposition of tin selenide thin films, Mater.Sci.Eng.B, 107(2), 181-185.

[8] V. E. Drozd, I. O. Nikiforova, V. B. Bogevolnov, A. M. Yafyasov, E. O. Filatova and D. Papazoglou, 2009, ALD synthesis of SnSe layers and nanostructures, J.Phys. D, 42, 125306-125310.

[9] D. P. Padiyan, A. Marikani and K. R. Murali, 2000, Electrical and photoelectrical properties of vacuum deposited SnSe thin films, Cryst.Res.Technol, 35(8), 949-957.

[10] N. Kumar, V. Sharma, U. Parihar, R. Sachdeva, N. Padha and C. J. Panchal, 2011, Structure, optical and electrical characterization of Tin selenide thin films deposited at room temperature using thermal evaporation method, J. Nano- Electron.Phys., 3(1), 117-126.

[11] J. P. Singh and R. K. Bedi, 1990, Tin selenide films grown by hot wall epitaxy, J. Appl. Phys., 68, 2776-2779.

[12] G. H. Chandra, J. Naveen Kumara, N. M. Raob, and S. Uthanna, 2007, Preparation and characterization of flash evaporated tin selenide thin films, J. Cryst. Growth., 306, 68-74.

[13] N. Kumar, V. Sharma, N. Padha, N. M. Shah, M. S. Desai, C. J. Panchal and I. Yu. Protsenko, 2010, Influence of the substrate temperature on the structural, optical, and electrical properties of tin selenide thin films deposited by thermal evaporation method, Cryst. Res. Technol., 45(1), 53-58.

[14] Z. Zainal, N. Saravanan, K. Anuar, M. Z. Hussein and W. M. M. Yunus, 2003, Tin Selenide thin films prepared through combination of chemical precipitation and vacuum evaporation technique, Mater.Sci., 21(2), 225-233.

[15] Z. Zainal, N. Saravanan, K. Anuar, M. Z. Hussein and W. M. M. Yunus, 2003, Tin Selenide thin films prepared through combination of chemical precipitation and vacuum evaporation technique, Mater.Sci., 21(2), 225-233.

[16]ZiaulRaza Khan, M. Zulfequar, Mohd. Shahid Khan, Chalcogenide Letters, 7, 431-438 (2010).

[17] G.K. Williamson and R. E. Smallman, 1956, III.Dislocation Densities in some annealed and cold-worked metals from measurements on the X-ray Debye- Scherrer spectrum, Philos. Mag., 1(1), 3445.

# Synthesis, characterization and functionalization of multi-walled carbon nanotubes by chemical vapour deposition method

## Parth Joshi[1], Dimple shah[2] and Pooja Kalaria[2]

[1]Department of Physics, Uka Tarsadia University, Bardoli, Gujarat-394350

[2]Applied Physics Department, Sardar Vallabhbhai National Institute of Technology, Surat-395007

Corresponding Author* - parth4570@gmail.com

**Abstract**

In this paper, multi-walled carbon nanotubes synthesized by chemical vapour deposition methods. To obtained carbon nanotubes has functionalization with carboxylic and groups. The exhibit of groups on the carbon nanotubes has been characterization by XRD, FT-IR and TEM. The X-ray differaction pattern at the angle ($2\theta$) of $26.5^o$ can be indexed as the (002) reflection of hexagonal graphite structure. The formation of the carboxylic group in the grafting reaction has been confirmed by FT-IR spectroscopy. The transmission electron microscopy study of pristine CNTs is inner length 10 nm, The result indicates that the further grafting is successful. The functionalized carbon nanotubes can be a new versatile platform for many interesting applications.

**Keywords:** Carbon nanotubes, functionalization, carboxylic groups.

## Introduction

Carbon Nanotubes(CNTs), long, thin cylinders of carbon, were discovered in 1991 by Sumio Iijima. It is unique for their size, shape, and remarkable physical and mechanical properties. Nowadays, MWNTs and SWNTs are produced mainly by three techniques: arc-discharge, laser-ablation, and catalytic growth.[1] However, synthesizing CNTs remains costly and difficult due to the high temperatures (around 500°C) and pressures required. Here we report on a chemical vapour deposition method which allows us to prepare CNTs. CVD is one of the slower methods of nanotube growth but affords a greater control over the tubes that are grown through the process. By selecting different process gases, a researcher can control whether CVD produces single or multi-walled tubes. These process gasses – methane and ethylene – are very stable at the temperatures in the furnace, typically 600 to 1200 degrees Celsius. Due to gasses' high molecular stability, they only decompose at catalyst sites, reducing the amount of amorphous

carbon generated during CVD. Decomposed carbon molecules then assemble themselves into nanotubes at the catalyst nano-particle sites. Using lithography, scientists can control the location of nanotube growth by seeding a substrate with catalyst nano-particles.They can also form nanotubes at an electrical connection, or at a site of physical significance such as a line etched in the silicon substrate. [2]**.** Since CNTs tend to agglomerate, serious dispersion problems must be solved. In order to realize the many potential applications that CNTs can offer, the chemical functionalization of CNTs is of fundamental importance. Introduction of functional groups, such as carboxyl and amino groups, not only can improve CNTs solubility in various solvents, but also are useful for the further chemical link with other compounds, such as inorganic compound [3], biomolecules[4] and polymers [5] and the CNTs self-assembly into devices structures [6]. Various functional groups attached to CNTs are possible via oxidation withconcentrated acids [7], cycloaddition [8], arylation [9], diazonium salt chemistry [10–12] and other reactions [13–15]. Applications in compound materials, electronic QC devices, nano sensors or as gas storage material are intensively explored. All these potential applications require an extended functionalization of the nanotubes to make them processable and to tune their properties. [16]

## Materials and Methods

### Materials and solvents

In present study, attempts were made to synthesize carbon nanotubes using xylene as carbonaceous precursors and Ferrocene as catalyst compounds & cobalt, nickel and iron were used as catalyst powder. Concentrated sulfuric acid ($H_2SO_4$) and nitric acid ($HNO_3$) were also used for functionalization.

### Preparation of substrate

Silica was taken in the bulk form and grinded in a ball mill for 24 hrs and then powder was oxidized in a furnace at $900^{o}$c for 1 hr . The amount of loss of silica is 9.98% of weight after oxidation.

### Synthesis methods of CNTs

Horizontal Quartz tube furnace was used for the growth of carbon nanotubes. The substrate was heated in high pure argon up to desired reaction temperature at specific heating rate. On attainment of desired reaction temperature, the mixture of carbonaceous source and catalyst was

passed for different reaction time from 30 min. The liquid hydrocarbons containing about 5 wt% of ferrocene (organometallic compound) was injected into the CVD reactor by the syringe pump along with argon containing $H_2$ atmosphere After the reaction, the furnace was allowed to cool under argon atmosphere. Substrates used in these studies were weighed before and after the reaction to determine the amount of carbon produced at different sites within the reactor.

**Purification of CNTs**

CNTs were placed in 50:50 solution of HF and distilled water and the solution was kept for 24 hrs. It was then filter with distilled water till the neutral pH is obtained. Purified CNTs were kept in oven to remove the moisture for 72 hrs at $80^o$c.

**Procedure for the synthesis of CNTs/COOH**

The pristine carbon nanotubes 0.1 g were first chemically functionalized with mixture of concentrated sulfuric acid and nitric acid under the ratio of 3:1 the ultrasonication bath for 1 hr. after the ultrasonication bath material put on stirring for 2 hr. Then 90 ml of water was added into the mixture. The dispersion was then centrifuged, washed with water until it turned neutral and dried at 50˚C over night.

**Material characterizations**

X-ray diffraction is patterns were obtained with a diffractometer using Cu pellet anode at 40 kV, wavelength 0.154 nm. Fourier transform infrared (FT-IR) spectra of the products were recorded with KBr pellet spectrometer ranging from $400cm^{-1}$ to $4000cm^{-1}$. The morphology and identify structural changes was examined by transmission electronic microscopy.

**Results and Discussion**

**Transmission electron microscopy**

TEM, as one of the most useful methods to characterize the morphologies of nanoparticles in Nano-composites, and also used for the investigation of the hybrid material.

To prepare TEM samples, some acetone was dropped on the nanotubes film, and then, these films were transferred with a pair of tweezers to a carbon coated copper grid. It is obvious from the images that all the nanotubes are hollow and tubular in shape. In some of the images, catalyst particles can be seen inside the nanotubes. TEM images indicate that the nanotubes are of high purity, with uniform diameter distribution, and contain no deformity in the structure while Figure

shows Transmission Electron Microscope of the carbon nanotube. It shows that a highly ordered crystalline structure of CNTs is present.
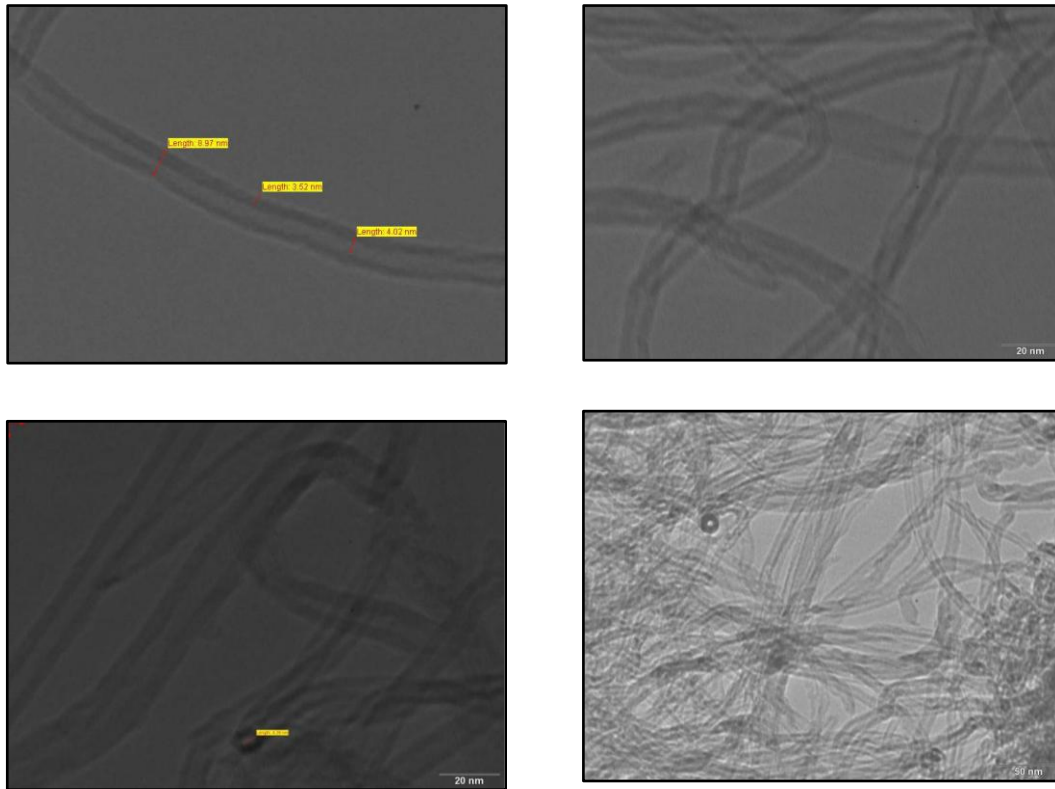


**Fig. 3.1** Transmission electron microscopy of pristine CNTs.

**X-Ray Diffraction**

This characterization method is not sample destructive and is used to obtain some information on the interlayer spacing, the structural strain and the impurities. However, carbon nanotubes have multiple orientations compared to the X-ray incident beam. Peak broadening and peak shift indicates that the strain is introduced in the nanotube structures due to surface functionalization and introduction of defects during ultrasonication reaction. The strongest diffraction peak at the angle ($2\theta$) of $26.5^o$ can be indexed as the c (002) reflection of hexagonal graphite structure. The sharpness of the peak at the angle ($2\theta$) of $26.5^o$ indicates that the graphite structure of the SWNTs was acid-oxidized without significant damage since any decrease in the order of crystalline in SWNTs will make XRD peaks broadening and shift the peak diffraction on towards lower angles.
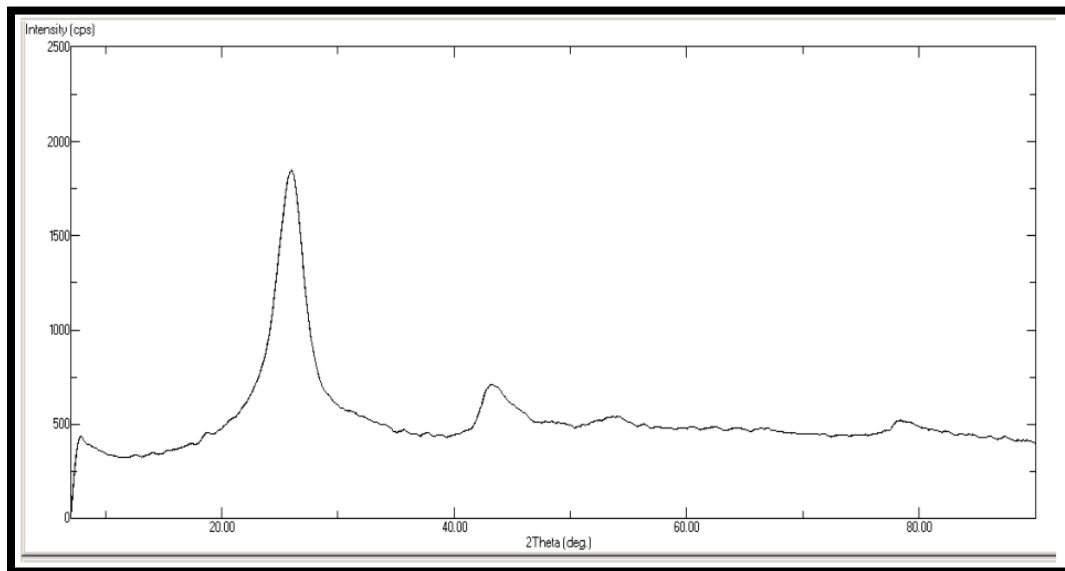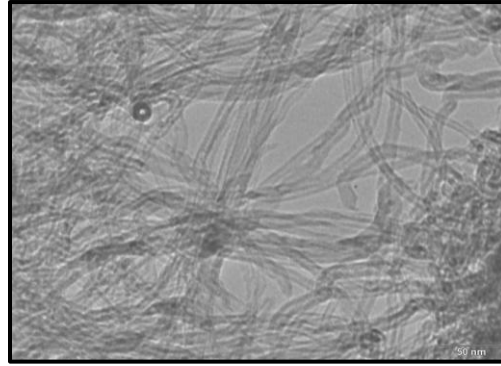
**Figure 3.2** X ray Diffraction graph of CNTs

**FT-IR study**

FT-IR was conducted on functionalized CNTs as shown in fig 3.3. The IR spectrum shows important bands at 3450 cm$^{-1}$ (attributing to OH stretching). 2900 cm$^{-1}$ and 2950 cm$^{-1}$ assigned to asymmetric and symmetric CH$_2$ stretching. 1725 cm$^{-1}$ assigned to stretching vibrations of carbonyl groups (C=O) present in carboxylic acids(RCOOH). 1625 cm$^{-1}$ assigned to conjugated C=C stretching. 1050 cm$^{-1}$ corresponding to C-O stretch in alcohols. The peak at 1589.40 cm$^{-1}$ and 1554.68 cm$^{-1}$ can be assigned to the C=C stretching, which indicates the graphite structure of MWNTs. Peak at 1400 cm$^{-1}$ is O-H band of carboxylic group. These results suggest that carboxylic acid groups have been successfully introduced on to the surfaces MWNTs by acid treatment.
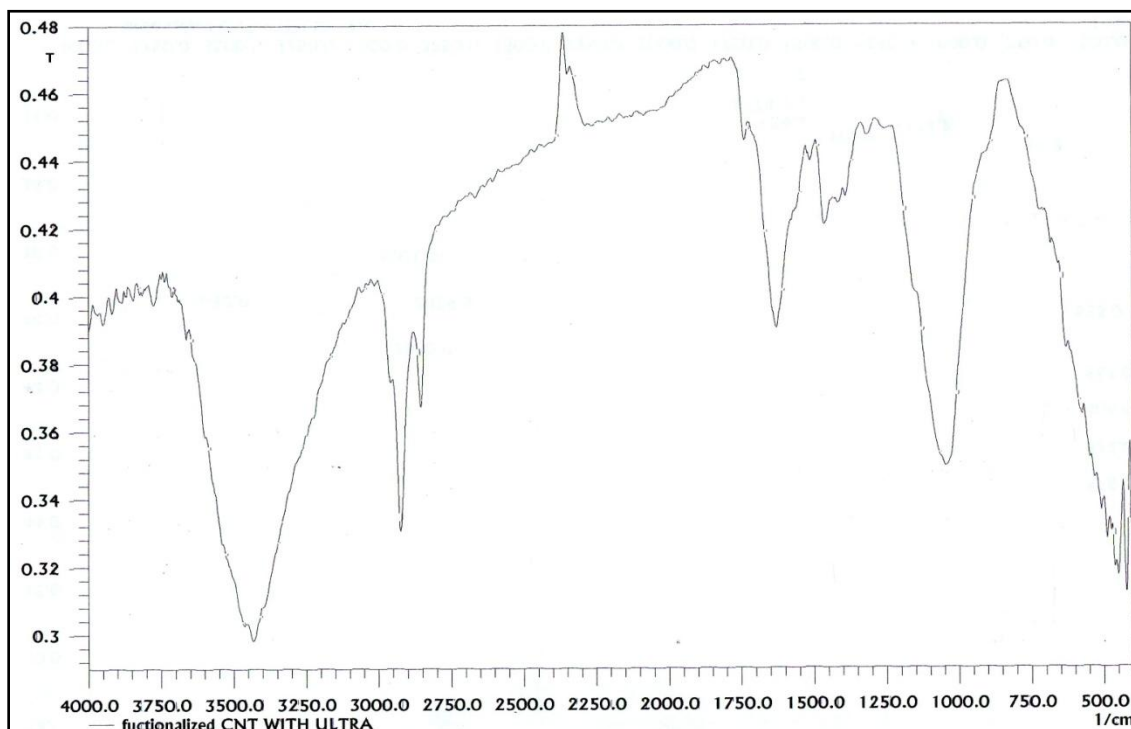
**Fig 3.3  FT-IR study of functionalized carbon nanotubes with carboxylic groups**

**Conclusion**

The research presents a CVD method for producing MWCNTs by using catalyst. In CNTs, the result of X-ray  differaction characterization shows the sharpness of the peak at the angle ($2\theta$) of indicates that the graphite structure of the MWNTs which match of CNTs JCPDS 75-1621 card. TEM characterizations of pristine CNTs form bundles which contain crystallized and Multi walled CNTs with a diameter of around 10 nm. Taking into account the importance of carboxyl groups on the surface of MWCNTs, these groups has been successfully introduced to achieve the

functionalization of MWCNTs via the mixed acid treatment. FT-IR result on samples confirms the presence of carboxyl on the MWCNTs. Moreover, carboxyl introduced onto the surfaces of MWCNTs are available to be further functionalized by conventional chemistry routes. MWCNTs-COOH may conveniently been served as flexible platforms for further functionalizations in materials science, cancer treatment, sensor and drug delivery applications.

**References:**

1. C. Oncel, Y. Yurum, Carbon Nanostructures, 2006, 14,17.
2. G.Gabriel  Carbon, 2006,  44 ,1891.

3. S.Banerjee, T. Hemraj-Benny, S. S.Wong, Advanced Materials, 2005,17,17.
4. D. Tasis, N. Tagmatarchis, A. Bianco, M. Prato, Chemistry of carbon nanotubes, Chemical Reviews 2006, 106 1105.
5. M.T. Byrne, Y.K. Gun'ko, Advanced Materials, 2010, 22, 1672.
6. C. Klinke, J. B. Hannon, A.  Afzali, P. Avouris, (2006). Field-effect transistors assembled from functionalized carbon nanotubes. *Nano letters*,*6*(5), 906-910.
7. F. Avilés, J. V. Cauich-Rodríguez, L. Moo-Tah, A. May-Pat, R. Vargas-Coronado, *Carbon*, 2009, *47*, 2970.
8. N. Tagmatarchis, M. Prato, Journal of materials chemistry, 2004, 14, 437.
9.  J. J. Stephenson, A. K. Sadana, A. L. Higginbotham, J. M. Tour, Chemistry of Materials, 2006,18, 4658.
10. J. L.Bahr, J. M. Tour, Chemistry of Materials, 2001. 13, 3823.
11. M. D.Ellison, P. J.  Gasda, . The Journal of Physical Chemistry C, 2008, 112, 738.
12. A. Amiri, M. Maghrebi, M. Baniadam, S.Z. Heris, Applied Surface Science, 2011, 257, 10261.
13. J.Y.Yook, J. Jun,  S. Kwak, Applied Surface Science, 2010,256, 6941.
14. Ajayan, M. Pulickel, Z. Otto Zhou. Springer Berlin Heidelberg, 2001. 391.
15. Khare, Rupesh,  and Suryasarathi Bose. *Journal of minerals and Materials Characterization and Engineering,* 2005, 4,31.
16. A.Hirsch, O.Vostrowsky, Springer Berlin Heidelberg, 2005, 193.

# Acoustical properties of aqueous solutions of paracetamol at different temperatures

## T. R. Pandit [1], V. A. Rana [2]

Dept. of Physics, University School of Sciences, Gujarat University, Ahmedabad, Gujarat, India.
E-mail: [1]tanmaypandit12@gmail.com, [2]ranava2001@yahoo.com

**Abstract**

Measurements of physical properties like refractive index, density, viscosity and ultrasonic velocity for aqueous solutions of Paracetamol across a temperature range of 293.15 K to 323.15 K were carried out in this study. Obtained results were analyzed for gathering structural information of solutions as well as to get an idea about its applications in formations of medicines from the drug. Thermodynamical properties like specific volume $(S_v)$, specific gravity $(S_G)$ for all solutions at all temperatures were also calculated using the values of density. Results of refractive index were used to calculate dielectric constant at optical frequency $(\varepsilon_\infty)$ of solutions. Acoustical parameters like adiabatic compressibility $(\beta_a)$, free length $(L_f)$, acoustic impedance $(Z_{aco})$, etc. were also calculated for all solutions from measured physical properties.

**Keywords: -** Physical properties, paracetamol; ultrasonic velocity; Abbe's refractometer; pharmaceuticals

**Introduction**

Physical properties of pharmaceutical drugs provide useful information regarding drug formulation, drug dosage, synthesis, etc. In bio-physical chemistry; it is required to understand drug - macromolecular interaction which involves a complex mechanism. Since most of the bio-chemical processes occur in aqueous medium; the study of physical properties of a drug in aqueous state provides useful information in pharmaceutical and medicinal chemistry. The drug - water interaction and their temperature dependence play an important role to understand the drug action in human body. Such results can be helpful to predict the absorption of drugs and transport of drugs across the biological membranes. [1]

Research into the physical properties like solubility, boiling point of thirteen different pharmaceutical powders has been measured by C.M.Mcloughlin et al. [2] Physical properties like refractive index, density and viscosity of three pharmaceutical drugs at different temperatures were measured by Iqbal and Chaudhary. [1] Literature survey confirms that no

attempts has yet been made to obtain physical properties for aqueous solutions of PCM which has been fulfilled in this study at four different temperatures.

Pharmaceutical drug selected for this study is Paracetamol (PCM) because it is the most common drugs used in the world for pain, fever and in many other medical issues. PCM has protein like structure and contains amide group ($R-CONH_2$) in its formulation which indicates many applications in the field of pharmaceutical sciences as well as in medical sciences.

The chemical formula of PCM is $C_8H_9NO_2$ and its molecular weight is 151.17 gm /mol. [3] PCM is used as an intermediate for pharmaceuticals, stabilizer for hydrogen peroxide, photographic chemicals and as an alternative to aspirin. [4] Schematic for structure of PCM is shown in figure - 1.
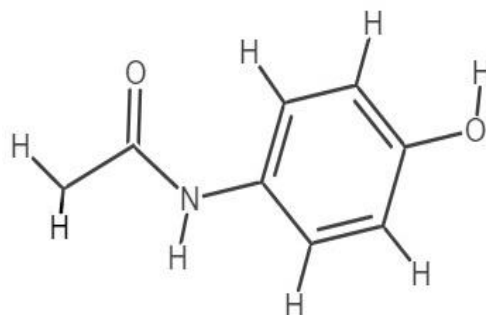
Figure-1: Structure of PCM

## Materials and Methods

Paracetamol (PCM) powder was supplied by "Farmson Pharmaceuticals Gujarat Pvt. Ltd.; Vadodara" and distilled water was purchased from "High Purity Laboratory Chemicals Pvt. Ltd.; Mumbai". Samples of sealed packets were kept in airtight glass container before to make its use in the experiment. Aqueous solutions of different weight fractions of PCM powder with 10 ml volume of distilled water were prepared. The maximum amount of weight fractions of PCM used for experiment is according to its solubility in water i.e. 140 mg / 10 ml. [5] The concentrations then converted into the unit of molarity using conversion formula described by E.M.Cheng et al. [6]

For measurements of physical properties refractive index, viscosity, density and ultrasonic velocity; Abbe's refractometer, Ostwald's Viscometer, Pycnometer and Ultrasonic interferometer were used respectively. Experimental setup and methodology as discussed by Rana and Chaube [7] has been followed to obtain physical and ultrasonic properties. Allied parameters from obtained physical properties were calculated using expressions stated in [8]. Comparison of measured values of R.I., density, viscosity and ultrasonic velocity with literature values at 303.15 K are presented in table - 1.

| Physical Property | Experimental Value | Literature Value |
|---|---|---|
| Refractive Index | 1.331 | 1.33105 [9] |
| Density (kg m$^{-3}$) | 995.41 | 995.70 [10] |
| Viscosity (m$^2$ sec$^{-1}$) | 8.008 | 8.010 [11] |
| Ultrasonic Velocity (m sec$^{-1}$) | 1507.78 | 1500 [12] |

Table - 1: Comparison of measured and literature values of physical properties of water at 303.15 K temperature

## Results and Discussion

Experimentally determined values of R.I., density, viscosity, ultrasonic velocity and other evaluated parameters for aqueous solutions of PCM at four temperatures are presented in table - 2. Refractometry (technique for measurements of RI) is important in pharmacy for identification of a pure substance, establishing the purity of some substances and determination of the concentrations of simple solutions.[13] Values of RI (n) increases with the molarity of PCM powder and decreases with temperature. Results are obvious because when temperature increases; solution become less dense that effects as decrement in the value of RI. Increment in RI value with molarity reflects the presence and increase in concentrations of PCM in water. RI is the square root of relative permittivity and using this relation; dielectric constant at optical frequency ($\varepsilon_\infty$) has been calculated for all solutions at all temperatures. With reference to this relation; it can be justified that the variation in temperature causes change in the electronic polarization due to increase in average expansion of charges and dipole moment.

Density for all solutions increases with the molarity of PCM - water solutions. Increment in density is the result of increment in weight fraction of PCM powder in solution. Density for all solutions decreases with temperature due to expansion of volume in the solution. In liquids, density variation with molarity is typically small at all temperatures but this could be much greater for gases. Obtained results for density are useful to find the macroscopic properties of matter to uncover the informations at the atomic level as well as to identify pure substances and to characterize the composition of many kinds of mixtures of drugs. [14] Using the values of density; thermodynamical properties specific volume ($S_v$) and specific gravity ($S_G$) have been calculated. Linear increment in $S_V$ with temperature was observed. Decrement in $S_V$ with molarity is a result of weak solute - solute interaction. [1] Results give an idea about accurate dosage selection for compositions of PCM with water. Values of $S_G$ shows minor variations with molarity and exhibit non - linear variation with temperature.

| Temp. T (K) | Molarity (M) | n | $\varepsilon_\infty$ | $\rho$ (kg/m³) | $S_r*10^{-3}$ (m³/kg) | $S_G$ | $\eta*10^{-5}$ (m²/sec) | u (m-sec⁻¹) | $\beta a*10^{-10}$ (m·s²/kg) | $L_f$ (10⁻⁶ m) | $Z_{aco}*10^6$ (m⁻²·s⁻¹) | $\tau_\eta*10^{-14}$ (sec) | $V_f*10^{-5}$ (ml mole⁻¹) | $V_M*10^{-4}$ (kg·m⁻³ mol⁻¹) | R (*10⁻³) | W (*10⁻⁶) | $\emptyset_r*10^3$ (m·kg⁻¹·s⁻² mole⁻¹) | $\emptyset_k*10^{-5}$ (ml mole⁻¹) |
|---|---|---|---|---|---|---|---|---|---|---|---|---|---|---|---|---|---|---|
| 293.15 | 0 | 1.332 | 1.774 | 998.00 | 1.002 | 1.000 | 10.076 | 1481.26 | 4.566 | 1.316 | 1.478 | 6.13 | 1.53 | 1.801 | 2.05 | 8.34 | ---- | ---- |
|  | 0.013 | 1.335 | 1.782 | 998.21 | 1.001 | 1.000 | 10.078 | 1484.48 | 4.546 | 1.313 | 1.481 | 6.10 | 1.57 | 1.831 | 2.08 | 8.47 | -76.820 | -3.49 |
|  | 0.026 | 1.335 | 1.782 | 998.51 | 1.001 | 1.000 | 10.080 | 1487.19 | 4.528 | 1.311 | 1.484 | 6.08 | 1.62 | 1.862 | 2.12 | 8.61 | -38.320 | -1.73 |
|  | 0.039 | 1.336 | 1.784 | 998.72 | 1.001 | 1.000 | 10.083 | 1490.65 | 4.506 | 1.307 | 1.488 | 6.05 | 1.66 | 1.892 | 2.16 | 8.74 | -25.487 | -1.14 |
|  | 0.052 | 1.336 | 1.784 | 998.93 | 1.001 | 1.000 | 10.236 | 1493.39 | 4.488 | 1.305 | 1.491 | 6.12 | 1.67 | 1.922 | 2.19 | 8.88 | -19.070 | -0.85 |
|  | 0.065 | 1.337 | 1.787 | 999.13 | 1.000 | 1.001 | 10.239 | 1496.87 | 4.466 | 1.302 | 1.495 | 6.09 | 1.71 | 1.952 | 2.23 | 9.01 | -15.220 | -0.67 |
|  | 0.079 | 1.337 | 1.787 | 999.55 | 1.000 | 1.001 | 10.394 | 1499.35 | 4.451 | 1.299 | 1.498 | 6.16 | 1.72 | 1.983 | 2.27 | 9.15 | -12.491 | -0.55 |
|  | 0.092 | 1.338 | 1.790 | 999.86 | 1.000 | 1.001 | 10.549 | 1502.97 | 4.427 | 1.296 | 1.502 | 6.22 | 1.73 | 2.013 | 2.30 | 9.28 | -10.701 | -0.47 |
| 303.15 | 0 | 1.331 | 1.771 | 995.41 | 1.004 | 1.000 | 8.008 | 1507.78 | 4.418 | 1.318 | 1.501 | 4.71 | 2.21 | 1.800 | 2.06 | 8.29 | ---- | ---- |
|  | 0.013 | 1.333 | 1.776 | 995.82 | 1.004 | 1.000 | 8.009 | 1511.02 | 4.398 | 1.315 | 1.504 | 4.69 | 2.28 | 1.832 | 2.09 | 8.43 | -77.052 | -3.35 |
|  | 0.026 | 1.333 | 1.776 | 996.03 | 1.003 | 1.000 | 8.011 | 1515.82 | 4.369 | 1.310 | 1.509 | 4.66 | 2.34 | 1.861 | 2.13 | 8.56 | -38.436 | -1.67 |
|  | 0.039 | 1.334 | 1.779 | 996.44 | 1.003 | 1.001 | 8.136 | 1519.62 | 4.345 | 1.307 | 1.514 | 4.71 | 2.35 | 1.891 | 2.17 | 8.69 | -25.564 | -1.11 |
|  | 0.052 | 1.334 | 1.779 | 996.96 | 1.003 | 1.001 | 8.261 | 1523.81 | 4.319 | 1.303 | 1.519 | 4.75 | 2.37 | 1.922 | 2.21 | 8.83 | -19.128 | -0.82 |
|  | 0.065 | 1.335 | 1.782 | 997.27 | 1.002 | 1.001 | 8.388 | 1527.25 | 4.298 | 1.300 | 1.523 | 4.80 | 2.38 | 1.952 | 2.24 | 8.96 | -15.266 | -0.65 |
|  | 0.079 | 1.335 | 1.782 | 997.68 | 1.002 | 1.002 | 8.514 | 1531.92 | 4.271 | 1.295 | 1.528 | 4.84 | 2.40 | 1.983 | 2.28 | 9.09 | -12.529 | -0.53 |
|  | 0.092 | 1.336 | 1.784 | 997.99 | 1.002 | 1.002 | 8.640 | 1535.27 | 4.251 | 1.292 | 1.532 | 4.89 | 2.41 | 2.013 | 2.32 | 9.22 | -10.733 | -0.45 |
| 313.15 | 0 | 1.327 | 1.760 | 992.82 | 1.007 | 1.000 | 6.565 | 1526.43 | 4.323 | 1.326 | 1.515 | 3.78 | 3.02 | 1.801 | 2.07 | 8.27 | ---- | ---- |
|  | 0.013 | 1.329 | 1.766 | 993.23 | 1.006 | 1.000 | 6.566 | 1531.52 | 4.292 | 1.322 | 1.521 | 3.75 | 3.12 | 1.831 | 2.11 | 8.40 | -77.286 | -3.29 |
|  | 0.026 | 1.331 | 1.771 | 993.54 | 1.006 | 1.000 | 6.671 | 1536.63 | 4.262 | 1.317 | 1.526 | 3.79 | 3.14 | 1.863 | 2.15 | 8.54 | -38.553 | -1.63 |
|  | 0.039 | 1.331 | 1.771 | 994.06 | 1.005 | 1.001 | 6.776 | 1541.91 | 4.231 | 1.312 | 1.532 | 3.82 | 3.16 | 1.892 | 2.18 | 8.66 | -25.642 | -1.07 |
|  | 0.052 | 1.332 | 1.774 | 994.27 | 1.005 | 1.001 | 6.882 | 1546.73 | 4.204 | 1.308 | 1.537 | 3.85 | 3.18 | 1.922 | 2.22 | 8.79 | -19.186 | -0.80 |
|  | 0.065 | 1.332 | 1.774 | 994.58 | 1.005 | 1.001 | 6.988 | 1551.25 | 4.178 | 1.304 | 1.542 | 3.89 | 3.20 | 1.954 | 2.26 | 8.93 | -15.313 | -0.63 |
|  | 0.079 | 1.333 | 1.776 | 994.99 | 1.005 | 1.002 | 7.199 | 1556.05 | 4.151 | 1.301 | 1.548 | 3.98 | 3.14 | 1.938 | 2.29 | 9.06 | -12.567 | -0.51 |
|  | 0.092 | 1.333 | 1.776 | 995.31 | 1.004 | 1.002 | 7.306 | 1561.39 | 4.121 | 1.295 | 1.554 | 4.01 | 3.16 | 2.013 | 2.33 | 9.18 | -10.766 | -0.44 |
| 323.15 | 0 | 1.325 | 1.755 | 989.44 | 1.010 | 1.000 | 5.347 | 1541.97 | 4.251 | 1.338 | 1.525 | 3.03 | 4.15 | 1.803 | 2.08 | 8.25 | ---- | ---- |
|  | 0.013 | 1.328 | 1.763 | 989.74 | 1.010 | 1.000 | 5.262 | 1548.37 | 4.214 | 1.332 | 1.532 | 2.95 | 4.40 | 1.832 | 2.12 | 8.38 | -77.520 | -3.26 |
|  | 0.026 | 1.328 | 1.763 | 989.95 | 1.010 | 1.000 | 5.349 | 1555.93 | 4.172 | 1.325 | 1.540 | 2.97 | 4.43 | 1.862 | 2.15 | 8.51 | -38.669 | -1.61 |
|  | 0.039 | 1.329 | 1.766 | 990.26 | 1.009 | 1.000 | 5.436 | 1562.94 | 4.133 | 1.319 | 1.547 | 2.99 | 4.46 | 1.892 | 2.19 | 8.64 | -25.719 | -1.06 |
|  | 0.052 | 1.329 | 1.766 | 990.67 | 1.009 | 1.001 | 5.610 | 1569.03 | 4.109 | 1.314 | 1.554 | 3.06 | 4.39 | 1.924 | 2.23 | 8.77 | -19.244 | -0.78 |
|  | 0.065 | 1.330 | 1.768 | 990.88 | 1.009 | 1.001 | 5.697 | 1576.95 | 4.058 | 1.307 | 1.562 | 3.08 | 4.43 | 1.954 | 2.27 | 8.89 | -15.359 | -0.62 |
|  | 0.079 | 1.330 | 1.768 | 991.18 | 1.008 | 1.001 | 5.785 | 1583.37 | 4.024 | 1.302 | 1.569 | 3.10 | 4.45 | 1.984 | 2.31 | 9.02 | -12.605 | -0.50 |
|  | 0.092 | 1.331 | 1.771 | 991.60 | 1.008 | 1.002 | 5.961 | 1590.94 | 3.984 | 1.295 | 1.577 | 3.16 | 4.40 | 2.015 | 2.35 | 9.15 | -10.798 | -0.43 |

Table - 2: Values of refractive index (n), permittivity at optical frequency ($\varepsilon_\infty$), density ($\rho$), specific volume ($S_v$), specific gravity ($S_G$), viscosity ($\eta$), ultrasonic velocity (u), adiabatic compressibility ($\beta_a$), free length ($L_f$), acoustic impedance ($Z_{aco}$), viscous relaxation time ($\tau_\eta$), free volume ($V_f$), molar volume ($V_M$), rao's constant (R), wada's constant (W), apparent molar volume ($\emptyset_v$) and apparent molar compressibility ($\emptyset_K$) for aqueous solutions of PCM at different temperatures

Viscosity ($\eta$) gives an idea about any liquid in pharmaceuticals, with how much resistance it can flow whether it is a cough syrup, ointment, etc. It is very important for drug manufacturers to predict how products will behave when users consumes it. Small variation in viscosity with molarity of PCM and a noticeable change with temperature have been observed which is a result of existance of small amount of resistance for flow of liquid. Low values of viscosity refers to the presence of small molecules in solution with which rearrangement ability is faster than that of long chain molecules.

It is observed from table that ultrasonic velocity (u) increases linearly with concentration of PCM and with temperature. Adiabatic compressibility ($\beta_a$) and Free length ($L_f$) show an opposite trend to that of velocity. Free volume ($V_f$) and molar volume ($V_M$) increases with the concentration of PCM and increases with temperature. Increase in ultrasonic velocity and decrease in adiabatic compressibility, free length with concentration indicates strong solute - solvent interactions [15]; which is also supported by increase in viscous relaxation time ($\tau_\eta$).
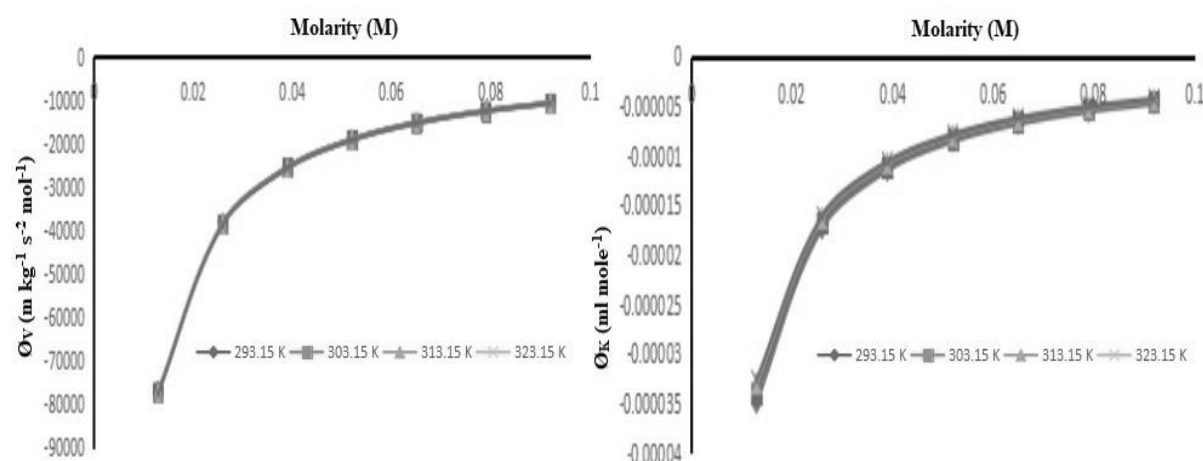


Figure - 2: Variation of apparent molar volume ($\emptyset_V$) and apparent molar compressibility ($\emptyset_k$) with molarity and temperature

It can be observed from figure - 2 that; Apparent molar compressibility ($\emptyset_k$) and apparent molar volume ($\emptyset_V$) also increases non- linearly with concentrations and temperature. Negative values of $\emptyset_V$ and $\emptyset_k$ are due to strong attraction between water molecules and paracetamol for occupying less space.

Linear increase in Rao's constant (R) and Wada's constant (W) with concentration can be observed from figure - 3; indicates solute - solvent molecules are coming close to each other and the space between them is decreasing with rise in temperature. [16]
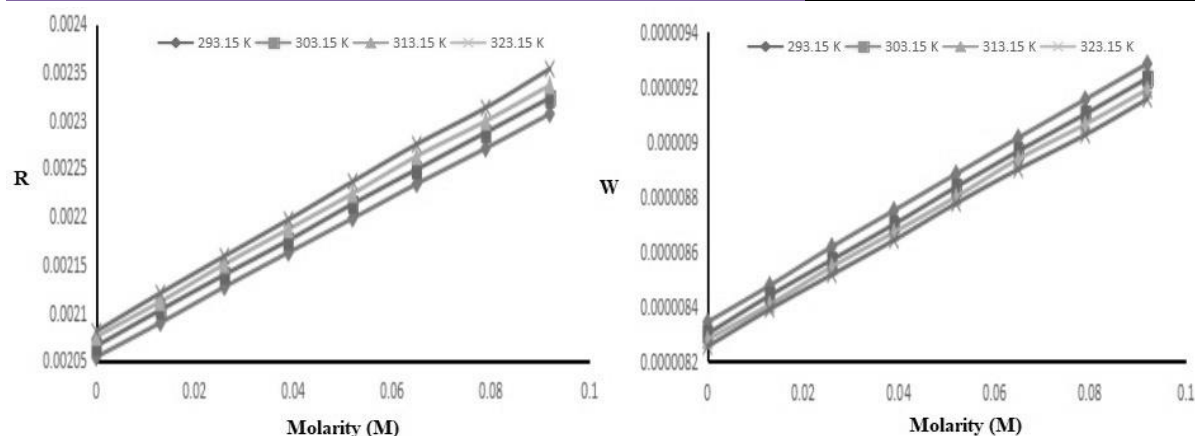
Figure - 3: Variation in Rao's constant (R) and Wada's constant (W) with molarity and temperature

## Conclusions

Measurements of physical quantities density, refractive index, viscosity and ultrasonic velocity for aqueous solutions of PCM of varying concentration within its solubility range over a temperature range of 293.15 K to 323.15 K were performed. Data of refractive index and dielectric constants at optical frequency for all solutions indicates change in electronic polarization with molarity of PCM due to increase in average expansion of charges. Density of solutions found to increase with molarity and decrease with temperature. Values for specific volume ($S_v$) and specific gravity ($S_G$) were calculated from density. These parameters are useful in pharmaceutical sciences for identification of purity of drugs and to estimate the concentration of drug in the solutions. Viscosity for all solutions exhibits very small variation with molarity but a noticeable variation with temperature has been observed. Small size of molecules / particles in solutions were predicted from the small variations of viscosity with concentration. Ultrasonic velocity increased with molarity as well as with temperature. Parameters obtained from ultrasonic velocity indicates strong solute - solvent interaction for all solutions and exhibit decrement in spacing between solute - solvent with rise in temperature.

## Acknowledgements

## References

1. M.J.Iqbal, M.A.Chaudhary; "J. Chem. Thermodynamics"; 2009; 41; 221 - 226.

2. C.M.Mcloughlin, W.A.M. McMinn, T.R.A. Magee; "Powder Technology"; 2003; 134; 40 - 51.

3. G.P.Johari, S.Kim, R.M.Shanker; "Journal of Pharmaceutical Sciences"; 2010; 99 (3); 1358 - 1374.

4. R.E.Mudgett; "Food Technology"; 1986; 40; 84 – 93.

5. M.S.Venkatesh, G.S.V.Raghavan; "Canadian Bio-Systems Engineering"; 2005; 97; 7.15 – 7.30.

6. E.M.Cheng, M. Fareq, F.S.Abdullah et al.; "IEEE International RF and Microwave Conference"; 2013; 409 - 413.

7. V.A. Rana, H.A. Chaube; "Journal of Molecular Liquids"; 2012; 173; 71–76.

8. S. Ajeetha, A.H.Malini, V.N.M.Devi; "Research journal of pharmaceutical, biological and chemical sciences"; 2013; 4(3); 218 - 224.

9. A.N.Bashkatov, E.A.Genina; "SPIE"; 2003; 5068; 393 - 395.

10. G.S.Kell; "J. Chem. Eng. Data"; 1975; 20 (1); 97 - 105.

11. J. Kestin, M.Sokolov, A.Wakeham; "Journal of Physical and Chemical Reference Data"; 1978; 7; 941 - 948.

12. C.J.Burton; "The journal of the acoustical society of America"; 1948; 20; 186 - 199.

13. D. R.Lide; "CRC Handbook of chemistry and physics"; 86th ed.; Boca Raten (FL): CRC Press; 2005.

14. R.Francesconi, A.Bigi, K.Rubini, F.Comelli; "J. Chem. Eng. Data"; 2005; 50; 1932 - 1937.

15. P.S.Naidu, K.R.Prasad; "Indian Journal of Pure & Applied Physics"; 2004; 42; 512 - 517.

16. J.P.Singh, R.Sharma; "International Journal of Engineering Research and Development"; 2013; 5(11); 48 - 51.

# Phonon dispersion curves and elastic moduli for Sn-Pb liquid metallic alloy

A. B. Patel[1#], C. H. Patel[2], N. K. Bhatt[3] and P. N. Gajjar[1]

[1]Department of Physics, School of Sciences, Gujarat University, Ahmedabad, Gujarat – 380009

[2]Gujarat State board of school textbooks, 'vidyayan', sector-10/A, Gandhinagar, Gujarat –382010

[3]Department of Physics, M K Bhavnagar University, Bhavnagar, Gujarat – 364001

[#]Corresponding author. Email: amit07patel@gmail.com

**Abstract**. The phonon dispersion curves of polyvalent liquid binary SnPb alloy are investigated using Hubbard and Bebby (HB) approximation at different temperatures. The calculation is based on pseudo potential due to Hasegawa is valid for all electrons which gives the occurrence of the true field, rather than a Columbic form in the pre-asymptotic region.In present work, the parameters of Sn-Pb alloy are obtained from the relation $P^{eff} = (1-x)P^{Sn} + x\,P^{Pb}$; where, P is the desired effective parameters like $r_c$, $\Omega_0$, σ, etc. and x is the concentration of individual elemental metals. The phonon frequencies in the large wave length limit, increased faster with q than predicted by classical hydrodynamics which is so-called positive dispersion. The temperature dependence of elastic moduli is calculated using the longitudinal and transverse phonon velocities. Because of the non-availability of any experimental results on PDCs and elastic moduli, it has not been possible to compare the computed results. Nevertheless, the results obtained may be useful for future comparison qualitatively as well as quantitatively.

**Keywords:** pseudo potential; SnPb alloy; phonon dispersion; elastic moduli

**Introduction:** In recent years, due to the prime technological importance, there has been great interest for the study of liquid metals and their alloys. Experimentally dispersion curves for longitudinal phonon and theoretically computer simulation technique have provided dispersion curves for both longitudinal and transverse phonons in liquids and its alloys [1].During the past few decades, metallic liquids have been extensively studied using the pseudo potential theory. Phonon dispersion in liquid metallic alloys is mostly studied for existing collective modes of motion of the constituent atoms. However, Sn and Pb is the heaviest non-simple element the d- bands in such less simple metals are completely filled by electrons, still the significant effect of the sp-d hybridization exists. Moreover, the structure of these less simple liquid metals shows anomalous behavior near their melting temperatures. In this connection, a careful and comprehensive study requires for various physical properties of liquid Sn-based alloys. The temperature dependent study of various alloy systems in liquid state is not

largely explored yet. It is a still question how the physical properties of liquid metallic alloys very with the temperature. Previously Patel *et. al.*[2] studied vibrational dynamics for liquid Sn and Pb metals over a wide range of temperature. So our main purpose of this paper is an extension work of Patel *et.al.*[2] for Sn-Pb liquid metallic alloys. Therefore, in the present work the vibrational dynamics and elastic properties of $Sn_{1-X}Pb_X$ liquid metallic alloy have been investigated for wide temperature range.

**Computational Approach:** The second order pseudo potential perturbation theory gives the effective inter-atomic pair potential V(r) of a metal as the sum of the direct Coulomb repulsive interaction between two ions and attractive interaction between ions and its screening electron gas is expressed by [3],

$$V_{eff}(r) = \frac{Z_{eff}^2 e^2}{r} + \frac{\Omega_{0eff}}{\pi^2} \int F_{eff}(q) \frac{\sin(qr)}{qr} q^2 dq \qquad (1)$$

Here, $Z_{eff}$ is the valence, e is the electronic charge and $\Omega_{eff}$ is the atomic volume of binary alloys. In the present work, the temperature dependent pair potential is calculated by multiplying a dimensionless damping term $\exp\left(-\frac{\pi k_B T}{2k_F} r\right)$ to the pair potential [4-6], which provides necessary Friedel-damping as expected at high temperatures. In Eq.-1, $F_{eff}(q)$ is the energy wave number characteristics. The first term gives the coulomb interaction between ions and the second term is due to the indirect interaction through the conduction electrons. This indirect interaction can be calculated using the energy wave number characteristics F(q).

$$F_{eff}(q) = -\frac{\Omega_{0eff} q^2}{16\pi} \left|W_{Beff}(q)\right|^2 \frac{\varepsilon_{Heff}(q)-1}{1+(\varepsilon_{Heff}(q)-1)(1-f_{eff}(q))}. \qquad (2)$$

Here, $\varepsilon_{Heff}(q)$ is the Hartree dielectric response function and $f_{eff}(q)$ is the local field correction function, which represents the exchange and correlation effects. In the present work, we used the Ichimaru-Utsumi [7] local filed correction function which accurately reproduces the Monte-Carlo results and it also satisfies the self consistency condition in the compressibility sum rule.

The choice of model potential is an important feature which describes the motion of valence electron in a metal. We have employed the pseudo potential due to Hasegawa *et al.*[8] for bare ion interaction potential. Earlier, the ionic potential for Li from first principles, which are extrapolated into the core region with delta function to describe the core pseudisation is proposed by Hoshino and Young [9]. It consists full electron-ion interaction and a delta function which represents the

orthogonalisation effect due to the s-core states in such sp-bonded metals. This gives the occurrence of the true field, rather than a Columbic form in the pre-asymptotic region. Following their calculations, Hasegawa *et al.*[8] have improved the model potential form by Coulombic tail by an exponentially decay term, and inside the core complete cancellation due to orthogonal properties of core and valence states. Application of this potential gives good results for describing the concentration fluctuation in structural study of Li-Na liquid alloy [10] and also predicting the correct sign of the phase shift in liquid potassium. This modified empty-core (MEC) bare ion potential includes non-locality and its q-space form of is,

$$W_{Beff}(q) = -\frac{4Z_{eff}\,\pi\,e^2}{q^2}\cos qr_{ceff}\left[1+\frac{a_{eff}\,q^2}{q^2+b_{eff}{}^2}\exp(-b_{eff}\,r_{ceff})(1+\frac{b_{eff}}{q}\tan qr_{ceff})\right]. \tag{3}$$

In the study of phonon dispersion curves (PDC) of liquid binary alloy the main ingredients are theinter-atomic pair potential V(r) and pair correlation function g(r). It contains useful information about the inter particle radial correlation can be obtain using different experimental techniques and theoretical models. In our previous work[11], we computed static structure factor S(q) and its Fourier transforms g(r) using Ashcroft-Lengrath [12] approximation is now used to calculate PDC. To compute the phonon frequencies the most frequently used approach of Hubbard and Beeby (HB) [13] is adopted. Under HB assumption, the expressions for longitudinal and transverse phonon frequencies are,

$$\omega_l^2 = \omega_E^2\left[1-\frac{3\sin(q\sigma)}{(q\sigma)}-\frac{6\cos(q\sigma)}{(q\sigma)^2}+\frac{6\sin(q\sigma)}{(q\sigma)^3}\right]. \tag{4}$$

$$\omega_t^2 = \omega_E^2\left[1+\frac{3\cos(q\sigma)}{(q\sigma)^2}-\frac{6\sin(q\sigma)}{(q\sigma)^3}\right]. \tag{5}$$

Where, $\omega_E = \frac{4\pi\pi_{eff}}{3M_{eff}}\int_0^{\infty}g(r)r^2\left\{V_{eff}''(r)+\frac{2}{r}V_{eff}'(r)\right\}dr$ is the maximum phonon frequency and $V_{eff}'(r)$ the first derivative and$V_{eff}''(r)$the second derivatives of V(r).

Within the long-wavelength limit, the phonon dispersion curve shows an elastic behavior. Hence, the longitudinal $v_l$ and transverse $v_t$ sound velocities are also computed by

$$\omega_l \propto q \qquad \text{and} \qquad \omega_t \propto q, \qquad\qquad \omega_l = V_l\,q \qquad \text{and} \qquad \omega_t = V_t\,q$$

Then using longitudinal and transverse sound speed, the bulk modulus B, Poisson's ratio '$\xi$', modulus of rigidity G, Young's modulus Y and the Debye temperature $\theta_D$ are computed byfollowing expressions,

$$B = \rho\left(V_l^2 - \frac{4}{3}V_t^2\right), \quad \xi = \frac{1 - 2\left(V_t^2/V_l^2\right)}{2 - 2\left(V_t^2/V_l^2\right)}, \quad G = \rho V_t^2, \quad Y = 2G(\xi+1) \text{ and } \theta_D = \frac{h}{k_\beta}\left[\left(\frac{9\rho}{4\pi}\right)^{\frac{1}{3}}\left(\frac{1}{V_l^3} + \frac{2}{V_t^3}\right)^{\frac{-1}{3}}\right]$$

where, 'h' is Plank constant, $k_B$ is the Boltzmann constant and $\rho$ is the isotropic density of the alloy.

**Results and Discussion:**

Table-1: The calculated input parameters effective volume and effective core radius at different temperatures and concentrations.

| T(K) Con. | 470 | | 523 | | 613 | | 973 | | 1173 | | 1500 | |
|---|---|---|---|---|---|---|---|---|---|---|---|---|
| | $\Omega_{0eff}$ | $r_{ceff}$ | $\Omega_{0eff}$ | $r_{ceff}$ | $\Omega_{0eff}$ | $r_{ceff}$ | $\Omega_{0eff}$ | $r_{ceff}$ | $\Omega_{0eff}$ | $r_{ceff}$ | $\Omega_{0eff}$ | $r_{ceff}$ |
| 0 | 189.36 | 1.5200 | 190.25 | 1.4830 | 191.77 | 1.4726 | 198.066 | 1.4300 | 201.749 | 1.4110 | 208.075 | 1.3820 |
| 0.1 | 191.80 | 1.5374 | 192.74 | 1.5030 | 194.36 | 1.4931 | 201.059 | 1.4487 | 205.087 | 1.4290 | 211.8305 | 1.3990 |
| 0.2 | 194.24 | 1.5549 | 195.22 | 1.5231 | 196.95 | 1.5135 | 204.052 | 1.4675 | 208.426 | 1.4480 | 215.5859 | 1.4161 |
| 0.3 | 196.68 | 1.5724 | 197.71 | 1.5431 | 199.55 | 1.5339 | 207.045 | 1.4863 | 211.764 | 1.4670 | 219.3414 | 1.4332 |
| 0.4 | 199.12 | 1.5898 | 200.20 | 1.5632 | 202.14 | 1.5544 | 210.038 | 1.5051 | 215.103 | 1.4860 | 223.0968 | 1.4503 |
| 0.5 | 201.55 | 1.6073 | 202.69 | 1.5832 | 204.73 | 1.5748 | 213.031 | 1.5239 | 218.441 | 1.5050 | 226.8523 | 1.4674 |
| 0.6 | 203.99 | 1.6248 | 205.18 | 1.6033 | 207.32 | 1.5952 | 216.023 | 1.5426 | 221.78 | 1.5230 | 230.6078 | 1.4844 |
| 0.7 | 206.43 | 1.6422 | 207.67 | 1.6233 | 209.91 | 1.6157 | 219.016 | 1.5614 | 225.118 | 1.5420 | 234.3632 | 1.5015 |
| 0.8 | 208.87 | 1.6597 | 210.15 | 1.6434 | 212.50 | 1.6361 | 222.009 | 1.5802 | 228.456 | 1.5610 | 238.1187 | 1.5186 |
| 0.9 | 211.31 | 1.6772 | 212.64 | 1.6634 | 215.09 | 1.6565 | 225.0027 | 1.5990 | 231.7954 | 1.5800 | 241.8741 | 1.5357 |
| 1 | 213.75 | 1.6947 | 215.13 | 1.6835 | 217.68 | 1.6770 | 227.9956 | 1.6178 | 235.1338 | 1.5990 | 245.6296 | 1.5528 |

The parameters used in the present calculation of the phonon dispersion curves of the Sn-Pb alloy are tabulated in Table-1. Patel $et.al.$[2] have determined the potential parameter $r_c$ by optimizing hard sphere diameter at a given (n,T) condition. It is noteworthy that this model provides accurate description of the interactions in the liquid polyvalent metals. In present work, the parameters of Sn-Pb alloy can be obtained from the relation $P^{eff} = (1-x)P^{Sn} + x P^{Pb}$; where, P is the desired effective parameters like $r_c$, $\Omega_0$, $\sigma$, etc. The $0 \leq x \leq 1$ is the concentration of individual elemental metals.
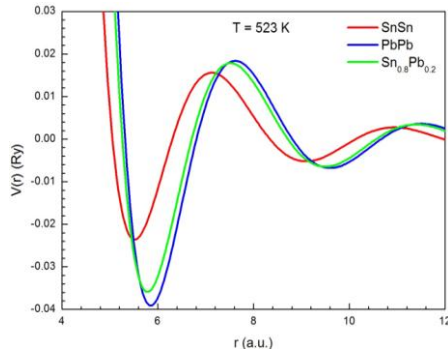
**Fig. 1 Inter atomic potential at T = 523 K**     **Fig. 2 Same as Fig. 1at T = 1500 K**
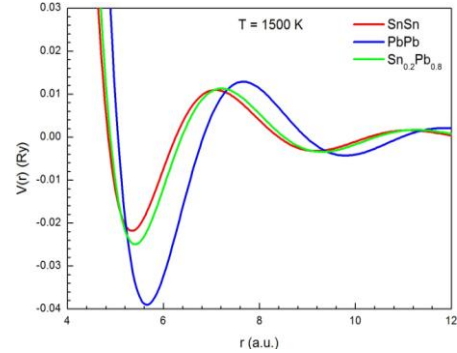
The inter atomic partial pair potential $V_{Sn-Sn}(r)$, $V_{Pb-Pb}(r)$ and $V_{Sn-Pb}(r)$ have been calculated using the eq.1 within the framework of pseudo potential formalism are shown in Fig.1 and Fig.2. The effective pair potential $V_{eff}(r)$ lies in between $V_{Sn-Sn}(r)$ and $V_{Pb-Pb}(r)$. We can infer from the Fig.1 and Fig.2, the effective inter atomic pair potentials have significant oscillations in the large r – region at T = 523 K while these Friedal oscillations are damped at T = 1500 K. This exponentially damped pair potential has the advantage of not containing the long ranged Friedal oscillations. We can also infer that, with inclusion of Pb the depth of V(r) decreases near equilibrium. We also observed that the depth of the principal minimum decreases and the width of well increases with increasing temperature. These observations are consistent to the fact that with temperature binding decreases resulting into shallower V(r).
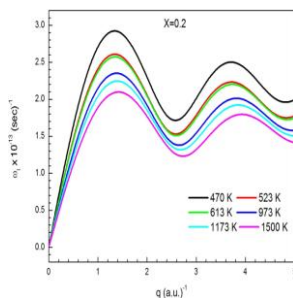


Fig.-3: Longitudinal phonon frequencies of $Sn_{0.2}Pb_{0.8}$ at different temperature.
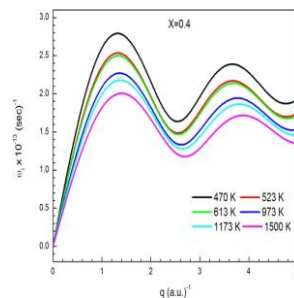
Fig.-4: Longitudinal phonon frequencies of $Sn_{0.4}Pb_{0.6}$ at different temperature.
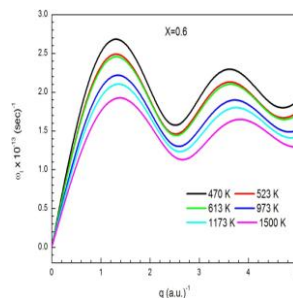
Fig.-5: Longitudinal phonon frequencies of $Sn_{0.6}Pb_{0.4}$ at different temperature.
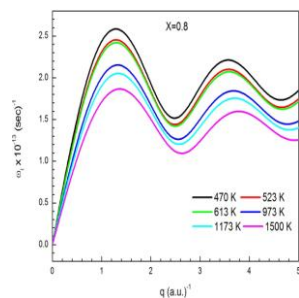
Fig.-6: Longitudinal phonon frequencies of $Sn_{0.6}Pb_{0.4}$ at different temperature.



Fig.-7: Transverse phonon frequencies of $Sn_{0.2}Pb_{0.8}$ at different temperature.
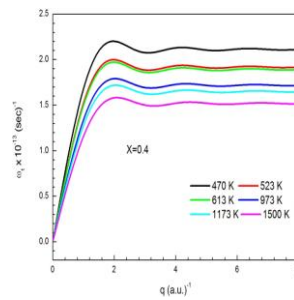
Fig.-8: Transverse phonon frequencies of $Sn_{0.4}Pb_{0.6}$ at different temperature.
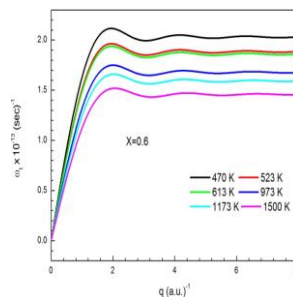
Fig.-9: Transverse phonon frequencies of $Sn_{0.6}Pb_{0.4}$ at different temperature.
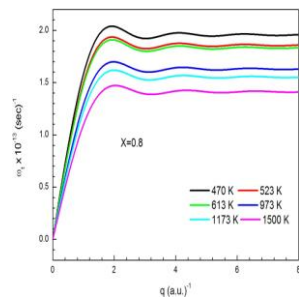
Fig.-10: Transverse phonon frequencies of $Sn_{0.8}Pb_{0.2}$ at different temperature.

Further, using above obtained effective pair potential the eigen frequencies of Sn-Pb liquid metallic alloy has been studied for longitudinal and transverse mode. The longitudinal and transverse phonon frequencies have been computed at different concentration and temperatures are shown in Fig.3-10. The curves obtain from HB approach reproduces all the broad characteristics of dispersion relation. Longitudinal phonon shows oscillatory behavior with prominent maximum frequency. We also examined the position of the first frequency minimum roughly coincides with the first peak of structure factor $S(q)$ which is around $2k_F$. It has been revealed that this minimum arises from a process analogous to the Umklapp scattering in the crystalline solids. Moreover, the maximum frequency of the transverse phonon is smaller and appears at larger q than longitudinal phonons. The oscillatory behavior of the transverse phonon is insignificant beyond the first peak. It indicates that the transverse phonons undergo large thermal modulation compared to longitudinal phonons, due to the anharmonicity in atomic vibrations, which may be connected with the instability of transverse phonons in liquid metal systems.The height of the peak decreases gradually where its width increases on raising the concentration of Pb in Sn.The phonon frequencies in the lower q range increased noticeably faster with q than predicted by classical hydrodynamics. This is the so-called positive dispersion which was already observed before in many other simple and non-simple liquid metals [14-17].
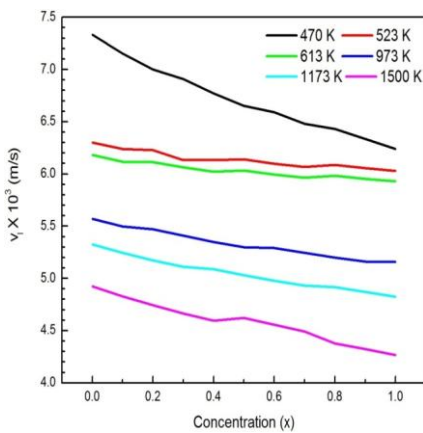


Fig.-11: Longitudinal sound speed ($v_l$) for different temperatures and concentrations.
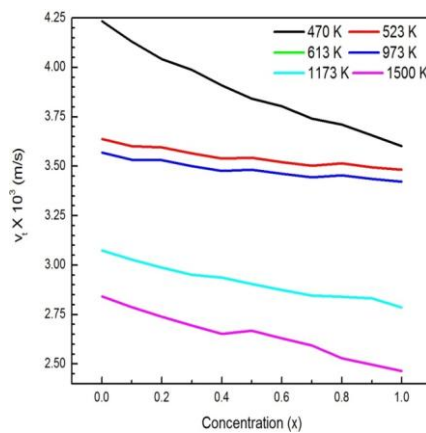
Fig.-12: Transverse sound speed ($v_t$) for different temperatures and concentrations.
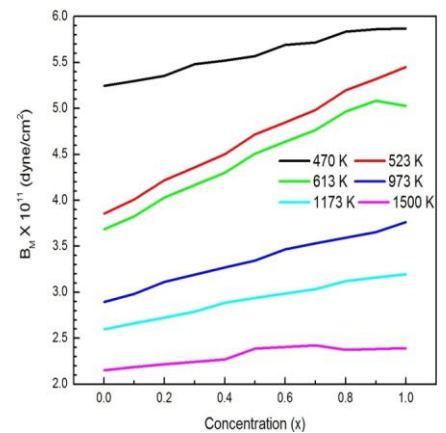
Fig.-13: Bulk Modulus ($B_M$) for different temperatures and concentrations.
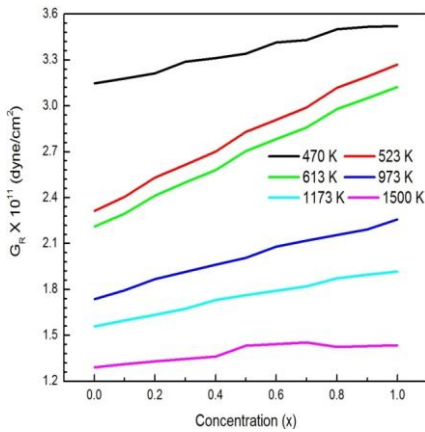
Fig.-14: Modulus of Rigidity ($G_R$) for different temperatures and concentrations.
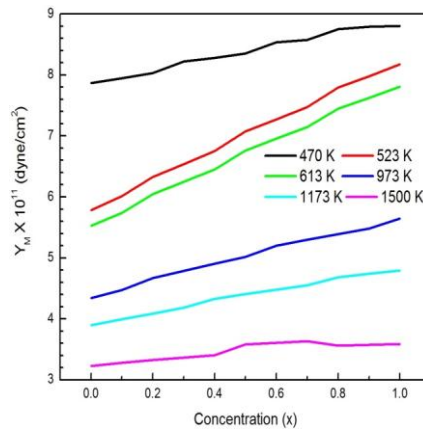
Fig.-15: Young Modulus ($Y_M$) for different temperatures and concentrations.
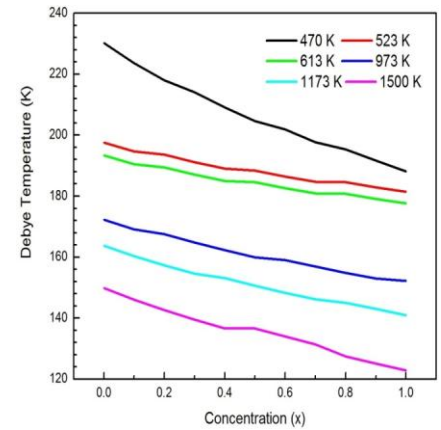
Fig.-16: Debye temperature for different temperatures and concentrations.

The dispersion curves show a linear variation in low the wave vector transfer region and depict the characteristic of elastic waves. The computed values of the elastic moduli for Sn-Pb liquid metallic alloy at different temperatures and concentrations are shown in Fig.11-16. We can infer that longitudinal and transverses sound velocities decreases with increasing temperature. In addition, both sound velocities are also decreases with increasing concentration of Pb in Sn. The elastic moduli ($B_M$, $G_R$ and $Y_M$) are found decreases with rising temperatures, while increases with higher concentration of Pb. From Fig.13-15, the increase in elastic moduli with concentration is observed upto around T = 1500 K and above this temperature they remains almost constants. The calculated values of Debye temperature decrease with increasing temperature and concentration of Pb.  In general, we can say that all the elastic parameters are decreases with increasing temperature.

**Conclusion:** The study indicates that, in liquid alloys, long-range oscillations are also present in the inter-atomic potential similar to the case of liquids and liquid metals. The Friedal oscillations in the inter-atomic potential are charge density oscillations, which cause and indirect electronic interaction between localized charges as pointed out by Haussler [18].  Overall, the PDC generated from the Hubbard and Beeby [13]approach reproduces satisfactorily the general characteristics of dispersion curves. The choice of the local field correction functions of the electron gas is also an important factor in the study of metallic properties. Hence, in present study the model potential along with Ichimaru and Utsumi local field correction function [7] seems to be capable of explaining the phonon dispersion curves (PDC) of liquid metallic alloys. We could not compare PDCs and elastic moduli due to unavailability of experimental and theoretical results, though our findings are guidelines for future investigation.

**References:**

1. S. Hosokawa, H. Sinn, F. Hensel, A. Alatas, E. E. Alp, W.-C. Pilgrim, J. Non-Cryst. Solids, 2002, 312–314, 163.
2. A. B. Patel, PhD Thesis, Sardar Patel University, 2014.
3. A. B. Patel, N. K. Bhatt, B. Y. Thakore, A. R. Jani, AIP Conf. Proc., 2013, 1536, 589.
4. A. B. Patel, N. K. Bhatt, B. Y. Thakore, P. R. Vyas, A. R. Jani, Phys. Chem. Liquids, 2014, 52 471.
5. A. B. Patel, N. K. Bhatt, B. Y. Thakore, P. R. Vyas, A. R. Jani, Mol. Phys., 2014, 112, 2000.
6. A. B. Patel, N. K. Bhatt, B. Y. Thakore, P. R. Vyas, A. R. Jani, Eur. Phys. J. B., 2014, 87, 1.
7. S. Ichimaru, K. Utsumi, Phys. Rev. B., 1981, 24, 3220.
8. M. Hasegawa, K.Hoshino, M. Watabe, H. Young, J. Non-Cryst. Solids, 1990, 117/118, 300.
9. K. Hoshino, W. H. Young, J. Phys. F: Met. Phys, 1986, 16, 1659.
10. K. Hoshino, M. Silbert, A. Stafford, W. H. Young, J. Phys. F., 1987, 17, L49.
11. C. H. Patel, N. K. Bhatt, P. N. Gajjar, Proc. Natl. Conf. on "Recent adv. in materials Sci. & Tech.", Dec. 22-23, 2014, MLV Govt. College, Bhilwara, Rajasthan.
12. N. W. Ashcroft, D. C. Langreth, Phys Rev., 1967, 156, 685.
13. J. Hubbard, J. L. Beeby, J. Phys. C, 1969, 2, 556.
14. W.-C. Pilgrim, S. Hosokawa, H. Saggau, H. Sinn, E. Burkel, J. Non Cryst. Solids, 1999, 250–252, 96, and references therein.
15. S. Hosokawa, J. Greif, F. Demmel, W.-C. Pilgrim, Nucl. Instrum. and Meth. B, 2003, 199, 161.
16. L. E. Bove et al., Phys. Rev. Lett., 2001, 87, 215504.
17. T. Scopigno et al., J. Phys.: Condens. Matter, 2000, 12, 8009.
18. P. Haussler, Physics Reports, 1992, 222, 65.

# Kinetic studies of sorption of zinc ions onto activated carbon

Parth Joshi[*1], Desai Avani[2] and Desai Riddhi[2]

[1]*Department of Physics, Uka Tarsadia University, Bardoli, Gujarat-394350*
[2]*Department of Physics, Veer Narmad South Gujarat University, Surat-395007*

*E-mail: parth4570@gmail.com*

**Abstract**

Carbon in dense as well as porous solid form is used in a variety of applications. Activated porous carbons are made through pyrolysis and activation of carbonaceous natural as well as synthetic precursors. The use of low-cost activated carbon derived from sugarcane baggase, an agricultural waste material, has been investigated as a replacement for the current expensive methods of removing zinc ions from wastewater. With a view to find a suitable application of the material, activated carbon has been derived, characterized and utilized for the removal of zinc. The kinetics of adsorption depends on the adsorbate concentration and the physical and chemical characteristics of the adsorbent. Therefore, this study revealed that sugarcane baggase can serve as a good source of activated carbon with multiple and simultaneous metal ions removing potentials and may serve as a better replacement for commercial activated carbons in applications that warrant their use.

**Keywords:** Adsorption, activated carbon, zinc removal.

## 1. Introduction

In recent times, carbon has been one of the magnificent elements which have revolutionized materials science. Carbon provides materials with excellent properties for a large spectrum of industrial applications [1]. From carbon we obtain the strongest fibers (carbon fibers), one of the best solid lubricants (graphite), one of the best electrically conducting materials (graphite electrodes), the best structural material for high temperature tribological application (carbon–carbon composites), one of the best porous gas adsorbers (activated carbon), an essentially non-crystalline impermeable material (vitreous carbon), the hardest material (diamond), and now the most fascinating material, the fullerenes. All these forms are made by meticulously choosing the raw materials and processing conditions.

Porous carbons can be grouped into two categories: (i) Carbon foams with desired architecture of pores for structural and thermal applications; recently, these have been used as templates for making ceramics, (ii) activated carbons consisting of porous carbons with added active surface chemical groups. Porous carbons, especially activated porous carbons, constitute one of the most important types of industrial carbons and have been in use for thousands of years. Their use in water purification can be dated back to 2000 BC when ancient Egyptians used charcoal to purify water for medicinal purposes. It was during World War I that major developments in the use of porous carbons began and there was no going back afterwards. Newer and more modern technologies have since then developed both for the manufacturing and application of this versatile material [2]. Activated carbon fibers with very high surface area (around 2000 $m^2$/gm) have been the latest addition in the family of porous carbons [3]. These fibrous materials have widened the application potential to gas storage and energy areas. The term activated carbon defines a group of materials with highly developed internal surface area and porosity, and hence a large capacity for adsorbing chemicals from gases and liquids. Activated carbons are extremely versatile adsorbents of industrial significance and are used in a wide range of applications which are concerned principally with removal of undesired species by adsorption from liquids or gases, in order to effect purification or the recovery of chemical constituents. They also find use as catalysts or catalyst supports [4]. The strong market position held by the activated carbon adsorbents relates to their unique properties and low cost compared with that of possible competitive inorganic adsorbents like zeolite. Moreover, in porous carbons a broad distribution in pore size and shape is usually obtained in sharp contrast to almost constant pore size in zeolite. This makes activated carbons more versatile adsorbing materials. Porous adsorbing carbons are associated with new processes for development of these materials, mechanisms, material characterization and newer application. More than 30% of the carbon research world over revolves around activated carbons; newer precursors, methods of activation and applications.

Zinc is one of the heavy metals considered toxic to plants, invertebrates and even vertebrate fish. Though zinc is useful to man but excess amount of zinc ions in waste waters may cause zinc toxicity which could lead to severe hemolytic anemia, liver and kidney damages; vomiting and diarrhea [5]. Zinc oxide is widely used as a white pigment in paints, and as a catalyst in the manufacture of rubber [6]. High release of zinc ions into the

environment is also toxic to agricultural activities, sediment entrainment and groundwater. As a result of this inevitable development due to industrial discharge, a few techniques for the removal of these heavy metals (lead, zinc, zinc, nickel, chromium, mercury, cadmium, aluminum, manganese and cobalt) were introduced by concerned researchers for the removal of these heavy metals from untreated water. These methods are reverse osmosis, ultra filtration, nano-filtration, coagulation, sedimentation, adsorption, etc. Though, it was discovered that these methods have been proved to have a lot of disadvantages which includes cost of operation and production of post sludge. Among the aforementioned treatment methods, adsorption had been reported as an efficient and economic option [7,8] especially when the source of adsorbent is economical. Adsorption is one of the cheap and most effective methods in water purification and activated carbon is preferred adsorbent that is wildly used to treat waste water containing different classes or types of metal ions. Activated carbon has the tendency of adsorbing large and small dissolved organic molecules such as gases, chemicals and metal ions.

Therefore the objectives of these work is to study the kinetics of the removal of zinc ions using activated carbon from Sugarcane baggase.

## 2. Processing of activated carbon

Activated carbons are manufactured by the pyrolysis of carbonaceous materials of vegetable origin, such as Sugarcane baggase, White straw, wood, coal, peat, fruit stones, and shells or synthetic polymers such as viscose rayon, polyacrylonitrile (PAN) or phenolics followed by activation of the chars obtained from them. m. The pyrolysis of any carbonaceous material in absence of air involves decomposition of organic molecules, evolution of tarry and gaseous products, and finally in a solid porous carbon mass. The porous carbons so obtained contain predominantly macropores and practically inactive materials with specific surface area of the order of several square meters per gram. An adsorbent with a highly developed porosity and a correspondingly large surface area is obtained only by activating the carbonized material either by physical or chemical activation. The processing of activated carbon basically involves selection of raw material, carbonization and activation.

### 2.1 Raw materials

Sugarcane baggase (SB), a by-product procured from a local sugar processing factory was the precursor used in this study. The collected sample was washed exhaustively with deionized

water to remove adhering dirt particles from the surface. Dried SB was cut, ground and screened to the desired mesh size of 1–2 mm.

## 2.2 Activation

The raw material produced was mixed in potassium hydroxide solution with a raw material (SB)/KOH impregnation with occasional stirring. After stirring the resultant sample was dried at room temperature for 12 hour and then the resultant sample was dried at $120^{o}$C for 24 hour.

After it the sample was again dried for 6 hour and weight loss measured at every half hour. The resultant sample was washed with hot and cold distilled water until the filtrate reached to neutral pH.

## 2.3 Carbonization

The carbonization process was performed by loading 90 gm of dried KOH activated sample into a furnace, and heated up to a carbonization temperature of $700^{o}$ C under purified $N_2$ flow and after carbonization 20 gm of activated carbon produced.

## 3. Results and Discussion

### 3.1 Effect of HA dosage

The adsorption capacity of zinc ions on HA was studied by changing the quantity of adsorbent keeping the initial zinc ions concentration (100 mg/l), temperature and pH constant. The  adsorption of zinc ions onto HA included two steps-a fast initial adsorption followed by a much slower gradual adsorption. The adsorption capacity increased sharply in the first 10 min and then increased slowly. The adsorption equilibrium was reached with a solution contact time of less than 3 h. Thus the time of 3 h was considered sufficient for the significant removal of zinc ions and was therefore used for all the further experiments.

### 3.2 Adsorption kinetics

Kinetics of adsorption describes speeds of reactions that permit to determine the contact time under agitation put to reach the adsorption equilibrium. In order to determine the adsorption kinetics of zinc ions on HA, pseudo-first-order and pseudo-second order kinetic models were applied to the experimental data.  Fig. 1 shows the linear plot of log $(q_e\text{-}q_t)$ versus t. Fig. 2 showed the linear plot of $t/q_t$ versus t.

Correlation coefficients of second-order equation for all HA dosage was higher than the first-order equation and its calculated equilibrium adsorption capacities, $q_{e2}$, fitted well the

experimental data. These suggest that the pseudo second-order adsorption mechanism is predominant and that the overall rate of the metal ions adsorption process appear to be controlled by the chemical process.  For the both pseudo equation, the rate constants increases with an increasing of initial HA dosage.
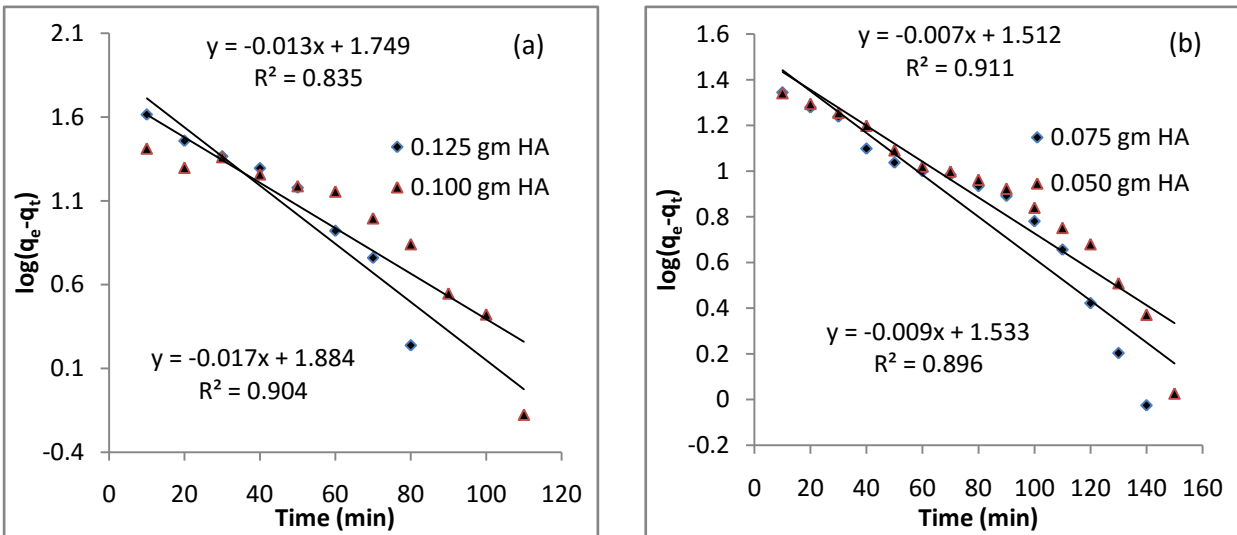


Figure 1. Adsorption kinetics of zinc ions by activated carbon by pseudo-first order.
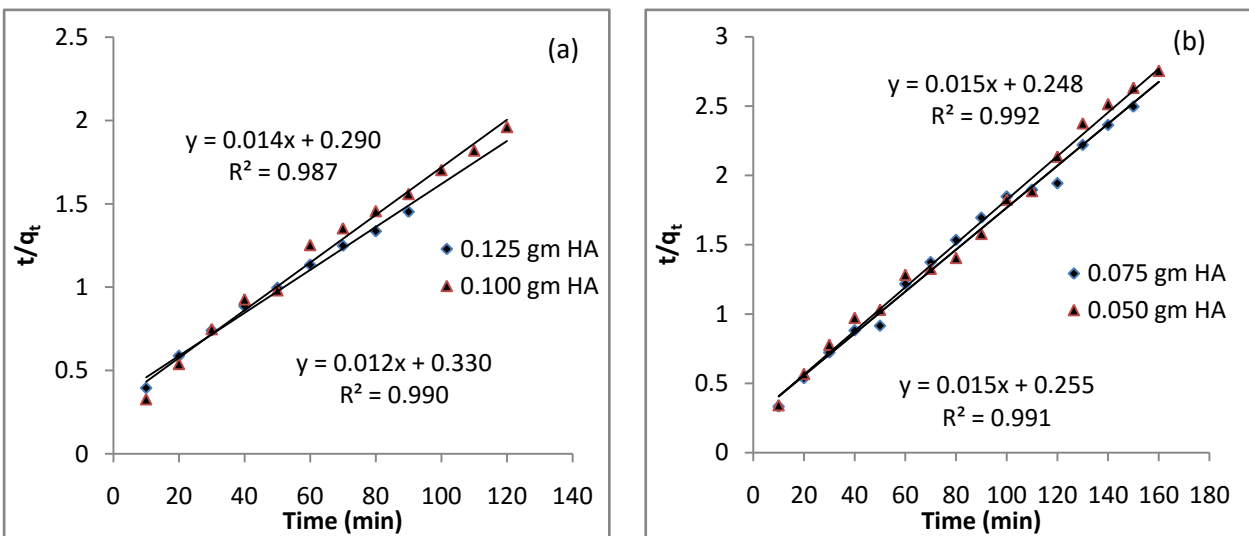


Figure 2. Adsorption kinetics of zinc ions by activated carbon by pseudo-second order.

Also, based on the comparison between experimental and theoretically calculated $q_e$ values, it was found that the pseudo second-order model fitted better than pseudo first order

model for removal of zinc ions. This model is more likely to predict the kinetic behavior of adsorption with chemical reaction being the rate-controlling step and it provides best correlation to describe chemical adsorption process between the adsorbent and adsorbate. This suggests that the rate-limiting step of this adsorption system may be chemical adsorption or chemisorption involved valence forces through sharing or exchange of electrons between adsorbent and adsorbate.

### 3.3 Effect of temperature

The temperature has two major effects on the adsorption process. Increasing the temperature is known to increase the rate of diffusion of the adsorbed molecules across the external boundary layer and the internal pores of the adsorbent particles, owing to the decrease in the viscosity of the solution. The removal of zinc ions increases from 23.51 mg/g to 42.12 mg/g by increasing the temperature of the solution from 283K to 323K, indicating that the process to be endothermic. This kind of temperature dependence of the amount of the zinc ions adsorbed may be due to the fact that a possible mechanism of interaction is the reaction between the zinc ions and the cationic sites of HA such a reaction could be favored at higher temperatures.

### 3.4    Thermodynamics study



$$y = -94.27x + 13129$$
$$R^2 = 0.986$$
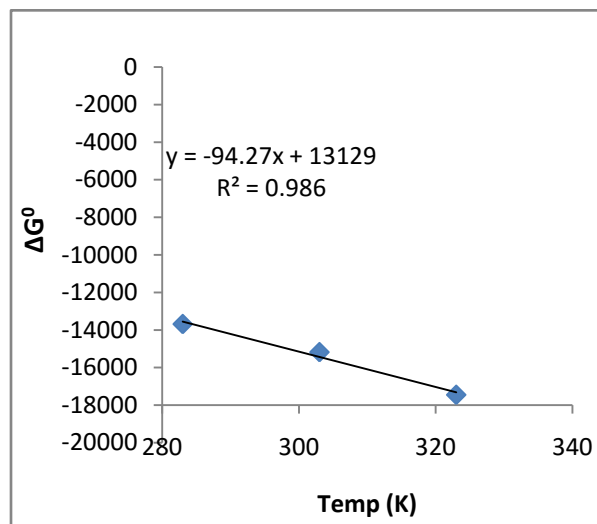
Fig. 3 - Enthalpy and Entropy determination curve for the adsorption of zinc ions using activated carbon.

The Gibbs free energy change ($\Delta G°$) is negative as expected for a spontaneous process under the ambient condition. The negative $\Delta G°$ values indicated that the adsorption of zinc ions

onto activated carbon was thermodynamically feasible and spontaneous. The enthalpy ($\Delta H°$) and entropy ($\Delta S°$) changes were determined as 13129 J/mol and 94.27 J/mol K, respectively, from $\Delta G°$ versus Temperature (K) plot as shown in Fig. 3. The positive value of $\Delta H°$ confirmed the endothermic character of the adsorption process. The positive values of $\Delta S°$ also revealed the increase of randomness at the solid‑solute interface during the adsorption of zinc ions onto activated carbon. The low value of $\Delta S°$ indicated that no remarkable change on entropy occurs. The positive value of entropy change ($\Delta S°$) reflects the affinity of activated carbon toward zinc ions in aqueous solutions and may suggest some structure changes in the adsorbents. A positive entropy change for adsorption of metal ions on activated carbon is due to the fixation of ions on the exchange sites of the randomly distributed surfactant species.

## 4. Conclusion

The result show that activated carbon , is a good adsorbent for zinc ions and therefore can be potential candidate for removal of zinc ions from wastewater.  The adsorption of zinc ions is found to increase significantly with the increase in temperature and dosage of the activated carbon. The thermodynamics of the system pointed out the system was spontaneous and endothermic. The adsorption process is found to be of second order with the surface diffusion as one of the rate determining steps. The present study concludes that the activated carbon could be employed as an efficient adsorbent to remove the zinc ions from wastewater.

## References

1) T. Burchell, In Carbon materials for advanced technologies (ed.), 1999, 95.

2) Derbyshier F, Porosity in carbons "Characterization and applications" (ed.),1995, 227.

3) Suzuki M., Active carbon fibre: fundamentals and applications. Carbon, 1994, 32, 577.

4) Patrick J W., Porosity in carbons, Characterisation and application, 1994, 124.

5) A .Muataz, 2nd International Conference on Environment Science and Technology Singapore, 2011.

6) M . Sekar, V . Sakthi, and S. Rengaraj, Journal. Colloid Interface Science, 2004,279, 307.

7) A. H. Mahvi, International Journal Environment Science Technology, 2008, 5 ,275.

8) M . Malakootian, J. Nouri, and H. Hossiani, Journal Environment Science Technology, 2009,6, 183.

9) S. Babel, T., Kurniawan, Journal of hazardous materials,2002, 219.

10) I.N. Jha, L. Iyengar, A.V.S.P. Rao, J. Environ. Eng., 1988, 114, 962.

11) J.-W. Shim, S.-J. Park, S.-K. Ryu, Carbon, 2001, 39, 1635.

12) S.K. Srivastava, V.K. Gupta, D. Mohan, J. Environ. Eng., 1997, 123 ,461.

13) Rodriguez R., Chemistry and physics of carbon (ed.) P A Thrower, 21, 1, 1995.

14) F. Ferrero, M.P.G. Prati, Annali di Chimica, 1986, 86, 125.

15) M.C. Sekhar, B. Chakravarthy, J. Indian Water Works Assoc. XXXII , 2000,4 ,305.

# Study of Atomic Force Microscopy On Tungsten Diselenide Single Crystals Doped By Copper

M. N. Parmar

Department of Physics, The H. N. S. B. Ltd. Science College, Himatnagar, Gujarat

*Corresponding author Email: manoj.5870@gmail.com

**Abstract**

Tungsten diselenide is a diamagnetic semiconductor which belongs to the family of group VI B layer type transition metal dichalcogenides. The material exhibits extreme anisotropy in electrical optical and mechanical properties along and perpendicular to vander waal planes. This paper deals with copper doping in tungsten diselenide single crystals by vapour phase technique. AFM are measured on $Cu_xWSe_2$ ( x= 0, 0.5, 1.0 ) single crystals. The results thus obtained from above measurements are discussed below in this paper.

Key Words :Crystal Growth ,Vapour phase technique, AFM

**Introduction**

The transition metal disulphides and diselenides have attracted considerable attention during the past few years [1,2]. These $MX_2$ (M = transition metal; X = Chalcogen) compounds are formed by a layer of transition metal atoms between two layers of sulphur or selenium atoms. There is a strong covalent bonding within the layers, but a weak van der Waals bonding between them. These materials are used in such diverse applications as catalysis [3], batteries [4] and lubricants [5]. Recently, these materials have found potential use in the fabrication of photoelectrochemical (PEC) solar cell for solar energy conversion. It has also been realized that selenides are more efficient as solar cell materials than sulphides[6]. In light of this realization, the growth of tungsten diselenide single crystals and its doped compounds using vapour transport technique have attracted more attention recently. This paper mainly focuses on Atomic Force Microscope(AFM) by taking real and fourier transform images of $Cu_xWSe_2$(x = 0, 0.5, 1.0) single crystals.

**Experimental Procedure:**

Scanning probe microscope (SPM) consists of family of microscopy where a sharp probe is scanned across a surface and some tip- sample interactions are monitored.

SPM consist of many forms like scanning tunneling microscope (STM), Atomic Force Microscope (AFM), magnetic force microscope (MFM), Electric force microscope (EFM) etc. AFM is one type of scanning probe microscope and also known as nanoscope. It has ability to create three dimensional micrograph of sample surface with resolution down to the nano-meter and angstrom scale. These are also capable of measuring or imaging force between tip and sample surface like van der Waal's force with resolution in the range of few nano-Newtons.

AFM operates in three modes.

1. Contact mode AFM.
2. Tapping mode AFM.
3. Non contact mode AFM.

AFM consists of microscope force sensor that responds to a force and a detector that measure the sensor's response. In the AFM, sensor is a cantilever with an effective spring constant k. At the end of the lever, is a sharp tip which is used to sense the force between the tip and sample. Lever deflects in accordance with the force acting on the tip. Detector measures the

deflection of the lever. In AFM we use the laser feedback detection system which can then be used to determine the force on the tip by using Hooke's law F= k z, where z is cantilever displacement. If the sample is scanned under the tip, force between tip and sample surface and image of the sample surface are generated. By scanning the AFM cantilever over a sample surface and recording the deflection of the cantilever the local height of the sample is measured, three dimensional topographical maps of the surface are then constructed by plotting the local sample height versus horizontal probe tip position. Several forces typically contribute to the deflection of an AFM cantilever which are intermolecular microscopic forces.

**Main components of AFM instrument:**
The various component of AFM are Scanning probe microscope (SPM), controller, computer, display monitor and control monitor. The main component of the system is scanning probe microscope (SPM). The main parts of the SPM are SPM head, scanner, cantilever, tip, control and feedback system.

**SPM head:**
It contains photodetector system, cantilever and tip. There are many types of detection systems like tunneling detection system, capacitance detection system, laser diode photo detection system etc. In AFM laser diode photo detection system is normally being used. In this a laser light is being used because it is highly coherent and the spot size is also short. Laser light is focused on the cantilever supporting the force-sensing tip. And it is reflected back to photodiode. If cantilever deflect with an angle then laser light reflect with twice the angle. In this system a four photodiode system is used and is known as quad photodiode.
The four elements of the quad photodiode are combined to provide the different information depending on the operation mode. At starting the cantilever is fixed at a constant deflection i.e., set point. And set the laser light with cantilever that after reflection laser light makes spot at the center of the quad photodiode. Then all photodiodes collect equal light and give it current that is same. When tip is deflected the laser light also shows the deflection on the photodiode. These minute deflections of the lever cause the photo detector to collect more light to other one. And this current fed to substractor and the output of this substractor is proportional to the deflection of the lever. This is used to image the force across the sample and maintained set point.

**Cantilever :**
Cantilever is a beam that is supported at one end and other end is free to move. In AFM force sensing tip is mounted at the free end of the lever. AFM cantilever is flexible beam whose geometrical and material property plays an important role in determining the sensitivity and resolution of AFM. In contact AFM mode cantilever's flexibility acts as a nanometeric spring allowing the tip to measure the surface force. For contact mode AFM imaging, it is necessary to have a cantilever which is soft enough to be deflected by very small forces (k is small) and has a high enough resonant frequency to not be susceptible to vibration instabilities. This is accomplished by making the cantilever short, to provide a high resonant frequency and thin to provide a small force constant. The silicon nitride tip and cantilever is being used normally. This tips exhibit excellent flexibility. For the typical silicon nitride tips, the value of spring constant k is 0.58, 0.32, 0.12 or 0.06 N/m depend upon geometry of cantilever. Cantilever lengths 100 to 200μm and tip radius of curvature is 20 – 60 nm. In tapping mode the cantilever is oscillating up and down at its resonance frequency while its amplitudes are monitored. In the tapping mode we use much stiffer crystal silicon probe which is oscillated to its resonance frequency, because tip describes a high frequency oscillating arc (100 kHz)

and larger force constant. It possesses sufficient energy to break free of surface tension force. This is also non-conducting material. The probe is considerably stiffer than silicon nitride making it more brittle and less forgiving .The tip and cantilever are an integrated assembly of single crystal silicon, produced by etching techniques. For typical single crystal silicon probes, spring constant k = 20 –100 N/m, resonant frequency 200 –400 kHz, tip radius of curvature 5 -10 nm and cantilever length is about 125μm.

**Scanner :**

In AFM scanner is used for movement of sample or tip. These scanners are made from piezo electric material (example ceramic polycrystalline material ) which expands and contracts proportionally to an applied voltage. Piezomaterial expands or contract depends upon the polarity of the voltage applied. Scanners are of many sizes and each scanner exhibits its own unique properties. In AFM a scanner tube is being used, which is constructed by combining independently, operated piezoelectrodes for x, y and z direction, which can manipulate sample and probes with extreme precision in three dimensions.

**Feedback loop :**

To produce images the SPM must be capable of controlling the tip sample interaction with the great precision with the use of feedback loop which safeguards tip and sample by keeping force between them at a user specified set point level. Set point refers to how much tip sample force is to be maintained which means that how much force can be applied on the tip which is just enough to trace the surface features and not so much that the tip is broken off or sample is damaged. In contact AFM mode the deflection of the cantilever, the tip's height above the surface can be precisely maintained. To control this we adjust various gains in the SPM feed back circuit. The main gains are:

Proportional gain   : Amount of correction applied in response to the error signal between set point force and actual force measured by the detection in direct proportion to the error.

Integral gain : Amount of correction applied in response to the average error between set point force and actual force measured by the detector.

Look ahead gain  : Amount of correction applied in response to the error signal between set point force and actual force measured by the detector based upon recorded information the adjacent scan line. Computer works as a controller of feed back loop. Atomic Force Microscope - Nanoscope is shown in Fig. 1



**Fig.1   Atomic Force Microscope (AFM) – Nanoscope**

## Results and Discussion

Surface morphological studies on single crystals of CuxWSe2 (x = 0, 0.5, 1.0) are carried out by above described Atomic Force Microscope ( in contact mode ) using silicon nitride tip. With the help of Nanoscope control software package, various section analysis like periodicity along specific direction, fourier transform of images are studied.

Fig.2 for WSe2 crystal shows the periodicity along any specific direction and the image clearly shows that atoms in the lattice are arranged in a regular fashion. The measured horizontal distance is 0.321nm and this value between any two consecutive atoms is maintained throughout.
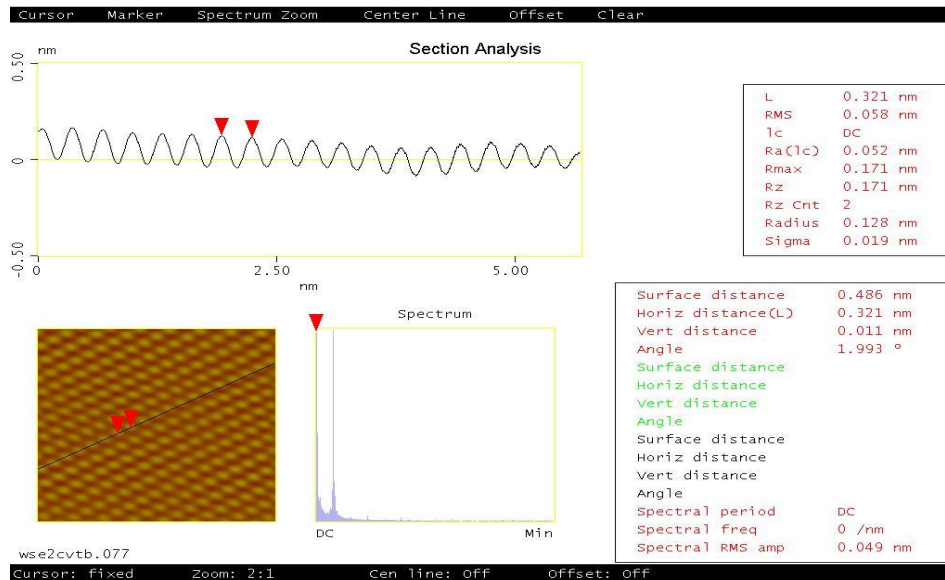


**Fig.2 Section analysis( periodicity) for WSe2 single crystal**

Fig.3 shows layers on the surface of WSe2 in a scanning region of 2.00μm with scan rate 10.17Hz. The depth profiling on the surface shows that layers are nearly separated by 20nm distance from each other.
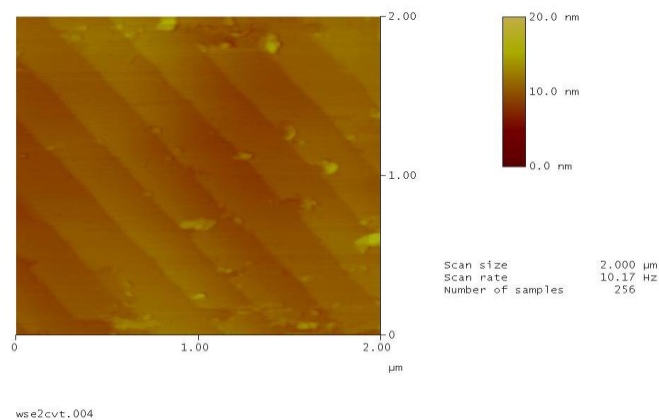


**Fig.3      Shows layers of WSe2 single crystal separated by 20nm distance.**

Fig.4 which is again a section analysis for periodicity and it clearly indicates that atoms are arranged in similar fashion as it was observed in  Fig.2. But the scanned region in this image is different then the previous image which means that crystal are possessing good periodicity in different region as well.
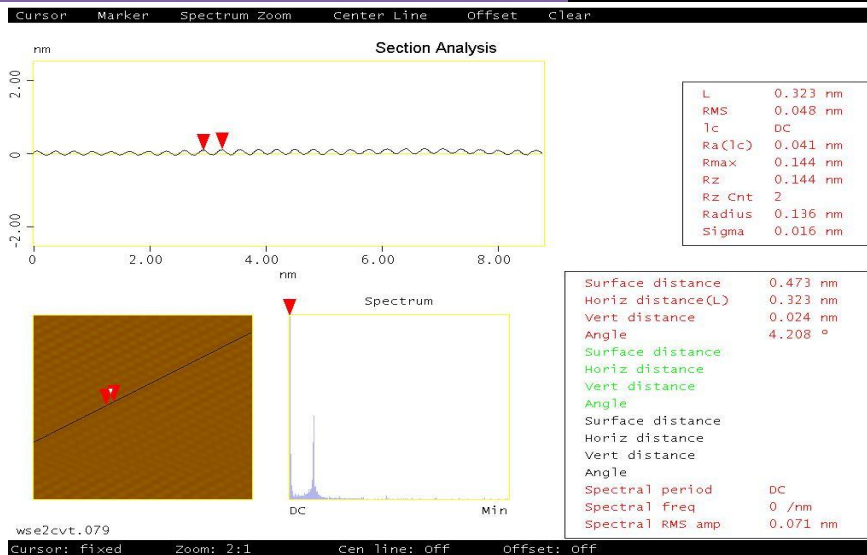
**Fig. 4 Section analysis( periodicity) from different region for WSe2 single crystal.**

Fig.5 and Fig.6 are three dimensional view of previous images for WSe2 single crystal showing periodicity at atomic level.
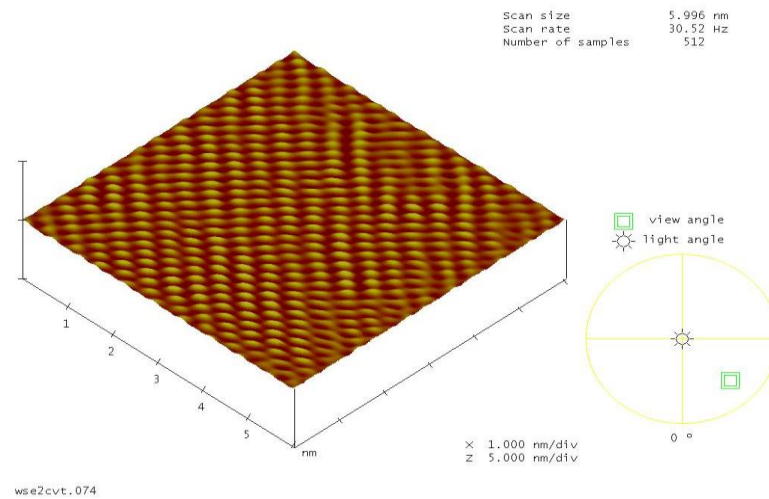


**Fig. 5 Three dimensional photograph for WSe2 single crystal**
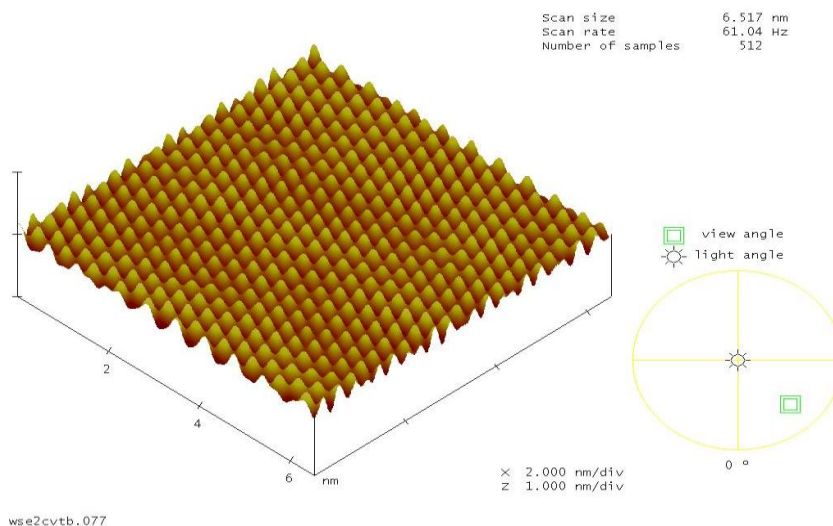


**Fig.6 Another view of three dimensional photograph for WSe2 single crystal**

Fig.7 is a section analysis (angle) of Fig.4 which shows pattern of hexagons in the figure. Now, if we measure the internal angle of hexagon it comes about 124.700 as it is well known that the internal angle of perfect hexagon is 1200 i.e. it represents perfect hexagonal shape at atomic level. Similar kind of pattern is obtained on MoS2 crystal using AFM by M. Remskar et al [7].
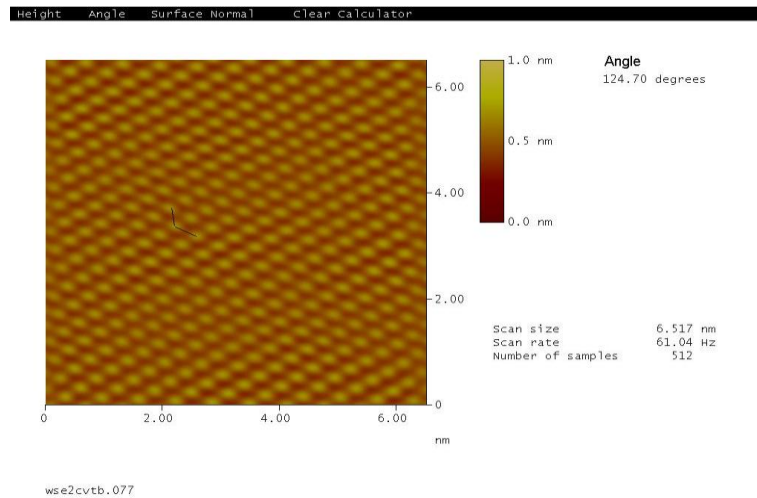


**Fig. 7 Section analysis (angle) for WSe2 single crystal**

Parallel kinds of studies are carried out on Cu0.5WSe2 and Cu1.0WSe2 single crystal and are discussed below.

Now Fig.8 is a section analysis of 2-D topograph of copper doped WSe2 single crystal and from the graph in the inset it is clear that atoms are arranged in periodic manner in all direction. The measurements are taken along one specific direction which shows that horizontal distance between two points is 0.321nm and that is maintained throughout the specific direction.
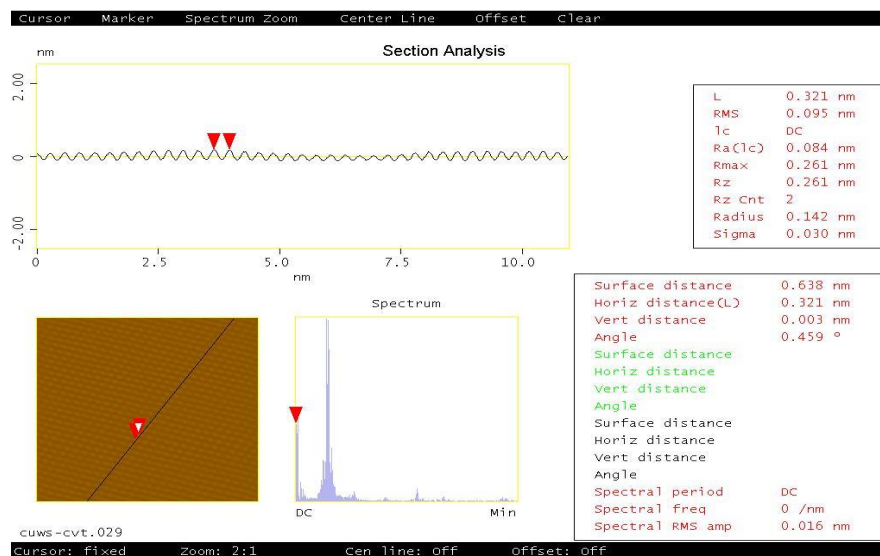


**Fig.8 Section analysis ( periodicity) for copper doped WSe2 single crystal.**

Fig.9 shows section analysis (angle) of copper doped WSe2 single crystal and shows that internal angle of hexagon is 123.21A0.
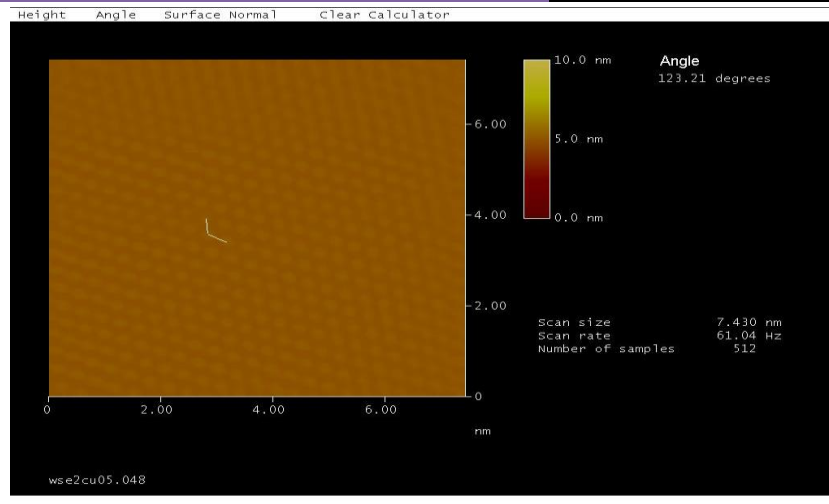
**Fig. 9 Section analysis (angle) for copper doped WSe2 single crystal**

### Conclusion

AFM pictures taken on these samples clearly reflects the periodicity in arrangement of atoms which  is very well maintained  throughout the material and also the internal angle obtained matches to that of on hexagon.

### Acknowledgment

### References:

[1]  J Legma, G Vacquier, Mater.Sci.Engg.,B8 (1991)167.

[2]  S. G. Patel Cryst. Res. Technol., 27 (1992)285.

[3]  R. R. Chianelli Catal.Rev.-Sci. Eng., 26 (1984) 361.

[4]  J Bouxel and R Brech Rev. Mater. Sci., 16 (1986) 137.

[5]  J.Lince and P Fleischauer J. Mater. Res., 2 (1987)827.

[6]  H. Tributsch J. Appl. Phys., 23 (1980)61.

[7]  M. Remskar, Z. Skraba, C. Ballif, R. Sanjines, F. Levy
     Surface Science, 433-435 ( 1999 ) 637-641.

# Sorption study of cadmium ion using activated carbon

Parth Joshi*[1], Desai Riddhi[2] and Desai Avani[2]

[1]*Department of Physics, Uka Tarsadia University, Bardoli, Gujarat-394350*
[2]*Department of Physics, Veer Narmad South Gujarat University, Surat-395007*
*E-mail: parth4570@gmail.com*

## Abstract

Carbon in dense as well as porous solid form is used in a variety of applications. Activated porous carbons are made through pyrolysis and activation of carbonaceous natural as well as synthetic precursors. The use of low-cost activated carbon derived from baggase, an agricultural waste material, has been investigated as a replacement for the current expensive methods of removing heavy metals from wastewater. With a view to find a suitable application of the material, activated carbon has been derived, characterized and utilized for the removal of cadmium and. The uptake of cadmium was found to be slightly greater and the sorption capacity increases with increase in temperature. The adsorption of cadmium ions on activated carbon prepared from Sugarcane Baggase obtained from local sugar industry was carbonized and chemically activated using potassium hydroxide solutions as activating reagents. Studies were conducted to delineate the effect of pH and initial metal ions concentration,. On the basis of these studies, various parameters were evaluated to establish the mechanisms. Therefore sugarcane baggase can serve as a good source of activated carbon with multiple metal-ions removing potential.

**Keywords:** Adsorption, Activated carbon, Baggase.

## 1. Introduction

 Heavy metals are toxic to aquatic flora and fauna even in relatively low concentrations. Some of these are capable of being assimilated, stored and concentrated by organisms. Cadmium is accumulated in the human body, causing erothrocyte destruction, nausea, salivation, diarrhea and muscular cramps, renal degradation, chronic pulmonary problems and skeletal deformity[1]. Heavy metals are present in the soil, natural water and air in various forms and may become contaminates in food and drinking water [2]. Some of them are constituents of herbicides, pesticides, paints and fertilizers applications. Hazards associated with the contamination of water have led to the

development of various technologies for water purification namely filtration and ion exchange, precipitation with carbonate or hydroxide [3]. Several treatment technologies exist for metal removal, but the process of adsorption using of activated carbon has been found to be an efficient technology for decolorization of west material.

In recent times, carbon has been one of the magnificent elements which have revolutionized materials science. Carbon provides materials with excellent properties for a large spectrum of industrial applications [4]. The term activated carbon define a group of materials with highly developed internal surface area and porosity, and hence a large capacity for adsorbing chemicals from gases and liquids. Activated carbons are extremely versatile adsorbents of industrial significance and are used in a wide range of applications which are concerned principally with removal of undesired species by adsorption from liquids or gases, in order to effect purification or the recovery of chemical constituents. They also find use as catalysts or catalyst supports [5]. The strong market position held by the activated carbon adsorbents relates to their unique properties and low cost compared with that of possible competitive inorganic adsorbents like zeolites. Moreover, in porous carbons a broad distribution in pore size and shape is usually obtained in sharp contrast to almost constant pore size in zeolite. This makes activated carbons more versatile adsorbing materials.

Heavy metals are non-biodegradable and they tend to accumulate in living organisms, causing various diseases and disorder. Cadmium causes serious renal damage, anemia and hypertension. Cadmium occurs naturally in the environment and the main anthropogenic pathway through which cadmium enters environment is through waste from industrial processes such as electroplating, smelting, alloy manufacturing, cadmium-nickel batteries, pesticides, mining, fertilizers, textile operations and refining [6].

In the last two decades, extensive studies have been made on the selection and pyrolysis behavior of new synthetic precursors to develop active carbons with very high adsorption capacitiesandcontrolledporesizedistributionsforspecificenergyapplications.Theseprecursors are polymer-based fibrous materials. The examples are viscose rayon, polyacrylonitrile, saran, phenolic, PFA [7-9].

During carbonization, most of the non-carbon elements, hydrogen and oxygen are first removed in gaseous form by pyrolytic decomposition of the starting materials, and the free atoms of elementary carbon are grouped into organized crystallographic formations known as elementary graphite

crystallites. The mutual arrangement of the crystallite is irregular, so that free interstices exist between them. Thus carbonization involves thermal decomposition of carbonaceous material, eliminating non-carbon species producing a fixed carbon mass and rudimentary pore structure [10]. The process is usually carried out at temperature below 800˚C in a continuous stream of an inert atmosphere. The important parameters that determine the quality and the yield of the carbonized product are: (i) rate of heating, (ii) final temperature and (iii) soaking time. The carbonization process involves various important stages that markedly determine the properties of the final product to be obtained. The basic microstructure of the char with micro porosity is formed around 500˚C. Some of these pores are blocked by the tarry products evolved during pyrolysis and could be available only when further heat treatment to about 800˚C is given. Further heat treatment to temperature of 1000˚C and above normally lead to hardening of the carbon structure due to partial alignment of graphitic planes and decrease in porosity which deaccelerate.

For quite some time we are involved in developing some low-cost activated carbons/adsorbents for the removal and recovery of organics/metal ions from wastewater. Continuing our activities in this direction, we have derived a new low-cost activated carbon from baggase (an agricultural waste material) for the removal of cadmium from synthetic wastewater in systems successfully.

## 2. Preparation of activated carbon

### 2.1 Raw materials

Sugarcane baggase were bought in large quantity from local sugar factory, Bardoli. The Sugarcane baggase were transported to the laboratory for immediate use. The Sugarcane baggase were sorted out and which were thoroughly washed with water to remove dirt/ unwanted parts and dried very well in an oven at 100˚C for one hour.

### 2.2 Activation

The raw material produced was mixed in potassium hydroxide solution with a raw material (SB)/KOH impregnation with occasional stirring. After stirring the resultant sample was dried at room temperature for 12 hours and then the resultant sample was dried at $120^{\circ}$C for 24 housr. After it the sample was again dried for 6 hours and weight loss measured at every half hour. The resultant sample was washed with hot and cold distilled water until the filtrate reached to neutral pH.

## 2.3 Carbonization

The carbonization process was performed by loading 90 gm of dried KOH activated sample into a furnace, and heated up to a carbonization temperature of $700^{°}$ C under purified $N_2$ flow and after carbonization 20 gm of activated carbon produced.

## 3. Results and Discussion

## 3.1 Effect of cadmium ions concentration

The adsorption of cadmium ions was carried out at different initial concentrations ranging from 50 to 150 mg/l, at pH 7. A higher initial concentration provides an important driving force to overcome all mass transfer resistances of the cadmium ions between the aqueous and solid phases, thus increases the uptake of metal ions.

The results show that removal of cadmium ions from solution by activated carbon was found to be dependent on the initial concentration of metal ions. The amount of adsorbed metal ions increased with an increase in initial concentration. At low concentrations the available surface for adsorbate is sufficient so the removal becomes independent of initial concentrations. However, in the case of higher concentrations of adsorbate, available adsorption sites are occupied by the adsorbate and the removal depends upon the initial concentrations.

## 3.2 Adsorption isotherms

The linearized Langmuir and Freundlich adsorption isotherms of cadmium ions obtained at the cadmium ions concentration of 50 to 150 mg/l are shown in **fig 3.1(a) & fig 3.1(b)**. An adsorption isotherm is characterized by certain constants, values of which express the surface properties and affinity of the adsorbent and can also be used to find the adsorption capacity of adsorbent.

As seen in figure, the values of $R^2$ indicate that the adsorption pattern for cadmium ions by HA followed both Freundlich isotherm ($R^2 > 0.852$) and Langmuir isotherm ($R^2 > 0.987$). It is clear that the Langmuir isotherm better fitted for the adsorption of cadmium ions by activated carbon. Results indicate that the capacity of activated carbon for adsorption of cadmium ions is increased with increase in concentration which is typical for adsorption of most metal ions from their solution.
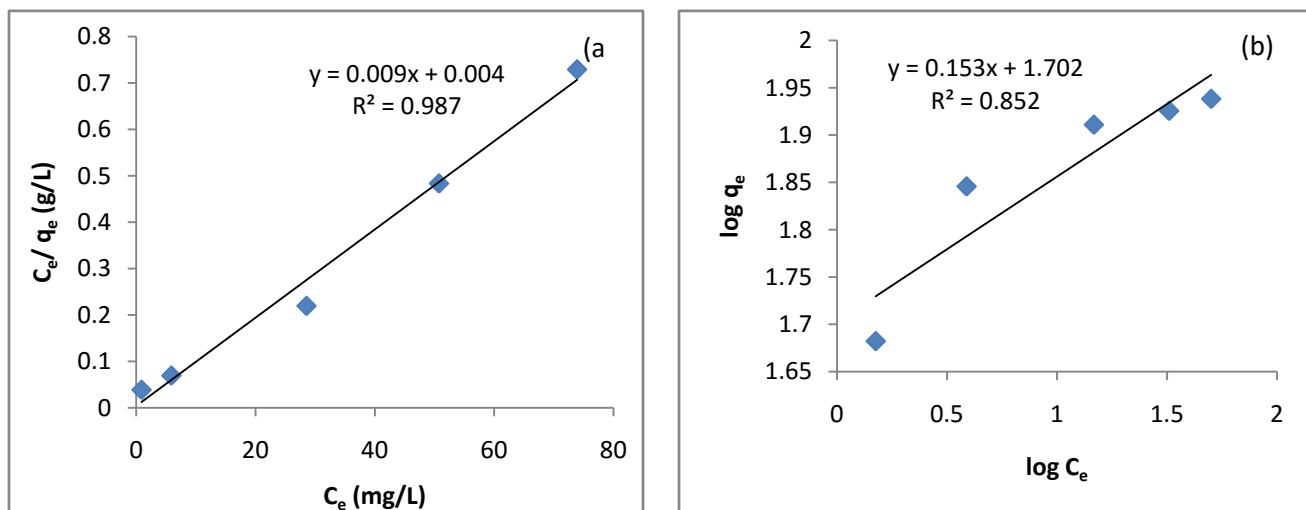
**Figure 3.1.** Isotherm plot of cadmium ions adsorbed on activated carbon powders according to (a) Langmuir adsorption model and (b) Freundlich adsorption model.

## 3.3 Effect of pH

pH of aqueous solution is an important controlling parameter for cadmium ions adsorption process and thus role of hydrogen ion concentration was examined from solutions at different pH values from 5 to 7. A neutral pH range was chosen because an optimum metal ions uptake could be attained without precipitation of the metal ions. The maximum uptake level of cadmium ions was observed at pH 7. It was observed from **figure 3.2**, that the percentage of adsorption of cadmium ions increased with an increase in pH of the solution.
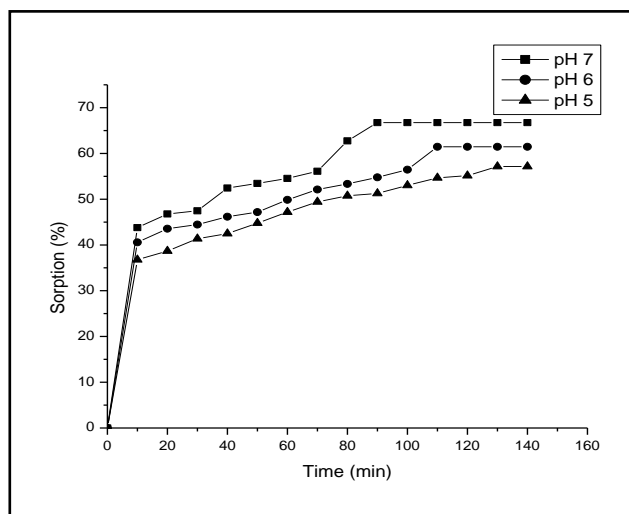


**Figure 3.2.** Adsorption studies of cadmium ions using different pH of initial solution.

## 4. Conclusion

Adsorption of cadmium ions on activated carbon achieves equilibration quickly. Adsorption of cadmium ions on activated carbon is strongly dependent on pH values. The adsorption increases with increasing pH values. The adsorption isotherms of cadmium ions on HA can be described well by the Langmuir model. The results support reported two-step mechanism involved in the removal of cadmium ions by activated carbon. Activated carbon can effectively remove cadmium ions in aqueous solution under different experimental conditions and show potential application prospect.

## Reference

1.  D. Mohan, K. singh, water research 2002, 36,1.
2.  D.N.Olowoyo, A.O.Garuba, Global Advanced Research journal food science technology(ed.),2012,1.
3.  T. Burchell, In Carbon materials for advanced technologies (ed.), 1999, 95.
4.  Jin H et al,  The shape selectivity of activated carbon fibres on a palladium support. Carbon, 1996 39, 421.
5.  Patrick J W , Porosity in carbons, Characterisation and applications,1995.
6.  I. Mochida, K. Kuroda, S. Miyamoto, C. Sotowa, Y. Korai, S. Kawano, K. Sakanishi, A. Yasutake, and M. Yoshikawa ,E*nergy Fuels*, 1997, 11 , 272.
7.  C.W. Cheung, J.F.  Poter, G.  McKay, Elovich. J. Chem. Technol. Biotechnol., 2000, 75, 963.
8.  J .Wu, J. Lu, T.H. Chen, Z. He, Y. Su, X.Y. Yao,  Environ. Earth Sci. 2010, 60, 421.
9.  M. Inagaki , New carbons: control of structure & functions , 2000,126.
10. T . Mays, Active carbon fibres. In Carbon materials for advanced technologies (ed.) 199, 95.

# Tailoring of Cu crystal phase withnon-face centred cubic phase: the tetragonal phase

Ghanshyam R. Patel[1*], Tushar C. Pandya[2], Ashok N. Patel[3] and Rajkumar G. Patel[4]

[1]Physics Department, Government Science College, Gandhinagar, Gujarat, India.

[2]Physics Department, St.Xavier's College, Navrangpura, Ahmedabad, Gujarat, India.

[3]Physics Department, M.N.Science College, Patan Gujarat, India.

[4]Electrical Engineering Department, Nirma Institute of Technology, Gujarat, India.

[*]Email:grpalp94@gmail.com

**Abstract**: Crystallization of noble metal atoms usually leads to the highly symmetric face-centered cubic phase that represents the thermodynamically stable structure. In the present work we have made an effort to tailor the crystal structure of non –face-centered cubic phase of Cu with the help of DFT using quantum espresso code. We have reported stable tetragonal crystal structures having three and four number of atoms per unit cells. We report the formation of nano wire having triangular and square cross section.

## Introduction

Nanowires are very important for studying for nanotechnology applications as well as nano science. In comparison to other low dimensional systems nano wires, have two quantum confined directions, while one direction is unconfined for electrical conduction. Hence nano wires are used in applications where electrical conduction, rather than tunnelling transport, is required [1]. Due to their distinctive density of electronic states, nano wires in the limit of small diameters are expected to exhibit significantly different optical, electrical and magnetic properties from their bulk crystalline counterparts. Nano wire is having enhanced surface to volume ratio, very high density of electronic states, size-dependent band gap, and increased surface scattering for electrons and phonons compared to their bulk counterpart. Due to their potential application in various field in the recent years, nano wires and nano rods of metallic and semi-conducting materials have drawn a lot of research interest.

Metallic nanoparticles with tuneable crystalline phases and internal microstructures exhibits a class of promising building blocks in achieving very high-strength materials [2].Noble metal nanoparticles with closely packed non-face-centred cubic (f.c.c.) crystalline phase is rarely reported. Yugang sun et al. [2] have observed that Ag nano plates with multiple parallel twin planes exhibited a partial phase transition from f.c.c. to b.c.t. under external pressures higher than 12GPa.Although Ag nano cubes without internal crystalline defects remain perfect f.c.c. phase at even higher pressures. These results indicate that controlling internal microstructures in nano particles may represent a promising strategy to achieve tetragonal phase even for nano particles with large lateral dimensions (for example,> 10nm) at ambient pressure.

By using first-principles calculations based on the density-functional theory, Mahmoud Jafri et al [3]have systematically investigated the equilibrium structure and the electronic properties of pentagonal and hexagonal copper nano wires (CuNWs) [3].

In the present work we have made an effort to tailor the crystal structure of non –face-centered cubic phase of Cu with the help of DFT using quantum espresso code. We have found stable tetragonal crystal structures having three and four number of atoms per unit cells.

## Method of analysis

All the calculations for the tetragonal Cu unit cell  with three and four atoms per unit cell have been performed using density functional theory with the generalized gradient approximation (GGA) using Perdew–Burke– Ernzerhof (PBE) parameterization of exchange correlation functional as implemented in the Quantum Espresso code [**4**]. These calculations are performed using a plane-wave basis [**5**]. The plane wave energy cutoff for three and four atoms are respectively 50 Ry and 60 Ry. For the Brillouin zone (BZ) integration we use a $1\times1\times30$ and $1\times1\times36$ sampling mesh for unit cell withthree atoms and four atoms calculations respectively. Further, we have checked force relaxation with 0.001118 Ry/au in three atoms per unit cell and 0.002545 Ry/au in four atoms per unit cell. Convergence threshold used 1.0E-10. The Broyde-Fletcher- Goldfarb-Shanno (BFGS) method is used for the geometry optimization. Here mixing beta was taken 0.7 and degauss 0.02 considered.

## Result and Discussion

Variation of energy versus  unit cell volume for tetragonal copper unit cell having three and four atoms are shown in Fig.1.and Fig.2.respectivly.Minima ofthe energies are found at unit cell volume $125.97 \, (A^0)^3$   and  $129.13 (A^0)^3$ for three and  four atoms per unit cell respectively.
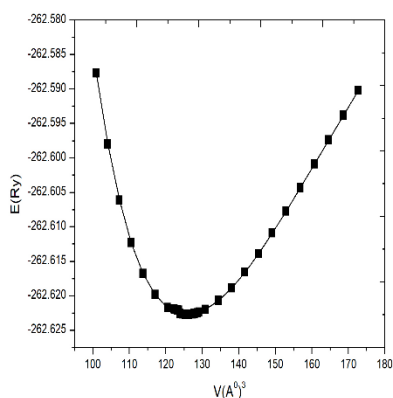


Fig.1 Energy versus Volume for tetragonal copper unit cell with three atoms
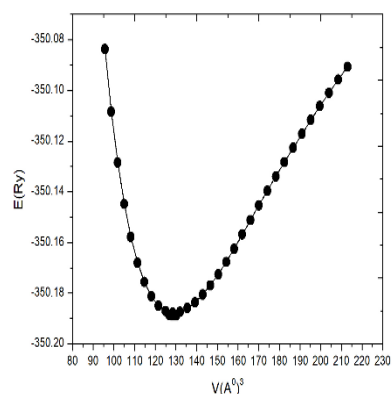
Fig.2 Energy versus Volume for tetragonal copper unit cell with four atoms

In the Fig.3 simulated image of tetragonal Cu unit cell having three atoms is shown. In Fig.4. proposed nano wire with triangular cross-section is shown along 2x2x10.
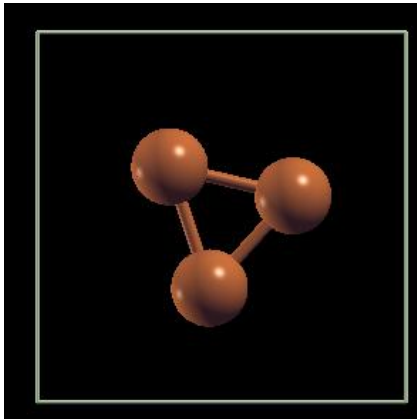


Fig.3. Image of simulated three atom tetragonal copper unit cell
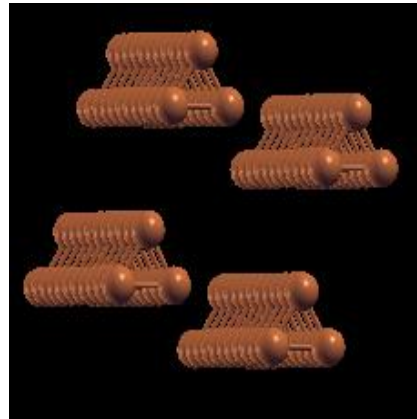


Fig.4 simulation of triangle cross section nanowire along 2x2x10

Similarly in the Fig.5 simulated image of tetragonal Cu unit cell having four atoms is shown. In Fig.6. proposed nano wire with square cross-section is shown along 2x2x10.
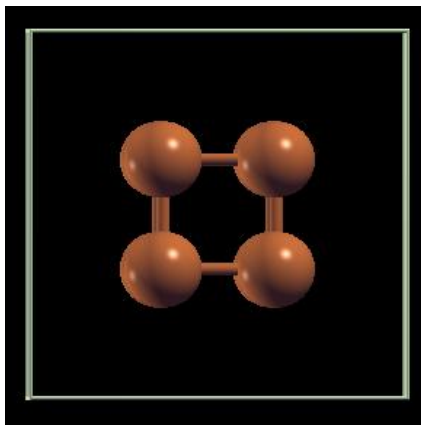


Fig.5.Image of simulated four atom tetragonal copper unit cell
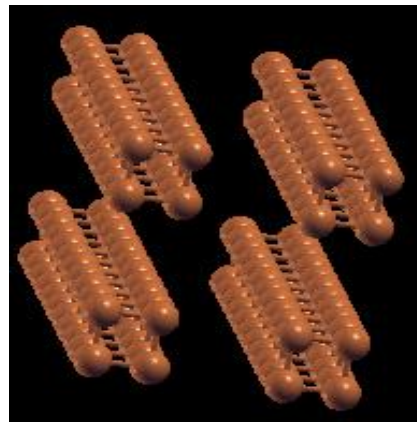


Fig.6 simulation of square cross section nanowire along 2x2x10

## Conclusion

We have found that tetragonal unit cell having three atoms is more stable triangular structure. In this case we have found three different   bond lengths, $2.4726A^0$, $2.4748A^0$ and $2.4290 A^0$ Similarly We have found that tetragonal unit cell having four atoms is also stable square structure. In this case the bond lengths and diagonal length are $2.1860A^0$and $3.0929 A^0$respectively.Both optimised stable unit cell can be extended in the direction of primitive translation vector c for the simulation of nano wire.

## References

[1] Nanotechnology and nano materials chapter 20, Hardevsingh virk. doi.10.572/16382 (2011).
[2] Yugang sun et al., nature communication (2012).

[3] Mahmoud Jafri et al. computational material science.**77**, 224-229.(2013)

[4] Baroni S.; Corso A. D.; Gironcoli S.; Giannozzi P.; http://www.pwscf.org

[5] Baroni S.; Gironcoli S. de. Corso D.; Giannozzi P. Rev. Mod. Phys. 73, 515. 2001

# Ultrasonic velocity and density of binary mixtures of 1-butyl-3-methylimadazolium and methanol at 293.15 K

D. K. Barot, V. A. Rana[*] , H. A. Chaube

Department of Physics, School of Sciences, Gujarat University, Ahmedabad, Gujarat, India

[*]E mail: ranava2001@yahoo.com

## Abstract

Physical properties such as ultrasonic velocity (u), density ($\rho$), viscosity ($\eta$) and refractive index (n) of 1-Butyl-3-methylimadazolium [BMiM][Cl] with methanol (MeOH) of varying concentration have been measured using ultrasonic interferometer, pyknometer, Ostwald's viscometer  and Abbe's refractometer respectively at 293.15K. From the measured values various acoustical parameters such as, adiabatic compressibility ($\beta$), acoustic impedance (Z) and free length ($L_f$), etc. have been calculated for all solutions to obtain some structural information. Results of refractive index are used to calculate dielectric constant at optical frequency. Obtained parameters were found to vary with the weight fractions of [BMiM][Cl] in MeOH.

**Keywords:** Ultrasonic velocity; density; Viscosity; adiabatic compressibility; free length; acoustic impedance

## Introduction

The study of physiochemical behavior and molecular interactions in ionic liquids in pure as well as in mixed state is of considerable importance and a number of experimental techniques have been used to investigate the interactions between the components of liquid mixtures. In recent years, the measurement of ultrasonic velocity has been extensively applied in understanding the nature of molecular systems, physicochemical behavior and molecular interactions in liquid mixtures [1-2]. Extensive application of isentropic compressibility of liquid mixtures in characterizing molecular association, dissociation and complex formation is available in literature. Ionic liquids are salts with melting points lower than 30$^{o}$C and look like a classical liquid but only contain ions.  The physicochemical properties of ionic liquids are as follows (i) under an inert atmosphere, they remain liquid over a temperature range of 200 to 300$^{o}$C; (ii) they have practically no vapor pressure; (iii) they are reported to have a wide window of electrochemical stability, good electrical conductivity, high ionic mobility and excellent chemical stabilities [3-5].  Binary polar liquid mixtures having ionic liquids as one of the constituents is of considerable interest among the industrialists.

One of the constituent of the binary liquid mixture under study is 1-Butyl-3-methylimadazolium [BMiM][Cl] member of ionic liquid and self associative and the other constituent of the binary mixture system is methanol (MeOH) which is also a self-associative, so it is thought that the binary liquid mixture of [BMiM][Cl] and MeOH will form an interesting and complex problem of liquid state physics and will provide a good scope to qualitatively analyze the physico-chemical data to gain some insight to the intermolecular interactions in the liquid mixture.

## Materials and Sample Preparation

[BMiM][Cl] (extra pure), and MeOH (AR grade) were obtained from HPLC Fine Chem. Limited and were used without further purification. Binary mixtures of [BMiM][Cl] with MeOH were prepared for nine concentrations by varying weight fractions. Samples were prepared by syringing weighed amounts of the pure liquids into stopper bottles, and weighed using digital balance with a precision of (1mg).

Experimental arrangements and methodology described by Rana and Chaube [6] has been followed to obtain physical and ultrasonic properties of the prepared samples. Allied parameters of obtained physical properties were calculated using appropriate mathematical expressions.

## Results and discussion

Experimental value of Density ($\rho$), viscosity ($\eta$), refractive index (n) and ultrasonic speed (u) of pure MeOH at 293.15 K are given in Table 1. They are in good agreement with the literature values.

**Table-1: Comparison of experimentally measured physical properties of MeOH with literature values at 293.15 K temperature**

| Physical property | Experimental value | Literature value |
|---|---|---|
| Refractive Index | 1.3312 | 1.33105 [7] |
| Density (kg m$^{-3}$) | 787.1 | 786.6 [8] |
| Viscosity (mPa.s) | 0.551 | 0.554 [8] |
| Ultrasonic Velocity (m sec$^{-1}$) | 1079.8 | 1097.6 [9] |

Measured values of Refractive Index,Density,Viscosity,Ultrasonic Velocity of mixtures of [BMiM][Cl] and MeOH are presented in Table 2.

**Table-2 Experimentally measured density (ρ), ultrasonic velocity (u), viscosity (η) and refractive index (n) of mixture of [BMiM][Cl] with MeOH at 293.15 K temperature**

| Weight Fraction ($x_1$) | Density (ρ) ($kg\ m^{-3}$) | Ultrasonic Velocity (u) (m / s) | Viscosity (η) (mPa.s) | Refractive Index (n) | Dielectric constant at optical frequency ($\varepsilon_\alpha$) |
|---|---|---|---|---|---|
| 0.001 | 792.1 | 1080 | 0.605 | 1.3315 | 1.7728 |
| 0.007 | 792.9 | 1094 | 0.606 | 1.3320 | 1.7742 |
| 0.010 | 793.8 | 1109 | 0.616 | 1.3330 | 1.7768 |
| 0.012 | 795.3 | 1120 | 0.626 | 1.3335 | 1.7782 |
| 0.014 | 796.8 | 1144 | 0.636 | 1.3345 | 1.7808 |
| 0.018 | 798.5 | 1163 | 0.647 | 1.3360 | 1.7848 |
| 0.021 | 800.2 | 1182 | 0.657 | 1.3370 | 1.7875 |
| 0.030 | 801.9 | 1204 | 0.677 | 1.3385 | 1.7915 |
| 0.042 | 803.6 | 1230 | 0.697 | 1.3395 | 1.7942 |

Density for all solutions increases with the increase in weight fractions of [BMiM][Cl] in MeOH. Obtained results can be useful for determination of macroscopic properties in order to reveal the information at atomic level. Low values of viscosity for all solutions refers to the presence of small molecules with which rearrangement ability is faster than compared to that of long chain molecules [8]. Values of refractive index (n) for different solutions are found to increase with weight fraction of [BMiM][Cl] which reflects the presence and enhancement of [BMiM][Cl] weight fractions. Using the values (n) dielectric constant at optical frequency has been calculated. The evaluated values of various acoustical parameters are reported in Table - 3.

**Table-3: Calculated values of adiabatic compressibility (β), free length ($L_T$), acoustical impedance (Z) of mixture of [BMiM][Cl] with MeOH at 293.15 K temperature**

| Weight Fraction Of [BMiM][Cl] $x_1$ | β/( $* 10^{-9}\ m^2N^{-1}$) | $L_T$ ( $* 10^{-8}$m) | Z( $* 10^5\ kgm^{-2}s^{-1}$) |
|---|---|---|---|
| 0.001 | 1.082 | 6.442 | 8.555 |
| 0.007 | 1.054 | 6.357 | 8.674 |
| 0.010 | 1.024 | 6.267 | 8.803 |
| 0.012 | 1.002 | 6.200 | 8.907 |
| 0.014 | 0.959 | 6.064 | 9.115 |
| 0.018 | 0.926 | 5.959 | 9.286 |
| 0.021 | 0.894 | 5.856 | 9.459 |
| 0.030 | 0.860 | 5.743 | 9.655 |
| 0.042 | 0.823 | 5.616 | 9.884 |

Ultrasonic speed is determined by the properties of the medium through which it propagates and it depends upon both the elastic property (stiffness or rigidity) and inertial property, i.e. mass density of the individual particles of the medium. In a single phase of matter longitudinal

sound wave travels faster in a less dense material than a more dense material [6]. From Table 2 it can be seen that values of ultrasonic velocity (u) increases with increase in concentration of [BMiM][Cl]. The evaluated parameters free length ($L_f$) and adiabatic compressibility ($\beta$) exhibit an opposite trend to that of measured ultrasonic velocity (Table 3). This observation is in agreement with the model proposed by Eyring and Kincaid [5]. Free length of 0.1 gm of [BMiM][Cl] with MeOH is $6.442 \times 10^{-8}$ m at 293.15 K and that of 0.9 gm of [BMiM][Cl] with MeOH is $5.616 \times 10^{-8}$ m at the same temperature. This suggests that the distance between the surfaces of two neighboring molecules of 0.1 gm [BMiM][Cl] with MeOH is more than that in 0.9 gm of [BMiM][Cl] with MeOH . Free length values are found to decrease with increase in concentration of [BMiM][Cl] in MeOH and the decrement is non-linear. This suggests that the ordering of the molecules increases with increasing concentration of [BMiM][Cl] in the mixture [10].



(a)



(b)



(c)
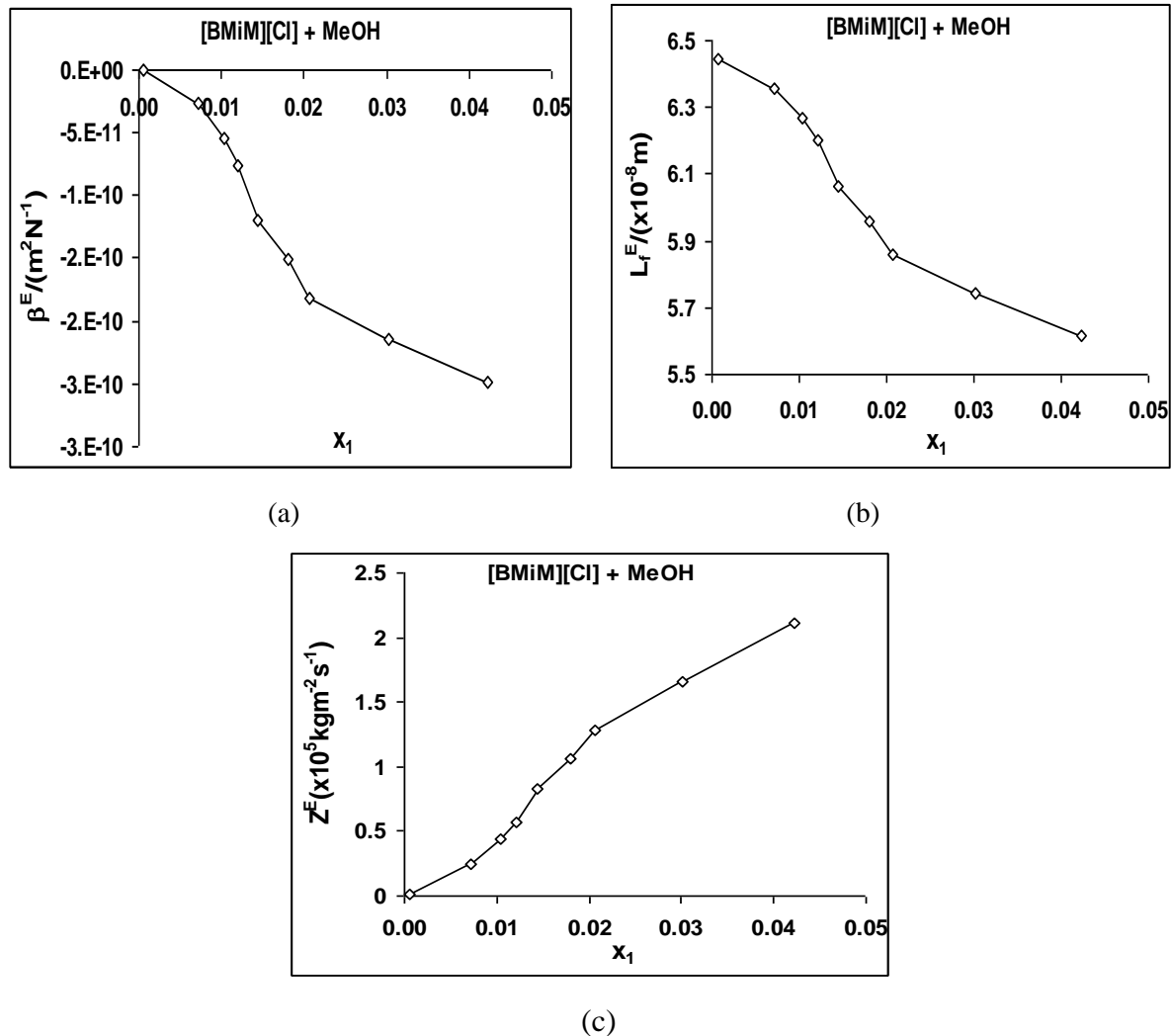
**Figure – 1: Excess adiabatic compressibility ($\beta^E$), excess free length ($L_f$) and excess acoustic impedance ($Z^E$) of mixtures of [BMiM][Cl] in MeOH at 293.15 K**

From the plot of excess adiabatic compressibility ($\beta^E$) against concentration (Fig. 1(a)), it can be seen that $\beta^E$ values are negative over the complete concentration range at given temperature. The negative $\beta^E$ values indicate that the corresponding ideal mixture is more compressible than the actual mixture [11]. [BMiM][Cl] and MeOH are self associative in their pure liquid state however when these two liquids are mixed, breaking of self associative ionic bonded structure takes place and new ionic bonded structures are formed due to the cross linkage between [BMiM][Cl] and MeOH molecules. This causes reduction in the compressibility and hence negative $\beta^E$ values. [12]

From Figure 1(c), it can be seen that excess specific acoustic impedance $Z^E$ is positive for entire concentration range of [BMiM][Cl]. This suggests the strengthening of the ionic bonds and dominance of the attractive forces between the component molecules.

## Conclusion

Measurements of physical properties density, viscosity, ultrasonic velocity and refractive index for solutions of different weight fractions of [BMiM][Cl] in MeOH at 293.15 K were performed. Values of all physical parameters for MeOH were compared with the literature value to validate the experimental results. All parameters were found to vary with the weight fractions of [BMiM][Cl] in mixture. Obtained results for density can be useful for determination of macroscopic properties in order to reveal the information at atomic level. Low values of viscosity for all solutions refers to the presence of small molecules with which rearrangement ability is faster compared to that of long chain molecules. Dominance of long range dispersive forces can be inferred from the excess free length values.

## Acknowledgement

## References

1) K R Seddon, A Stark, M J Torres, Pure Appl. Chem., 2000, 72, 2275–2287.

2) T Welton, Chem. Rev., 1999, 99, 2071-2083.

3) Y Chauvin, H O Bourbigou, Chemtech, 1995, 25, 26-30.

4) H L Ngo, K LeCompte, L Hargens, A B McEwen, Thermochim. Acta, 2000,357,97-102.

5)  H Eyring, J F Kincaid, J. Chem. Phys., 1938, 6, 620-630.

6)  V A Rana, H A Chaube, J. Mol. Liq., 2012, 173, 71-86.

7)  V A Rana, H A Chaube, D H Gadani, J.Mol. Liq., 2011, 164, 191-196.

8)  P S Nikam, L N Shrisat, M Hasan, J. Chem. Eng. Data, 1998; 43; 732-737.

9)  G V Ramana, E Rajagopal, N M Murthy, Indian J. Pure Appl. Phys., 2005, 43, 259-264.

10) M Vatandas, A B Koc, C Koc, Eur. Food Res. Tech., 2007, 225, 525-532.

11) A Tadd, B D Djordjevid, D K Grozdandid, J. Chem. Eng. Data, 1992, 37, 310-313.

12) P S Naidu, K R Prasad, Indian J. Pure Appl. Phys., 42, 2004, 512-517.

# Vertical growth of Van der Wall's heterostructure by depositing SnSe thin films on to crystalline WSe$_2$ and its characterization

Chetan K. Zankat, Pratik Pataniya, Alkesh B. Patel,  K. D. Pathak, G. K. Solanki,V. M. Pathak

*(Department of Physics, Sardar Patel University, Vallabh Vidyanagar- 388120, Gujarat, India)*

**Email:**mycreatphysics1@gmail.com

**(1) Chetan K.Zankat**

Department of Physics, Sardar Patel University, Vallabh Vidyanagar, Anand-388120, Gujarat, India.

Email: mycreatphysics1@gmail.com

**(2) Pratik Pataniya**

Department of Physics, Sardar Patel University, Vallabh Vidyanagar, Anand-388120, Gujarat, India.

Email: pm.pataniya9991@gmail.com

**(3) Alkesh B.Patel**

Department of Physics, Sardar Patel University, Vallabh Vidyanagar, Anand-388120, Gujarat, India.

Email:alkeshpatel51@yahoo.co.in

**(4) K. D. Patel**

Department of Physics, Sardar Patel University, Vallabh Vidyanagar, Anand-388120, Gujarat, India.

Email: kdptflspu@yahoo.com

**(5) G. K. Solanki**

Department of Physics, Sardar Patel University, Vallabh Vidyanagar, Anand-388120, Gujarat, India.

Email: solankigunvant@yahoo.co.in

**(6) V. M. Pathak**

Department of Physics, Sardar Patel University, Vallabh Vidyanagar, Anand-388120, Gujarat, India.

Email: yogvmpathak@yahoo.co.in

**Abstract:**

Amorphous SnSe thin films of thickness 150nm were deposited on glass substrates as well as on $WSe_2$ crystals using thermal evaporation technique in vacuum better than $10^{-5}$Torr. The elemental analysis was made by Energy dispersive analysis of X-ray (EDAX). The structural properties of deposited thin films were studied by powder X-ray diffraction (XRD) and transmission electron microscopy (TEM). The selected area electron diffraction pattern (SAED)of SnSe thin films was analyzed by VSPEC image processing software. The current-voltage characteristic of prepared hetero-interface (SnSe/$WSe_2$) shows reasonably good current rectification. The fabricated heterojunction was analyzed in dark and under illumination of 80mW power intensity. For quantitative analysis, the typical device parameters such as ideality factor and saturation current are evaluated from the observed I-V characteristics on the basis of thermionic-emission model of current conduction through such hetero-interfaces..

**Keywords:** TMDC, thermal evaporation, XRD, TEM, heterojunction.

**Introduction:**

The study of transition metal dichalcogenide(TMDC) materials in recent time has become one of the most attractive area of research in nano-science due to their vast application in electronic, optoelectronic devices and sensors [1-2]. Inspired from the success of graphene, many other 2D materials, such as GaS, GaSe, SnSe, transition metal oxides, etc.have been extensively studied [3–10]. Many Transition metal dichalcogenides (TMDCs) e.g. $WSe_2$, $MoSe_2$ etc. are Van der Waals layered materials with hexagonal lattice structure constituting stacked tri-layers in X-M-X form. The structures of layered TMDCs ($MX_2$, where M is a transition element and X is a chalcogen) incorporate each layer with strong in-plane covalent bonding and weak out-of-plane van der Waals interactions [11]. Each layered material has its own advantages and disadvantages. For example, the carrier mobility in black phosphorus (BP) is greater than that in TMDCs, but TMDCs have larger absorption coefficient compared with BP in visible range of light spectrum. The band gap of about 1-1.4 eV is the most attractive feature of TMDCs; which corresponds to their optimum efficiency in solar cell applications. In particular, research interest in the family of TMDCs has increased dramatically due to their layer-thickness dependent physical properties, for example, they exhibit transition from an indirect bandgap in bulk to direct bandgap in monolayer form [12–21]. One of the most explored members of IV-VI group, SnSe has orthorhombic crystal structure with lattice parameters: a = 11.50 Å, b = 4.15 Å and c = 4.44 Å [22]. In present work, we report the structural properties of SnSe thin film deposited by

thermal evaporation technique. The SnSe/WSe$_2$ heterojunction is fabricated and characterized by current-voltage measurement technique in dark and illuminated condition.

**Materials and methods:**

The SnSe films of thickness 150nm are deposited on ultrasonically cleaned glass substrates and freshly cleaved surface (by mechanical exfoliation) of WSe$_2$ crystals in vacuum better than $10^{-5}$ mbar. During deposition process, deposition rate of ~ 2Å/sec is maintained constant by Quartz crystal digital thickness controller (SQC-310). The chemical confirmation of deposited thin film was carried out by EDAX. The structural properties like lattice parameters and crystallographic planes were determined by powder X-ray diffraction (Rigaku) and transmission electron microscopy. The hetero junction device was then completed by bonding thin copper wires by highly conducting silver paste. I-Vcharacteristics of hetero-interface (SnSe/WSe$_2$) were measured using Keithly-source measure Unit SMU-2400 in dark and under polychromatic illumination.

**Results and discussion:**

The EDAX results show the stoichiometry of prepared SnSe thinfilm and weight (%) are also measured, as mentioned in Table 1. No extra peaks are found in EDAX spectrum, which confirms the purity of prepared thinfilm.

**Table 1**Results of EDAX for SnSe thin film.

| Wt % of the elements | Sn | Se |
|---|---|---|
| Stoichiometric proportion taken | 49.3 | 50.7 |
| Obtain from the EDAX | 46.2 | 53.8 |
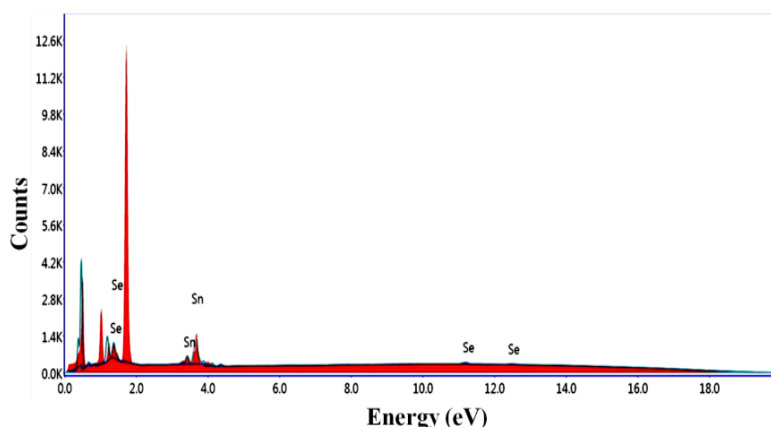


**Figure 1**EDAX spectra of deposited SnSe thin film.

The structural properties of SnSe thin films were studied by powder X- ray diffraction and transmission electron microscopy. The XRD pattern reveals (011) and (111) reflections at angle 29.44˚ and 30.46˚ respectively, as shown in Figure 2 (a). The SnSe thinfilm has orthorhombic lattice structure and the determined values of lattice parameters, a = 11.50 Å, b = 4.15 Å and c = 4.44 Å are well in agreement with reported data[22]. The transmission electron microscopy as used in imaging mode shows uniform SnSe thin film with ~16nm average particle size (Fig.-2b). Selected area electron diffraction pattern (Fig.-2c) shows diffused ring pattern that indicates amorphous nature of grown SnSe thin film. For accurate determination of lattice parameters and indexing of crystallographic planes, we have used VSPEC image processing software. The obtained (*hkl*) values (111), (400), (311) and (112) are good in agreement with the standard JCPDF file [23].
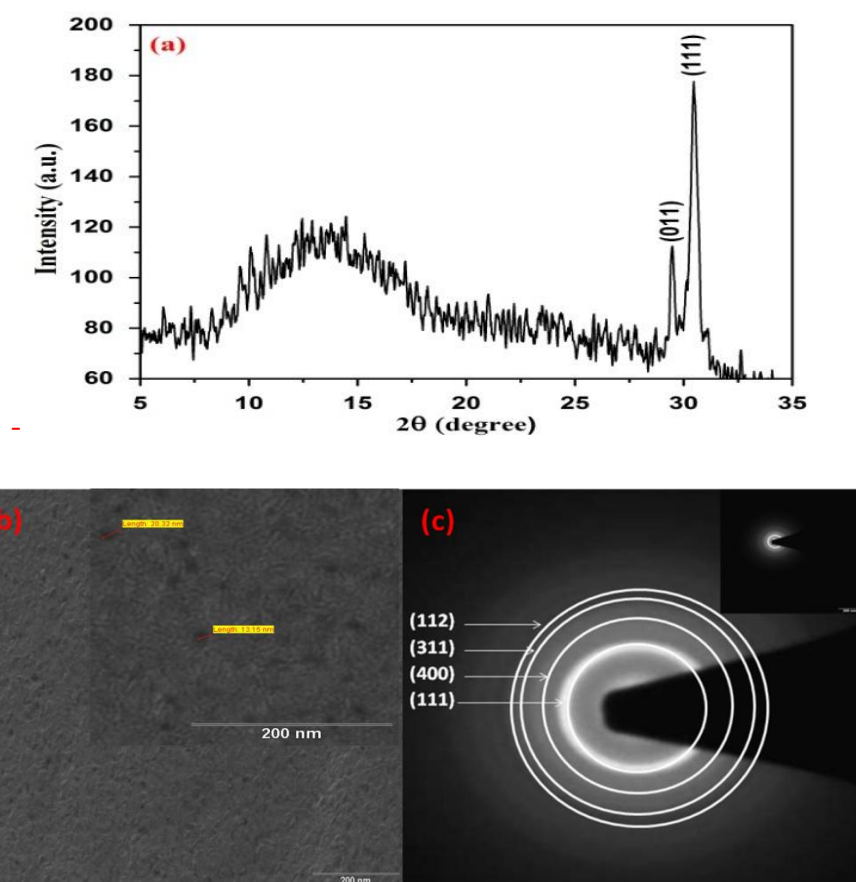


**Figure 2** (a) X-ray diffraction pattern,(b) grown thin film surface,(c) Indexed SAED pattern, of Deposited SnSe thin film.

The SnSe/WSe$_2$ hetero junction was characterized by current-voltage measurement technique at room temperature and in dark and under illumination, as shown in Figure 3. The I-V measurements show the good current rectification and rectification ratio is determined at ±0.8V. The current across the junction is found to increase slightly on illuminating the SnSe/WSe$_2$

interface. The current rectification ratio also increases under illumination.The typical parameters such as ideality factor and saturation current are also determined from the thermionic emission theory for fabricated device, as mentioned in Table 2. Despite of having good rectification ratio, the ideality factor is found in excess of unity that indicates domination of non-ideal current conduction mechanisms originating from lattice mismatch at the interface due to structural mismatch as well as barrier inhomogeneity. The lattice mismatch may lead to interfacial strain that leads to formation of strained lattice or lattice defects. Apart from this it is a case of interface between amorphous material to crystalline material where in grain boundaries of amorphous material add inhomogeneities when in contact with the crystalline material surface. This in turn adds additional scattering centers and thus it results in to a system with ideality factor well in excess of unity.
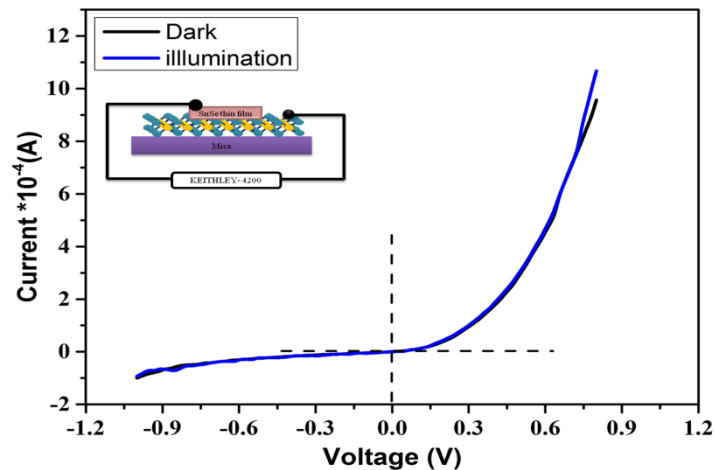


**Figure 3** I-V characteristics of SnSe/WSe$_2$heterojunction.

**Table 2** Typical parameters of fabricated device

| Illumination (mW/cm$^2$) | Ideality factor η | Saturation current $I_0(\mu A)$ |
|---|---|---|
| dark | 5.57 | 0.697 |
| 80mw | 5.65 | 0.747 |

**Conclusion:**

The SnSe thin film was prepared by thermal evaporation technique. The XRD and TEM analysis of 150 nm thick films reveals that deposited films of SnSe possess orthorhombic structure with lattice parameter values matching to standard reported values adhering their stoichiometric proportion in thin film form. For SnSe/WSe$_2$ junction, the determined value of ideality factor is

greater than one. Hence, it suggests the present interface is the case of inhomogeneous hetero structure having lattice mismatch.

**Reference:**

[1] A. Mihai. Popescu, Solid State Science and Tec., 2000 8.

[2] K R Willardson and R E Weber, Semiconducting Chalcogenide Glass I, 2004 78.

[3] P. Hu et al,  Nano Lett. 2013 13 1649–54.

[4] D J Late, B Liu, J Luo, A Yan, H S Matte, M Grayson, C N Rao and V P Dravid, Adv. Mater., 2012 24 3549–54.

[5] L Li, Z Chen, Y Hu, X Wang, T Zhang, W Chen and Q Wang, J. Am. Chem. Soc., 2013 135 1213–6.

[6] W Dang, H Peng, H Li, P Wang and Z Liu, Nano Lett., 2010 10 2870–6.

[7] D Kong, W Dang, J J Cha, H Li, S Meister, H Peng, Z Liu and Y Cui, Nano Lett., 2010 10 2245–50.

[8] K K Kim et al, Nano Lett. 2012 12 161–6.

[9] R Ma and T Sasaki, Adv. Mater., 2010 22 5082–104.

[10] H Li, G Lu, Y Wang, Z Yin, C Cong, Q He, L Wang, F Ding, T Yu and H Zhang, Small 2013 9 1974–81.

[11]  M. Chhowalla, H.S. Shin, G. Eda, L. Li, K.P. Loh, H. Zhang, Nat. Chem., 2013 5 263.

[12] B Radisavljevic, A Radenovic, J Brivio, V Giacometti and A Kis, Nature Nanotechnol., 2011 6 147–50.

[13] Wu Sanfeng, H Chunming, A Grant, S R Jason, H C David and Xu Xiaodong,  ACS Nano., 2013, 7 (3),  2768–2772.

[14] J N Coleman et al, Science., 2011 331 568–716.

[15] Y H Lee et al, Adv. Mater., 2012 24 2320–5.

[16] G A Castellanos, E Cappelluti, R Roldan, N Agrait, F Guinea and B G Rubio, Adv. Mater., 2013 25 899–903.

[17] S Larentis, B Fallahazad and E Tutuc , Appl. Phys. Lett. 2012 101 223104.

[18] D Kong, H Wang, J J Cha, M Pasta, K J Koski, J Yao and Y Cui, Nano Lett. 2013 13 1341–7.

[19] H R Gutierrez, L N Perea, A L Elias, A Berkdemir, B Wang, R Lv, U F Lopez, V H Crespi, H Terrones and M Terrones, Nano Lett. 2013 13 3447–54.

[20] H Zeng et al, Sci. Rep. 2013 3 1608.

[21] W J Zhao, Z Ghorannevis, L Q Chu, M L Toh, C Kloc, P H Tan and G Eda, ACS Nano, 2013 7 791–7.

[22] N. kumar, U. Parihar, R. Kumar, K. J. Patel, C. J. Panchal,  N. Padha American Journal of Materials Science, 2012, 2(1)  41-45

[23] JCPDF card no. 32-1382.

# Optical properties of pure and off-stoichiometric tin selenide single crystals

Mohit Tannarana, G. K. Solanki, Pratik Pataniya, K. D. Patel, V. M. Pathak

Department of Physics, Sardar Patel University, Vallabh Vidyanagar-388120, Anand, Gujarat, India.

Email: mohittanna6@gmail.com

**Abstract:**

The single crystals of pure SnSe and $Sn_{0.4}Se_{0.6}$ (off-stoichiometric) were grown by direct vapour transport technique. The optical response of grown single crystals was studied by UV-Visible-NIR spectroscopy. The absorption spectra were recorded for grown single crystals in spectral range 250 nm to 1500 nm. Absorption near the fundamental edge was found to be due to direct allowed transition and the optical band gap corresponding to this transition has also been determined. The optical parameters like absorption coefficient, extinction coefficient and refractive index have also been calculated for grown single crystals. The results thus obtained have been described and discussed in this paper.

**Keywords:** Single crystal growth, optical properties, band gap, tin selenide, off-stoichiometry.

**Introduction:**

Recently, transition metal chalcogenides have attracted great attention due to their excellent optical properties. Moreover, IV-VI compounds having band gap of 1-2 eV and high absorption co-efficient are useful for the applications in solar cell and photovoltaic devices. These layered semiconductors, namely SnS, SnSe, GeS and GeSe have direct as well as indirect band gap, which may improve efficiency of solar cell. One of the important compounds of chalcogenide family, SnSe has orthorhombic structure with eight atoms per unit cell forming bi-planar layers normal to the largest c axis [1-3]. In each bi-layer, atoms are joined to three nearest neighbors by covalent bond which forms zigzag chains along ab-plane while SnSe bi-layers are stacked upon each other by weak van der Waals interaction. As the bonds between adjacent double layers are van der Waals type, this material cleaves easily along a-b (001) planes. In crystalline form, SnSe shows a wide variety of optical and electrical properties and presence of anisotropy increases the curiosity of researcher. Besides this, SnSe has shown great potential for applications in phase change

memory devices due to its low crystallization and high melting temperature in certain conditions [4, 5]. The SnSe is found to be crystallize in orthorhombic lattice structure with space group $P\bar{3}m1$ and lattice parameters a=4.16Å, b=4.45Å and c=11.55 Å. Many researchers studied the optical properties of SnSe pure single crystals [6-9] but the off-stoichiometric tin selenide has been less explored.

**Materials and Methods:**

The single crystals of SnSe and $Sn_{0.4}Se_{0.6}$ were grown by direct vapour transport technique. The optical properties of grown crystals were examined by UV-Visible spectroscopy. The absorption spectra of samples were recorded using Beckman Model DK-A spectrophotometer (UV-VIS-NIR spectrophotometer) (Make: Perkin Elmer, Model: Lambda with the light source having radiant energy in the ultraviolet to near infrared regions of the electromagnetic spectrum. Samples used for UV-Visible spectroscopy is cleaved mechanically using scotch tape. Cleaved samples are covered by black opaque paper used for analysis. The absorbance was measured in spectral range 250 nm to 1500 nm at ambient temperature. The optical parameters have been calculated for as grown samples. For quantitative analysis, optical parameters like bandgap, refractive index and extinction co-efficient were also determined.

**Results and discussion:**

The absorption spectra of SnSe and $Sn_{0.4}Se_{0.6}$ samples were recorded in spectral range 250 nm to 1500 nm is as shown in Figure 1. The increased absorption near the edge is due to the transition of electron from the valance band to conduction band [10]. The absorption coefficient ($\alpha$) can be estimated from Lambert's law [11].

$$\alpha = \frac{2.303A}{t}$$

(1)

where, $t$ is thickness of the absorbing layer and A is the absorbance from the spectra. The most prominent peaks are found to be at 1150 nm and 840 nm for SnSe and $Sn_{0.4}Se_{0.6}$, respectively. The optical band gap of samples is calculated using following relation:

$$\alpha h\nu = A(h\nu - E_g)^r$$

(2)

for direct transition

$$\alpha h\nu = \sum_j B_j (h\nu - E'_g \pm E_{pj})^r$$

(3)

for indirect transition
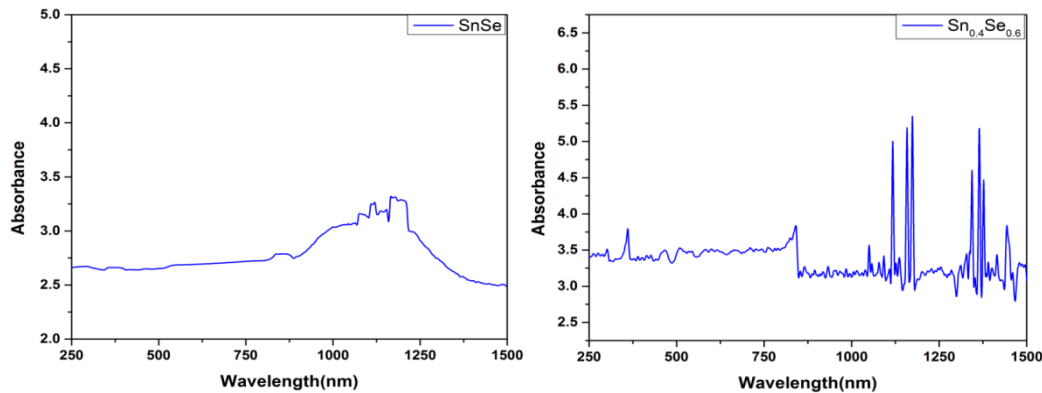


**Figure 1:** Absorption spectra of SnSe and $Sn_{0.4}Se_{0.6}$ crystals

The variation of $(\alpha h\nu)^2$ vs. photon energy (hν) is shown in Figure 2. The Values of band gap obtained from the extrapolation of the straight line portion [7]. The direct bandgap was determined and found to be 1.0 eV for SnSe and 1.45 eV for $Sn_{0.4}Se_{0.6}$ single crystals. Figure 3 shows the plot of $(\alpha h\nu)^{1/2}$ versus photon energy (hν) which gives the values of indirect transition for grown single crystals. The determined value of indirect band gap is 0.95 eV and 1.37 eV for for SnSe and $Sn_{0.4}Se_{0.6}$ samples respectively. Value of the band gap for SnSe compound is matched with reported values [6-9]. The change in band gap is due to off-stoichiometry present in $Sn_{0.4}Se_{0.6}$ compound in which proportion of tin is (less compared to pure SnSe) reduced to 40%.
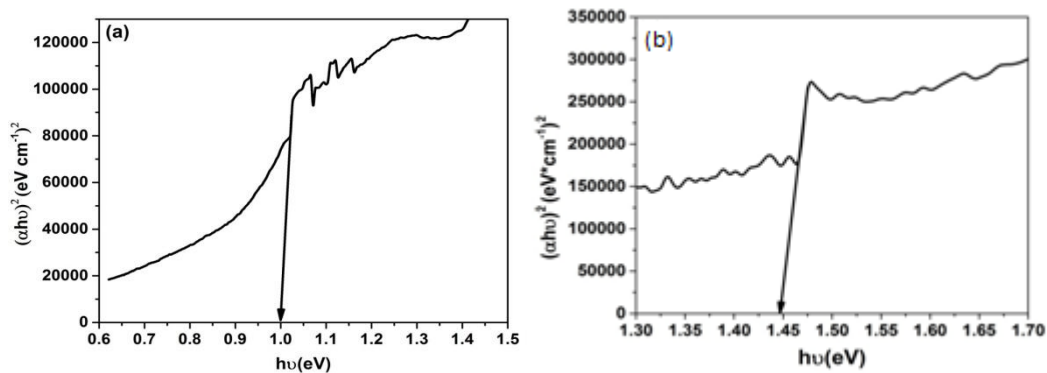


**Figure 2:** direct band gap of (a) SnSe and (b) $Sn_{0.4}Se_{0.6}$ crystals
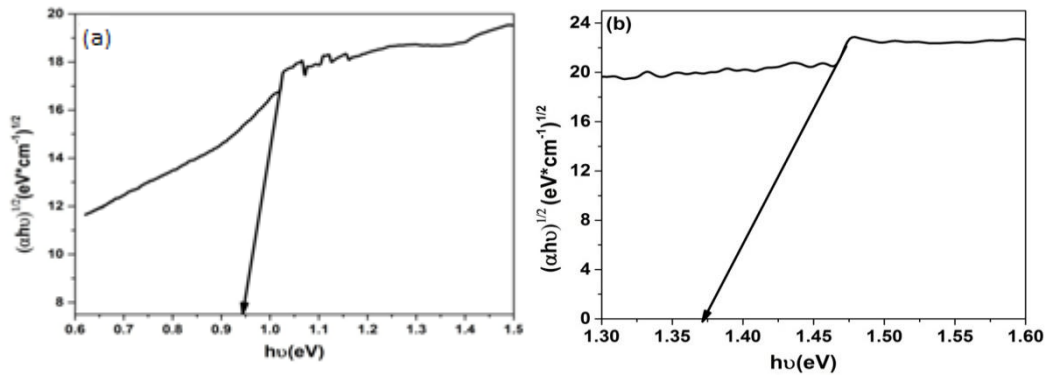
**Figure 3:** indirect band gap of (a) SnSe and (b) Sn$_{0.4}$Se$_{0.6}$ crystals
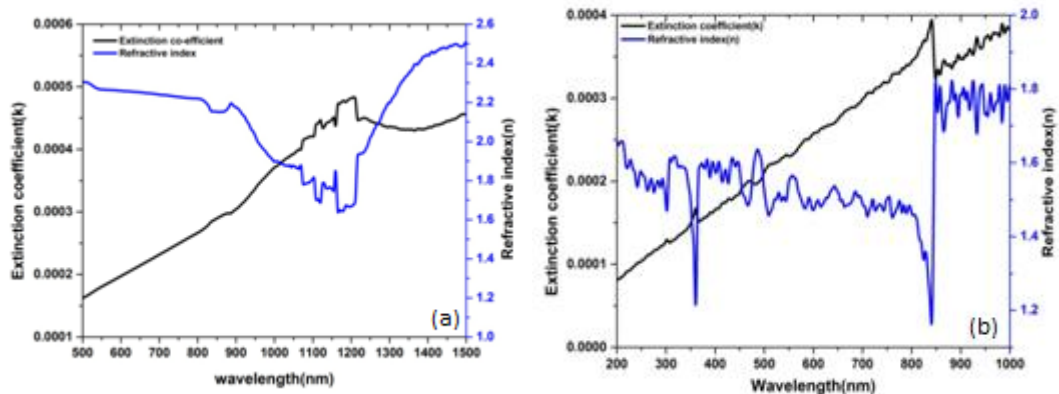


**Figure 4:** Variation of Extinction co-efficient and Refractive index at different wavelengths for (a) SnSe and (b) Sn$_{0.4}$Se$_{0.6}$.

The optical parameters such as extinction co-efficient (k) and refractive index (n) have been calculated using following relations:

$$k = \frac{\alpha \lambda}{4\pi} \tag{4}$$

$$n = \frac{(R-1)^2 + k^2}{(R+1)^2 + k^2} \tag{5}$$

Where, α = absorbance co-efficient

λ = Wavelength

R= Reflection

The refractive index (n) and extinction coefficient (k) are shown in Figure 4 (a) and (b) for grown single crystals. These plots show the promising variation of both the parameters for different wavelengths.

**Conclusions:**

The single crystals of SnSe and $Sn_{0.4}Se_{0.6}$ were grown by direct vapour transport technique. Study of optical properties like direct and indirect band gap, refractive index, extinction co-efficient has been carried out. Variation in the values of band gap is due to off-stoichiometry present in $Sn_{0.4}Se_{0.6}$ compound. Nearly 1.0 eV value of band gap for SnSe is quite promising for its application in opto-electric devices and solar cell.

**References:**

[1] Okazaki, J.Phys.Soc., Japan, 1958, 13, 1151- 1155.

[2] S. Logothetidis and H. M. Polatoglou, Phys. Rev. B, 1987, 36, 7491-7499.

[3] G. Valiukonis, D. A. Gussienova, G. Krivaite and A. Sileika, Phys. Stat.Solidi (b), 1986, 135, 299-307.

[4] K. M. Chung,D. Wamwang, M. Wod, M. Wutti and W. Bensc, J.Appl. Phys., 2008,103, 083523(1-7).

[5] K. A. Campbell and C. M. Anderson, Microelectronics Journal, 2007, 38, 52-59.

[6] M. Parentau and M. Carlone, Phys. Rev. B, 1990, 41: 5227-5234.

[7] B.B. Nariya, A.K. Dasadia and A.R. Jani, PRAJNA -Journal of Pure and Applied Sciences, 2011, 19, 79 - 81.

[8] A. M. Elkorashy, journal of Physics and Chemistry of Solids, 1986, 47, 3, 497-504.

[9] C.Julien, M.Eddrief, I.Samaras and M.Balkanski, Materials Science and Engineering: B, 1992, 15, 1, 70-72.

[10]   M. M. Parvathi, A. Mohan, V.Arivazhagan and S.Rajesh, AIP conf.proc., 2012, 206, 1451-1454.

[11]   S. A.Khan and A. A. Al-Ghamdi, Mater. Lett., 2009,63, 1740-1742.

# Disharmonic Identification of EEG data through Wavelet Transform

Dhwanilnath Gharekhan [1], Prakash L. Patel[2,3] and Anita Gharekhan[3]

[1]M.Tech Student, M.Tech (Geomatics), Faculty of Technology, CEPT University, Ahmedabad, India, dhwanilnath@gmail.com

[2]Research Scholar, Pacific University, PAHER, Rajasthan, India

[3]Associate Professor, Department of Physics, C U Shah Science College, Ahmedabad, India, anitaghare@gmail.com

**Abstract**

Although the structure of a brain is highly complicated; Brain scans provide an opening to understand the functionality which a body undergoes during various activities. The brain's cells produce tiny electrical signals when they send messages to each other. The brain's electrical charge is maintained by huge number of individual neurons. Neurons are electrically charged (or "polarized") by membrane transport proteins that pump ions across their membranes. Each neuron interacts with its neighbouring neurons as well as with remote neurons. Electroencephalography (EEG) is the recording of these electrical activities along the scalp. In situations with diseases, there are numerous undulation which enter in the EEG. Identification of these pattern can provide a better insight of a human's condition. Wavelet transform can sometimes diagnose a pathological condition more easily when the frequency content of the signal is analysed. The frequency spectrum of a signal is basically the frequency components (spectral components) in that signal. The peaks of a wavelet can be used in diagnosing such conditions.

**Keywords:** EEG, Wavelet Transform, Signal, DWT, CWT.

## Introduction

### Electro-Encephalography

The brain's electrical charge is maintained by huge number of individual neurons. Neurons are electrically charged (or "polarized") by membrane transport proteins that pump ions across their membranes[1]. Each neuron interacts with its neighbouring neurons as well as with remote neurons. They constantly exchange ions with the extracellular milieu, for example to maintain resting potential and to propagate action potentials. Ions of similar charge repel each other, and when many ions are pushed out of many neurons at the same

time, they can push their neighbour's', who push their neighbours, and so on, in a wave. This process is known as **volume conduction**.

When the wave of ions reaches the electrodes on the scalp, they can push or pull electrons on the metal on the electrodes. Since metal conducts the push and pull of electrons easily, the difference in push or pull voltages between any two electrodes can be measured by a voltmeter. Recording these voltages over time gives us the EEG.  EEG measures voltage fluctuations resulting from ionic current flows within the neurons of the brain. Routine EEG is typically used in the following clinical circumstances:

- to distinguish epilepticseizures from other types of spells, such as psychogenic non-epileptic seizures, syncope (fainting), sub-cortical movement disorders and migraine variants.
- to differentiate "organic" encephalopathy or delirium from primary psychiatric syndromes such as catatonia
- to serve as an adjunct test of brain death
- to prognosticate, in certain instances, in patients with coma
- to determine whether to wean anti-epileptic medications

The pattern of electrical activity produced on an EEG can be used to help diagnose a number of conditions that affect the brain [2]. An EEG is mainly used to diagnose and manage epilepsy (a condition that causes repeated brain seizures). EEGs can also be used to diagnose and manage sleep disorders such as insomnia. An EEG can identify areas of the brain that are not working properly. This helps doctors to make decisions about the type of treatment that is most suitable for you. EEGs are also sometimes used to determine the level of brain function in people who are in a coma. The patterns can be undertaken by analyzing them.

**Wavelet Transform**

Wavelet transform provides information by taking the EEG scans as direct signals [3].Wavelets refer to small waves and wavelet transform refers to the representation of a signal in terms of a finite length or fast decaying oscillating waveform. This waveform, known as the *mother wavelet*, is scaled and translated to match the input signal. In this representation, a wavelet series, which is the coordinate representation of a square integral function with respect to a complete, orthonormal set of basic functions for the discrete

wavelets under consideration. Wavelet transforms are broadly classified into the discrete wavelet transform (DWT) and the continuous wavelet transform (CWT) [4].

Discrete Wavelet transform is known as mathematical microscope which provides a multi-resolution analysis of the data under consideration. The data is separated into high frequency and low frequency components at multiple scales, known respectively as high pass and low pass coefficients. The basic functions consist of father wavelet $\phi(x)$ and mother wavelet $\varphi(x)$ satisfying $\int \phi dx = A$, $\int \varphi dx = 0$ and $\int \phi * \varphi dx = 0$

$\phi$ and $\varphi$ are also square integrable : $\int |\phi|^2 dx = 1 = \int |\varphi|^2 dx.$

A completely orthonormal basis is constructed through translated and scaled versions of $\phi(x)$ and $\varphi(x)$. Explicitly, $\phi(x-k) \equiv \phi_k(x)$ and $\varphi_{j,k} \equiv 2^{j/2} \varphi(2^j x - k)$, for $-\infty \le k \le \infty$ and $0 \le j \le \infty$, provide a complete orthonormal basis through which a data set can be expanded in the form,

$$f(t) = \sum_k c_k \phi_k + \sum_k \sum_{j=0}^{\infty} d_{j,k} \varphi_{j,k}$$

Here $c_k$'s the low pass and $d_{j,k}$'s the high pass coefficients. For our analysis, we will make use of Haar wavelets, in which $c_k$'s can be interpreted as average of data points of appropriate size around space location k, $d_{j,k}$'s the high pass coefficients at level j. These represent differences around location k, over a window of appropriate size, depending on level j [4].

Continuous wavelet transform was developed as an alternative approach to the short time Fourier transforms to overcome the resolution problem. The wavelet analysis is done in a similar way to the STFT analysis, in the sense that the signal is multiplied with a function, similar to the window function in the STFT, and the transform is computed separately for different segments of the time-domain signal. The continuous wavelet transform is defined as follows [5].

$$CWT_x^{\varphi}(\tau, s) = \varphi_x^{\varphi}(\tau, s) = \frac{1}{\sqrt{s}} \int x(t) \varphi * \left( \frac{t-\tau}{s} \right) dt$$

## Materials and Method

Five sets (denoted A–E) each containing 100 single channel EEG segments of 23.6-sec duration, were composed for the study [6].These segments were selected and cut out from continuous multichannel EEG recordings after visual inspection for artefacts, e.g., due to muscle activity or eye movements. Sets A and B consisted of segments taken from surface EEG recordings that were carried out on five healthy volunteers using a standardized electrode placement scheme. Volunteers were relaxed in an awake state with eyes open (A) and eyes closed (B), respectively. Sets C, D, and E originated from our EEG archive of presurgical diagnosis. For the present study EEGs from five patients were selected, all of whom had achieved complete seizure control after resection of one of the hippocampal formations, which was therefore correctly diagnosed to be the epileptogenic zone [2]. Segments in set D were recorded from within the epileptogenic zone, and those in set C from the hippocampal formation of the opposite hemisphere of the brain. While sets C and D contained only activity measured during seizure free intervals, set E only contained seizure activity. Here segments were selected from all recording sites exhibiting ictal activity.

All EEG signals were recorded with the same 128- channel amplifier system, using an average common reference [omitting electrodes containing pathological activity (C, D and E) or strong eye movement artefacts (A and B)].After 12 bit analog-to-digital conversion, the data were written continuously onto the disk of a data acquisition computer system at a sampling rate of 173.61 Hz. Band-pass filtersettings were 0.53–40 Hz (12 dB/Oct.). Exemplary EEGs are depicted in fig. 1. More information about the recorded data can be found in ref 1-5 and data is available in public domain ref. 6.Amplitudes of surface EEG recordings are typically in the order of some mV. For intracranial EEG recordings amplitudes range around some 100 mV. For seizure activity these voltages can exceed 1000 mV [7].

There are infinite varieties of discrete wavelets; the choice of a basis set depends on the application at hand. For our application, we make use of the simplest Haar wavelet, since the interpretation of the wavelet coefficients is quite transparent here; it is also free from artefacts arising due to the finite size of the data.

For the Haar wavelet $h(0) = h(1) = \dfrac{1}{\sqrt{2}}$ and $\tilde{h}(0) = -\tilde{h}(1) = \dfrac{1}{\sqrt{2}}$, these coefficients are different for different wavelet basis sets. Haar basis is special, since it is the only wavelet, which is symmetric and compactly supported. In a level one Haar wavelet decomposition, the nearest neighbour averages and differences are calculated with the normalization factor of

$1/\sqrt{2}$ .The alternate coefficients are thrown out in a process called down-sampling or decimation, which leaves half of the data in the form of low-pass coefficients and the other half in terms of Level-I high-pass coefficients. Subsequently, the same procedure can be applied once more to the low-pass coefficients to decompose them into level-II high-pass coefficients and level-II low-pass coefficients. One can now clearly see that the level-I high-pass coefficients are the nearest neighbour differences in the Haar wavelet. The level-II high-pass coefficients are the differences of the nearest neighbour averages. In this manner, one can find out the differences of progressively larger chunks of data, which are the other higher level high-pass coefficients. The fluctuations considered here are these Haar wavelet coefficients, which are the simple differences of intensities at neighbouring wavelengths. This illustrates how the high-pass coefficients at higher levels separate out the fluctuations over progressively bigger neighbourhoods.
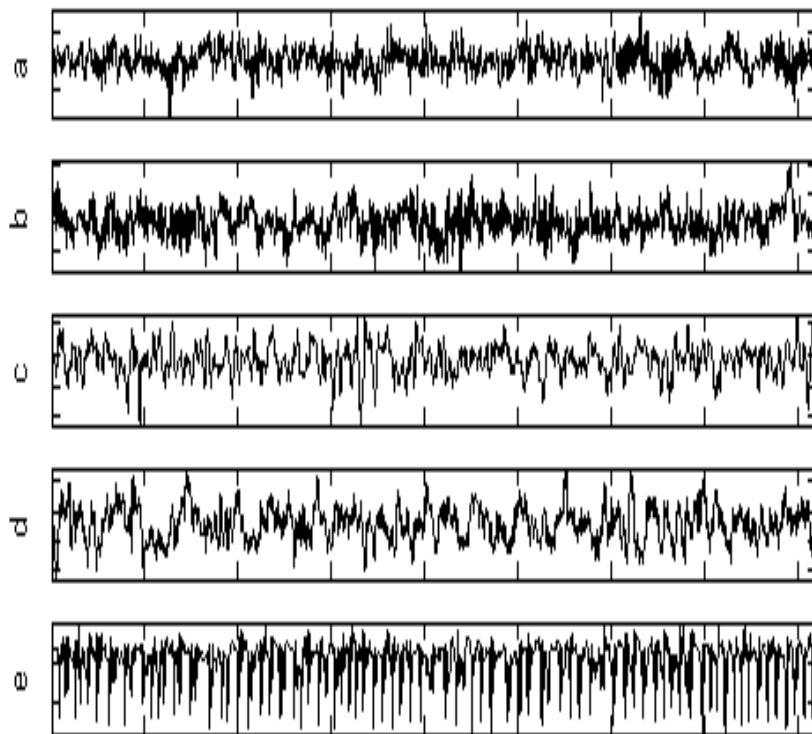


Figure I: Exemplary EEG time series from each of the five sets. From top to bottom: set A to set E (denoted a to e).

If the data set contains $2^N$ elements, with N an integer then one can have a N-level decomposition, after which one is left with only one low-pass coefficient, which is the

average of all points, modulo a normalization factor. It is evident that the high-pass coefficients, progressively capture differences at a broader scale starting from the nearest neighbor ones. In more sophisticated wavelets, the above averaging and differentiation is replaced by a suitable weighted averaging and differentiation. If the data is not $2^N$, one needs to append the same with the required number of points by padding or other procedures. It is worth mentioning that, apart from Haar wavelets, the process of computing wavelet coefficients needs a suitable extension of data e.g., circular or periodic, which also brings in artifacts to be clearly differentiated from the true variations. In order to avoid these complications, we have taken the Haar wavelets for our analysis. The studied data is having 4096 points so it can be decomposed up to twelve levels, without encountering any artificial features. It should be pointed out that, wavelet transform satisfies the Parseval theorem implying that

$$\sum I_i^2 = \sum (c_k)^2 + \sum_{j,k} (d_{jk})^2 ,$$

where $I_i$ is the voltage in mV and $c_k$'s and $d_{jk}$'s are the low and high-pass coefficients respectively.

## Results and Discussion

The original EEG signal consist of at least a million entries over its 30 mins time span, out of which a couple of patches of 4096 entries have been taken into account for studying and analysing. For the analysis of studied EEG data, the convenient decomposition level is taken up to 8. Discrete wavelet transform (DWT) means time series will be transformed into high pass and low pass components and these respective values are being studied individually.

The level-1 low pass coefficients are the averages of nearest neighbour data points, level-2 low pass coefficients represent averages of 4-data points etc. It is clear that, there are 2048 level-1 coefficients, 1024 level-2 coefficients etc. For 4096 data points, we can have twelve level decomposition. It is observed that, progressive averaging of data in discrete wavelet transform reduces statistical and experimental uncertainties. The variations at lower level represent the high frequency components, corresponding to variations in smaller window sizes.

### Discrete Wavelet Transform

As an illustration one typical DWT decomposition in its corresponding low pass coefficients and high pass coefficient is shown in figure II and III respectively.
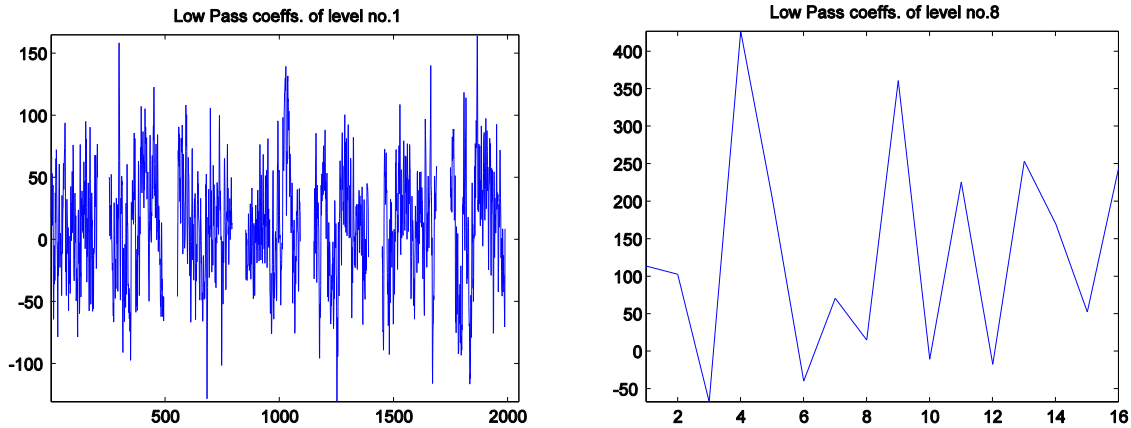
Figure II: Low-pass wavelet coefficients of level -1 and level – 8 of condition A.
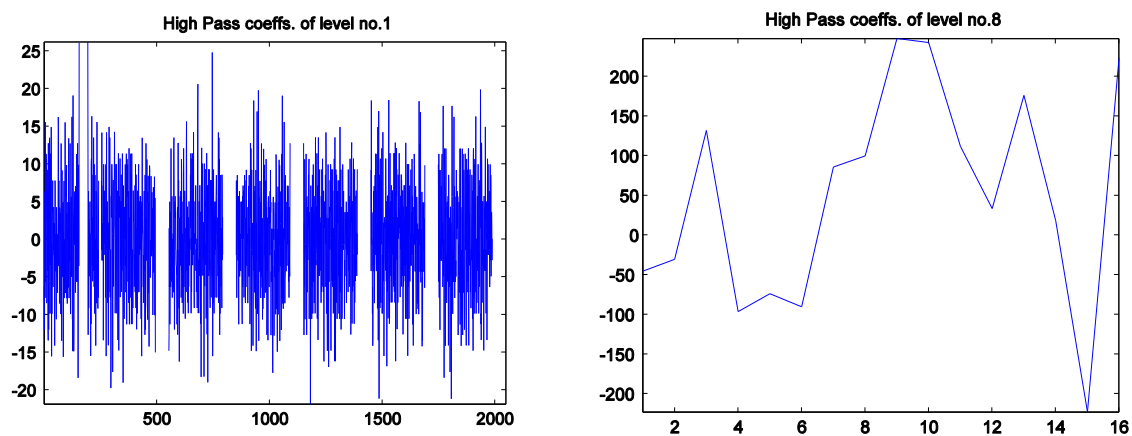


Figure III: High-pass wavelet coefficients of level -1 and level – 8 of condition A.

While computing wavelet power one take the sum of the square of wavelet coefficients at particular level e.g., low pass power at level-3 corresponds to sum of square of low pass coefficients of 3rd level. Usually for the sake of normalization, we normalize it i.e., divides it by total power P which is the sum of the squares of all the data points. Similarly, one can compute high pass power. In wavelet transform total power is conserved i.e., sum of low pass and high pass power yield the total power.The rate of decrease of low pass power, as a function of levels, is almost same in all conditions except patient is in totally relaxed mode. While high pass shows variation with levels and can be used for diagnostics purpose.
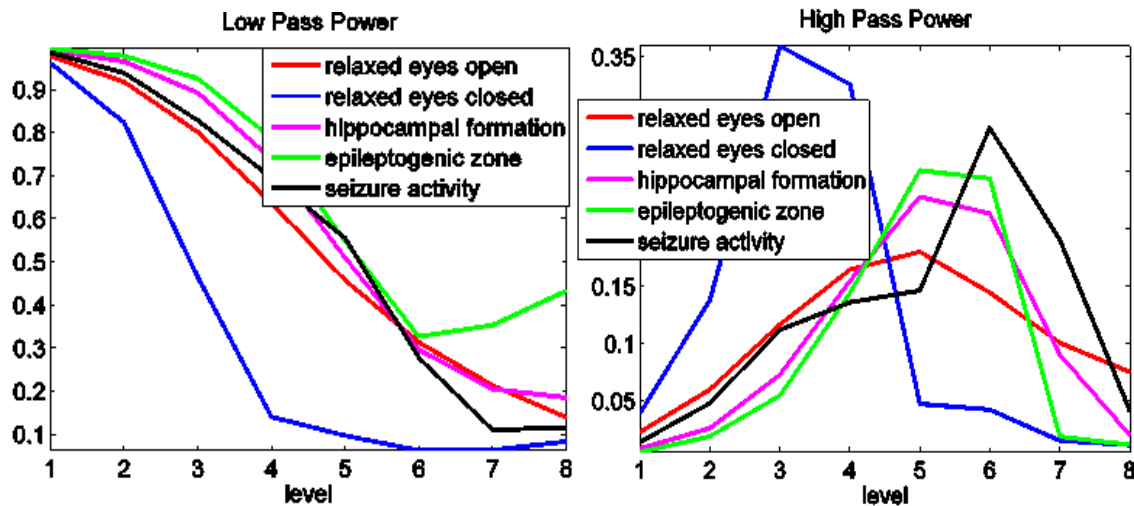
Figure IV: Plot of typical eight level normalized low pass and high pass power of all conditions.

**Cumulative Sum of CWT Coefficients**

In statistical quality control cumulative sum is a sequential analysis technique typically used for monitoring change detection. In statistical quality control the **CUMSUM** (or **cumulative sum**) is a sequential detection. As its name implies, CUMSUM involves the calculation of a cumulative sum (which is what makes it "sequential"). Samples from a process $x_n$ are assigned weights $\omega_n$, and summed as follows:

$$S_{n+1} = \max(0, S_n + x_n - \omega_n), S_0 = 0$$

When the value of *S* exceeds a certain threshold value, a change in value has been found. The above formula only detects changes in the positive direction. When negative changes need to be found as well, the min. operation should be used instead of the max.operation, and this time a change has been found when the value of *S* is *below* the (negative) value of the threshold value.

In order to properly study the scalogram behaviour at different scales, the cumulative sum of the magnitude of wavelet coefficients over time and also on log scale is computed. It is very interesting to note that, in all the data samples, cumulative power shows different behaviour between different conditions at certain scale range. A typical plot of cumulative power as a function of scale values between 1-30 is shown in figureV. This behaviour is observed in almost all samples, albeit at different scale values. It is found that power is more between the scales 12 to 14 in relaxed closed eyes condition. It may be attributed to alpha wave.
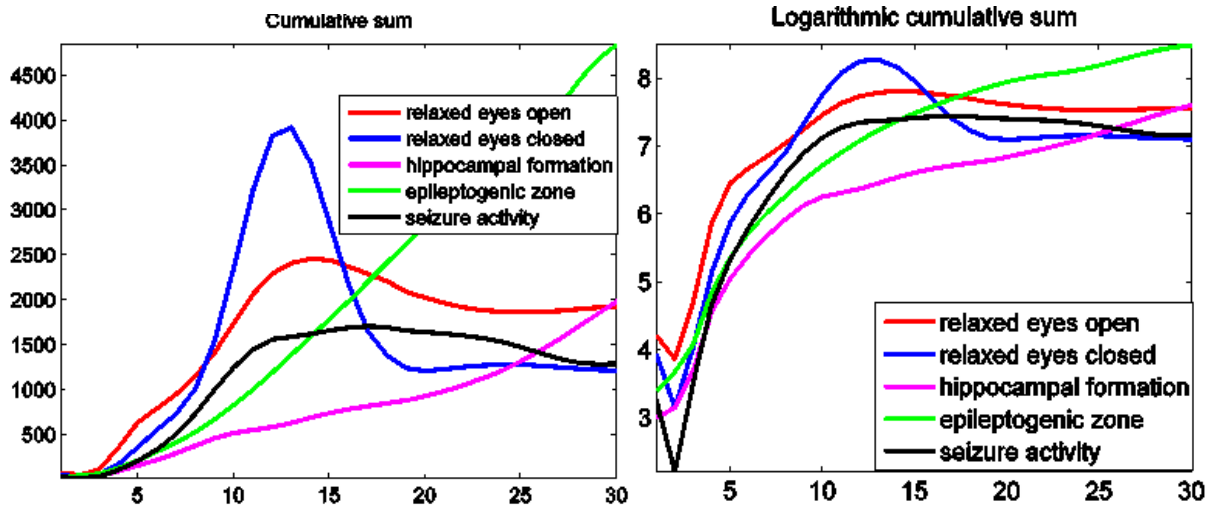
Figure V: (a) Cumulative sum of wavelet coefficients and on (b) logarithmic scale.

Alpha is the frequency range from 8 Hz to 12 Hz [1]. Hans Berger named the first rhythmic EEG activity he saw, the "alpha wave." This is activity in the 8–12 Hz range seen in the posterior regions of the head on both sides, being higher in amplitude on the dominant side. It is brought out by closing the eyes and by relaxation. It was noted to attenuate with eye opening or mental exertion.Its location is in posterior regions of head, both sides, higher in amplitude on dominant side. All the results with sensitivity 85% of the different brain scans, depict a similar result pattern.

**Conclusion**

The continuous wavelets have pinpointed significant differences in the different conditions of EEG. The multiresolution ability and the overcomplete nature of the continuous Morlet wavelets are responsible in finding out these minute differences with a high sensitivity of 85%. High pass power and cumsum of wavelet coefficients together can give better insight of EEG conditions and can be robust diagnostic parameters. In conclusion the use of wavelet transform allowed a scale dependent separation of average behaviour, which is less prone to statistical and experimental uncertainties.

**References**
1. F.H. Lopes da Silva, Electroencephalogr. Clin. Neurophysiol.**79**, 81 (1991).

2. H. O. Lu¨ders and I. Awad, in *Epilepsy Surgery*, edited by H. O. Luders (Raven  Press, New York, 1991), pp. 51–61.

3. S. Weigend and N. A. Gershenfeld, *Time Series Prediction: Forecasting the Future and Understanding the Past*, Proceedings of the Santa Fe Institute Studies in the Science of Complexity Vol. XV (Addison -Wesley, Reading, 1993).

4. Daubechies, *Ten Lectures on Wavelets*, (CfreBMS-NSF regional conference series in applied mathematics, Philadelphia, PA, 1992, Vol. 64).

5. B. B. Hubbard, *The World According to Wavelets,* 2nd edition, UniversityPress (India), Hyderabad, (2003).

6. EEG time series are available under http://www.meb.unibonn. de/epileptologie/science/physik/eegdata.html

7. Lorena Orosco, Agustina Garces Correa, Eric Laciar, *Review: A survey of performance and techniques of automatic epilepsy detection.* Journal of Medical & Biological Engg. 33(6), 2013, 526 – 537

# Quarkonium: a comparison with Positronium

Tanvi Bhavsar[1,*] and Manan Shah [2] and P.C. Vinodkumar[1]

*tanvibhavsar1992@yahoo.com

[1]Department of Physics, Sardar Patel University, Vallabh Vidyanagar, Gujarat.

[2]P. D. Patel Institute of Applied Sciences, CHARUSAT, Changa, 388421, India

**Abstract:**

Quarkonium is a flavorless meson whose constituents are quark (c,b) and its anti quark($\bar{c}, \bar{b}$) where as Positronium (Ps) is a composition  of an electron and its anti-particle, a positron. Positronium consists of two fermionic particles, the total spin of the system couples to a singlet s = 0 and a triplet s= 1 state same as quarkonia. To study the mass spectrum of quarkonium we have used two-Body Dirac equations  to investigate the problem of highly relativistic quarks in meson bound states. From our observations it has been noticed that at low energies,  quarkonium spectrum is very similar to that of Positronium.  Similarity in both the cases they decay  either through the annihilation of its constituents or through electromagnetic transitions . The only difference between quarkonium  and Positronium is with respect to the fundamental forces which hold them together. Positronium is held together solely by the electromagnetic force, as it consists of a pair of colorless leptons, while quarkonium not only feels electromagnetic attraction, but  also the much stronger colour force, which dominates the potential.  The spectra of quarkonium (Charmonium and bottomonium) will be compared with the spectra of positronium to highlight the similarities and differences.

**Keywords:** Quarkonium, mass spectra, similarities and differences

**Introduction:**

Quarkonium the flavorless colourless quark-antiquark systems are of great interest in the field of hadron physics. The high energy experiments world over have recorded many many quarkonia states in the charm and bottom sector [1] etc. Theoretically many of these states are standard as analogy with positronium.



Positronium          Charmonium          Bottomonium
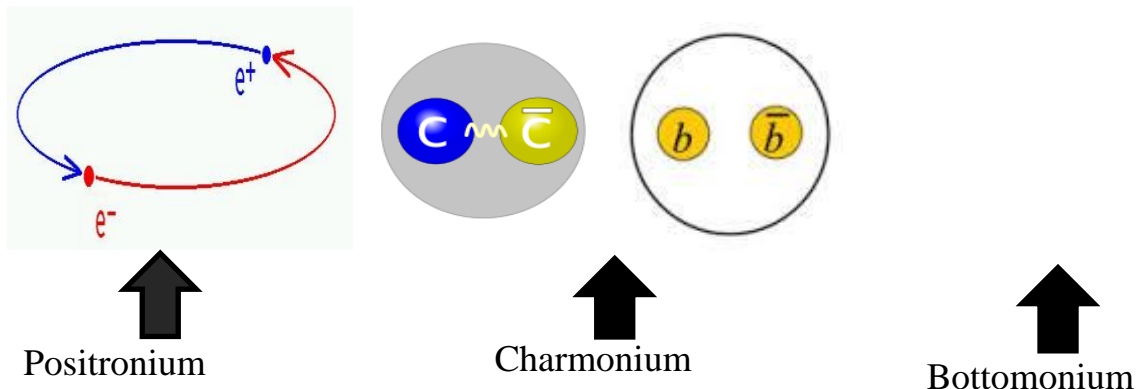
The spectrum of Positronium is very much similar to of that charmonium and bottomonium at least at low energies. To study the mass spectrum of quarkonium we have used Relativistic Dirac Formalism to investigate the problem of relativistic quarks inside the meson. Aim of our work is to compare mass spectra of quarkonium (Charmonium and bottomonium) with the spectra of positronium to get more information about Hadron Structure and strong interactions. This paper is organized as follows: after the introduction, in section II we present our theoretical formalism that we have used to obtain mass spectra of charmonium and bottomonium. In section III, mass spectra of charmonium, bottomonin and positronium are comparedand in section IV we discuss our results and in view of the latest experimental data.

**Theoratical formalism**

In the present study we assume that meson which is containing quark and anti quark is independently confined by a potential [2,3],

$$V(r) = \frac{1}{2}(1 + \gamma_0)(\lambda r^{1.0} + V_0)$$

Where $\lambda$ is the strength of the confinement part of the potential and $V_0$ is a constant negative potential depth. To first approximation, the confining part of the interaction is believed to provide the zero[th] order quark dynamics inside the meson through the quark Lagrangian density [2,3],

$$\mathcal{L}_q^0(x) = \bar{\psi}_q(x)\left[\frac{i}{2}\gamma^\mu \overrightarrow{\partial_\mu} - V(r) - m_q\right]\psi_q(x)$$

The Dirac equation is obtained from $\mathcal{L}_q^0(x)$ ,4],

$$[\gamma^0 E_q - \gamma.\mathbf{P} - m_q - V(r)]\psi_q(\mathbf{r}) = 0$$

To obtain binding energy we have to solve the two component (positive and negative energy) Dirac equation. Its solution can be written as [4,5],

$$\psi_{nlj}(r) = \begin{pmatrix} \psi_{nlj}^{(+)} \\ \psi_{nlj}^{(-)} \end{pmatrix}$$

where the positive and negative energy solutions corresponds to the quark and antiquark respectively are written as [4,5],

$$\psi_{nlj}^{(+)}(\mathbf{r}) = N_{nlj}\begin{pmatrix} ig(r)/r \\ (\sigma.\hat{r})f(r)/r \end{pmatrix}\mathcal{Y}_{ljm}(\hat{r}),$$

$$\psi_{nlj}^{(-)}(\mathbf{r}) = N_{nlj} \begin{pmatrix} i(\sigma.\hat{r})f(r)/r \\ g(r)/r \end{pmatrix} (-1)^{j+m_j-l} \mathcal{Y}_{ljm}(\hat{r})$$

$N_{nlj}$ is the overall normalisation constant. The corresponding energy eigen value is given by[4,5],,

$$\epsilon = (E_D - m_q - V_0)(m_q + E_D)^{\frac{1}{3}} \lambda^{\frac{-2}{3}}$$

Mass of particular Quark-Antiquark system can be written as [4,5],

$$M_{Q\bar{Q}} = E_D^Q + E_D^{\bar{Q}} - E_{cm}$$

Here, $E_{cm}$ in general can be state dependent which we absorb in our potential parameter $V_0$, making $V_0$ as state dependent parameter.

**Comparis on of mass spectra  of charmonium and bottomonium with positronium**
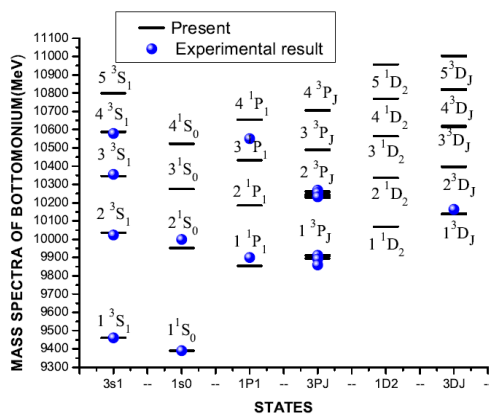


Fig 1 represents the mass spectra of bottomonium (in MeV)
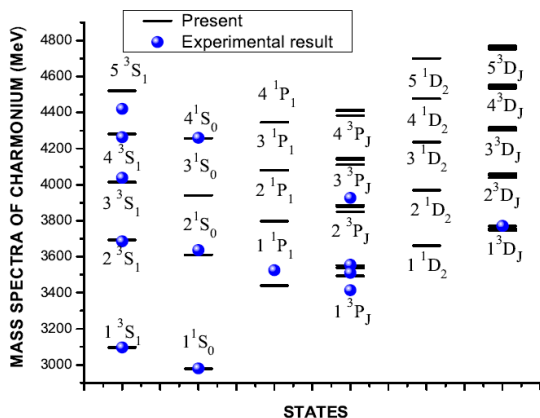


Fig 2 represents the mass spectroscopy of Charmonium (in MeV)
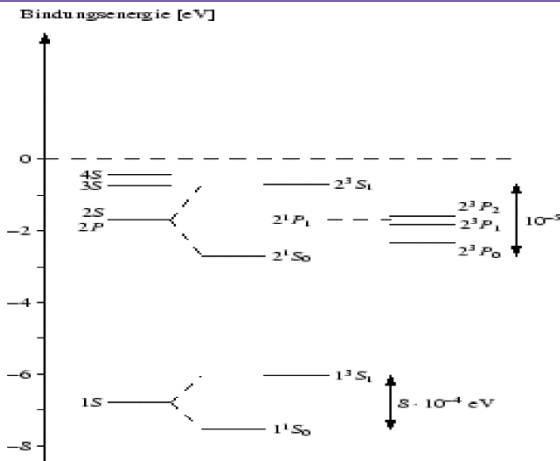
Fig 3 represents the mass spectra of Positronium (in MeV)

**Results and discussion**

- Our computed mass spectra for quarkonium is in good agreement  with experimental results.

- From our observations it has been noticed that at low energies,  quarkonium spectrum is very similar to that Positronium and deviations from the spectrum of the positronium are only obtained with higher excitations. Another similarity is  their binding energies are relatively small.

**ACKNOWLEDGMENTS**

**Reference:**

[1] K.A.Olive et al.(Particle data group) chin. Phys.C,  2014,  **38**,090001.

[2] M. Shah, B. Patel and P. C. Vinodkumar, Phys. Rev. D 2014, **90**, 014009.

[3] M. Shah, B. Patel and P. C. Vinodkumar, Phys. Rev. D 2016, **93**, 094028.

[4] W.Greiner,'Relativistic Quantum Mechancs - Wave Eqautions', Springer-Verlag Berlin Heidelberg 1990, NY. U.S.A.

[5] G. Aruldhas , 'Quantum mechanics', PHI Learing Private Limited, New Delhi, Second Edition.

# Theoretical Study of Knight-Shifts in Liquid Alkali Metals

A. M. Vora and P. N. Gajjar

Department of Physics, University School of Sciences, Gujarat University,

Ahmedabad-380009, Gujrat, India

E-mail : voraam@gmail.com, pngajjar@rediffmail.com

**Abstract**

In the present paper, we report the knight-shifts of liquid alkali metals at their melting point temperature using a model potential formalism. A universal model potential given by Fiolhais *et al.* is used for the first time with five local field correction functions proposed by Hartree (H), Taylor (T), Ichimaru-Utsumi (IU), Farid *et al.* (F) and Sarkar *et al.* (S) in the present computation and found suitable for such study. The theoretical structure factors due to PY theory is adopted for generating the structure factor. It is concluded that, the comparisons of present results with theoretical findings wherever exists are highly encouraging.

**Keywords    :**    Pseudopotential; knight-shifts; structure factor; liquid alkali; local field correction functions.

## Introduction

Knight-shift measurements in metals and alloys are of interest because they provide a delicate probe of both the electronic and magnetic properties in the vicinity of the resonant nucleus. In spite of the extensive theoretical work done in this field, it can still be said that a description of the knight-shift which consistently incorporates all the effects that have been considered important (such as self constancy and core polarization) is still lacking. Also, the Knight-shift of simple metals at their melting temperature based on pseudopotential has been studied by many authors [1-13]. Previously, Styles and Tranfield [4] have studied the knight-shift of about 18 simple liquid metals using non-local pseudopotential theory with reasonable accuracy. Mishra *et al.* [7] have used non-local form of pseudopotential for the calculation of the knight-shift of simple liquid metals. Their results show deviation from the experimental values ranging 0%-15% and 0%-69% respectively. Halder [10, 11] has reported knight-shift of liquid metals and their alloys using model potential formalism. Zaremba and Zobin [12] have studied knight-shifts in simple metals using density functional approach. Very recently, knight-shifts of some liquid non-transition and transition metals using newly proposed model potential was

reported by Baria [13] and found suitable for his study. We have also reported knight-shift data of large number of metals [3] with empty core model (EMC) potential of Ashcroft [14].

In the present paper, we are intended to report the knight-shifts of liquid alkali metals based on the universal model potential of Fiolhais *et al.* [15]. In the present work, the theoretical structure factors are computed from the Percus-Yevic (PY) hard sphere model with proper packing density $\eta$ [16]. Five different types of the local field correction functions proposed by Taylor (T) [17], Ichimaru-Utsumi (IU) [18], Farid *et al.* (F) [19] and Sarkar *et al.* (S) [20] are employed for the first time to investigate the influence of the exchange and correlation effects with reference to the static Hartree (H) [21] screening function in the present computations.

**Computational Methodology**

The knight-shift in liquid metals is described by the equation [1-13]

$$K = \frac{2}{3} \chi_S \Omega_O \left\langle \left| \Psi_{k_F}(0) \right|^2 \right\rangle. \tag{1}$$

Where, $\Omega_O$ is the atomic volume, $\chi_S$ is the Pauli susceptibility per unit volume of the conduction electrons and $\Psi_{k_F}(r)$ is the wave function of an electron at the Fermi surface.  In the free electron approximation the temperature dependence of the knight-shifts at a constant volume in the liquid phase is given by [1-13]

$$\frac{\partial \ln K}{\partial T} = \frac{-3Z}{4T_m E_F k_F^2} \int_0^\infty a(q) W(q) \left( \frac{q}{2k_F} \right) \ln \left| \frac{q + 2k_F}{q - 2k_F} \right| d\left( \frac{q}{2k_F} \right), \tag{2}$$

and the knight-shift of a liquid metal is given by [5, 9]

$$\frac{K_1}{K_O} = \frac{-3Z}{4E_F k_F^2} \int_0^\infty a(q) W(q) \left( \frac{q}{2k_F} \right) \ln \left| \frac{q + 2k_F}{q - 2k_F} \right| d\left( \frac{q}{2k_F} \right). \tag{3}$$

Here $a(q)$ is the structure factor derived via the Percus-Yevic (PY) hard sphere model [16] and depends only on the packing fraction $\eta$, $W(q)$ the screened form factor, $T_M$ the melting

temperature, $E_F = \left(\hbar k_F^2 / 2m\right)$ the Fermi energy and $k_F = \left(3\pi^2 Z / \Omega_O\right)^{1/3}$ the Fermi wave vector with $\Omega_O$ the atomic volume of the liquid metals.

The universal model potential of Fiolhais *et al.* [15] is used in the present computation including five different types of the local field correlation functions [17-21]. The form factor explored in the present investigation is of the form [15],

$$V(q) = \frac{4\pi Z e^2 R^2}{\Omega_O \, \varepsilon(q)} \left[ \frac{-1}{(qR)^2} + \frac{1}{\left[(qR)^2 + \alpha^2\right]} + \frac{2\alpha\beta}{\left[(qR)^2 + \alpha^2\right]^2} + \frac{2A}{\left[(qR)^2 + 1\right]^2} \right], \qquad (4)$$

with $x = r/R$, $R$ being a core decay length, and with $\alpha > 0$. An analyticity condition at $r = 0$ determines the parameters $A$ and $\beta$ in terms of $\alpha$ as follows,

$$\beta = \frac{\alpha^3 - 2\alpha}{4\left(\alpha^2 - 1\right)} \quad \text{and} \quad A = \frac{1}{2}\alpha^2 - \alpha\beta. \qquad (5)$$

Also, $Z$ is the valence, $\Omega_O$ the atomic volume and $\varepsilon(q)$ the modified Hartree dielectric function [21].

**Results and Discussion**

The input parameters and constants used in the present calculations are given in Table 1. Our present investigation of the knight-shifts $\left(K_1/K_O\right)$ and the temperature coefficients of knight-shifts of alkali metallic elements are narrated in Tables 2-3 with the theoretical [13] data wherever exists in the literature.

**Table 1.        Input parameters and other constants.**

| Metals | Z | $\Omega_O$ (au) | T (K) | η | $\alpha$ (au) | R (au) |
|--------|---|-----------------|-------|------|---------------|--------|
| Li | 1 | 142.47 | 453 | 0.46 | 3.546 | 0.361 |
| Na | 1 | 254.25 | 378 | 0.46 | 3.074 | 0.528 |
| K | 1 | 480.84 | 343 | 0.46 | 2.806 | 0.745 |
| Rb | 1 | 588.98 | 313 | 0.43 | 2.749 | 0.823 |
| Cs | 1 | 743.53 | 323 | 0.43 | 2.692 | 0.919 |

**Table 2.** **Knight-shifts$(K_1/K_O)$ of liquid alkali metals at melting point.**

| Metals | Present results | | | | | Others [13] |
| --- | --- | --- | --- | --- | --- | --- |
| | H | T | IU | F | S | |
| Li | 0.0994 | 0.1318 | 0.1066 | 0.1375 | 0.1172 | 0.126 |
| Na | 0.1270 | 0.1769 | 0.1375 | 0.1856 | 0.1546 | 0.206 |
| K | 0.1639 | 0.2438 | 0.1798 | 0.2574 | 0.2075 | 0.303 |
| Rb | 0.2094 | 0.318 | 0.2305 | 0.3367 | 0.2685 | 0.378 |
| Cs | 0.2295 | 0.3587 | 0.2539 | 0.3807 | 0.299 | 0.425 |

Table 3.The temperature coefficients of knight-shifts (in $10^{-4}$ K$^{-1}$) of liquid alkali metals at melting point.

| Metals | Present results | | | | | Others [13] |
| --- | --- | --- | --- | --- | --- | --- |
| | H | T | IU | F | S | |
| Li | 3.2025 | 3.3424 | 3.2349 | 3.2254 | 3.2244 | 3.9 |
| Na | 3.0591 | 3.2148 | 3.0975 | 3.0449 | 3.0729 | 3.5 |
| K | 3.0930 | 3.2687 | 3.1399 | 3.0123 | 3.0902 | 2.5 |
| Rb | 3.3125 | 3.4646 | 3.3586 | 3.1355 | 3.2743 | 3.8 |
| Cs | 3.2445 | 3.3944 | 3.2927 | 3.026 | 3.1945 | 1.9 |

From the study of Table 2-3, it can be noted that among the five employed local field correction functions, the local field correction function due to H (without exchange and correlation) gives the lowest value of knight-shifts$(K_1/K_O)$ and the temperature coefficients of knight-shifts of liquid alkali metals at melting point while the local field correction function due to T and F gives the highest values of the properties. The presently computed all results are found in qualitative agreement with the available theoretical [13]. In comparison with the presently computed results of the knight-shifts of various local field correction functions with respect to static H-function, the percentile influence for all liquid alkali metals is found of the order of 0.09%-15.11% while those found for the temperature coefficients of knight-shifts of liquid alkali metals at melting point is of the order of 0.46%-15.10%, respectively.

According to the Styles and Tranfield [4], have concluded that the knight-shifts calculations are not particularly sensitive to the exact values of the structure factor of the metallic elements and

uncertainties in the results cannot account for the differences between theory and experiment. Also, the values of the conduction electron spin susceptibility used in the present computation of the knight-shifts are responsible for significant variations. The numerical values of the knight-shifts $(K_1/K_O)$ and the temperature coefficients of knight-shifts are found to be quite sensitive to the selection of the local field correction functions and showing a significant variation with the change in the functions. Neither the experimental result for alkali metallic elements at a constant volume and the knight-shifts are available, so the present investigations are found in predictive nature.

## Conclusions

It is concluded that, we are reporting here the knight-shifts of some liquid alkali metals for the first time using a Fiolhais *et al.*'s universal model potential with PY structure factor and different local field correction functions. Hence, such potential can predict the trend of the potential over the alkali elements.

## Acknowledgements

## References

[1] M. Shimoji, Liquid metals, Academic Press, London, 1977.

[2] T. E. Faber, An Introduction to the theory of liquid metals, Cambridge University Press, London, 1972.

[3] Aditya M. Vora, Chinese J. Phys., 2008, 46, 426.

[4] G. A Styles, G. Tranfield, J. Phys. F.: Metal Phys., 1978, 8, 2035.

[5] F. Seitz, D. Turnbull, Solid State Physics, Vol. 2, Academic press, New York, 1956.

[6] A. L. Ritter, J. A. Gardner, Phys. Rev., 1971, 3, 46.

[7] B. Mishra, L. K. Das, T. Sahu, G. S. Tripathi, P. K. Mishra, J. Phys.: Conden. Mat., 1990, 2, 9891.

[8] J. Behari, Phil. Mag., 1972, 26, 737.

[9] M. Watabe, M. Tahaka, H. Endo, B. K. Jones, Phil. Mag., 1965, 12, 347.

[10] N. C. Halder, J. Chem. Phys., 1970, 52, 5450.

[11]    N. C. Halder, Phys. Rev. 1969, 177, 471.

[12]    E. Zaremba, D. Zobin, Phys. Rev. Lett., 1980, 44, 175.

[13]    J. K. Baria, Chinese J. Phys., 2003, 41, 528.

[14]    N.  W.  Ashcroft, Phys. Lett., 1966, 23, 48.

[15]    C. Fiolhais, J. P. Perdew, S. Q. Armster, J. M. MacLaren, M. Brajczewska, Phys Rev B, 1995, 51, 14001.

[16]    J. K. Percus, G. J. Yevick, Phys. Rev., 1958, 110, 1.

[17]    R. Taylor, J. Phys. F: Metal Phys., 1978, 8, 8.

[18]    S. Ichimaru, K. Utsumi, Phys. Rev. B, 1981, 24, 7385.

[19]    B. Farid, V. Heine, G. E. Engel, I. J. Robertson, Phys. Rev. B, 1993, 48, 11602.

[20]    A. Sarkar, D. S. Sen, S. Haldar, D. Roy, Mod. Phys. Lett. B, 1998, 12, 639.

[21]    W. A. Harrison, Elementary Electronic Structure, World Scientific, Singapore, 1999.

# Some static and vibrational properties of strontium using local pseudopotential

## B.S. Pandya[1*], D.D. Satikunvar[1], R. H. Joshi[1], N. K. Bhatt[2] and B. Y. Thakore[1]

[1]Department of Physics, Sardar Patel University, Vallabh Vidyanagr – 388 120, Gujarat, India.

[2]Department of Physics, M. K. Bhavnagar University, Bhavnagar – 364 001, Gujarat, India.

E-mail : bhumispandya@gmail.com

## Abstract

Within the frame work of second order perturbation theory based on pseudopotential we have calculated the interatomic pair potential for the elemental strontium employing two parametric *evanescent* form of local pseudopotential along with Ichimaru and Utsumi dielectric screening function which plays a role of exchange and correlation. Presently, we have calculated interatomic force constants up to 37 shells, dynamical elastic constants, bulk modulus, deviation from Cauchy relation, Poisson's ratio, Young's modulus and propagation velocity of elastic waves. Overall, we found an excellent agreement of our results with other available results experimental as well as theoretical.

## Keywords

Strontium, elastic constants, pseudopotential, central force

## Introduction

The alkaline earth metals make up group IIA of the modern periodic table. Naturally occurring element strontium occupies all most middle position in the family and it is more reactive than Ca and Mg but less active than Ba, preserving face centered cubic structure at the ambient environment. The alkaline earth metal recognized as the empty *d*-band metals and the band structure and the other physical properties of them strongly influenced via hybridization effects at and below Fermi level. All though the vast amount of work has been carried out by the researchers on the alkaline earth metals but the case of strontium is not much attempted. As much as the technological applications are concern, the comprehension of the elastic properties of any metal is at prime importance. The behavior of the elasticity of the Sr can be studied by

investigating the static and vibrational properties of it. The simplest approach is assumption of central force between the pair of ions or atoms. Also, keeping in mind that the non local effects are negligible in the effective electron-ion interaction and local potential is sufficient to describe behavior of interaction, we can calculate elastic properties by the method of homogeneous deformations. The lattice dynamical properties, within the framework of second order perturbation treatment on the pseuedopotential, has been subject of many studies. Following to this, hereby we have calculated the effective ion-ion potential along with interatomic force constants which are useful while studying the dynamical elastic constants, shear modulus and bulk modulus. This set of data is efficient in evaluation of violation of Cauchy's relation, Poisson's ratio, Young's modulus and propagation velocities of elastic waves. We have used local form of pseudopotential proposed by Fiolhais *et al.* [1] for exploration of above properties and dielectric screening function due to Icihmaru and Utsumi [2] is bring into play to mimic the role of exchange and correlation. Our main objective is  to compare our results with the available experimental as well as other theoretical data and to check the applicability of the formalism.

## Evanscent pseudopotential

A "structured" local electron-ion pseudopotential have been proposed by the Fiolhais *et al.* [1] which resolves the drawback of the structureless pseudopotential. This proposed pseudopotential depends on the density on the surface of Wigner-Seitz cell, which is given as equilibrium number of valence electrons in the interstitial region, instead of density parameters $R_s$ and valence Z. This potential was formulated directly in and for the solid state so the complexity of transferability to the solid state does not occur.

After motivated by earlier proposed pseudopotential due to Hellmann [5,6] and orthogonality arguments [7], authors given the smooth local pseudopotential which has evanescent form (i.e. as $r \rightarrow \infty$) exponential decay of the core repulsion) as,

$$V(r) = -\frac{ze^2}{R}\left\{\frac{1}{x}[1 - (1 + \beta x).e^{-\alpha x}] - Ae^{-x}\right\}. \tag{1}$$

Having,  $x = \frac{r}{R}$; R stands for the core decay length and $\alpha$ is a positive parameter.

The local pseudopotential in the form of equation (1) is continuous and its derivatives are also continuous. This is specially constructed to have a finite value at $r \rightarrow 0$ and first and third

derivatives are zero. A and $\beta$ can be determine in terms of $\alpha$ by an analytical condition at $r = 0$. By expanding the equation (1) about x within limit $x \to 0$, we have

$$\omega \to -\frac{ze^2}{R} \left\{ \begin{array}{c} [\alpha - \beta + A] \; + \frac{x}{1!}\left[-\frac{1}{2}\alpha^2 + \alpha\beta \; + A\right] \\ + \frac{x^2}{2!}\left[\frac{1}{3}\alpha^2 - \alpha^2\beta + A\right] \\ + \frac{x}{3!}\left[-\frac{1}{4}\alpha^4 + \alpha^3\beta + A\right] + \cdots \end{array} \right\} \tag{2}$$

As first and third derivatives vanish so one can write,

$$-\frac{1}{2}\alpha^2 + \alpha\beta \; + A = 0 \quad\text{and}\quad -\frac{1}{4}\alpha^4 + \alpha^3\beta + A = 0$$

By solving above equations, we have A and $\beta$ as,

$$A = \left(\frac{\alpha^2}{2} - \alpha\beta\right) \quad\text{and}\quad \beta = \frac{(\alpha^3 - 2\alpha)}{4(\alpha^2 - 1)} \tag{3}$$

By the Fourier transform of equation (1) we have q-space representation for the pseudopotential as,

$$V(q) = \frac{8\pi Ze^2 R^2}{\Omega}\left[\frac{-1}{(qR^2)} + \frac{1}{[(qR^2)+\alpha^2]} + \frac{2\alpha\beta}{[(qR^2)+\alpha^2]^2} + \frac{2A}{[(qR^2)+1]^2}\right], \tag{4}$$

At $r = 0$, smoothness and analyticity are responsible for better convergence of sums over reciprocal lattice vectors ($\lim q \to$, $\omega(q) \sim q$-8).

Authors have determined two parameters R and $\alpha$ by employing two conditions. One is zero pressure at observed density $R_s$. (i.e. $R_s$ is the empirical input) and second is valence interstitial electron number $N_{int}$. There are two different ways for the determination of parameters R and $\alpha$ namely, "Universal" and "Individual". If $N_{int}$ is kept equal to uniform-electron-value at zero pressure condition, one can attain "Universal set of Parameters" and if the $N_{int}$ is evaluated to actual value for each metal, the "individual set of Parameters" can be conquered. But it is found that bulk properties can be more accurately determined by individual set of parameters so

we have used the individual set of parameters throughout the calculations. Table 1 shows the individual set of parameters and other input data used for computations.

## Table1

Pseudopotential parameters (proposed by Fiolhais *et al*. [1] ) and supplementary input data for computations.

| Metal | Crystal Structure | Pseudopotential Parameters [1] | | Valence (Z) | Mass of ion M [3] (a.m.u.) |
|-------|-------------------|--------------------------------|----|-------------|----------------------------|
| | | $\alpha$ | R (a.u.) | | |
| Sr | FCC | 3.176 | 0.614 | 2 | 87.62 |

## Effective ion-ion potential

In the second order perturbation theory, the effective interatomic pair potential of a given metal is a sum of the Coulombian repulsive interaction between two ions and attractive interaction between an ion and screening electron cloud. This effective inter-atomic pair potential can be given as,

$$V(r) = \frac{Z^2 e^2}{r} + \frac{\Omega_o}{\pi^2} \int F(q) \frac{\sin(qr)}{qr} q^2 \, dq \tag{5}$$

In this equation, Z is the valence. e and $\Omega$ are the electronic charge and atomic volume respectively. The first term in the above equation represents the direct repulsive coulombian interaction between the ions and the second term gives the indirect interaction of the conduction electrons and ions. This indirect interaction can be evaluated using the energy wave number characteristics as,

$$F(q) = -\frac{\Omega_o q^2}{16\pi} |W_B(q)|^2 \frac{\varepsilon_H(q) - 1}{1 + (\varepsilon_H(q) - 1)(1 - f(q))} \tag{6}$$

Here, $\varepsilon_H(q)$ is the Hartree dielectric screening function [4] and f(q) represents the local field correction function, which represents the exchange and correlation effects and as mentioned earlier we have used IU [3] screening function throughout the present work. To investigate the

various physical properties at different temperature one should have the knowledge about the temperature dependent pair potential. The temperature dependent pair potential can be obtained by the multiplication of the dimensionless damping term $\exp\left(-\frac{\pi k_B T}{2 k_F} r\right)$ with pair potential. It will provide the necessary Friedel damping at high temperature as anticipated. With the following equation we can obtain the pair potential at desired temperature.

$$V(r, T) = V(r) \exp\left(-\frac{\pi k_B T}{2 k_F} r\right) \tag{7}$$
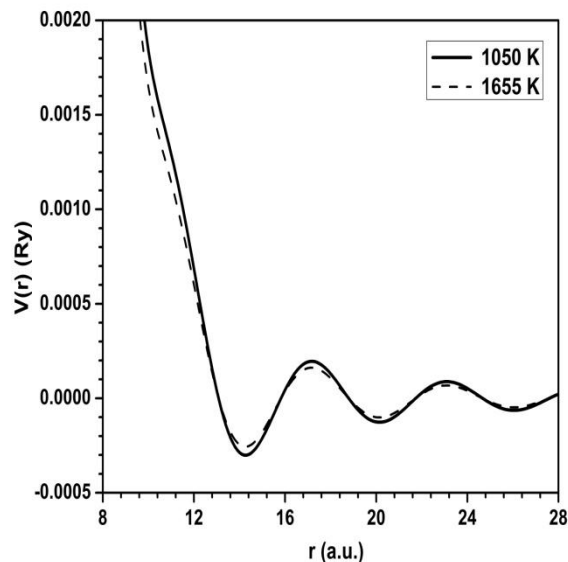


**Figure 1** Interatomic potential for solid Sr. Full line is for the temperature 1050 K and dotted line is for 1655 K.

## Radial ($K_r$) and Tangential ($K_t$) Force Constants

The force acting between two atoms or ions depends on the distance between them.  A pair of the ions interacting due to a central interaction have two independent interatomic force constant, namely tangential ($K_t$) and radial ($K_r$). Exploiting interionic potential V(r), we can acquire tangential and radial force constant in real space as follows [8-12].

The tangential force constants ($K_t$) given as,

$$K_t = \frac{1}{r} \frac{dV(r)}{dr}$$

$$= \frac{-Z^2 e^2}{r^3} + \frac{\Omega}{\pi^2 r^2} \int_0^\infty F(q) q^2 \left( \cos qr - \frac{\sin qr}{qr} \right) dq \qquad (8)$$

The radial force constants ($K_r$) given as,

$$
\begin{aligned}
K_r &= \frac{d^2 V(r)}{dr^2} \\
&= \frac{2Z^2 e^2}{r^2} + \frac{\Omega}{\pi^2 r^2} \int_0^\infty F(q) q^2 \left[ \frac{2 \sin qr}{qr} - 2 \cos qr - qr \sin qr \right] dq
\end{aligned} \qquad (9)
$$

By utilizing $K_r$ and $K_t$ we can attain the interatomic force constants $K_{\alpha\beta}$ as a tensor [13,14] as,

$$
\begin{aligned}
K_{\alpha\beta} &= \frac{d^2 \Phi(r)}{dr_\alpha dr_\beta} \\
&= \left[ \delta_{\alpha\beta} - \frac{r_\alpha r_\beta}{r^2} \right] K_t + \frac{r_\alpha r_\beta}{r^2} K_r
\end{aligned} \qquad (10)
$$

Here, $r_\alpha$ and $r_\beta$ stands for the $\alpha^{th}$ and $\beta^{th}$ cartesion components of the position vector r of the ion, correspondingly.

Presently, we have generated the interatomic force constants for 37 shells in the nearest neighbor region in real space. Table 2 contains results of our computations. Our results are in a good agreement with the others. For the sack of simplicity we do not compare our results with other available results.

## Table 2

Radial and Tangential Force Constants in dyne/cm

| Shell No. (n) | Shell Type | No of Atoms N(n) | Radial Force Constants (in dyne/cm) | Tangential Force Constants (in dyne/cm) |
|---|---|---|---|---|
| 1 | (011) | 12 | 7179.075464 | -413.213293 |
| 2 | (002) | 06 | -257.591505 | -35.121496 |
| 3 | (112) | 24 | 228.663676 | 0.077415 |
| 4 | (022) | 12 | -101.013444 | 5.094013 |
| 5 | (013) | 24 | -13.048369 | -3.568812 |
| 6 | (222) | 08 | 52.192484 | -0.295125 |
| 7 | (123) | 48 | -6.242830 | 1.681401 |
| 8 | (004) | 06 | -29.996404 | -0.004955 |
| 9 | (033) | 12 | 1.240236 | -0.934775 |
| 10 | (411) | 24 | 1.240236 | -0.934775 |
| 11 | (420) | 24 | 20.218919 | -0.185348 |
| 12 | (233) | 24 | 6.257654 | 0.527905 |
| 13 | (422) | 24 | -11.666087 | 0.348283 |

| 14 | (510) | 24 | -11.108290 | -0.177179 |
| 15 | (431) | 48 | -11.108290 | -0.177179 |
| 16 | (521) | 48 | 9.849224 | -0.113136 |
| 17 | (440) | 12 | 6.333602 | 0.174637 |
| 18 | (433) | 24 | -2.537991 | 0.227012 |
| 19 | (530) | 24 | -2.537991 | 0.227012 |
| 20 | (600) | 06 | -7.419626 | 0.063720 |
| 21 | (442) | 24 | -7.419626 | 0.063720 |
| 22 | (611) | 24 | -4.961898 | -0.117610 |
| 23 | (532) | 48 | -4.961898 | -0.117610 |
| 24 | (620) | 24 | 1.215748 | 1.215748 |
| 25 | (541) | 48 | 5.417775 | -0.071591 |
| 26 | (622) | 24 | 4.805896 | 0.056829 |
| 27 | (631) | 48 | 0.733630 | 0.119888 |
| 28 | (444) | 08 | -3.280619 | 0.087479 |
| 29 | (017) | 24 | -4.492987 | 0.001386 |
| 30 | (435) | 48 | -4.492987 | 0.001386 |
| 31 | (640) | 24 | -2.566634 | -0.071323 |
| 32 | (633) | 24 | 0.760550 | -0.087229 |
| 33 | (127) | 48 | 0.760550 | -0.087229 |
| 34 | (642) | 48 | 3.208340 | -0.047193 |
| 35 | (730) | 24 | 3.437833 | 0.014906 |
| 36 | (651) | 48 | -0.890747 | 0.064447 |
| 37 | (732) | 48 | -0.890747 | 0.064447 |

## Dynamical Elastic Constants, Shear Modulus and Bulk Modulus

When a crystal is under an external stress and if the deformation is relatively small then the strain is directly proportional to the stress as per the Hooke's law. Thus, the stress and strain components are linear functions of each other and they are associated by elastic stiffness constant. In the cubic crystals there are four three-fold rotation axes. So in cubic crystals there are three independent elastic constants viz. $C_{11}$, $C_{12}$ and $C_{44}$.

The dynamical elastic constants $C_{11}$, $C_{12}$ and $C_{44}$ can be obtained by long wave length phonon velocity method [12] that is the dynamical treatment for computation of the elastic constants as well as incorporating the interatomic force constants $K_{\alpha\beta}^{n}$ at nth neighbour separation.

$$C_{11} = \frac{1}{12a} \sum_n N(n) \left[ x^2 K_{xx}^n + y^2 K_{yy}^n + z^2 K_{zz}^n \right] \qquad (11)$$

$$C_{44} = \frac{1}{24a} \sum_n N(n)\left[(y^2 + z^2)\, K_{xx}^n + (z^2 + x^2)\, K_{yy}^n + (x^2 + y^2)\, K_{zz}^n \right] \qquad (12)$$

$$C_{12} + C_{44} = \frac{1}{6a} \sum_n N(n)\left[ yz\, K_{yz}^n + zx\, K_{zx}^n + xy\, K_{xy}^n \right] \qquad (13)$$

Where, a is a lattice constant and $N(n)$ represents the number of atoms at the nth neighbour separation. Here the atomic position at $n^{th}$ neighbour separation is demonstrated as $\frac{a}{2}(x, y, z)$.

Shear Modulus $(C')$ using equation (11) and (12) can be given as,

$$C' = \frac{(C_{11} - C_{12})}{2} \qquad (14)$$

Similarly the Bulk Modulus (B),

$$B = \frac{[C_{11} + 2C_{12}]}{3} \qquad (15)$$

While evaluating the elastic constants and bulk modulus using interatomic force constants, it is necessary to consider the long-range character for the conversion of calculation. Regarding to this we have performed the real-space sum up to 37 shells. Table 3 contains the calculated elastic constants, shear modulus and bulk modulus along with other experimental and theoretical results. Our results are in a better agreement with them. Little difference in a some of values is due to choice of screening function and form of pseudopotential as far as the theoretical results are concern.

**Table 3**

Elastic constants[$C_{11}$, $C_{12}$ and $C_{44}$ ], Shear modulus [$C'$] and Bulk modulus [B] for Sr. All quantities are in [$10^{12}$ dyne /cm$^2$].

| | Present | Experimental | Other Theoretical Results |
|---|---|---|---|
| $C_{11}$ | 0.2080 | 0.1700 [18] | 0.1910 [24] 0.1888 [19] 0.2500 [20] |
| $C_{12}$ | 0.1588 | 0.1221 [18] | 0.1480 [24] 0.1473 [19] |

| | | | 0.1700  [20] |
|---|---|---|---|
| $C_{44}$ | 0.1005 | 0.099   [18] | 0.0780  [24] |
| | | | 0.1180  [19] |
| | | | 0.1300  [20] |
| $C'$ | 0.0240 | 0.0230  [18] | 0.0215  [24] |
| | | | 0.0400  [20] |
| B | 0.1752 | 0.1200  [18] | 0.1620  [24] |
| | | | 0.1190  [22] |
| | | | 0.1420  [21] |
| | | | 0.1960  [20] |
| | | | 0.1250  [23] |

**Table 4**

Deviation from Cauchy's relation [in $10^{12}$ dyne /cm$^2$], Cauchy's ratio, Poisson's ration and Young's modulus [in $10^{12}$ dyne /cm$^2$] for Sr.

| | Present | Experimental | Other theoretical results |
|---|---|---|---|
| $C_{11} - C_{12}$ | 0.0582 | 0.0470  [18] | 0.0430  [24] |
| $C_{12} / C_{44}$ | 1.5793 | 1.2330  [18] | 1.8970  [24] |
| σ | 0.4329 | 0.4180  [18] | 0.4360  [24] |
| Y | 0.0705 | 0.0590  [18] | 0.0610  [24] |

## Propagation Velocities of the Elastic Waves

Determination of the elastic constants $C_{11}$, $C_{12}$ and $C_4$ gives provision to evaluate the propagation velocity of the elastic waves.

Concerning to the cubic system, the propagation velocity for the longitudinal and transverse waves in symmetry direction [100] are [3,17],

$$v_L \ [1\ 0\ 0] = \left(\frac{C_{11}}{\rho}\right)^{\frac{1}{2}} \tag{21}$$

$$v_T \ [1\ 0\ 0] = \left(\frac{C_{44}}{\rho}\right)^{\frac{1}{2}} \tag{22}$$

Here, $\rho$ is the density of the crystal. The velocity of the elastic waves in [110] direction are [3,17],

$$v_L \ [1\ 1\ 0] = \left[\frac{C_{11} + C_{12} + 2C_{44}}{2\rho}\right]^{\frac{1}{2}} \tag{23}$$

$$v_{T1} \ [1\ 1\ 0] = \left(\frac{C_{44}}{\rho}\right)^{\frac{1}{2}} \tag{24}$$

$$v_{T2} \ [1\ 1\ 0] = \left[\frac{C_{11} - C_{12}}{2\rho}\right]^{\frac{1}{2}} \tag{25}$$

[110] is the face diagonal direction of a cubic crystal. Here three elastic constants can be found from the three different propagation velocities in this direction. The propagation velocity in the [111] direction are [3,17],

$$v_L \ [1\ 1\ 1] = \left[\frac{C_{11} + 2\ C_{12} + 4C_{44}}{3\rho}\right]^{\frac{1}{2}} \tag{26}$$

$$v_T \ [1\ 1\ 1] = \left[\frac{C_{11} - C_{12} + C_{44}}{3\rho}\right]^{\frac{1}{2}} \tag{27}$$

Table 5 shows our computed results as well as other experimental and theoretical results. Results are in a excellent agreement with them.

**Table 5**

Propagation velocities [in $10^5$ cm /sec] of elastic waves in Sr.

| | Present | Experimental | Other Theoretical Results |
|---|---|---|---|
| $V_L$ (100) | 2.83 | 2.62 [18] | 2.78 [24] |
| $V_T$ (100) | 1.97 | 2.00 [18] | 1.77 [24] |
| $V_L$ (110) | 4.68 | 4.26 [18] | 4.48 [24] |
| $V_{T1}$ (110) | 1.97 | 1.40 [18] | 1.77 [24] |
| $V_{T2}$ (110) | 0.97 | 0.98 [18] | 0.93 [24] |
| $V_L$ (111) | 3.45 | 3.30 [18] | 3.28 [24] |
| $V_T$ (111) | 1.38 | 1.40 [18] | 1.27 [24] |

## Conclusion

We have carried out theoretical investigation of static properties of strontium on the basis of pseudopotential method. Our computed results are in outstanding agreement with the experimental results and better than the available other theoretical investigations. The present result has confirmed that the pseudopotential characterized with good $q_0$ value can yield very good results for metalic properties. To extend this work we can also calculate the anisotropy of crystal, temperature variation of the all of above properties. Based on present formulation, the investigation of the electronic properties would be interesting and open problem for future work.

## References

[1]     C. Fiolhais, J. P. Perdev, S.Q. Armster, J.M. MacLaren and Brajazewska, Phys. Rev. B, (1996), **51**, 14001;ibid., **53**, 13193 (E).

[2]     S. Ichimaru and K. Utsumi, Phys. Rev., B**,** (1981), **24**, 7385.

[3]     C. Kittle, "Introduction to the Solid State Physics", Wiley Eastern University Edition, Berkely, CA, (1966).

[4]     W. A. Harrison, "Pseudopotential in the Theory of Metals", W. A. Benjamin, New York, (1966).

[5]     H. Hellmann, Acta Physicochim., USSR, (1934). **1,** 913.

[6]     H. Hellmann, J. Chem. Phys., (1935), **3,** 61.

[7]     B. J. Austine, V. Heine and L. J. Sham, Phys. Rev., (1968). **127**, 276.

[8]     W. M. Shyu and G. D. Gaspari, Phys. Rev., (1968), **170**, 687.

[9]     W. M. Hartmann and T. O. Milbrodt, Phys. Rev. B, (1971). **3**, 4133.

[10]    V. B. Gohel, C. K. Acharya and A. R. Jani, J. Phys. F, (1985), **15**, 279.

[11]    R. F. Wallis, A. A. Maradudin, V. Bortolani, A. G. Eguiluz, A. A. Quong, A. Franchini and G. Santoro, Phys. Rev. B, (1993), **48,** 6043.

[12]    E. G. Brovman and M. Yu. Kagan, "Dynamical Properties of Solids", *Vol. 1 ed*, G. K. Horton and A. A. Maradudin, North-Hollend: Amsterdam, (1974).

[13]    G. L. Krasko and Z. A. Guruskii, Sov. Phys. Solid State, (1971), **13**, 2062.

[14]    Z. A. Gurskii and G. L. Krasko, Sov. Phys. Doklady, (1971), **16,** 298.

[15]    D. Sen and S. K. Sarkar, Phys. Rev. B, (1980), **22**, 1856.

[16]   W. A. Harrison and J. M. Wills, Phys. Rev. B, (1982), **25**, 5007.

[17]   D. L. Jules, "Solid State Physics", *Vol. 2 ed.,* F. Seitz and D. Turnbull, Academic Press: New York, (1956).

[18]   U. Buchenau, M. Heiroth and M. Schober, Phys. Rev. B, (1984), **30**, 3502.

[19]   S. Das and A. Sarkar, Pramana J. Phys., (1987), **28**, 689.

[20]   J. A. Moriarty, Phys. Rev. B, **34**, (1986), 6738.

[21]   D. J. Gonzalez, C. M. Zapata and J. A. Alonso, Phys. Stat. Sol. (b), (1985), **29**, 483.

[22]   G. K. White, J. Phys. F, (1972), **2**, 865.

[23]   L. Pollack, J. P. Predew, J. He, M. Marques, F. Nogueira and C. Fiolhais, Phys. Rev. B, (1997), **55**, 23.

[24]   T. C. Pandya, "A Comprehensive Study of Physical Properties of Alkaline Earth Metals (A Pseudopotential Approch)", Thesis, Gujarat University, (2000).

[25]   E. G. Brovman, Yu. Kagan and A. Kholas, Sov. Phys. Solid Stat., (1970), **12**, 786.

# Electron induced Interactions Cross sections for Methanimine (CH₂NH)

Yogesh Thakar[1], RakeshBhavsar [2], Chetan Limbachiya[3,*]
[1,2]M.N. College, Visnagar -384315
[3]The M.S. University of Baroda, Vadodara – 390001
[*]E-mail:cglimbachiya-appy@msubaroda.ac.in

**Abstract**

In present work electrons induced processes with important astro-compound, Methanimine found in tholins of Titan are investigated. We report calculated total elastic cross sections $Q_{el}$, andtotal cross sections $Q_T$ for Methanimine($CH_2NH$), upon electron impact for energies from ionization threshold to 5 keV. We have employed Spherical Complex Optical Potential (SCOP) formalism to calculate total elastic cross section, total cross sections for compound methanimine total cross sections.

*Keywords*: **Astrocompound compounds, spherical complex optical potential (SCOP), Total cross sections.**

## Introduction

Methanimine is astromolecule, detected in sagattarius-B. Since molecule are in gaseous phase their interaction with electron play important role. Methanimine is of great interest since it is aminoacid precursor. Methaniminecan form simplest amino acid, glycine when it reacts with hydrogen cyanide thus it play significant role in life building block. Methanimine is protonated imines and is detected in an ion composition in agreement with Titan's INMS measurements reinforcing the suspected role in chemical species on aerosol production. [1]Calculations of various cross sections of these targets are in demand in astrophysics
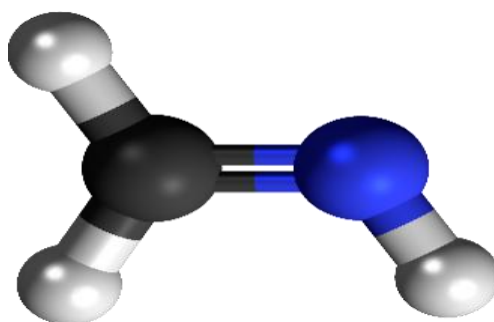


Fig1.Methanimine CH₂NH

**Table 1: Properties of target molecule** [2,3]

| Molecule | I.P. (eV) | Bond lengths(Å) | Polarizability($Å^3$) | Dipole-moment (D) |
|---|---|---|---|---|
| Methanimine ($CH_2NH$) | 10.70 | C=N 1.273 N=H 1.023 C–H 1.081 | 2.47 | 2.00 |

**Theoretical Methodology**

In the present work we have attempted to study the electron driven elastic processes for methanimine molecule through total elastic cross sections relative to the total cross sections. The present calculations are done with Spherical Complex Optical Potential(SCOP) method which is moreappropriate to energy range from threshold to 5 keV.

In order to calculate the total cross sections, we have employed a well-known spherical complex optical potential (SCOP) formalism [4-7] in which the electron-molecule system can be represented by a complex potential,

$$V(r, E_i) = V_R(r, E_i) + iV_I(r, E_i) \tag{1}$$

Where, $V_R(r, E_i)$ is real potential term and $V_I(r, E_i)$ is an imaginary potential term which represents the absorption potential.

Here,

$$V_R(r, E_i) = V_{st}(r) + V_{ex}(r, E_i) + V_{pol}(r, E_i) \tag{2}$$

The three terms on the RHS of Eq. (2) represent various real potentials*viz.*static, exchange and polarization potentials which arise due to electron target interactions. To evaluate all these potentials, the most basic input is charge density of the target. The spherically averaged charge density$\rho(r)$ of the molecule and static potential $V_{st}(r)$ are determined from the constituent atomic charge densities derived from the Hartree-Fockwave functions of given by Cox and bonham [8].

The static potential $V_{st}(r)$ is the potential experienced by the incident electron uponapproaching a field of an unperturbed target charge cloud which is calculated at the Hartree-Fock level using fixed nuclei approximation.

For the exchange potential, we have employed Hara's free electron gas exchange model [9] which is parameter free and energy dependent. For the polarization potential$V_{pol}$, we have used a parameter free model of correlation potential by Zhang et al. [10].

The imaginary part $V_I$ of the complex potential in equation (1) contains absorption potential which represents the effects of all inelastic channels. Here we have employed a well-known non-empirical quasi-free model form given by Staszeweska et al. [11] as given below.

$$V_{abs}(r, E_i) = -\rho(r)\sqrt{\frac{T_{loc}}{2}}\left(\frac{8\pi}{10\,k_f^3 E_i}\right) \times \theta(P^2 - k_F^3 - 2\Delta) \times (A_1 + A_2 + A_3) \qquad (3)$$

The local kinetic energy of the incident electron is $T_{loc} = E_i - (V_{st} + V_{ex})$

The parameters $A_1$, $A_2$, and $A_3$ in equation (3) are given as,

$$A_1 = 5\,\frac{k_f^3}{2\Delta}, \qquad A_2 = \frac{k_f^2(5p^2 - 3k_f^2)}{(5p^2 - 3k_f^2)} \text{ and } A_3 = \frac{2\theta(2k_f^2 + 2\Delta - p^2)(2k_f^2 + 2\Delta - p^2)^{5/2}}{(p^2 - k_f^2)^2}. \qquad (4)$$

The absorption potential is not sensitive to long-range potentials like $V_{pol}$. In equation (4), $p^2 = 2E_i$, $k_F = [3\pi^3\rho(r)]^{1/3}$ is the Fermi wave vector and $\Delta$ is an energy parameter. Further $\theta(X)$ is the Heaviside unit step-function, such that $\theta(X) = 1$ for $X \geq 0$ and is zero otherwise. The dynamic functions $A_1, A_2$ and $A_3$ occurring in equation (4) depend differently on $\theta(X), I, \Delta$ and $E_i$, where $I$ is the ionization threshold of the target. The energy parameter $\Delta$ determines a threshold below which $V_{abs} = 0$, and the ionization or excitation is prevented energetically. In fact $\Delta$ is the governing factor which decides the value of the total inelastic cross sections and that is one of the characteristics of the Staszewska model [11]. We have modified the original model by considering $\Delta$ as a slowly varying function of $E_i$ around $I$ in order to incorporate the inelastic processes occurring even below the ionization potential viz. excitation processes [12-16]. Further $\Delta$ as a variable, accounts for the screening of the absorption potential in the target charge-cloud region as suggested by Blanco and Garcia [17]. This is meaningful since $\Delta$ fixed at $I$ would not allow excitation at incident energy $E_i \leq I$. On the other hand, if the parameter $\Delta$ is much less than the ionization threshold, then $V_{abs}$ becomes exceedingly high near the peak position. The modification introduced in our paper is aimed at assigning a reasonable minimum value 0.8I to $\Delta$ and express this parameter as a function of $E_i$ around $I$ as follows [18]

$$\Delta(E_i) = 0.8I + \beta(E_i - I) \qquad\qquad (4)$$

In equation (4) β is obtained by requiring that $\Delta = I$(eV) at $E_i = E_p$, beyond which $\Delta$ is held constant and equal to $I$. Here $E_p$ is the value of incident energy at which the total inelastic cross sections $Q_{inel}$ reaches its peak. After generating the full complex potential given in equation (1), we solve the Schrodinger equation numerically using partial wave analysis to obtain complex phase shifts that are then used to find the total elastic cross section $Q_{el}$ relative to the total cross sections $Q_T$.

## Results and Discussion



**Figure 2 TCS for e-CH$_2$NH scattering**

**Solid line: Present Q$_T$; Dash line: Present Q$_{el}$**
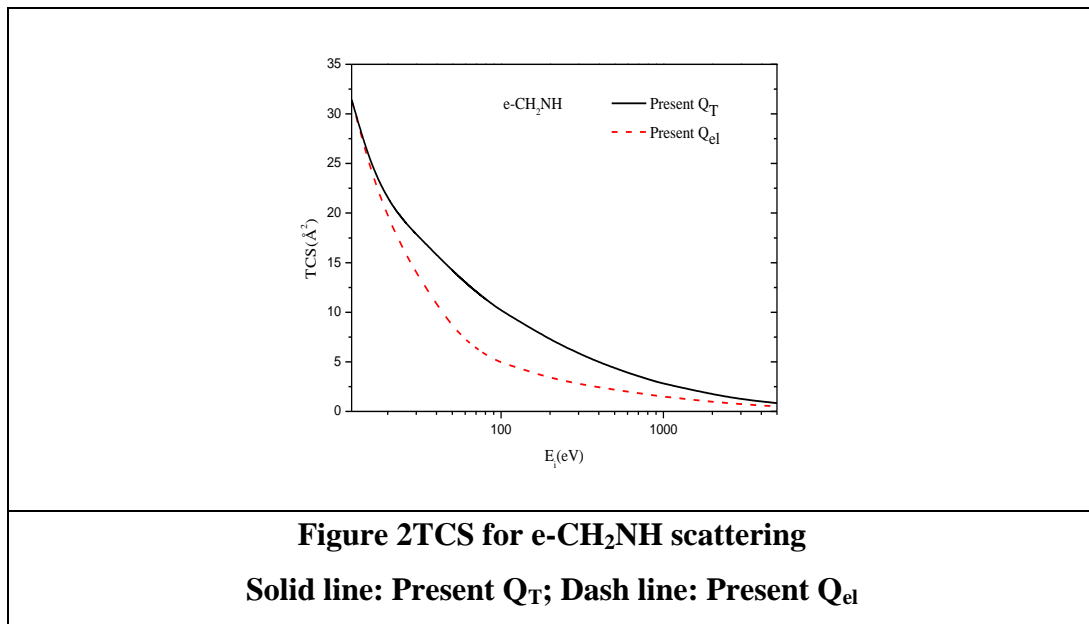
Figure 2 shows present total cross section and present elastic cross sections. Both $Q_{el}$ as well as $Q_T$ tend to follow the ln(E)/E nature at higher energies as expected. Here at high energy electrons are so fast that they do not have sufficient time to interact with target molecule so $Q_{el}$ , and $Q_T$ reduces faster. No theoretical data as well as experimental data is available to the best of our knowledge. The present results of $Q_T$ and $Q_{el}$ showing same tendency of variation as other target like these. % elastic cross sections are also having uniformality with other similar molecule.

## Conclusion

The theoretical approach of SCOP method discussed above allows us the determination of various total cross sections $Q_T$, $Q_{el}$. All these cross sections are computed under the same formalism and hence render relative reliability for the data. This study of methanimine - electron interaction studies are rare cross sections reported are for very first time. In this paper

we report for the first time several total cross sections viz. $Q_{el}$, $Q_{inel}$. Theoretical Calculations for molecules presented here for first time with no experimental and theoretical comparison available. We are expectingexperimental and theoretical calculations to get boost to our work.

**References**

[1] ICARUS, vol. 219(1) May 2012, Volatile products controlling Titan's tholins production. Ncarraso, T Gautir

[2]http://cccbdb.nist.gov

[3]D R Lide, CRC Handbook of Physics and Chemistry, 74th edn. (Chemical Rubber Company, Boca Raton, FL, 1993-94

[4] Jain A, Baluja K, 1992, Phys. Rev. A **45**, 202

[5] Jain A, 1986, Phys. Rev. A **34**, 3707

[6] Jain A, 1988, J. Phys. B **22**, 905

[7] Limbachiya C, Vinodkumar M, Mason N, 2011, Phys. Rev. A, **83**,042708

[8] H. L. JR Cox and R. A. Bonham,1967, J. Chem. Phys. **47,** 8

[9] Hara S, 1967, J. Phys. Soc. Japan **22**,710

[10] Zhang X, Sun J and Liu Y, 1992, J. Phys. B: At. Mol. Opt. Phys. **25**, 1893

[11] Staszewska G, Schwenke D W, Thirumalai D and Truhlar D G, 1983, Phys. Rev. A **28**, 2740

[12] Vinodkumar M, Limbachiya C, Barot M, and Mason N, 2012, Eur. Phys. J. D, **66:74**

[13] M.A Rahman , S.Gangopadhyay, C. Limbachiya and K. N. Joshipura, 2012 International Journal of Mass Spectrometry **319 ,** 48-54

[14]K. N. Joshipura, C. G. LimbachiyaB.G.Vaishnav 2006 Pramana**66(2),** 403-414

[15] Vinodkumar M, Bhutadia H, Limbachiya C, Joshipura K, 2011, Int. J. Mass Spectrom, **308**, 35

[16] Vinodkumar M, Limbachiya C, Joshipura K and Mason N, 2011, Eur. Phys. J. D, **61**,579

[17] Blanco F and Garcia G, 2003, Phys. Lett. A **317**,458

[18] Vinodkumar M, Limbachiya C and Bhutadia H, 2010, J. Phys. B: At. Mol. Opt.Phys. **43**,015203

# Electron induced ionization cross sections for carbon-tetraflouride(CF$_4$)

**Rakesh Bhavsar[1], Yogesh Thakar[2], Chetan Limbachiya[3,*]**

[1,2]M.N. College, Visnagar -384315

[3]The M.S. University of Baroda, Vadodara – 390001

[*]E-mail:cglimbachiya-appy@msubaroda.ac.in

## ABSTRACT

We report electron impact inelastic, ionization and excitation cross sections for plasma feed gas CF$_4$ from ionization threshold to 5 keV. We have employed Spherical Complex Optical Potential (SCOP) to calculate total inelastic cross sections Q$_{inel}$ and have used Complex Scattering Potential – ionization contribution (CSP-ic) formalisms to compute total ionization cross sections Q$_{ion}$ and summed total excitation cross sections $\sum$Q$_{exc}$. We have compared our cross sections with available experimental as well as theoretical results and have found good agreement wherever available. This is the maiden attempt to report the total excitation cross sections for this target.

**Key Words:**   plasma processing gas, ionization cross sections, spherical complex optical potential, complex scattering potential-ionization contribution.

## INTRODUCTION

The plasma phase exclusive properties provide powerful remedy to a number of industrial and manufacturing problems. In semiconductor etching, plasmas can give access to chemically active species ions and radicals from a relatively inert processing  gas[1].The industry relies upon the development of plasma technology to produce progressively more detailed and compact systems while also meeting increasingly severe environmental legislation. Technological plasmas are partially ionized.  They contain electrons, atomic ions, molecular ions, and neutrals [1]

Electron-impact ionization of atoms and molecules are significant process in any plasma. Electron-impact ionization cross-sections of molecules are important quantities in a variety of applications as diverse as low-temperature processing plasmas, fusion edge plasmas, gas discharges, planetary, stellar, and cometary atmospheres, radiation chemistry, mass spectrometry, and chemical analysis [1]

The carbon-tetrafluoride (CF$_4$) molecule is a frequently used compound in fluorocarbon plasmas that are widely used in the semiconductor industry, primarily for the plasma etching of Si based microelectronic devices.
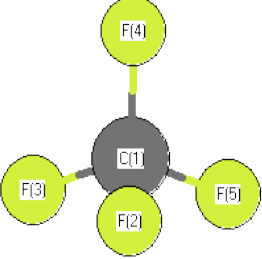
| Schematic of CF$_4$ | Bond length(Å) | Ionization Potential (eV)[2] | Electric dipole Polarizability ($10^{-30}$ m$^3$) [2] |
|---|---|---|---|
|  | C(1)-F(2)1.3151<br>C(1)-F(3)1.3151<br>C(1)-F(4)1.3151<br>C(1)-F(5)1.3151 | 14.700 | 2.824 |

Table 1: Schematic and properties of CF$_4$

**Theoretical Methodology**

An important inequality $Q_{inel}(E_i) \geq Q_{ion}(E_i)$ forms the basis for Complex Scattering Potential – ionization contribution (CSP-ic) method [3-5]. Here Q$_{inel}$ cross-sections are computed with the help of SCOP method[6]. Total ionization cross section may be estimated from total inelastic cross section by defining an energy dependent ratio R(E$_i$) given by

$$R(E_i) = \frac{Q_{ion}(E_i)}{Q_{inel}(E_i)} \qquad (1)$$

such that, $0 < R \lesssim 1$.

As total ionization cross section is a continuous function of energy, we can express this ratio also as a continuous function of energy for $E_i>I$.

$$R(E_i) = 1 - f(U) = 1 - C_1\left(\frac{C_2}{U+a} + \frac{\ln(U)}{U}\right) \qquad (2)$$

here, U is the dimensionless variable defined as, $U = \frac{E_i}{I}$.

The reason for adopting such explicit form of $f(U)$ could be explained as follows. At high energies the total inelastic cross section follows the Born Bethe term according to which the cross sections falls of as $\ln(U)/U$, but at low and intermediate energies they obey $1/E$ form [7]. Accordingly the first term takes care of the cross sections nature at low and intermediate energies while the second term describes high energy behavior of cross sections. The dimensionless parameters $C_1$, $C_2$ and '$a$' involved in the above equation are deduced by imposing the three physical conditions on the ratio as discussed below.

$$R(E_i) \begin{cases} = 0 \ for \ E_i \leq I \\ = R_p \ for \ E_i = E_p \\ \cong 1 \ for \ E_i >> E_p \end{cases} \tag{3}$$

The first condition is an exact condition wherein it states that no ionization process is possible below the ionization threshold of the target. At very high energies ($\sim 10 \ E_p$) the ionization cross sections are almost equal to inelastic cross sections as affirmed in the last condition of equation (3). This is justified by the fact that at such high energies there are innumerable channels open for the ionization as against very few channels for excitation.  At such high energies the contribution of excitation is negligible leading the ratio approach unity.

The second condition is empirical in nature. $R_P$ is the value of $R(E_i)$ at $E_i = E_P$, and it was observed that the contribution for ionization to total inelastic cross sections is about 70 - 80 % at the peak of inelastic cross section. Perhaps a first ever estimate of ionization in the relation to excitation process was made by Turner et al. [8]. They conclude from semi-empirical calculations that in gaseous $H_2O$, ionization was more probable than excitation above $\sim 30$ eV. If $\sigma_{ion}$ and $\sigma_{exc}$ are the cross sections of the ionization and excitation respectively then above 100 eV,

$$\frac{\sigma_{ion}}{\sigma_{ion} + \sigma_{exc}} \approx 0.75 \tag{4}$$

It should be noted here that the denominator in equation (4) represents the total inelastic cross sections. This ratio is similar to the ratio defined in this paper vide equation (1).The value of the ratio is attributed to the faster fall of the contribution of the first term $\Sigma Q_{exc}$ to the total inelastic cross sections beyond $E_p$ in Eq. (3). In order to make our method consistent and predictive we choose a single value of$R_p=0.7$ for all the targets studied in this work. Using this

ratio we calculate the ionization cross sections for present targets vide equation (1) and the total excitation cross sections vide equation (5).

$$Q_{inel}(E_i) = \sum Q_{exc}(E_i) + Q_{ion}(E_i) \qquad (5)$$

**Results and Discussion**
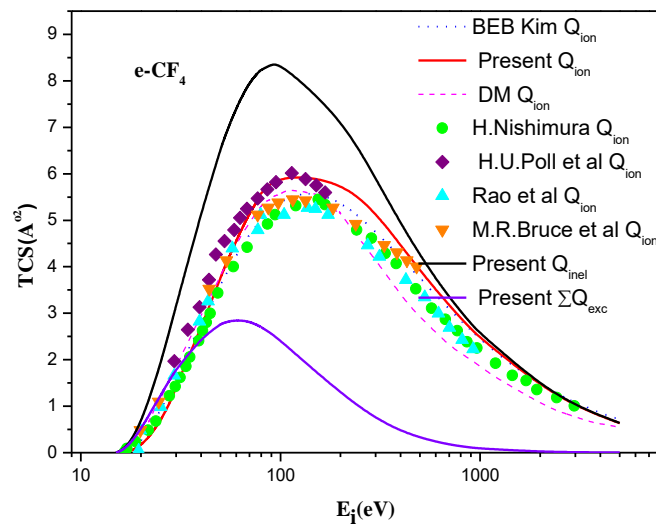


Fig. 1   **Total ionization cross sections for e-CF$_4$**

The present calculations $Q_{ion}$ for CF$_4$ molecule are in very good agreement with theoretical result of BEB[9] and DM[10]  within the required accuracy  in energy range from threshold to 5 keV. Experimental results of H. Nishimura [11]shows good agreement with our results for energy upto 3keV, Rao et al[12] for energy upto 900eV, M.R.Bruce et al[13] for energy  upto 500eV and H.U. Poll et al[14] for energy upto 150eV.

**Conclusion**

In the present work we studied inelastic electron interactions with plasma compound CF$_4$ and calculated various inelastic cross-sections for threshold to 5 keV. The result shows good agreement with theoretical and experimental cross-sections. In the cross-section values the nature of the curve is consistent with the molecular target charge density, target geometry and ionisation potential. Present work give us confidence hence we are motivated for calculation of complex target with better accuracy. This will be quite helpful in plasma modelling.

## Reference

[1] I. Rozum, P.Limao-Vieira, S.Eden, J.Tennyson and N.Meson, American Institute of Physics. **35**(2006) 267

[2] http://cccbdb.nist.gov

[3]K. N. Joshipura, M. Vinodkumar, C. G. Limbachiya, B. K. Antony, Phys. Rev.  A,**69**, 022705(2004)

[4] M.A Rahman , S.Gangopadhyay, C. Limbachiya and K. N. Joshipura, 2012 International Journal of Mass Spectrometry **319 ,** 48-54

[5]K. N. Joshipura,C. G. Limbachiya B.G.Vaishnav 2006 Pramana **66(2),** 403-414

[6] M.Swadia , R.M. Bhavsar, Y.J. Thakar,M.Vinodkumar and C. G. Limbachiya, Molecular Physics. DOI: 10.1080/00268976.2017.1333645

[7] G. Garcia, F. Blanco, Phys. Rev. A,**62**, 044702(2000)

[8]J. E. Turner, H. G. Paretzke, R. N. Hamm, H. A. Wright, and R. H. Ritchie, Radiation Research. **92**, 47-60(1982)

[9] Y.K. Kim, M.E. Rudd, Phys. Rev. A **50** (1994) 3954.

[10] H.Deutsch, K.Becker , S. Matt, T.D.Mark, Int. J. Mass Spectrom,**197**(2000) 37-69

[11] H.Nishimura, W.M.Huo, M.A.Ali, Y.K.Kim, J.Chem. Phys. **110**(1999) 3811

[12] M.V.V.S. Rao, S.K. Srivastava, Contributed Papers, XXthInternational Conference on the Physics of Electronic andAtomic Collisions (ICPEAC), Abstract Mo150, F. Aumayr,G. Betz, H.P. Winter (Eds.), July 1997, Vienna,Austria.

[13] M.R. Bruce, R.A. Bonham, Int. J. Mass Spectrom. IonProcesses **123** (1993) 97.

[14] H.U. Poll, C. Winkler, D. Margreiter, V. Grill, T.D. Ma¨rk, Int. J. Mass Spectrom. Ion Processes **112** (1992) 1-17

# Dielectric Properties of Binary Mixtures of Methyl Iso Butyl Ketone and Dimethyl Silicone Fluid

KunjanN.Shah[1], VipinchandraA.Rana[2] and Hemalkumar P.Vankar[3]

[1, 2, 3](Department of Physics, Electronics and Space Science, School of Sciences, Gujarat University,Ahmedabad,Gujarat,India)

[1]kunjanshah_91@yahoo.com

[2]varana@gujaratuniversity.ac.in

## ABSTRACT

Complex dielectric permittivity $\varepsilon^*(\omega) = \varepsilon'(\omega) - \varepsilon''(\omega)$ of the binary mixtures of methyl iso butyl ketone and dimethyl silicone fluid were measured using precision LCR meter in the frequency range 20 Hz to 2 MHz at 303.15 K temperature. The permittivity at optical frequency of the samples was also determined. Measured dielectric dataare used to gain information about the effect of concentration variations of the component of the mixtures on their dielectric properties. The electrode polarization effect was observed under the effect of low frequency A.C. electric field. The ionic and non-ionic behaviour of the mixtures are also enlightened.

**Keywords.** Precision LCR meter, Methyl iso butyl ketone, Dimethyl silicone fluid, Dielectric Permittivity

## INTRODUCTION

Dimethyl silicone fluid (D.M.S.F.) is a type of silicone fluids, whose structure is the combination of the silicone and oxygen skeleton. It is available in the form of the crystal clear liquid of viscosities from less than one to one million centistokes. It is most efficient and reliable material as dielectrics and used as a coolant in transformers. It is widely used in electrical and electronics applications. It is used as one of the ingredient for the cosmetics items. It is soluble in hydrocarbon solvents, in chlorinated solvents, and in low molecular weight aromatic solvents. D.M.S.F. is easily soluble in the ketones like methyl iso butyl ketone and methyl ethyl ketone. Methyl iso butyl ketone (M.I.B.K.) is an organic colourless liquid. They have low viscosity and high solvency trend. They are widely used in paint, ink and in coating industry.Recently we reported [1] dielectric properties of binary mixtures of methyl iso butyl ketone and amino silicone oil.To gain more information about dielectric behaviour of silicone fluid in polar solvents, we have studied dielectric properties of the dimethyl silicone fluid and methyl iso butyl ketone in this paper. The literature survey

suggests that the dielectric properties of D.M.S.F. and M.I.B.K. in the frequency range of 20 Hz to 2 MHz have not been reported, so far.

In the present investigation, we measured complex permittivity of the binary mixtures of methyl iso butyl ketone and dimethyl silicone fluid of varying concentration in the frequency range 20 Hz to 2 MHz at 303.15 K temperature. Value of dielectric constant ε' (real part of complex permittivity ε*) at 2 MHz frequency was taken as static permittivity and square of measured value of refractive index $n_D$, was taken as permittivity at optical frequency ($\varepsilon_\infty = n_D^2$) for all mixtures samples and are reported in this paper. The relative static permittivity of the material is highly important property in the field of physics, chemistry and material science. Investigation of static permittivity of binary mixtures is important in design of mixed solvents of required solvating powder for suitable solubility and for chemical solubility of the solute in the solutions [2-4]. Dielectric properties are used to gain the information about the polarization phenomena taking place under the effect of low frequency A.C. electric field. The effect of the concentration of the components of the binary mixtures on the dielectric properties is studied.

## MATERIALS AND METHODS

The samples M.I.B.K. (AR Grade) and D.M.S.F. (With 350 Centistokes Viscosity) were used to make binary mixtures and they were provided by A.C.S. Chemicals Pvt. Ltd. (India) and Narayan Co-operation Pvt. Ltd. (India) respectively. They were used directly without purification. The sixteen different samples were prepared by weight fraction of the binary mixtures of D.M.S.F. and M.I.B.K. The samples were prepared using digital analytical weight meter and have an accuracy of ± 0.0001 g. Complex permittivity of the liquid samples in the frequency range 20 Hz to 2 MHz were measured using an Agilent E-4980, precision LCR meter and self-designed sample holder. Sample holder was designed in our laboratory and was fabricated by a local manufacturer. The simplified diagram of the sample holder is shown in Figure (1). While performing the measurements the test fixture correction coefficient was also considered to cancel the effect of the stray capacitance. The open and short measurement was also carried out to cancel out the effect of stray capacitance. The capacitance and parallel resistance of the liquid samples with and without samples were measured at each frequency point to find out the complex permittivity spectra. The complex dielectric function of the samples was determined as stated in reference [5]. The refractive

index of the samples was measured using an Abbe's refractometer and have an accuracy of ±0.001. The square of the refractive index was taken as permittivity at optical frequency.
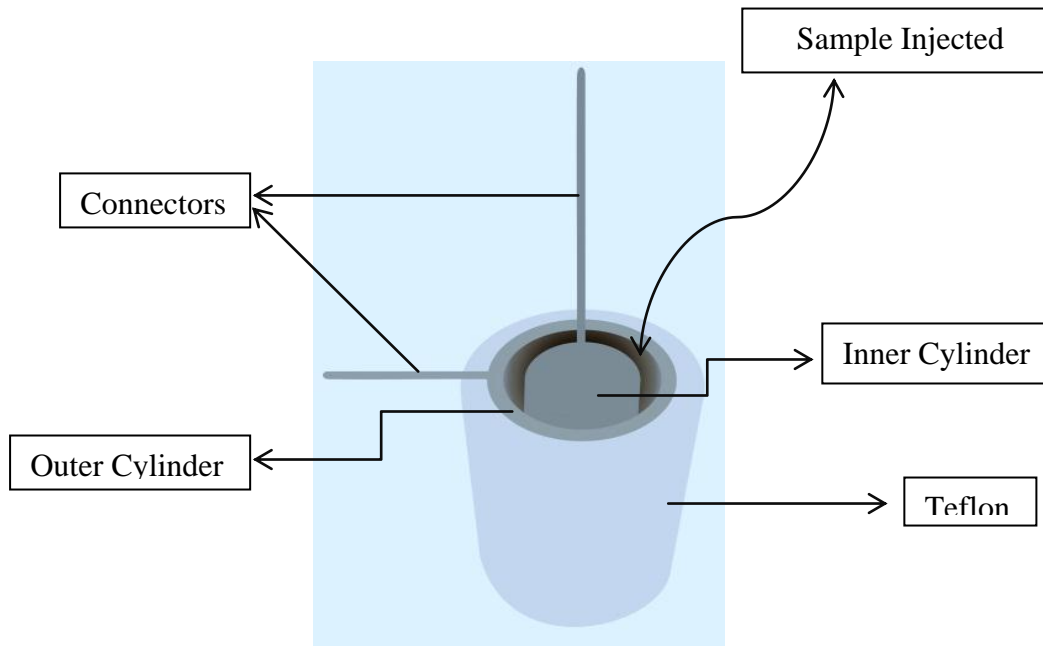


Figure 1: Simplified diagram of sample holder.

## RESULT AND DISCUSSION

The frequency and concentration dependent real ($\varepsilon'(\omega)$) and imaginary ($\varepsilon''(\omega)$) part of complex dielectric functionfor the binary mixture of M.I.B.K. and D.M.S.F. at 303.15 K temperature is shown in Figure (1). The value of the $\varepsilon'(\omega)$ is high at the lower frequency and it decreases as the frequency increases. The high value of the $\varepsilon'(\omega)$ at the lower frequency indicates the dominance of electrode polarization phenomena taking place under the effect of the A.C. electric field and also it is because of the blocking of the electrode which impede free charge motion at the boundary between the electrode surface and bulk material [6]. The $\varepsilon'(\omega)$ spectra divides into two different region, for the frequency below $10^3$ Hz it decreases rapidly with frequency and beyond that frequency it becomes frequency independent. The value of the $\varepsilon'(\omega)$ is high for the higher concentration of M.I.B.K. in D.M.S.F. over the entire range of frequency. It is interesting to note that for pure D.M.S.F. and up to 0.580 concentration of D.M.S.F. in the mixture $\varepsilon'$ values remain constant over the entire range of frequency. However when concentration of M.I.B.K. in the mixtures increases $\varepsilon'$ values are found to increase with decrease in the frequency below $10^3$ Hz. Above this frequency $\varepsilon'$ values remains independent of frequency. Rate of increase of $\varepsilon'$ with frequency is found to

increase with increase in concentration of M.I.B.K. This suggests polar and non-polar nature of M.I.B.K. and D.M.S.F. in their pure states. Increase in ε' values with decrease in frequency below $10^3$Hz frequency for M.I.B.K. and higher concentration of M.I.B.K., suggest electrode polarization effect. This effect is due to presence of unidentified ionic and charge contaminants in the dipolar solvents. Unidentified ionic and charge contaminants in the dipolar liquids are predominantly produced by the natural electromagnetic irradiations. Presence of ionic impurities in dipolar solvents is confirmed by many researchers [5-6, 8].

The higher value of the ε"(ω) at the lower frequency is because of the conduction loss.The ε"(ω) spectra is also divided in two different region, for the frequency below $10^4$ Hz it decreases rapidly with increase in frequency and beyond that it decreases slowly. The value of ε"(ω) is high for the higher concentration of M.I.B.K in D.M.S.F. and as the concentration decreases the systematic decrease is observed.
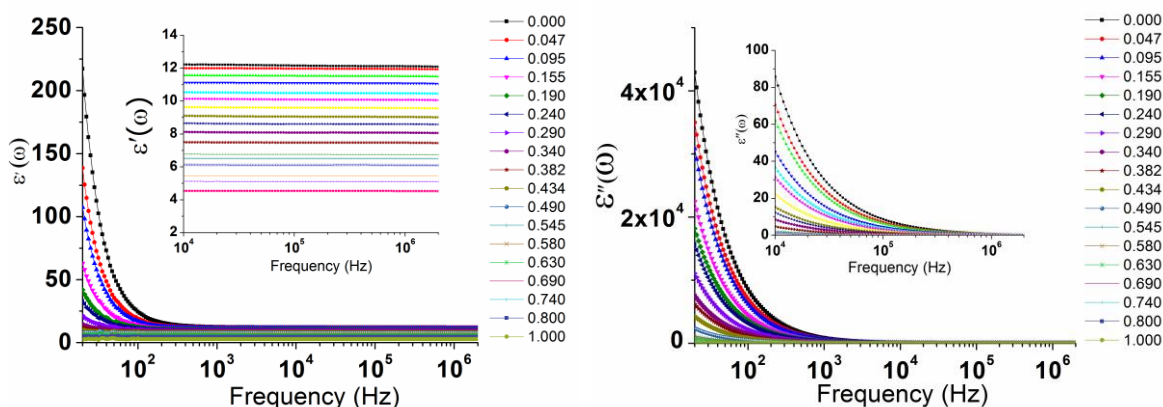


Figure 2: Real (ε'(ω)) and imaginary (ε"(ω)) part of complex dielectric function frequency range 20 Hz to 2 MHz. Insets show the enlarged view of ε' and ε" plots in higher frequency regime.

The graphical representation of the loss tangent for binary of the M.I.B.K and D.M.S.F. at 303.15 K temperature is shown in Figure (3). The tan δ peak is observed at 89.34 Hz frequency for pure M.I.B.K and as the concentration of M.I.B.K., decreases the peak is shifting towards the lower frequency. Peak value of tan δ is minimum for pure M.I.B.K. and increases with decrease in its concentration.

The graphical representation of the static permittivity and permittivity at optical frequency is shown in Figure (4). The value of static permittivity for M.I.B.K and D.M.S.F. are 12.09 and 2.76 respectively. Static permittivity of M.I.B.K is in the good agreement with literature

value 12.92 at 297.15 K temperature [7]. The static permittivity values for all the binary mixtures of M.I.B.K. and D.M.S.F lies between 12.09 and 2.76 and vary linearly with concentration of D.M.S.F. in M.I.B.K. This suggests absence of intermolecular interaction between D.M.S.F. and M.I.B.K. The refractive index for M.I.B.K and D.M.S.F. is 1.390 and 1.399 respectively. The refractive index value for the M.I.B.K is in good agreement with the literature value 1.390 at 303.15 K temperature [1]. It is clearly observed from the Figure (4), that the permittivity at optical frequency increases linearly as the weight fraction D.M.S.F. increases in the binary mixtures. This suggests that electronic polarization of M.I.B.K. and D.M.S.O. is not affected on mixing.
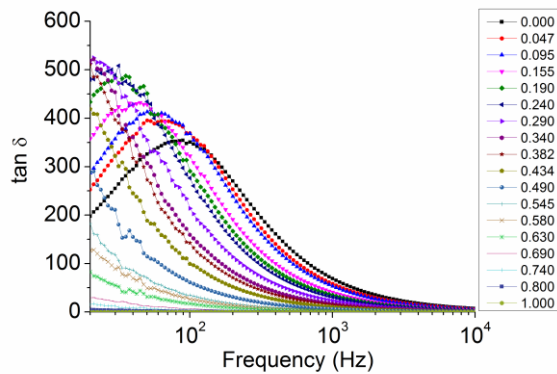


Figure (3) Loss tangent (tan δ) plots for mixtures of M.I.B.K. and D.M.S.F.
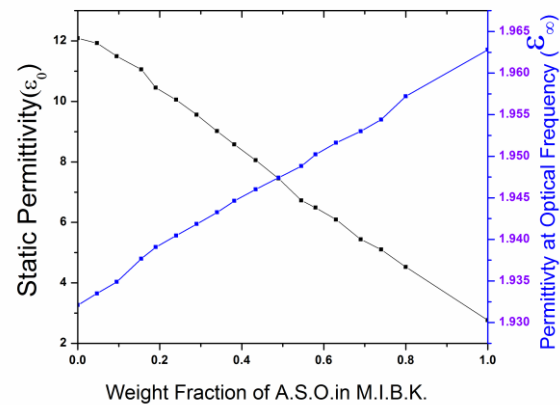


Figure (4) Variation of static permittivity and permittivity at optical frequency with concentration of D.M.S.F. in M.I.B.K.

The frequency at which the bulk material property and E.P. phenomena are separated is known as the electrode polarization frequency ($f_{EP}$) [8]. That frequency is shown in Figure (3) for the higher concentration of M.I.B.K. in D.M.S.F. The electrode polarization relaxation time ($\tau_{EP}$) is calculated using the relation $\tau_{EP} = (2\pi f_{EP})^{-1}$ [8]. Variation in the electrode polarization relaxation time with change in weight fraction of D.M.S.F. in M.I.B.K. is shown in Table (1). As the concentration of M.I.B.K. decreases in D.M.S.F, the electrode polarization relaxation time increases. The peak is not observed for the higher concentration of D.M.S.F. in M.I.B.K. in the considered frequency range.

Table 1: Variation in electrode polarization relaxation time ($\Upsilon_{EP}$) and electrode polarization frequency ($f_{EP}$)

| Weight Fraction of D.M.S.F. in M.I.B.K. | $f_{EP}$ (Hz) | $\Upsilon_{EP}$ (ms) |
| --- | --- | --- |
| 0.000 | 89.34 | 1.782 |
| 0.047 | 50.24 | 3.169 |
| 0.095 | 47.43 | 3.358 |
| 0.155 | 44.78 | 3.556 |
| 0.190 | 35.56 | 4.478 |
| 0.240 | 22.44 | 7.096 |

## CONCLUSION

The concentration and frequency dependent dielectric properties of the M.I.B.K. and D.M.S.F. and their binary mixtures were studied at 303.15 K temperature in the frequency range 20 Hz to 2 MHz. Static permittivity and permittivity at optical frequency of the same system were also measured. An electrode polarization phenomenon is taking place under the effect of low frequency A.C. electric field in M.I.B.K. rich region. The loss tangent tan δ peak is observed in the higher concentration of M.I.B.K in the D.M.S.F. The electrode polarization relaxation time increases as the concentration of the M.I.B.K. decreases in D.M.S.F. Static permittivity and permittivity at optical frequency of M.I.B.K. is in good agreement with the literature value. The imaginary part of permittivity is high at the lower frequency this is because of the conduction loss. The static permittivity and permittivity at optical frequency variation with concentration of D.M.S.F. in M.I.B.K. exhibits linear but increase trend.

## ACKNOWLDEGEMENT

## REFERNCES

1) K.Shah, V.Rana, C.Trivedi&H.Vankar, AIP Conf. Proc, 2017, 1837, 040026_1 – 040026_3

2) A.Chmielewska, M.Urada, K.Klimaszewski & A.Bald, J.Chem.Eng.Data, 2009, 54,801-806

3) G.Goldoni, L.Marcheselli, A.Marchetti,L.Tassi&G.Tosi, J.Sol.Chem, 1992, 21,953-962

4) Ch.Ramana, A.KiranKumar, M.Ashok Kumar,M.Moodley, J.Of.Chem, 2013,687106, 1-4

5) H.Chaubeand V.Rana ,Adv.Mat.Res.,2013,665,194-201

6) N.Shah, P.Shah &V.Rana, Ionics, 2015, 21, 3217-3222

7) H.Eckstrom, J.Berger &L.Dawson, 1960, 64, 1458-1461.

8) R.Sengwa,S.Choudhary, P.Dhatarwal,J.Mol.Liq,2017,225,42-49

# Continuous Wavelet Transform on Soil Data
# – A study of Surendranagar District of Gujarat

Prakash H. Patel[1,2], Nirmal P. Patel[1,2], Anita Gharekhan[1]

[1]Associate Professor, Department of Physics, C U Shah Science College, Ahmedabad, India.

[2]Research Scholar, Pacific University, PAHER, Rajasthan, India.

Email:prakashhpatel1970@yahoo.com

**Abstract**

Soil quality depends on multi-dimensional factors such as land use, soil management practices, ecosystem and environmental interactions, so it is considered as complex characteristic. However, to manage and maintainsoils in an acceptable state for future generations, soil quality must be adequately defined. At present "Soil Health Card program of the Government of Gujarat, India" is going on at different Science Colleges and STL (Soil Test Laboratories). From this program, the district Surendranagar (Gujarat -India) and its nearest geographical districts are selected for the Soil study and Analysis by Continuous Wavelet transform and wavelet variance derived from transform as it can provide scientific basis for monitoring and controlling the tillage management.

**Keywords**:Soil Study Testing, CWT, Wavelet variance

## Introduction

Soil is a naturally occurring porous medium that supports the growth of plant roots by retaining air, heat, water, and nutrients; and provides mechanical support to the plant. Soil provides a reservoir of nutrients required by crops. The purpose of soil analysis is to assess the adequacy, surplus or deficiency of available nutrients for crop growth and to monitor changes brought about by farming practices. This information is needed for optimum production, to avoid transferring undesirable levels of some nutrients into the environment and to ensure a suitable nutrient content in crop products. Regular soil analysis, every 3-5 years, should be undertaken as a vital part of good management practice.The composition of soil varies from region to region and requirement of the nutrients varies from crop to crop. So it is very essential to link the quality of soil with the requirement of the crop. If any deviation or lacunas found in ideal composition, it can be corrected by supplementing the deficient element to have better crop.

A soil test is the analysis of soil sample to determine nutrient and contaminant content,

composition and other characteristics, such as acidity or pH level. A soil test can determine fertility, or the expected growth potential of the soil, indicate nutrient deficiencies, potential toxicities from excessive fertility and inhibitions from the presence of non-essential trace minerals. Soil nutrients vary with depth and soil components change with time. With the help of soil analysis one can find out the shortfall of essential elements and can take corrective steps to have good crop.

Several elements take part in the growth and development of plants, and those absorbed from the soil are generally known as plant nutrients. In all, 16 elements have been identified and are established to be essential for plant growth. They are carbon (C), hydrogen (H), Oxygen (O), nitrogen (N), phosphorus (P), potassium (K), calcium (Ca), magnesium (Mg), iron (Fe), sulphur(S), zinc (Zn), manganese (Mn), copper (Cu), boron (B), molybdenum (Mo) and chlorine (Cl). These elements serve as raw materials for growth and development of plants, and formation of fruits and seeds. Although plants absorb a large number of elements, all of them are not essential for the growth of crops. Some of these are required in large amounts and some in traces; these are classified as major and micro nutrients.

The objective of the soil examination is to assess the accessible supplement status, response of the soil. It is additionally helpful to assess the richness status of soils of a nation or a state or an area and to arrange a logical or efficient supplement administration program. Remedy compost utilize, in view of exact data about soil fruitfulness levels in fields, can bring about expanded harvest yield, decreased cost, less utilization of normal assets and limited natural effect. Knowing a field's supplement status inconstancy implies compost application can be balanced all the more nearly to meet the supplemental supplement needs of a yield or soil for particular field zones. There are at least twelve fundamental supplements that plants require in an adjusted manner from the dirt keeping in mind the end goal to deliver a decent yield.

**Materials**

Research is carried out to examine the impact of corporeal and physio-chemical analysis of nutrition and intensity of crop in Surendranagar District of Gujarat state. At present "Soil Health Card program of the Government of Gujarat" is going ahead with various Science Colleges and STL (Soil Test Laboratories). From this program, the region Surendranagar and its closest topographical locale are chosen for the Soil study and Analysis.The review territory - Surendranagar is situated between 22° 43'N Latitude and 71° 43'E Longitude can be appropriately named as entryway to Saurashtra. The region involves a range of 10,489

square kilometers. It has a populace of roughly 1.7 million individuals, out of which 26 percent live in urban communities. It is otherwise called Cotton City of India. It is presently a noteworthy exchange and handling place for agrarian items, cleanser, glass, cotton, salt, pharmaceuticals, chemicals and plastics, material course, pottery and sterile product. The district is divided with major 10 tehsils i.e. Dhrangadhra, Halvad, Wadhwan, Limdi, Patdi (Dasada), Lakhtar, Muli, Sayla, Chotila and Chuda.There are majorly three types of soils found in Surendranagar District i.e. Medium Black Soils, Sandy Soils and Saline & Alkaline Soils. The specification of each of the soil area is presented in following table I.

Table I: Type of Soil in Surendranagar District

| Lane No. | Type of Soil | Area ('000 | Percent |
|---|---|---|---|
| 1 | Medium Black Soil | 633.4 | 60.5 |
| 2 | Sandy Soil | 252.5 | 24.2 |
| 3 | Saline & Alkaline | 160.2 | 15.3 |
|  | Total | 1046.1 | 100 |

Source: Soil Test Laboratories Gujarat

The study lane covers, Medium Black Soil under the various tehsil places i.e.

    A) Patdi: which covers Makhanpur, Haripur, Jarvala, Savlas, Bajana, Pipadi

    B) Muli: which covers Raisangar, Jepar and

    C) Chotila which have Morthala

Total 62 soil samples are collected at a distance gaps of 500 mt., which covers above statedthreeTehsilhaving9 major villages with total distance of 31 km.

**Method**

**Wavelet Transform**

Wavelet transform is a scientifically magnifying instrument which gives a multi-dimensional investigation of the information under thought. It is an intense apparatus for advanced picture handling and example acknowledgment. There is as of now an amazing rundown of utilization, including picture handling and video pressure, programmed target acknowledgment, picture upgrade, edge identification, clamor diminished and surface examination. The researcher applies this for large scale soil properties and attributes.Wavelet changes are comprehensively grouped into the discrete wavelet change (DWT) and the continuous wavelet change (CWT). The discrete wavelet has an entirely

limited size, so DWT utilize a particular subset of all scale and interpretation values, though the nonstop change works over each conceivable scale and interpretation.

The wavelets shaping a CWT are liable to Heisenberg's vulnerability standard and, proportionally, discrete wavelet bases might be considered with regards to different types of the instability guideline.In wavelet changes the information under thought is isolated into high recurrence and low recurrence parts at numerous levels, referred to individually as high pass and low passes coefficients. For instance, high pass coefficients at level-1 speak to varieties at littlest scale and the ensuing more elevated amount coefficients speak to varieties over greater frame sizes. The low pass coefficients at different levels speak to normal conduct of the information over relating window sizes.Wavelet changes might be thought to be types of time-recurrence portrayal and are, in this manner, identified with the subject of consonant examination. All for all intents and purposes valuable discrete wavelet changes make utilization of channel banks containing limited drive reaction channels.

### CWT Analysis

The data under consideration is composite signal type i.e. a mixture of periodic and non-periodic components. These type of pattern occurs may be due to the influence of several processes (e.g. climate change, weather disturbance, random use of fertilizers, crop pattern etc.) over the time. So it is difficult to get description of composite signals and identification of specific pattern. So heterogeneity in study area is studied by continuous wavelet transform to get better insight.

CWT graphs of all parameters are shown in figure I along with original data, where the horizontal axis is for distance in meters. The orange and red colors in CWT graphs indicate high coefficients of CWT at a particular frequency and location. The smaller coefficients are represented by yellow or blue. The very high frequency components are located in the lower portion of the graphs in shades of blue, indicating lower energies. The figureIshows that most of the sample data are within acceptable limits i.e. upper control limit (UCL) and lower control limit (LCL). In CWT graphs y-axis corresponds to scales and z-axis to wavelet coefficients. The scale to scale analysis is suited to detect local features of aperiodic data.
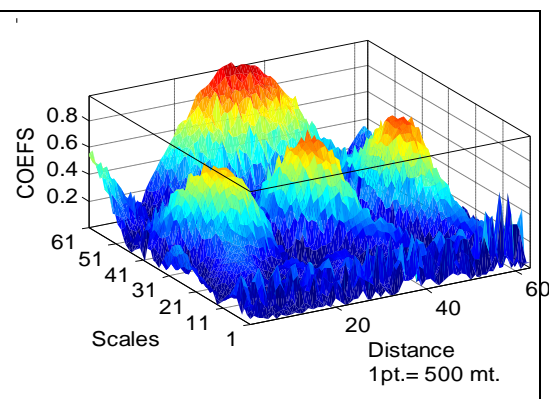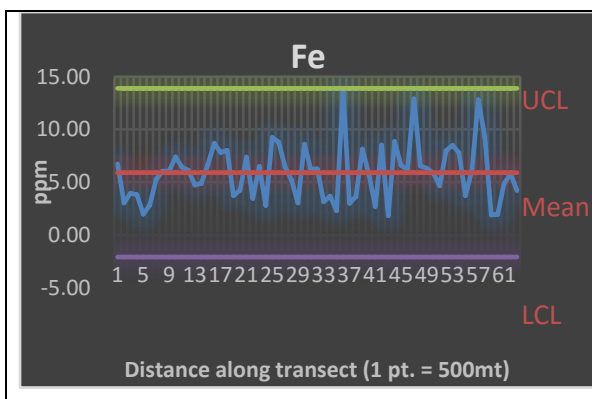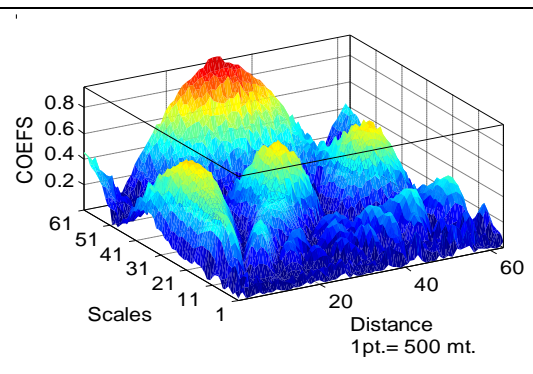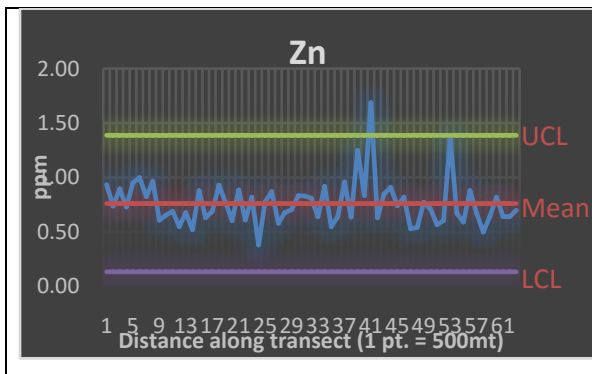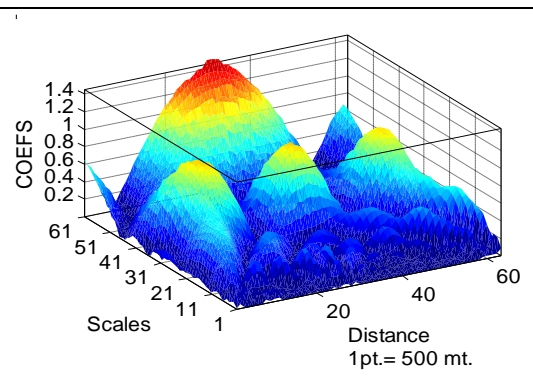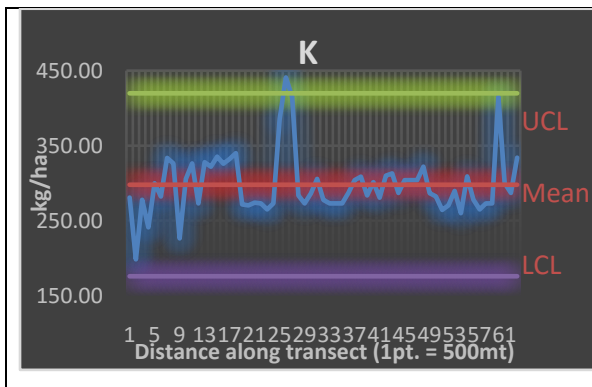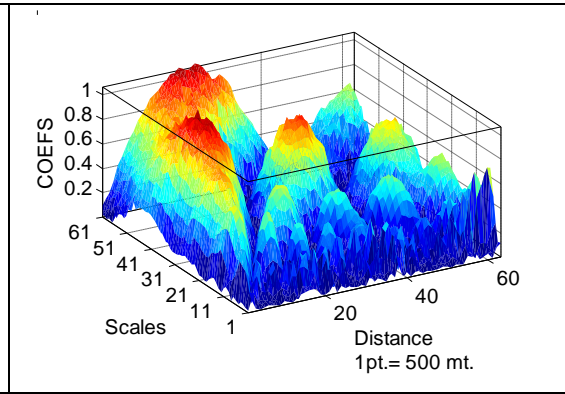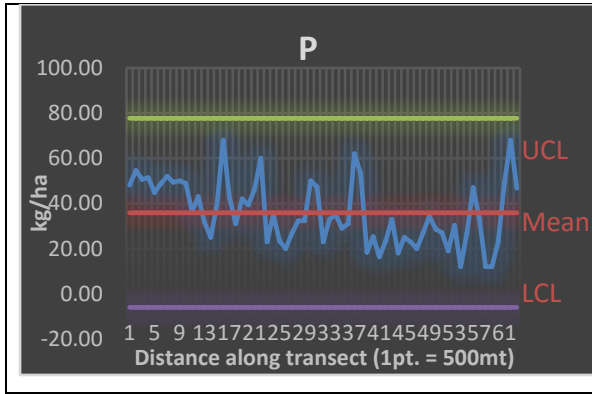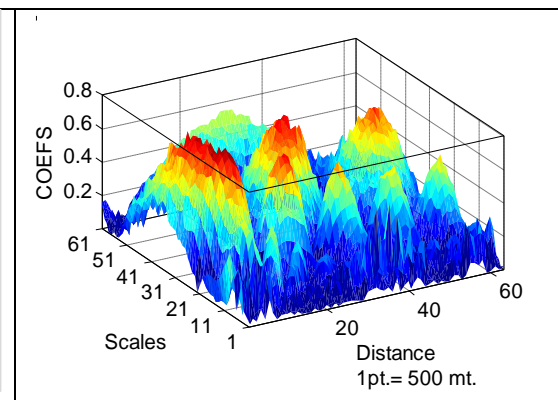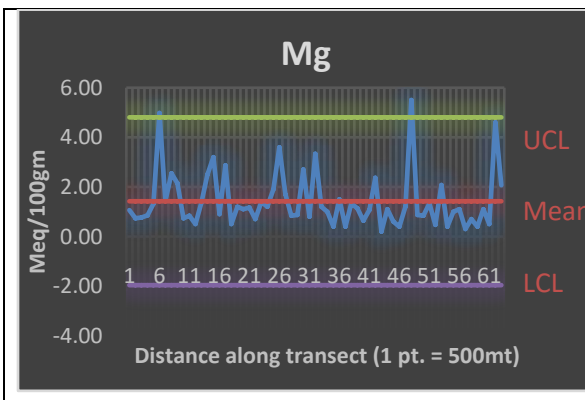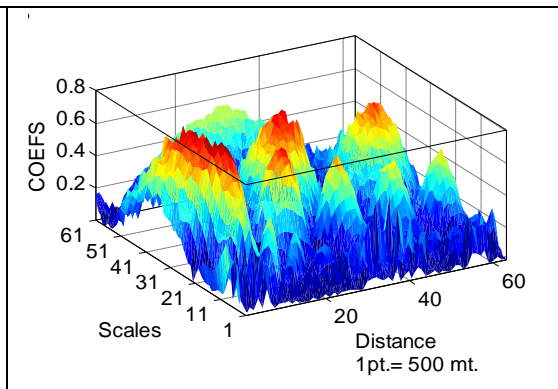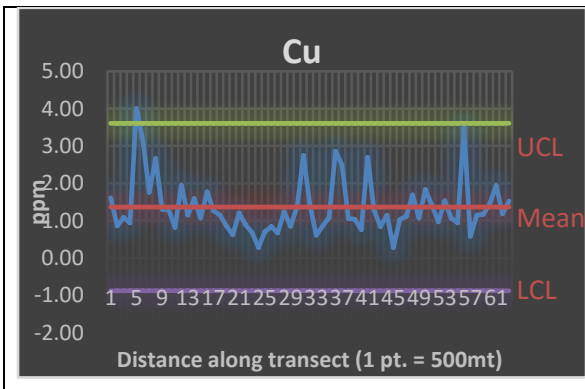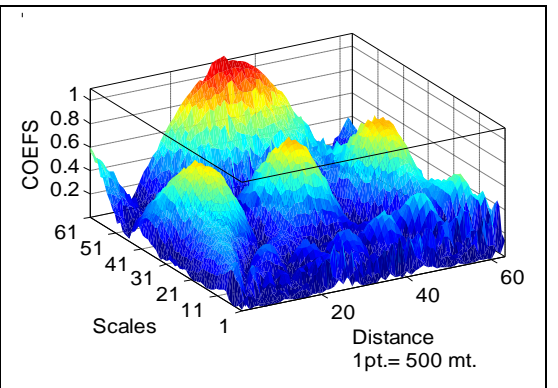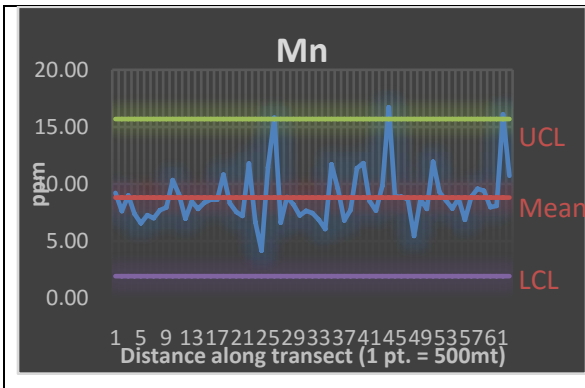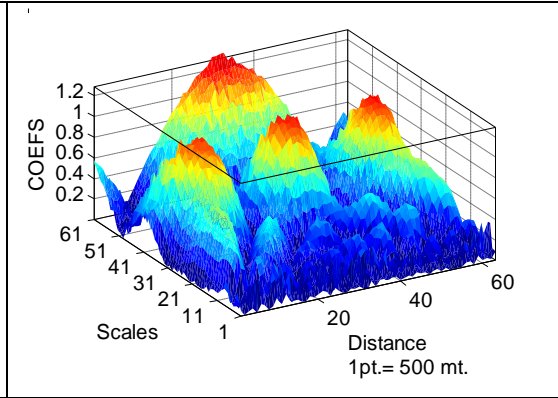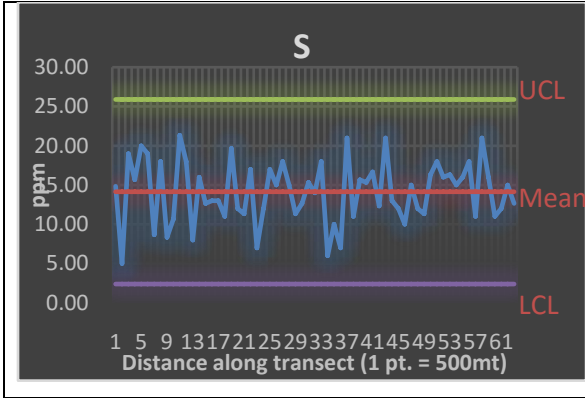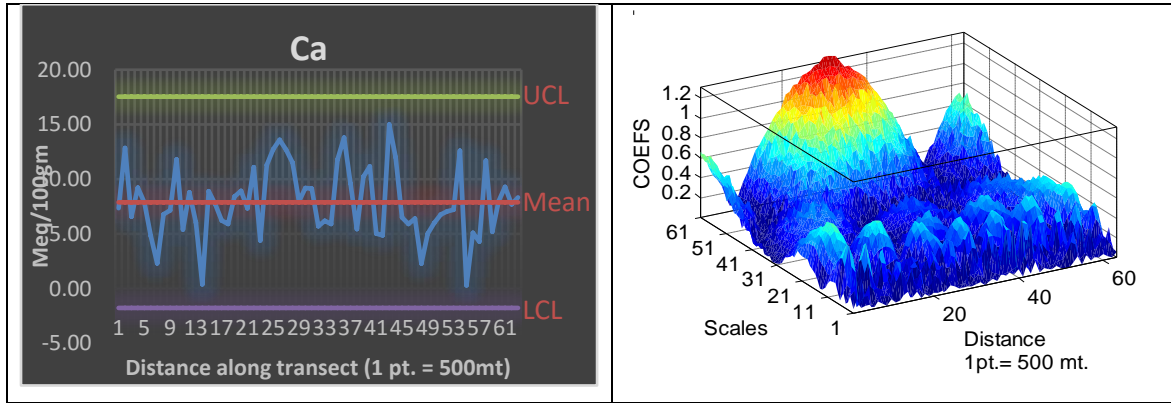
Figure I: Transect of P, K, Zn, Fe, S, Mn, Cu, Mg and Ca of studied Lane with their CWT presentation

As the wavelet transform is a function of both scale and location, the interpretation of transform is difficult, so wavelet variance is the solution to facilitate analysis. Wavelet variance is simply the average of square of wavelet coefficients of a scale.  The wavelet variance is proportional to the number and intensity of a feature of a given scale, a peak in the wavelet variance indicates presence of high number of low intensity values or low number of high intensity values. In studied data it is seen the dominant peak is directly proportional to number of data in a series. It is found from this study that the dominant peak is following a pattern, it is normally within the range: Half the number of samples + 10% and Half the number of samples + 20%.In all parameters it is checked, where ever this range is not followed, heterogeneity is found. In some parameters along with dominant peak, small multiple peaks are also seen at lower scales, indicating variability and other characteristics of studied area with low intensity. The values of wavelet variance of macro and micro nutrients at dominant peak with scale and their respective contribution in percentage is incorporated in figure II and table II.
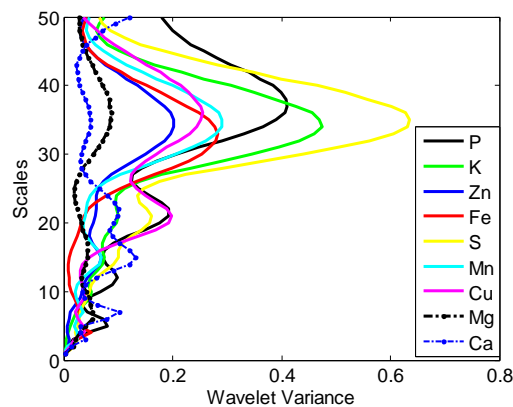


Figure II: Shows the wavelet variance of P, K, Zn, Fe, S, Mn, Cu, Mg and Ca data. The horizontal axis corresponds to wavelet variance as a function of scale.

Table II: Varianceinmacro and micro nutrition

|  | Peak Scale | WaveletVariance Value | Weightage in % |
|---|---|---|---|
| **P** | **37** | **0.41** | **14.8%** |
| **K** | **34** | **0.47** | **17%** |
| Zn | 34 | 0.2 | 7.22% |
| Fe | 33 | 0.28 | 10.1% |
| **S** | **35** | **0.64** | **23.1%** |
| Mn | 34 | 0.29 | 10.46% |
| Cu | 36 | 0.26 | 9.38% |
| Mg | 36 | 0.09 | 3.24% |
| Ca | 15 &7 | 0.13  & 0.1 | 8.3% |

Table II and CWT graphs reveal that

1. P, K and S are dominating the site.

2. Ca is also a higher contributor but the multiple peaks shows not the entire site is under its influence but it is localized, as dominant peak is not following the pattern and it can be seen through CWT graph low intensity values are contributing more and giving rise to low scale multiple peaks.

3. Zn, Fe, Mn and Cu are normal contributor.

4. Cu, Sand P are also showing multiple peaks at lower scale.

5. Sulphur is the highest contributor.

6. It is very interesting to see though Magnesium is following the scale pattern but least contributor.


With scale we can get information of pattern, if any parameter is not following the pattern, we can predict variation in data due to some factors (like excess amount of fertilizers, weathering effect alter the values of particular nutrient, previous crop dependency, so one should change the next crop).So from dominant peak we can get idea of whole distance area and with small peaks and multiple peaks district wise as well as village wise also can be predict. Deviation from the general trend can be directly linked to random events and site conditions. In this study main event may be lack of knowledge of using fertilizers, quality of fertilizers, weather conditions etc.

**Reference:**

1. G. A. Bradshaw and T. A. Spies (1992), "Characterizing canopy gap structure in forests using wavelet analysis", Journal of Ecology, Vol.:80, pp. 205–215.

2. R. M. Lark and R. Webster (1999), "Analysis and elucidation of soil variation using wavelets" European Journal of Soil Science, Vol.:50, pp. 185-206.

3. Walker, J. S. (1999). A Primer on Wavelets and Their Scientific Applications, 1st ed. Boca Raton (FL) CRC Press.

4. Polikar, R. (2001). The Engineer's Ultimate Guide to Wavelet Analysis: The Wavelet Tutorial.

# Electron Impact Ionization of Carbon and Silicon based molecules

Hitesh Yadav[1,3*], Hardik Desai[2], Minaxi Vinodkumar[3] and P.C. Vinodkumar[1]

[1]Department of Physics, Sardar Patel University, Vallabh Vidyanagr, Gujarat.
[2]Department of Physics, UkaTarsadia University, Bardoli, Surat, Gujarat.
[3]Electronics Department, V.P & R.P.T.P. Science College, Vallabh Vidyanagar, Gujarat.

*hitesh0507@gmail.com

**Abstract:**

We report electron impact total ionization cross sections for Silicon-based molecules such as (*SiC, SiN, SiO, SiF$_2$*) and Carbon-based molecules (*CF$_4$, CF$_3$Br, C$_3$H$_4$*) from the threshold of the target to 5000 *eV*. We have employed Spherical Complex Optical Potential (*SCOP*) to compute total inelastic cross sections ($Q_{inel}$). The total ionization cross section ($Q_{ion}$) is extracted from the total inelastic cross section using the Complex Scattering Potential–ionization contribution (*CSP-ic*) method. The results of most of the targets studied here compare well with the measurements and the theoretical data wherever available. The correlation between the peaks of ionization cross sections with the number of target electrons is also reported. It is observed that not only numberof electrons contribute to ionization cross sections but also the number of molecular bonds of the target. This correlation is shownfor the iso-electronic molecule.


**Keywords:**SCOP, CSP-ic, Ionization cross section, Iso-electroinc molecule.

**Introduction:**

Atomic-molecular collision study has a history of more than 100 years now and has found important place in the exploration of basic processes like excitation, ionization and dissociation or fragmentation at the subatomic level. The problem of electron scattering with atoms and molecules has been extensively addressed by many theoretical and experimental scientists in recent past,as these processes have gained much importance in environmental science, study of aurora, ionosphere of the earth and other astrophysical environments and low temperature plasmas.

Energetic electrons striking the atomic or molecular targets are responsible for many physical and chemical processes, which can be classified into elastic and inelastic processes.

Quantitatively, these processes are represented by the elastic and inelastic cross sections. Inelastic channel includes discrete excitations to higher orbits or ionization that is excitation to the continuum. Both the processes are important and are responsible for the loss of flux from the incident channel into the inelastic channel. In fact, the active fragments (ions, radicals and atoms) generated in the inelastic channels as electrons colliding with the molecular targets are responsible for several chemical reactions, such as etching, coating and polymerization leading to surface and material treatment or modifications. Furthermore, the knowledge of ionization cross sections is a fundamental step in theion–molecule reactions in chemical reactors [1, 2]. The ionization cross sections play pivotal role in applications of plasma physics, atmospheric science, mass spectrometry and vacuum technology.

Among the targets of present study, silicon is an important constituent of interstellar dust, silicon cluster are also found in the atmospheres of planets and their moons [3]. The silicon based molecules (*SiC, SiN, SiO*) are of important in applied physics, quantum chemistry and have a big impact in the interstellar region [4].*SiO* and *SiN* are of great interest in discharges and plasmas as well as in gas lasers, planetary, cometary, radiation chemistry and mass spectrometry [5]. $SiF_2$ radical isknown to be product of the etching of Si by fluorinated gases [6, 7]. Electron scattering from small fluorocarbon compounds has been of recent interest due to the prominent role these molecule plays as feedstock gases for industrial plasmas such as $CF_4$. Carbon tetrafluoride ($CF_4$) is one of the most widely used components of feed gas mixture employed for a variety of plasma environment [8]. $CF_3Br$ is attractive choice of precursor for generation of radical beams as the bromine elimination is expected to be the dominant elimination channel, making $CF_3Br$ a likely efficient source of $CF_3$ and *Br* radicals [9, 10, 11].Propyne ($C_3H_4$) also known as methylacetylene is commonly used as substitute for acetylene as fuel for welding torches and it's also being investigated as possible fuel for rockets in space craft.

Thus, from literature survey it is quite clear that work on these targets are of great importance.We report total ionization cross sections for*SiC, SiN, SiO, SiF$_2$, CF$_4$, CF$_3$Br and C$_3$H$_4$*from the threshold of the target to 5000 *eV*. The ionization cross sectional data for the discussed targets are fragmentary and for few of the molecules the ionization cross section are reported for the first time. In the next section, we discuss the theoretical methodology and its salient features.

**Theoretical Methodology:**

We briefly discuss the theoretical methodology employed here for the calculation of the various cross sections. The details of the methodology can be obtained from our earlier publications [12-14]. As discussed in the earlier section that the scattering phenomenon is characterized quantitatively into two important processes namely elastic and inelastic. They combine to give the total scattering phenomenon.

$$Q_T(E_i) = Q_{el}(E_i) + Q_{inel}(E_i) \qquad (1)$$

where $Q_{el}$ represents the elastic cross section and $Q_{inel}$ represents the total inelastic cross sections. The Spherical Complex Optical Potential $SCOP$ formalism [12-14] to describe the electron molecule scattering is represented by the interaction potential,

$$V_{opt}(E_i, r) = V_R(E_i, r) + iV_I(E_i, r) \qquad (2)$$

where the real part, $V_R(E_i, r)$ consist of static potential $(V_{st})$, exchange potential $(V_{ex})$, and polarization potential $V_p$ and the complex part $V_I$ of the optical potential takes care of all the inelastic processes via absorption potential $(V_{abs})$ which accounts for the total loss of flux scattered into the allowed electronic excitation or ionization channels. It is to be noted that the $SCOP$ program doesn't require any fitting parameters. All the potential described by equation (2) are charge-density dependent. In the $SCOP$ formalism [12-14], the complex optical potential is used to solve the Schrödinger equation numerically using the partial wave analysis. Using these partial waves, the complex phase shifts are generated which are key ingredients to find the relevant cross sections. The phase shifts contain all the information regarding the scattering events.

Total inelastic cross sections are not directly measurable quantities and hence do not provides a direct comparison with experiment. But it is obtained by subtracting the elastic cross section from the total cross sections. Though it is difficult to measure, but it contains an important quantity which is directly measurable i.e ionization cross section and electronic excitation cross sections. Thus, the total inelastic cross section $(Q_{inel})$ can be written as [12]

$$Q_{inel}(E_i) = \sum Q_{ex}(E_i) + Q_{ion}(E_i) \qquad (3)$$

where the first term represents the sum of all total discrete electronic excitation and the second term represents the total ionization cross section. The discrete transition arise mainly from the low-lying dipole allowed transitions for which the cross sections decreases beyond $E_p$ the energy at which $Q_{inel}$ is maximum therefore by definition we can write,

$$Q_{inel}(E_i) \geq \sum Q_{ion}(E_i) \qquad (4)$$

This is an important inequality and it forms the basis for the complex spherical potential-ionization contribution (*CSP-ic*) method. The ionization cross-section may be estimated from total inelastic cross sections by defining an energy dependent ratio $R(E_i)$,

$$R(E_i) = \frac{\sum Q_{ion}(E_i)}{Q_{inel}(E_i)} \qquad (5)$$

such that $0 \leq R \leq 1$,

it is apparent from the above ratio that when the incident energy is less than or equal to the ionization threshold ($I$) of the target, this ratio is zero as the ionization process has not started. Also at very high energy say for about then times the energy at which the inelastic peak occurs, the only dominant process is the ionization and hence the ratio $R(E_i)$ approaches to 1.

$$R(E_i) \begin{cases} = 0 \quad for\ E_i \leq I \\ = R_p for\ E_i = E_p \\ \cong 1\ for\ E_i \gg E_p \end{cases} \qquad (6)$$

As the ionization, cross section is continuous function of energy, we can express this ratio as [12,14]

$$R(E_i) = 1 - f(U_i) = 1 - C_1\left(\frac{C_2}{U_i + a} + \frac{lnU_i}{U_i}\right) \quad (7)$$

where $U_i = \frac{E_i}{I}$ dimensionless variable, $E_p$ stands for the incident energy at which the calculated $Q_{inel}$ attains its maximum value. $R_p$ is the value of $R$ at $E_i = E_p$. The reason for adopting such term is that, at higher energies the total cross sections follows the Bron Bethe term according to which the cross section falls as $\frac{lnU}{U}$, but at low energy and intermediate energies it obeys $\frac{1}{E_i}$ [15]. Equation (7) involves dimensionless parameters $C_1$, $C_2$ and $a$ that depends on the target properties. To determine these parameters, we have used the three conditions given in equation (6) for the ratio $R(E_i)$.

## Results and Discussion:

The theoretical approach of *CSP-ic* method outlined above is employed to determine electron impact total ionization cross sections. We have presented our graphical results in figure 1-9.
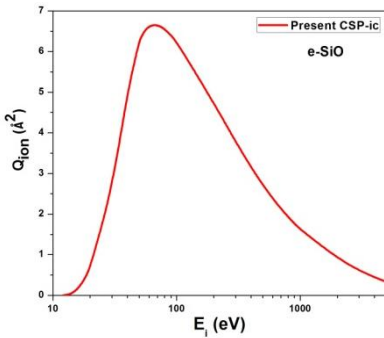


**Figure 1 Total Ionization Cross section ($Q_{ion}$) for e-SiC.**

In figure 1-3 we have presented the calculated Ionization cross section for the diatomic molecular target (*SiC, SiO & SiN*) using the *CSP-ic* method. Where we have used the $R_p$ value to be 0.7 i.e. assuming 70% ionization contribution in the inelastic cross sections [15]. The result presented here are been reported for the first time to the best of our knowledge.
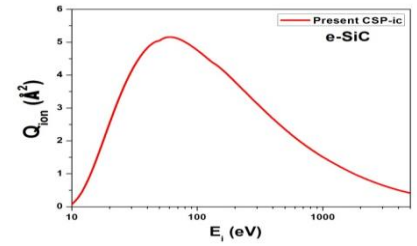


**Figure 2 Total Ionization Cross section ($Q_{ion}$) for e-SiO.**
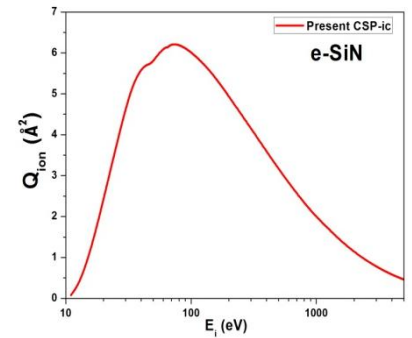


**Figure 3 Total Ionization Cross section ($Q_{ion}$) for e-SiN.**

In figure 4 we have reported the calculated ionization cross section for the $SiF_2$ molecule. In figure 5, we present the dependency of the ionization cross section ($Q_{ion}$) on the number of electron present in the target. Where $SiF_2$ having the maximum number of the electrons i.e. 32 and *SiC* has the least i.e. 20. Thus the conclusion can be drawn from the graph that the $Q_{ion}$ peaks depend on the number electrons present in the molecular or the atomic target.
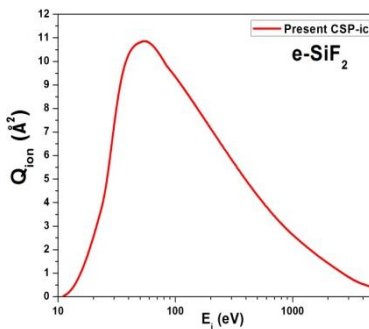


**Figure 4 Total Ionization Cross section ($Q_{ion}$) for e-SiF$_2$**
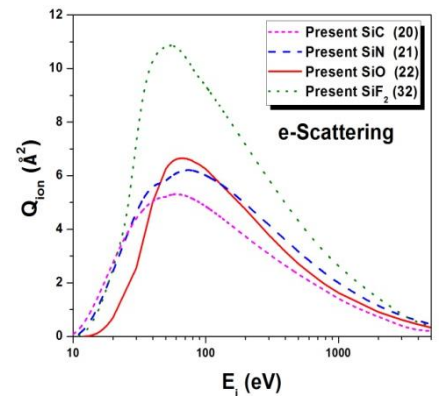


**Figure 5 Comparison of the ($Q_{ion}$) peaks for all silicon based molecules**

In the figure 6-7 we have presented the calculated result for the fluorine containing molecules. It's very difficult to ignore the presence of the high electron affinity of the fluorine atom and that can be clearly seen in the case of experimental results. In figure 6 we have presented the calculated $Q_{ion}$ for the CF$_4$ molecule. And it is in good agreement with S. Pal et. al [16] , S. Pal et. al [17],
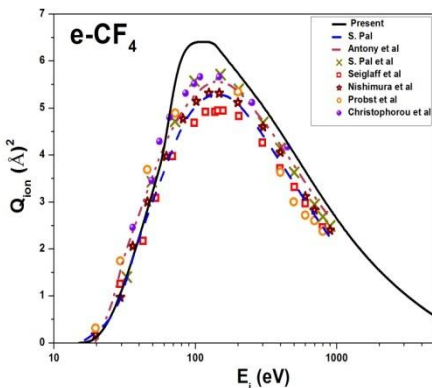


**Figure 6 Total Ionization Cross section ($Q_{ion}$) for e-CF$_4$**
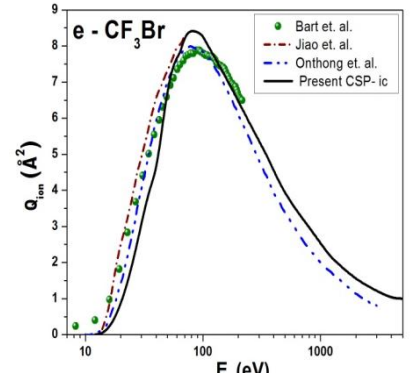


**Figure 7 Total Ionization Cross section ($Q_{ion}$) for e-CF$_3$Br**

Nishimura et. al [18] and Seiglaff et. al [19], at lower energy regime but at higher energy the nature of the cross section is qualitatively same but differs quantitatively. While in the figure 7 we have reported the ionization cross section for *e-CF$_3$Br*. The presented data finds overall a good agreement with available data in the literature [9, 10, 11]. In figure 8 the present calculated data for the *C$_3$H$_4$* is plotted. We have compared our data with the lone data of Szmytkowski et. al [20] calculated using the BEB method. The data findsgood agreement at low and high energy regime and it over estimates the BEB cross section in the intermediate energy regime.
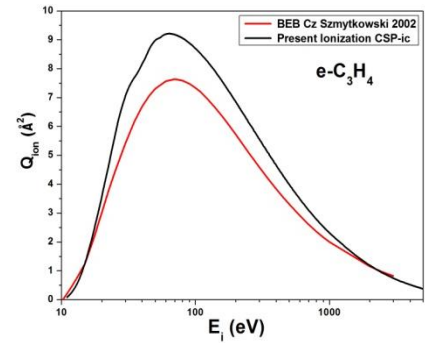


**Figure 8 Total Ionization Cross section ($Q_{ion}$) for e-C$_3$H$_4$**

Figure 9 represents the $Q_{ion}$ of two iso-electronic molecules i.e. the molecule having the same number of the electrons.In the case of SiO and C$_3$H$_4$where they have the same number of electrons, i.e. 22,from figure 9, it is evidentthat not only the number of electron responsible for ionizations cross sections but also the number of atoms present in the molecule. The dissociative ionization also plays a role in the cross sections. This comparison between Propyne (C$_3$H$_4$) and SiO indicates the same.
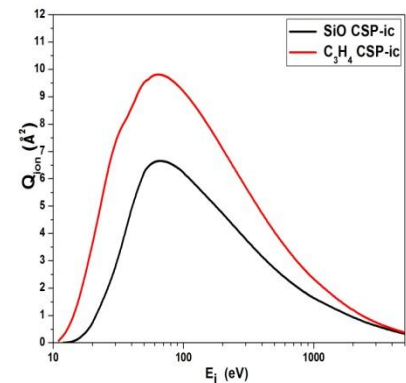


**Figure 9 Iso-electronic molecules ionization cross sections of SiO and C$_3$H$_4$.**

**Conclusion:**

 In the present work we have reported the results for ionization cross sections (see figure 1-9) of silicon based and carbon based molecules of industrial applications. It is also seen that the ionization peak increases with no. electrons present in the molecule (size of the molecule). It is further noticed that molecules having the higher number of molecular bonds have higher ionization cross sections even though their electron numbers are identical. This may be due to the contributions coming from various dissociative ionization processes of the inelastic channels.

**Acknowledgement:**

**Reference:**

[1.] J. L Franklin, Ion-Molecule Reactions (Butterworth, London, 1972) pp:1-2.

[2.] M. T. Bowers, Gas Phase Ion chemistry (Academic Press, London, 1973) pp:1-2.

[3.] M. C. Necarthy, C. A. Gottlieb & P. Thaddeus, Mol Phys. 2003, 101, 4.

[4.] J. Cernicharo, C.A Gottlieb, M. Guelin, P. Thaddeus & J. M. Vrtiek, Astrophys. J. 1989, 341,L25.

[5.] B. E. Turner, Astrophys. J. 1996, 468,694.

[6.] H. F. Winter & F. A. Houle, J. Appl. Phys., 1983, 54, 1218.

[7.] Y. Matsumi, S. Toyoda, T. Hayashi, M. Miyarnura, H. Yoshikawa & S. Komiya, J. Appl. Phys., 1986, 60, 4102.

[8.] L. G. Christophorous, J. K. Olthoff & M. V. V. S. Rao, J. Phys. Chem. Ref. Data., 1996, 25, 1341.

[9.] M. Bart, P. W. Harland, J. E. Hudson and C. Vallance, Phys. Chem. Chem. Phys., 2001, 3, 800.

[10.] C.Q. Jiao, B. Ganguly, C.A. DeJoseph, A. Garscadden, Int. J. Mass. Spect., 2001, 208, 127.

[11.] U Onthong, H Deutsch, K Becker, S Matt, M Probst, T.D Märk, Int. J. Mass Spect., 2012, 214,53.

[12.]  M Swadia, Y Thakar, M Vinodkumar, C Limbachiya, Euro. Phys. J. D 2017, 71, 85.

[13.] H Yadav, M Vinodkumar, C Limbachiya, PC Vinodkumar,  Mol. Phys. 2017, 115, 952.

[14.] H Bhutadia, A Chaudhari, M Vinodkumar, Mol. Phys., 2015, 113, 3654.

[15.] J. Turner, H. Paretzke, R. Hamm, H. Wright, R. Richie, Radiat. Res., 1982, **92**, 47.

[16.] S. Pal, P. Bhatt, Int. J. Mass Spect., 2003, 229,151.

[17.] S. Pal, Phs. Scr. 2008, 77, 055304.

[18.] H. Nishimura, W. M. Huo, J. Chem. Phys. 1999, 110, 3811.

[19.] D RSeiglaff, RRejoub, J. Phys. B, 2001,  34, 799.

[20.] C. Szmytkowski, J. R. Brunton, M. J. Brunger & S. J. Buckman, Plasma Sources Sci. Thechnol. 2010, 19, 065021.

# The Study of Lattice Dynamics and Lattice Mechanical Properties Using First Principles Local Pseudopotential

Kamaldeep G Bhatia[1*], Amit B Patel[2], Nisarg K Bhatt[3], Pulastya R Vyas[2] and Vinod B Gohel[2]

[1]*Department of Physics, L.J.I.E.T., Gujarat Technological University, S. G. Highway, Ahmedabad- 382210, Gujarat, India*

[2]*Department of Physics, School of Science, Gujarat University, Ahmedabad, Gujarat, India*

[3]*Department of Physics, M. K. Bhavnagar University, Bhavnagar- 394001, Gujarat, India*

[*]Corresponding author: kamaldeep.bhatia1991@gmail.com

**Abstract:**

The local form of the pseudopotential without adjustment of any parameter has been used for the theoretical study of partly d band transition metal Copper. We have also computed phonon density of states, temperature variations of Debye Waller factor, mean square displacement and Debye temperature. Presently obtained results are in excellent agreement with experimental results. From present study we conclude that the local pseudopotential without adjustment of any parameter provides more transparent way for understanding of ionic interaction. Such approach is very simple and identical to first principles approach.

**Keywords:** Transition metal; local pseudopotential; phonons and lattice mechanical properties.

**PACS:**63 20Dj, 65 50 +m

**Introduction:**

Over the past 40 years, phonon spectra of crystals have been determined by using neutron scattering experiments for a wide class of systems ranging from elements to multicomponent materials, metals to semiconductors, insulators and alloys. The theoretical and experimental studies are helpful for the understanding of many static and lattice mechanical properties at ambient condition and even at extreme environment (High Temperature and High Pressure). With the increasing computational power of modern work stationsab initio calculations of phonons have become possible.These investigations all based on a density functional theory differ, however, in the treatment ofthe tightly bound core electrons and/or in the basis setused for describing the wave functions[1]. Since very accuratefull- potential calculations [e.g.,

full-potential linearizedaugmented-plane wave(FLAPW)calculations]arevery time consuming, even with modern work stations,most studies have been restricted to selected phononmodes by using the frozen phonon approach [2]. During literature survey it has been observed that Embedded (EMBM) atom method and Tight Binding [TB] method are also used for the study of lattice dynamics.

A more elaborated approach is due to the pseudopotential theory. Even transition elements may be described bya local pseudopotential, provided that the valence is chosenappropriately[3].For transition metals, unlike what happens for simplemetals, there is not a large number of suitable pseudopontentials.Essentially, for transition metals, one has to consider the fact that the tightly bound d-electrons hybridize withthe nearly free electrons, resulting in a partially filled d-band,crossing the Fermi energy. The presence of the dband has been a serious impediment to the applicationof pseudopotential perturbation theory for such systems [4]. Number of attempts have been made in recent past for the study of lattice dynamics and lattice mechanical properties of transition metals with complex electronic and structural behaviour [1,4-8]. Nevertheless, for transition metals, it hasbecome necessary to introduce some sophistication in orderto obtain satisfactory agreement with experimentalphonon frequencies. During literature survey it has been observed that theoretical study based on local pseudopotential requires fitting of parameters to predict phonon spectra of transition metals [1,4]. Keeping this in our mind, in the present communication, we attempt to uselocal pseudopotential due to Kumar [9] without any adjustments of parameter for the study of lattice dynamics and lattice mechanical properties of Cu in the framework of second order perturbation theory. Such calculation is identical with the one carried out with first principles method.

**Theory:**

The total dynamical matrix $D_{\alpha\beta}(q)$ will consist of three terms,

$$D_{\alpha\beta}(q) = D_{\alpha\beta}^{C}(q) + D_{\alpha\beta}^{E}(q) + D_{\alpha\beta}^{R}(q) \qquad (1)$$

Here superscripts stand for Columbic, Electronic and Repulsive contributions.$D_{\alpha\beta}^{C}(q)$, $D_{\alpha\beta}^{E}(q)$ and$D_{\alpha\beta}^{R}(q)$ can be found in [10]. In the harmonic approximation, the Debye-Waller exponent $2W_T$ is directly obtained from the computed phonon density of states. If g(v) is the frequency distribution function for the phonons giving the number of vibrational modes in the frequency interval between v and v + dv [11], then

$$2W_T = \frac{8\pi^2\hbar}{3MN}\left(\frac{sin\theta}{\lambda}\right)^2 \int_0^{v_{max}} \frac{g(v)}{v} \coth\left\{\frac{hv}{2k_BT}\right\}dv \quad (2)$$

where Q is the glancing angle and $\lambda$ is the wave length of incident radiation. M is mass of the atom and N denotes the total number of unit cells in the crystal. In the harmonicapproximation, the mean square displacement of the atoms in the crystal is given by the relation [11],

$$\overline{U}^2 = \frac{3}{8\pi^2}\left(\frac{\lambda}{sin\theta}\right)^2 W_T \quad (3)$$

**Results and Discussion:**

In the present study we have used Kumar's pseudopotential [9] which has the following form in r-space, $V_{ion}(r) = \frac{-Ze^2r}{r_m r_c}$ for $0<r<r_c$; $V_{ion}(r) = \frac{-Ze^2r}{r_m}$ for $r_c< r <r_m$ and $V_{ion}(r) = \frac{-Ze^2r}{r}$ for $r_m< r$.In above pseudopotential, there are two adjustable parameters core radius $r_c$ and some model radius $r_m$. We have taken core radius $r_c$ as experimental ionic radius and $r_m$ as experimental atomic radius in the present study. In the region $r <r_c$, there is no complete cancellation of potential but it decreases linearly and in the region $r_c$ to $r_m$ it remains constant. It possesses pure coulombic behaviour for the region outside $r_m$.The potential between region$r_c$ to $r_m$ accounts hybridization effects because in case of d-band metals there is no complete cancellation of potential within this range. In this sense the local form of the pseudopotential is free from any kind of adjustments of parameter and considered as first principles pseudopotential. The values of $r_c$ and $r_m$ are 1.3797 a.u. and 2.9673 a.u. respectively. The value of effective valency Z=1.1937 obtained from first principles calculation has been used. It is well known fact that in case of transition metals due to oscillations of ions there is core-core repulsion which is short range in nature and plays an important role for the complete understanding of ionic interaction. We have also accounted such core-core repulsion by using Born-Mayer type of potential. The value of the coefficient of the Born-Mayer potential is 125 and exponent value is 2.42. The calculated phonon frequencies in symmetric directions are compared with experimental results as shown in Fig. 1.
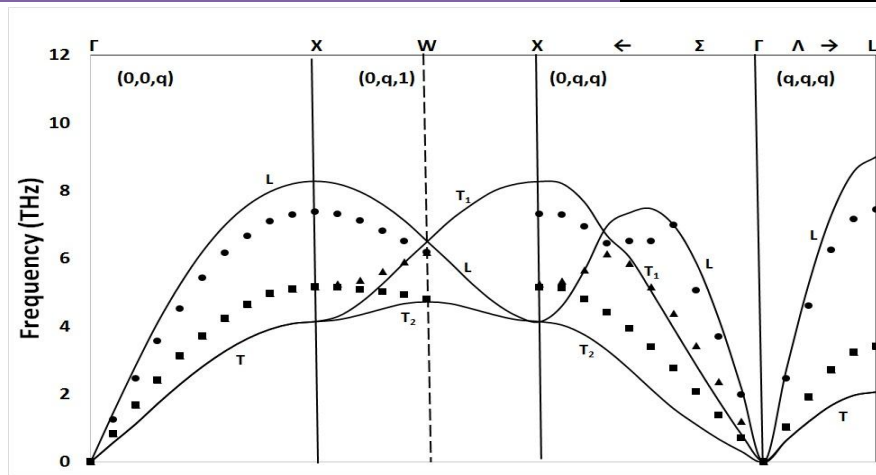
**FIG. 1** Phonon Dispersion curves for Cu.

The agreement between experimental findings [12] of our computed frequencies are in good agreement with having maximum deviation less than 20% in both longitudinal and transverse modes. Again we would like to comment that the parameters are not adjusted to reproduce any phonon frequency. The best of our knowledge such approach has not been used previously for the study of lattice dynamics using local pseudopotential. In order to verify the reliability of present scheme we have computed frequency distribution (phonon density of states). The frequency spectra of the lattice vibrations is computed by the numerical sampling of the frequencies according to Blackmann's technique.We have considered a mesh of evenlyspaced 64000 wave vectors in the first Brillouin zone. The detailsof the calculations may be found in [13].

The variations of $W_T$ and $\overline{U}^2$ alongwith the experimental results due to Peng et. al. [14] are shown in Fig. 2. The agreement between experimental and theoretical results are very good. Using phonon density of states we have computed $C_v/3R$ upto $300^o$ K using expression given in [10]. From such numerical values of temperature variation of $C_v/3R$ we have computed temperature variation of Debye Temperature upto $300^o$ K as shown in Fig. 3. Computed results are in excellent agreement with experimental findings due to [15]. Here we would like to point that the Debye temperature$\theta_D$ at $0^o$ K is computed using method discussed by Raju [16].
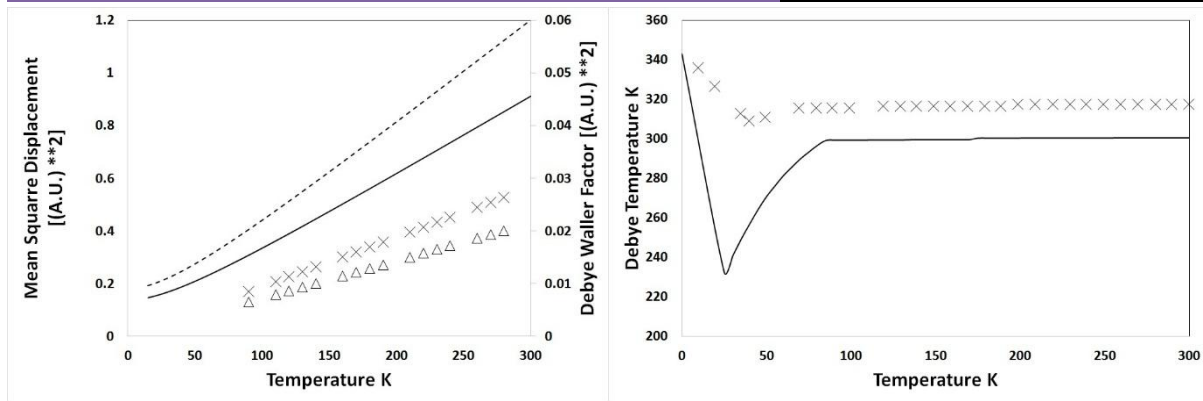
**FIG. 2** Temperature variations of $W_T$ and $\overline{U}^2$ **FIG.3** Temperature variations of $\theta_D$

## Conclusions:

From the present study we conclude that parameter free (first principles) local pseudopotential explains lattice dynamics and lattice mechanical properties with good degree of success. The use of experimental values of ionic and atomic radii is more realistic in comparison with those obtained by favoring some physical properties. We have also find that for the better description of the physical properties valency do play an important role. Here we would also like to comment that the pseudopotential constructed using experimental data can be fully justified when it is used for the study of comprehensive physical properties (static, lattice mechanical and transport).

## Acknowledgements:

## References:

1. C. V. Pandya, P. R. Vyas, T. C. Pandya, N. Rani and V.B. Gohel,Journal of the Korean Physical Society, 2001, 38(4), 377.
2. K. Kune, Electronic Structure, Dynamics and QuantumStructural Properties of Condensed Matter, editedby J. T. Devreese and P van Camp, Plenum, New York,1985.
3. T. Starkloff and J. D. Joannopoulos Phys. Rev. B, 1977, 16,5212.

4. C. V. Pandya, P. R. Vyas, T. C. Pandya, N. Rani and V.B. Gohel, Physica B Condensed Matter,2001, 307(1-4), 138.

5. A. Eichler, K. P. Bohnen, W. Reichardt and J. Hafner, Phys. Rev. B, 1998, 57, 324.

6. M. I. Katsnelson, I. I. Naumov, A. V. Tre_lov, M. N. Khlopkin and K. Yu Khromov, Phil. Mag. B,1997, 75, 389.

7. B. A. Greenberg, M. I. Katsnelson, V. G. Koreshkov, Yu N. Osetskii, G. V. Peschanskikh, A. V. Frefilov, Yu F. Shamanacv and L. I. Yakovenkova, Phys. Stat. Sol. (b), 1990, 158, 441.

8. A. S. Ivanov, M. I. Katsnelson, A. G. Mikhin, Yu N. Osetskii, A. Yu Rumyantsev, A. V.Trefilov, Yu F. Shamanaev and L. I. Yakovenkova, Phil. Mag. B, 1994, 69, 1183.

9. J. Kumar, Solid State Communications, 1977, 21, 945.

10. D. C. Wallace, Thermodynamics of Crystals, Dover's Publication, New York, 1998.

11. P. R. Vyas, C. V. Pandya, T. C. Pandya and V. B.Gohel, Indian J. Phys., 2001,75, 271.

12. G. Nilsson and S. Rolandson, Phys. Rev. B, 1973, **7**:6, 2393.

13. P. R. Vyas, PhD thesis, Gujarat University (Ahmedabad, India, 2000).

14. L. M. Peng, G.Ren, S. L.Dudarev and M. J. Whelan, ActaCryst. A, 1996, 52, 456.

15. D. L. Martin, Phys. Rev., 1966,141**,** 576.

16. S. Raju, E. Mohandas and V. S. Raghunathan, Z. Metallkd, 1996, 87,51.

# Study of molecular interactions in aqueous solutions of diclofenac potassium through acoustical parameters

Jigna B. Karakthala[1] and Vipinchandra A. Rana[2]

*Department of Physics, Gujarat University, Ahmedabad, Gujarat, India.*

Email: [1]jigna.karakthla@gmail.com,[2]varana@gujaratuniversity.ac.in

## Abstract

Physical properties like Density ($\rho$), ultrasonic velocity ($n$), viscosity ($h$) of aqueous solutions of diclofenac potassium were measured. Diclofenac potassium is non-steroidal and anti-inflammatory drug applied to reduce inflammation and analgesic reducing pain. As the drug's efficiency is affected by the degree to which it binds to protein within blood plasma, knowledge of drug interaction with water and protein is of paramount importance. To understand such interaction, acoustical parameters such as adiabatic compressibility ($\beta_a$), free length ($L_f$), acoustic impedance($Z$), Viscous relaxation time ($\tau_\eta$), apparent molar volume ($\Phi_v$) and apparent molar compressibility ($\Phi_k$) were determined using measured physical properties. All these measurements were done at 303.15 K.

**Keywords:** Density, ultrasonic velocity, viscosity, diclofenac potassium, protein, acoustical parameters.

## Introduction

In medicinal physics, drug-molecular interaction in physiological media involved in drug transport, protein binding and anesthesia are important phenomena [1]. An effort has been made in the present investigation to study the behavior of the diclofenac potassium (NSAID-nonsteroidal anti-inflammatory drug) in water solvent (since most of the biochemical activities occur in aqueous media) by measuring ultrasonic velocity ($n$), density ($\rho$), viscosity ($h$) and thereby computing related acoustical and thermal parameters. Diclofenac potassium is non-steroidal and anti-inflammatory drug applied to reduce inflammation and analgesic reducing pain. Thermodynamic and transport properties of drug in the aqueous state provides useful information in pharmaceutical science [2]. A drug's efficiency may be affected by the degree to which it binds to the protein within blood plasma. Thus, the knowledge about interaction of drug with water and protein is of paramount importance [3-5]. Understanding of such interactions based on solvation which depends on the polarity of solute and solvent, findapplicationin several

industrial and technological processes. Besides in pharmaceutical science for instance drug delivery, solubility, protein binding is essential [3-10]. The variation in these parameters with concentration gives idea about changes in molecular structures having weak or strong interactions[11,12]. In the present investigation physical properties like density ($\rho$), ultrasonic velocity (n), viscosity (h) of aqueous solutions of diclofenac potassium were measured, from these various acoustical parameters are calculated at 303.15 K. The results are interpreted in terms of molecular interactions between diclofenac potassium and water molecules.

**Materials and Methods**

2.1 Materials

Diclofenac potassium (with purity 99.98%) was obtained from Shree Parikh Trading, Ahmedabad, India. The Structural formula of Diclofenac Potassium ($C_{14}H_{10}Cl_2KNO_2$) is shown in scheme 1. Distilled water was obtained from High Purity Laboratory Chemicals (HPLC), Mumbai, India and was used for preparation of solutions. Which were made on mass basis at room temperature over the concentration range from 0 M to 0.0822 M using an electronic balance.

2.2 Measurements

The concentration is converted into the molarity using conversion formula described by E. M. Cheng et al. [13]. Density of solutions was measured by pycnometer which was calibrated using water with 995.6 kg/m³ as its density. Viscosity was measured by Ostwald viscometer and was calibrated with distilled water. All the experiments were repeated thrice. The ultrasonic velocity for the solutions was measured with ultrasonic interferometer (model F-81S) working at 2 MHz frequency. The various acoustical parameters like adiabatic compressibility ($\beta_a$), free length ($L_f$), acoustic impedance (Z), viscous relaxation time ($t_\eta$), apparent molar volume ($\Phi_v$) and apparent molar compressibility ($\Phi_k$) were evaluated using equations mentioned in ref. [5,14]. All these measurements were performed at 303.15 K.

**Results and Discussion**

Density, viscosity and ultrasonic velocity vary with concentration at 303.15 K for aqueous diclofenac potassium solutions as illustrated in figure 1. Density of solution increases with increase in the concentration of diclofenac potassium in distilled water as shown in figure 1.This might be the result of decreased volume of solution due to the attractive interaction between solvent-solute molecules which leads to increase in the overall mass of the solution [15]. The

rise in viscosity with concentration (figure 1) can be due to the increased no. of ions/molecules subjected to torsional force. This causes rotation of molecules/ions and hence absorption of energy [5]. Ultrasonic velocity increases on increasing the concentration of solute which may be attributed to cohesion brought about by the association among the molecule and greater solute -solvent interaction [16].
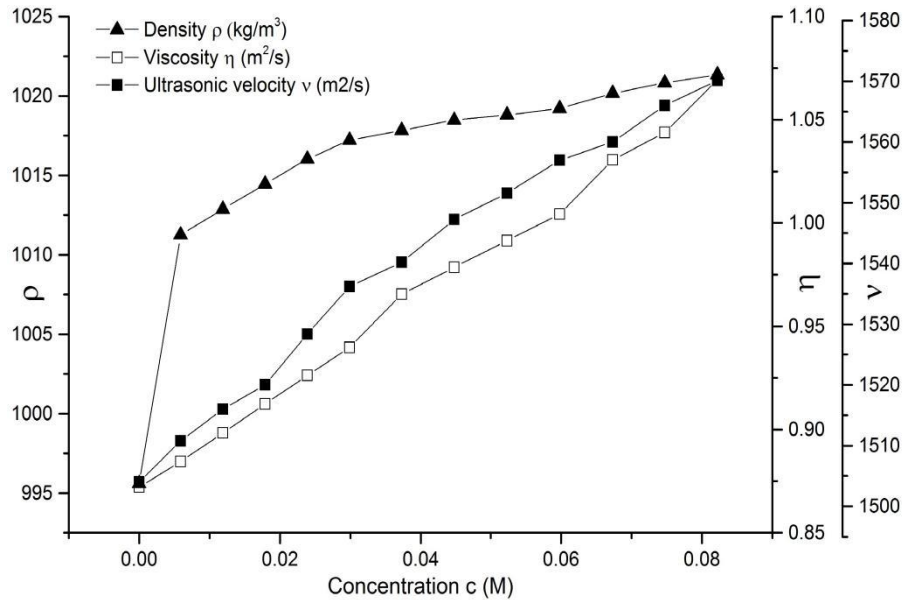


Figure 1. Variation of density ($\rho$), viscosity (h) and ultrasonic velocity (n) with concentration of aqueous solutions of diclofenac potassium at 303.15 K
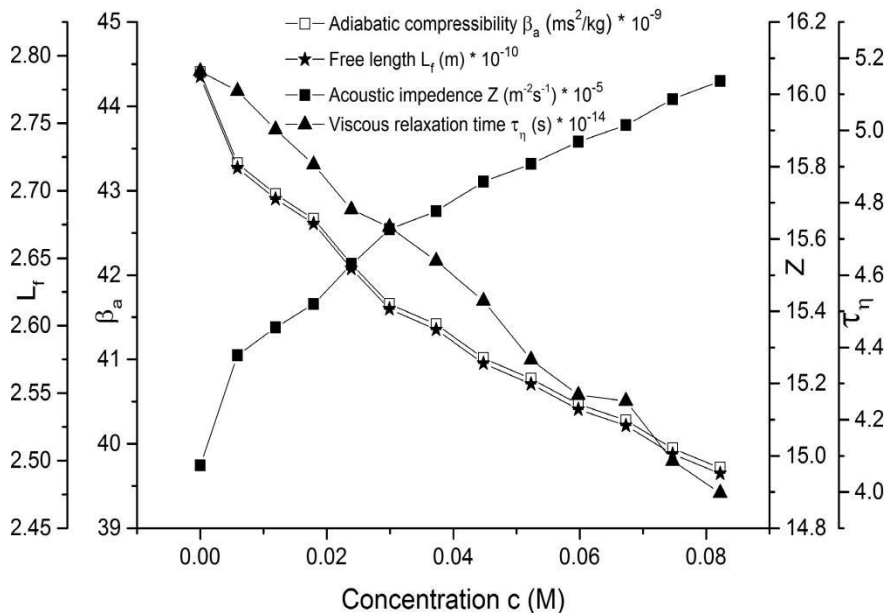


Figure 2. Variation of adiabatic compressibility ($\beta_a$), intermolecular free length ($L_f$), acoustic impedance (Z), viscous relaxation time ($t_\eta$) for aqueous solutions of diclofenac potassium at 303.15 K

As shown in figure 2, values of adiabatic compressibility decrease with concentration which indicates formation of strong hydrogen bonding between solute and solvent. This can also be verified by viscous relaxation time [17]. It is observed that the values of acoustic impedance increase and inter-molecular free length (distance between the surfaces of the neighboring molecule) decreases as concentration increases which shows strong interaction between solute and solvent [15,18].

Water is a polar solvent that solvates polar solutes and ions as they can orient the appropriate partially charged portion of the molecule towards the solute through electrostatic attraction. This stabilizes the system and creates hydration (solvation of Diclofenac potassium by water) shell around each particle of solute. Since diclofenac have hydrogen (H) bond acceptors and donor, it forms a strong H-bond with water which may be due to the solvated anion as shown in scheme 1 [2].
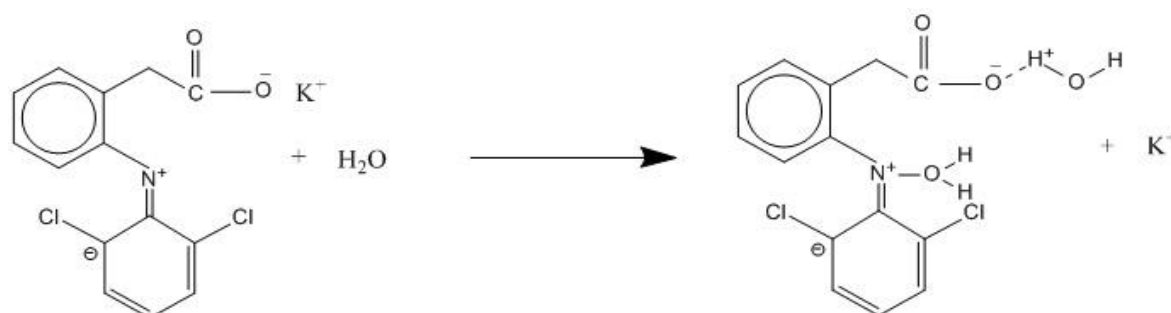


Scheme 1. Possible interaction of diclofenac potassium with water

Figure 3 shows negative values of apparent molar volume represents weak interaction but positive values for higher concentration shows that interaction becomes stronger with increase in the no. of solute ions in the solution which is in good agreement with the above statements. Studies of D. V. Jahagirdar et al. shows that negative value of compressibility is a sign of hydrophobic behavior of solute [5,19,20], which may result into lower binding with protein. Present study shows negative values of compressibility for the considered concentration range of aqueous diclofenac potassium. Due to lower protein binding diclofenac potassium gets release easily at appropriate position of the body and being a weak acid with a $pK_a$ 4.0, it has a protein binding ability of more than 99%, study of determination of drug release was done with the help of UV spectroscopy for diclofenac sodium by Aseri Ajay, et al. [21]. Drug binding may affect the drug dose response in the body as the drug is less bound, the more efficiently it traverse cell membranes or diffuse which satisfied with hydrophobic drug to be a better transporter throughout membranes than others [22].
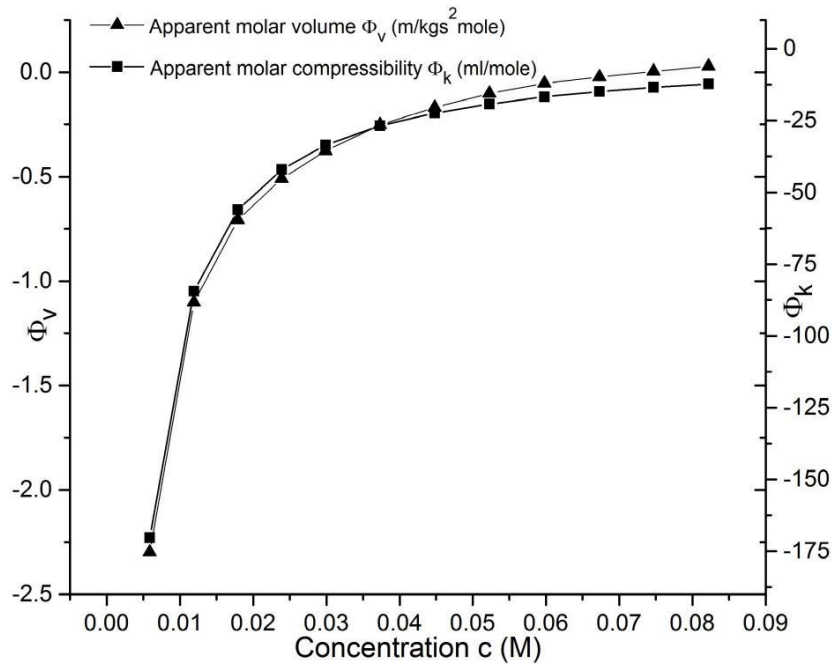
Figure 3. Variation of Apparent molar volume and apparent molar compressibility with concentration of aqueous diclofenac potassium solutions at 303.15 K

## Conclusion

Experimental Density($\rho$), ultrasonic velocity(n), viscosity (h) were measured for aqueous solutions of diclofenac potassium (non-steroidal and anti-inflammatory drug). Possible structure for the interaction of diclofenac potassium with water is proposed in this study. Efficiency of drug is affected by its binds to protein within blood plasma, information of drug interaction with water and protein is of paramount importance. To interpret such interaction, acoustical parameters are derived using above three experimentally measured properties. Since negative values of apparent molar compressibility for given concentration range of aqueous solutions of diclofenac potassium shows hydrophobic behavior of drug. Besides hydrophobic is a better transporter throughout membranes than others. Such kind of behavior shows that drug binds less with protein of blood plasma. Being less bind to the protein, Diclofenac potassium is having property to release easily at suitable area of body. Thus, appropriate protein binding was affected by selection of drug dose, so that the selection dose of drug is an important criterion and it should be taken in keen interest.

## Acknowledgement

acknowledged.We are also thankful to Prof. P. N. Gajjar, Head, Department of physics, School of Sciences, Gujarat University, Ahmedabad for his constant encouragement.

## References

[1]   S. J. Synder, J. R. Synder, J. Chem. Eng., 1974, 19, 207.

[2]   M. J. Iqbal, M. A. Chaudhary, J. Chem. Thermodyn., 2009, 41, 221.

[3]   J. C. McElnay, P. F. D'Arcy, ADIS Press Australasia, 1983, 25, 495.

[4]   S. Stephan, G. Daniel, D. Hartmut, J. Pharm. Sci., 2009, 99, 1107.

[5]   D. V. Jahagirdar, B. R. Arbad, S. R. Mirgane, M. K. Lande, A. G. Shankarwar, J. mol. Liq., 1998, 75, 33.

[6]   R. G. Rao, S. C. Rambabu, Indian J. Pure Appl. Phys., 2004, 42, 820.

[7]   A. Pal, H. Kumar, J. Chem. Thermodyn. 2004, 36,173.

[8]   T. S. Rao, N. Veeraiah, C. Rambabu, Indian J. Pure Appl. Phys. 2002, 40, 850.

[9]   A. Valen, M. C. Lopez, J. S. Urieta, F. M. Royo, C. Lafuente, J. Mol. Liq., 2002, 95,157.

[10] P. S. Nikkam, B. S. Jagdale, A. B. Sawant, M. Hasan, Indian J. Pure Appl. Phys. 2001, 39, 433.

[11] S. Thirumaran, K. Sathish, Bull. Pure Appl. Sci., 2008, 27, 239.

[12] S. Thirumaran, N. Karthikeyan, Int. J. Chem. Res. 2011, 3, 83.

[13] E. M. Cheng, M. Fareq, F. S. Abdullah et al., IEEE International RF and Microwave Conference, 2013, 409.

[14] S. Ajitha, H. A. Malini, M. V. Devi., Res. J. Pharm. Bio. Chem. Sci. 2013, 4, 218.

[15] S. D. Deosarkar, T. M. Kalyankar, Russ. J. Phys. Chem. 2013, 87, 1060.

[16] A. Dhote, S. Aswale, Adv. Appl. Sci. Res. 2012, 3, 2299.

[17] P. S. Naidu, K. R. Prasad, Indian J. Pure Appl. Phys. 2004, 42, 512.

[18] C. Sharma. Indian J. Pure Appl. Phys., 1989; 27, 32.

[19] K. Shakshi, K Arakawa, Bull. Chem. Soc. 1973, 2738.

[20] S. Prakash, F. M. Ichikaporia, J. D. Pandey., J. Phy. Chem., 1964, 3078.

[21] A. Aseri, D. Duggal, A. Nayak, J. Katewa, Asian J. Pharm. Res. Dev., 2013, 3, 98.

[22] J. Philip, L. Robert, V. prasad, Pharm. Res. Jpn., 2003, 20, 264.

# Study of Electrode Polarization and Ionic Conductivity Relaxation in Binary Mixtures of 3-Bromoanisole and Methanol at 293.15 K

Hemalkumar P. Vankar[a] and Vipinchandra A. Rana[b]

[a, b] Department of Physics, School of Sciences, Gujarat University, Ahmedabad, Gujarat,

India

Email ID: [a]hemal5drm@gujaratuniversity.ac.in, [b]ranava2001@gujaratuniversity.ac.in.

## Abstract

The complex relative dielectric permittivity $\varepsilon^{*}(\omega)=\varepsilon'-j\varepsilon''$ of the binary mixtures of 3-bromoanisole (3-BA) and methanol (MeOH) in the frequency range 20 Hz to 2 MHz at 293.15 K temperature were fitted to Coelho model. The electrode polarization relaxation time $\tau_{EP}$ were obtained using fitted model and compared with the electrode polarization relaxation time $\tau_{EP}'$ which were obtained by the tanδ spectra. The real and imaginary part of complex electric modulus ($M^{*}$) were determined for the binary mixtures. The ionic conductivity relaxation time $\tau_{\sigma}$ were also determined to understand the relaxation processes.

**Keywords:** Complex relativedielectric permittivity, Coelho Model, Electrode polarization relaxation time, Ionic conductivity relaxation time.

## Introduction

Recently we reported concentration dependent dielectric behaviour of the binary mixtures of 3-bromoanisole (3-BA) and methanol (MeOH) in frequency range 20 Hz to 2 MHz at 293.15 K temperature [1]. As an extension of this work, experimental data of complex relative dielectric function of binary mixtures of 3-bromoanisole (3-BA) and methanol (MeOH)were fitted to Coelho model [2, 3] and fitted parameters are reported in this paper. The present paper concerns mainly with different relaxation phenomenon taking place in the low frequency region (20 Hz to 2 MHz) in binary mixtures of 3-BA and MeOH of varying concentration. The relaxation processes were investigated with the help of electrode polarization relaxation time $\tau_{EP}$ and ionic conductivity relaxation time $\tau_{\sigma}$.

**Materials and Methods**

Details of materials and sample preparation were reported in our recent publication [1]. The low frequency complex permittivity data were fitted to the Debye type Coelho model [2,3]

$$\varepsilon^*(\omega) = \varepsilon_s + \frac{\Delta\varepsilon_{EP}}{1+j\omega\,\tau_{EP}} \tag{1}$$

Where, $\Delta\varepsilon_{EP} = \varepsilon_{s,EP} - \varepsilon_s$, $\varepsilon_{s,EP}$ is low frequency dielectric constant in presence of EP, $\varepsilon_s$ is static dielectric constant and $\tau_{EP}$ is electrode polarization relaxation time.

Fitting parameters $\Delta\varepsilon_{EP}$, $\varepsilon_s$ and $\tau_{EP}$ were obtained by fitting the experimental data of complex relative dielectric permittivity $\varepsilon^*(\omega)$ to equation (1) by using a complex nonlinear least square (CNLS) fit method [4].

Complex electric modulus is correlated to the complex relative dielectric function by the following relation [5]

$$M^*(\omega) = M^{'}(\omega) + M''(\omega) = \frac{\varepsilon'}{\varepsilon'^2+\varepsilon''^2} + \frac{\varepsilon''}{\varepsilon'^2+\varepsilon''^2} \tag{2}$$

**Results and Discussion**

Frequency dependent plots of real ($\varepsilon'$) and imaginary ($\varepsilon''$) parts of relative dielectric function ($\varepsilon^*$) with fitted Coelho model for 3-BA, MeOH and mixture of 3-BA (50%) + MeOH (50%) are shown in Figure 1. From this figure it can be seen that the experimental data can be well fitted to Coelho model. The Coelho model is used to fit complex permittivity data of all other mixture samples. It was observed that the Coelho model provide good fitting for 3-BA and it start to show deviation in lower frequency region with decrease the concentration of 3-BA in MeOH. The values of the fitting parameters are reported in Table 1.

**Table 1.** Fitting parameters $\varepsilon_s$, $\Delta\varepsilon_{EP}$, and $\tau_{EP}$ of the Coelho model.

| Concentration of MeOH | $\varepsilon_s$ | $\Delta\varepsilon_{EP}$ | $\tau_{EP}$ (ms) |
|---|---|---|---|
| 0 | 7.12 | 6.292E+05 | 903.75 |
| 0.1 | 8.34 | 6.021E+05 | 40.27 |
| 0.2 | 10.29 | 5.307E+05 | 8.60 |
| 0.3 | 12.53 | 5.250E+05 | 4.44 |
| 0.4 | 14.89 | 5.273E+05 | 3.23 |
| 0.5 | 17.40 | 5.191E+05 | 2.60 |
| 0.6 | 19.95 | 5.143E+05 | 2.39 |
| 0.7 | 22.51 | 4.996E+05 | 2.36 |

| 0.8 | 25.39 | 4.947E+05 | 2.59 |
| --- | --- | --- | --- |
| 0.9 | 27.55 | 4.552E+05 | 2.72 |
| 1 | 30.49 | 3.930E+05 | 4.86 |

The fitted and experimental value of static dielectric constant of 3-BA is 7.12 and 7.11 [1] while that for MeOH is 30.49 and 32.95 [1] respectively. The electrode polarization relaxation time for MeOH is about 4.86ms and for 3-BA is 903.75 ms, which is around 186 times higher than that of MeOH.
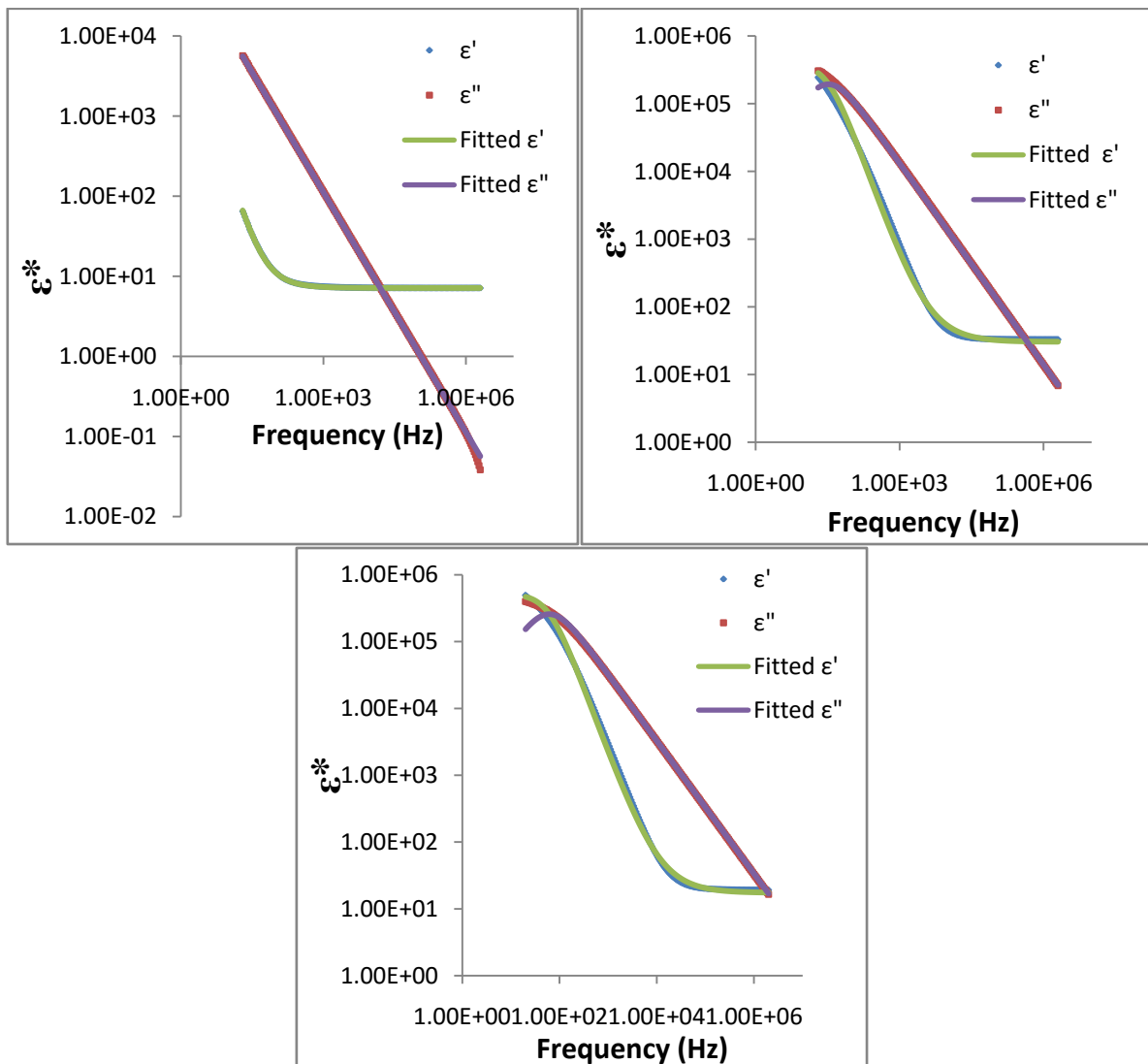


**Figure 1.** Complex dielectric function ($\varepsilon^{*}$) versus frequency for (a) 3-BA, (b) MeOH and (c) mixture of 3-BA (50%) + MeOH (50%). The solid line indicates best fit of Coelho model.

The electrode polarization (EP) relaxation time $\tau_{EP}$ for different concentration of 3-BA and MeOH were obtained by Coelho model. Variation of EP relaxation time $\tau_{EP}$ with

concentration of MeOH is shown in Figure 2. As shown in figure 2 the behaviour $\tau_{EP}$ is very similar to EP relaxation time $\tau_{EP}'$ which was derived using tan$\delta$ plot in our earlier publication [1]. The $\tau_{EP}$ and $\tau_{EP}'$ are correlated by the relation $\tau_{EP}' = (\tau_{EP}\tau_{\sigma})^{1/2}$[3] where $\tau_{\sigma}$ is ionic conductivity relaxation time which will determined in later part of this paper.
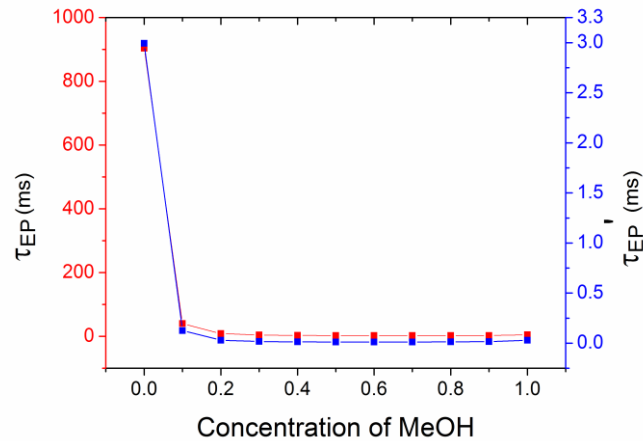


**Figure 2.** Plot of electrode polarization relaxation time $\tau_{EP}$ (Using Coelho model) and $\tau_{EP}'$ (Using tan$\delta$ spectra) versus concentration of MeOH

The frequency and concentration dependent real (M') and imaginary (M") part of complex electric modulus (M$^*$) for binary mixture of 3-BA and MeOH are shown in Figure 3 and 4 respectively. The complex electric modulus is basically inverse of the complex relative dielectric function ($\varepsilon^*$) as a result in Figure 3 the value of M' is very high in high frequency region. The higher value of M' in high frequency region is due to ionic conduction. In Figure 3, M" spectra of these mixtures have peaks and frequency $f_{\sigma}$ corresponding to these peaks is related to the ionic conductivity relaxation time $\tau_{\sigma}$ by the relation $\tau_{\sigma} = (2\pi f_{\sigma})^{-1}$[6, 7]. The variation of $\tau_{\sigma}$ as a function of concentration of MeOH is shown in Figure 5.
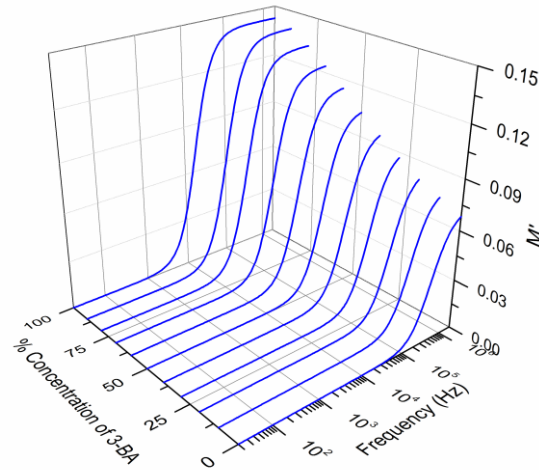
**Figure 3.** 3D Plot of real part of electric modulus (M') versus % concentration of 3-BA and frequency

Ionic conductivity relaxation time $\tau_\sigma$ of 3-BA and MeOH are about 8.93 µs and 0.38 µs respectively. The $\tau_\sigma$ value decrease up to 80% concentration of MeOH, and remain same up to 90% concentration and then it increases reaching to $\tau_\sigma$ value of pure MeOH.
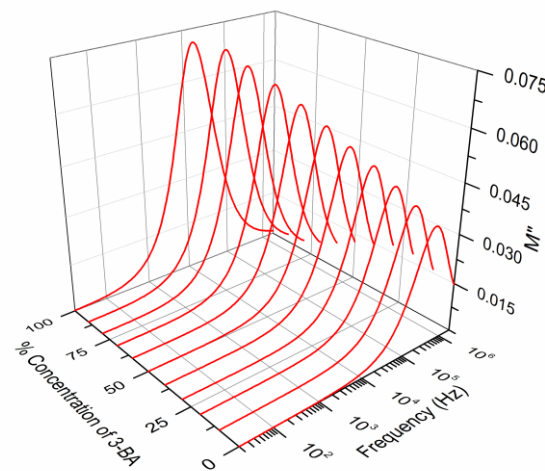


**Figure 4.** 3D plot of imaginary part of electric modulus (M") versus % concentration of 3-BA and frequency
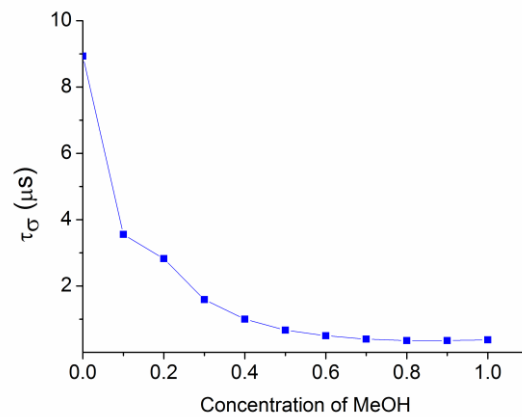
**Figure 5.** Plot of ionic conductivity relaxation time (τ$_σ$) versus concentration of MeOH

Figure 6 presents' complex plane electric modulus spectra of studied system and all are single Debye type in the static dielectric region which indicates single ionic conductivity relaxation process.
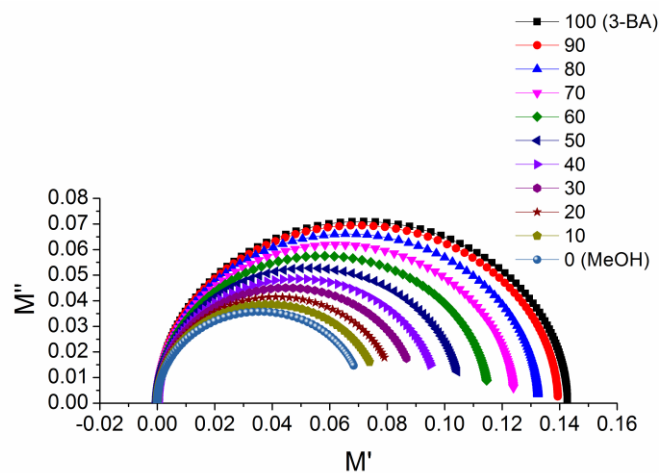


**Figure 6.** Electric modulus spectra for the binary mixture of 3-BA and MeOH in complex plane

**Conclusions**

The complex relative dielectric spectra of the binary mixtures of 3-BA and MeOH were fitted to Coelho model in the frequency range of 20 Hz to 2 MHz at 293.15 K. The Coelho model gives good fitting in higher concentration of 3-BA. The EP relaxation time obtained by Coelho model and tan δ spectra, gives similar behaviour. The ionic conductivity relaxation time is maximum for 3-BA and it decrease with increase in concentration of MeOH. Modulus spectra in complex plane show single Debye type ionic conductivity relaxation.

## Acknowledgements

## References

[1] H. P. Vankar and V. A. Rana, In: D. G. Kuberkar (Ed.), International Conference on Functional Oxides and Nano materials, 11-13 Nov. 2016, Rajkot, India (AIP, United States, 2017) 040008.

[2] R. Coelho, J. Non-Cryst. Solids, 1991, 131, 1136.

[3] R. J. Klein, S. Zhang, S. Dou, B. H. Jones, R. H. Colby and J. Runt, J. Chem. Phys., 2006, 124, 144903.

[4] J. R. Macdonald, LEVM/LEVMW manual, Version 8.12, 2013.

[5] J. Jadzyn, J. Swiergiel, Ind. Eng. Chem. Res., 2012, 51, 807.

[6] S. Zhang, S. Dou, R. H. Colby, J. Runt, J. Non-Cryst. Solids, 2005, 351, 2825.

[7] R. J. Sengwa, S. Sankhla, Colloid. Polym. Sci., 2007, 285, 1237.

# Protein-ligand Docking Studiesof Novel Silver Complex of 4-Amino-N-(4,6-dimethyl-2-pyrimidinyl)benzene sulfonamide

Bhavesh N. Socha[2], Sachin B. Pandya[2], Kaushik P. Chaudhary[2], Khushbu k. Lalvani[2], U. H. Patel[1]

X-ray Crystallographic Laboratory, Department of physics, Sardar Patel University Vallabh vidhyanagar-388120, Gujarat, India.

Email: Bhaveshsocha@gmail.com

**Abstract:**

This paper deals with molecular docking studies of a novel Silver complex of4-Amino-N-(4,6-dimethyl-2-pyrimidinyl)benzene sulfonamide (sulfamethazine)with (A) Dihydropteroate synthase enzymes[ Plague (Yersinia Pestis)](1) 3TZF (2) 5JQ9.(B) Dihydropteroate synthase enzymes (Homo sapiens) – (1) 4J7U (2) 4HWK.The Molecular Docking performed using a software package from Schrödinger. Hydrogen-bonding interactions of the title molecule with the amino acids of the target protein have been analyzed.

**Key words:** Molecular docking studies, Silver complex of sulfamethazine, hydrogen bondInteractions, receptors.

**Introduction:**

Sulfonamides [1] are the first 'chemotherapeutic' agents which are employed systematically for the prevention and cure of bacterial infections in human beings also used in the treatment of inflammatory bowel disease. Sulfa drugs are bacteriostatic. They act by interfering with the synthesis of folic acid (folate), a member of the vitamin B complex present in all living cells. Most bacteria make their own folic acid from simpler starting materials; humans and other higher animals, however, must obtain folic acid in the diet. Thus, sulfa drugs can inhibit the growth of invading microorganisms without harming the host. Silver ions and silver compounds show a toxic effect on some bacteria, viruses, algae and fungi, typical for heavy metals like lead or mercury, this ion forms strong molecular bonds with other substances used by bacteria to respire, such as molecules containing sulphur, nitrogen, and oxygen. When the $Ag^+$ ion forms a complex with these molecules, they are rendered unusable by the bacteria, depriving them of necessary compounds and eventually leading to the bacteria's death. **[1],**

Sulfamethazine **[1]** as shown in **Figure 1.1** is one of the active member of antibacterial sulfonamides family. It has spectrum of antimicrobial action similar to other sulfonamides. The Sulfamethazine (4-amino-N-(4, 6- dimethyl-2-pyrimidinyl) benzene sulfonamide) is commonly incorporated into swine feed as promotants of growth and for control of certain diseases in animals. Transition metal complex of sulfamethazine has been synthesized and its structure has been reported by us. **[2]**(M.phil. dissertation)
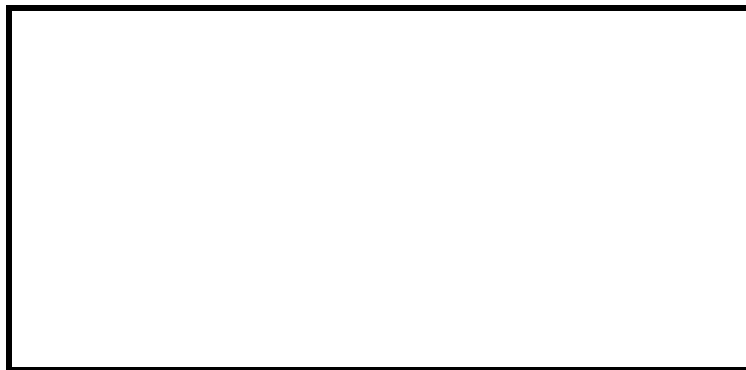


**Figure 1.1 Sulfamethazine (SMZ)**

Plague is a disease that affects humans and other mammals. It is caused by the bacterium, Yersinia Pestis. Human usually get plague after being bitten by a rodent flea that is carrying the plague bacterium or by handling an animal infected with plague. **[3]**

To correlate the structure-function relationship, we have carried out molecular docking studies of the title molecule using glide docking module of Schrodinger software. The small molecule called ligand usually interacts with protein's binding sites. Binding sites are areas of protein known to be active in forming of compound. There are several possible mutual conformations in which binding may occur. These are commonly called binding modes. It also predicts the strength of the binding, the energy of the complex; the types of signal produced and calculate the binding affinity between two molecules using scoring function. The most interesting case is the type protein-ligand interaction, which has its applications in medicine. It aims to achieve an optimized conformation for both the protein and ligand and relative orientation between protein and ligand such that the free energy of the overall system is minimized. Molecular docking can be referred as "lock and key" model **[4]**. Here the protein can be called as a lock and the ligand can be called as key, which describes the best fit orientation of the ligand to which it goes and

binds to a particular protein. To perform a docking study, in which the protein structure and ligand are the inputs and the protein structure data used to be collected from PDB(Protein Data Bank).

Our interest has focused biological response of novel title molecule shown in **Figure 1.2**. The biological activity gets enhanced on undergoing complexation with metals. Several metal complexes of sulfonamides showed higher activity than free ligand. In this paper the study of molecular docking has been carried out for the two different types of protein (Yersinia Pestis)and Homosepiance)[5, 6] in which glide energy, docking score, hydrogen bond interactions and types of interactions has been presented in **Table 1**.and compared.
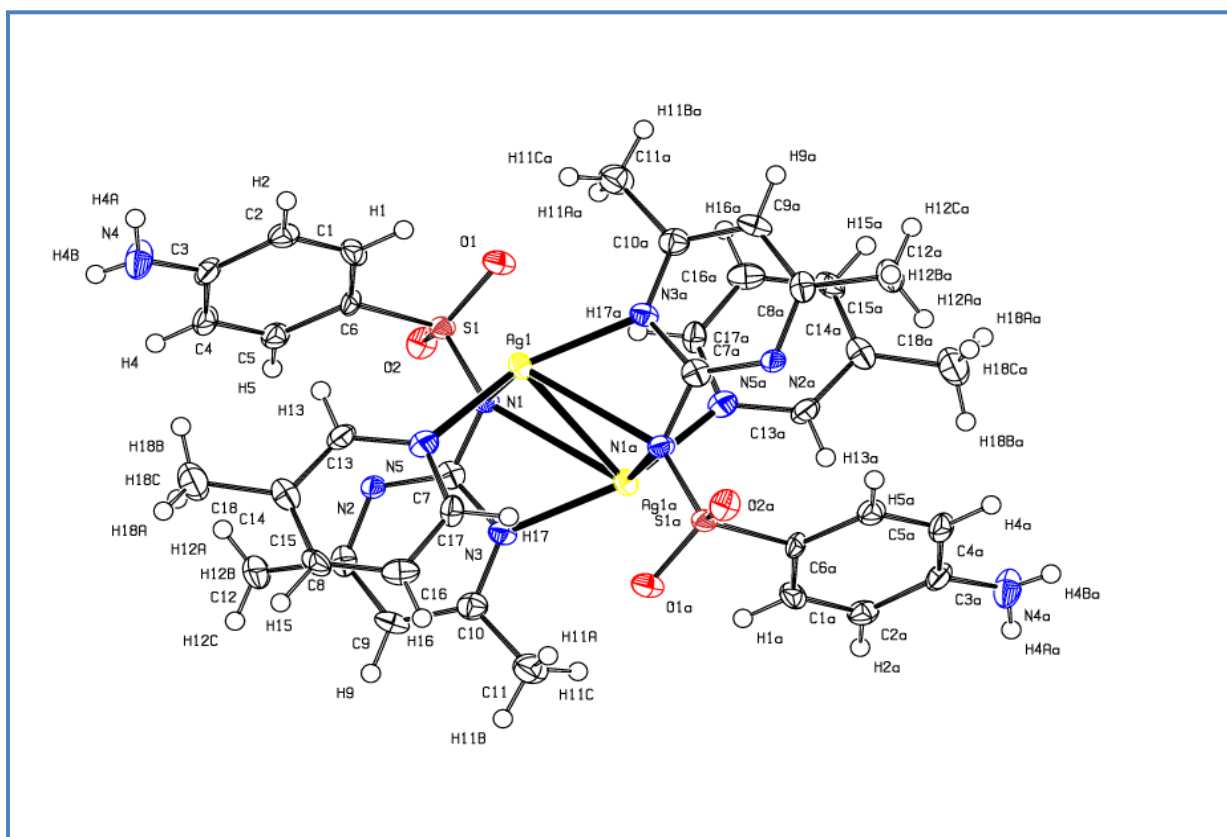


**Figure 1.2 Silver complex of sulfamethazine**

**Materials and methods:**

**Methodology:**

In the present study, we carried out the docking studies of transition metal complex of sulfamethazine with target proteins (A) Dihydropteroate synthase enzymes[ Plague (Yersinia

Pestis)] (1) 3TZF  (2) 5JQ9.(B) Dihydropteroate synthase enzymes (Homo sapiens) – (1) 4J7U (2) 4HWK which were extracted from PDB. The Protein Data Bank (pdb) is the single, global archive for information about the 3D structure of bio macromolecules and their complexes, as determined by X-ray crystallography, NMR spectroscopy and includes more than a few Nobel Prize winning structures. The crystal structure of the target protein, (A) Dihydropteroate synthaseenzymes [Plague (Yersinia Pestis)] (1) 3TZF (2) 5JQ9 (B) Dihydropteroate synthase enzymes (Homo sapiens) – (1) 4J7U (2) 4HWK are downloaded from the PDB with the specific resolution.

PREPARATION OF PROTEIN

A typical PDB structure file consists only of heavy atoms and may include water molecules, metal and ions. Some structures are multimeric, and may need to be reduced to a single unit. In Schrödinger package a set of tools are accumulated to prepare proteins in a form that is suitable for modeling calculations.

PREPARATION OF LIGAND:

The Schrödinger ligand preparation product LigPrep is designed to prepare different conformations of the title molecule.

GLIDE GRID GENERATION:

Glide (Grid-based Ligand Docking with Energetics) is a ligand binding tool provided by Schrödinger package that searches for favorable interactions between one or more ligand molecules and a receptor molecule, usually a protein. It provides a complete solution for ligand-receptor docking. The combination of position and orientation of a ligand relative to the receptor, along with its conformation in docking, is referred to as a ligand pose. The ligand poses that Glide generates pass through a series of hierarchical filters that evaluate the ligand's interaction with the receptor. Finally, the minimized poses are re-scored to generate the Glide score (G score) that is the sum of total various figures generated for each ligand during the docking process. The scoring function (G score), for computing binding affinity is an extension of an empirically based Chem-Score function of Eldridge et al. [7]. The best G Score is obtained as the

most negative and the most active ligands in terms of G Score are enlisted in descending order.**[8, 9]**

**Results and Discussion:**

**Molecular Docking**

Molecular docking predicts the binding strength of ligand with different receptors. GLIDE docking method has been applied to build a binding affinity model for the title molecule with different protein complexes. The binding is predicted with help of mainly three parameters Glide score, Glide energy and H-bond interactions. On the basis of these parameters the binding affinity of ligand towards the receptors are discussed. The more negative value of G-score indicates the good binding affinity of the ligand with particular protein. The minimum energy for the formation of complex between ligand and receptor indicates the good binding affinity. More number of H-bond interactions in the structure revealsligand having good binding mode to receptor.

Here, silver complex of sulfamethazine is docked with (A) Dihydropteroate synthaseenzymes [Plague (Yersinia Pestis)] (1) 3TZF (2) 5JQ9. (B) Dihydropteroate synthase enzymes (Homo sapiens) – (1) 4J7U (2) 4HWK. Docking results are tabulated in **Table 1**, which clearly reflects that Silver complex of sulfamethazine molecule binds well with 4HWK receptor

The title molecule is found to have high docking score of -6.0and energy -46.4 kcal/mol with 4HWK receptor.  The 5JQ9 receptor gives G-score of -4.0with glide energy -35.8kcal/mol. The title molecule interacts with 4HWK and 5JQ9 proteins at sites: SER222, ASP214 and ASP212, (Figure 3). In addition, 4HWK receptor forms hydrogen bond interaction via HID1048 with pyrimidine nitrogen of SMZ molecule. The binding sites of 4HWK and 5JQ9 proteins after GLIDE docking with title molecule are depicted in Figure 3 and Figure 4represents hydrogen bond interactions between 4HWK and 5JQ9 receptors with title molecule.

.

**Table 1: Docking results of Silver complex of Sulfamethazine molecule with different receptors**

| Protein | Receptors | Glide Score | Glide energy | H-Bond Interactions | Hydrophobic Interaction |
|---|---|---|---|---|---|
| Yersinia Pestis | (1)3TZF | -2.1 | -41.6 | (1)N-H.....O (SER222) = 1.91Å (2)O-H…O (SER222) =2.84Å (3)N-H…O (SER222) =3.15Å | PRO64, MET148, PHE188, PHE190, PHE28 |
| | (2) 5JQ9 | -4.0 | -35.8 | (1)N-H.....O (GLU122) = 2.82Å (2)N-H…O (GLU68) =2.82Å (3)N-H…O (GLU68) =3.02Å (4)N-H…O (GLU68) =2.91Å | nil |
| Homo sapiens | (3)4J7U | -5.4 | -29.3 | (1)N-H.....O (ASP254) = 2.73Å | PRO195, TYR167 CYS156 ALA194 LEU155 |
| | (4) 4HWK | -6.0 | -46.4 | (1)N-H.....O (ASP212) = 2.96Å (2)O-H…O (ASP214) =3.72Å (3)N-H…O (ASP214) =3.55Å | PRO160 CYS156 LEU155 PRO197 LEU219 |
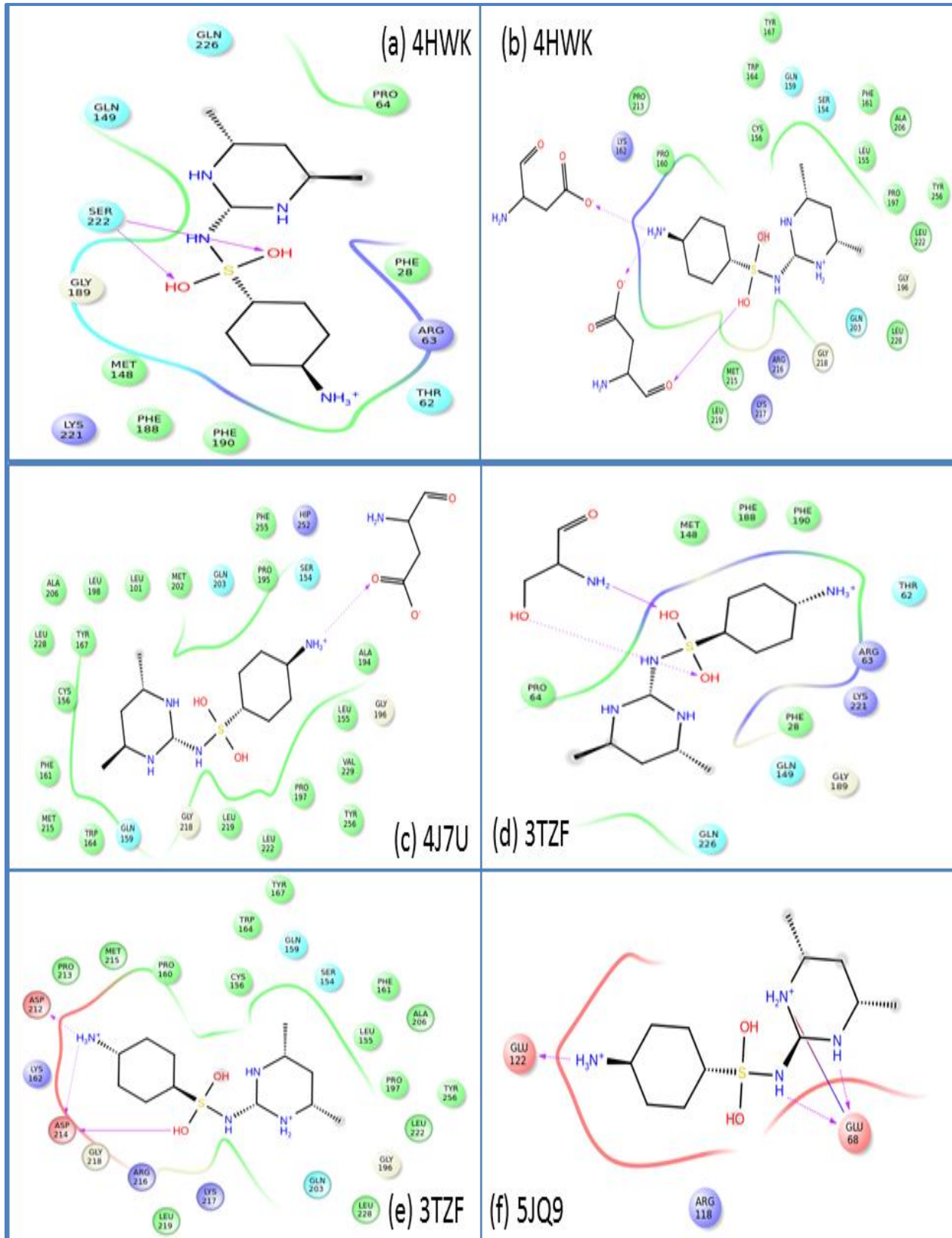
**Figure 3: The binding sites of Silver complex of sulfamethazine with (a, b) 4HWK (c) 4J7U**

**(d, e) 3TZF (f) 5JQ9 of the protein receptors after GLIDE docking**
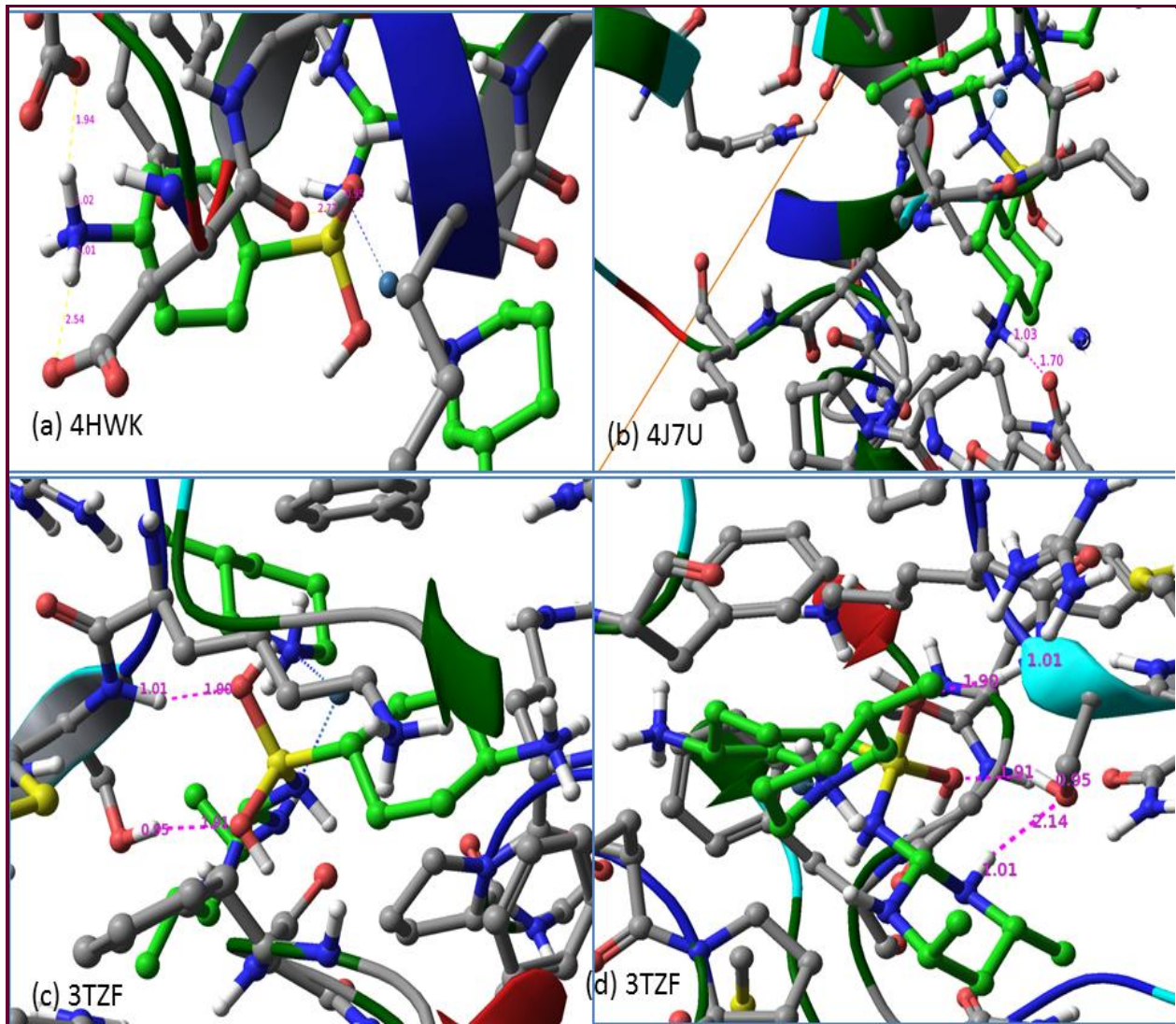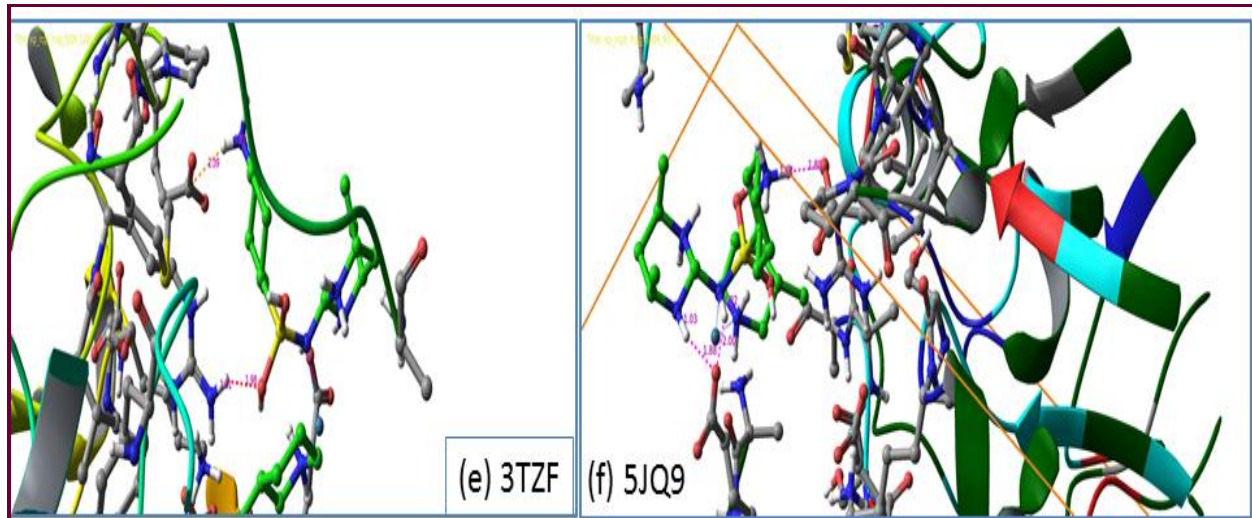
**Figure 4: Interaction of Silver complex of sulfamethazine with (a) 4HWK (b) 4J7U (c, d, e) 3TZF (f) 5JQ9 receptors**

**Conclusion:**

The title molecule Silver complex of Sulfamethazine (SMZ) has been docked with different receptors. Docking results reveals that the title molecule has the lowest Glide score of-6.0    and Lowest Glide energy with the receptor-46.4.

**Acknowledgement:**

**Reference list**

1. www.wikipedia.com
2. Bhavesh N.Socha, M.Phil./Dissertation,Sardar Patel University(Vallabh Vidhyanagar, India , June-2017)
3. CDC. Plague. Atlanta, GA: US Department of Health and Human Services, CDC; 2015. Available at http://www.cdc.gov/plague/
4. .D. B. Kitchen, H. Decornez, J. R. Furr, J. Bajorath, Nature reviews Drug discovery, 2004, 3(11), 935.
5. W. L. Jorgensen, Science, 1991, 254 (5034), 954.

6.  Mi-Kyung Yun1, Yinan Wu1,2, Zhenmei Li1, Ying Zhao3, M. Brett Waddell4, Antonio M. Ferreira1,5, Richard E. Lee3, Donald Bashford1,2, Stephen W. White1,2, Science  02 Mar 2012, 335, 6072, 1110-1114.

7.  Hirohito Haruki, Miriam Grønlund Pedersen, Katarzyna Irena Gorska, Florence Pojer, Kai Johnsson,Science, 24 May 2013, 340,  6135, 987-991.

8.  ELDRIDGE, M.D., C.W. MURRAY, T.R. AUTON, G.V. PAOLINI, R.P. MEE, Empirical scoring functions: empirical scoring function to estimate the binding affinity of ligands in receptor complexes, J. Comput. Aided. Mol. Des., 1997, 11, 425–445.

9.  GOHLKE, H., G. KLEBE, Approaches to the description and prediction of the binding affinity of small-molecule ligands to macromolecular receptors, Angew. Chem. Int. Ed.., 2002, 41, 2644–2676.

# Elastic Properties of $Mg_{65}Cu_{25}Tb_{10}$ Bulk Metallic Glass Using Pseudopotential Theory

A .C.  Khunt[#1], D. D. Satikunvar[1], R .H. Joshi[1], N. K. Bhatt[2] and B. Y. Thakore[1]

[1]Department of Physics, Sardar Patel University, Vallabh Vidynagar-388120, Gujarat

[2]Department of Physics, M. K. Bhavanagr University, Bhavanagr -364001, Gujarat

[#]Corresponding author email: ankitkhunt@spuvvn.edu

**Abstract**: The phonon dynamics of Mg-based Bulk metallic glass(BMG) has been reported through this paper. Longitudinal and Transverse modes for phonon eigen frequencies were studied using the approach proposed by Hubbard-Beeby. Further to calculate the ion-ion interaction we have used our recently proposed local pseudopotential. In the present study we have calculated the elastic properties of $Mg_{65}Cu_{25}Tb_{10}$. Along with the phonon frequencies different elastic properties are also evaluated. Five different forms of the static local field correction functions, viz., Hartree (H), Taylor (T), Ichimaru and Utsumi (IU), Farid (F) and Sarkar and Sen.(S) are employed to investigate the influence of the screening effect on the vibrational dynamics of $Mg_{65}Cu_{25}Tb_{10}$ BMG . Result for bulk modulus, modulus of rigidity, Poisson's ratio, Young modulus, propagation velocity of elastic waves and dispersion curves are studied. Good agreement of presented results and others findings confirms the use of our model pseudopotential to study elastic properties of such a glassy system.

**Keywords:** elastic constant, pseudopotential.

## Introduction

Atoms inside the matters always perform the motion. However, the interaction among the atoms results into the cooperative motion. These motion of the atoms are provides base to the macroscopic dynamics of liquids and solids. As we know that the main boundary between the solid and liquid is periodicity of atoms. Liquids or amorphous structure both has the short range order [1]. BMG matrix materials are fast developing and promising materials in modern industry. Bulk metallic glasses have found wide ranging application in the field of materials science and engineering during the last three decades [2,3]. Such solids have electronic properties normally associate with metals but atomic arrangement is not spatially periodic. Ternary metallic glasses made up of components of simple metals provide us with physically interesting systems for theoretical investigations. Bulk metallic glasses usually show high strength, large elastic limit and excellent wear and corrosion resistances along with

other remarkable engineering properties. Researchers have developed families of binary and multicomponent systems [4,5] to from BMGs. Appreciating the continuous success of applicability of pseudopotential in the study of metallic glasses we thought it worthwhile to test a typical local pseudopotential. Hence in the present work we have proposed such application of model pseudopotential. Deviating from a routine approach we have made use of five prominent screening functions to examine the relative influence of exchange and correlation effects. This has been carried out by studying collective modes and elastic properties of $Mg_{65}Cu_{25}Tb_{10}$ glass.

## Computational Methodology

Very first ingredient to calculate the different properties of the matter is the interaction among the atoms inside the matter. This interaction between the atoms is calculated using the different form of pair potential. There are many methods are present to calculate the pair potential, among all of them one is the simplest method is pesudopotential method [6,7]. In this study we have calculate the pair potential using two different form of pseudopotential. The first form is recently proposed by us, which is referred as model potential-1 (MP-1), while another form is referred as model potential-2 (MP-2). Eq.(1) and Eq.(2) represents the form of MP-1 and MP-2 respectively, in r-space. The core radius $R_c$ is potentail parameter and calculated as given in Ref [8]. Here, Z and e represent effective valance and electronic charge, respectively, for model potential 1, the whole effective region is splitted into two parts which satisfies the boundary conditions. We have included both the feactures of the pseudopotential cancellation as well as remaining interaction around the ion. Inside the core region cancellation effect is more and become weaker. A study of form factor gives correct limiting value of $-\frac{2}{3}k_f{}^2$ as q→0 which is required for local pseudopotential. The most interesting feature is that this present potential is applicable to almost all metal in periodic table.

For model potential-2, Inside the core $-\frac{ze^2}{r}$ coloumbian term is modified by exponential term. At r→0, it approches a constant value of $-\frac{ze^2}{R_c}$ and outside the core it retains the coloumbian term.

$$W(r) = -\frac{Ze^2e}{R_c}\left[\frac{2r}{R_c} - \frac{r^2}{R_c{}^2}\right]e^{\frac{-r}{R_c}} \qquad\qquad r \le R_c$$

$$= -\frac{Ze^2}{r} \qquad\qquad r \ge R_c \qquad (1)$$

$$W(r) = -\frac{Ze^2}{r} + \frac{Ze^2}{r}\exp\left(\frac{-r}{Rc}\right) \qquad\qquad r \ge R_c$$

$$= -\frac{Ze^2}{r} \qquad\qquad r < R_c \qquad (2)$$

Since all physical properties can be computed within the pair potential formalism, based on these model potentail-1 and potential-2, an effective pair potential $V_{eff}$ is calculated. This allows us to compute $\omega_E{}^2$, where, $\omega_E$ is the maximum phonon frequency.

$$\omega_E{}^2 = \frac{4\pi\rho_{eff}}{3M_{eff}}\int_0^\infty g(r)r^2 V_{eff}{}''(r)\,dr \qquad\qquad (3)$$

In equation (3), $g(r)$ is pair correlation function.

$$g(r) = 1 + \frac{\Omega}{2\pi r}\int_0^\infty q\,[S(q)-1]\sin(qr)\,dq \qquad\qquad (4)$$

The upper limit in the integration is decided by the length of $g(r)$ in the computation. $M_{eff}$ is the effective atomic mass and $\rho_{eff}$ is the effective number density. The input parameters used in the calculation are show in Table 1.

The longitudinal and transverse phonon frequencies in Hubbard and Beeby [9,10] approach are given by following equations.

$$\omega_L^2(q) = \omega_E^2\left[1 - \frac{3\sin(q\sigma)}{q\sigma} - \frac{6\cos(q\sigma)}{(q\sigma)^2} + \frac{6\sin(q\sigma)}{(q\sigma)^3}\right] \qquad\qquad (5)$$

$$\omega_T^2(q) = \omega_E^2\left[1 + \frac{3\cos(q\sigma)}{(q\sigma)^2} - \frac{6\sin(q\sigma)}{(q\sigma)^3}\right] \qquad\qquad (6)$$

Since in the long wavelength limit the phonon dispersion curves show elastic behaviour, which permits us to write the longitudinal $v_l$ and transverse $v_t$ sound velocities using the expressions

$$\omega_l \propto q \quad \text{and} \quad \omega_t \propto q$$

Therefore,

$$\omega_l = v_l q \quad and \quad \omega_t = v_t q \tag{7}$$

The elastic properties such as bulk modulus $B_T$, rigidity modulus $G$, Poisson's ratio $\xi$, Young's modulus $Y$ and Debye temperature $\theta_D$ are computed using the following expressions depending on longitudinal $v_l$ and transverse $v_t$ sound velocities as [11]

$$B_T = \rho \left( v_l^2 - \frac{4}{3} v_t^2 \right) \tag{8}$$

$$\xi = \left[ \frac{1 - 2\left(\frac{v_t^2}{v_l^2}\right)}{2 - 2\left(\frac{v_t^2}{v_l^2}\right)} \right] \tag{9}$$

$$\tag{10}$$

$$G = \rho v_t^2$$

$$Y = 2G(\xi + 1) \tag{11}$$

$$\theta_D = \frac{h}{k_B} \left[ \left( \frac{9\rho}{4\pi} \right)^{\frac{1}{3}} \left( \frac{1}{v_l^3} + \frac{2}{v_t^3} \right)^{\frac{-1}{3}} \right] \tag{12}$$

Where $\rho$ is the isotropic density, $h$ is Planck's constant and $K_B$ is Boltzman's constant.

## Result and Discussion

Input parameter used in the calculations is given in table no.i. The longitudinal and transverse phonon frequencies are shown in figure 1 and 2 for both potential. It is seen form the results of phonon frequencies that the nature of peak positions are not much affected by different screening functions. here two different potential are used with the five local field corrections functions due to [12-16] to generate pair potential.

**Table i.** Input parameter of $Mg_{65}Cu_{25}Tb_{10}$ BMG

| Parameter | Z | $\Omega_{eff_3}$ [au] | $r_c$ [au] | $M_{eff}$ [amu] |
|---|---|---|---|---|
| $Mg_{65}Cu_{25}Tb_{10}$ | 2.65 | 161.52 | 1.24 | 47.77 |

It is obvious from the figures that the oscillations are prominent in the longitudinal mode, which indicated that the collective excitations at larger wave vector transfer due to the dispersion of longitudinal excitation. On the other hand the transverse modes undergo larger thermal modulation due to the anharmonicity of the vibrations in the alloys. It can also be seen that the first minimum in longitudinal branch of the dispersion curve falls at a value $q \approx 0.75 Å^{-1}$ in the model potential 1 and 2. In the long wavelength limit the dispersion curves are linear and confirming characteristics of elastic waves. Thephonon dispersion curves (PDC)for transverse phonons attain maxima at a higher q value than the longitudinal phonon curves.
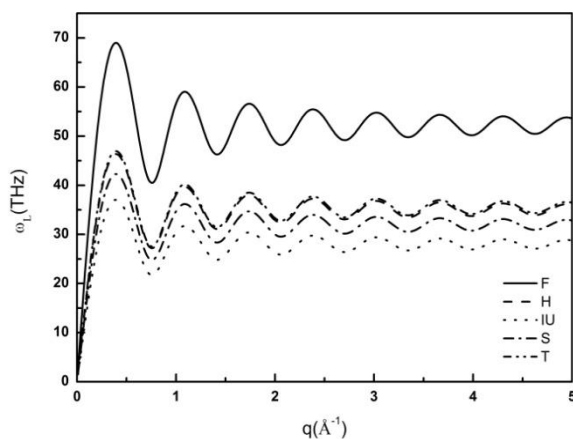


Fig.1: Longitudinal phonon frequency using MP-1     Fig .2: Transverse phonon frequency using MP-1
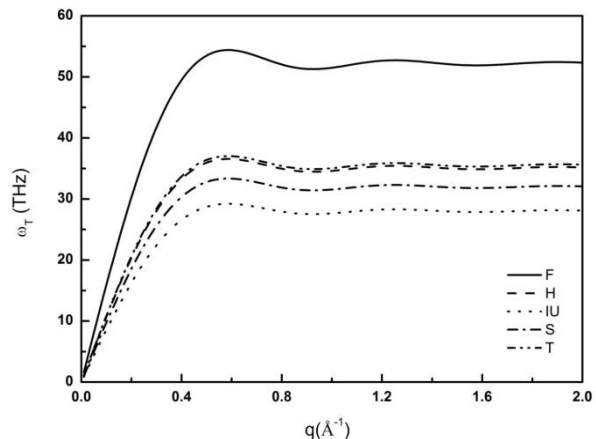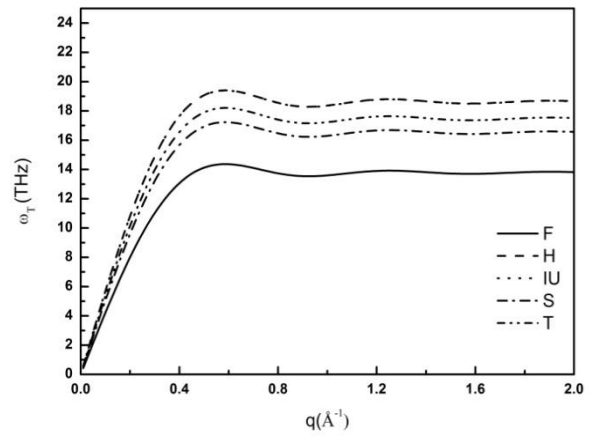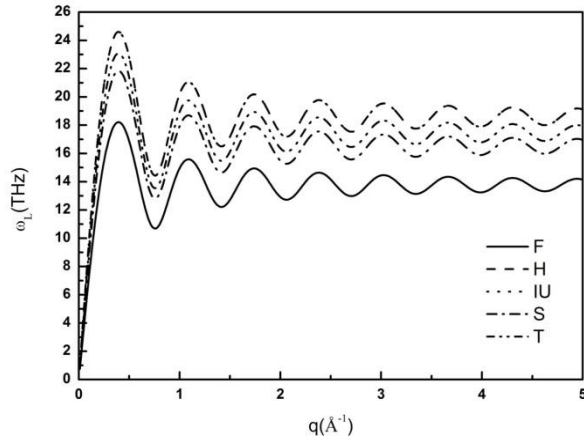
Figure.3: Longitudinal phonon frequency using MP-2



Figure 4: Transverse phonon frequency using MP-2

Presently calculated bulk modulus $B_T$, rigidity modulus of $G$, Poisson's ratio Poisson's ratio $\xi$, Young's modulus $Y$ and Debye temperature $\theta_D$ of ternary of liquid alloys are listed in Table II.

From the table, one can see that by using the H, S, T, IU and F screening functions, the results are very close to one another as compared to the F screening function. From the slope of phonon dispersion curve at q ≈ 0, the bulk modulus and other elastic properties are computed; we see that value of bulk modulus is cloase to experiemental value for both the potential when employed with Ichimaru and Utsumi screening function.

Table II: Elastic properties (First and Second entries show results for MP-1 and MP-2).

| | Potential | $v_l$ $(10^5$ cm/s) | $v_t$ $(10^5$ cm/s) | $B_T$ (Gpa) | $G$ (Gpa) | $\xi$ | $Y$ (Gpa) | $\theta_D$ (K) |
| --- | --- | --- | --- | --- | --- | --- | --- | --- |
| Expt.[17] | | 4.22 | 2.22 | 44.70 | 19.60 | 0.309 | 51.30 | 272.90 |
| Hartree (H) [12] | MP-1 | 3.78 | 2.18 | 68.49 | 15.80 | 0.25 | 39.51 | 250.63 |
| | MP-2 | 2.80 | 1.62 | 37.75 | 87.35 | 0.25 | 21.78 | 186.0 |
| Sarkar *et al.* (S)[13] | MP-1 | 3.45 | 1.99 | 56.95 | 13.14 | 0.25 | 32.85 | 228.55 |
| | MP-2 | 2.49 | 1.43 | 29.75 | 68.66 | 0.25 | 17.16 | 165.20 |
| Taylor (T)[14] | MP-1 | 3.83 | 2.21 | 70.24 | 16.20 | 0.25 | 40.52 | 253.82 |
| | MP-2 | 2.62 | 1.52 | 33.2 | 87.35 | 0.25 | 19.16 | 174.56 |
| Ichimaru and Utsumi(IU)[15] | MP-1 | 3.02 | 1.74 | 43.72 | 10.08 | 0.25 | 25.22 | 200.25 |
| | MP-2 | 2.80 | 1.62 | 37.71 | 87.25 | 0.25 | 21.75 | 185.98 |
| Farid *et al* (F) [16] | MP-1 | 4.22 | 2.44 | 85.58 | 19.76 | 0.25 | 49.35 | 280.17 |
| | MP-2 | 2.98 | 1.78 | 46.52 | 96.20 | 0.25 | 28.63 | 223.20 |

The same conclusion can be drawn for other elastic properties as well, except for Poisson ratio. Experimental Poisson ratio is as high as 0.309, whereas the present calculation predicts its value as 0.25 ( same for all screening functions and both potentails upto third digit). Calculated elastic constants due to HB approach are in agreement with the available experiment data.

## Conclusion

Finally, we conclude here that the PDC generated from the HB approach reproduces sastifactorily general characteristics of dispersion curves. We have studied the collective dynamics of $Mg_{65}Cu_{25}Tb_{10}$ BMG using two Pseudopotential. The computed dispersion curves show all broad features of collective excitation in the system studied here by both the potentials. The overall picture reveals the importance of local field correction function. it is seen that the peak position are not affected much by the different screening functions. The oscillations are more prominent in the longitudinal modes as compared to transverse modes. This shows the existence of collective excitations at larger momentum transfer due to longitudinal modes only and the instability of the transverse modes due to anharmonicity of the atomic vibration in bulk metallic system. Screening function due to Farid et al gives good overall results compared to other screening functions. Further, elastic constant have calculated which are in good agreement with the experimental data. We therefore conclude that both the potentials with proper choice of the parameter in presence of the employed screening functions may give good vibrational and elastic properties.

## References

[1] T. A. Jr and T. Masumoto, J. Phys. Con. Matt., 1995, 7, 1525.

[2] W.L. Johnson MRS Bull. 1999,24, 42.

[3] A. Inoue Acta Mater., 2000, 48, 279 2000.

[4] A. Peker and W. L. Johnson Appl. Phys. Lett., 1993, 63, 2342.

[5] V. Ponnambalam, S. J. Poon, and G. J. Shiflet J. Mater. Res., 2004, 19, 1320.

[6] W. A. Harrison, "Pseudopotential in the theory of metals" W A Benjamin Pub. Co., New York, 1967.

[7] E. Fermi, Ricerca Sci., 1936, 7, 13.

[8 V. Heine, M. L. Cohen and D. Weaire Solid state Phy., 1970, 24, 249.

[9] J. Hubbard and J. L. Beeby J.Phys., 1969, 2, 556.

[10] P. B. Thakore, P. N. Gajjar, and  A. R. Jani, Comm in Phy., 2004, 14, 15.

[11] A. K. Varshneya, A. N. Sreenam and S. R.Swiller Phys.Chem. Glasses., 1993, 34, 179.

[12] W. A. Harrison,  Phys. Stat. Sol. B., 1969, 181, 1036.

[13] A. Sarkar, D. S. Sen, S. Haldar, D. Roy  Mod. Phys. Lett. B., 1998, 12,  639.

[14] R. Taylor, J. Phys.F, 1981, 8, 1699.

[15] S. Ichimaru  and K.Utsumi,P hys. Rev. B., 1981, 24, 3220.

[16] B. Farid, V. Heine, G. E. Engel and I. S. Robertson, Phys. Rev., 1993, 48, 11602.

[17] W. H. Wang, F. Y. Li, M. X. Pan, D. Q. Zhou and R. J. Wang, Acta Materialia, 2004, 52, 715.

.

# The Theoretical Study of Electron Dispersion Curves of Some Divalent and Trivalent Rare Earth Metals

Hiral Patel[1], A. B. Patel[2], N. K. Bhatt[3], P. R. Vyas[4] and V. B. Gohel[5]

[1]*Ahemdabad Institute of Technology, Ahmedabad-380060, Gujarat, India.*

[3]*Department of Physics, M. K. Bhavanagar University, Bhavanagar - 364001, Gujarat, India.*

[2,4,5] *Department of Physics, School of Sciences, Gujarat University, Ahmedabad - 380009, Gujarat, India.*

[1]*hiralpateltm@yahoo.com*

**Abstract**

We have used a pseudopotential having two parameters for the theoretical study of electronic energy employing second order perturbation theory for some divalent (Eu and Yb) and trivalent (La, Ce and Gd) rare earth metals. We have carried out theoretical study of electron dispersion curves (E(k)→k), Fermi energy ($E_F$) and density of states at Fermi energy ($N(E_F)$). The order of the magnitude of all physical properties is in accordance with previously computed results for simple metals. Such theoretical results will be helpful for the understanding of many liquid state properties like free energy of electron gas, entropy, thermal conductivity etc. of liquid metals.

**Keywords** - Liquid rare earth metals; local pseudopotential; electron dispersion; Fermi energy and density of states.

## I.    Introduction

The rare earth elements have proven of increasingly great commercial value. The demand of rare earth elements has been increased because of the technological uses like hybrid engines, metal alloys, lasers, fluorescent lamps, ceramics and magnets [1]. The rare-earth metals form a series of elements with almost identical chemical properties. When electrons are added to these atoms, as the nuclear charge is increased, they go into the 4f shell, and since this shell lies in the interior of the xenon core region, the bulk properties of the metals are thereby essentially unchanged. In most of the geological settings, rare earth elements (La, Ce, Gd, Eu and Yb) are of great importance as they help in the understanding of wide variety of geological, geochemical and cosmochemical processes that take place on Earth, other planets and other planetary bodies.

This is however, due to the occurrence of different types of electronic configurations of the rare earths. La, Ce and Gd hold $[Xe]5d^1 6s^2$, $[Xe]4f^1 5d^1 6s^2$ and $[Xe] 4f^7 5d^1 6s^2$ (trivalent) electronic configurations respectively, while Eu and Yb have $[Xe] 4f^7 6s^2$ and $[Xe] 4f^{14} 6s^2$ (divalent) electronic configurations respectively. In the solid phase, however, most of the

elements are found in the trivalent configuration, and therefore in the condensation of the atoms one of the 4f electrons has been promoted into the 5d state. In solid state, only europium and ytterbium remain in a divalent state [2]. If the behaviour of the rare earth elements is known, some of their metallic properties can be predicted with good degree of success. The studies of liquid metal resistivity using Ziman's nearly free electron approach have been carried out by many researchers [3-6]. It is also found that the order of magnitude of liquid metal resistivity of some transition metals Mn, Fe and Co is same as that of La, Ce, Gd and Yb. In case of Eu, the value of the liquid metal resistivity is found to be higher which is same as that of liquid Ba [7].

Looking to all aforesaid facts, researchers are interested in the study of liquid state properties of this group of metals. In order to carry out study of physical properties of materials, one must have enough knowledge about all electron-ion interactions (pseudopotential). The study of metallic properties using pseudopotential helps to understand interactions persisting in the corresponding solid metals. The study of comprehensive physical properties (static, lattice-dynamical and transport) using pseudopotential is found to be very well. For such study the parameters of the pseudopotential must be determined from most general method. Pollack et. al. [8] have mentioned that the study of liquid state properties using ab-intio method is difficult and pseudopotential method has proven to be successful. The study of electron dispersion curves $(E(k) \rightarrow k)$ will help to understand energy distribution in Brillouin Zone. For such study, one must require knowledge of structure factor and screened electron-ion interaction. To the best of our knowledge, such study is limited up to simple metals.

Looking to the importance and need of the theoretical predication of electron dispersion, in the present communication, we have studied electron dispersion curve of liquid rare earth metals. In our previous paper [10], we have used local pseudopotential due to Kumar [9] and calculated liquid metal resistivity using nearly free electron Ziman's approach. In the present paper, alongwith electron dispersion curves, we have studied density of states at Fermi energy $(N(E_F))$.

## II.    Theory

In the framework of second order perturbation theory, the electronic structure of a liquid metal is sum of ground state energy $E_0$ and first and second order corrections to the energy $E_1$ and $E_2$, which is given in atomic unit as,

$$E(k) = k^2 + \langle k|V(q)k|\rangle + \sum \frac{S(q)S^*(q)|V(q)|^2}{k^2 - |k+q|^2} \tag{1}$$

Here $\langle k|V(q)|k\rangle$ is the matrix element of pseudopotential form factor between two zeroth order plane waves which gives first order correction to the energy and $V(q)$ is the screened pseudopotential $[V(q) = V_{ion}(q)/\varepsilon(q)]$

Here $\varepsilon(q)$ is modified Hartree dielectric function which is expressed as,

$$\varepsilon(q) = [H(q) - 1][1 - Y(q)]$$

and $Y(q)$ is exchange and correlation function. We have used Hubbard-Sham exchange and correlation function [11, 12].

In the present study, we have used bare-ion pseudopotential $V_{ion}(q)$ due to Kumar [9] which has following form in a.u

$$V_{ion}(q) = -\frac{4\pi Z^* e^2}{\Omega_0 q^2} \cos(qR_m) - \frac{4\pi Z^* e^2}{\Omega_0 q^4 R_c R_m}\left[-q^2 R_c^2 \cos(qR_c) + 2qR_c \sin(qR_c) + 2\cos(qR_c) - Z\right]$$

$$-\frac{4\pi Z^* e^2}{\Omega_0 q^3 R_m}\left[qR_c \cos(qR_c) - qR_m \cos(qR_m) + \sin qR_m - \sin(qR_c)\right] \tag{2}$$

In case of liquid metals, eq. [1] becomes [13-14],

$$E(k) = k^2 + \Delta(k) - \Delta(0) \tag{3}$$

Where,

$$\Delta(k) = \frac{3Z}{8\vec{k_F} E_F \vec{k}} \int_0^\infty S(q)V(q)^2 q \ln\left|\frac{2\vec{k}+q}{2\vec{k}-q}\right| dq \tag{4}$$

and

$$\Delta(0) = \frac{3Z}{2\vec{k_F} E_F \vec{k}} \int_0^\infty S(q)V(q)^2 dq \tag{5}$$

Here $k_F$ is the Fermi momentum, $E_F$ is the Fermi energy and $S(q)$ is the structure factor. We have used Percus-Yevick form with packing fraction $\eta = 0.45$.

### III.  Result and discussion

In the present study, we have used pseudopotential due to Kumar [9]. In our previous paper, [10] we have calculated liquid metal resistivity of La, Ce, Gd, Eu and Yb metals using nearly

free electron Ziman's approach. The pseudopotential parameters $R_c$ (core radius) and some atomic radius-$R_m$ were determine in the previous paper [10]. In the present study, we have used the same set of parameters. The presently used pseudpotential is discontinuous in r-space while continuous in q-space. We have also presented variations of screened pseudopotential $V(q) \rightarrow q/k_F$ for all metal [10]. In the present study we have calculated $\Delta E(k) = \Delta(k) - \Delta(0)$ using equations 3, 4 and 5 as a function of k up to k=4$k_F$ which are shown in figures 1-5 for all the metal studied.


Fig: 1 Electron Dispersion for Lanthanum


Fig:2 Electron Dispersion for Cerium


Fig:3 Electron Dispersion for Gadolinium


Fig: 4 Electron Dispersion for Europium


Fig: 5 Electron Dispersion for Ytterbium
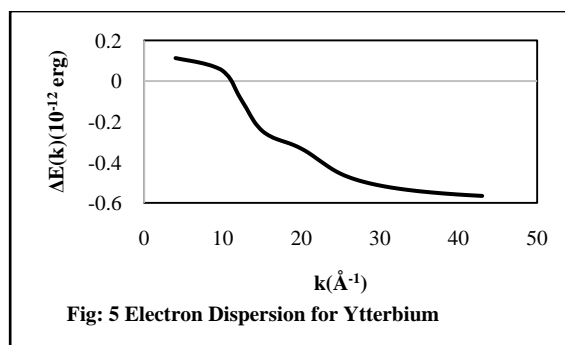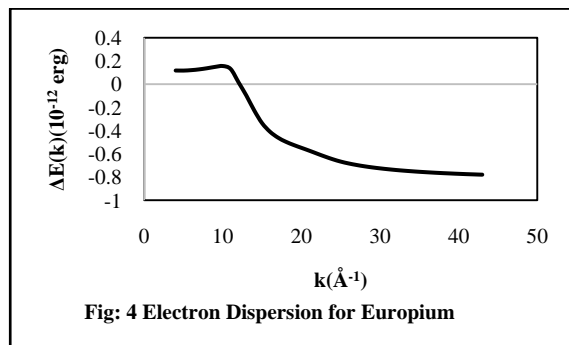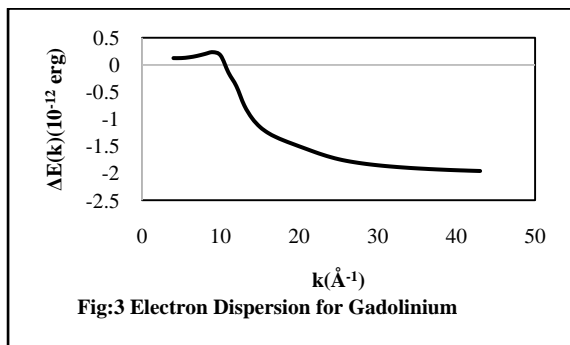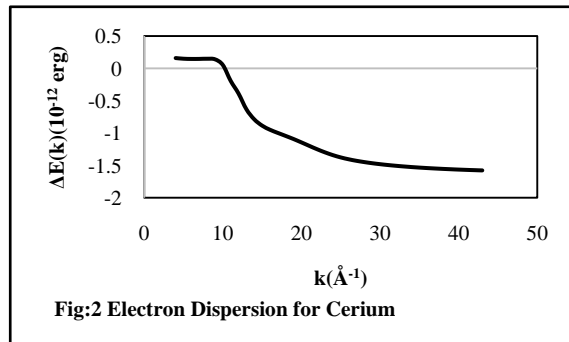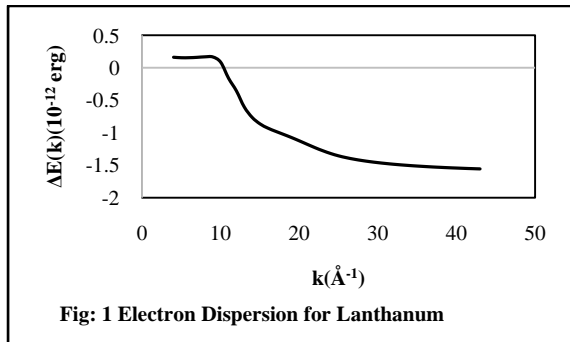
For calculation of electron dispersion, the behaviour of the screened pseudopotential must be smooth in the sense that it should be wiggle-less. Such behaviour is found in presently used screened pseudopotentials for all the metals studied. Here we would like to point out that no extra term is used to make the pseudopotential zero. For the calculation of $\Delta(k)$, one has to evaluate integration precisely due to presence of logarithmic term which depends on q as well as k. Such term has highly oscillatory behaviour. In the present study, evaluation of

integration has been carried out with upper limit q=80 $k_F$ in step of 0.1 $k_F$. The calculated electron dispersion curve, in absence of any experimental and other theoretical result may be considered as a prediction which explains the behaviour of $\Delta E(k)$.

In the next step of calculation we have computed Fermi-energy by using following relations in atomic unit.

$$E_F = k_F^2 + \Delta(k_F) - \Delta(0)$$

$\Delta(k_F)$ can be obtained by replacing $k$ with $k_F$ in equation 4. The computed values of $E_F$ are displayed in Table 1.

The density of states at Fermi energy $N(E_F)$ has been calculated by using following equation,

$$N(E_F) = \frac{k_F^2}{n\pi^2}\left[\frac{dE}{dk}\right]^{-1}$$

Where n = number of atoms per unit volume. The calculated values of $N(E_F)$ are also shown in Table 1.

**Table.1** The calculated values of Fermi energy ($E_F$) and density of states at Fermi level ($N(E_F)$)

| Metal | $E_F$ (x $10^{-12}$ erg) | $N(E_F)$(x $10^{11}$ (energy-atom)$^{-1}$) |
|---|---|---|
| La | 18.3107 | 3.32099 |
| Ce | 18.9935 | 3.20160 |
| Gd | 18.3660 | 3.31098 |
| Eu | 14.2886 | 2.83722 |
| Yb | 15.1846 | 2.69588 |

The order of computed values of $N(E_F)$ is similar to those obtained by Srivastava [13] for simple metals. The calculation of $N(E_F)$ at liquid density is important ingredient for the theoretical understanding of many liquid state physical properties like free energy due to electron gas, entropy, thermal conductivity etc. of liquid metals.

## IV. Conclusions

The present study confirms that local pseudopotential with proper form of exchange and correlation function can be used for the study of liquid state properties of transition and f-

shell metals with good degree of success. During literature survey, it has been observed by us that many researchers have employed the method of adjusting the valency for the better understanding of physical properties of this group of metals in solid and liquid phases. Such study may also be carried out with the help of non-local pseudopotentials. But non-local pseudopotentials are conceptually complicated and mathematically lengthy while local pseudopotentials are computationally simple and physically more transparent alongwith their accuracy. Looking to the success of present study, we would like to extend the presently used pseudopotential for the study of electronic properties of liquid metal alloys.

## Acknowledgements

## References

[1]  D. Atwood, The Rare Earth Elements: Fundamentals and Applications, United Kingdom, Wiley Publications, 2012.

[2]  B. Johansson and A. Rosengren, Phys. Rev. B, 1975, 11, 8, 2836.

[3]  J. Gasser, J. Phys.: Cond. Matter, 2008, 20, 114103.

[4]  A. B. Patel, N. K. Bhatt, B. Y. Thakore, P. R. Vyas and A. R. Jani, Molecular Physics, 2014,112, 15, 2000.

[5]  E. Apfelbaum, Phys. Che. of Liquids, 2010, 48, 4, 534.

[6]  K. G. Bhatia, N. K. Bhatt, P R. Vyas and V. B. Gohel, AIP conference proceedings, 2015, 1665, 1, 110014.

[7]  B. Delley and H. Beck, J.Phys. F: Metal Phys., 1979, 9, 3, 517.

[8]  L. Pollack, J. P. Perdew, J. He, M. Marques, F. Nogueira and C. Fiolhais, Phys. Rev. B, 1979, 55, 15544.

[9]  J. Kumar, Solid State Comm., 1977, 21, 945.

[10] M. B. Pathak, N. K. Bhatt, P. R. Vyas and V. B. Gohel, Journal of international academy of physical science, 2012, 16, 4, 1.

[11] J. Hubbard, Proc. Roy. Soc. A, 1958, 243,336.

[12] L. J. Sham, Proc. Roy. Soc. A, 1965, 283, 33.

[13] S.K. Srivastava, J. Phys. Chem. Solids, 1975, 36, 993.

[14] P. N. Gajjar, B. Y. Thakore and A. R. Jani, Acta Physica Polonica A, 1998, 94, 33.

# Total Ionization cross sections of transition atoms

## A.  Y. Barot[1#], M.Y. Barot[2] D.N. Bhavsar[3] and M. Vinodkumar[4]

[1#] Sigma Institute of science and commerce, Vadodara-390001, gujarat, India

[2] Government Science College Gandhinagar-382016, Gujarat, India

[31] Bhavan's Sheth R. A. College of Science, Khanpur, Ahmedabad-380001, Gujarat, India

[4] V. P. & R. P. T. P. Science College, Vallabh Vidyanagar – 388120, Gujarat, India

**Corrosponding author:** barotavani29@yahoo.com, Contact: **09601251449**

**ABSRACT:** In this paper the detailed study on the electron scattering with metallic and transition atoms are presented. Atoms are simpler in view of their well-studied structure and spherical shapes. We have employed the Complex Optical Potential – ionization contribution (CSP-ic) method to extract total ionization cross sections from total inelastic cross sections. We have compared our results with the available theoretical as well as experimental data.

**Key Words:** Ionization cross sections, Spherical Complex Optical Potential (SCOP) Complex Optical Potential – ionization contribution (CSP-ic)

**Highlights:**

- Here we compute the total ionization cross sections of transition metals like Fe, Co, Ni, Cu, Zn and other industrially important metals such as Al and Ga.
- Complex Optical Potential – ionization contribution (CSP-ic) method is used to extract total ionization cross sections from total inelastic cross sections.

**PACS number(s)**: 34.80.Bm

## 1 INTRODUCTION

Atomic collision phenomena are of fundamental importance in atomic and molecular physics and play an important role in other fields such as astrophysics, chemistry, plasma physics and laser physics. The applications of electron impact total ionization cross section ($Q_{ion}$) data in the fields of atmospheric sciences, astrophysical context and technological plasmas, radiation physics, mass spectroscopy and semiconductor industry [1] have already been realized. However, the compilation

of all the required data in a single database is still a distant reality. One of the reasons for this is the scarcity of cross section data for many targets like heavy atoms and exotic molecules and radicals. Also, the reliability of the available data has been a major concern. Here we compute the total ionization cross sections of transition metals like Fe, Co, Ni, Cu, Zn and other industrially important metals such as Al and Ga. We present total ionization cross sections ($Q_{ion}$) of these atomic targets from their ionization potential (IP) to 2keV incident electron energies.

The Spherical Complex Optical Potential (SCOP) [2, 3] and Complex Optical Potential – ionization contribution (CSP-ic) method [4, 5] is used to extract total ionization cross sections from total inelastic cross sections.

Many research groups have determined the electron impact total and ionization cross sections for molecules [6, 7]. Kim and co-workers [8, 9], Deutsch and Märk [11] and Huo et al. [13] are engaged in calculating total ionization cross sections. Many groups began by using the additivity rule (AR) [14] to investigate ionization cross section data for molecules. The AR is a crude high energy approximation in which the total ionization cross sections of molecules are a simple sum of the Total Ionization Cross Sections (TICS) of its constituent atoms. This has led to different variants called modified additivity rules (MAR) [12]. MAR could produce much better results than AR, but still lacks reliability. This reasons motivated us to pursue a better method, which is more reliable and easy to handle.

**Aluminium (Al)** is a silvery white metal belongs to the boron group element.  It has an atomic number **13** and is the third most abundant metal in the earth's crust after oxygen and silicon. It makes up about 8% by weight of the earth's solid surface [10].

**Iron (Fe)** is a metal in the first transition series having atomic number **26** and is the most common element forming the planet earth's outer and inner core. It is the fourth most common element in the earth's crust. Iron plays an important role in biology, forming complexes with molecular oxygen in hemoglobin and myoglobin. Iron is also the metal used at the active site of many important redox enzymes dealing with cellular respiration and oxidation and reduction in plants and animals [10].

**Cobalt (Co)** is a chemical element with atomic number **27**and is found naturally only in chemically combined form [10].

**Nickel (Ni)**is a chemical element with atomic number **28**. It is silvery white transition metal and is hard and ductile. Nickel is reactive enough with oxygen so that native nickel is rarely found on

earth's surface, being mostly confined to the interiors of larger nickel–iron meteorites that were protected from oxidation during their time in space. An iron–nickel mixture is thought to compose earth's inner core [10].

**Copper (Cu)** is a ductile metal with atomic number **29**. It has very high thermal and electrical resistivity. Approximately 65% of copper produced is used for electrical applications [10].

**Zinc (Zn)** is a metallic chemical element with atomic number **30**. It is the first element of group 12 of the periodic table. Zinc is the 24th most abundant element in the Earth's crust and has five stable isotopes [10].

**Gallium (Ga)** is a chemical element with atomic number **31**. Elemental gallium does not occur in pure form in nature, but as gallium (III) compounds are in trace amounts in zinc ores and in bauxite. Roughly 90-95% of gallium consumption is in the electronics industry. Gallium arsenide (GaAs) can convert light directly into electricity. Further, gallium arsenide is also used in LEDs and transistors. Scientists employ an alloy with Gallium for the plutonium pits of nuclear weapons to stabilize the allotropes of plutonium [10].

The Ionization Potential (IP) [15] for these atoms are listed in Table 1

**Table 1** Ionization Potential (IP) for Atoms

| ATOMS | Al | Fe | Co | Ni | Cu | Zn | Ga |
|-------|------|------|------|------|------|------|------|
| **IP (eV)** | 5.98 | 7.90 | 7.88 | 7.63 | 7.72 | 9.39 | 5.99 |

## 2. THEORY

The absorption potential takes care of loss of flux into all allowed inelastic channels. For this we have used model potential of Staszewska et al. [10] which is non-empirical, quasifree, Pauli-blocking and dynamic in nature. The full form of model potential is represented by,

$$V_{abs}(r, E_i) = -\rho(r)\sqrt{\frac{T_{loc}}{2}} \times \left(\frac{8\pi}{10k_F^3 E_i}\right) \times \theta(p^2 - k_F^2 - 2\Delta) \cdot (A_1 + A_2 + A_3)$$

(1)

And

$$T_{loc} = E_i - (V_{st} + V_{ex}) \qquad (2)$$

After generating the full complex optical potential for a given electron molecule system, we solve the Schrödinger equation numerically with Numerov method using partial wave analysis. Using these partial waves the complex phase shifts are obtained which are key ingredients to find the relevant cross sections. The phase shifts contains all the information regarding the scattering event. Using these complex phase shifts we evaluate total inelastic cross sections. The two vital components of total inelastic cross sections are given by,

$$Q_{inel}(E_i) = \sum Q_{exc}(E_i) + Q_{ion}(E_i) \qquad (3)$$

Total ionization cross section may be estimated from total inelastic cross section by defining an energy dependent ratio $R(E_i)$ given by,

$$R(E_i) = \frac{Q_{ion}(E_i)}{Q_{inel}(E_i)} \qquad (4)$$

such that, $0 < R \lesssim 1$.

As total ionization cross section is a continuous function of energy, we can express this ratio also as a continuous function of energy for $E_i > I$, used in earlier studies as [4, 5 ].

$$R(E_i) = 1 - f(U) = 1 - C_1 \left( \frac{C_2}{U+a} + \frac{\ln(U)}{U} \right) \qquad (5)$$

here, $U$ is the dimensionless variable defined by, $U = \dfrac{E_i}{I}$ .

The dimensionless parameters $C_1$, $C_2$ and 'a' involved in the above equation are deduced by imposing the three conditions on the ratio as discussed below.

$$R(E_i) \begin{cases} = 0 \ for \ E_i \leq I \\ = R_p \ for \ E_i = E_p \\ \cong 1 \ for \ E_i >> E_p \end{cases}$$

(6)

where $E_p$ is the peak of inelastic cross section.

The first condition is an exact condition wherein it states that no ionization process is possible below the ionization threshold of the target. According to the last condition, ionization contribution is almost equal to inelastic contribution at very high ($\sim 10 \ E_p$) energies. $R_P$ is the value of $R$ at $E_i = E_p$, and it was observed that at the peak of inelastic cross section the contribution for ionization is about 70 to 80%. Here we have taken $R_p$ as 0.7 for all the targets studied here.

## 3 Results and Discussion

Figure 1 shows comparison of total ionization cross section for e – Al scattering with other available data. There is only one measurement performed by Freund et al. [16] while theoretical data are provided by Bartlett and Stelbovics [17], Kim and Stone [18] Talukdar et al. [19] and Joshipura et al. [20].
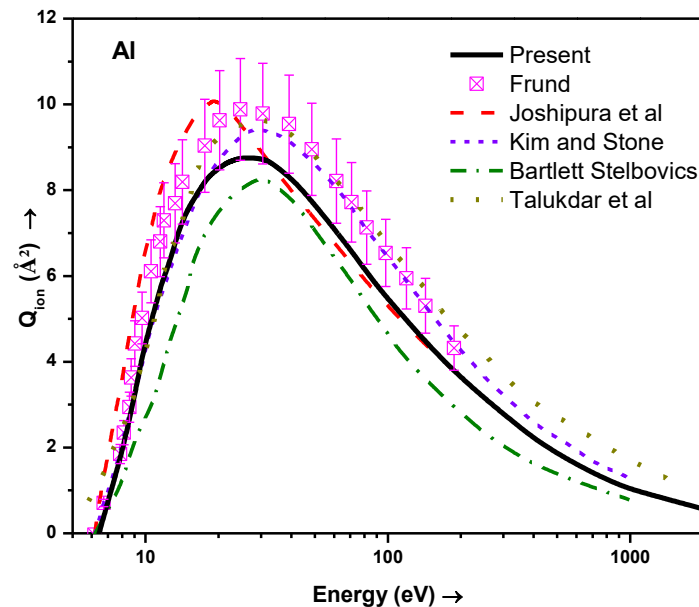


**Figure 1** Total ionization cross section ($Q_{ion}$) for Al atom

*Solid line: Present Results,Short Dash dot: Bartlett and Stelbovics [17], Short Dashed line: Kim and Stone[18], dashed line: Joshipura et al. [20], Dotted line: Talukdar et al. [19], Square with cross: Freund et al. [16].*

Below 30 eV our results are in good agreement with the Kim and Stone [18] and Talukdar et al. [19]. After 40 eV our theory falls between other theories [17-19] but in good agreement with Joshipura et al. [20]. We get the peak of 8.77 $Å^2$ at 24 eV same as Freund et al. [16] and Talukdar et al. [19] but the cross section of Freund et al. [16] at peak  is 9.87 $Å^2$ which is around 1 $Å^2$ higher compared to present result.
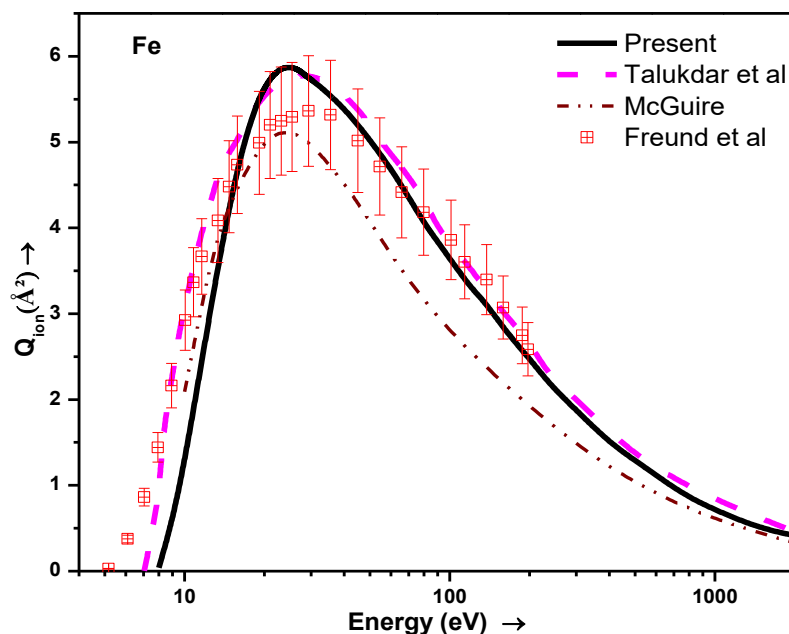


**Figure 2** Total ionization cross section for Fe atom

*Solid line: Present Results, Dashed Line: Talukdar et al. [19], Dashdot dot: McGuire et al.[21], Square with cross: Freund et al.[16].*

Figure 2 shows comparison of total ionization cross section for e – Fe scattering with available comparisons. There is single measurement available for the comparison by Freund et al. [16] while theoretical data is provided by Talukdar et al. [19] and McGuire et al. [21]. McGuire et al. [21] has employed generalized Oscillator-Strength formulation of the Born approximation for the calculation of total ionization cross sections. Talukdar et al. [19] have calculated ionization cross

sections using empirical method. Present data is in very good agreement with measurements of Freund et al. [16] and Talukdar et al. [19] beyond 30 eV, below which there is little deviation with present data. Theoretical data of McGuire et al. [21] are in very good agreement with present data below 10 eV above which they are lower compared to all other data. The cross section at peak is $5.87\text{Å}^2$ at 24 eV incident energies which matches with Talukdar et al. [19] as well as Freund et al. [16].
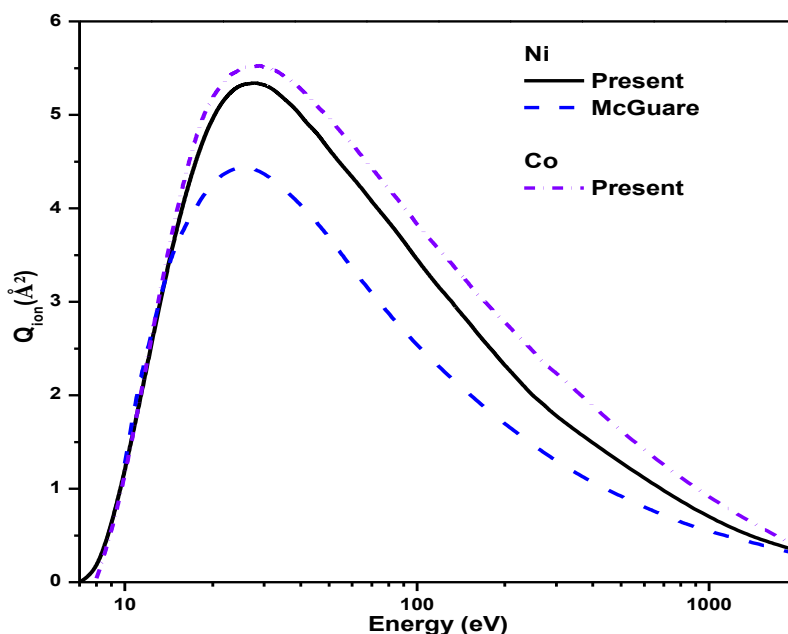


**Figure 3** Total ionization cross section forCo and Ni atoms

*Solid line: Present Results, Deshed line: McGuire et al. [21].dash dotted line: present Co*

Figure 3 shows the present result of total ionization cross sections for Co and Ni atoms. There are no theoretical or experimental results available for Co atom to the best of our knowledge. The peak of ionization cross sections for Co is 5.52 $\text{Å}^2$ at 27 eV. For Ni, there is lone theoretical data by McGuire et al. [21]. The peak of ionization cross sections for Ni is 5.34 $\text{Å}^2$ at 28 eV while peak obtained by McGuire et al. [21] is 4.43 $\text{Å}^2$ at 26 eV. The peak of McGuire et al. [21] is lower compared to the present results for all the atoms studied here.

Figure 4 shows the comparison of total ionization cross sections of e – Cu scattering with available comparisons. The experimental data are provided by two groups [16, 22]. Theoretical data are provided by Joshipura et al. [20] using CSP-ic method, Kim and Stone [18] by using BEB formalism and Talukdar et al.[19] by employing some empirical formula. Present results are in good agreement with both the measurements. Theoretical data of Kim and Stone [18] is lower compared to all data presented here. Present data is in good agreement with data of Joshipura et al. [20] till 20 eV beyond which they are higher compared to all other data presented here. Theoretical data of Talukdar et al. [19] is higher compared to the present data till 100 eV, beyond which they are in excellent agreement with present data.
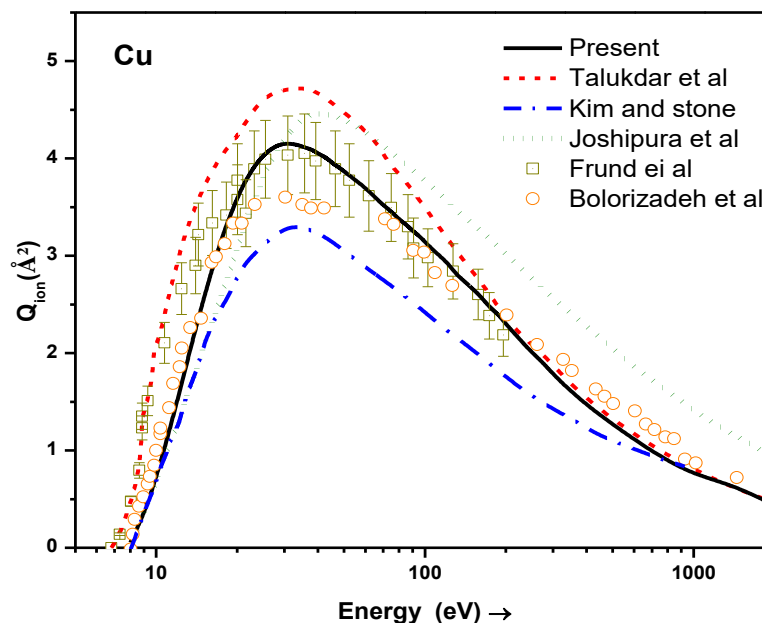


**Figure 4** Total ionization cross section for Cu atom

*Solid line: Present Results, Short dashed Line: Talukdar et al. [19], Dash dot dot: Kim and Stone [18], short dotted line: Joshipura et al. [20], Circle: Bolorizadehet al.[22], Square with cross: Freund et al. [16].*

Figure 5 shows the present result of total ionization cross sections ($Q_{ion}$) for Zn atom. As per our knowledge, there is only one theoretical result available by McGuireet al. [21] using generalized Oscillator-Strength formulation of the Born approximation for the calculation. Overall range of the energy, good matching obtained between both the theories but slide variation at the peak of the

cross sections observed. We get the peak of 4.42Å$^2$ at 30 eV, while McGuire et al. [21] gets the peak of 4.24 Å$^2$ at 30 eV.
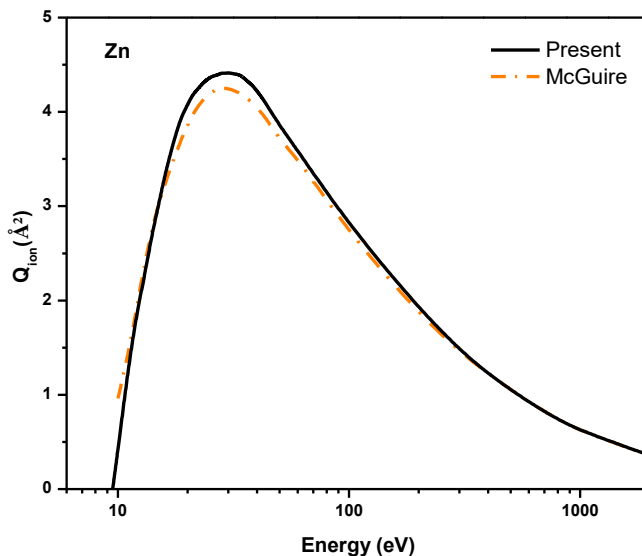


**Figure 5** Total ionization cross section for Zn atom

*Solid line: Present Results, Dashed line: McGuire et al. [21].*
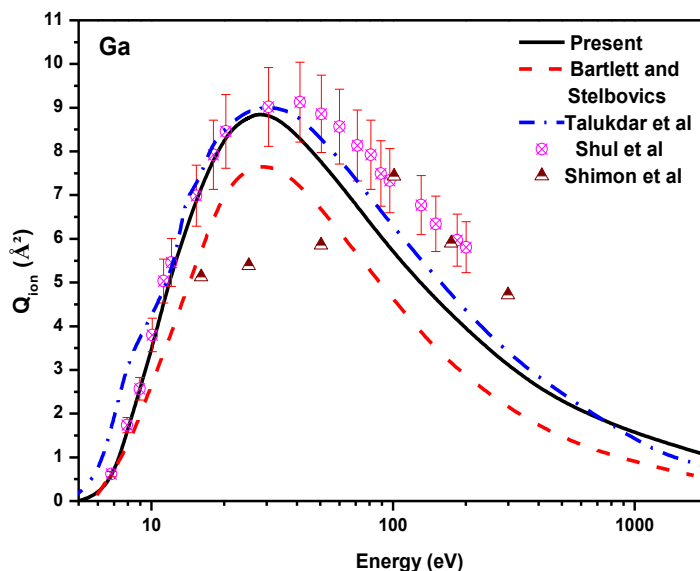


**Figure 6** Total ionization cross section for Ga atom

*Solid line: Present Results, Dashed Line: Bartlett and Stelbovics [17], Dash dot line: Talukdar et al.[19], Circle with cross: Shulet al.[23], Half-filled triangle: Shimon et al. [24].*

Figure 6 shows the comparison of total ionization cross sections for Ga atom. Present results are going well with the theoretical values of Talukdar et al. [19] and higher compared to Bartlett-Stelbovics [17]. The measured results of Shul et al. [23] are in agreement with our present results up to 40 eV. After that the experimental data of Shul et al. [23] goes higher than all the theoretical results. The results of Shimon et al. [24] are lower at intermediate energies but in good agreement with the Shul et al. [23] at high energies. Our results lie between the both available theories [17, 19] throughout the energy range. The peak obtained in present result is 8.88 $\text{Å}^2$ at 30 eV. The peak energy of all theories are similar while experimental peak of Shul et al. [23] is 9.11 $\text{Å}^2$ at 30 eV, which is slightly shifted right side from the others [17, 19, 24].

The present computational data of all atoms are given in table 2. Cross sections at peak are indicated in bold in table 2.

**Table 2** Total Ionization Cross sectionsforstudied atoms

| Energy (eV) | Total Ionization Cross Section ($Q_{ion}$) ($\text{Å}^2$) | | | | | | |
|---|---|---|---|---|---|---|---|
|  | Al | Fe | Co | Ni | Cu | Zn | Ga |
| 6 | 0.04 | -- | -- | -- | -- | -- | 0.27 |
| 7 | 0.76 | -- | -- | 0.02 | 0.02 | -- | 0.81 |
| 8 | 2.15 | 0.04 | 0.04 | 0.18 | 0.41 | -- | 1.58 |
| 9 | 33 | 0.60 | 0.53 | 0.70 | 0.66 | 0.002 | 2.80 |
| 10 | 4.32 | 1.28 | 1.14 | 1.39 | 1.23 | 0.407 | 3.76 |
| 15 | 7.61 | 4.34 | 3.94 | 3.75 | 2.49 | 2.99 | 8.20 |
| 20 | 8.48 | 5.63 | 5.18 | 4.96 | 61 | 4.09 | 8.54 |
| 23 | 8.75 | 5.86 | 5.43 | 5.24 | 3.89 | 4.29 | 8.59 |
| 24 | **8.77** | **5.87** | 5.46 | 5.27 | 3.93 | 4.33 | 8.81 |
| 25 | 8.77 | 5.86 | 5.49 | 5.31 | 4.00 | 4.37 | 8.82 |
| 26 | 8.77 | 5.84 | 5.50 | 5.33 | 4.07 | 4.39 | 8.84 |
| 27 | 8.76 | 5.83 | **5.52** | 5.33 | 4.09 | 4.40 | 8.86 |

| 28 | 8.76 | 5.80 | 5.51 | **5.34** | 4.10 | 4.41 | 8.87 |
| 30 | 8.75 | 5.72 | 5.50 | 5.32 | **4.16** | **4.42** | **8.88** |
| 50 | 7.64 | 5.03 | 4.97 | 4.62 | 3.88 | 3.87 | 7.74 |
| 100 | 5.38 | 62 | 3.82 | 4.5 | 14 | 2.81 | 2.81 |
| 1000 | 1.07 | 0.74 | 0.87 | 0.62 | 0.77 | 0.64 | 1.55 |
| 2000 | 0.57 | 0.41 | 0.18 | 0.33 | 0.46 | 0.37 | 0.37 |

## 4. Conclusion

In this article series of calculations to obtain total ionization cross sections for atoms were carried out. We have employed the well-known SCOP and CSP-ic formalisms to perform these calculations. The total ionization results obtained are presented in the article numerically in Table 2 and are graphically compared (Fig. 1-6) with other available measurements and theories. We find that the present results are over all very consistent in strength and shape and hence prove that present method can produce reliable cross sections. So we are now confident to use this method for complex targets as well as targets which are difficult to study experimentally for e.g. exotic targets or radicals. It can be easily employed for the targets where experiments are difficult.

### References

1. B. Boudaiffa, P. Cloutier, D. Hunting, M. A. Huels and L. Sanche Science **287**, 1658 (2000).
2. A. Jain and K. L. Baluja, Phys. Rev. A **45** (1992) 202.
3. K. N. Joshipura and M. Vinodkumar, Z. Phys. D **41**, 133 (1997).
4. B. K. Antony, K. N. Joshipura, N. J. Mason and J. Tennyson, J.Phys.B: At. Mol. Opt.  Phys. **37**, 1689 (2004).
5. M. Vinodkumar, K. Korot and H. Bhutadia, Int. J. Mass Spectrom. **294**, 54 (2010).
6. S. P. Khare, "*Introduction to the Theory of Collisions of Electrons with Atoms and Molecules*" (Kluwer Academic / Plenum Publishers, London, 2002).
7. L. G. Christophorou, "*Electron molecule interactions and their applications*"   (Academic press inc., London, 1984).
8. Y-K Kim and M. E. Rudd, Phys. Rev. A **50,** 3954 (1994).

9. Y. K Kim, W. Hwang, N. M. Weinberger, M. A. Ali and M. E. Rudd, J. Chem. Phys. **106**,1026(1997).

10. From: http://www.explainthatstuff.com

11. H. Deutsch, K. Becker, S. Matt and T. D. Märk, Int. J. Mass Spectrom. **197,** 37(2000).

12. M. Vinodkumar, Ph. D. book, Sardar Patel University, India, (1999).

13. W. M. Huo, Phys. Rev. A **64,** 042719 (2001).

14. K. N. Joshipura and M. Vinodkumar, Phys. Letts. A **41** (1997) 361.

15. R Lide, "*CRC Handbook of Chemistry and Physics"* (CRC Press LLC, Boca RatonFL, 2003).

16. R. S. Freund, R.C. Wetzel, R. J. Shul, T.R. Hayes, Phys. Rev. A41, 3575 (1990).

17. P. L. Bartlett and A T. Stelbovics, Phys. Rev. A **66**, 012707 (2002)

18. Y. K. Kim and P.M. Stone, J. Phys. B: At. Mol. Opt. Phys.**40**,1597(2007).

19. M. R. Talukder, S. Bose, M. A. R. Patoary, A. K. F. Haque, ,M. A. Uddin, A. K. Basak, and M. Kando, Eur. Phys. J. D **46**, 281(2008).

20. K. N. Joshipura, B. G. Vaishnav and C G. Limbachiya, Pramana**66,** 403 (2006).

21. E. J. McGuire, Phys. Rev. A **16**, 62 (1977).

22. M. A. Bolorizadeh, C. J. Patton, M. B. Shah, and H. B. Gil-body, J. Phys. B: At. Mol. Opt. Phys.**27**, 175 (1994).

23. R. J. Shul, R.C. Wetzel, R.S. Freund, Phys. Rev. A **39**,5588 (1989).

24. L. L. Shimon, E. I. Nepiipov, and I. P. Zapesochnyi, Zh. Tekh. Fiz. **45**, 688 (1975) [Sov. Phys. Tech. Phys. 20, 434 (1975)]

# Investigation of Resistivity and Activation energy of WSe$_2$ crystal with Temperature

Dr.B.A.Thakar[1],Dr.R.J.Pathak[*],Dr. Dipak sahay[2],Dr.Ripal parmar[3]andDr.R.K.Shah[4]

[1]B.S. Patel Polytechnic, Ganpat Vidhyanagar, Kherva

[*]R.R.Mehta College of Science, Palanpur

[2]Government Engineering College, Modasa

[3]Department of Physics, HNGU, Patan

[4]Arts, Science and Commerce College,Bhadran

**Email: bhavesh.thakar@ganpatuniversity.ac.in**

## ABSTRACT

Single crystals of tungstendiselenide (WSe$_2$) have been grown using direct vapour transport technique (DVT). The variation of resistivity with temperature was studied along perpendicular and parallel to c-axis of crystal plane using four probes method. Electrical properties variation with temperature and parameters are discussed. Activation energy in various temperature range were analyzed in detail for the crystal of WSe$_2$.

*Key words: TMDC crystals,* Resistivity, Activation energy.

## *INTRODUCTION

The energy levels of semiconductors can be grouped into two bands, the valence band and the conduction band. In the presence of an external electric field it is the electrons in the valence band that can move freely, thereby responsible for the electrical conductivity of the semiconductors. In case of intrinsic semiconductors the Fermi level lies in between the conduction band minimum and valence band maximum. Since the conduction band lies above the Fermi level, at 0K, when no thermal excitations are available, the conduction band remains unoccupied. So conduction is not possible at 0K, and resistance is in infinite. As temperature increases, occupancy of the conduction band goes up, thereby resulting in decreases of electrical resistance of the semiconductor. The temperature dependence of resistance follows an exponential relation with temperature, $R = R_0\, e^{(-\alpha)/T}$

## Experimental Methodology

The dc resistivity (ρ) of $WSe_2$ crystals perpendicular to c-axis was investigated by using dc resistivity apparatus. It can be investigated by the following techniques:  (1) Van deer Pauw techniqueand (2) four probe resistivity method.  The resistivity of the specimens can be measured at different temperatures by four probe method.The high temperature dc resistivity measurements performed on the basal plane in the direction parallel to c-axis and in the temperature range 312K-673K is made by resistivity apparatus using four probe resistivity method. The crystals having irregular shape and larger size were normally selected to investigate their electrical behavior through four probe resistivity method [7].

Four probes are placed on a flat surface of the material whose resistivity is to be measured. Current is passed through the two outer electrodes and floating potential is measured across the inner pair. The four probe set up consists of probe arrangement, oven, constant current source, millimeter and electronic voltmeter. Collinear and equally spaced spring loaded four probes are coated with zinc at the tips to ensure good electrical contact with the sample. The resistivity variations with temperature in the range from ambient to 673 K were studied on the grown crystals using conventional four probe method. The resistivity at each temperature was evaluated by using the formula [7],

$$\rho = 2\pi \, sR \qquad (1)$$

Where s is the distance between two probes, and 'R' is the resistance between two probes. The resistivity data obtainedfrom the above equation are plotted as a function of inverse of temperature and are shown in Fig.1 for $WSe_2$.

## *RESULTS AND DISCUSSIONS:

### TABLE-1DATA TABLE OF THE EXPERIMENT

| T(K) | $R_\parallel$(k Ω) | $\rho_\parallel$ (Ω · m) | Log($\rho_\parallel$) | R⊥ (k Ω) | $\rho_\perp$ (Ω · m) | Log( $\rho_\perp$) | 1000/T (K$^{-1}$) |
|---|---|---|---|---|---|---|---|
| 312 | 101 | 1268.56 | 3.1033 | 43.30 | 543.85 | 2.74 | 3.2051 |
| 318 | 95 | 1193.20 | 3.0767 | 32.30 | 405.69 | 2.61 | 3.1447 |
| 323 | 87 | 1092.72 | 3.0385 | 25.40 | 319.02 | 2.50 | 3.0960 |
| 328 | 81 | 1017.36 | 3.0075 | 23.09 | 290.01 | 2.46 | 3.0488 |

| 333 | 75 | 942.00 | 2.9741 | 20.53 | 257.86 | 2.41 | 3.0030 |
| --- | --- | --- | --- | --- | --- | --- | --- |
| 338 | 71 | 891.76 | 2.9502 | 18.12 | 227.59 | 2.36 | 2.9586 |
| 343 | 68 | 854.08 | 2.9315 | 16.30 | 204.73 | 2.31 | 2.9155 |
| 348 | 66 | 828.96 | 2.9185 | 14.76 | 185.39 | 2.27 | 2.8736 |
| 353 | 63 | 791.28 | 2.8983 | 12.29 | 154.36 | 2.19 | 2.8329 |
| 358 | 62 | 778.72 | 2.8914 | 11.81 | 148.33 | 2.17 | 2.7933 |
| 363 | 60 | 753.60 | 2.8771 | 10.71 | 134.52 | 2.13 | 2.7548 |
| 368 | 56 | 703.36 | 2.8472 | 9.08 | 114.04 | 2.06 | 2.7174 |
| 373 | 54 | 678.24 | 2.8314 | 8.41 | 105.63 | 2.02 | 2.6810 |
| 378 | 51 | 640.56 | 2.8066 | 7.38 | 92.69 | 1.97 | 2.6455 |
| 383 | 49 | 615.44 | 2.7892 | 6.92 | 86.92 | 1.94 | 2.6110 |
| 388 | 46 | 577.76 | 2.7617 | 6.15 | 77.24 | 1.89 | 2.5773 |
| 393 | 43 | 540.08 | 2.7325 | 5.71 | 71.72 | 1.86 | 2.5445 |
| 398 | 41 | 514.96 | 2.7118 | 5.43 | 68.20 | 1.83 | 2.5126 |
| 403 | 39 | 489.84 | 2.6901 | 5.03 | 63.18 | 1.80 | 2.4814 |
| 408 | 37 | 464.72 | 2.6672 | 4.71 | 59.16 | 1.77 | 2.4510 |
| 413 | 36 | 452.16 | 2.6553 | 4.43 | 55.64 | 1.75 | 2.4213 |
| 418 | 34 | 427.04 | 2.6305 | 4.01 | 50.37 | 1.70 | 2.3923 |
| 423 | 32 | 401.92 | 2.6041 | 3.83 | 48.10 | 1.68 | 2.3641 |
| 428 | 30 | 376.80 | 2.5761 | 3.73 | 46.85 | 1.67 | 2.3364 |
| 433 | 28 | 351.68 | 2.5461 | 3.65 | 45.84 | 1.66 | 2.3095 |
| 438 | 27 | 339.12 | 2.5304 | 3.51 | 44.09 | 1.64 | 2.2831 |
| 443 | 25 | 314.00 | 2.4969 | 3.28 | 41.20 | 1.61 | 2.2573 |
| 448 | 23 | 288.88 | 2.4607 | 3.12 | 39.19 | 1.59 | 2.2321 |
| 453 | 20 | 251.20 | 2.4000 | 3.09 | 38.81 | 1.59 | 2.2075 |
| 458 | 20 | 251.20 | 2.4000 | 3.01 | 37.81 | 1.58 | 2.1834 |
| 463 | 18 | 226.08 | 2.3543 | 2.81 | 35.29 | 1.55 | 2.1598 |
| 468 | 17 | 213.52 | 2.3294 | 2.78 | 34.92 | 1.54 | 2.1368 |
| 473 | 17 | 213.52 | 2.3294 | 2.71 | 34.04 | 1.53 | 2.1142 |
| 478 | 15 | 188.40 | 2.2751 | 2.65 | 33.28 | 1.52 | 2.0921 |
| 483 | 14 | 175.84 | 2.2451 | 2.51 | 31.53 | 1.50 | 2.0704 |
| 488 | 13 | 163.28 | 2.2129 | 2.41 | 30.27 | 1.48 | 2.0492 |
| 493 | 12 | 150.72 | 2.1782 | 2.30 | 28.89 | 1.46 | 2.0284 |
| 498 | 12 | 150.72 | 2.1782 | 2.27 | 28.55 | 1.46 | 2.0080 |
| 503 | 13 | 163.28 | 2.2129 | 2.23 | 28.01 | 1.45 | 1.9881 |
| 508 | 14 | 175.84 | 2.2451 | 2.22 | 27.86 | 1.44 | 1.9685 |
| 513 | 13 | 163.28 | 2.2129 | 2.11 | 26.50 | 1.42 | 1.9493 |
| 518 | 11 | 138.16 | 2.1404 | 2.02 | 25.32 | 1.40 | 1.9305 |
| 523 | 10 | 125.60 | 2.0990 | 1.98 | 24.91 | 1.40 | 1.9120 |
| 528 | 12 | 150.72 | 2.1782 | 1.84 | 23.14 | 1.36 | 1.8939 |
| 533 | 12 | 150.72 | 2.1782 | 1.89 | 23.78 | 1.38 | 1.8762 |

| 538 | 10 | 125.60 | 2.0990 | 1.87 | 23.50 | 1.37 | 1.8587 |
|-----|----|--------|--------|------|-------|------|--------|
| 543 | 11 | 138.16 | 2.1404 | 1.85 | 23.17 | 1.36 | 1.8416 |
| 548 | 12 | 150.72 | 2.1782 | 1.84 | 23.15 | 1.36 | 1.8248 |
| 553 | 10 | 125.60 | 2.0990 | 1.83 | 22.97 | 1.36 | 1.8083 |
| 558 | 11 | 138.16 | 2.1404 | 1.82 | 22.80 | 1.36 | 1.7921 |
| 563 | 12 | 150.72 | 2.1782 | 1.81 | 22.73 | 1.36 | 1.7762 |
| 568 | 10 | 125.60 | 2.0990 | 1.80 | 22.62 | 1.35 | 1.7606 |
| 573 | 11 | 138.16 | 2.1404 | 1.80 | 22.55 | 1.35 | 1.7452 |
| 578 | 10 | 125.60 | 2.0990 | 1.80 | 22.62 | 1.35 | 1.7301 |
| 583 | 10 | 125.60 | 2.0990 | 1.81 | 22.75 | 1.36 | 1.7153 |
| 588 | 9  | 113.04 | 2.0532 | 1.82 | 22.80 | 1.36 | 1.7007 |
| 593 | 9  | 113.04 | 2.0532 | 1.81 | 22.77 | 1.36 | 1.6863 |
| 598 | 8  | 100.48 | 2.0021 | 1.85 | 23.24 | 1.37 | 1.6722 |
| 603 | 8  | 100.48 | 2.0021 | 1.89 | 23.79 | 1.38 | 1.6584 |
| 608 | 7  | 87.92  | 1.9441 | 1.91 | 23.93 | 1.38 | 1.6447 |
| 613 | 5  | 62.80  | 1.7980 | 1.92 | 24.17 | 1.38 | 1.6313 |
| 618 | 2  | 25.12  | 1.4000 | 1.95 | 24.47 | 1.39 | 1.6181 |
| 623 | 2  | 25.12  | 1.4000 | 1.99 | 24.98 | 1.40 | 1.6051 |
| 628 | 2  | 25.12  | 1.4000 | 1.99 | 24.99 | 1.40 | 1.5924 |
| 633 | 2  | 25.12  | 1.4000 | 2.11 | 26.49 | 1.42 | 1.5798 |
| 638 | 2  | 25.12  | 1.4000 | 2.28 | 28.57 | 1.46 | 1.5674 |
| 643 | 2  | 25.12  | 1.4000 | 2.33 | 29.21 | 1.47 | 1.5552 |
| 648 | 3  | 37.68  | 1.5761 | 2.33 | 29.29 | 1.47 | 1.5432 |
| 653 | 3  | 37.68  | 1.5761 | 2.38 | 29.94 | 1.48 | 1.5314 |
| 658 | 3  | 37.68  | 1.5761 | 2.45 | 30.82 | 1.49 | 1.5198 |
| 663 | 2  | 25.12  | 1.4000 | 2.52 | 31.66 | 1.50 | 1.5083 |
| 668 | 2  | 25.12  | 1.4000 | 2.61 | 32.79 | 1.52 | 1.4970 |
| 673 | 2  | 25.12  | 1.4000 | 2.60 | 32.61 | 1.51 | 1.4859 |
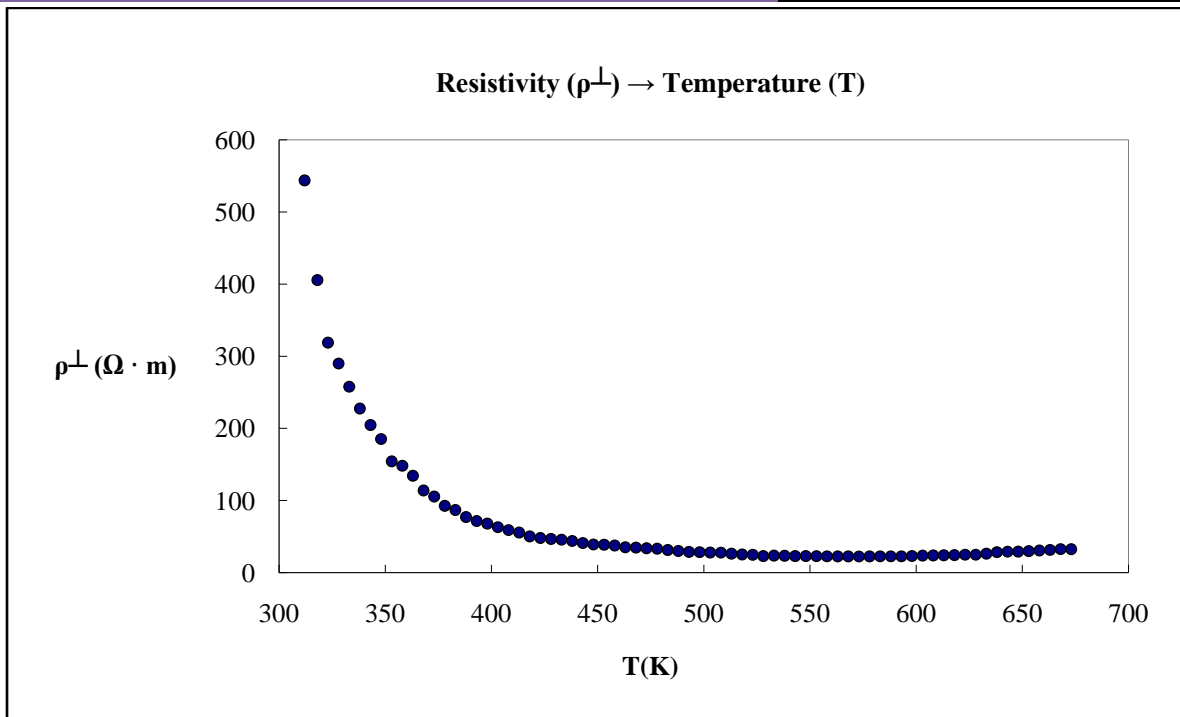
**Fig.1: Variation of resistivity** ($\rho\perp$) **with temperature (T) of WSe$_2$ crystal**

Results of resistivity ($\rho\perp$) perpendicular to c axis in the temperature range (328K-673K) for a sample of WSe$_2$is shown in Fig.1.It is fairly evident that resistivity decreases exponentially with an increase in temperature. This is the typical characteristic of semiconducting material. The graph of log($\rho$)verses 1000/T in Fig.2shows astraightlineregion similar to that observed by*voraet.el* in there research work.
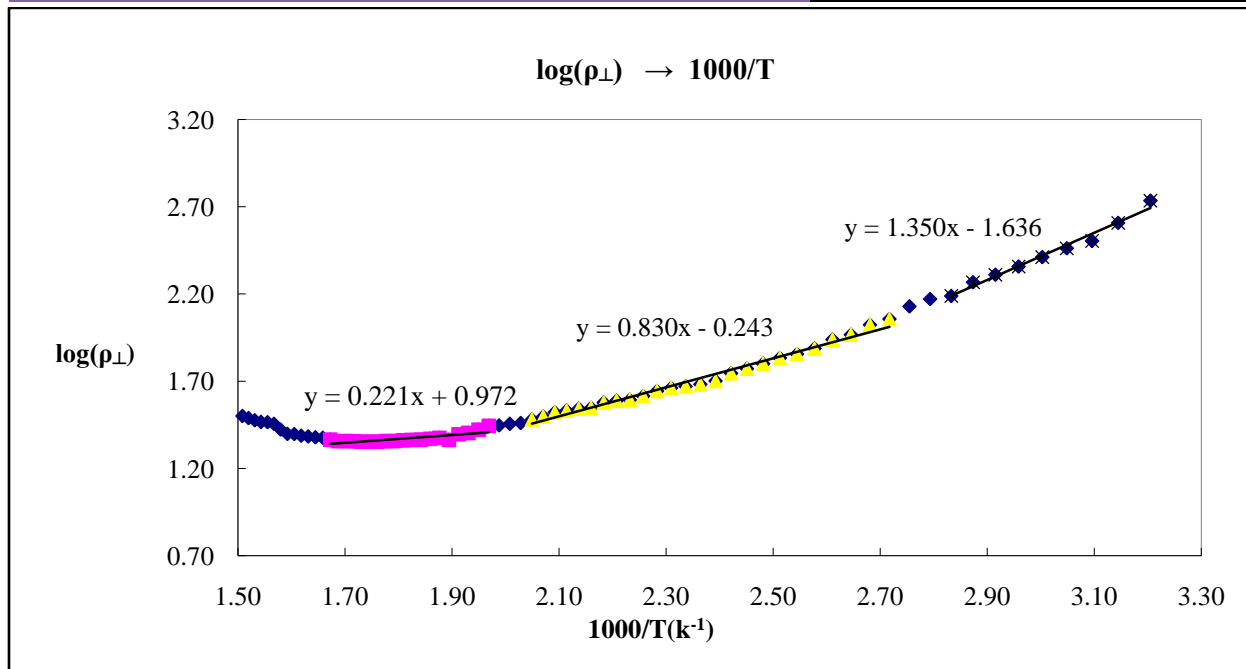
**Fig.2: Variation of resistivity with reciprocal of temperature of WSe$_2$ crystals**
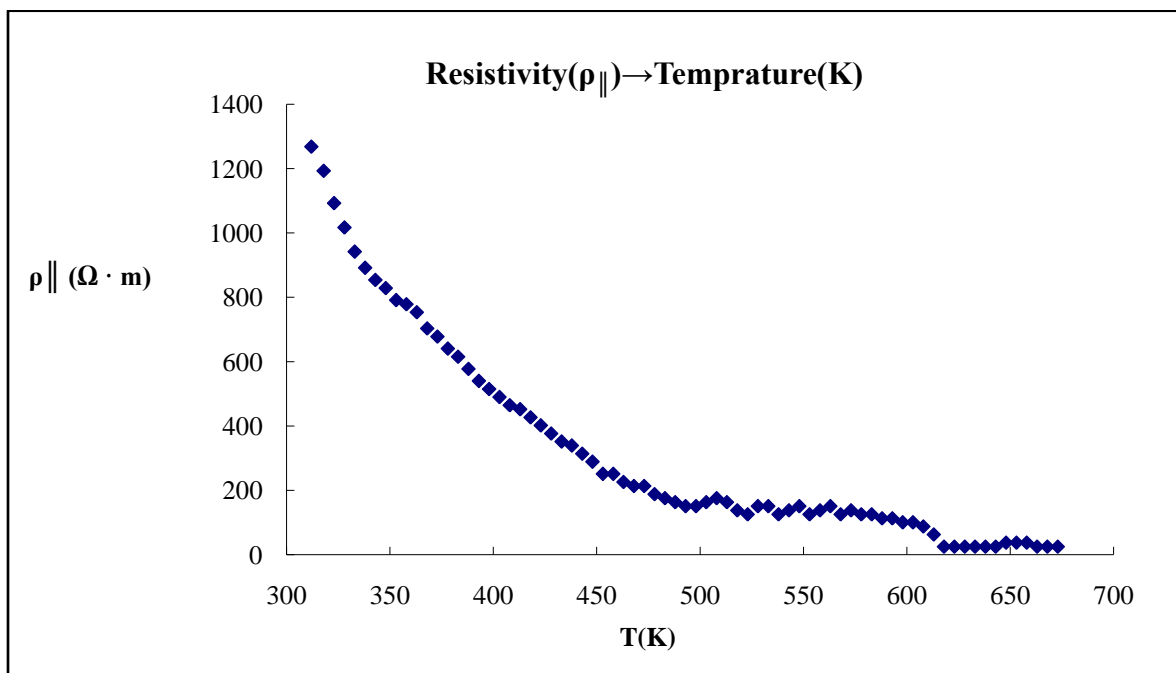


**Fig.3: Variation of resistivity ($\rho_\parallel$)with Temperature (T) of WSe$_2$ crystals**

Experiment have been repeated to found out variation in resistivity ( $\rho_\parallel$ ) parallel to c axis in temperature range (328K-673K) for a sample of WSe$_2$. Fig:3 shows the outcome of the

experiment. Fig: 3 shows that resistivity parallel to c axis decreases exponentially with temperature. The above graph demonstrate typical characteristics of semiconducting materials.
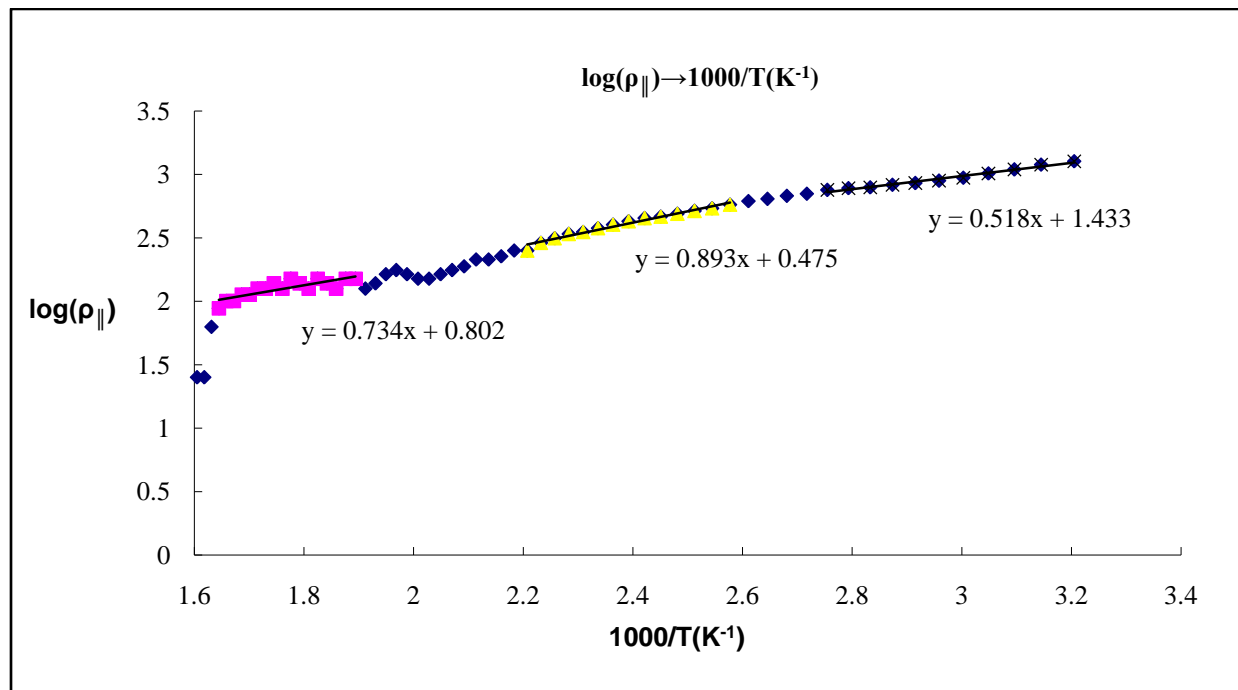


**Fig.4: Variation of resistivity with reciprocal of temperature of WSe$_2$ crystals**

Fig.4shows avariation of log ρ verses 1000/T.  Using the value of a slop of a straight line found in various temperature range,we have calculated the value of activation energy in a respective temperature range.

The activation energy is determined from the above plots (Fig. 2  andFig. 4) using equation,

$$Ea = 2.303 \times K_B \times slope \times 1000 \ (eV) \tag{2}$$

Where Ea = Activation energy

$K_B$=Boltzmann constant

$K_B$=8.6173 X $10^{-5}$eV/K

For the samples of WSe$_2$ the resistivity perpendicular and parallel to c-axis decreased with increase of temperature analogous to semiconducting behavior. The activation energy values determined from the Fig. 2 and Fig. 4is tabulated in Table 2.

**Table 2**: The activation energies calculated from the plotsLog(ρ)vs. 1000/T.

| Material | Resistivity type | Temp. rang | Slop | Activation energy (Ea (eV)) |
| --- | --- | --- | --- | --- |
| WSe$_2$ | $\rho\perp$ $(\Omega \cdot m)$ | 598-508 | 0.221 | 0.0439 |
| | | 488-368 | 0.8301 | 0.1647 |
| | | 353-312 | 1.3507 | 0.2680 |

| Material | Resistivity type | Temp. rang | Slop | Activation energy (Ea (eV)) |
| --- | --- | --- | --- | --- |
| WSe$_2$ | $\rho\parallel$ $(\Omega \cdot m)$ | 608-528 | 0.7349 | 0.1458 |
| | | 453-388 | 0.8931 | 0.1772 |
| | | 378-312 | 0.518 | 0.1028 |

## *Anisotropy:

In our investigation anisotropy measurements have been carried out in the temperature range 378K-673K from the ratio of the data of high dc resistivity measured from parallel and perpendicular to the c-axis. It is seen in Fig.5 that the anisotropy ratioincreases with the increase in temperature. This variation of anisotropy with temperature shows an identical behavior to that reported by *deshpande et.al.*[2] in their research work.
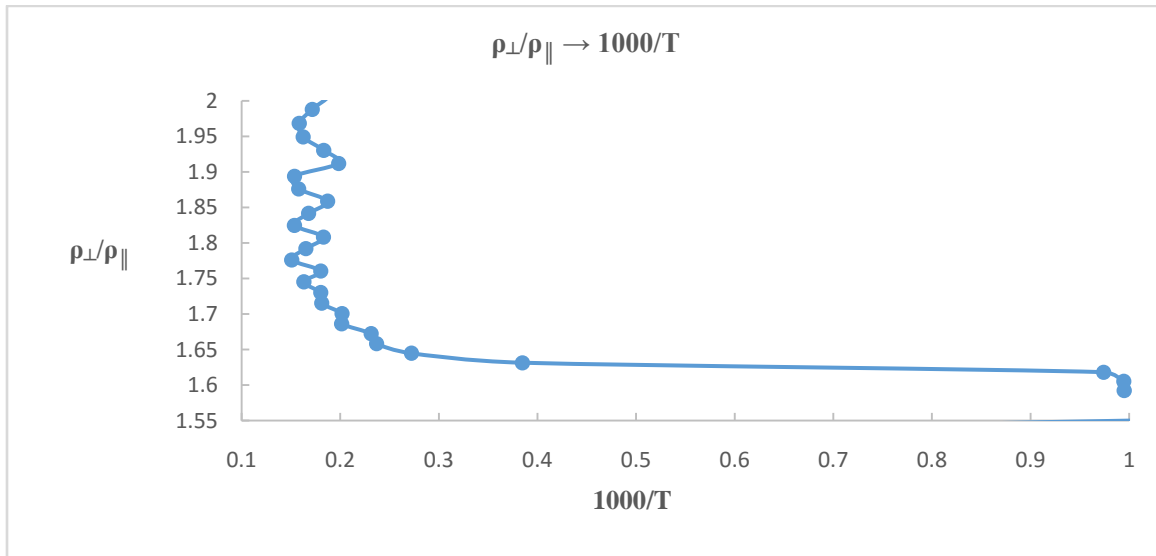
**Fig.5: Variation in anisotropy ratio with reciprocal of temperature**.

## *CONCLUSIONS:

1. Resistivity of $WSe_2$ decreases with an increase in temperature. Hence we can confirms that DVT grown crystal of $WSe_2$ have semiconducting nature.

2. Resistance in parallel to c-axis found to be larger than that of perpendicular to c axis. Hence we can confirms that DVT grown crystal of $WSe_2$ have layered kind of a solid state structure.

3. The activation energy's in various temperature range can be found out using slops of the plots of $\log(\rho)$ versus reciprocal of the temperature.

4. The crystals of $WSe_2$ grown by a direct vapour transport technique are found to have an anisotropic semiconducting nature.

5. The anisotropy ratio increases with the increase in temperature.

**REFERENCES**

[1]     Pankaj R. Patel, H. S. Patel, J. R. Rathod, K. D. Patel, and V. M. Pathak, *American J.Cond.Matt. Phys*., **3(1)** (2013) 13-20.

[2]     M. P. Deshpande, Sunil Chaki, Nilesh N. Pandya and Sagar C. Shah, *PRAJNA – J. P. and App. Sci.*, **18** (2010) 132 – 135.

[3]     H. S. Patel, J. R. Rathod, K. D. Patel and V. M. Pathak, *Research Expo, International Multidisciplinary Research J.*, **1** (2011) 127.

[4]     Sandip R.Unadkat, Ph.D. Thesis.Sardar Patel University, 2012.

[5]     P. R. Patel and V. M. Pathak,
        *J. Ele. and Elec. Eng.*, (2012) 44-46.

[6]     Mihir M. Vora and Aditya M. Vora,
        *The African Review of Physics*, **6** (2011) 15.

[7]     KalyaniBhoi,
        Master of Science Thesis, National Institute of Technology, Rourkela, (2010).

[8]     G K Solanki, Dipika.B.Patel, SandipUnadkatAnd M. K. Agarwal,
        *PRAMANA – J.Phys.*,**74** (2010) 813-825.

[9]     DeepaL.Makhija*, K.D.Patel, V. M. Pathak, R. Srivastava,
        *J.Ovonic Research*, **4** (2008) 141 – 145.

[10]    Priyanka Desai*, D.D. Patel, D.N. BhavsarAnd A.R. Jani,
        *PRAJNA – J.P.andApp.Sci.*, **19** (2011) 68 -70.

[11]    MoussaBougouma, BoubiéGuel, TirianaSegato, Jean B. Legma and Marie-Paule,
        *Bull. Chem. Soc*. Ethiop, **22(2)** (2008) 225-236.

[12]    Mihir M. Vora and Aditya M. Vora,
        *The African Review of Physics*, **6** (2011) 15.

[13]    C. K. Sumesh, K. D. Patel, V. M. Pathak, R. Srivastava,
        *Chalcogenide Letters*, **5** (2008) 177-180.

[14]    P. C. Yen, Y. S. Huang and K. K. Tiong,
        *J. Phys: Condensed Matter*, **16** (2004) 2171-2181.

[15]    S. Y. Hu, M. C. Cheng, Tiong, K. K. Tiong, and Y. S Huang,
        *J. Phys. Condensed Matter*, **17** (2005) 3573-3583.

[16]    S.Mattila, J. A.Leiro, M.Heinonen and T. Laiho,
        *Core level Spectroscopy of $MoS_2$. Surf. Sci.*, **60** (2006) 5168-5175.

[17]    V.Podzorov, M.E.Gershenson, R.Zeis, and E. Bucher,
        *Appl. Phys. Lett.*, **84** (2004) 3301-3303.

[18]    K.K.Tiong, T.S.Shou, and C.H.Ho,
        *J. Phys.: Condensed Matter*, **12** (2000) 3441–3449.

[19]    J.C.Bernede, C. Amory, L. Assmann, and M.Spiesser,
        *Appl. Surf. Sci,.***219** (2003) 238-348.

[20]    H. J Goldsmith,
        *Applications in Thermoelectricity*, Methuen Monograph, London, (1950).

[21]    H. P. R Frederikse,
        *Phys. Rev.*, **91** (1953) 491.

# TOTAL SCATTERING CROSS SECTIONS CALCULATIONS FOR ELECTRON IMPACT ON $CF_2$ RADICAL

## M. Y. Barot[1#], A. Y. Barot[2], D. N. Bhavsar[3] and M. Vinodkumar[4]

[1]Government Science College Gandhinagar-382016, Gujarat, India

[2]Sigma Institute of science and commerce, Vadodara-390001, gujarat, India

[3]Bhavan's Sheth R. A. College of Science, Khanpur, Ahmedabad-380001, Gujarat, India.

[4]V. P. & R. P. T. P. Science College, Vallabh Vidyanagar – 388120, Gujarat, India

#correspondant author *:* barot_mayuri@yahoo.com  Tel. No.: +919624045206

**Abstract:** Total scattering cross sections for electron impact on $CF_2$ in the gas phase are presented from 0.1 eV to 2000 eV. Computation of such e - $CF_2$ cross sections over such a wide range of energy is reported for the first time employing two distinct formalisms. From 0.1 eV to the ionization threshold of the target we employed the *ab-initio* R-matrix method, while at higher energies we used the Spherical Complex Optical Potential (SCOP) method. At the crossing point, the two theories match one another quite well and hence prove that they are consistent with one another. The total cross sections presented here are in good agreement with other experimental and theoretical calculations. These results show that the techniques employed here can be used to predict cross sections for other targets for which data is scarce or not available. This methodology may be integrated into online databases such as the Virtual Atomic and Molecular Data Centre (VAMDC) to provide cross section data required by many desperate users.

**Key Words:** R-matrix method, *ab-initio* calculations, Spherical Complex Optical Potential, Total  cross sections, $CF_2$.

**PACS number(s)**: 34.80.Bm

**Highlights:**

- Here we have presented Eigen phase sum, Excitation cross section, Differential cross sections, Momentum transfer cross section, and Total cross sections for e-$CF_2$.

- The calculations of total cross sections show a peak at 0.81 eV using the Static Exchange Polarization (SEP) model and at 1.86 eV using a Static Exchange (SE) model which is a reflection of the formation of a $\Pi_u$ shape resonance state.

- These values are close to theoretical calculations by Rozum *et al.* [J. Phys. Chem. Ref. data, **35,** 267 (2006)] with a peak at 0.89 eV for SEP model and 1.91 eV for SE model. Lee *et al.* [Phys. Rev. A, **74,** 052716 (2006)] have also reported a peak at 1.65 eV.

## 1 INTRODUCTION

Molecular radicals play an important role in many electron-driven processes, including radiation damage in tissue, gas discharges, low-temperature plasma etching environments and waste deposition technologies. In particular, radicals of the fluorocarbons play a significant role in the etching processes and evolution of plasmas used in micro and nano-structure assembly, for example it is now well established that the concentration of $CF_x$ (x = 1–3) radicals have  a significant effect on the behavior of fluorocarbon plasmas [1, 2]. Such $CF_x$ radicals are predominantly formed by electron impact induced dissociation of the fluorocarbon feed gases.

In this paper we study the scattering of $CF_2$ radicalon electron impact. Experimental studies of electron collision cross sections with $CF_2$ are difficult and hence to date measured data has only been reported by one group [3]. Francis-Staite *et al.* [3] used a crossed–beam electron scattering experiment to measure e -$CF_2$ differential cross sections at specific angles (20° – 135°) for incident energies between 2 and 20 eV. They also reported calculated data for absolute differential cross sections and integral cross sections using the Schwinger multichannel method for impact energies between 2 and 20 eV. Earlier Maddern*et al.* [4] reported absolute differential cross sections for incident electron energies of 30–50 eV and over an angular range of $20^o$–$135^o$. Theoretical investigations of the total elastic cross sections for e -$CF_2$ scattering have been reported by four groups [3, 5-7]. Lee *et al.* [5] used the Iterative Schwinger variational method and calculated elastic differential, integral and momentum transfer cross sections as well as total absorption cross sections in the energy range 1 – 500 eV. Rozum*et al.* [6] used the R-matrix method to evaluate the total elastic and excitation cross sections of the six lowest lying electronic excited states of the $CF_2$. Antony *et al.* [7] have reported total elastic and total inelastic cross sections using a Spherical Complex Optical Potential for impact energies between 50 and 2000 eV. Owing to the difficulties involved in experiments with $CF_2$ radicals, total ionization cross sections have been reported experimentally by two groups, Huo*et al.* [8] and Tarnovsky*et al.* [9] while theoretical estimates of the total ionization cross sections are reported by three groups [7,10,11]. Thus, reviewing the literature, it is quite clear that the work on e -$CF_2$ is scarce, as most of the authors have focused their results over a specific range of impact energies as well as for specific cross sections. This work reports various cross section data for a wide energy range which can be used for plasma modeling.

This paper reports electron impact excitation, differential, momentum transfer, ionization and total cross sections for e -$CF_2$ scattering over a wide range of energy starting from a very low energy of 0.1 eV to 2000 eV. Electron-molecule collision cross sections from very low

energy up to threshold play an important role in determining electron transport properties and electron energy distribution of a swarm of electrons drifting through various gases. They also play significant role in modeling low temperature plasmas. In addition to the practical interest, electron scattering data are of fundamental theoretical importance towards the understanding of various electron assisted molecular chemistry [12]. The motive behind such study is twofold; (1) to study the resonance processes which are more prominent at low impact energies below 10 eV through which  knowledge of dissociative electron attachment and negative ion formation can be gathered and (2) to compare the results of this work with available data. In order to achieve these goals we employed two different formalisms that are consistent and widely used over specific ranges of impact energies. For low impact energies up to the ionization threshold of the target we employ the *ab-initio* R-matrix method [13] while at higher energies  computation of the total cross sections is carried out using a quantum mechanical approach through Spherical Complex Scattering Potential [14, 15].

This paper is organized as follows, in Section 2 we describe first the target model and then describe the salient features of the oretical methodologies employed for low energy as well as high energy calculations. Section III is devoted to results and discussions of the results obtained and finally we end up with conclusions of the present study.

## 2 THEORETICAL METHODOLOGIES

The energy range of this study (0.1 to 2000 eV) cannot be modeled by any single theoretical formalism. Hence the present calculations are based on two distinct methodologies, one valid below the ionization threshold of the target and the other above it. This paper reports low energy (0.1 eV to about 15 eV) *ab-initio* calculation using the Quantemol-N package [16] employing the UK molecular R-matrix code [13] and the Spherical Complex Scattering Potential formalism above 15eV. The target model plays an important role as its correct representation ensures accuracy and stability in the calculation, therefore before discussing the scattering formalisms we must discuss the target model employed.

### A Target Model Used For Low-Energy Calculations

According to equilibrium geometry, $CF_2$ is a triangular radical with a C–F bond length of 2.45 $a_0$ and a bond angle F–C–F of 104.98$^o$ [17]. We employed a double zeta plus polarization (DZP) basis set similar to 6-31G for the target wave function representation and assumed $C_{2v}$ point group symmetry of order four. For the optimized nuclear geometry of the target we employed second order Möller-Plesset perturbation theory in the 6–31G (*d*) basis set and the

occupied and virtual molecular orbitals obtained using Hartree–Fock–Self consistent field (HF–SCF) opt0imization which was used to set up the $CF_2$ electronic target states. The ground state Hartree–Fock electronic configuration is $1b_2^2$, $1a_1^2$, $2a_1^2$, $3a_1^2$, $2b_2^2$, $4a_1^2$, $3b_2^2$, $5a_1^2$, $1b_1^2$, $1a_2^2$, $4b_2^2$ and $6a_1^2$. To establishing a balance between the amount of correlation incorporated in the N-electron target representation, $\varphi N_i$, and the (N+1) electron scattering wavefunction in our configuration integration (CI) model, out of 24 electrons, we froze 16 electrons in ten molecular orbitals ($1a_1$, $2a_1$ $3a_1$, $4a_1$, $5a_1$, $1b_1$, $1b_2$, $2b_2$, $3b_2$, $1a_2$). The remaining 8 electrons were allowed to move freely in the active space of 6 target occupied and virtual molecular orbitals ($6a_1$, $7a_1$, $2b_1$, $3b_1$, $4b_2$, $5b_2$).

**TABLE I.** Target properties for $CF_2$ molecule.

| Properties of Target | Present | Theoretical Results | Experimental Results |
|---|---|---|---|
| Ground state energy (Hartree) | –236.7341 | –236.7305 [5] –236.7275 [18] | ----- |
| First excitation energy (eV) | 3.28 | 2.49 [6] 2.42 [19] 2.46 [20] | 2.30 [3] |
| Rotational constant $(cm^{-1})$(A)(B) (C) | 2.95 0.403 0.353 | 2.83 [6] | 2.95 [17], 2.947 [21] 0.417 [21] 0.364 [21] |
| Dipole moment (D) | 0.301 | 0.246 [Ref.5] 0.440 [Ref.18] 0.448 [Ref.6] | 0.469 [Ref.21] |

Our self-consistent field (SCF) calculation yielded the ground state energy for $CF_2$ as –236.7341 Hartree whichis in good agreement with –236.7305 Hartree calculated by Lee *et al.* [5] and –236.7575 Hartree of Russo *et al.* [18]. The nuclear coordinates will determine the molecular orbitals, rotational constants, dipole moment and symmetries of the molecule. These parameters highly affect the cross section (differential, momentum transfer and total cross sections) calculations. Hence it is imperative to use proper nuclear coordinates. The calculated rotational constants for $CF_2$ are 2.95 $cm^{-1}$, 0.403 $cm^{-1}$ and 0.353 $cm^{-1}$ which are very close with measured data of 2.947 $cm^{-1}$, 0.417 $cm^{-1}$ and 0.364 $cm^{-1}$ reported by Kirchhoff *et al.* [21] and

also same as 2.95 cm$^{-1}$ reported in Computational Chemistry Comparison and Benchmark Data Base [17] and is slightly lower than the theoretical value of 2.83 cm$^{-1}$ reported by Rozum*et al.* [6].  The calculated first excitation energy is 3.28 eV is higher compared to measured value of 2.3 eV reported by Francis-Staite *et al.* [3] and theoretical values of 2.49 eV reported by Rozum*et al.* [6], 2.42 eV reported by Cai [19]. The calculated dipole moment is 0.301 D which is higher compared to 0.246 D reported by Lee *et al.* [5] but is lower than the experimental value of 0.469 D of Kirchhoff *et al.* [21] and the theoretical value of 0.44 D of Russo *et al.* [18] and 0.448 D of Rozum*et al.* [6]. The target properties along with available comparisons are listed in Table I and the eight electronic excitation thresholds for $CF_2$ are listed in Table II.

**TABLE II.** Vertical excitation energies for e -$CF_2$.

| State | Energy (eV) | State | Energy (eV) |
|-------|-------------|-------|-------------|
| $1A_1$ | 00.00 | $1A_2$ | 11.06 |
| $3B_1$ | 03.28 | $3B_2$ | 11.45 |
| $1B_1$ | 06.14 | $1B_2$ | 12.66 |
| $3A_2$ | 10.96 | $3A_1$ | 12.99 |

**B Low Energy Scattering Formalism (0.1 eV To ~ 15 eV)**

The most popular methodologies employed for low energy electron collision calculations are the Kohn variational method [22], the Schwinger multichannel method [23] and the R-matrix method [24], of which the R-matrix is the most widely used method. The underlying idea behind the R-matrix method relies on the division of configuration space into two spatial regions, namely an inner region and outer region. The spatial R-matrix spherical boundary is chosen such that the complete electronic charge distribution of the target electrons plus the scattering electron is embedded in it. Thus the all N target electrons plus one scattering electron are contained in the inner region which makes the problem numerically complex, but physically very precise. All short range interactions between the target electrons and scattering electron are dominant in this region which includes static, exchange and correlation polarization potentials. Consequently the accuracy of scattering calculation depends critically on how appropriately the inner region physics is defined. The solution of the inner region problem involves rigorous quantum chemistry methods and thus consumes most of the time needed for calculation. However, the inner region problem is solved independently of the energy of the scattering electron and hence is done only once.

In the outer region where the scattering electron is at large distance from the center of mass of the target, the probability of swapping its identity with any one of the target electrons is negligible, resulting in a negligible contribution from the exchange and correlation effects. This makes the problem very simple since only multipolar interactions between the scattering electron and the target are included. A single center close coupling approximation with direct potentials leads to a set of coupled differential equations and this allows quick, simple and fast solutions in the outer region. The outer region calculations are repeated for each set of energies. In the present calculation the inner R-matrix radius is taken as 10 $a_0$. In the outer region the R-matrix on the boundary is propagated to a sufficiently large distance where the interaction between target electrons and scattering electron is assumed to be zero. In the present case this distance is 100 $a_0$. Asymptotic expansion techniques are used to solve the outer region functions [24].

In the inner region target electrons are placed in some combination of target molecular orbitals which are represented by Gaussian-type orbitals and these are multiplied by spin functions to generate configuration state functions (CSF's). The target molecular orbitals are also supplemented by a set of continuum orbitals which have longer range such that they extend beyond the inner region R-matrix boundary and hence the inner region wave function is constructed using a close coupling approximation [25] for all N+1 electrons. In the close coupling method, scattering cross sections are calculated including the effect of Polarization and in the presence of resonances due to formation of transient negative ions and various threshold effects. The total wave function for the system is expressed as,

$$\psi_k^{N+1} = A \sum_I \psi_I^N(x_1, \cdots, x_N) \sum_j \zeta_j(x_{N+1}) a_{Ijk} + \sum_m \chi_m(x_1, \cdots, x_{N+1}) b_{mk} \tag{1}$$

where A is the anti–summarization operator that takes care of exchange effect among N+1 electrons, $x_N(r_n, \sigma_n)$ is the spatial and spin coordinate of the $n^{th}$ electron, $\xi_j$ is a continuum molecular orbital spin-coupled with the scattering electron. $a_{Ijk}$ and $b_{mk}$ are variational coefficients determined by the diagonalization of N+1 Hamiltonian matrix.

The accuracy of the calculation depends solely on the accurate construction of the wave function given in equation (1). The first summation runs over the target states used in the close-coupled expansion and a static exchange calculation has a single Hartree-Fock target state in the first sum. Here one electron is placed in the continuum orbital of the target and the rest of the electrons move in available target molecular orbitals thus generating target + continuum configurations. In the second term $\chi_m$ are multi-center quadratically integrable functions, known as $L^2$ functions constructed from target occupied and virtual molecular orbitals, and are used to

represent correlation and Polarization effects. This sum runs over the minimal number of configurations, usually 3 or fewer, required to relax orthogonality constraints between the target molecular orbitals and the functions used to represent the configuration. The continuum orbitals are centered on the center of mass of the molecule. The present close-coupled calculation uses the lowest number of target states, represented by a configuration interaction (CI) expansion in the first term and over a hundred configurations in the second. These configurations allow for both orthogonality relaxation and short-range Polarization effects.

The complete molecular orbital representation in terms of occupied and virtual target molecular orbitals are constructed using the Hartree-Fock Self-Consistent Field method with Gaussian-type orbitals (GTOs) and the continuum orbitals of Faure *et al.* [26] and included up to g ($l = 4$) orbitals. The benefit of employing a partial wave expansion for low energy electron molecule interaction is its rapid convergence. In the case of dipole-forbidden excitations ($\Delta J \neq 1$), where J represents the rotational quantum number, the convergence of the partial waves is rapid but in the case of dipole-allowed excitations $(\Delta J = 1)$ the partial wave expansion converges slowly due to the long range nature of the dipole interaction. In order to account for the higher partial waves not included in the fixed nuclei T-matrices, the born correction is applied. The effect of partial waves higher than $l = 4$ were included using a Born correction which requires expressions for the partial waves as well as full Born cross sections. These expressions were drawn from the work of Chu and Dalgarno [27]. We were constrained to employ partial waves for the continuum orbital up to $l = 4$ only, as the representation in Gaussian type orbitals for the Bessel functions higher than $l = 4$ were not available. For low partial waves $(l \leq 4)$ T matrices computed from the R-matrix calculations are employed to compute the cross sections. The low partial wave contributions arising from the Born contribution are subtracted in order that the final cross section set only contains those partial waves due to the R-matrix calculation. We have performed the calculations with and without dipole Born corrections.

The R-matrix provides the link between the inner region and the outer region. The R-matrix is propagated to an asymptotic region where the radial wave-functions describing the scattering electron can be matched to analytical expressions. For this purpose the inner region is propagated to the outer region potential until its solution matches with the asymptotic functions given by the Gailitis expansion [28]. Coupled single center equations describing the scattering in the outer region are integrated to identify the K-matrix elements. The K-matrix is a symmetric

matrix whose dimensions are the number of open channels. All the observables can be deduced from it and it can be used to obtain T-matrices using the definition,

$$T = \frac{2iK}{1-iK} \qquad (2)$$

These T-matrices are in turn used to obtain various total cross sections. The K-matrix is diagonalized to obtain the eigenphase sum. The eigenphase sum may be further used to obtain the position and width of resonances by fitting them to the Breit Wigner profile [29]. Differential and Momentum transfer cross sections (MTCS) are calculated using POLYDCS program [30]. In fact the MTCS is obtained by integrating the differential cross sections (DCS) with a weight factor (1-cosθ).

## C  The high energy scattering formalism

Even with the latest computing facilities available the R–matrix code cannot be extended to scattering calculations beyond about 15 to 20 eV hence if intermediate to high energy electron scattering is to be modeled we must use the well–established SCOP formalism [31, 32]. We employ partial wave analysis to solve the Schrödinger equation with various model potentials as input. The interaction of incoming electron with the target molecule can be represented by a complex optical potential comprising of real ($V_R$) and imaginary parts ($V_I$) ,

$$V_{out}(E_i, r) = V_R(E_i, r) + iV_I(E_i, r) \qquad (3)$$

such that,

$$V_R(r, E_i) = V_{st}(r) + V_{ex}(r, E_i) + V_p(r, E_i) \qquad (4)$$

where, the real part $V_R$ comprises of static potential ($V_{st}$), exchange potential ($V_{ex}$), and Polarization potential ($V_p$). The static potential, ($V_{st}$) arises from Coulombic interactions between the static charge distribution of the target and projectile. It is calculated at the Hartree–Fock level. The exchange potential ($V_{ex}$) term accounts for electron exchange interaction between the incoming projectile and one of the target electrons. The Polarization potential ($V_p$) represents approximately short range correlations and long range Polarization effects arising from the temporary redistribution of the target charge cloud. Note that the SCOP as such does not require any fitting parameters. The most important basic input for evaluating all these potentials is the charge density of the target. We have used the atomic charge density derived from the Hartree Fock wave functions of Bunge *et al.* [33]. Any e –molecule system is more complex compared to any e -atom system but this complexity is reduced by adopting a single center approach [34, 35] so as to make a 'spherical approximation' applicable. In case of $CF_2$ we reduce the system to single centre by expanding the charge density of both carbon and fluorine atoms at the center of

mass of the system by employing the Bessel function expansion detailed in Gradshetyn and Ryzhik [36]. The spherically averaged molecular charge–density $\rho(r)$, is determined from the constituent atomic charge density using the Hartree Fock wave functions of Bunge *et al.* [33]. The molecular charge density $\rho(r)$ obtained is then renormalized to incorporate the covalent bonding [37]. In the SCOP method the spherical part of the complex optical potential is treated exactly by a partial wave analysis to yield various cross sections [38]. Here we have neglected the non-spherical terms arising from the vibrational and rotational excitations in the full expansion of the optical potential.

The atomic charge densities and static potentials ($V_{st}$) are formulated from the parameterized Hartree–Fock wave functions given by Bunge *et al.* [33]. The parameter free Hara's 'free electron gas exchange model' [39] is used to generate the exchange potential ($V_{ex}$). The Polarization potential ($V_p$) is constructed from the parameter free model of the correlation–Polarization potential given by Zhang *et al.* [40]. Here, various multipole non-adiabatic corrections are incorporated into the intermediate region which will approach the correct asymptotic form at large '$r$' smoothly. In the low energy region, the small '$r$' region is not important due to the fact that higher–order partial waves are unable to penetrate the scattering region. However in the present energy region, a large number of partial waves contribute to the scattering parameters and correct short range behavior of the potential is essential.

The imaginary part in $V_{opt}$ is called the absorption potential, and $V_{abs}$ or $V_I$ accounts for the total loss of flux scattered into the allowed electronic excitation or ionization channels. $V_{abs}$ is not a long range effect and its penetration towards the origin increases with increasing energy. This implies that at high energies the absorption potential accounts the inner-shell excitations or ionization processes that may be closed at low energies.

The well-known quasi-free model form of Staszeweska *et al.* [41, 42] is employed for the absorption part and is given by,

$$V_{abs}(r, E_i) = -\rho(r)\sqrt{\frac{T_{loc}}{2}}\left(\frac{8\pi}{10k_F^3 E_i}\right)\theta(p^2 - k_F^2 - 2\Delta)(A_1 + A_2 + A_3)$$

(5)

where the local kinetic energy of the incident electron is,

$$T_{loc} = E_i - (V_{st} + V_{ex} + V_p)$$

(6)

where $p^2 = 2E_i$, $k_F = [3\pi^2\rho(r)]^{1/3}$ is the Fermi wave vector and $A_1$, $A_2$ *and* $A_3$ are dynamic functions that depend on $\theta(x)$, $I$, $\Delta$ and $E_i$. $I$ is the ionization threshold of the target, $\theta(x)$ is the Heaviside unit step–function and $\Delta$ is an energy parameter below which $V_{abs} = 0$. Hence, $\Delta$ is the principal factor which decides the value of total inelastic cross section, since below this

value ionization  or excitation is not permissible. This is one of the main characteristics of the Staszeweska model [41, 42]. In the original Staszeweska model [41, 42] $\Delta = I$ and hence it ignores the contributions coming from discrete excitations at lower incident energies. This had been realized earlier by Garcia and Blanco [43] who elaborately discussed the need to modify $\Delta$ value. In our calculations we have treated $\Delta$ as a slowly varying function of $E_i$ around $I$. Such an approximation is meaningful since $\Delta$ fixed at $I$ would not allow molecular excitation at energies $E_i \leq I$ . If $\Delta$ is taken as being much lower than the ionization  threshold then $V_{abs,}$ becomes unexpectedly high near the peak position so in order to overcome this  we  give a reasonable minimum value of $0.8I$ to $\Delta$ [35] and express the parameter as a function of $E_i$around $I$ as follows,

$$\Delta(E_i) = 0.8I + \beta(E_i - 1) \tag{7}$$

The value of the $\beta$ parameter is obtained by requiring that $\Delta = I$ (eV) at $E_i= E_p$, the value of incident energy at which $Q_{inel}$ reaches its peak. $E_p$ can be found by calculating $Q_{inel}$ by keeping $\Delta = I$. Beyond$E_p,$ $\Delta$ is kept constant and is equal to the ionization threshold, $I$. The theoretical basis for assuming a variable $\Delta$ is discussed in more detail by Vinodkumar *et al*. [35].

The complex optical potential thus formulated is used to solve the Schrödinger equation numerically through a partial wave analysis. This calculation will produce complex phase shifts for each partial wave which carries a signature of the interactions of the incoming projectile with the target. At low impact energies only a few partial waves are significant, but as the incident energy increases, more partial waves are needed for convergence. The phase shifts $(\delta_l)$ thus obtained are employed to find the relevant cross sections, the total elastic ($Q_{el}$) and the total inelastic cross sections ($Q_{inel}$) using the scattering matrix $S_l(k) = \exp(2i\delta_l)$ [44].   Total cross sections such as the total elastic ($Q_{el}$) and the total inelastic cross sections ($Q_{inel}$) can be derived from the scattering matrix [44]. The sum of these cross sections will then give the total scattering cross section ($Q_T$).

## 3 RESULTS AND DISCUSSION

In this study we have carried out comprehensive computations of the total cross section produced by the collision of electrons with $CF_2$ in the gas phase from 0.01 eV to 2000 eV. Both of the theoretical formalisms used have their own limits over the range of impact energies. More elaborately, the *ab-initio* calculations are computationally viable only up to around 20 eV, while

the SCOP formalism can be employed successfully from threshold of the target to 2000 eV. In this work we compute the total cross section below the ionization threshold using a close coupling formalism employing the R-matrix method where total cross section is obtained as sum of total elastic and total electronic excitation cross sections while beyond ionization threshold we use the SCOP formalism and the total cross section is obtained as the sum of the total elastic and inelastic cross sections. The results we obtained are consistent and there is a smooth transition at the overlap of two formalisms (around 14 eV). Thus it is possible to provide the total cross section over a wide range of impact energies from meV to keV. We have presented our results in graphical form and numerical values are tabulated in Table III.

**TABLE III.** Total cross sections (TCS) for e - $CF_2$ scattering in ($\text{Å}^2$)

| Energy (eV) | TCS ($\text{Å}^2$) Q-mol | Energy (eV) | TCS ($\text{Å}^2$) SCOP |
|---|---|---|---|
| 0.1 | 23.64 | 12.0 | 16.65 |
| 0.3 | 21.95 | 15.0 | 15.06 |
| 0.5 | 25.95 | 20.0 | 13.80 |
| 0.7 | 59.47 | 25.0 | 13.23 |
| 0.8 | 77.79 | 30.0 | 12.93 |
| 1.0 | 34.40 | 50.0 | 12.33 |
| 1.06 | 30.01 | 60.0 | 12.04 |
| 2.0 | 18.86 | 70.0 | 11.70 |
| 3.0 | 16.59 | 80.0 | 11.29 |
| 4.0 | 15.22 | 90.0 | 10.85 |
| 5.0 | 14.46 | 100.0 | 10.43 |
| 6.0 | 13.81 | 300.0 | 5.81 |
| 7.0 | 13.22 | 500.0 | 4.19 |
| 8.0 | 12.91 | 700.0 | 3.34 |
| 9.0 | 12.91 | 1000.0 | 2.58 |
| 10.0 | 13.34 | 1500.0 | 1.89 |
| 11.0 | 14.18 | 2000.0 | 1.50 |

Figure 1 shows a comparison of the present total cross section for e -$CF_2$ scattering for 0.1 eV to 20 eV. We performed calculations using static exchange (SE) and static exchange plus Polarization (SEP) models. Our data is compared with the theoretical data of Rozum*et al.* [6]

Lee *et al.* [4] and Francis Staite *et al* [3] and experimental data of Francis staite*et al.* [3] and recommended data of Yoon *et al.* [45].
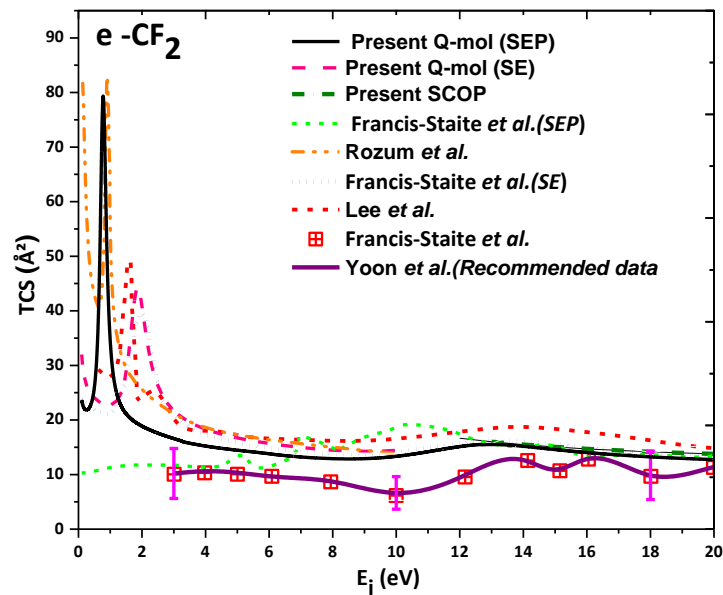


**Fig. 1. (Color online)** Total cross section for e -CF$_2$ scattering. Black solid line: Present Q-mol results (SEP); Dash line: Present Q-mol results (SE);  Dash dot line: Present SCOP results; Short Dash: Francis-Staite *et al.* (SEP) [3]; Dash Dot Dot line: Rozum*et al.* [6] (SEP); Short dash  line: Francis-Staite *et al.* (SE) [3];  Short Dash line: Lee *et al.* [5]; Open Square: Francis-Staite *et al.* [3]; Solid circle: Yoon *et al.* [45]

Rozum*et al.* [6] have also performed R-matrix calculations using SE and SEP models. We obtained a prominent peak of 79.20 Å$^2$at 0.82 eV in the SEP model and 44.20 Å$^2$ at 1.86 eV from the SE model which is a reflection of $\Pi_u$shape resonance state. This shift (0.79 eV to 1.04 eV) in the peak is attributed to the attractive nature of Polarization potential which improves the results. The theoretical results of Rozum*et al.* [6] shows peak value of 80.64 Å$^2$ at 0.89 eV for SEP model and 39.57 Å$^2$ at 1.91 eV for SE model which are in excellent agreement with our results both qualitatively as well as quantitatively. Overall there is good agreement of our results with the results of Rozum*et al.* [6] throughout their reported range. The theoretical SEP results of Francis Staite et al [3] do not show first shape resonance at low energy but their SE results show resonance at 2.02 eV with a peak of 39.98 Å$^2$ which is close to present value at 1.86 eV with a slightly higher peak of 44.20 Å$^2$. The SE results of Francis Staite *et al.*[3] are in good agreement with our results beyond 3 eV. Finally the theoretical results of Lee *et al.* [5] reported a peak at 1.65 eV with magnitude of 49.3 Å$^2$. The shape resonance peak of Lee *et al*. [5] is slightly shifted compared to all other reported SEP data. Beyond 3 eV their data are slightly

higher compared all data presented here. The low energy shape resonance structure is not visible in the available experimental as the experimental data reported by Francis Staite *el al.* [3] is from 2 eV to 20 eV and the shape resonance occurs below 2 eV. We also observed another small structure at 13.42 eV in our low energy total cross section results which is also seen at the same energy in the data of Lee *et al.* [4]. This structure is also reflected in the experimental result of Francis-Staite *et al.* [3] at 10.35 eV. This is due to $2B_2$ scattering channel. The experimental data of Francis-Staite *et al.* [3] and recommended data of Yoon *et al*. [45] are lower compared to all theoretical results. This discrepancy in ICS is due to the fact that they obtained their ICS data by integrating the DCS data which introduces an error of 45% due to extrapolation of DCS data in the range $20^o$ to $0^o$ and from $135^o$ to $180^o$. However our data show very good agreement with the experimental data of Francis Staite *et al.* [3] beyond 15 eV. There is smooth crossover of the our R matrix data with SCOP data at around 14 eV.

In Figure 2 we present a comparison of our total cross section data over a wide energy range from 0.1 eV to 2000 eV. The data over such a wide range is an amalgamation of data obtained through the two formalisms, R-matrix and SCOP. The data obtained through R-matrix and SCOP agrees and confirms a smooth transition at around 14 eV from one methodology to the other. We have not shown our SE data and SE data of Francis Staite *et al.* [3] and Rozum *et al.* [6] in Figure 2 as they are already discussed in Figure 1. Also we have already discussed the low energy data (up to 20 eV) in Figure1. hence we discuss here only intermediate to high energy data. The lone theoretical data reported from low to high energy is from Lee *et al.* [5]. The total cross section of Lee *et al.* [5] is obtained by summing their elastic cross sections and absorption cross section beyond 15 eV. The present SCOP data finds excellent agreement with data of Lee *et al.* [5] beyond 50 eV below which their data are higher compared to the present data. Theoretical data reported by Antony *et al.* [7] are much higher compared to our data at 50 eV but this discrepancy decreases with increase in energy and after 200 eV they merge with present data. The experimental data reported by Maddern *et al.* [4] are slightly lower compared to our data but within experimental uncertainty. There is a lone experimental data set reported by Francis-Staite *et al.* [3] at 50 eV beyond which no other experimental data is reported. There are only two theoretical data sets at higher energies with which to compare our data; one reported by Lee *et al.* [4] and other reported by Antony *et al.* [6]. The results of Lee *et al.* [4] are lower compared to the present results while those of Antony *et al.* [6] are higher up to 300 eV beyond which all data tend to merge. There is discrepancy between our data and measured data of Francis Staite *et al.* [3]. This is attributed to large error (~45%) which arises due to extrapolation

of DCS from $20^o$ to $0^o$ and $135^o$ to $180^o$ to obtain the integral cross section as discussed earlier. The discrepancy is more at low energy below 10 eV and above 10 eV there is better agreement with our data.
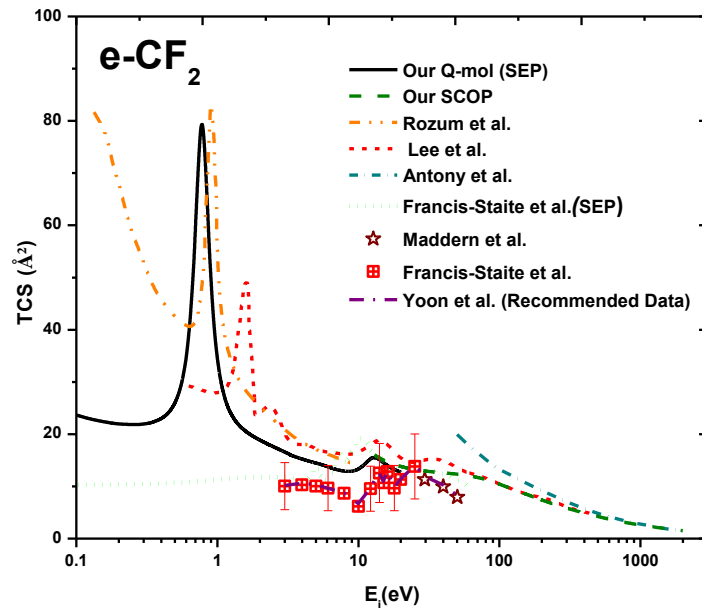


**Fig. 2.(Color online)** Total cross section for e -$CF_2$ scattering. Black solid line: OurQ-mol results (SEP);  Dash dot line: Our SCOP results;  Short Dash dot line: Antony et al. [7]; Short Dot: Francis-Staite *et al.* (SEP) [3]; Dash Dot Dot line: Rozum*et al.* [6] (SEP); Short Dash line: Lee *et al.* [5]; Open star: Maddern *et al.* [4];  Open Square: Francis-Staite *et al.* [3]; Solid circle: Yoon *et al.* [45]

Figure 3 shows the eigenphase sum for various doublet scattering states ($^2A_1$, $^2B_1$, $^2A_1$ and $^2B_2$) of the $CF_2$ system. It is important to study eigenphase sum as they indicate the position of electron scattering resonances which are important features in low energy regime. Resonances occur when the incident electron is temporarily captured by the target to form a negative ion (an anion) which subsequently decays either by auto detachment (often leaving the target vibrationally/electronically excited) or by dissociating the molecule to produce a net product anion (a process known as Dissociative Electron Attachment (DEA)). A recursive procedure for detecting and performing Breit-Wigner fits to the eigenphase diagram and is done through program RESON [13]. This program generates new energy points and marks those points where the numerically computed values of second derivative changes sign from positive to negative. Finer grids are constructed about each of these points which are used as inputs for Breit-Wigner fit [13] and the two most important parameters (position and width) related to resonances are

obtained. Table IV gives the positions and widths of resonances obtained in the our case using *R*-matrix calculations.

**TABLE IV:** Position and width of resonance states.

| Resonance state | Position (eV) | Width (eV) | Resonance state | Position (eV) | Width (eV) |
|---|---|---|---|---|---|
| | **Present** | | | **Others** | |
| $^2B_1$ | 0.81 | 0.24 | $^2B_1$ | 0.95[6] | 0.18[6] |
| $^2A_1$ | 6.14 | --- | $^2A_1$ | 5.61[6] | 2.87[6] |
| $^2B_2$ | 13.4 | --- | $^2B_2$ | 13.5[5] | -- |
| | | | $^2B_2$ | 15.0[4] | -- |

The $^2B_1$ state shows a prominent structure in the eigenphase sum which is reflected as a strong peak of 65.59 $Å^2$ in the TCS curve at 1.04 eV and it may be attributed to formation of a $^2\Pi_u$ shape resonance. We also observe resonance structure around 6.14 eV due to $^2A_1$ scattering which is also reflected in our MTCS curve (Figure 6) and this structure is also observed at 5.6 eV by Rozum *et al*. [6]. The $^2B_1$ excitation cross section also shows an increase around 13.5 eV and this is seen as structure in the TCS curve at 13.4 eV. The $^2B_2$ resonance was reported at 13.5 eV by Francis Staite *et al.* [3] and same was reported by Lee *et al.* [5] at 15 eV. No other prominent structures are seen in the eigenphase sum below 14 eV for any symmetry and the same holds true for the total cross section curve. Eigenphase sums also show the important channels to include in the calculations. It is to be noted that as more states are included in the CC expansion and retained in the outer region calculation, the eigenphase sum increases reflecting the improved modeling of Polarization interaction.
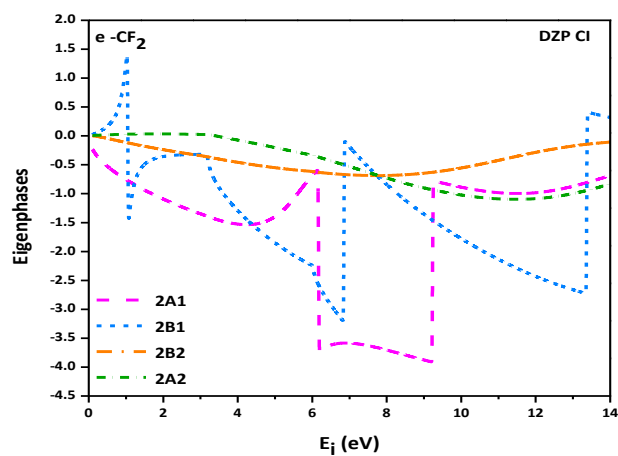


**Fig. 3.(Color online)** Eigenphase sums of *e* –CF$_2$ for a 10-state CC calculation.

Figure 4(a) presents the electronic excitation cross section for excitation of $CF_2$ from the ground state $1A_1$ to target states $3B_1$, and $1B_1$ for incident energies 2 to 10 eV. We have compared the excitation cross sections for first two states with Rozum *et al.* [6] and have found in general good qualitative agreement except for our excitation cross sections which are quantitatively slightly lower compared to that of Rozum *et al.* [6]. However the peak position and magnitude remains the same for $3B_1$ state in our as well as Rozum *et al* [6] data. From the excitation curve it is evident that first electronic excitation energy for $CF_2$ is at 3.28 eV. The highest contribution to the total excitation cross section comes from the transition $1A_1$ to $3B_1$ with a peak of ~1.00 $Å^2$ at 5.8 eV. The transitions beyond 10 eV do not contribute much to the total cross section.
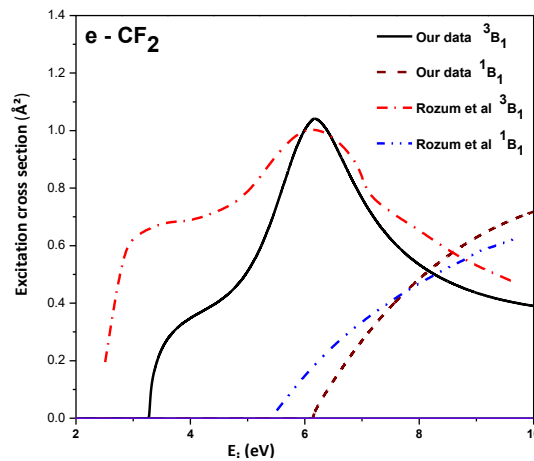


**Fig. 4. (Color online)** Electronic excitation cross sections of *e* - $CF_2$ for a 10-state CC calculation from an initial state $1A_1$.

A study of differential cross sections (DCSs) is very important as they are more accurately measured experimentally, and provide a stringent test for any scattering theory. DCSs are sensitive to effects which are averaged out in the integral cross sections. Hence, we have calculated DCSs for the elastic scattering of electron from $CF_2$ at incident energies 3, 5, 7, 10, 15, and 20 eV over the angular range from $0°$ to $180°$. Figures 5(a) –5(f) show DCSs as a function of angle theta (θ) for incident energies 3, 5, 7, 10, 15, and 20 eV, respectively. We have compared our theoretical data with the other available theoretical results of Rozum *et al.* [6], Lee *et al.* [5] and measured data reported by Francis-Staite *et al.* [3] and observe that present data are in agreement with available theories but lower compared to the experimental data of Francis-Staite *et al.* [3].and another observation is that as energy increases, the discrepancies with other theoretical and experimental data decreases and in general a good agreement is observed.
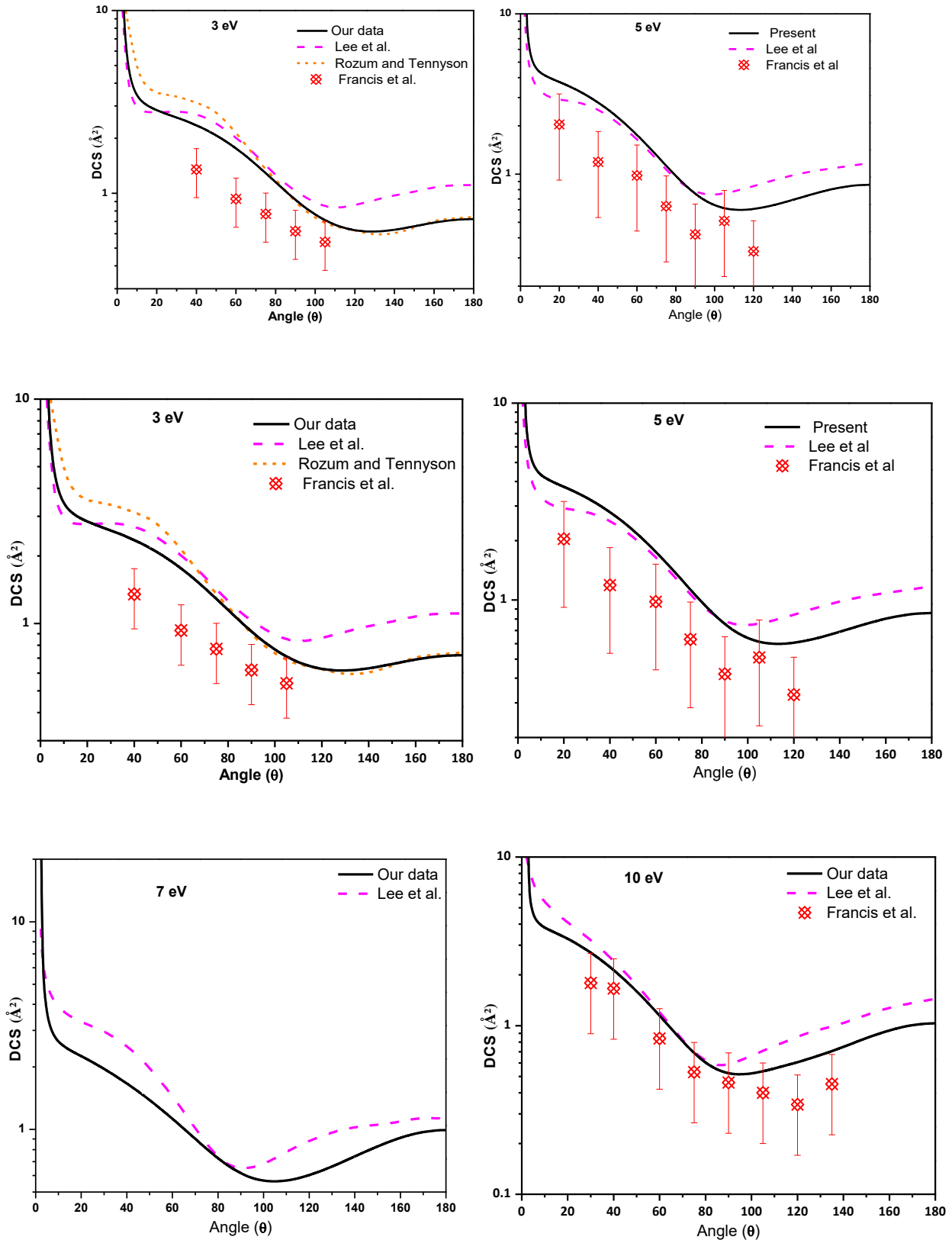
**Fig. 5.** (Color online) DCS of e – CF$_2$ scattering at (a) 3 eV, (b) 5 eV, (c) 7 eV, (d) 10 eV, (e) 15eV and (f) 20 eV.
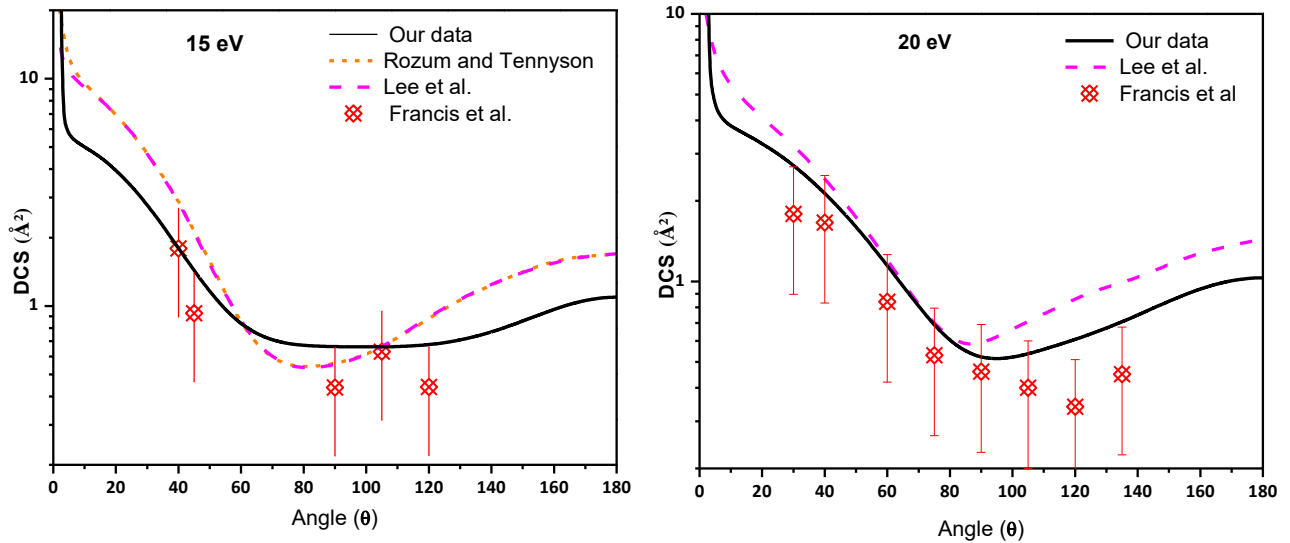
A test on the quality of our DCS is further judged by momentum transfer cross sections (MTCS) as shown in figure 6 for energies 0.01 eV to 10 eV. The MTCS indicate the importance of the backward scattering and is an important quantity that forms the input to solve the Boltzmann equation for the calculation of electron distribution function of swarm of electrons drifting through a molecular gas. In contrast to the divergent behavior of DCS in the forward direction, the MTCS does not diverge due to the multiplicative factor $(1 - \cos\theta)$. The various peaks or structures observed in MTCS correspond to various resonance processes. Figure 6 shows comparison of present MTCS with theoretical results of Lee *et al.* [5] and Rozum*et al.* [6] Our results show very good agreement with results of Rozum*et al.* [6] both quantitatively as well as qualitatively except around 6 eV.
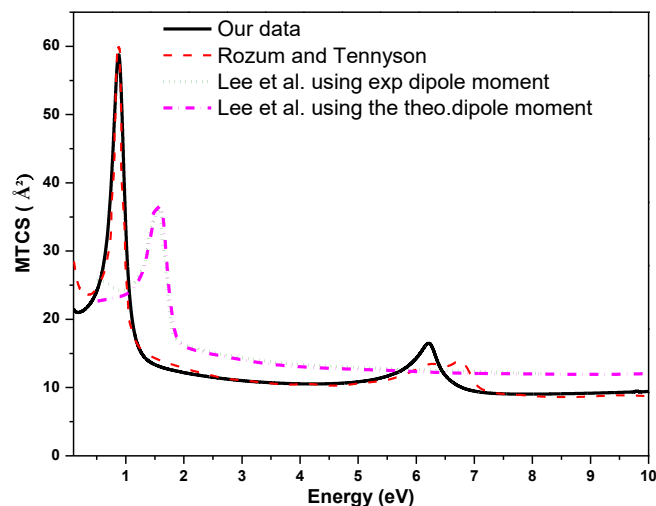


**Fig. 6.(Color online)** Total momentum transfer cross section for e -CF$_2$ scattering. Black solid line: Our results; Dash Line: Rozum*et al.* [6]; Short Dot line: Lee *et al.* [5] using exp. μ; Dash Dot Line using theoretical μ.

The first prominent peak is the reflection of $^2B_1$ scattering which has identical magnitude and position (0.88 eV and 60.01 Å$^2$) as seen in results of Rozum *et al.* [6] and this peak is also reflected in the TCS (see Figs. 1 & 2). The second peak is at 6.22 eV with magnitude of 16.52 Å$^2$ and it is at 6.77 eV with magnitude of 14.30 Å$^2$ in the results of Rozum *et al.* [6]. The results of Lee *et al.* [5] show only one structure and shows shifted first peak compared to our results and the results of Rozum *et al.* [6] at 1.62 eV with magnitude of 36.85 Å$^2$.
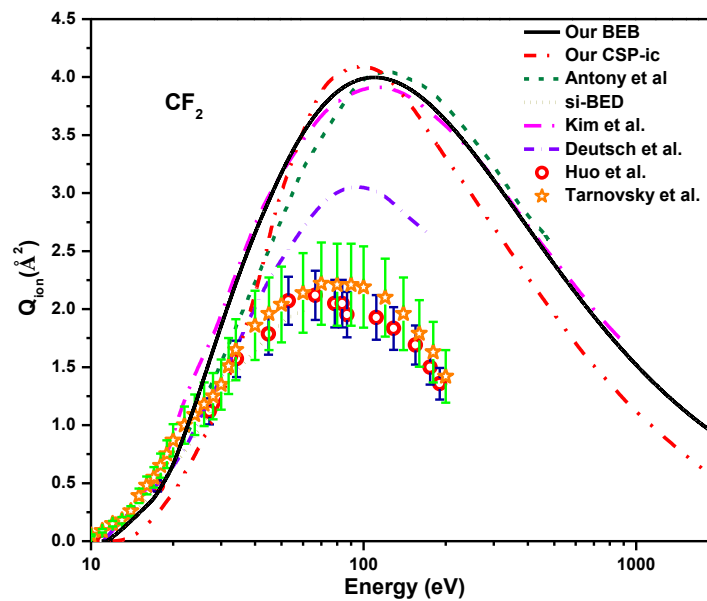


**Fig. 7.** (Color online) Total ionization  cross section for e -CF$_2$ scattering. Black solid line: Our BEB results; Dash Dot Dot line: Present CSP-ic results; Dash line: Antony *et al.* [7]; Dotted line: si-BED [3]; Dash Dot line: Kim *et al.* [11]; Short Dash Dot line: Deutsch *et al.* [10]; Open Circle: Huo *et al.* [8]; Open circle: Tarnovsky *et al.* [9]

Finally in Figure 7 we show the comparison of our total ionization cross section of e – CF$_2$ scattering with available results. The theoretical results are reported by three groups [7, 10, 11] and experimentally by two groups [9, 10]. Antony *et al.* [7] used CSP-ic method, Deutsch *et al.* [10] used DM formalism and Kim *et al.* [11] used BEB formalism to calculate total ionization cross section. We have reported total ionization cross sections using CSP-ic method and BEB formalism. The CSP-ic method is described in detail in our earlier publication [35] and hence not repeated here. We find here that experimental data are much lower compared to all theoretical results and have high uncertainty of ~25%. This is due to the fact that CF$_2$ is reactive radical and it has tendency to adhere to the wall of the chamber [3]. All theoretical results are quantitatively and qualitatively in good agreement with one another except siBED results provided by Deustch et al. [10]. However our CSP-ic data show a peak at same energy as both the experimental

results [8, 9] at ~80 eV. Experimental data provided by Huo *et al.* [8] and Tarnovsky *et al.* [9] are lower compared to all theoretical data except siBED data [10].

## 4 CONCLUSIONS

A detailed study of e -$CF_2$ system in terms of eigenphase, electronic excitations, differential cross sections, momentum transfer, ionization and total cross sections has been performed and interaction cross sections are reported in the article. We demonstrate here with the help of eigenphase diagram (Figure 3.) that a CC calculation can give much more information than a simple static-exchange calculation at low energies. We can readily obtain the position of resonances that may arise due to temporary negative ion formation from the eigenphase plots. We obtained a prominent peak of 70.20 $\mathring{A}^2$ at 0.81 eV for SEP model and 44.20 $\mathring{A}^2$ at 1.86 eV for SE model which is reflection of $\Pi_u$ shape resonance state. This resonance is also reflected in the MTCS curve (Figure 6) at 0.88 eV with magnitude of 60.01 $\mathring{A}^2$. We also observed another small structure at 13.4 eV in our low energy total cross section results which is also seen at the same energy in the data of Lee *et al.* [5]. This structure is also reflected in the experimental result of Francis–Staite *et al.* [3] at 10.35 eV. This is due to $2B_2$ scattering.

We have performed close coupling calculations employing the UK molecular R-matrix code below the ionization threshold of the target while the SCOP formalism is used beyond it [46 – 49]. We have demonstrated through Figures 1 and 2 that results obtained using these two formalisms are consistent and show a smooth transition at the overlap energy (~14 eV). This confirms the validity of our theories and hence enables us to predict the total cross sections from low energy (0.1 eV) to high energy (2000 eV).

$CF_2$ is a moderately studied target both by theoreticians and experimentalists for reasons discussed earlier. Hence we have chosen this target so that present methodology may be put to the test while still benchmarking our results by comparing with previous works. From the results presented here we conclude that our results are in good agreement with available data. Therefore, we are confident that this methodology may be employed further to calculate total cross sections over a wide range of impact energies in other molecular systems where experiments are difficult or impossible to perform. Total cross section data is important in a variety of applications from aeronomy to plasma modeling. Accordingly such a methodology maybe built into the design of online databases to provide the 'data user' with the opportunity to request their own set of cross sections for use in their own research. Such a prospect will be explored by the emerging Virtual Atomic and Molecular Data Centre (VAMDC) [50].

## REFERENCES

1. P. Chabert, H. Abada, J. -P. Booth, and M. A. Lieberman, J. Appl. Phys. **94**, 76 (2003)

2. T. Nakano and H. Sugai, J. Phys. D Appl. Phys. **26**, 1909 (1993)

3. J. R. Francis-Staite, T. M. Maddern, M. J. Brunger, S. J. Buckman, C. Winstead, V. McKoy, M. A. Bolorizadeh, and H. Cho, Phys. Rev. A **79**, 052705 (2009)

4. T. M. Maddern, L. R. Hargreaves, J. R. Francis-Staite, M. J. Brunger, S. J. Buckman, C. Winstead and V. McKoy, Phys. Rev. Lett. **100,** 063202 (2008)

5. M. -T. Lee, I. Iga, L. E. Machado, L. M. Brescansin, E. A. y Castro, and G. L. C. de Souza, Phys. Rev. A **74**, 052716 (2006)

6. I. Rozum, P. Lima˜o-Vieira, S. Eden, J. Tennyson, and N. J. Mason,J. Phys. Chem. Ref. Data, **35,** 267 (2006)

7. B. K. Antony, K. N. Joshipura,and N. J. Mason, J. Phys. B: At. Mol. Opt. Phys. **38,** 189 (2005)

8. W. M. Huo, V. Tarnovsky and K. H. Becker, Chem. Phys. Lett.**358,** 328 (2002)

9. V. Tarnovsky, P. Kurunczi, D. Rogozhnikov and K. Becker, Int. J. of Mass Spectrom. andIon Pro. **128,** 181(1993)

10. H. Deutsch, T. D. Meark, V. Tarnovsky, K. Becker, C. Cornelissen, L. Cespiva, and V. Bonacic-Koutecky, Int. J. Mass Spectrom. Ion-Process. **137**, 77, (1994)

11. Y.-K. Kim and K. K. Irikura, Proceedings of the 2$^{nd}$ International Conference on Atom Molecular Data and their Applications, edited by K. Barrington and K. L. Bell, AIP Conf. Proc. No. 543 p. 220 (AIP, New York, 2000)

12. I. Schneider, Adv. At., Mol., Opt. Phys., 1994, 33,183.

13. J. Tennyson, Phys. Rep. **491**, 29 (2010)

14. A. Jain, J. Chem. Phys. **86**, 1289 (1987)

15. L. E. Machado, R. T. Sugohara, A. S. dos Santos, M.-T. Lee, I. Iga, G. L. C. de Souza, M. G. P. Homem, S. E. Michelin, and L. M. Brescansin, Phys. Rev. A **84**, 032709 (2011)

16. J. Tennyson, D. B. Brown, J. M. Munro, I. Rozum, H. N. Varambhia, and N. Vinci, J. Phys.: Conf. Ser. **86**, 012001 (2007)

17. See http://cccbdb.nist.gov/.

18. N. Russo, E. Sicilia, and M. Toscano, J. Chem. Phys. **97**, 5031 (1992)

19. Z. -L. Cai, J. Phys. Chem., **97**, 8399 (1993)

20. B. I. Schneider and T. N. Rescigno, Phys. Rev. A 37, 3749 (1988)

21. W. H. Kirchhoff, D. R. LideJr, and F. X. Powell, J. of Mol. Spec., **47,** 491498 (1973)

22. K. Takatsuka and V. McKoy, Phys. Rev. A 30, 1734 (1984)

23. H. D. Meyer, Chem. Phys. Lett. 223, 465 (1994)

24. C. J. Noble and R. K. Nesbet, Comput. Phys. Commun. **33,** 399 (1984)

25. A. M. Arthurs and A. Dalgarno, Proc. Phys. Soc. London, Sect. A **256**, 540 (1960)

26. A. Faure, J. D. Gorfinkiel, L. A. Morgan, and J. Tennyson, Comput. Phys. Commun. **144**, 224 (2002)

27. S. I. Chu and A. Dalgarno, Phys. Rev. A **10**, 788 (1974)

28. M. Gailitis, J. Phys. B **9**, 843 (1976)

29. J. Tennyson and C. J. Nobel, Comput. Phys. Commun. **33,** 421 (1984)

30. N. Sanna and F. A. Gianturco, Comput. Phys. Commun. **114,** 142 (1998)

31. M. Vinodkumar, K. N. Joshipura, C. G. Limbachiya, and B. K. Antony, Eur. Phys. J. D **37**, 67 (2006)

32. K. N. Joshipura, M. Vinodkumar, C. G. Limbachiya, and B. K. Antony, Phys. Rev. A **69**, 022705 (2004)

33. C. F. Bunge, J. A. Barrientos, and A. V. Bunge, At. Data Nucl. Data Tables **53**, 113 (1993)

34. M. Vinodkumar, C. Limbachiya, K. Korot, and K. N. Joshipura, Eur. Phys. J. D **48**, 333 (2008)

35. M. Vinodkumar, K. Korot, and P. C. Vinodkumar, Int. J. Mass Spectrom. **305**, 26 (2011)

36. I. Gradashteyn and I. M. Ryzhik, *Tables of Integrals, Series and Products* (Academic, New York, 1980)

37. M. Vinodkumar, K. N. Joshipura, C. Limbachiya, and N. Mason, Phys. Rev. A **74**, 022721 (2006)

38. A. Jain and K. L. Baluja, Phys. Rev. A **45**, 202 (1992)

39. S. Hara, J. Phys. Soc. Jpn. **22**, 710 (1967)

40. X. Zhang, J. Sun, and Y. Liu, J. Phys. B **25**, 1893 (1992)

41. G. Staszewska, D. W. Schwenke, D. Thirumalai, and D. G. Truhlar, Phys. Rev. A **28**, 2740 (1983)

42. G. Staszewska, D. M. Schwenke, and D. G. Truhlar, J. Chem. Phys. **81**, 3078 (1984)

43. F. Blanco and G. Garcia, Phys. Rev. A **67**, 022701 (2003)

44. C. J. Joachain, *Quantum Collision Theory* (North - Holland, Amsterdam, 1983)

45. J.-S. Yoon, M.-Y. Song, H. Kato, M. Hoshino, H. Tanaka, M. J. Brunger, S. J. Buckman and H. Cho, J. Phys. Chem. Ref. Data. **39,** 033106 (2010)

46. M. Vinodkumar, A. Barot, and B. Antony, J. Chem. Phys. **136**, 184308 (2012)

47. M. Vinodkumar and M. Barot, J. Chem. Phys. **137**, 074311 (2012)

48. M. Vinodkumar, C. Limbachiya, A. Barot, and N. Mason, Phys. Rev. A **87,** 012702 (2013)

49. A. Barot, D. Gupta, M. Vinodkumar, and Bobby Antony, Phys. Rev. A **87,** 062701 (2013)

50. M. L. Dubernet, V. Boudon, J. L. Culhane, M. S. Dimitrijevic, A. Z. Fazliev, C. Joblin, F. Kupka, G. Leto, P. Le Sidaner, P. A. Loboda, H. E.Mason, N. J. Mason, C. Mendoza, G. Mulas, T. J. Millar, L. A. Nũnez, V. I. Perevalov, N. Piskunov, Y. Ralchenko, G. Rixon*et al.*, J. Quant. Spectrosc. Radiat. Transfer **111**, 2151 (2010)

# Frequency and temperature dependent dielectric study of MoSe$_2$ crystals

Dipak Sahay[#], Ripal Parmar[1], B.A.Thakar[2], R.K.Shah[3], R.J.Pathak*

[#]Government Engineering College, Modasa, Gujarat

[1]Department of Physics, Hemchandracharya North Gujarat University, Patan, Gujarat

[2]B.S.Patel Polytechnic,Ganpat University,Kherva,Gujarat

[3]Art,Science and R.A.Patel Commerce College, Bhadran, Gujarat

*R.R.Mehta College of Science, Palanpur

[#]Email: dipaksahay86@gmail.com

**Abstract**: Transition-metal dichalcogenide (TMDC) crystals have emerged as a new class of semiconductors that display distinctive properties. An interesting group of compounds which has received Increasing attention from the fundamental as well as the industrial point of view in recent years. Studying the dielectric constant as a function of frequency and temperature, the various polarization mechanisms in solids can be understood. The real part of dielectric constant $\varepsilon'$, imaginary part of dielectric constant $\varepsilon''$, the dissipation factor tan $\delta$ and the alternating current conductivity $\sigma_{ac}$ were measured in an applied ac electric field of frequencies extending from 100 Hz to 1MHz with temperature variation of 303 k to 525 k. Based on the dependencies of these dielectric parameters on both the frequency and temperature, the dielectric properties of the crystals under investigation were elucidated and analyzed.

**Keywords**: Transition-metal dichalcogenide (TMDC)

## 1. Introduction:

The study of dielectric properties of solids often gives good insight into the electric field distribution within the solids. The various polarization mechanisms in solids can be understood by studying the dielectric constant as a function of frequency and temperature. A careful study of the MoSe$_2$ suggests to study the variation of dielectric constant and loss factor of crystalline MoSe$_2$ crystals with respect to frequency and temperature.

The present chapter embodies an in-depth analysis of the variation of dielectric parameters of MoSe$_2$ crystals in the frequency range 100 Hz to 1 MHz using LCR meter model Agilent 4284A and temperature range 303K to 523K.

## 2. Experimental set up:

## 2.1 High temperature LCR measurement setup :

The grown crystals or pallets were employed. The geometrical dimension of all the samples were measured using a traveling microscope and the thickness has been measured using micrometer screw. The dielectric measurements were carried out using the standard two electrode method. The specimen was mounted in between two flat stainless steel parallel electrodes of a specially designed sample holder. Both the upper and lower base of the holder can be screwed in for proper contact of the sample with the electrode. The sample holder was enclosed in a specially built resistance heating furnace which is capable to provide temperature upto 625K. The whole measurement setup is shown in Figure 1. To measure all dielectric parameters Automation and Controlling software "LABVIEW" is used. The parameters like the thickness and area of the sample, starting and ending temperature and frequency as well as desired steps to increase temperature and frequency has been set in software. These input data are essential in order to measure dielectric parameters at desired temperature and frequencies. The digital temperature controller DT84848 is used to monitor the preferred temperature of the specimen. When preferred temperature is achieved HP4284A LCR meter will scan all the frequencies and resultant data is feeded in the storage device.
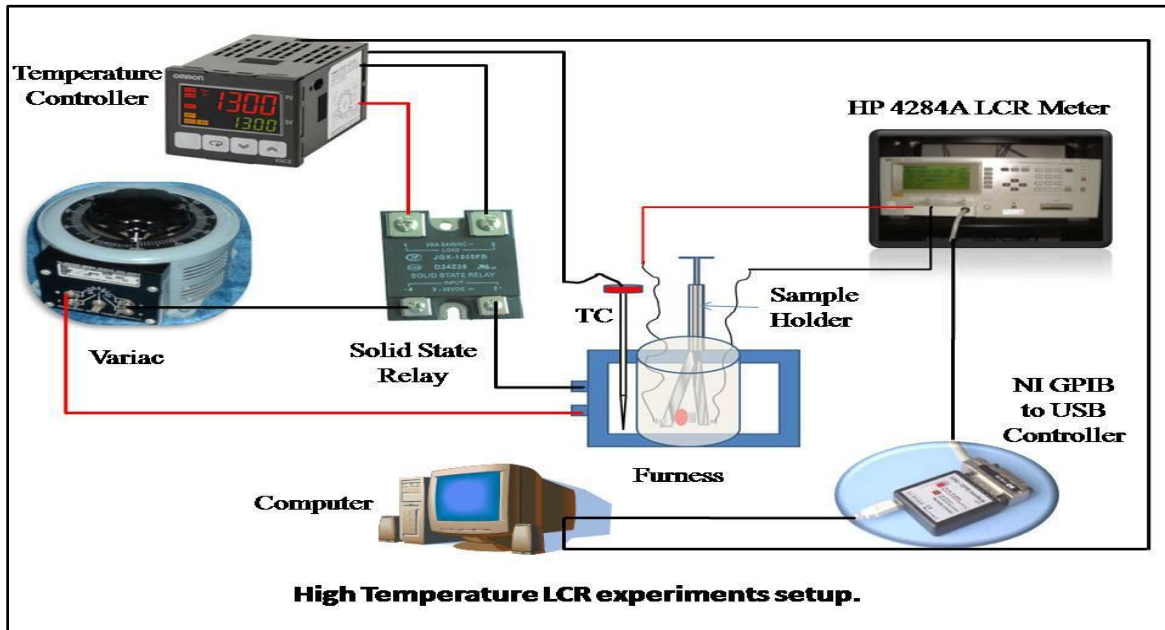
**Figure 1: High temperature LCR experiment set up.**

## 2.2 Experimental Details

The grown crystals of MoSe$_2$ by Direct Vapor Transport (DVT) technique were mounted in the sample holder. The capacitance and the dissipation factor were measured in the frequency range 100 Hz to 1 MHz with different temperature from room temperature to 523K, in the step of 50K temperature using 4284A LCR meter. From capacitance and dissipation factor all the other parameter can be calculated.

The dielectric constant "ε" of the sample is calculated using the formula

$$\varepsilon = \frac{C}{C_0}$$

where C is measured capacitance and C$_0$ is calculated by the given equation.

$$C_0 = \frac{\varepsilon_0 A}{t}$$

where ε$_0$ is the permittivity of free space (8.854 X 10$^{-12}$ fm$^{-1}$), "A" and "t" are the area and thickness of the samples respectively.

The dielectric loss tangent was computed as

$$\tan \delta = f\, D$$

where "D" is the dissipation factor and "$f$" is the frequency in kHz.

The resistivity has been determined using the formula:

$$\rho_{ac} = \frac{1}{\sigma_{ac}} = \frac{1}{\omega \varepsilon_0 \varepsilon''} = \frac{A}{2\pi f C t \tan \delta}$$

where ω = 2πf, $\varepsilon_0$ is free space permittivity and ε′′ = (ε′tanδ) is the dielectric loss factor, $f$ is the applied frequency, C and tanδ are the measure capacitance and dielectric loss.

### 2.3 Results and discussions

The variation of capacitance (c), dielectric constant (ε'), loss tangent (tanδ), a.c. resistivity ($\rho_{ac}$), a. c. conductivity($\sigma_{ac}$) and imaginary part(ε") of permittivity of the as grown $MoSe_2$ crystals have been shown on Figure 2 (a, b, c, d, e, f) with different frequency and from 303K to 523K temperature in the step of 50K temperature.
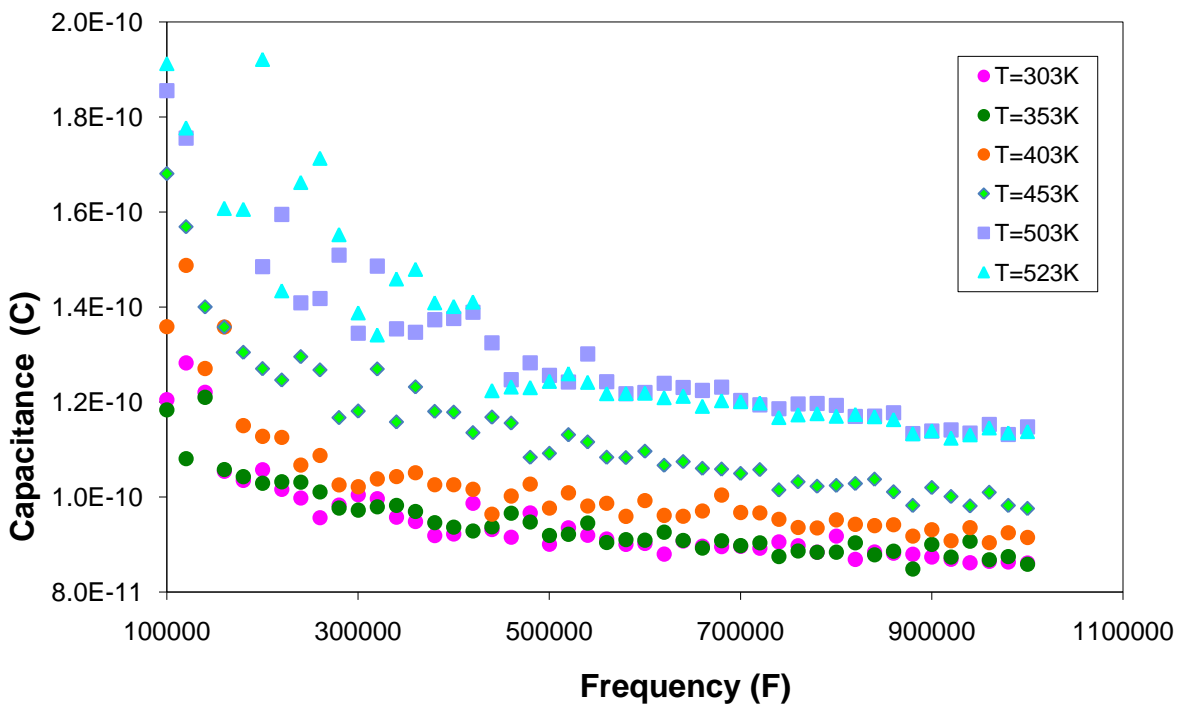


**Figure 2 (a): Variation of Capacitance with Frequency and Temperature for MoSe$_2$ crystals.**
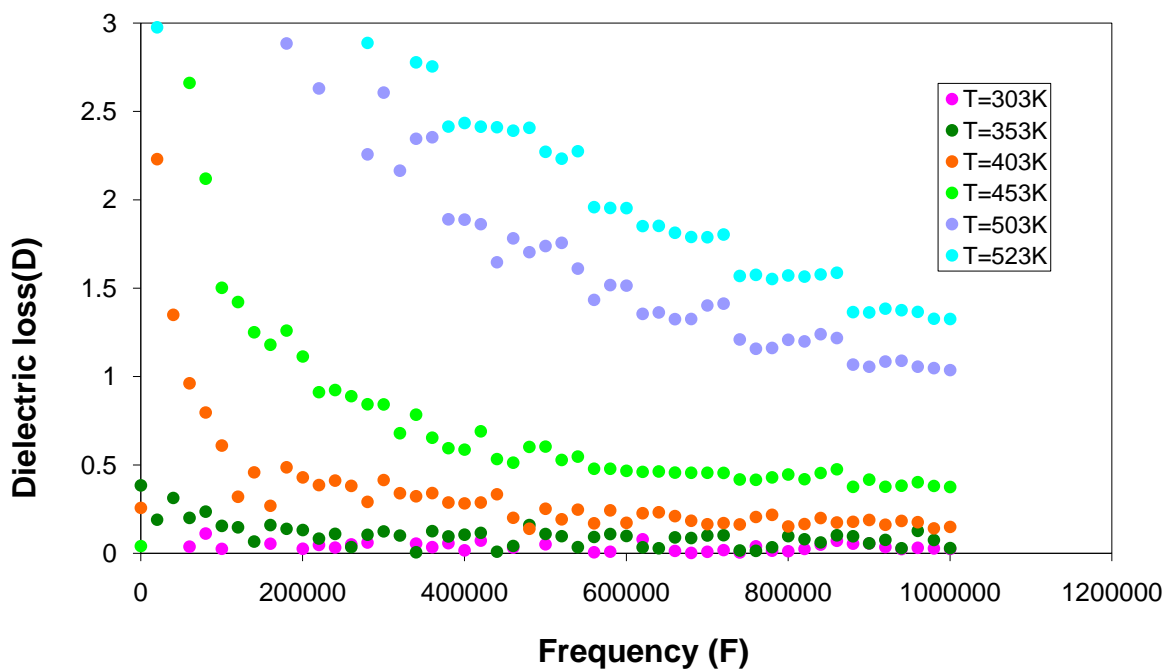
**Figure 2 (b): Variation of Dielectric loss with Frequency and Temperature for MoSe$_2$ crystals.**
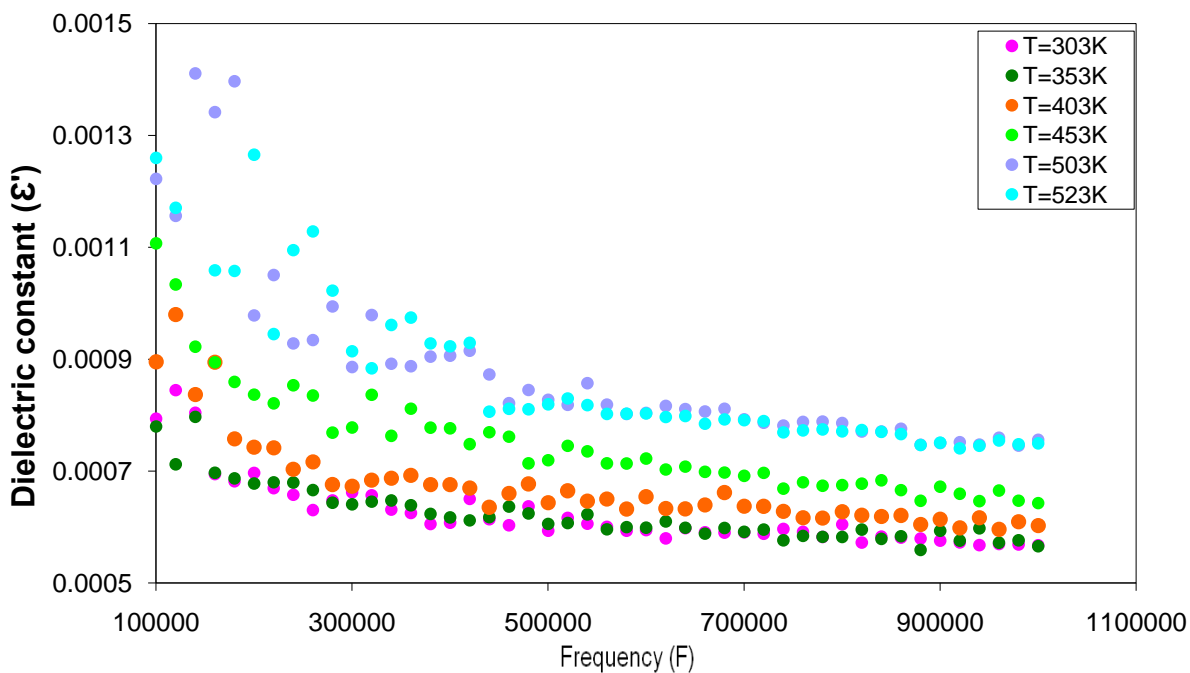


**Figure 2 (c): Variation of Dielectric Constant with Frequency and Temperature for MoSe$_2$ crystals.**
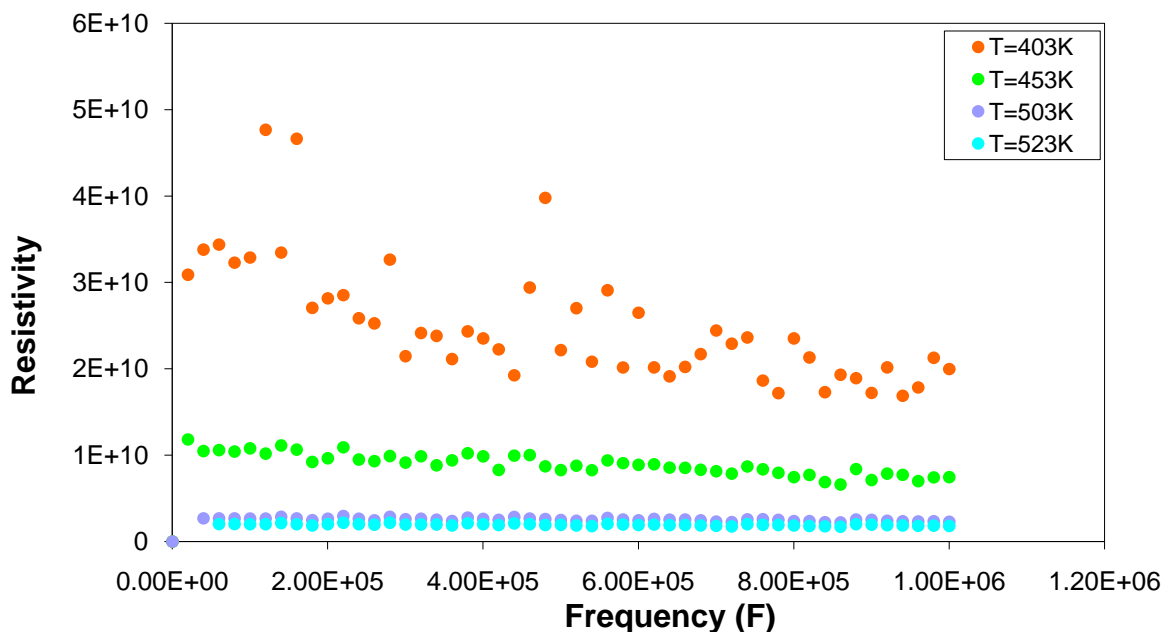
**Figure 2 (d): Variation of resistivity with Frequency and Temperature for MoSe$_2$ crystals.**
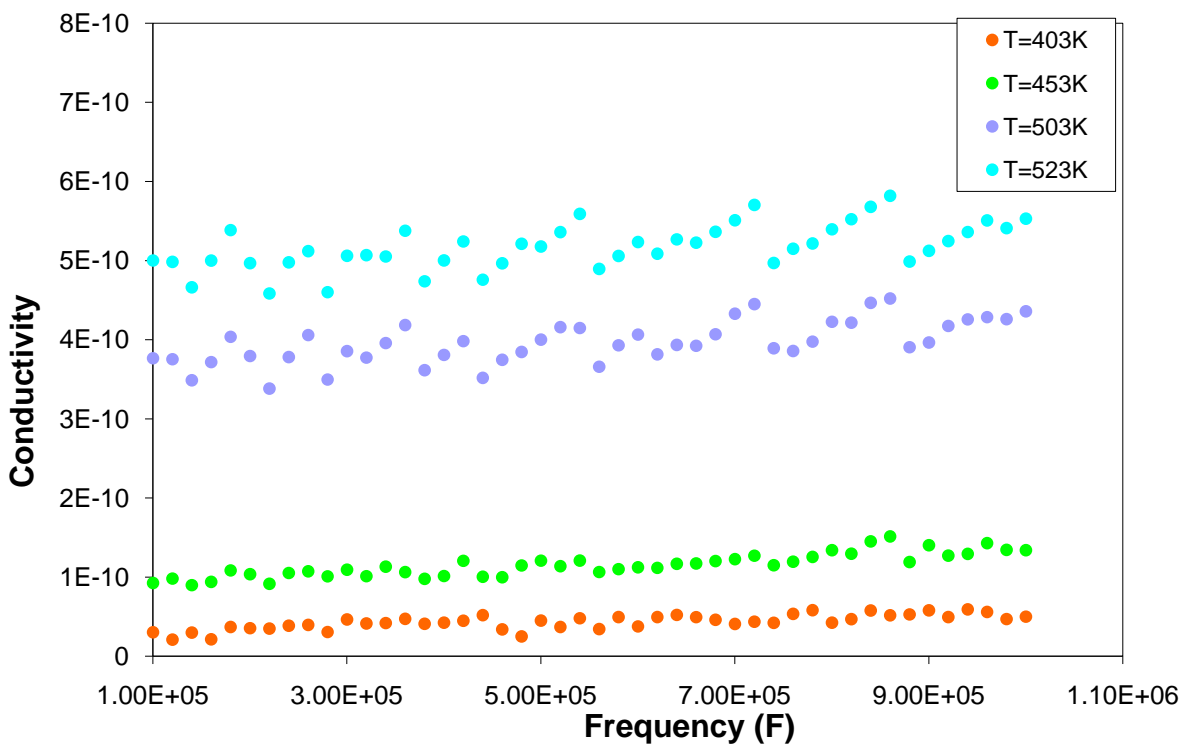


**Figure 2 (e):Variation of Conductivity with Frequency and Temperature for MoSe$_2$ crystals.**
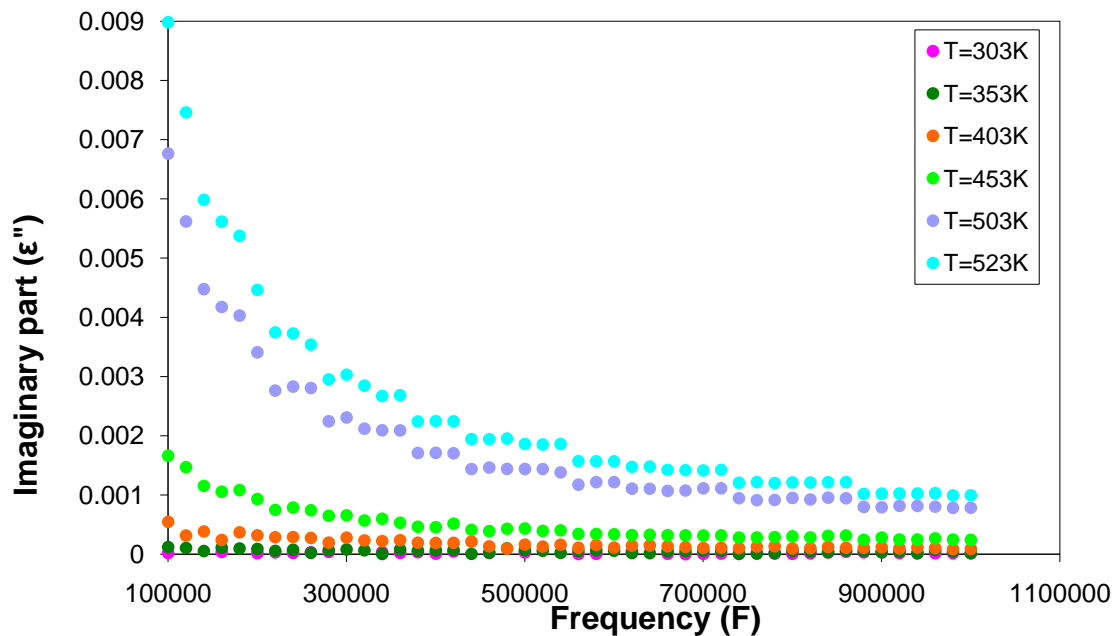
**Figure 2 (f): Variation of Imaginary part (Ɛ") with Frequency and Temperature for MoSe₂ crystals.**

For MoSe$_2$ crystals, One can see that dielectric behavior is frequency dependent. The capacitance is increases with increasing temperature and decrease with increasing frequency. Because at low temperature the mobility of ions is very low and so is the conductivity, resulting a lower value of capacitance. With temperature, the mobility of charge carriers increases, resulting the increase in space charge polarization and capacitance both. From Figure 2(c) In plot the dielectric constant ($\varepsilon'$) is observed to be higher at lower frequency and it monotonously decreases with increasing frequency up to 1MHz.

The dielectric constant of solids is known to consist of contribution from electronic, ionic, dipolar and space charge polarization exhibits itself potentially at lower frequency. This polarization is known to arise from defects or impurity present, grain boundaries etc. [1, 2] and also due to creation and distributions of either within the bulk or at surface of the crystals. Hence the higher values of the dielectric constant at lower frequency in the present investigation may be because of a large amount of space charge polarization [3-5]. Less frequency dependent value of dielectric constant ($\varepsilon'$) is taken as static dielectric constant. This indicates the probable presence of ionic and electrical polarization, since the concentration of crystal defects controlling the space charge polarization negligible. The dispersion of $\varepsilon'$ with frequency can be attributed to the Maxwell – Wagner type interfacial polarization i.e. the fact that in-homogeneities give rise to a frequency

dependence of conductivity because charge carriers accumulate at the boundaries of less conducting regions, thereby creating interfacial polarization [10-12].

The temperature is also found to exhibit an interesting influence on the dielectric properties. The value of dielectric constant ($\varepsilon$') increases with temperature for all samples. From Figure 2 (c), one can notice that at low temperature the variation in dielectric constant is much less frequency dependent, while at higher temperature the increase in dielectric constant is stronger and much more frequency dependent. This is due to lattice expansion, polarizability of the constituent ions due to increase in temperature and available volume together with the increase of atomic polarizability [6]. The faster increase with temperature is contributed by the thermally generated charge carriers.

In the most of the semiconducting compounds the number of charge carriers increases with temperature while the mobility decreases with rise in temperature. These changes are probably impeded by trapping a space charge there by building up polarization which results in macroscopic field distortion [7]. This leads to a large increase in $\varepsilon$'. And also the lattice defect concentration can rise with temperature making the space charge polarization dominant and hence the $\varepsilon$' increases with temperature. The changes in $\varepsilon$' with temperature are of similar nature at all frequency[10-12].

Figure 2(b) shows the variation in dielectric loss tan$\delta$, it decreases with increasing frequency and it is also increases consistently with temperature for all the samples. For many materials it has been observed that the dielectric loss decreases as frequency increases [8, 9]. The response of the normal materials to applied fields depends on the frequency of the applied fields. In fact, polarization of material does not respond instantaneously to an applied filed so the permittivity is often treated as a complex function of frequency. The change in complex dielectric constant with frequency is shown in Figure 2 (f). This indicates that as the frequency increases the value of imaginary part of the permittivity decreases. But it increases with temperature for MoSe$_2$ crystals. The observed decrease in $\varepsilon$'' values with frequency and increase in $\varepsilon$'' with temperature, which are the common features of all the compositions and it can be on explained on similar arguments as for $\varepsilon$' [10-12].

The conductivity of the materials is increases with temperature and frequency both while at lower frequency it is much more independent of frequency. The resistivity decreases with frequency and temperature both with can be seen from Figure 2 (d). So at higher temperature MoSe$_2$ all single crystals become more conducting so its resistivity decreases with temperature. At lower frequency the increase in conductivity is more rapid and at higher frequency the conductivity increases very slowly [10-12].

**References:**

[1] J. C. Maxwell., "Electricity and Magnetism" (New York: Oxford Uni. Press), 1 (1973) 828.

[2] K. W. Wagner., Am. Phys., 40 (1973) 817.

[3] K. V. Rao and A. Smakula., J. Appl. Phys., 37 (1966) 319.

[4] Y. R. Reddy and L. Sirdeshmukh., Solid State Comm., 40 (1981) 353.

[5] S. S. Sastry, G. Satynandam, A. Subrahmanyan and V. R. K.Murthy., Phys. Stat. Solidi (a),105 (1988) K71.

[6] C. P. Smyth., "Dielectric Behaviour and Structure", John-Wiley & Sons, New York, (1953) 132.

[7] A. P. Von Hipple.,"Dielectric behaviour and Structure", John Wiley & Sons, New York, (1954) 47.

[8] B. B. Parekh and M. J. Joshi., Cryst. Res. & Tech., 42 (2007) 127.

[9] B. B. Parekh, P. M. Vyas, Sonal R. Vasant, M. J. Joshi., Bull. Mater. Sci., 31(2008) 143-147.

[10] Maga D, Igor P and Sergei M 2000 J. Mater. Chem. 10 941

[11] Jona A, Kundu T K, Pradhan S K and Chakrvorty D 2005 J. Appl. Phys. 97 44311

[12] Ismailzade I H and Ismailov R M 1980 Phys. Stat. Sol. (a) 59 K 191

[13] Smolenski G A and Isupov V A 1954 Dokl. Akad. Nauk. SSSR 9 653

[14] Sandip R Unadkat, Thesis, May 2012.

# Exact Solution of Schrodinger Equation with Harmonic plus Inverse Square plus  non Central Potential Via Nikiforov-Uvarov Method

Rajendrasinh H Parmar

Sir P T Science College, Modasa, Gujarat, India

09102003dev@gmail.com

**Abstract**

Here we presented the solution of Schrodinger equation with harmonic plus inverse square plus new non central potential.  We used  Nikiforov-Uvarov Method to obtain energy eigenvalues and eigenfunctions for this potential. Radial eigenfunctions are expressed  in terms of Laguerre polynomials and angular part of the eigenfunctons are expressed  terms of Jacobi polynomials. Solution of these type potentials having important role in physical science and quantum chemistry.

**Keyword** : Schrodinger equation ;non central potential; inverse square potential; eigenfunctons; eigenvalues

## 1   Introduction

It is well known that  Schrodinger equation (SE) is second order differential equation, no of methods are developed to solve the relativistic and non  relativistic  SE. Solution of SE for a given system   gives the wavefunction and eigenvalues, from the  wavefunction, we can understand most of  all the properties and behavior  of the quantum-physical system. However form of  wavefunction depends on co-ordinate system and type of potential. Transforming SE into known ordinary  differential equation (ODE) whose solutions are available in terms of special functions like associated Laguerre polynomials, hypergeometric functions etc. is one of the  old methods. Second method is factorization techniques like supersymmetric (SUSY) method[1], the  asymptotic iteration method(AIM) [2-3], the  exact quantization rule(EQR) method [4]method, the Lie algebraic method [5] , the  Nikiforov-Uvarov (NU) method [6] etc for exact solution of  SE. Only few potentials are there which the SE can be solved exactly for all n and l values. Mainly two types potentials have been used to solve SE one is central potentials and non  central potentials. No off researcher are working on analytical  exact and approximate solution of Dirac equation of non central potentials. Central potentials (depends only on radial part ) have important role in the molecular chemistry , quantum chemistry and atomic  physics to describe the properties qualitatively[7] where as   non central potentials depends on radial as well as angular part of the system. Description of dynamical properties of the  system depends on non central potentials,  so we have to take into account non central potentials. No of papers have been

published by different researchers for non central potentials like Makarov potential[8], , modified-Kratzer plus ring-shaped potential[9], double ring-shaped Kratzer potential[10], modified non central potential[11], ring shaped non-spherical oscillator potential[12], ring shaped pseudo harmonic oscillatory potential[13], Killingbeck radial potential plus central potential[14], Hartmann ring shaped potential, Mie-type potential, pseudo harmonic oscillatory plus ring shaped potentia. The solutions of the Schrodinger equation with non-central potentials are important role in quantum chemistry [[15,16,17]

No of research have been studies for the non central potentials, the eigenvalues and eigenfunctionsare obtained via seperation of variables in spherical or other coordinate systems.

The concept of the Harmonic oscillator gives us a very good first approximation for understanding the spectroscopy and the structure of diatomic molecules in their ground electronic states. Recently, Berkdemir [18] proposed a novel angle-dependent (NAD) potential and obtained the exact solutions of the Schrodinger equation for the Coulomb and harmonic oscillator potentials with NAD potential. Here we presented harmonic plus inverse square plus non central potential (HINP) and its solve using Nikiforov-Uvarov (NU) method. Using NU method, we obtained eigenvalues and eigenfunctions of this type potential

In section two, we presented NU methods, in third section, we used the separation of variable method and solve the Schrodinger equation for radial part, in forth part we solve the Schrodinger equation for angular part. Concluded our work in fifth and last section.
.
## 2. Nikiforov-Uvarov Method
.
 The NU (Niki-forov-Uvarov) method is very good method to obtaining exact answers of certain states , of energy eigenvalues and the related functions based on Orthogonal polynomials. NU method is based on reducing a SE into hypergeometric type equation.

Using proper variable $s = s(r)$ to transform second orderdifferential equation into particular form in which can be solved using NikiforovUvarov Method is

$$\psi_n''(s) + \frac{\tilde{\tau}(s)}{\sigma(s)}\psi_n'(s) + \frac{\tilde{\sigma}(s)}{\sigma^2(s)}\psi_n(s) = 0 \tag{1}$$

Where $\tilde{\tau}(s)$ is first degree polynomial, $\tilde{\sigma}(s), \sigma(s)$ are second degree polynomial mostly and $\psi_n(s)$ hypergeometric type function.

consider $\psi_n(s)$ as,

$$\psi_n(s) = a_n(s)b_n(s) \tag{2}$$

Using equation (2) in equation (1),

$$\sigma(s)\frac{d^2 b_n(s)}{ds^2} + \tilde{\tau}(s)\frac{db_n(s)}{ds} + \Lambda b_n(s) = 0 \tag{3}$$

Wave function $a_n(s)$ is defined as a logarithm derivative,

$$\frac{1}{a(s)}\frac{da(s)}{ds} = \frac{\pi(s)}{\sigma(s)} \tag{3a}$$

Parameter $\Lambda$ and function $\pi(s)$ are defined as follows

$$\pi(s) = \frac{\frac{d\sigma}{ds}-\tilde{\tau}(s)}{2} \pm \sqrt{\left(\frac{\frac{d\sigma}{ds}-\tilde{\tau}(s)}{2}\right)^2 - \tilde{\sigma}(s) + K\sigma} \tag{4}$$

$$\Lambda = K + \frac{d\pi}{ds} \tag{5}$$

To find the value of K in (5),the value under the square root of (4) must be the square root of polynomial which is mostly first degree polynomial and this is possible when its determiner is zero i.e $b^2 - 4ac = 0$. There fore a new eigenvalue of (3) becomes,

$$\Lambda = \Lambda_n = -n\frac{d\tau}{ds} - \frac{n(n-1)}{2}\frac{d^2\sigma}{ds^2} \text{ , n=0,1,2,3,……} \tag{6}$$

where $\tau = \tilde{\tau}(s) + \pi(s)$ (7)

From (5) and (6), we obtain the new energy eigenvalue. $\frac{d\sigma}{ds}$ must be negative to generate igenvalues and corresponding eigenfunction. The solution of $b_n(s)$ of (3) is connected to Rodrigues relation which is given as,

$$b_n(s) = \frac{B_n}{\rho(s)}\frac{d^n}{ds^n}(\sigma^n(s)\rho(s)) \tag{8}$$

In above equation $B_n$ is normalization constant and $\rho(s)$ is weight function which satisfy the below condition

$$\frac{d(\sigma\rho)}{ds} = \tau(s)\rho(s) ,$$
$$\frac{dw(s)}{ds} = w(s)\frac{\tau(s)}{\sigma(s)} \tag{9}$$

Here $w(s) = \sigma(s)\rho(s)$ (10)

## 3. Schrodinger equation with harmonic plus inverse square plus new non central potential

$$V(r,\theta) = \frac{\hbar^2}{2\mu}\left\{Ar^2 + \frac{B}{r^2} + \frac{1}{r^2}(\alpha \cot^2\theta + \beta \operatorname{cosec}^2\theta)\right\} \tag{10a}$$

Where $V(r) = \frac{\hbar^2}{2\mu}\left(Ar^2 + \frac{B}{r^2}\right)$ (10b)

The schrodinger equation in spherical coordinate with non central potential as,

$$\nabla^2 \Psi(r, \theta\varphi) + \left(\frac{2\mu}{\hbar^2} E - V(r, \theta)\right) \Psi(r, \theta, \varphi) = 0 \qquad (11)$$

$$\frac{1}{r^2}\left(\frac{\partial}{\partial r}\left(\frac{r^2 \partial}{\partial r}\right) + \frac{1}{sin\theta}\frac{\partial}{\partial \theta}\left(sin\theta\frac{\partial}{\partial \theta}\right) + \frac{1}{sin^2\theta}\frac{\partial^2}{\partial \varphi^2}\right) \Psi(r, \theta\varphi) + \left(\frac{2\mu}{\hbar^2} E - V(r, \theta)\right) \Psi(r, \theta, \varphi) = 0 \quad (12)$$

Where $\alpha, \beta, A \; and \; B$ are constant, $\mu$ is mass of particle. Using equation (10) in equation (12) and separation of variable method with taking

$$\Psi(r, \theta, \varphi) = \frac{U(r)}{r} G(\theta)\Phi(\varphi) \qquad (13)$$

$$\frac{d^2 U(r)}{dr^2} + \left(\xi - Ar^2 - \frac{B}{r^2} - \frac{\lambda}{r^2}\right) U(r) = 0 \qquad (14)$$

$$\frac{d^2 G(\theta)}{d\theta^2} + cot\theta \frac{dG(\theta)}{d\theta} + \left(\lambda - \frac{m^2}{sin^2\theta} - (\alpha \, cot^2\theta + \beta \, cosec^2\theta)\right) G(\theta) = 0 \qquad (15)$$

$$\frac{d^2\Phi(\varphi)}{d\varphi^2} + m^2\Phi(\varphi) = 0 \qquad (16)$$

Solution of equation (16) is,

$$\Phi_m(\varphi) = \frac{1}{\sqrt{2}} e^{\pm im\varphi} \qquad\qquad , m = 0, \pm 1, \pm 2, \pm 3, \dots \dots .. \qquad (17)$$

Where $\xi = \frac{2\mu E}{\hbar^2}$ , Here $\lambda = l(l+1)$ and $m$ are real and dimensionless separation parameters.

## 4. Solution of radial part of schrodnger equation

### 4.1 Energy eigenvalues

Taking $s(r) = r^2$ and $B + \lambda = \lambda'$ in the equation (14)

$$\frac{d^2 U(s)}{ds^2} + \frac{1}{2s}\frac{dU(s)}{ds} - \frac{(As^2 - \xi s + \lambda')}{4s^2} U(s) = 0 \qquad (18)$$

Comparing equation (18) with equarion (1),

$$\tilde{\tau}(s) = 1, \quad \sigma(s) = 2s \quad and \quad \tilde{\sigma}(s) = -(As^2 - \xi s + \lambda') \qquad (19)$$

Using equation (52) in equation (4),

$$\pi(s) = \frac{1}{2} \pm \sqrt{\frac{1}{4} + As^2 + (2K - \xi)s + \lambda'} \qquad (20)$$

To solve quadric equation (20) for K , taking this quadric equation $b^2 - 4ac = 0$,

The possible values of $K_{\pm}$ as,

$$K_{\pm} = \frac{\xi}{2} \pm \frac{1}{2}\sqrt{A(4\lambda' + 1)} \tag{21}$$

$$\pi(s) = \frac{1}{2} \pm \sqrt{A} \begin{cases} \left(s + \sqrt{\frac{4\lambda'+1}{4A}}\right), & For\ K = \frac{\xi}{2} + \frac{1}{2}\sqrt{A(4\lambda'+1)} \\ \left(s - \sqrt{\frac{4\lambda'+1}{4A}}\right) & For\ K = \frac{\xi}{2} - \frac{1}{2}\sqrt{A(4\lambda'+1)} \end{cases} \tag{22}$$

According to NU method, derivative of $\tau(s)$ must be negative. Here acceptable solution of $\pi(s)$ is,

$$\pi(s) = \frac{1}{2} - \sqrt{A}\left\{\left(s - \sqrt{\frac{4\lambda'+1}{4A}}\right)\right\} \text{ for } K = \frac{\xi}{2} - \frac{1}{2}\sqrt{A(4\lambda'+1)} \tag{23}$$

Putting values of equation (19) and equation (23) in equation (7),

$$\tau(s) = 2\left[1 - \sqrt{A}\left(s - \sqrt{\frac{4\lambda'+1}{4A}}\right)\right] \tag{24}$$

from equation (5) and (6)

$$\Lambda = \frac{\xi}{2} - \sqrt{A}\left(1 + \frac{1}{2}\sqrt{4\lambda'+1}\right) \tag{25}$$

$$\Lambda_n = 2n\sqrt{A} \tag{26}$$

There fore eigen spectra of potential given by equation (10a) is

$$\xi = 2\sqrt{A}\left(2n + 1 + \sqrt{\lambda' + \frac{1}{4}}\right) \tag{27}$$

$$E_n = \frac{\hbar^2}{\mu}\sqrt{A}\left(2n + 1 + \sqrt{(B+\lambda) + \frac{1}{4}}\right) \tag{27a}$$

Equation (27a) is eigenvalue equation of radial part of SE.

## 4.2 Wavefunction of radial part of SE

Using equation (9) we can obtained [19,20,21]

$$\rho(s) = \frac{1}{2}s^{\sqrt{\lambda'+\frac{1}{4}}}e^{-\sqrt{A}s} \tag{28}$$

And

$$a_n(s) = s^{\frac{1}{4}\left(1+\sqrt{4\lambda'+1}\right)} e^{-\sqrt{A}s} \tag{29}$$

So equation (8),

$$b_n(s) = B_n \, 2^n s^{\sqrt{\lambda'+\frac{1}{4}}} e^{-\sqrt{A}s} \frac{d^n}{ds^n}\left(s^{n+\frac{1}{2}\left(\sqrt{4\lambda'+1}\right)} e^{-\sqrt{A}s}\right) \tag{30}$$

Now redial wave functioin can be obtained as,

$$U_n(s) = N_n \, 2^n s^{\frac{1}{4}\left(1+\sqrt{4\lambda'+1}\right)} e^{\frac{\sqrt{A}s}{2}}\left\{s^{-\frac{1}{2}\left(\sqrt{4\lambda'+1}\right)} e^{-\sqrt{A}s} \frac{d^n}{ds^n}\left(s^{n+\frac{1}{2}\left(\sqrt{4\lambda'+1}\right)} e^{-\sqrt{A}s}\right)\right\} \tag{31}$$

$N_n$ is normalizatiionconstant.

In terms of Laguerre polynomial equation (31) as,

$$U_n(s) = N_n \, 2^n s^{\frac{1}{4}\left(1+\sqrt{4\lambda'+1}\right)} e^{\frac{\sqrt{A}s}{2}} L_n^{-\frac{1}{2}\left(\sqrt{4\lambda'+1}\right)}(\sqrt{A}s) \tag{32}$$

For $s = r^2$ equatioin (32) is

$$U_n(s) = N_n \, 2^n r^{\frac{1}{2}\left(1+\sqrt{4\lambda'+1}\right)} e^{\frac{\sqrt{A}r^2}{2}} L_n^{-\frac{1}{2}\left(\sqrt{4\lambda'+1}\right)}(\sqrt{A}r^2) \tag{33}$$

Equation (33) is wavefunction of radial part of SE.

## 5.  Solution of angle dependent part

### 5.1 Eigenvalues of angular part of SE

Using coordinate transformation $s = cos\theta$ in equation (15),

$$\frac{d^2G(s)}{ds^2} - \frac{2s}{(1-s^2)}\frac{dG(s)}{ds} + \frac{1}{(1-s^2)^2}\left(-(\alpha+\lambda)s^2 + \beta' - m^2\right)G(s) = 0 \tag{34}$$

Where $\lambda - \beta = \beta'$. Equating equation (25) with equation (1),

$$\tilde{\tau}(s) = -2s, \quad \sigma(s) = (1-s^2) \quad \text{and} \quad \tilde{\sigma}(s) = -(\alpha+\lambda)s^2 + \beta' - m^2 \tag{35}$$

From equation (4),

$$\pi(s) = \sqrt{(\alpha'+\beta'-K)s^2 + (K+m^2-\beta')} \tag{36}$$

where $\alpha' = \alpha + \beta$ .To solve quadric  equation  (29) in terms of K , taking this quardric $b^2 - 4ac = 0$,The possible values of $K_\pm$ as,

$K_+ = \beta' + \alpha'$ and $K_- = \beta'\text{-}m^2$

$$\pi(s) = \pm \begin{cases} \sqrt{m^2 + \alpha'}, & For \quad K_+ = \beta' + \alpha' \\ \sqrt{m^2 + \alpha'}\, s \ , & For \quad\quad K_- = \beta' - m^2 \end{cases} \tag{37}$$

According to NU method, derivative of $\tau(s)$ must be negative. So here acceptable solution of $\pi(s)$ is,

$$\pi(s) = -\sqrt{m^2 + \alpha'}\, s \ , \quad and \quad\quad K_- = \beta' - m^2 \tag{38}$$

Using equation (7)

$$\tau(s) = -2\left[1 + \sqrt{m^2 + \alpha'}\right] s \tag{39}$$

from equation (5) and (6)

$$\Lambda = (\beta' - m^2) - \sqrt{m^2 + \alpha'} \tag{40}$$

$$\Lambda_n = 2n\left[1 + \sqrt{m^2 + \alpha'}\right] - n(n-1) \tag{41}$$

but $\Lambda = \Lambda_n$,

$$\beta' = n(3 - n) + (2n + 1)\sqrt{m^2 + \alpha'} \tag{42}$$

$$\lambda = n(3 - n) + (2n + 1)\sqrt{m^2 + \alpha'} + \beta \tag{43}$$

### 5.2 Eigen function of angular part

Using equation (9) below equations are obtained[19,20,21].

$$\rho(s) = (1 - s^2)^{\sqrt{m^2 + \alpha'}} \tag{44}$$

$$a_n(s) = (1 - s^2)^{\frac{\sqrt{m^2 + \alpha'}}{2}} \tag{45}$$

So equation (8),

$$b_n(s) = C_n \ \frac{1}{(1-s^2)^{\sqrt{m^2+\alpha'}}} \frac{d^n}{ds^n}\left((1 - s^2)^{n + \sqrt{m^2 + \alpha'}}\right) \tag{46}$$

Now $b_n(s)$ can be write in terms of Jacobi polynomials $P_n^{(\sqrt{m^2+\alpha'},\sqrt{m^2+\alpha'})}(s)$,

So equation (46) can be written as,

$$b_n(s) = (C_n 2^n n! (-1)^n)(s-1)^{-2\sqrt{m^2+\alpha'}} P_n^{(\sqrt{m^2+\alpha'},\sqrt{m^2+\alpha'})}(s) \tag{47}$$

Therefore total angular wavefunction obtained from equation (45) and equation(47) as,

$$G(s) = a_n(s)b_n(s)$$

$$G(s) = (C_n 2^n n! (-1)^n)(s-1)^{-2\sqrt{m^2+\alpha'}}(1-s^2)^{\frac{\sqrt{m^2+\alpha'}}{2}} P_n^{(\sqrt{m^2+\alpha'},\sqrt{m^2+\alpha'})}(s) \tag{48}$$

## 5. Conclusion

In this paper, we calculated eigenfunctions and eigenvalues of harmonic plus inverse square plus non central potential (HINP). It is solved using Nikiforov-Uvarov (NU) method with proper coordinate transformation. Our result is applicable in nuclear physics and quantum chemistry. By choosing proper values parameters $\alpha, \beta, A \ and \ B$, we can calculate eigenfunctions and eigenvalues of particular atom or molecules and from wavefunction, we can find different dynamical properties of system. For $\alpha, \beta \ and \ B = 0$, it is form of simple harmonic potential. We are looking  for further studies along this direction.

## References

[1]  F. Cooper, A. Khare and U. Sukhatme: "Supersymmetry and quantum mechanics and large-N expansions ", Phys. Rep., , (1995), Vol. 251,pp. 267–385

[2] S.M. Ikhdair and R. Sever:  Int. J. Mod. Phys. A, (2006), Vol. 21, pp. 6465–6476.

[3] S.M. Ikhdair and R. Sever: , J. Mol. Struc.-Theochem, (2007), Vol. 809,  pp. 103–113.

[4] Z.–Q. Ma and B.–W. Xu, Euro phys Lett.,   (2005), Vol. 69, pp. 685–691.

[5] M.R. Setare and E. Karimi:, Phys.Scr.,    (2007), Vol. 75, pp. 90–93.

[6] A.F. Nikiforov and V.B. Uvarov: Special Functions of Mathematical Physics,Birkhauser, Basel, 1988.

[7] R. J. Le Roy and R. B. Bernstein, J. Chem. Phys. (1970), 52, 3869.

[8] A. A. Makarov, J. A. Smorodinsky, K. H. Valiev and P. Winternitz, Nuovo Cimento (1967), A 52, 1061.

 [9] C. Berkdemir, A. Berkdemir and J. G. Han, Chem. Phys. Lett (2006) . 417, 326.

[10] A. Durmus and F. Yasuk, J. Chem. Phys. (2007) 126, 074108.

[11] E. Fues, Ann. Phys, (1926) . 80, 367.

[12] S. H. Dong, G. H. Sun and M. Lozada-Cassou, Phys. Lett. A (2004), 328, 299.

[13] H. X. Quan, L. Guang, W. Z. Min, N. L. Bin, and M. Yan, Commun. Theor. Phys. (2010) 53(2),        242.

[14] C. Cari, A. Suparmi, M. Yunianto and B. N. Pratiwi Journal of Physics: Conference Series 776       (2016) 012092

[15]M. Kibler and T. Negadi, Int. J. Quantum Chem. (1984), 26, 405.

 [16] M. V. Carpido-Bernido and C. C. Bernido, Phys. Lett. (1989), 134A 315.

[17] M. V. Carpido-Bernido, J. Phys. (1991) , A 24, 3013.

[18] C. Berkdemir, J. Math. Phys. (2009), 46, 13

[19] H. Salehi ,Applied Mathematics, (2011), 2, 999-1004

[20] H Goudarzi, A Jafari at al. Adv. Studies Theor. Phys., (2012), Vol. 6,  no. 26, 1253 – 1262

[21] D. Akaninyene, . Antia and Okon P. Akpan; Journal of Applied and Theoretical Physics Research (2017), 1(2),9-13.

# Temperature dependent electrical resistivity of $WS_xSe_{2-x}$ (X = 2, 1.5, 0.5) crystals

**(1) Payal Chauhan**

Department of Physics, Sardar Patel University, Vallabh Vidyanagar -388120, Anand, Gujarat, India.

Email: payalnchauhan64@gmail.com

**(2) Pratik Pataniya**

Department of Physics, Sardar Patel University, Vallabh Vidyanagar -388120, Anand, Gujarat, India.

Email: pm.pataniya9991@gmail.com

**(3) G. K. Solanki**

Department of Physics, Sardar Patel University, Vallabh Vidyanagar -388120, Anand, Gujarat, India.

Email: solankigunvant@yahoo.co.in

**(4) K. D. Patel**

Department of Physics, Sardar Patel University, Vallabh Vidyanagar -388120, Anand, Gujarat, India.

Email: kdptflspu@gmail.com

**(5) V. M. Pathak**

Department of Physics, Sardar Patel University, Vallabh Vidyanagar -388120, Anand, Gujarat, India.

Email: yogvmpathak@yahoo.co.in

**Abstract:**

Transition metal dichalcogenides have been intensively studied due to quasi two dimensional charge transport characteristic. The electrical resistivity of $WS_xSe_{2-x}$ (X = 2, 1.5, 0.5)was measured perpendicular to crystallographic c- axis in temperature range from 313 K to 673 K in the step of 5 K. The resistivity of $WS_xSe_{2-x}$ (X = 2, 1.5, 0.5)samples decreases on increasing the temperature. This study confirms the semiconducting behaviour of grown samples.The activation energy at different temperature range was calculated using Arrhenius relation.

**Keywords:** Activation energy, crystalgrowth, resistivity.

## Introduction:

The transition metal dichalcogenides (TMDCs) with generalised formula MX2, where M is the metal atom and X is the chalcogen atoms are crystalized by stacking of X-M-X sandwiched structure. In each layer the atoms are bonded by relatively strong covalent bond and layers are stacked upon each other by weak van der Waals interaction [1]. The anisotropy in interaction results into the anisotropic charge transport mechanism. The most intensively explored members of TMDCs family, $WSe_2$ and $WS_2$ are found to be semiconducting in nature with indirect band gap around 1.2-1.4 eV. They have shown great potential for the applications in the fields of optoelectronics due to exotic band structure and distinct physical properties [2-4]. The chemical and environmental stability makes them most suitable sustainable electronics. Besides this, tenability of electric properties, like conductivity, carrier concentration and mobility have been demonstrated [5-12]. In order to produce high performance device, the band gap have been engineered by doping of semiconductors and by alloying different semiconductors. In present research, tuning of electric transport have been demonstrated in $WS_xSe_{2-x}$(X = 2, 1.5, 0.5)by varying S and Se content into grown samples[13]. The electrical resistivity have been measured in parallel and perpendicular to c-axis in temperature range 313K to 673K  in the step of 5 K and activation energy has also been calculated using Arrhenius relation.

## Experimental:

The $WS_xSe_{2-x}$(X = 2, 1.5, 0.5)samples were grown by direct vapour transport technique using high temperature dual zone horizontal furnace. The electrical resistance of samples was measured in perpendicular to crystallographic c-axis in temperature range 313K to 673 K using two probe method. The experimental set up for this study comprises of steel sample holder with two wire probes and high temperaure single zone vertical furnace. The resistance was measured by Keithly-2700 multi meter and resistivity was also calculated. The activation energy was also calculated for grown sample using Arrhenius relation.

## Results and discussion:

The temperature dependent electrical resistivity ($\rho$) measurements perpendicular to c-axis were performed systematically in temperature range 313 K to 673 K in the step of 5 K. The temperature- resistivity curves of $WS_xSe_{2-x}$ (X = 2, 1.5, 0.5)are shown in Figure1. The resistivity of $WS_xSe_{2-x}$ (X = 2, 1.5, 0.5)samples decreases as the temperature increases. It depicts the semiconducting behaviour of grown samples.The conductivity curves seen to be in good agreement with the models related to the thermal carrier emission across grain boundary barriers where a temperature dependence of conductivity is expected to yield straight line in Arrhenius plots in the whole temperature range [13].
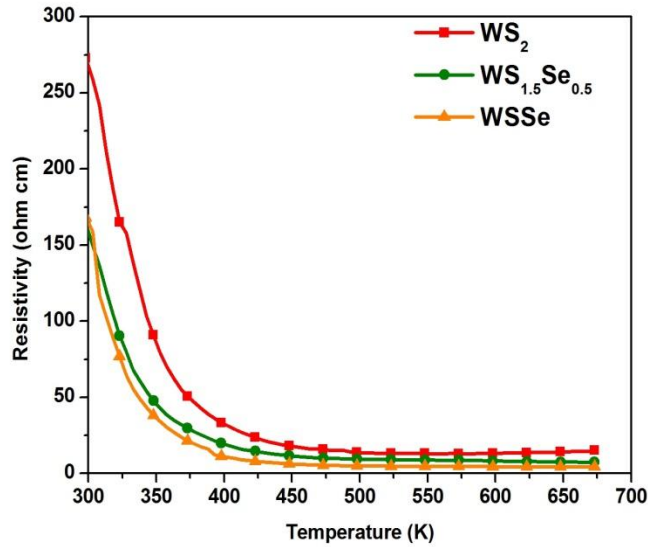
**Figure 1** Temperature-resistivity curves for $WS_xSe_{2-x}$ (X = 2, 1.5, 0.5) samples
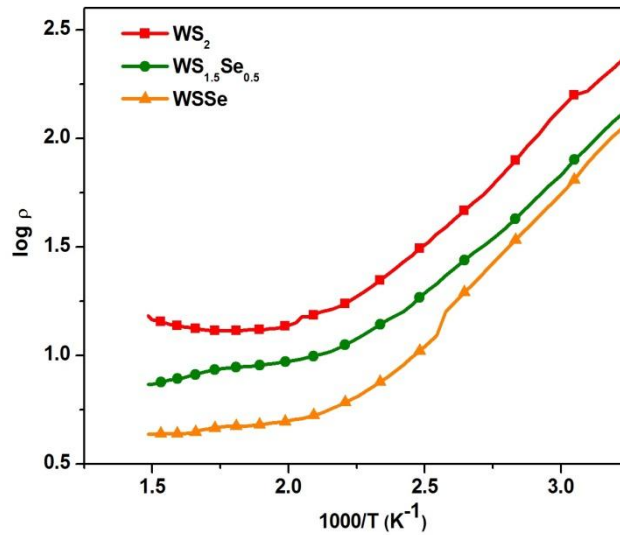


**Figure2** log ρ vs 1000/T for $WS_xSe_{2-x}$ (X = 2, 1.5, 0.5) samples.

The activation energy was also calculated using following relation:

$$\rho = \rho_0 \left[ -\frac{E_a}{k_B T} \right] \qquad (1)$$

where, $E_a$ is activation energy, $k_B$ is Boltzmann constant and T is absolute temperature.

The logρ vs. 1000/T curves are divided into two regions, as shown in Figure 2. The activation energy was determined for all the regions and mentioned in Table 1. The relatively lower values of activation energy attribute the presence of extrinsic conduction mechanism in $WS_xSe_{2-x}$ (X = 2, 1.5, 0.5) samples.

**Table 1** Activation energy for $WS_xSe_{2-x}$ (X = 2, 1.5, 0.5)samples.

| Compositions | Perpendicular to c-axis | |
|---|---|---|
| | Temperature range (K) | Activation energy (eV) |
| $WS_2$ | 298-413 | 0.108 |
| | 418-673 | 0.197 |
| $WS_{1.5}Se_{0.5}$ | 298-413 | 0.182 |
| | 418-673 | 0.198 |
| WSSe | 298-413 | 0.168 |
| | 418-673 | 0.198 |

The study of change in electrical resistivity by variation of S and Se is the key part of present research. The resistivity seems to be decreases on increasing the Se content in grown samples. In ternary compounds i.e. WSSe and $WS_{1.5}Se_{0.5}$, the Se-atoms replace the S-atoms from the host lattice. The activation energy is also found to be decreases as the content of Se increases.

**Conclusions:**

The electrical transport properties of$WS_xSe_{2-x}$ (X = 2, 1.5, 0.5)crystals have been studied with high temperature resistivity measurements. This work has shown that $WS_xSe_{2-x}$ (X = 2, 1.5, 0.5)crystal are a semiconducting in nature. The resistivity is decreases as temperature is increasing in all respective samples.

**References:**

[1]   K. Xu, Z. Wang, X. Du, M.Safdar, C. Jiang and J. He, Nanotechnol., 2013, **24,**465-705.
[2]   Q. H. Wang, K.Kalantar-Zadeh, A.Kis, J. N. Coleman and M. S.Strano, *Nat. Nanotech.,* 2012,**7,** 699–712.
[3]   K. A. Patel, C. K. Sumesh, P. Pataniya, G. K. Solanki and K. D. Patel,*Eur. Phys. J. Plus*, 2017,**132,**191.
[4]   S.Zheng, L.Sun, T.Yin, A. M. Dubrovkin, F. Liu, Z.Liu, Z. X. Shen and H. J. Fan,*Applied Physics Letters,* 2015,**106,** 063113.
[5]   P. Desai, D. D. Patel and A. R. Jani,*Journal of Crystal Growth,* 2014,**390,** 12–17.
[6]   P. Desai, D. D. Patel and A. R. Jani,*Mate. Sci. in Sem. Proces.,* 2014,**24,** 40–43.
[7]   D. D. Patel, P Desai and A. R. Jani, *Journal of Crystal Growth,* 2014,**400,**43–48.
[8]   Y. Chen, J.Xi, D. O. Dumcenco, Z.Liu, K.Suenaga, D. Wang, Z. Shuai, Y. S. Huang and L.Xie,*ACS Nano,* 2013,**7,** 4610.
[9]   Y.Chen, D. O. Dumcenco, Y.Zhu, X.Zhang, N.Mao, Q.Feng, M.Zhang, J.Zhang, P. H. Tan, Y. S. Huang and L.Xie,*Nanoscale,* 2014,**6,** 2833.
[10]  D. O. Dumcenco, H.Kobayashi, Z.Liu, Y. S. Huang and K.Suenaga,*Nat. Commun.,* 2013,**4,** 1351.
[11]  M.Zhang, J. Wu, Y.Zhu, D. O. Dumcenco, J.Hong, N. Mao, S.Deng, Y.Chen, Y.Yang, C.Jin, S. H. Chaki, Y. S. Huang, J.Hang and L.Xie,*ACS Nano,* 2014, **8,** 7130.
[12]  P.Yu, J.Lin, L.Sun, Q.L. Le, X.Yu, G.Gao, C. H. Hsu, D.Wu, T. R. Chang, Q.Zeng,

F.Liu,  Q. J. Wang, H. T. Jeng, H. Lin, A.Trampert, Z.Shen, K.Suenaga and Z.Liu,*Adv. Mater.,* 2017,**29,**1603991.

[13]  G. K.Solanki, P Pataniya, C. K. Sumesh, K. D. Patel and V. M. Pathak,*Journal of Crystal Growth,* 2016 ,**441,** 101–106.

# Growth and anisotropic behavior of  $GeS_{0.5}Ge_{0.5}$   single crystals grown using direct vapour transport technique

**Dipika B. Patel[a)]∗ , Sandeep G. Chovatiya[a)], Gunvant K. Solanki[b)]**

a)*ARIBAS, Sardar Patel University, New Vallabh Vidyanagar 388121, India

b)Department of Physics, Sardar Patel University, Vallabh Vidyanagar 388 120, India

[*]Corresponding author email Id: dipikapatel@aribas.edu.in

## Abstract

This paper report the growth of single crystals of ternary mixed compounds of group IV–VI in the form of  $GeS_{0.5}Se_{0.5}$  using direct vapour transport technique. The grown crystals were characterized by the X-ray diffraction analysis for their structural parameter determination. All the grown crystals were found to be orthorhombic structure. The microstructure analysis of the grown crystals reveals their layered type growth mechanism and are therefore highly anisotropic. The d.c. electrical resistivity measurements perpendicular to c-axis (i.e. along the basal plane) and parallel to c-axis (i.e perpendicular to basal plane) in the temperature range 303–723 K were carried out for grown crystals using four-probe method. The electrical resistivity measurements showed an anisotropic behavior of electrical resistivity for the grown crystals. The anisotropic behavior $GeS_{0.5}Ge_{0.5}$ is presented systematically.

**Keywords.** Crystal growth; layered structure; resistivity; anisotropy;

## Introduction

Natural crystals of many materials are available in nature but they cannot be used directly for device applications. Instead they should give some sort of treatment because of the main problem of purity and perfection. The crystal growth study in the last 10 years [1-5] led to the conclusion that the artificial crystals of most of the materials can be grown in the laboratories.

Sulphides and selenides of the fourth group and metals like germanium and tin (GeS, GeSe, SnS and SnSe) form an interesting family of layered compounds. These compounds are considered intermediate between the three dimensional and the two dimensional materials. The bonding between the layers is weak being of Van der Waal's type and therefore they can be easily cleaved in the (001) plane [6]. From this fact one might expect them to exhibit the typical anisotropy of

electrical properties i.e. conductivity or mobility of a layered structure. Mechanically, single crystals of these layered materials behave extremely two-dimensional. Although layered materials are indeed anisotropic, there is a great variation in the anisotropy ratio among them. In some cases anisotropy factor up to $10^6$ have been reported [7]. Since most of the semiconductor applications are governed by the electrical properties of the materials, the electrical properties of the IV–VI compounds (GeS, GeSe, SnS and SnSe) have been carried out by different investigators [8-11]. Most of these studies are nearly confined to investigations of electrical properties along the basal plane and very few of them report the interesting question of electrical transport along the c-axis. These lamellar compounds have attracted considerable attention because of their important properties in the field of optoelectronics, lubricants, photovoltaic/photocatalytic, solar energy converters, liquid junction solar cell, holographic recording systems, electronic switching and infrared production and detection. These compounds have been grown in a crystalline form using various techniques. The vapor transport technique has been proved as a very good technique to grow good quality single crystal and to avoid the contamination of transporting agent; it is preferable to grow crystals by DVT technique. They all exhibit an orthorhombic structure belonging to space group h D2 16 (Pcmn).  This paper reports the growth of $GeS_{0.5}Ge_{0.5}$ crystals and a systematic study on the anisotropic behavior of $GeS_{0.5}Ge_{0.5}$.

**Material and Methods**

The author has grown $GeS_{0.5}Ge_{0.5}$ crystals using direct vapour transport technique. By setting a precise temperature gradients between two zones to enhance the transport of material in vapour form. The mixture was slowly heated to the required temperature. The slow heating was necessary to avoid any explosion due to the strong exothermic reaction between the elements. A total charge of nearly 10 g was kept in the furnace. Energy Dispersive Analysis of X-rays (EDAX) has been carried out for determination of the chemical composition of grown crystals. The X-ray diffractrograms (XRD) of these compounds were recorded on Philips PW 1710 diffractometer using $CuK_\alpha$ radiation. For the study of variation in resistivity with temperature of the grown crystals a high temperature measurement set has been designed and developed in University Shophesticsted Instrumentation Centre (USIC), Sardar Patel University. Using this experimental set up, resistance of sample has been measured from room temperature to 723K temperature in the step of 10K and

for each step the corresponding resistivity can been calculated. To avoid excessive heating of the sample chamber, it is cooled by circulating cold water around it with the help of tubes.

The crystal is mounted in the sample holder which is then in inserted in the sample chamber and closed at the top. Introducing this assembly in vertical tabular furnace.  The temperature of the sample is raised using variac. The temperature of the sample is measured with the help of Cr-Al thermocouple kept in vicinity of the sample which is connected to the digital temperature controller which can control and display the acquired temperature. Starting from room temperature (303 K), the temperature of the sample is increased slowly from room temperature to 723 K, in steps of 10 K and at each step the corresponding value of the resistivity of the sample is calculated. Electrical resistivity parallel c-axis and perpendicular to c-axis has been measured and anisotropy ratio has been calculated for all the samples.

**Result and Discussion**

The appropriate growth conditions for $GeS_{0.5}$ $Ge_{0.5}$ crystals is shown in table 1. The ampoule containing the crystals was broken and crystals having maximum size shown in Table 1.

**Table 1.Growth parameters of $GeS_{0.5}Se_{0.5}$  single crystal.**

| Crystal | Temperature distribution | | Growth Period [Days] | Dimension of the grown crystals $(cm^2)$ |
|---------|---------|---------|---------|---------|
| | Reaction Zone (K) | Growth Zone (K) | | |
| $GeS_{0.5}Se_{0.5}$ | 923 | 873 | 7 | 0.75 X 0.65 |

The results of the EDAX report shown in table 2, confirms that the stoichiometry of the elements has been maintained in the grown crystals.
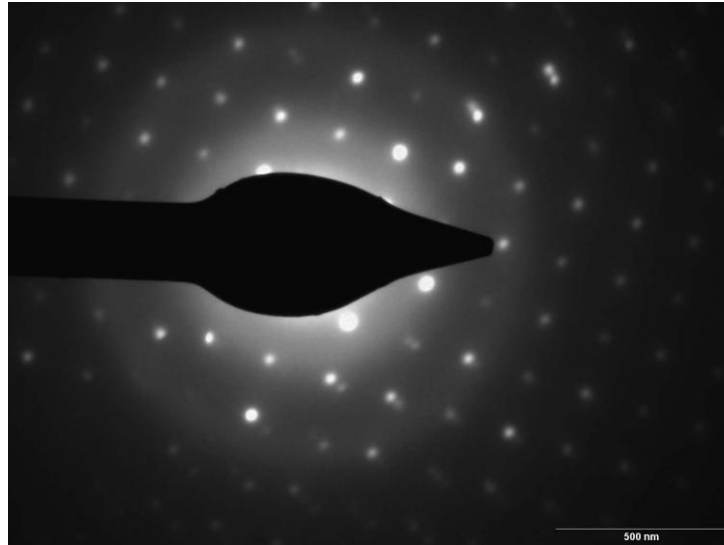
**Figure 1.Electron diffraction pattern of GeS$_{0.5}$Se$_{0.5}$ crystal**

**Table 2 Chemical composition (wt. %) of as grown GeS$_{0.5}$Se0.5 single crystal obtained by EDAX analysis**

| Crystal | Wt (%) of elements from EDAX | | | Wt % of elements taken for growth experiment | | |
|---|---|---|---|---|---|---|
| | Ge | S | Se | Ge | S | Se |
| GeS$_{0.5}$Se$_{0.5}$ | 55.90 | 12.10 | 32.00 | 56.66 | 12.5 | 30.81 |

The values of lattice parameters obtained for GeS$_{0.5}$ Se$_{0.5}$ single crystals are compared and found in agreement with those reported earlier by different investigators. The values of lattice parameter for the crystal shown in table 3 confirms the orthorhombic structure of grown crystals.

**Table 3. Lattice parameters, unit cell volume and X-ray density of GeS$_{0.5}$Se$_{0.5}$**

| Crystal | A in Å | b in Å | c in Å | Unit Cell Volume (Å)$^3$ | X-ray Density g cm$^{-3}$ |
|---|---|---|---|---|---|
| GeS$_{0.5}$Se$_{0.5}$ | 4.395 | 3.712 | 10.695 | 174.48 | 4.875 |

The variation of log of electrical resistivity parallel to c-axis and perpendicular to c-axis in the temperature range 303–723 K are shown in figures 2 & 3 , respectively. The decrease in electrical resistivity with increase in temperature suggests the semiconducting nature of the grown crystals. Using the resistivity values, anisotropy ratio was calculated using the relation

$$\gamma = \frac{\rho_\Pi}{\rho_\perp}$$

where $\rho_\parallel$ is the resistivity parallel to c-axis and $\rho_\perp$ the resistivity perpendicular to c-axis.

**Table 4. The values of activation energies perpendicular to c-axis and parallel to c-axis for GeS$_{0.5}$Se$_{0.5}$ single crystal**

| Sample | Activation energy (eV) | | | |
| --- | --- | --- | --- | --- |
| | Temp. Range | Along a-b axis | Temp. Range | Along c-axis |
| GeS$_{0.5}$Se$_{0.5}$ | 304-428 | 0.161 | 308 – 368 | 0.189 |
| | 433-533 | 0.120 | 373 – 543 | 0.491 |
| | 538-723 | 0.407 | 553 -723 | 1.743 |
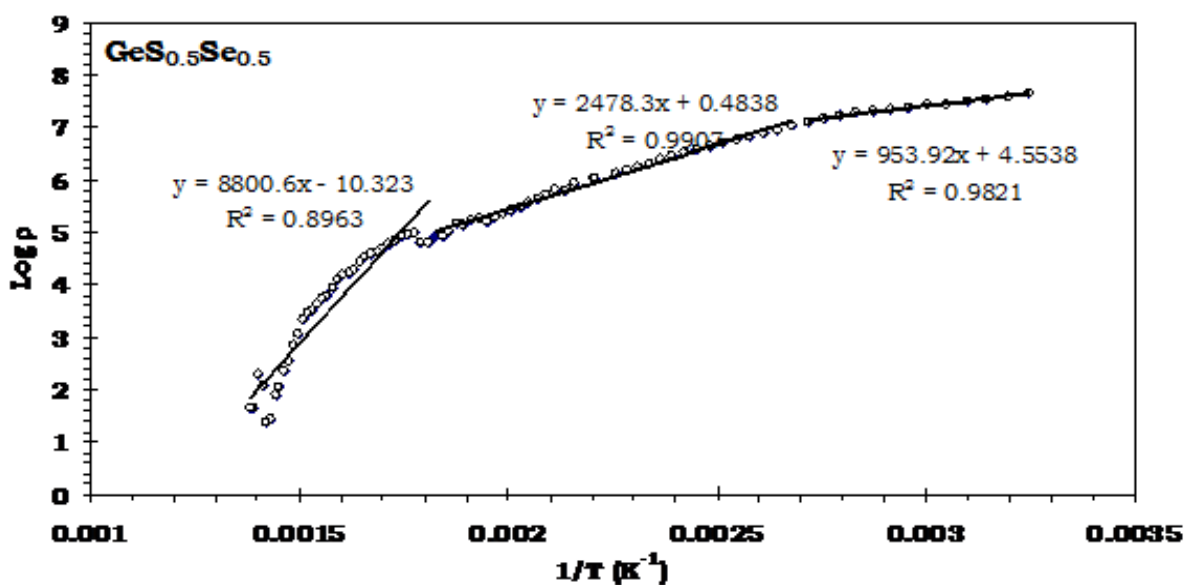


**Figure 2. Variation of lnρ vs. inverse of temperature for GeS$_{0.5}$Se$_{0.5}$ single crystal along the basal plane.**

The anisotropy ratio was determined at different temperatures in the range 303– 723 K for grown crystals. Figure 4 shows the variation of log of anisotropy ratio with reciprocal of temperature for grown crystal. The anisotropy ratio increases as the temperature decreases.
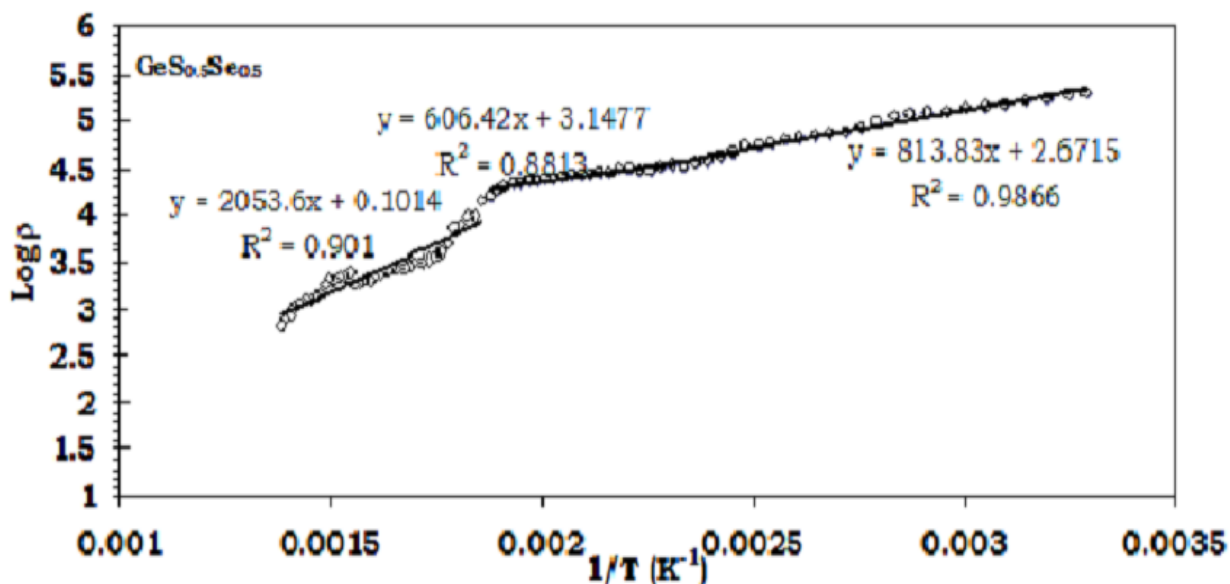


**Figure 3. Variation of lnρ vs. inverse of temperature for GeS$_{0.5}$Se$_{0.5}$ single crystal normal to the basal plane.**
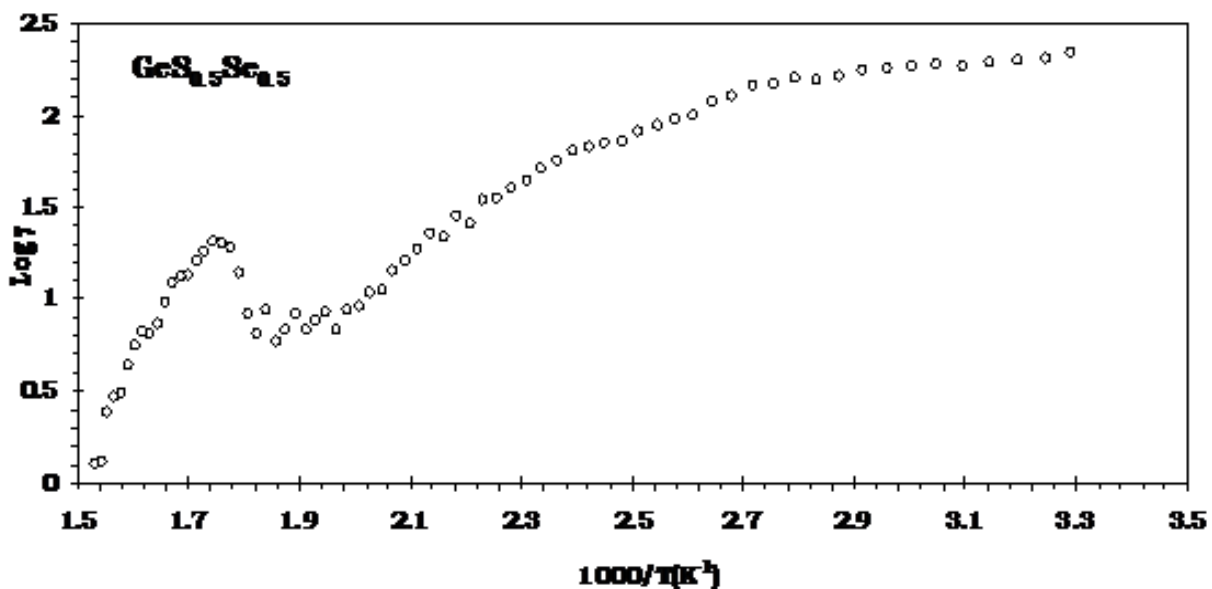


**Figure 4. Variation of logγ with temperature for GeS$_x$Se$_{1-x}$ (x= 0.25, 0.5, 0.75)**

For the materials, which are intermediate between two and three dimensions, there is anisotropy of strength of the bonds between atoms. Application of temperature or chemical alloying causes greater changes in the lengths of the weaker bonds than those of stronger ones [12]. This type of anisotropy behavior is an interesting question for the strongly layered materials and it can also be explained as an effect of stacking disorder i.e. effect of a nonperiodic stacking sequence. Since the stacking-fault energy in layered materials is small, real crystals grown at high temperatures usually exhibit a nonperiodic stacking sequence [13]. The disorder produced by the stacking faults is sufficient to localize the electron states normal to the layer. While considering the stacking between the adjacent layers, the whole crystal always remains invariant under the primitive translations parallel to the layers. So the d.c. resistivity parallel to layers is not affected by the presence of stacking disorder. However, the variation of resistivity along the basal plane is attributed to the change in nature. Layered crystals often show predominance of stacking faults [14]. Perpendicular to the layers, however, there is a probability of transport due to the localization of the electron states because of the presence of stacking faults. This will therefore give rise to a fairly large amount of conduction parallel to c-axis. Further the amount of conduction will be more for the crystals where the likelihood of stacking faults is more. However, according to [13] phenomenon of conduction along c-axis is formally a hopping process. It probably occurs in these crystals via a large overlap between states, which extend over many layers.

## Conclusion

The growth experiments carried out in this paper clearly indicate that it is possible to grow crystals of fairly large size using direct vaopur transport technique. The electron diffraction photograph in figure 1 confirms their crystalline nature. The lattice parameters shown in table 3 are nearly in agreement with those obtained earlier investigator. From the lattice parameters it has been confirmed that all the crystals having orthorhombic crystal structure. High temperature resistivity curves confirm the semiconducting nature of all the crystals. It is also proved that  the crystal having anisotropic nature and having two dimensional as well as three dimensional behaviors. The increase in anisotropy ratio can be attributed to decrease in conduction along c-axis due to decrease in presence of stacking disorder. The increase in anisotropy ratio can be attributed to the change in bond lengths between the anion and cation.in the single crystals.

References

[1]   H. E. Buckley, " Crystal growth", John Wiley and Sons, New York, (1951).

[2]   W. H. Brattain and G. B. Gareett, Bell. Syst.Tech.J., **32** (1955) 1.

[3]   W. H. Brattain and G. B. Garrett, Bell. Syst. Tech. J., **34** (1955) 129.

[4]   J. G. Burke, Origin of the Science of the Crystals (Berkeley , University of California Press), (1966).

[5]   D. Elwell and H.J. Scheel, Crystal Growth from High Temperature Solutions (New Yprk, Academic Press), (1975)

[6]  Agarwal A 1998 J. Cryst. Growth 183 347

[7]  Agarwal M K, Patel P D and Vijayan O 1983 Phys. Status Solidi A79 103

[8]  Maier H and Daniel D R 1977 J. Electron. Mater. 6 693

[9]  Clemen C, Saldhana X I, Munz P and Bucher E 1978 Phys. Status Solidi A49 437

[10]  Yue Y G, Yue A S and Stafsudd O M Jr 1981 J. Cryst. Growth 54 248

[11]  Nagard N Le, Clement C Levy, Katty A and Lieth R M A 1990 Mater. Res. Bull. 25 495

[12]  Peters M J and McNeil L E 1990 Phys. Rev. B41 5893

[13]  Maschke K and Schmid Ph. 1975 Phys. Rev. B12 4312

[14]  Trigunayat G C 1971 Phys. Status Solidi (a)4 281

# Study on Fourier Transform Infrared (FTIR) Spectroscopy of Charge Transfer Complexes (CTCs) of Ubiquinone (Coenzyme Q10) and Menaquinone (Vitamin K2)

**D. N. Bhavsar[1#], M. B. Patel[2], S. G. Patel[2], M. Y. Barot[3] and A. T. Oza[2]**

[1]Bhavan's Sheth R. A. College of Science, Khanpur, Ahmedabad-380001, Gujarat, India.

[2]Department of Physics, Sardar Patel University, Vallabh Vidyanagar-388120, Gujarat, India.

[3] Government Science College, Gandhinagar

[#]corresponding author: div.bhavsar@gmail.com, Tel. No.: +919429382908

Physics and Astronomy Classification Scheme Number (PACS): 82.39.jn, 87.85.jf, 87.14.Pq.

**Abstract:** The infrared spectra of four charge transfer complexes namely perylene-ubiquinone, benzidine-ubiquinone, perylene-menaquinone and benzidine-menaquinone have been studied. Band assignments have been carried out for vibrational bands. Featureless ranges have been analyzed for nature of transitions which are interband transitions with band gap in the infrared range. Ubiquinone complexes have shown Gaussian bands as electron absorption envelopes while menaquinone complexes have shown triangular distributions as envelopes. Both quinones have shown semiquinone ion bands in infrared (IR) range. A relation between Lorentzian function and triangular distribution is briefly discussed.

**Keywords:** FTIR Spectroscopy, vitamin $K_2$, donors and acceptors, triangular distributions.

**Highlights:**

- We report the FTIR spectroscopic study of perylene- ubiquinone, benzidine-ubiquinone, perylene-menaquinone and benzidine-menaquinone.

- Gaussian bands as electron absorption envelopes for ubiquinone complexes and triangular distributions as envelopes for menaquinone complexes have been verified.

- Triangular distribution reveals imperfect nesting of Fermi surface.

## 1. Introduction

Organic charge transfer complexes are very famous [1-3] but only limited study exists on charge transfer complexes of biomolecules [4]. Only homo-molecular bio-macromolecular materials were reported to be semiconducting [5]. Here we have studied charge transfer complexes of Ubiquinone (Coenzyme $Q_{10}$) and Menaquinone (Vitamin $K_2$) using infrared spectroscopy. Ubiquinone is a fat-soluble quinone with a very long isoprenoid side chain of 10 isoprenoid units and therefore also called coenzyme $Q_{10}$. This compound is found in mammalian tissues. Ubiquinone is found in the inner membrane occurring in free and bound protein forms. The function is to collect reducing equivalents from mitochondria vitamins $K_1$ and $K_2$ are found in plants. Vitamin K functions in a blood-clotting mechanism and converts fibrinogen in to fibrin as an enzyme [6-8]. Menaquinone (Vitamin $K_2$) contains six isoprenoid units on the one side and an aromatic ring on the opposite side.

**Figure 1 (a-b)** Molecular structures of donors and acceptors, **(c)** Ubiquinone (Coenzyme $Q_{10}$)

**(d)** Menaquinone (Vitamin $K_2$).

Here, ubiquinone and menaquinone are selected as quinones containing ortho-substituted isoprenoid side chain as compared to p-Benzoquinone which forms charge transfer complexes with organic donors. There are two methoxy groups in ubiquinone and an aromatic ring in menaquinone. Molecular structures of donors and acceptors are shown in figure 1.

## 2. Experimental details

Benzidine (0.000656 gm) and ubiquinone (0.003 gm) were taken and grinded in agate mortar to form a blue-coloured 1:1 charge transfer complex. Similarly, perylene (0.0088 gm) and ubiquinone (0.003 gm) were grinded to form a green complex. Perylene and menaquinoneformed green 1:1 complex. Benzidine and menaquinone formed a bluish green complex in a similar manner.

The samples for infrared spectroscopic measurements were prepared by mixing the four complexes in 5% with spectrograde anhydrous KBr powder in 95% and compressing in a die after regrinding in a mortar to form circular pallets. The pallets were placed at infrared window in Nicolet 400 D spectrophotometer and the spectra were recorded in 400 cm$^{-1}$ range of infrared frequencies.

## 3. Results and Discussion

**Figure 2 (a)** FTIR spectrum of ubiquinone, **(b)** Nature of transition in ubiquinone and

**(c)** ln A vs. $(k-K_0)^2$ for Gaussian profile in ubiquinone.

The infrared spectrum of homo-molecular ubiquinone was also taken and it is shown in figure 2. There is a gap in sharp bands between 1700 cm$^{-1}$ and 2800 cm$^{-1}$ and no sharp band is found in this interval of wave numbers. There are sharp bands above 2800 cm$^{-1}$.

**Table 1.**   Band assignments in FTIR spectra of Ubiquinone, Perylene-Ubiquinone

Benzidine-Ubiquinone.

These six bands are assigned to C-H stretching vibrations of methyl groups as well as those of isoprenoid units (table 1). The band assignments were carried out in full IR range (Table 1), taking guidance from elsewhere [9, 10]. Four semiquinone ion bands were found at 1220 cm$^{-1}$ (8.2 μ), 1150 cm$^{-1}$ (8.4 μ), 1060 cm$^{-1}$ (9.5 μ) and 880 cm$^{-1}$ (11.3 μ) which show presence of semiquinone ion.

This reveals that a semiquinone is formed upon a transfer of proton from the end of the isoprenoid chains towards the oxygen atom of p-benzoquinone. Such materials in which one part of a macromolecule behaves like a donor and the other part behaves like acceptor are called self-complexes. Thus, ubiquinone is a self-complex in which side chain of 10 isoprenoid units is folded in three-dimension such as to form a C-H----O contact with oxygen at para-position of p-benzoquinone. It is either a hydrogen bonding contact or a charge transfer contact forming an H$^+$-semiquinone anion ionic material.

There is a featureless absorption between 1700 cm$^{-1}$ and 2800 cm$^{-1}$ apart from very small and broad bands which can be analyzed as optical absorption edge with E$_g$=0.225 eV (1800 cm$^{-1}$). Thus, the semiquinone ion form stacks which are semiconducting with this band gap (figure 2 (b)). Ubiquinone is unique acceptor having negative charge on oxygen atom. In both cases, dipole-dipole interaction leads to small intermolecular distance along the stacks. The other evidence of semiconducting nature of ubiquinone is the presence of noise between 3500 cm$^{-1}$ and 4000 cm$^{-1}$ which is likely to exist in photoconducting materials. This is a region of free carrier absorption which can be present in the conduction band. Thus, ubiquinone is a photoconductor. There is also noise due to localization near the band edges near 1800 cm$^{-1}$. There is Lorentzian Line-shape around 3450 cm$^{-1}$, in the spectrum of ubiquinone which shows that either it is an intrinsic broadening or there is collision broadening. Other background envelope is around 1400 cm$^{-1}$ which fits a Gaussian curve (figure 2 (c)) which shows there is a Doppler broadening of spectral line in this range.

**Figure 3** **(a)** FTIR spectrum of perylene-ubiquinone, **(b)** FTIR spctrum of benzidine-ubiquinone, **(c)** Nature of transition in perylene-ubiquinone, **(d)** Nature of transition in benzidine-ubiquinone    and **(e)** ln A vs. (k-K$_0$)$^2$ for Gaussian profile in perylene-ubiquinone.

The IR spectra of perylene-ubiquinone and benzidine-ubiquinone are also shown in figure 3 (a-b) respectively. The spectrum of perylene-ubiquinone contains featureless absorption between 1700 cm$^{-1}$and 2800 cm$^{-1}$. This extends as background absorption down to 800 cm$^{-1}$. Thus, the forbidden energy gap between valence and conduction bands is very small of the order of 0.10 eV which is analyzed (figure 3(c)). It is a forbidden direct transition and therefore does not involve absorption and reemission of a phonon. Although ubiquinone is a macromolecule which should lead to indirect transition, the transition is found to be direct because the electronic conduction seems to be along the segregated perylene stacks rather

than along the mixed stacks. Perylene cation interacts with ubiquinone which exists in the form of semiquinone. Again semiquinone ion bands are observed at appropriate frequencies. Here condensed hydrocarbon perylene with its hydrogen atom shifted towards oxygen atom of substituted benzoquinone. The IR spectrum of benzidine-ubiquinone is similar (figure 3(b)) to that perylene-ubiquinone (figure 3(a)) except bands of N-H stretching and C-N stretching of benzidine molecule (table 1). The benzidine– ubiquinone shows an indirect allowed transition fitting $Ah\nu=B(h\nu-E_g)^2$ with $E_g=0.22$ eV (figure 3(d)). This gap is along stacks of semiquinone ions.

The Lorentzian line shape of only ubiquinone around 3450 cm$^{-1}$ is broadened by Doppler effect in perylene-ubiquinone and benzidine-ubiquinone shows very broad and weak Gaussian band almost approaching a Cauchy distribution for large damping coefficient and a comparatively sharp Gaussian band in the case of benzidine-ubiquinone (figure 3(e)). The photoconducting noise of only ubiquinone is considerably reduced in perylene-ubiquinone and benzidine-ubiquinone complexes. Benzidine-ubiquinone is more photoconducting than perylene-ubiquinone. Benzidne-ubiquinone and perylene-ubiquinone both show four semiquinone ion bands. In benzidine complex, benzidine condenses into hydroquinone with N-H---N bonds and hydrogen forming semiquinone ion of ubiquinone.

**Figure 4 (a)** FTIR spectrum of perylene- menaquinone, **(b)** FTIR spectrum of benzidine-menaquinone, **(c)** Nature of transition in perylene- menaquinone, **(d)** Nature of transition in benzidine-menaquinone.

The IR spectra of perylene-menaquinone and benzidine-menaquinone are shown in (figure 4(a-b) respectively. Both of the spectra show triangular distribution with peak at 3470 cm$^{-1}$. This peak is symmetric triangle in perylene-menaquinone while it is an asymmetric triangle having tail towards low frequency side, i.e. the slope of line forming triangle is smaller towards low frequency side in benzidine-menaquinone. The Lorentzian is thus

broadened into triangle. The triangular barrier in an internal Franz-Keldysh effect [11] related with tunneling of charge carriers across the band gap is tracked. The triangular distribution is the distribution of averages when the statistical meaning is concerned. Either a binomial distribution or a Lorentzian distribution is broadened to form such a triangular distribution. There is an increase in electrical conductivity by three orders of magnitude when a rectangular potential barrier is replaced by triangular distribution.

The wave function of an electron can become half-power beta density given by,

$$\psi = Ak^{*\,1/2}(1-k^*)^{1/2} \tag{1}$$

Where $k^* = \dfrac{K-a}{b}$ and A is constant which is based on Bernoulli trials, i.e. either charge carrier hops it does not hop. The electrical conductivity is related with wave function according to $\sigma = ne\mu = e|\psi|^2\,\mu$ where $e|\psi|^2$ is the charge density. This leads to

$$\sigma = e\mu A^2 K^*(1-K^*) \tag{2}$$

which is the equation of symmetric triangle. Thus, absorption coefficient $\alpha$ becomes

$$\alpha = \left(\frac{4\pi}{n_1 c}\right)\sigma = \left(\frac{4\pi e\mu A^2}{n_1 c}\right)k^*(1-k^*) \tag{3}$$

which is the triangular distribution. This shows how the triangular distribution is also related to the hopping conduction.

When the wave function itself is a triangular distribution given by

$$\psi = Ak^*(1-k^*) \tag{4}$$

Then the absorption coefficient is square-power beta density according to

$$\alpha = Bk^{*2}(1-k^*)^2 \tag{5}$$

which is the case of ionic materials related with optical phonons rather than acoustic phonons. The potential barrier is triangular when there is Franz-Keldysh effect in a semiconductor.

The featureless absorption in both menaquinone complexes show forbidden indirect transition obeying $Ah\nu=B(h\nu-E_g)^3$ in disordered or amorphous materials (figure 4(c-d)) respectively. The band gap of 0.225 eV is the standard band gap in charge transfer complexes.

The aromatic ring in menaquinone resulting in an asymmetric molecule is responsible for sharp triangular distribution. The aromatic ring localizes charge carrier while methoxy group in ubiquinone delocalize charge carriers.

Long isoprenoid side chain in ubiquinone suppresses Peierls transition compared to perylene-benzoquinone. Only in benzidine-ubiquinone the repulsive interactions dominate and Peierls transition with $E_g=0.225$ eV is not suppressed. This may be related to the ionic nature of benzidine because of ease of quaternization of N-atoms of amine groups.

**Table 2.**   Band assignments in FTIR spectra of Perylene-Menaquinone Benzidine-Menaquinone.

There is pronounced noise in perylene-menaquinone which shows more photoconducting nature than benzidine-menaquinone which shows lesser noise. There are three oscillator models below 1800 cm$^{-1}$ in both of the menaquinone complexes, which reveal more electron-phonon coupling as compared to ubiquinone complexes. Band assignments in the spectra of menaquinone complexes are summarized in table 2.

Lorentzian and Gaussian distributions are related through large damping coefficient. A harmonic oscillator model leads to Gaussian shape when the full-width at half-maximum (FWHM) is large [12]. Further, a Gaussian distribution leads to Cauchy distribution when width is further increased. This is as follows:

$$A = A_0 \exp\left(-\frac{(K-K_0)^2}{2M_{12}}\right) \cong A_0\left(1-\frac{(K-K_0)^2}{2M_{12}}\right) \cong \frac{A_0}{\left(1+\frac{(K-K_0)^2}{2M_{12}}\right)} \tag{6}$$

Where, $A_o$ is the maximum of the Gaussian curve and $M_{12}$ is the second moment of the distribution related with FWHM. Benzidine-ubiquinone shows a Gaussian band while perylene-ubiquinone shows a Cauchy distribution described by above approximation for large $M_z$. Such an approximation was also discussed earlier [13].

A triangular distribution observed in menaquinone complexes can be described by the triangular distribution given in the form of

$$f(x) = \frac{dF}{dx} = \frac{1}{\alpha}\left(1 - \frac{|x - \beta|}{\alpha}\right) \tag{7}$$

Where $f(x)$ is probability density function and $F$ is total probability [14]. Here the mean is $\beta$ and variance is $\alpha^2/6$. This triangular function can be derived from Lorentzian Line-shape as follows. The Lorentzian function is

$$g_L(\omega) \cong \frac{\gamma}{2\pi}\left[\frac{1}{(\omega - \omega_0)^2 + \frac{\gamma^2}{4}}\right] \tag{8}$$

Where $\omega_0$ is the resonance frequency and $\gamma$ is the damping coefficient. This can be also written as [15].

$$g_L(\omega) \cong \frac{2}{\pi(\Delta\omega_0)}\left[\frac{1}{1 + \frac{(\omega - \omega_0)^2}{\left(\frac{\Delta\omega_0}{2}\right)^2}}\right] \tag{9}$$

For large $\Delta\omega_0$,

$$g_L(\omega) \cong \frac{2}{\pi(\Delta\omega_0)}\left[1 - \frac{(\omega - \omega_0)^2}{\left(\frac{\Delta\omega_0}{2}\right)^2}\right] \tag{10}$$

For $\omega \leq \omega_{1/2}$ where $\omega_{1/2}$ is the frequency where amplitude reduces to half, one of $\omega$-$\omega_0$ cancels with $\Delta\omega_0$ to give

$$g_L(\omega) \cong \frac{2}{\pi(\Delta\omega_0)}\left[1 - \frac{(\omega - \omega_0)}{\left(\frac{\Delta\omega_0}{4}\right)}\right] \qquad (11)$$

This is of the form of triangular distribution with $\alpha$ proportional to $\Delta\omega_0$. Thus, a Lorentzian Line-shape can be approximated to a triangular function in the vicinity of resonance frequency $\omega_0$. $\omega_0$ is the mean and $\Delta\omega_0$ is related with the variance. The triangular distribution is in-between Lorentzian and Gaussian shapes.

**Conclusions**

In both menaquinone complexes electron-phonon coupling leads to triangular distribution and in ubiquinone complexes, it leads to Gaussian or Cauchy distribution. Electronic absorption envelope when Gaussian reveals free charge carriers while triangular distribution reveals localization. Triangular distribution also reveals imperfect nesting of Fermi surface.

**Acknowledgements**

**References**

1.  R Foster, in Organic Charge Transfer Complexes and References Therein (London-New York: Academic, 1969).

2.  F Gutman, & L E Lyons, in Organic Semiconductors and References Therein (John Wiley & sons, Inc., New York, 1967).

3. S Kanda, & H A Pohl, in Macromolecular Chemistry [Monograph]: J E Katon and Dekker, Marcel. Organic Semiconducting Polymers and References Therein (John Wiley & sons, Inc., New York, 1968) Vol. 87.

4. M A Slifkin, in Charge Transfer Interactions of Bio-molecules and References Therein (Academic Press, London-New York, 1971).

5. D D Eley, in Macromolecular Chemistry [Monograph]: Katon, J. E. Dekker, Marcel. Organic Semiconducting Polymers and References Therein (John Wiley & sons, Inc., New York, 1968).

6. L Albert & Lehninger, in Principles of Biochemistry: (CBS publishers and Distributors, Delhi (India), 1984) p. 269-479.

7. A N Nesmeyanov, in Fundamentals of Organic Chemistry (Mir Publishers, Moscow, 1978) Vol. 4, p. 471.

8. M V Volkenshtein, in Biophysics (Mir Publishers, Moscow, 1983).

9. P S Sindhu, in Molecular Spectroscopy: (Tata Mac Graw-Hill Pub. Co. Ltd., New Delhi, 1984) Vol. 104.

10. R S Drago, in Physical Methods in Inorganic Chemistry (Affiliated East-West Press Pvt. Ltd., Madras, 1971) p. 222.

11. J I Pankov, in Optical Processes in Semiconductors (Prentice-Hall Inc. Englewood Cliffs, New Jersy, 1974).

12. A T Oza, Spectroscopic theory for organic and organometallic conductors. Canadian Journal of Physics, **80**, 1175 (2002).

13. H O Parmar, Ph.D. Thesis (Sardar Patel University, Gujarat (India), 2012), p. 180.

14. P Mukhopadhayay, Mathematical Statistics (Books and Allied Pvt. Ltd., Calcutta, 2002) p. 58-92.

15. B B Laud, Lasers and Non-Linear Optics (Wiley Eastern Limited, New Delhi, 1985) p. 66.

## TABLES:

**Table 1.**  Band assignments in FTIR spectra of Ubiquinone, Perylene-Ubiquinone Benzidine-Ubiquinone.

**Table 2.**  Band assignments in FTIR spectra of Perylene-Menaquinone Benzidine-Menaquinone.

## FIGURES:

**Fig. 1 (a-b)** Molecular structures of donors and acceptors, **(c)** Ubiquinone (Coenzyme $Q_{10}$) **(d)** Menaquinone (Vitamin $K_2$).

**Fig. 2 (a)** FTIR spectrum of ubiquinone, **(b)** Nature of transition in ubiquinone and **(c)** ln A vs. $(k-K_0)^2$ for Gaussian profile in ubiquinone.

**Fig. 3 (a)** FTIR spectrum of perylene-ubiquinone, **(b)** FTIR spectrum of benzidine-ubiquinone, **(c)** Nature of transition in perylene-ubiquinone, **(d)** Nature of transition in benzidine-ubiquinone    and **(e)** ln A vs. $(k-K_0)^2$ for Gaussian profile in perylene-ubiquinone.

**Fig.4 (a)** FTIR spectrum of perylene- menaquinone, **(b)** FTIR spectrum of benzidine-menaquinone, **(c)** Nature of transition in perylene- menaquinone, **(d)** Nature of transition in benzidine-menaquinone.

**Tables:**

**Table 1.** Band assignments in FTIR spectra of Ubiquinone, Perylene-Ubiquinone Benzidine-Ubiquinone.

| Band assignments Ubiquinone | | Band assignments Perylene-Ubiquinone | | Band assignments Benzidine-Ubiquinone | |
|---|---|---|---|---|---|
| Wavenumber $(cm^{-1})$ | Band Assignment | Wavenumber $(cm^{-1})$ | Band Assignment | Wavenumber $(cm^{-1})$ | Band Assignment |
| 3080, 3050 | C-H stretching in $CH_3$ groups | 3060 | C-H stretching in C-H groups | 3480, 3440, 3350, 3200 | $\nu_{N-H}$, N-H stretching |
| 2930, 2970, 2900, 2850 | C-H stretching in isoprenoid units | 2980, 2850 | C-H stretching in isoprene units | 3060 | C-H stretching |
| 1650, 1600 | C=O stretching | 1650 | C=O stretching | 2950 | C-H stretching in isoprene units |
| 1460 | C=C stretching | 1500 1400 1260 | C=C stretching C-H bending C-O stretching | 1650 | C=O stretching |
| 1400 | C-H bending (deformation) | 1220, 1150, 1060 | Semiquinone ion bands | 1500, 1300 | C=C stretching |
| 1250 | C-O stretching in C-$OCH_3$ and in O-$CH_3$ | 880 | Semiquinone ion band | 1220, 1150, 1060 | Semiquinone bands and C-N stretching |
| 1220, 1150, 1060, 1000 | C-C stretching | 850, 800 | $\pi_{C-H}$ in C-$CH_3$ and C-O-$CH_3$ | 870 | Semiquinone ion band |
| 900 | $\pi_{C-H}$ in C-$CH_3$ | 700, 500 | $\pi_{C-H}$ in isoprene units | 800 | $\pi_{C-H}$ |
| 880 | Semiquinone ion band | | | 700, 500 | $\pi_{C-H}$ in isoprene units |
| 850 800 | $\pi_{C-H}$ in C-O-$CH_3$ | | | | |
| 700, 500 | $\pi_{C-H}$ in isoprene units | | | | |

**Table 2.** Band assignments in FTIR spectra of Perylene-Menaquinone Benzidine-Menaquinone.

| Band assignments Perylene-Menaquinone | | Band assignments Benzidine-Menaquinone | |
|---|---|---|---|
| Wavenumber $(cm^{-1})$ | Band Assignment | Wavenumber $(cm^{-1})$ | Band Assignment |
| 3053 | C-H stretching | 3469, 3322 | N-H stretching of benzidine |
| 2912, 2865 | C-H stretching in isoprene units | 2979, 2919, 2858 | C-H bending |
| 1670 | C=O stretching | 1669 | C=O stretching |
| 1454 | C=C stretching | 1508 | C=C stretching |
| 1387 | C-H bending | 1454 | C=C stretching |
| 1293 | C-O stretching | 1387 | C-H bending |
| 1220, 1150, 1060 | Semiquinone ion bands | 1293 | C-O stretching |
| 870 820 | $\pi_{C-H}$ in C-CH$_3$ and C-O-CH$_3$ | 1220, 1172, 1060 | Semiquinone ion bands and C-N stretching |
| 770, 722, 628, 554 | $\pi_{C-H}$ in isoprene units | | |
| 3053 | C-H stretching | | |

**Figures:**



Fig. 1 (a-b) Molecular structures of donors and acceptors, (c) Ubiquinone (Coenzyme $Q_{10}$)

(d) Menaquinone (Vitamin $K_2$).

**Fig. 2 (a)** FTIR spectrum of ubiquinone, **(b)** Nature of transition in ubiquinone and **(c)** ln A

vs. $(k-K_0)^2$ for Gaussian profile in ubiquinone.

**Fig. 3 (a)** FTIR spectrum of perylene-ubiquinone, **(b)** FTIR spectrum of benzidine-ubiquinone,

**(c)** Nature of transition in perylene-ubiquinone, **(d)** Nature of transition in benzidine-ubiquinone   and **(e)** ln A vs. $(k-K_0)^2$ for Gaussian profile in perylene-ubiquinone.

**Fig. 4 (a)** FTIR spectrum of perylene- menaquinone, **(b)** FTIR spectrum of benzidine-menaquinone, **(c)** Nature of transition in perylene- menaquinone, **(d)** Nature of transition in benzidine-menaquinone.

# "Synthesis and Characterization of Pure and Mg Doped ZnO Thin films and Nanorods"

**Kaushal V. Kadiya**

Research scholar, Central university of Gujarat, Gandhinagar

**E-mail ID**:  dhkaushal320@gmail.com

**Abstract**

In this paper, The optical absorption edge and the near-absorption edge characteristics of Mg undoped and doped  ZnO as  $Mg_x Zn_{1-x} O$ thin film and Nanorods(NR) using low cost chemical solution deposition techniques for growing seed layers of pure and Mg doped ZnO via Spin Coating Method method on glass substrate. Their optical    properties were investigated using UV-Vis spectroscopy and its surface topography and grain size were investigated using  AFM . The Mg dopant was found to be improving optical band gap. Accurate band gap estimation studied was obtained by using the general equation of absorbance coefficient proportional to  photon  energy graph which has discussed  below result and discussion with n = 1/2 for an  indirect allowed transition and n = 2 for a direct allowed transition.

**Keywords**

ZnO , MgO , $Mg_x Zn_{1-x} O$ ,  2-Methoxy ethanol and MEA. UV detector, AFM.

**Introduction:**

Nanotechnology is a vast empire of unknown things brought into light and certainly is the future of the days to come where the size would not be an issue[1-4]. It defines a particle as a single unit in terms of its properties and transport. Assuming a particle to be roughly spherical, classification can be done on the basis of their diameters and nanoparticles have size less than 100 nanometres[5-7]

**Synthesis Details:**

We have followed the Sol-Gel Route for the synthesis of the Mg doped ZnO (i.e. ; where x = doping in %) thin films with varied doping concentrations (viz. 0% and 4%)[8-9].  In order to

prepare the Solution and pursue the deposition, following steps were undertaken, The preparation of 0.3M solution of Zinc Acetate and Magnesium Chloride was accomplished for seed layer growth by weighing the respective compounds as precursors in accordance with the solid state calculation route suggested by Dr. Utpal Joshi. These compounds were then dissolved in the 20ml 2-Methoxy ethanol and MEA (Mono Ethanol Amine) in a ratio of 19.5:0.5 respectively by constant stirring for 30 minutes at $35^o$C[10-12]. After completion of the stirring process the samples were provided aging for 24 hours in order to observe the behaviour of the solution under the atmospheric conditions. These samples were then used for deposition of the solution on the RCA cleaned glass surface (sec. 2.2) using the Spin Coating Method (sec. 2.1). The Spin coating was approached under identical conditions for all the samples for 10 coats at 2000 rpm. After each coat the films were provided drying on the Hot Plate for 10 minutes at $215^o$C[13-14]. These films were then subjected to the oven at $75^o$C for 24hrs and then were subjected to Air Annealing at two different temperatures viz. $350^o$C 90 minutes to form the seed layer. These films were then approached Dip Coating Process prepared with a molarity of 0.5M containing the same precursors for 0% and 4% concentrations of doping for 1 hour[15]. These films were then subjected to Air Annealing @ $450^0$C for 2 hours for the growth of Nanorods[16].

**Configuration**
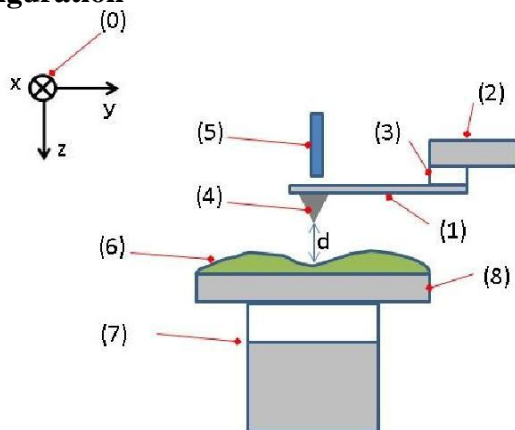


**Fig. 1: Typical configuration of an AFM.**

(1):: Cantilever, (2): Support for cantilever, (3): Piezoelectric element(to oscillate cantilever at its Eigen frequency.), (4): Tip (Fixed to open end of a cantilever, acts as the probe), (5): Detector of deflection and motion of the cantilever, (6): Sample to be measured by AFM, (7): xyz drive, (moves sample (6) and stage (8) in x, y, and z directions with respect to a tip apex (4)), and (8): Stage. The small spring-like cantilever (1) is carried by the support (2). Optionally, a piezoelectric element (3) oscillates the cantilever (1). The sharp tip (4) is fixed to the free end of the cantilever (1). The

detector (5) records the deflection and motion of the cantilever (1). The sample (6) is mounted on the sample stage (8). An xyz drive (7) permits to displace the sample (6) and the sample stage (8) in x, y, and z directions with respect to the tip apex (4). Although Fig. 4 shows the drive attached to the sample, the drive can also be attached to the tip, or independent drives can be attached to both, since it is the relative displacement of the sample and tip that needs to be controlled. Controllers and plotter are not shown in Fig. 4. Numbers in parentheses correspond to numbered features in Fig. 1. Coordinate directions are defined by the coordinate system (0).According to the configuration described above, the interaction between tip and sample, which can be an atomic scale phenomenon, is transduced into changes of the motion of cantilever which is a macro scale phenomenon. Several different aspects of the cantilever motion can be used to quantify the interaction between the tip and sample, most commonly the value of the deflection, the amplitude of an imposed oscillation of the cantilever, or the shift in resonance frequency of the cantilever (see section Imaging Modes). The detector (5) of AFM measures the deflection (displacement with respect to the equilibrium position) of the cantilever and converts it into an electrical signal. The intensity of this signal will be proportional to the displacement of the cantilever.

**Image Formation:**

When using the AFM to image a sample, the tip is brought into contact with the sample, and the sample is raster scanned along an x-y grid (fig 4). Most commonly, an electronic feedback loop is employed to keep the probe-sample force constant during scanning. This feedback loop has the cantilever deflection as input, and its output controls the distance along the z axis between the probe support (2 in fig. 3) and the sample support (8 in fig 3). As long as the tip remains in contact with the sample, and the sample is scanned in the x-y plane, height variations in the sample will change the deflection of the cantilever. The feedback then adjusts the height of the probe support so that the deflection is restored to a user-defined value (the set-point). A properly adjusted feedback loop adjusts the support-sample separation continuously during the scanning motion, such that the deflection remains approximately constant. In this situation, the feedback output equals the sample surface topography to within a small error. Historically, a different operation method has been used, in which the sample-probe support distance is kept constant and not controlled by a feedback (servo mechanism). In this mode, usually referred to as 'constant height mode', the deflection of the cantilever is recorded as a function of the sample x-y position. As long as the tip is in contact with the sample, the deflection then corresponds to surface topography. The main reason this method is not very popular anymore, is that the forces between tip and sample are not controlled, which can

lead to forces high enough to damage the tip or the sample. It is however common practice to record the deflection evenwhen scanning in 'constant force mode', with feedback. This reveals the small tracking error of the feedback, and can sometimes reveal features that the feedback was not able to adjust for. The AFM signals, such as sample height or cantilever deflection, are recorded on a computer during the x-y scan. They are plotted in a pseudocolor image, in which each pixel represents an x-y position on the sample, and the colour represents the recorded signal.

## Results and discussion

### Optical Properties

Underlying are the UV data for the MZO thin films in accordance with the synthesis with the doping varied as 0% and 4%. The plots shown are for Transmittance and Absorbance versus Wavelength in nm. The transmittance spectra and optical properties of the ZnO NRs in the wavelength range of 300 to 800 nm were investigated through UV-visible spectroscopy at RT. The UV-visible transmittance spectra of the ZnO NRs are shown in Figure 1. The inset of Figure 1 shows the magnified view of transmittance spectrum in the wavelength range of 100 to 800 nm.
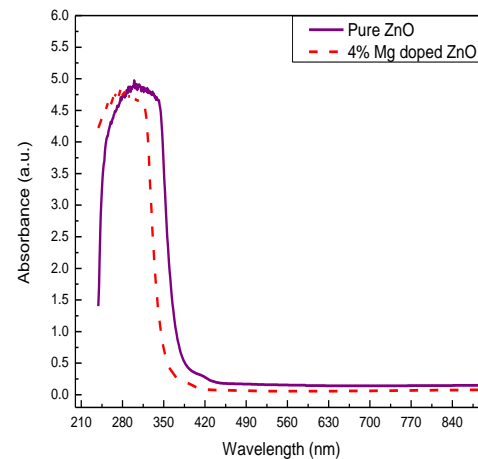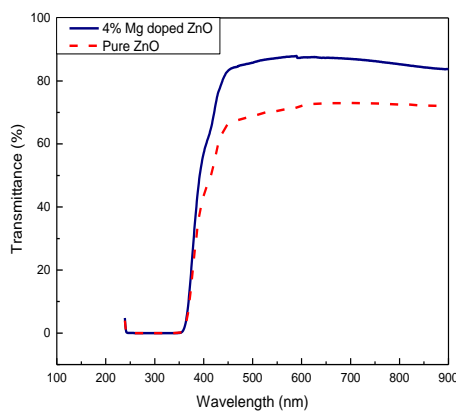


**Fig 1.** Optical transmittance spectra of ZnO NRs



**Fig.2** Graph of Absorbance vs Wavelength

The graph showed that all of the ZnO NRs that were prepared using different dopping exhibited strong excitonic absorption peaks at 300 nm. These peaks indicated that the grown ZnO NRs possessed good optical quality good exciton binding energy. Here we o find value of band gap  by usually use the Tauc relation by plotting a graph between $(\alpha h\nu)^n$  versus (hν).Here The absorption coefficient (α) for the direct transition of the ZnO NRs was studied using Equation

**absorption coefficient  (α) = 2.303 A / t**

where (A) is absorbance  and (t) is thickness of thin film.

while  *(hν)* is the photon energy, where

**hν(eV) = 1240 / incident wavelength (nm)**

The optical bandgap $(\alpha h\nu)^2$ dependence on the absorption coefficient (α) over the energy range of 3 to 3.5 eV at RT was calculated, where the line intercept with   **X** axis which shows photon energy as showed in below figure (3),
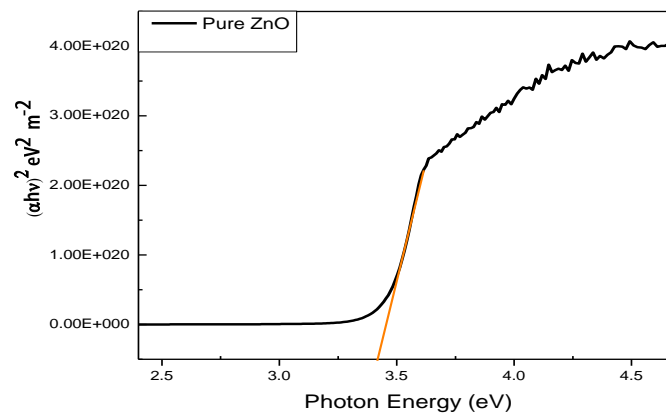


**Fig.3 (a**) For  Pure ZnO
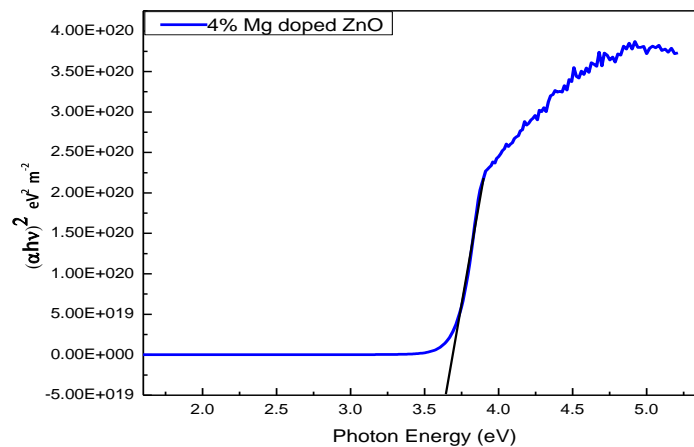


**Fig.3 (b**) For 4% Mg doped ZnO
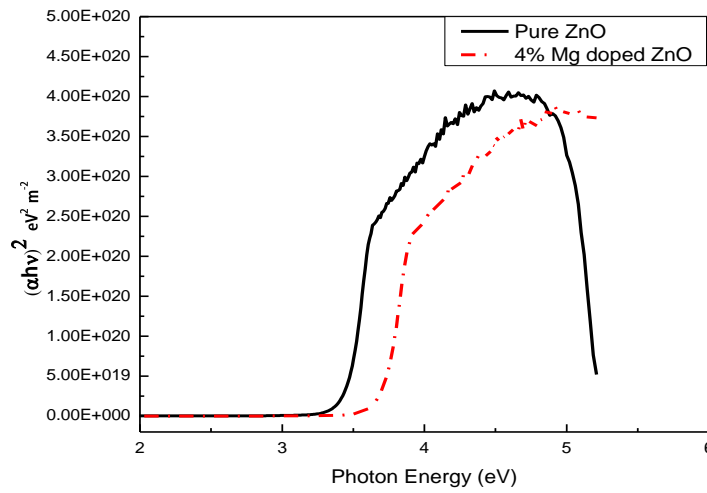
**Fig.3 (c)**

## AFM DATA
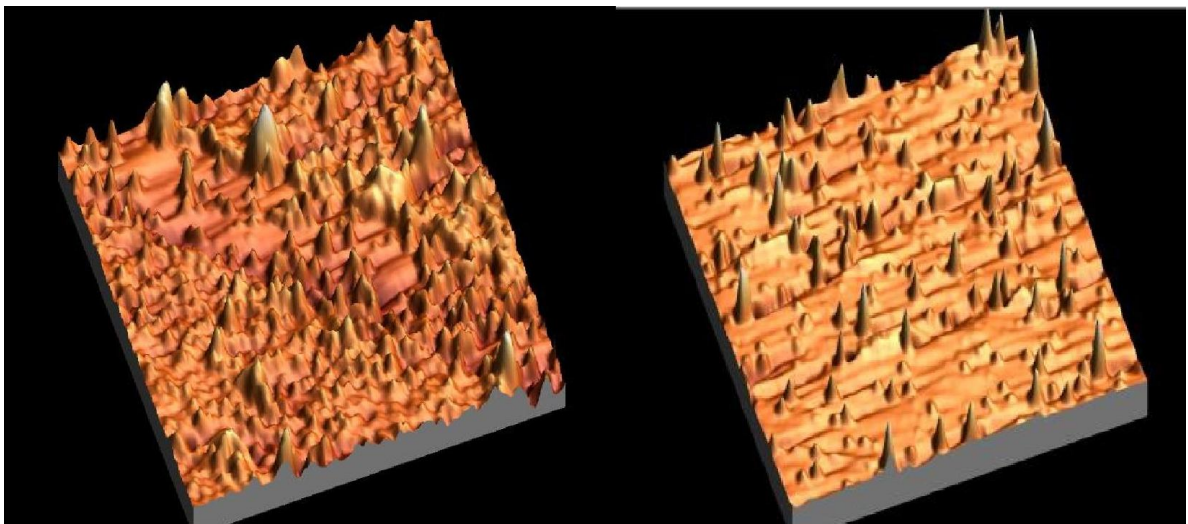


### 5.3 Observations:

| % of Mg doped in ZnO | Band gap (eV) |
|:---:|:---:|
| 0% | 3.4121 |
| 4% | 3.6469 |

## ACKNOWLEDGEMENT

## References:

1.  Y. T. Yin, W. X. Que, C. H. Kam, J Sol-Gel Sci Technol (2010) 53:605–612.
2.  Z.Q. Ma, W.G. Zhao, Y. Wang, Thin Solid Films 515 (2007) 8611–8614.
3.  Dongxu Zhao, Yichun Liu, Dezhen Shen, Youming Lu, Jiying Zhang, Xiwu Fan, Journal of Growth 234 (2002) 427–430.
4.  M. Sahal, B.Hartiti, A.Ridah, M.Mollar, B.Marı´, Microelectronics Journal 39 (2008) 1425–1428.
5.  Masashi Ohyama, Hiromitsu Kozuka, Toshinobu Yoko, Thin Solid Films 306 (1997) 78-85.
6.  J. Liu, H. Xia, D. Xue, L. Lu, J. Am. Chem. Soc. 131 (2009) 12086.
7.  C. Yan, D. Xue, Adv. Mater. 20 (2008) 1055.
8.  H. Xia, W. Xiao, M.O. Lai, L. Lu, Funct. Mater. Lett. 2 (2009) 13.
9.  T.H. Fang, S.H. Kang, J. Phys. D: Appl. Phys. 41 (2008) 245303.
10. Anna Og. Dikovska, P.A. Atanasov, A.Ts. Andreev, B.S. Zafirova, E.I. Karakoleva, T.R. Stoyanchov, Appl. Surf. Sci. 254 (2007) 1087.
11. D.X. Jiang, L. Cao, W. Liu, G. Su, H. Qu, Y.G. Sun, B.H. Dong, Nanoscale Res. Lett. 4 (2009)
12. D.K. Hwang, M.C. Jeong, J.M. Myoung, Appl. Surf. Sci. 225 (2004) 217.
13. Investigation on the properties of pure and doped nanocrystalline ZnO films,Ali Fatima A, December, 2011
14. Tang H, Prasad K, Sanjines R, Schmid PE, Le´vy F (1994) J Appl Phys 75:2042
15. Akl AA, Kamal H, Abdel-Hady K (2006) Appl Surf Sci 252:8651
16. Fan  X, Yu T, Zhang L, Chen X, Zou Z (2007) J Chem Phys  20:73347

# Infrared spectra of ternary complexes using benzidine and quinoline as donors

Ashok N. Patel[1*],  G. K. Solanki[2,], Ajay T. Oza[2]

[1]Sheth M.N. Science College, Hemchandracharya North Gujarat University, Patan-384 265, Gujarat, India

[2]Department of Physics, Sardar Patel University, Vallabh Vidyanagar- 388 120, Gujarat, India

[*]Correspondence: patelashok_patan@yahoo.co.in

**Abstract:** The charge transfer complexes of ternary type are prepared using benzidine and quinoline as donor molecules and studied with FTIR spectroscopy. Direct interband transitions are found around 0.22 eV except TCNE complex. The lower absorption edge is found to be of indirect type. TCNQ and chloranil complexes show half- power beta density and DDQ and TCNE complexes show triangular distributions. Only iodine complex shows Gaussian distribution. The low frequency background absorption is Gaussian distributed in TCNQ, chloranil and iodine complexes. Only TCNE complex shows a square power beta density. Iodine complex has highest conductivity with a range of free-carrier absorption.

**Keywords:** Infrared, ternary complexes, beta density, Gaussian distribution, nature of transition

**Introduction**

The earlier studies on ternary organic CT complexes included doped $(TMTSF)_2$ $ClO_4$, alkyl-ammonium donors with TCNQ-iodine, pyrene-TCNQ-ferrocene, substituted anthraquinone complexes and others [1-6]. $(TMPD)_{1.5}$ –$KI$-$I_2$ and $(TMPD)_{1.5}$ –$HI$-$I_2$ can be also considered as ternary systems [7]. There are two types of ternary systems. (1) one-donor and two-acceptor based systems which include, $K$-$(BEDT$-$TTF)_2$ $Cu[(CN)_2]NX$ where $X=Cl$, $Br$, $I$, $(C_1$-$TET$-$TTF)(FeBr_4)_{1-x}$ $Fecl_4)_x$ etc. [8-15] some of which were organic superconductors. (2) Two-donors and one acceptor based systems including $\alpha$-$(BEDT$-$TTF)_2MHg(SCN)_4$ where $M=K,NH_4$, $\alpha$-$(BEDT$-$TTF)_2RbZn(SCN)_4$ and $\beta$-$(CH_3)_4AS[Pd(dmit)_2]$ [16-23],   some of which were also superconducting. Ternary charge transfer complexes and radical-ion salts possess unique physical properties which are absent in binary (bimolecular) complexes. These properties include two-band transport, incommensurate to commensurate transition, alloy properties, cooperative and competitive  binding, more than two oscillator models or three absorption

envelopes, complex-salt character, superconduction and electron-exciton interactions. In the present work, we report CT complexes of benzidine-quinoline-$(TCNQ)_2$ , benzidine-quinoline-$(TCNE)_2$, benzidine-quinoline-$(chloranil)_2$, benzidine-quinoline-$(DDQ)_2$ and benzidine-quinoline-$(I_2)_2$ all in 1:1:2 molecular weight proportions.

**Experimental**

The donor benzidine was grinded with acceptors like TCNQ(7,7,8,8-tetra-cyano-p-quinodimethane), TCNE(N,N,N′,N′-tetracyano-p-ethylene), chloranil (2,3,5,6-tetrachloro-p-benzoquinone), DDQ(2,3-dichloro-5,6-dicyano-p-benzoquinone) and iodine in 1:2 molecular weight proportions. The liquid donor quinoline was added with the help of micropipette in a few drops needed in molecular weight proportions to form 1: 1:2 ternary complexes. The infrared spectra were recorded using a standard Perkin-Elmer spectra-photometer on the KBr-based semi-transparent pellets of all the five ternary complexes.

**Results and discussion**

The first is the infrared spectrum of benzidine-quinoline-$(TCNQ)_2$ which is shown here (Figure 1a). This spectrum can be divided in to three parts according to background absorption governed by electronic absorption. The first range is the 1700-3600 $cm^{-1}$ where a very broad half-power beta density distribution is observed given by

$$\alpha=\alpha_0 E^{*1/2}(1-E^*)^{1/2} \tag{1}$$

where $E^* = (E-a)/b$ is the reduced, dimensionless energy variable.

But difference in the spectrum between this and that of benzidine-pyridine-$(TCNQ)_2$ reported recently is in the splitting of the above distribution at 2317 $cm^{-1}$ by a dispersion shape of $\varepsilon_1(\omega)$ the real part of dielectric constant. Because of this splitting the distribution becomes asymmetric below 2317 $cm^{-1}$. The second range 1700-2170 $cm^{-1}$ correspond more to a transition across the usual band gap around 1700 $cm^{-1}$, rather than being a part of beta density. This splitting and asymmetry arise from stronger interaction between quinoline and TCNQ than pyridine-TCNQ interaction. The third part is below 1700 $cm^{-1}$ down to 500 $cm^{-1}$. This range consists of a very broad symmetric Gaussian band around 1100 $cm^{-1}$. There are no two envelopes below 1700 $cm^{-1}$. This also is a consequence of strong interaction between quinoline and TCNQ.

The second spectrum is that of benzidine-quinoline-$(DDQ)_2$ (Figure 1b). Here too, the spectrums can be divided in three main parts. The first range is above 1800 $cm^{-1}$ where a very large triangular distribution centered around 3082 $cm^{-1}$ is observed. This is a consequence of screening

of interaction between benzidine and DDQ by quinoline. In this range, spectrum significantly differs from that of TCNQ complex. This arises from asymmetric nature of DDQ molecule leading to more electronic molecular polarizability. It can not be attributed to the halogen end-group interacting with donor because iodine complex shows different features in this range.

The triangular distribution can be attributed to the nesting of Fermi surface, i.e. scattering of $q=2k_F$ electrons by phonons, which remains imperfect as revealed by an symmetric distribution. Then comes the second range which contains an interband electronic transition.

The third range is below 1800 cm$^{-1}$ down to 400 cm$^{-1}$. The background absorption is a monotonic function rather than a Gaussian distribution, the later found in the TCNQ complex. The absorption decreases as the frequency (or energy) decreases. The absorption is minimum at or below 0.05eV (400 cm$^{-1}$). Thus in the both ranges spectrum differs for DDQ complex from that of the TCNQ complex. Benzidine-DDQ interaction is stronger than benzidine-TCNQ interaction. Benzidine is enable to screen strongly in the DDQ complex. There is a steep rise in transmission above 1560 cm$^{-1}$ towards the high frequency side. The absorption is minimum near 1750 cm$^{-1}$ and there is a long band-tailing towards low frequency side. This may be related with imperfect nesting leading to this feature [24]. The real part of optical conductivity $\sigma_1$ ($\omega$) and the imaginary part of dielectric  constant $\varepsilon_2$ ($\omega$) are related. If we look at the high-frequency behaviour, it is a broad dispersion shape between 3600 cm$^{-1}$ and 1750 cm$^{-1}$. The constant high frequency background above 3600 cm$^{-1}$ is extrapolated and considered to be zero level, the curve in 1750 – 3600 cm$^{-1}$ is cut to give a dispersion shape governed by $\varepsilon_1$ ($\omega$). There is anomalous dispersion in this range. It is a fluctuation in absorption around zero level and if we apply lever rule, there is no net absorption. The integration (area under the band) is almost zero in this range. The second range of absorption below 1400 cm$^{-1}$ mainly consists of absorption across a very small band gap ($E_g < 0.05$ eV). These transitions coupled two bands through a Gaussian distribution in the TCNQ salts. The transitions are hindered in TCNQ complex while the transitions occur without being screened in the DDQ complex. In both of TCNQ and DDQ complexes, the lowest-lying envelope around 750 cm$^{-1}$ is not observed because it merges in the mid-IR envelope.

The third spectrum is that of benzidine-quinoline-(chloranil)$_2$ (Figure 2a). In this case, three envelopes are observed because of lack of delocalization due to screening effect. Benzidine-chloranil binary complex is weaker in interaction than benzidine-DDQ binary complex. As  a result, the interaction is screened by quinoline molecules. The highest-lying half power beta density envelope is somewhat similar to the one found in the TCNQ complex but somewhat

asymmetric rather than symmetric with more absorption on high-frequency side. This is between 1800 $cm^{-1}$ and 3600 $cm^{-1}$. The mid-IR envelope between 1000 $cm^{-1}$ and 1800 $cm^{-1}$ is also a flat beta density peak following a half-power law as given by equation 1. In this case, sharp bands are neglected and either background is considered or inflexion points of the spikes are joined. The lowest lying Gaussian-shaped envelope around 750 $cm^{-1}$ is clearly seen. Thus the spectrum is similar to that of benzidine-pyridine-(chloranil)$_2$.

The next is the IR spectrum of benzidine-quinoline-(TCNE)$_2$ (Figure 2b). The interaction is stronger than in the chloranil complex. The high-frequency envelop above 1800 $cm^{-1}$ is a triangular envelope associated with imperfect nesting as observed in the DDQ complex. This similarity reveals that this special spectral feature arises out of molecular polarizability of TCNE. TCNE does not contain aromatic ring as in TCNQ but contains C=C bridge. The four cyano-groups are more flexible and rotatable in three-dimensions leading to orientational polarizability. These rotations are hindered by the charge cloud of aromatic ring in TCNQ.

The mid-IR envelope between 950$cm^{-1}$ and 1800 $cm^{-1}$ is highly asymmetric with low-frequency tailing as compared to the envelope of chloranil complex. The lowest-lying envelope between 400 $cm^{-1}$ and 900 $cm^{-1}$ shows with square power beta density asymmetric distribution compared to that in the case of chloranil complex.

Thus there are two triangular distributions around 3000 $cm^-$ and 1400 $cm^{-1}$. The one at higher frequency is due to nesting of Fermi surface and the other at lower frequency is due to triangular interband gap connected with slant band edges in internal electric field. The later is related with tunneling of charge carriers.

The last spectrum of benzidine-quinoline-(iodine)$_2$ is also shown (Figure 2c). This spectrum is similar to its pyridine analog above 1700 $cm^{-1}$. The range below 1700 $cm^{-1}$ consists of a large number of absorption bands but leaving a scope for the background absorption which increases as the frequency decreases. This may correspond to a negative band gap as in semi-metals or free-carrier absorption above a very small band gap lying in far-infrared range. Also there is a possibility of a transition to an impurity level [25].

There is almost a semicircular distribution related with either isotropically disordered and positively charged quinoline molecules or disordered molecular iodine in this ternary complex. There is a small range of free carrier absorption between 1400 $cm^{-1}$ and 1600 $cm^{-1}$. This is realized by increase in absorption with an increase in wavelength of EM waves.

The beta density distribution is the fitted for the TCNQ complex having the highest-frequency envelope of this type. The plot of $F/(1-k^*)^{1/2}$ vs $k^{*1/2}$ where $F=\alpha-\alpha_0$ and $K^*=(K-a)/b$ is a straight

line indicating half-power beta density based on Bernoulli trials (Figure 3a). The broad lower frequency envelope is fitted a Gaussian distribution (Figure 3b) described by

$$A = A_0 \exp\left( \frac{\left(K - K_0\right)^2}{2M_2} \right) \qquad (2)$$

where $A_0$ is the maximum absorption, $K_0$ is the central wave-number and $M_2$ is the second moment of the distribution. This last parameter is related with the full-width at half-maximum W according to

$$M_2 = \frac{W^2}{8\ln 2} \qquad (3)$$

W is in turn related with electron-phonon coupling constant. Strong electron-intermolecular vibration coupling in TCNQ complex leads to very broad Gaussian band spanning more than half-IR-range and leads to a merging of central envelope and lowest-lying envelope associated with rocking and wagging vibrations. The part of the profile lying above the 2170 cm$^{-1}$ split, is fitted for a nature of transition. This transition is found to be allowed direct type (Figure 3 c), not involving any phonon.

Next is the analysis of spectrum of benzidine-quinoline-(DDQ)$_2$. The analysis indicates that the higher transition across the gap of about 0.2 eV is forbidden direct and the lower transition across the gap of nearly 0.05 eV is indirect and forbidden type. The lower band gap can be assigned to the quinoline- DDQ interaction because it is not found in the spectrum of binary benzidine-DDQ system. This analysis is shown  (Figure 4a and 4b)

These graphs reveal direct  exciton band around 0.25 eV and involvement of phonon of energy 0.01 eV, in the cases of a forbidden direct transition and forbidden indirect transition, respectively. In the later case the break  between phonon absorption and phonon emission is found at 0.15 eV.

Similar analysis of the nature of transition for the chloranil complex  is also carried out (Figure 5a) having indirect exciton. An allowed direct transition is evident. The high-frequency and mid-IR envelopes are both beta distribution with half-power beta densities   (Figure 5b and 5c). The lowest-frequency envelope is analyzed to be Gaussian curve (Figure 5d).

Thus there is an allowed direct transition with a break due to indirect exciton at 0.245 eV and exciton threshold at 0.225 eV. The Gaussian envelope  has maximum absorption , central wavenumber and full-width at half maximum (FWHM) as noted in Table 2.

More strongly interacting TCNE-based ternary complex shows two band gaps of 0.2 eV and 0.1 eV with corresponding forbidden indirect and allowed indirect transitions, respectively (Figure 6a and b). Thus TCNE complexes are small band gap semiconductor-phonon

The higher edge at 0.21 eV shows a break in $(\alpha h\nu)^{1/3}$ Vs $h\nu$ (eV) transition involving a phonon of energy of 0.02 eV. The  TCNE complex also  shows a square power beta density in the IR spectrum around 700 cm$^{-1}$. The analysis of the last spectrum of benzidine-quinoline-(iodine)$_2$ complex reveals an allowed direct transition (Figure 7a) and two Gaussian envelopes (Figure 7b and 7c).

The plot of allowed direct transition shows a direct exciton of energy of 0.24 eV. There are two Gaussians whose parameters are tabulated in table 2. The analysis of free-carrier absorption  is made by plotting $\log\alpha$ Vs $\log\lambda$ giving a slope of 2-5 which  corresponding to scattering of charge carriers by phonons.

Details of upper and lower absorption edges and both absorption envelopes are summarized (Table 1)


**Conclusion**

The three out of five ternary complexes based on TCNQ, DDQ and iodine show unusual spectral features which are making use of benzidine-quinoline combination. The TCNQ complex shows merging of two lower envelopes with unusually broad Gaussian band DDQ complex shows two triangular distributions related with imperfect nesting and the second due to one Franz-Keldy effect. TCNE and chloranil show three envelopes related with three band model. Iodine complex seems to be having highest conductivity because of negative band gap or free-carrier absorption.

**References**

[1]    C. Coulon, S. Flandrois, P. Delhaes, C. Hauw, P. Dupis, Phys. Rev. B, 1981, 23, 2850.

[2]    C. Coulon, P. Delhaes, J. Amiell, J. P. Monceau, L. M. Fabre, L. Giral, J. Physique (France), 1982, 43, 1721.

[3]    Andre Barraud, Pierre Lasieur, Annie Ruaudel-Teixier, Michel Van Devyer, Thin Solid Filam, 1995, 134, 195.

[4]    M. G. Abd El Wahed, S. Aaly, H. A. Hammad, S. M. Metwally,  J. Phys. Chem. Solids, 1974, 55, 31.

[5]    K. Kudo, M. Nagqoka, S. Kuniyoshi, H. Tanaka, Synthetic Metals, 1995, 71, 2059.

[6]    Jeong-Woo Choi, Gun-Yung Jung, Se Young Oh, Won Hong Lee, Dong Myung Shin, Thin Solid Films, 1996, 284-285, 876.

[7]     A.T. Oza, Solid State Commun., 1989, 71, 1005.

[8]     J. Wosnitza, H. Elsinger, J. Hagel, S. Wanka, D. Schweizer, Synthetic Metals, 2001, 120, 705.

[9]     J. J. McGuire, T. Room, A. Pronin, T. Timusk, J. A. Sch-Wieter, M. E. Kelly, M. A. Kini, Phys. Rev. B, 2001, 64, 094503.

[10]    S. Kamiya, Y. Shimojo, M. A. Tanatar, T. Ishiguro, H. Yamohi, G. Saito, Phys. Rev. B, 2002, 65, 13410.

[11]    K. D. Truong, S. Jandl, M. Poirier, Synthetic Metals, 2002, 130, 229.

[12]    Akane Sato, Hiroki Ahutsu, Kazuya Saito, Michio Sorai, Synthetic Metals, 2001, 120, 1035.

[13]    A. Paoneli, A. Girlando,  A. Fortuneli, Phys. Rev. B, 2001, 64, 054509.

[14]    M. A. Tanatar, S. Kagoshima, T. Ishiguro, H. Ito, V. S. Yefanov, V. A. Bonderenko, N. D. Kushah, E. B. Yagubskii, Phys. Rev. B, 2000, 62, 15561.

[15]    M. Enomoto, A. Miyazaki, T. Enoki, Synthetic Metals, 2001, 121, 1800.

[16]    D. Andres, M.V. Kartsovnite, W. Biberacher, H. Weiss, E. Balthes, H. Muler, N. Kulshch, Phys. Rev. B, 2001, 64, 161104.

[17]    N. Harrison, C.H. Mielke, A.D. Christianion, J.S. Brooks, M. Tokumoto, Phys. Rev. Letters, 2001, 86, 1586.

[18]    N. Harrison, L. Balicas, J.S. Brooks, M. Tokumoto, Phys. Rev. B, 2000, 62, 14212.

[19]    M. Maesato, Y. Kaga, R. Kondo,  S. Kagoshima, Phys. Rev. B., 2001, 64, 155104.

[20]    M. Maesato, Y. Kaga, R. Kondo, H. Hirai, S. Kagoshima, Synthetic Metals, 2001, 120, 941.

[21]    Y. Shimajo, T. Ishiguro, H. Yamochi, G. Saito, Synthetic Metals, 2001, 120, 751.

[22]    N. L. Wang, H. Mori,  S. Tanaka, J. Dong, B.P. Claymany,  J. Phys. Condens. Matter, 2001, 13, 5463.

[23]    Reizo Kato, Naoya Tajima, Masafumi Tamura,  Jun-Ichi Yamaura, Phys. Rev. B, 2002, 66, 020508.

[24]    Balazs Dora, Kazumi Maki, Attila Virosztek, Phys. Rev. B, 2002, 266, 15116.

[25]    J.I. Pankove; Optical processes in semiconductors, Eglewood Cliffs, Prentice – Hall Inc., New Jercy, 1971.

**Table 1.** **Infrared absorption edges for the ternary complexes based on benzidine quinoline combination.**

| Name of the complex | Upper edge | | | Lower edge | | |
| --- | --- | --- | --- | --- | --- | --- |
| | Absorption function | Type of transition | Band gap $E_g$ (eV) | Absorption function | Type of transition | Band gap $E_g$ (eV) |
| Benzidine-quinoline-$(TCNQ)_2$ | $\alpha h\nu = A(h\nu - E_g)^{1/2}$ | Allowed direct | 0.22 | — | — | — |
| Benzidine-quinoline-$(DDQ)_2$ | $\alpha h\nu = A(h\nu - E_g)^{3/2}$ Direct exciton 0.25 eV $E_p = 0.01$ | Forbidden direct | 0.18 | $\alpha h\nu = A(h\nu - E_g)^3$ Phonon $E_p = 0.01$ eV | Forbidden indirect | 0.006 |
| Benzidine-quinoline-$(chloranil)_2$ | $\alpha h\nu = A(h\nu - E_g)^{1/2}$ Indirect exciton 0.23eV | Allowed direct | 0.22 | — | — | — |
| Benzidine-quinoline-$(TCNE)_2$ | $\alpha h\nu = A(h\nu - E_g)^3$ Phonon 0.02 eV | Forbidden indirect | 0.21 | $\alpha h\nu = A(h\nu - E_g)^2$ | Allowed indirect | 0.11 |
| Benzidine-quinoline-$(I_2)_2$ | $\alpha h\nu = A(h\nu - E_g)^{1/2}$ Direct exciton 0.16 eV | Allowed direct | 0.21 | — | — | — |

**Table 2. Types and parameters of electronic absorption envelopes in the spectra of ternary complexes based on benzidine-quinoline combination.**

| Name of the complex | First envelope | | | Second envelope | | |
|---|---|---|---|---|---|---|
| | $K_o$ (cm$^{-1}$) | $\delta K$ (cm$^{-1}$) | $\alpha_m$ % | $K_o$ (cm$^{-1}$) | $\delta K$ (cm$^{-1}$) | $\alpha_m$ % |
| Benzidine-quinoline-(TCNQ)$_2$ | 2800   1300   30% (Half power-Beta density) And NT-1 | | | 1100   1050   35% (Gaussian distribution) NT-2 | | |
| Benzidine-quinoline-(DDQ)$_2$ | 3200   1100   50% (Triangular distribution) | | | NT-1 and 2 | | |
| Benzidine-quinoline-(chloranil)$_2$ | 2800   1700   20% (Half-power beta density)  1400   800   16% (Half power beta density) | | | 770   600   16% (Gaussian distribution) | | |
| Benzidine-quinoline-(TCNE)$_2$ | 3200   1200   65% (Triangular distribution) 1450   500   60 (TD) | | | SPBD 650   250   35 | | |
| -Benzidine-quinoline-(Iodine)$_2$ | 2800   1700   25% (Gaussian distributions) Or CD | | | 850   800   20% (Gaussian distribution) | | |

**Figure 1.** Infrared spectra of

    (a)    benzidine-quinoline-(TCNQ)$_2$ and

    (b)    benzidine-quinoline-(DDQ)$_2$.

**Figure 2.**     Infrared spectra of

(a) benzidine-quinoline-(chloranil)$_2$

(b) benzidine-quinoline-(TCNE)$_2$ and

(c) benzidine-quinoline-(iodine)$_2$.

**Figure 3.**  (a) Beta density fit

(b) Gaussian fit and

(c) Nature of transition above 0.2 eV gap

– all of the TCNQ complex.

**Figure 4.**   (a) Nature of transition above 0.2 eV gap and

(b) nature of transition above 0.05 eV gap.

Figure 5.    (a) Nature of transition above 0.225 eV gap with indirect exciton
(b) beta density peak
(c) second beta density peak and
(d) Gaussian band analysis.
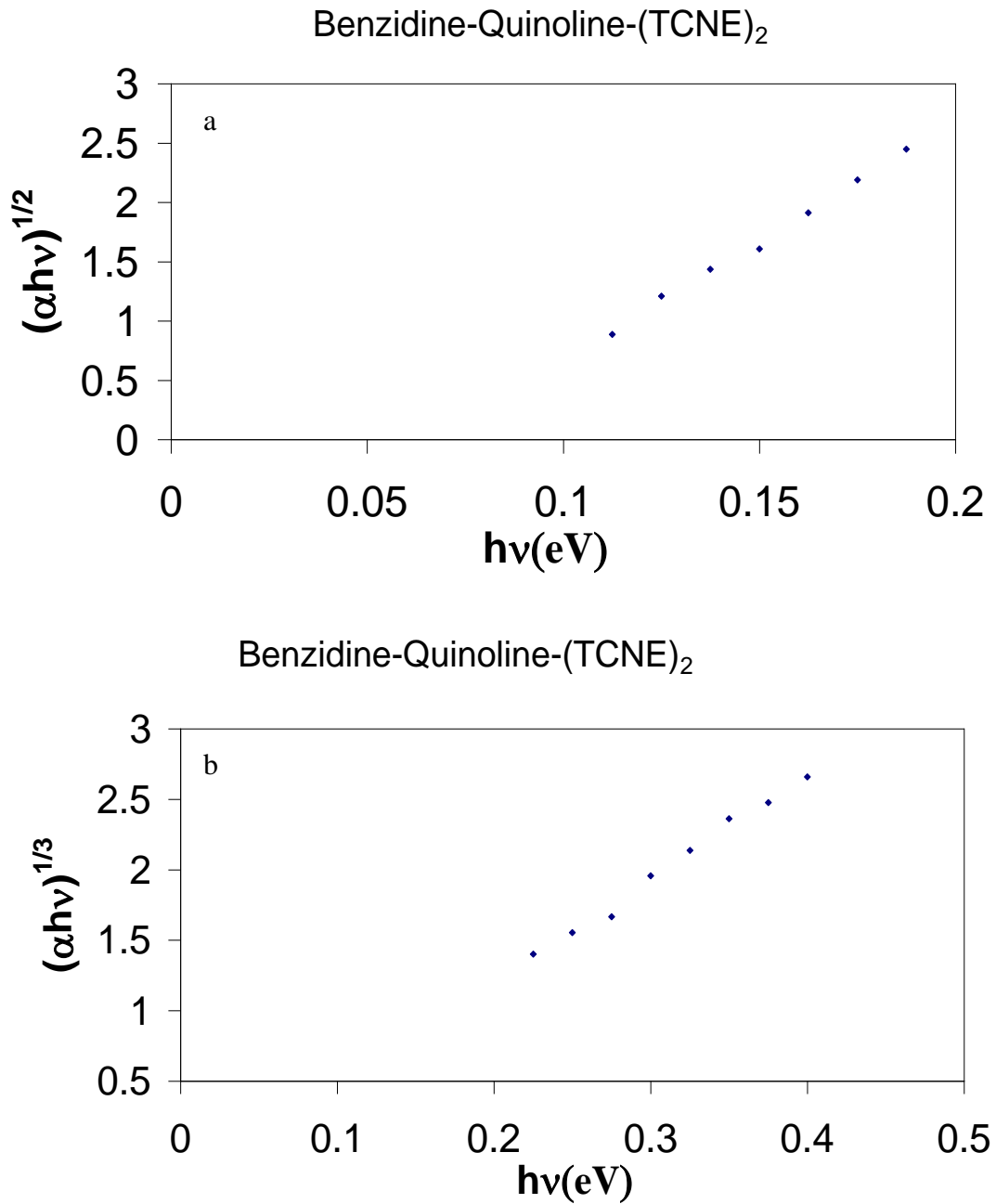
**Figure 6.** (a) nature of transition above 0.1 eV gap and
(b) nature of transition above 0.2 eV gap.
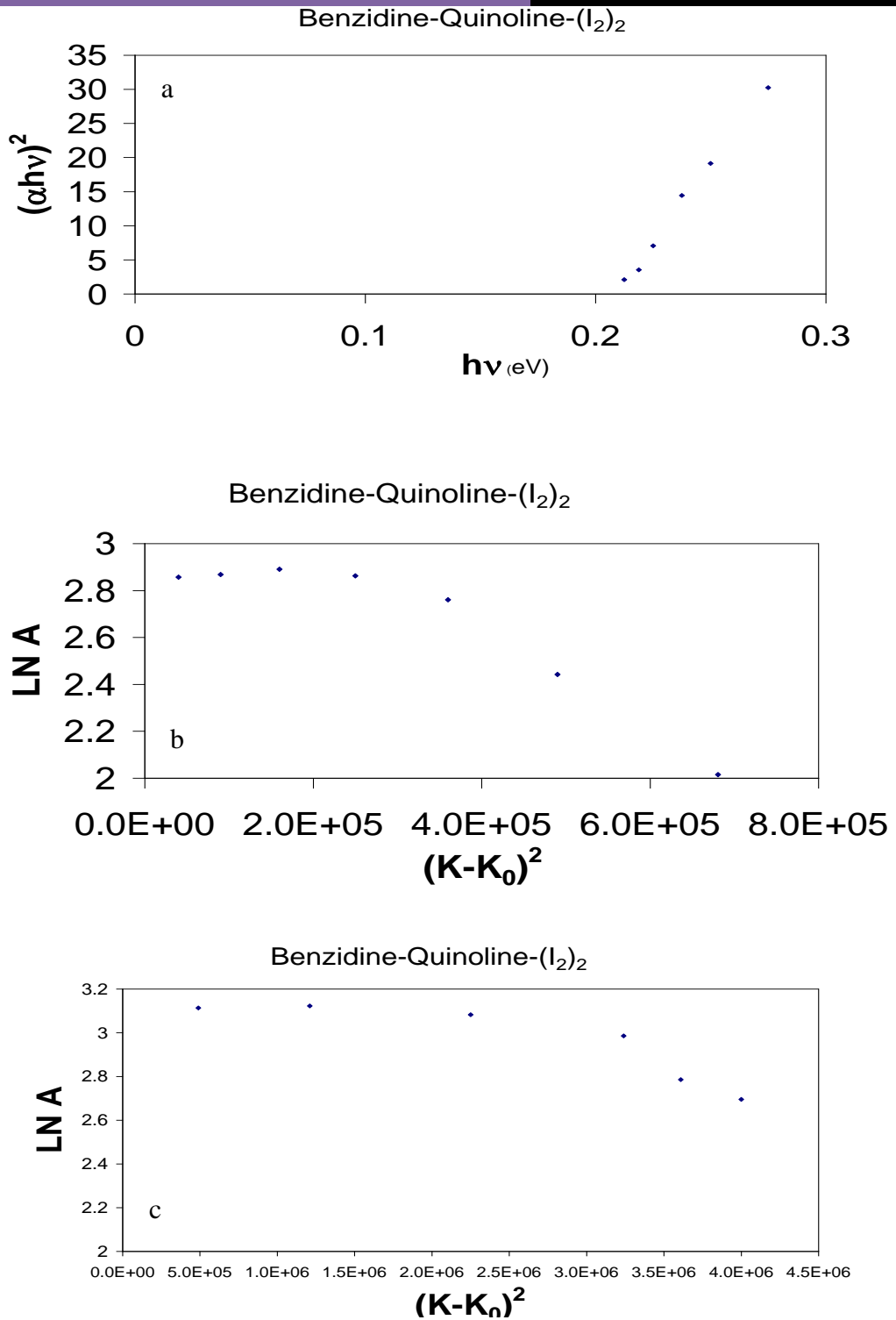
**Figure 7.**    (a) Nature of transition above 0.21 eV gap

(b) The first Gaussian peak and

(c) The second Gaussian peak.

# Growth characterization and Studies of some Mixed Tartrate single crystal

**Sanjay B.Kansara[1], Tarun J.Patel , Ram N.Nandaniya[1], Girish L.Vekaria[2]**

*1. Shri P.H.G.Muni.Arts And Science College Kalol*

*2. Sir P.T.Science College Modasa.*

sankansara35@yahoo.in

## Abstract

There are many applications of different tartrate compounds. In present study Strontium-Manganese Mixed Tartrate Crystals were grown by sol gel growth technique in silica hydro-gel medium. The test tubes were used as crystallization vessels while silica gel as a growth media. The optimum growth conditions for crystals were determined. Optimum conditions were established by varying various parameters such as pH, concentration gel solution, setting time of the gel solution and concentration of the reactance. These crystals were characterized by using X-ray diffraction and FTIR analysis.

Key Words:

 **Keywords**: *Crystal Growth, Sol-gel preparation, XRD, FT-IR*

## 1. INTRODUCTION

In recent years crystals growth in gel medium has attracted the attention of many investigators [1-2]. Scientifically and technologically crystal growth and characterization have became an interesting research area in the past decades. All basic solid materials are made up of single crystals and they are backbone of the modern technology. Mainly tartrate crystals possess application as dielectric, ferroelectric and piezoelectric materials. Some tartrate compounds are used in military applications. Manganese tartrate crystals are used in chemical temperature indicators. Among the several tartrate compounds, strontium tartrate has received greater attention on account of its ferroelectric, nonlinear optical and spectral characteristics [3-5].

Currently, great attention has been devoted to the growth and characterization of pure and doped metal tartrate crystals with the aim of identifying new materials for device applications. Investigating the effect of dopants on various properties of single crystals is of great interest in the

technological point of view[1]. In the present study single crystals of pure and manganese doped strontium tartrate trihydrate crystals were grown by the gel technique and the grown crystals were characterized by carrying out  X-ray diffraction (XRD), Fourier transform infrared (FTIR) spectral. The results obtained are reported herein and discussed.

## 2 Materials and Methods

### 2.1Gel Preparation: -

Commercial sodium metasilicate is generally used for the manufacture of soap. In the present case AR grade sodium metasilicate powder is used for preparation of the gel medium. To remove the impurities 250g sodium metasilicate was dissolved in one liter of water taken in a beaker. On stirring it thoroughly, dense milky solution of sodium metasilicate was formed. It was left for a couple of days, so that heavy insoluble impurities accumulate at the bottom of the beaker. This was decanted into another beaker and filtered twice with Whatman (cat No 1001 125) filter paper of 12.5 cm diameter. Then the solution was centrifuged on MSE high-speed centrifuge unit for about half an hour at 10000 revolutions per minute. Practically all suspended impurities were got rid off, and as a result transparent golden colored solution of sodium metasilicate was obtained. This could be preserved as a stock solution for quite a long period [6-9].

### 2.2 Crystal Growth: -

The crystallization apparatus employed for the present investigation consist of glass test tubes of 25mm diameter and 140mm length. The AR grade chemicals were used to grow the crystals. One of the reagents, 1 M levo tartaric acid, was mixed with sodium metasilicate solution to prepare the gel in such a way that the pH of mixture was maintained 4.5. The specific gravity of the gel was chosen 1.04. After setting the gel, the supernatant solutions containing various amounts of SrCl2 and MnCl2 having concentrations of 1M were gently poured without disturbing the gel surfaces, in respective test tubes. The growth of crystals was completed within the period of one month [10-12].
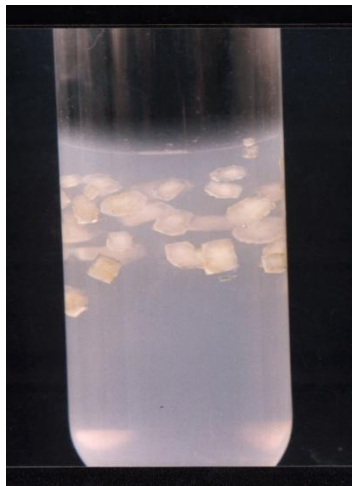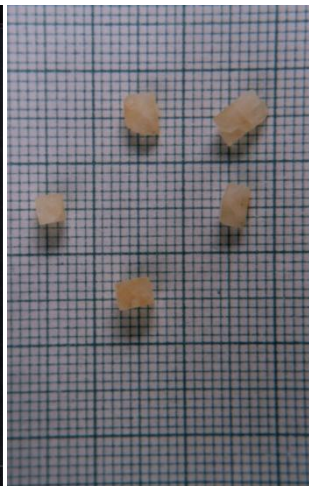
Fig 1                                   Fig 2

## 3. Characterizations

### 3.1 FTIR Spectroscopic Studies : -

The FTIR spectra of pure and mixed strontium and calcium lavo tartrate crystals as well as pure and mixed manganese and iron levo tartrate were reported. In the present investigation three different strontium and three different strontium and manganese mixed crystals, namely $Sr_{0.8}Mn_{0.2}C_4H_4O_6$ $3H_2O$, $Sr_{0.6}Mn_{0.4}C_4H_4O_6$ $3H_2O$, $Sr_{0.2}Mn_{0.8}C_4H_4O_6$ $2H_2O$, were investigation by FTIR spectroscopy.

Figure is FTIR spectra of $Sr_{0.8}Mn_{0.2}C_4H_4O_6$ $3H_2O$. The assignments of different absorption band are given in Table. From the table one can confirm the presence of water of crystallization ($\sim 3400 cm^{-1}$),C=O ($\sim 1600$ $cm^{-1}$), C-O ($\sim 1000$ cm to $12000$ $cm^{-1}$), metal oxygen ($\sim$ $<800$ $cm^{-1}$)bond. No systematic variation in the bond due to metal oxygen bond is found on increasing the contain of manganese in the crystal.

Fig 3
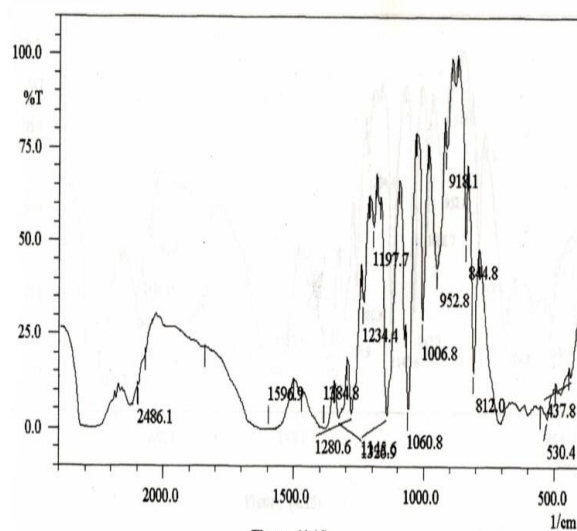


Table 1

| Wave number ($cm^{-1}$) | Assignments |
|---|---|
| 3450.0 | Broad O – H stretching due to water of crystalization |
| 1596.8 | C = O stretching |
| 1280.6 | C – O stretching |
| 1184.8 | C – O stretching |
| 1234.4 | C – O stretching |
| 1197.7 | C – O stretching |
| 1060.8 | O – H deformation out of plane and C – O stretching |
| 1006.8 | O – H deformation out of plane and C – O stretching |
| 952.8 | O – H deformation out of plane and C – O stretching |
| 918.1 | O – H deformation out of plane and C – O stretching |
| 844.8 | Metal – oxygen stretching |
| 812.0 | Metal – oxygen stretching |
| 530.4 | Metal – oxygen stretching |
| 437.8 | Metal – oxygen stretching |

**X – Ray diffraction results for $Sr_{0.8} Mn_{0.2}C_4H_4O_6$  $nH_2O$**

The present analysis the following cell parameters were taken as the standard one. An X-ray study of gel grown strontium tartrate tetra hydrate was reported by Bohandy and Murphy [15-18]. The following lattice parameter were found:

$a = 9.48  \pm 0.04$ Å

$b = 10.96 \pm 0.04$ Å

$c = 9.46  \pm 0.04$ Å

Which is orthorhombic structure. The space group was $P2_12_12_1$

For manganese tartrate crystals the following lattice parameters were reported [15].

$a =  9.4388$ (8)

$b =  11.6925$ (1)

$c =  5.0706$  (4)

Whereas, Table  gives the values of cell parameters calculated for pure and mixed strontium and manganese levo tartrate crystals.

The orthorhombicity is calculated by using the following formula,

orthorhimbicity $= [b - a / b + a] \times 100$

Where, $a$ and $b$ are the lattice parameters. The values of orthorhombicity are tabulated in table . The X-ray density $(d_x)$ is calculated by the following relation,

$d_x = 8M/N_a abc$

Where,

$M$ = Molecular weight

$N_a$ = Avogadro number

$abc$ = Cell volume

Fig.4
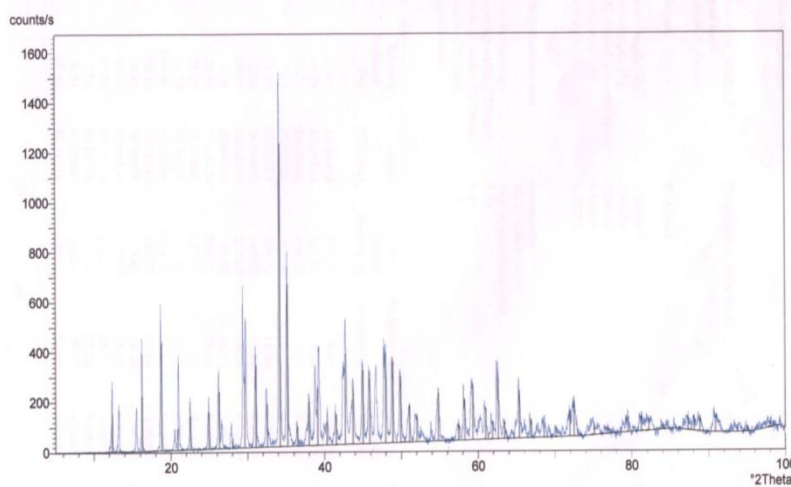


| 2 θ degrees | Relative Intensity % | $d$ (Å) | $h\,k\,l$ |
|---|---|---|---|
| 18.7880 | 35.78 | 4.7191 | 002 |
| 29.6360 | 23.45 | 3.0008 | 301 |
| 31.0786 | 26.95 | 2.8792 | 113 |
| 34.2379 | 100.00 | 2.6268 | 203 |
| 35.2160 | 53.46 | 2.5463 | 213 |
| 39.1449 | 19.09 | 2.2993 | 401 |
| 42.7101 | 29.64 | 2.1153 | 204 |
| 43.7169 | 18.27 | 2.0683 | 043 |
| 45.0288 | 24.21 | 2.0200 | 143 |
| 45.8834 | 23.54 | 1.9761 | 422 |
| 47.9509 | 29.73 | 1.8956 | 243 |
| 48.9013 | 26.78 | 1.8609 | 015 |

Table 3

| Sample | a (Å) | b (Å) | c (Å) | Cell volume (Å)$^3$ | Orthoro-hmbicity | X– ray density gm/cm$^3$ |
|---|---|---|---|---|---|---|
| $Sr_{0.8}Mn_{0.2}C_4H_4O_6$ $3H_2O$ | 9.4828 | 10.9578 | 9.4503 | 981.98 | 7.21 | 3.83 |

Table 4

The present results were compared with the results of pure and mixed calsium and strontium levo tartrate crystals as well as pure and mixed iron-managanese levo tartrate crystals.

**Result Discussion and Conclusion**

Single crystals of pure and manganese doped strontiumtartrate trihydrate have been grown successfully by the gel technique

The FTIR spectra indicate the present of water of crystallization C = O, C – O, O – H, and metal oxygen bond. The values of lattice parameters of $Sr_{0.8}Mn_{0.2}C_4H_4O_6$ $3H_2O$ corresponding to the strontium tartrate lattice parameters,
One can find a phase transition occurring in the crystal structure from XRD

**References**

[1] H.K.Henisch,J.Dennisand J. I. Hanoka, J. Phys. Chem. Solids, **26**, 493 (1965).

[2] H.K.Henisch,Crystal Growth in Gells, Pennsylvania State University Press, UniversityPark, Pennsylvania, 1970.

[3] S.M.Dharma Prakash,P.Mohan Rao Bull. Mater. Sci**. 4**, 511 (1986).

[4] M.R.Shedam,Venkateswara Rao Bull.. Mater Sci. **16**, 309 (1993).

[5] S.L.Garud,K.B. Saraf Bull. Mater. Sci. **31**, 639 (2008).

[6] Koisse, G. A.Crystal Structure Of Inorganic Compounds", Edited By Malinowski, T. I., Shteintsa Press, Kishinev, (1974) P-103 In Russian.

[7] Henisch, H. K. Dennis, J.And Hanoka, J. I.J. Phys. Chem. Solids, **26** (1965) 493.

[8] Patel, A. R. And Arrora S. K. J. Mater. Sci. , **11** (1976)843.

[9]  Patel, A. R. And Arrora S. K.J. Mater. Sci., **12**(1977)2124.

[10]   Patel A. R. And Arrora, S. K.J. Crystaql Growth, **37**(1977)343.

[11] Patel A. R. And Arrora S. K. Kryst. Technol. **13**(1978)899.

[12]  Raina K. K. J. Mater Sci. (1986)

[13]  J. Bohandy and J. c. Marphy*, Acta Cryst*, **B24** (1968) 286.

[14]  Natl. Bur. Stand (U. S.) Monogr. **25, 19, 57** (1982).

[15]  P.N. Kotru, K. K. Raina and M.L.Koul; *J. Mater. Sci*., **21** (1986) 3933.

[16] S. Joseph, H. S. Joshi and M. J. Joshi; *Cryst. Res. Technol*., **32** (1997) 110.

[17]  V.S. Joshi and M. J. Joshi; *Indian J. Phys*., **75A** (2001) 159.

[18] B. Ptaszynski, E. Skkiba, J. Krystek; *J. of Thermal Analysis and Calorimetry*,**65 (1)** (2001) 3.

# Preparation and Characterization of Activated Carbon Produced from Azadirachta indica (Neem leaf)

Parth Joshi*, Chirag Patel and  Meet Vyas

*Department of Physics, Uka Tarsadia University, Bardoli, Gujarat-394350*

*E-mail: parth4570@gmail.com*

## Abstract

Activated carbon are unique and versatile adsorbents having extended surface area, micro porous structure,  universal adsorption effect, high adsorption capacity and high degree of surface reactivity. Activated carbons were prepared from Azadirachta indica by phosphoric acid activation. The effects of activation temperature on activated carbon production were investigated. The resulting samples were characterized by nitrogen adsorption measurements at 77 K to obtain surface area and pore size distributions. The morphology of the resulting sample was studied by scanning electron microscopy. Physico-Chemical characteristics such as ash content, pH, iodine number, porosity, yield percentage and surface area have been carried out to assess the suitability of the carbon as absorbent. Results of this investigation indicate that the activated carbon prepared using Azadirachta indica impregnation process followed by activation at 900°C under nitrogen atmosphere yield activated carbon with the high surface area and more developed porosity. Activated carbon prepared from Azadirachta indica by chemical processes shows excellent improvement in the surface characteristics.

**Key words**: Activated carbon, carbonization, activation.

## 1. Introduction

Activated carbon is a form of carbon process to have small, low volume pores that increase the surface area available for adsorption or chemical reactions. Activated carbon is also known as activated charcoal. Activated carbon is a predominantly amorphous solid carbon material with highly developed internal surface area, porous structure and high degree of surface reactivity. These unique characteristic properties make activated carbon materials very

versatile adsorbent materials for adsorption of both gaseous and liquid phase pollutants. Activated carbons are useful adsorbents of industrial significance and are used in a wide range of applications which are concerned principally with removal of undesired species by adsorption from liquids or gases [1-6], in order to effect purification [7] or the recovery of chemical constituents.

Common forms are beads, granules, pellets, fibers, cloths and powder. Some typical applications are: water and wastewater treatment to remove hazardous organic compounds [8] or those that impart odor or taste [9], for natural gas storage [10] and odoriferous chemicals which are merely trapped, upgrading methane from substandard natural gas wells [11], food decolorization, and pharmaceutical purification. Impregnated activated carbons are widely used in gas masks and to remove other specific contaminants in gas or water. Impregnants include sulfuric acid [12-13] (for ammonia or mercury), iron oxide (for hydrogen sulfide or mercaptans), zinc oxide (for hydrogen cyanide) [14-15], and a combination of heavy metal salts (for phosgene, arsine, and nerve gases).

## 2. Processing of activated carbon

Activated carbon is usually derived from charcoal and is sometimes utilized as biochar. Those derived from coal and coke is referred as activated coal and activated coke respectively. Activated carbon is carbon produced from carbonaceous source materials such as nutshells, coconut husk, peat, wood, coir, lignite, coal, and petroleum pitch.

### 2.1 Raw materials

Azadirachta indica (neem leaves) were collected from Uka Tarsadia university campus was the precursor used in this study. The collected sample was washed exhaustively with deionized water to remove adhering dirt particles from the surface. Azadirachta indica (Neem leaves) were dried till it became yellow and then ground and screened to the desired mesh size of 1–2 mm.

### 2.2 Activation

The raw material produced was mixed in potassium hydroxide solution with a raw material (AI)/KOH impregnation with occasional stirring. After stirring the resultant sample was dried at room temperature for 12 hour and then the resultant sample was dried at $120^{\circ}C$ for 24 hour.

After it the sample was again dried for 6 hour and weight loss measured at every half hour. The resultant sample was washed with hot and cold distilled water until the filtrate reached to neutral pH.

## 2.3 Carbonization

The carbonization process was performed by loading 50 gm of dried KOH activated sample into a furnace, and heated up to a carbonization temperature of $800^{\circ}C$ under purified $N_2$ flow and after carbonization 10 gm of activated carbon produced.

## 3. Results and Discussion

### 3.1 Scanning electron microscopy(SEM)

Figures 3.1 show SEM micrographs of prepared activated carbon using chemical activation. These results show that on activation with KOH, enhanced the bigger pores as shown in Fig. The filled massgets highly decomposed resulting in clear pore structure. The SEM photographs of samples show a smooth surface with many orderly pores developed.
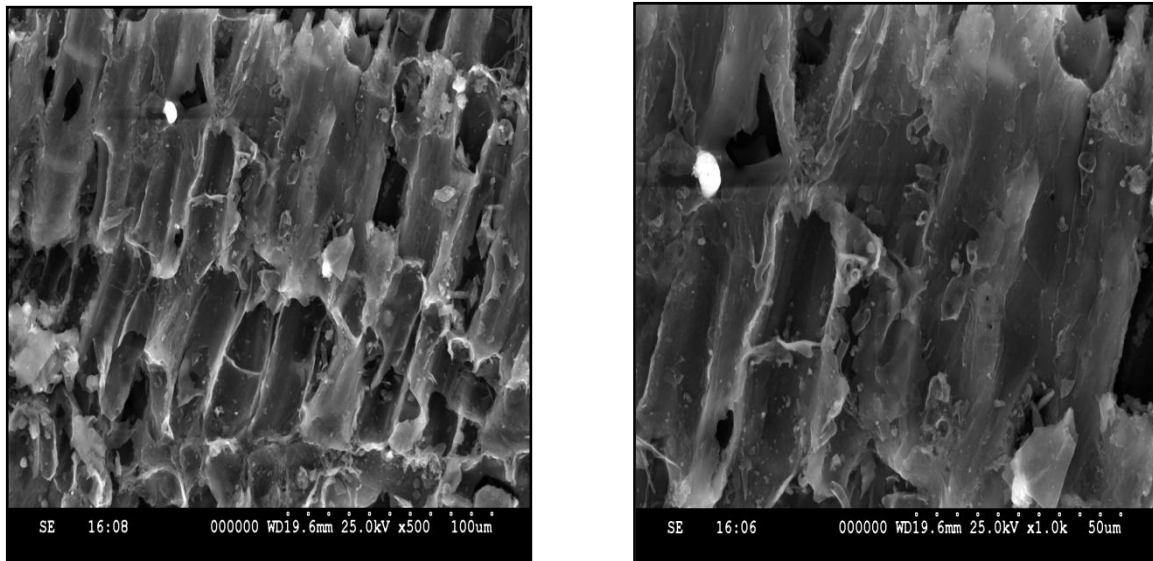


**Figure 3.1** SEM micrographs of Activated carbon produced by potassium hydroxide activation

### 3.2 Yield after Carbonization

The Carbonize yield is defined as the mass of carbonize carbon obtained per mass of raw material (Azadirachta indica). Table 3.1 shows the yields calculated for carbonize sample at 900°C.

**Table: 3.1** Yield after Carbonization

| Initial weight (gm) | After carbonization weight (gm) | Yield (%) |
|---|---|---|
| 50 | 11.52 | 23.04 % |

### 3.3 Ash content of the product

The ash content of activated carbon primarily depends on precursor material and these mineral matters are desired to be as low as possible to obtain an activated carbon of high quality. It is known that mineral content of activated carbon causes undesirable effects such as decreasing the activity and regeneration efficiency of activated carbon.

The amount of ash of activated carbons can range from 1% to 20% and the ash content of the all produced activated carbon is between these values. As shown in the table 3.2 the values of ash contents of the activated carbons are 3.24%.

**Table: 3.2** Ash content of the activated carbon from azadirachta indica

| Temperature ($^{\circ}$C) | Initial weight (gm) | After heating weight (gm) | Ash content |
|---|---|---|---|
| 700 | 5 | 0.162 | 3.24 % |

### 3.4 pH Values of Products

pH is an indicator of nature of the surface functional groups of activated carbon because, they give an idea about the presence and absence of oxygen or hydrogen containing functional groups. Also pH of the solution influences the adsorption process by changing behaviour of the adsorbate-adsorbent interactions significantly. pH of the potassium hydroxide activated carbons was found 8.5 as it can be seen Potassium hydroxide activation made these products slightly basic.

### 3.5 Surface area determination

Methylene blue method can be used as an indicator of the adsorptive capacity of activated carbons. Methylene blue method of activated carbons indicates the ability of adsorbent to adsorb on super micropores and mesopores.  Surface area by methylene blue before activation is 35 m$^2$/gm and after activation  is 650 m$^2$/gm.

### 3.6 Iodine number

Many carbons preferentially adsorb small molecules. Iodine number is the most fundamental parameter used to characterize activated carbon performance. It is a measure of activity level (higher number indicates higher degree of activation – needs citation), often represented as mg/g. It is a measure of the micropore content of the activated carbon by adsorption of iodine from solution. Iodine number is a measure of the iodine adsorbed in the pores and as such, is an indication of the pore volume available in the activated carbon of interest. The measure Iodine number of activated carbon is 754 mg/g**.**

### 4. Conclusion

The type of raw material well as the activation conditions determines the properties and yield of activated carbon. Activated carbon produced from azardicha  indica is cost effective as it easily available. The prepared activated carbon attained surface area 650 $m^2$/gm and surface area before activation was 35 $m^2$/gm. From which we conclude that surface area after activation was increased.  Prepared Activated carbon has large surface area so it will increase it adsorption capacity, and it can utilize in water purification, air purification etc. A low cost and high quality active carbon should be of high surface area, produced at low temperature. Methods of activation of carbon materials have opened up a new avenue to tune the structural, textural, morphological and surface properties of carbon materials to suit to the problem in hand.

### References

1) A. Kumar, S. Kumar and S. Kumar, Carbon, 2003, 41, 3015.

2) L. R. Radovic, I. F. Silva, J. I. Ume, J. A. Menendez and C. A. Leon Y Leon, Carbon, 1997, 35, 1339.

3) D. Mohan, K. P. Singh, S. Sinha and D. Gosh, Carbon, 2004, 42, 2409.

4) A. Bagreev, J. A. Menendez, I. Dukhno and Y. Tarasenko , Carbon, 2005, 43, 208.

5) A. A. Bagreev, W. Kuang and T. J. Bandosz, Adsorption, 2005, 11, 461.

6) K. L. Foster, R. G. Fuerman, J. Economy, S. M. Larson and M. J. Rood, Chemistry of Materials, 1992, 4, 1068.

7) W. J. Huang, C. Y. Chen and M. Y. Peng, Water SA, 2004, 30, 369.

8) D. Rajkumar, K. Palanivelu and N. Balasubramanian, J. Environ. Eng. Sci.,2005, 4, 1.

9) R. S. Juang, R. L. Tseng and F. C. Wu, Adsorption, 2001, 7, 65.

10) V. C. Menon, S. Komarneni, J. Porous Mater., 1998, 5, 43.

11) A. Herbst and P. Harting, Adsorption, 2002, 8, 111.

12) J. Guo, W. S. Xu, Y. L. Chen, A. C. Lua, J. Colloid Int. Sci., 2005, 281, 285.

13) W. Feng, S. Kwon, X. Feng, E. Borguet, R. D. Vidic and M. Asce, J. of Environ. Eng., March 2006, 292.

14) Y. Kikuchi, Q. Qian, M. Machida and H. Tatsumoto, Carbon, 2006, 44, 195.

15) M.P. Cal, B.W. Strickler, A.A. Lizzio, Carbon, 2000, 38, 1757.

# Synthesis and characterisation of some acid dyes based on 4, 4'-diamino diphenyl amine derivative and their application on various fibres

Yogesh S. Patel* and Keshav C. Patel

The Patidar Gin Science College, Bardoli-394601, Di-Surat, Gujarat, India.

* Corresponding author's email address: patelyogesh5@rediffmail.com , Mob. No. 9879267042

## Abstract

Various acid dyes have been prepared by coupling diazotized 4, 4'-diamino diphenyl amine with various acid coupling components and their dyeing performance as acid dyes has been assessed on silk, wool and nylon fibres. All the dyes gave orange to maroon shades with good to very good light fastness on each fibres. The purity of dyes was checked by thin layer chromatography. The IR spectra showed all characteristics bands and a representative dyes PMR spectra showed all the signals. The percentage dye bath exhaustion on different fibres was reasonably good and acceptable. The dyes fibres showed moderate to very good fastness to light, washing and rubbing.

## Keywords

4, 4'-diamino diphenyl amine, acid coupling components, dyeing, exhaustion, spectra.

## Introduction

Acid dyes are divided in to three group based on their difference in affinity, which is primarily a function of the molecular size [1]. Acid dyes are water soluble anionic dyes that are applied to by printing on protein fibres and by the vigorous process selected dyes may be printed on viscose from a paste containing area, other important use includes the dyeing of leather, paper, jute, straw and anodized aluminium the coloring of food and drink, drugs, cosmetics, insecticides, fertilizers, wood, stains, varnishes, ink, plastics, resins and the manufacture of toners and pigments of the lake type [2].

We wish to describe a simple and efficient protocol for the rapid preparation of acid dyes were probably originally so named because of the presence of one or more sulphonic acid or other acidic groups in the molecules. These dyes give very bright hues and have a wide range of fastness properties from very poor to very good [3, 4].

Chemically the acid dyes consist of azo [5], anthraquinone [6], azine [7], pyrazolone [8], nitro and nitroso compounds. R.S.Patel and K.C.Patel [9] have synthesised some novel acid dyes and evaluate

their dyeing application on various fibres. Moreover, various reports are available in the literature on dyeing of wool and nylon with acid dyes the reason being that, acid dyes are used on fibres with cationic sites [10].

We report here the synthesis and characterization of the dyeing properties of the acid dyes base on 4, 4'-diamino diphenyl amine. The acid dyes of the following structure were prepared.
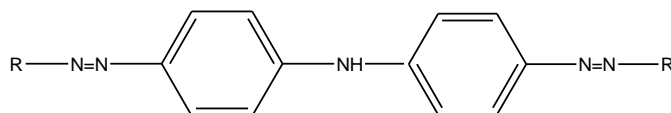


Where R = acid coupling component such as H-acid, K-acid, J-acid, T-acid, R-acid, Gamma acid, N-phenyl J-acid, Tobias acid, Bronner's acid, Chicago acid, Laurent's acid, Peri acid, Sulfotobias acid, Schaeffer's acid and Cleve acid.

**Materials and Methods**

[I] Synthesis of 4,4'-diamino diphenyl amine:

(i) Synthesis of 4,4'-dinitro diphenyl amine:

Concentrated sulphuric acid (25ml) is added to a well stirred solution of diphenyl amine (3.83gm, 0.02mole) in glacial acetic acid (20ml). The clear solution is cooled (freezing mixture of ice-salt), stirred and a mixture of concentrated nitric acid (7.5ml) and concentrated sulphuric acid (4.8ml) is added slowly through a dropping funnel. The temperature of the reaction mixture is maintained below 5-10ºC. The mixture is allowed to attain room temperature and left for 30 minutes. It is poured on to crushed ice and the mixture stirred well. The separated product is filtered, washed with cold water (until free of acid) and crystallized from alcohol, yield 80%, m.p. 222 ºC.

(ii) Synthesis of 4,4'-diamino diphenyl amine:

4,4'-dinitro diphenyl amine (5.18gm, 0.02mole) was suspended in a solution of sodium sulphide (non hydrated 14.4gm, 0.06mole) in water (75ml) was refluxed for 2 hours, yielding a deep reddish brown solution, after cooling and diluted with water (75ml) and strongly acidifying with hydrochloric acid, the solution was boiled for 20 minutes and filtered. Addition for sodium carbonate precipitated free amine. The product was crystallized from ethanol, yield 70%, m.p. 158 ºC.

[2] Diazotization of 4,4'-diamino diphenyl amine:

4,4'-diamino diphenyl amine (1.99gm, 0.01mole) was suspended in water(60ml). Hydrochloric acid (10ml) was added drop wise to this well stirred suspension. The solution was cooled to 0-5 ℃ in an ice bath. A solution of $NaNO_2$ (1.2gm) in water (8-10ml) previously cooled to 0 ℃, was the added over a period of 5 minutes with stirring. The stirring was continued for an hour; maintain the same temperature, with positive test for nitrous acid on starch iodide paper. After just destroying excess of nitrous acid with required amount of a solution of sulphamic acid, the clear diazotize solution at 0-5 ℃ obtained was use for subsequent coupling reaction.

[3] Synthesis of various acid dyes:

H-acid (6.38gm, 0.02mole) was suspended in water (20ml) and dissolved at neutral pH with sodium carbonate (10% W/V) to obtain a clear solution. The solution was cooled below 5 ℃ in an ice bath. To this well stirred solution, the above mentioned solution of diazotize was added drop wise over period of 10-15 minutes, maintaining the pH 7-8 by simultaneous addition of sodium carbonate solution (10% W/V), during coupling purple solution was formed. The stirring was continued for three hours keeping the temperature at 0-5 ℃. The reaction mixture was heated up to 60 ℃ and sodium chloride added until the colouring material was precipitated. It was stirred for an hour, filtered and washed with a small amount of sodium chloride solution (50% W/V). The solid was dried at 80-90 ℃ and extracted with DMF solvent. The dye was purified by coupling the DMF extract with excess of chloroform. A purple dye was filtered, washed with chloroform and dried at 60 ℃, yield 85%. Different acid coupling components were used to form various acid dyes.

Dyeing of Fibres:

All the dyes were applied on silk, wool and nylon fibres using the reported procedure [11,12].

Fastness Test:

Fastness to light was assessed in accordance with BS: 1006-1978. The rubbing fastness test was carried out with a crockmeter (Atlas) in accordance with AATCC-1961, and the wash fastness test in accordance with IS: 765-1979.

**Result and Discussion**

All the dyes were orange to marron in colour and obtained in excellent yield (75% to 85%). The purity of all dyes was checked by Thin Layer Chromatography [13]. The absorption spectra of all the dyes were recorded on Beckmann DB-GT grafting spectrophotometer. The characterization data of dyes are given in table-1.

Infrared Spectra:

The IR spectra of the dyes $D_1$ to $D_{15}$ were recorded on Perkin-Elmer spectrophotometer (Model 830) using KBr pellets. Dyes $D_1$ to $D_{15}$ showed characteristic band at 2810-2820 (-$CH_2$-) [14], 1650-1660 (-NH-), 1370-1380 (-N=N-), 1040-1070 (S=0) and 3420-3410 cm$^{-1}$ due to (O-H and N-H) stretching vibration.

PMR Spectra:

The PMR spectra (300MHz, $CDCl_3$) of a representative dye showed signals at 3.45 (-OH), 8.24 (-NH), 2.10 (-$CH_2$-) and 6.82-8.14 (aromatic proton).

Fastness Properties:

The percentage exhaustion, fixation and fastness propertied of dyes $D_1$ to $D_{15}$ are given in table 2 and 3. All the dyes $D_1$ to $D_{15}$ showed good affinity for silk, wool and nylon gave moderate to very good light, washing and rubbing fastness and good to very good exhaustion and fixation.

**Conclusion**

Various acid dyes based on 4, 4'- diamino diphenyl amine have been synthesized. These dye mostly orange, yellow, brown and marron shaded on silk, wool and nylon fabric having good fastness properties. The variation in the hues of the dyed fabric result from the both the nature and position of the substituent present on the coupler ring. The exhaustion and fixation of these dyes are very good; this indicates that the dyes have good affinity and solubility with the fabric. The remarkable degree of levelness after washing indicates the good penetration and affinity of these dyes to the fabric. The intrinsic conjugation in the diazo structure results in very good colour strength.

**Acknowledgements**

**Reaction Scheme:**

[1] Synthesis of 4,4'- diamino diphenyl amine:

(i) Synthesis of 4,4'- dinitro diphenyl amine:



(ii) Synthesis of 4,4'- diamino diphenyl amine:
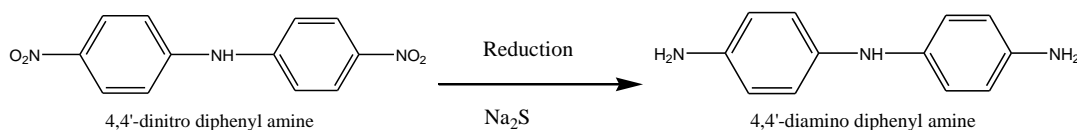


[2] Diazotization of 4,4'- diamino diphenyl amine:
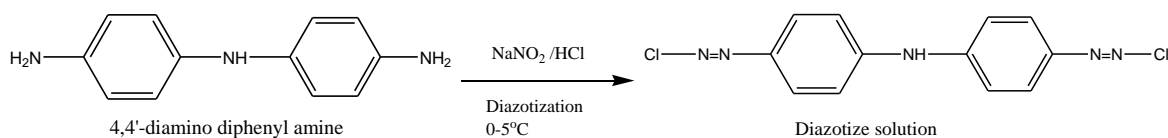


[3] Synthesis of Dyes:
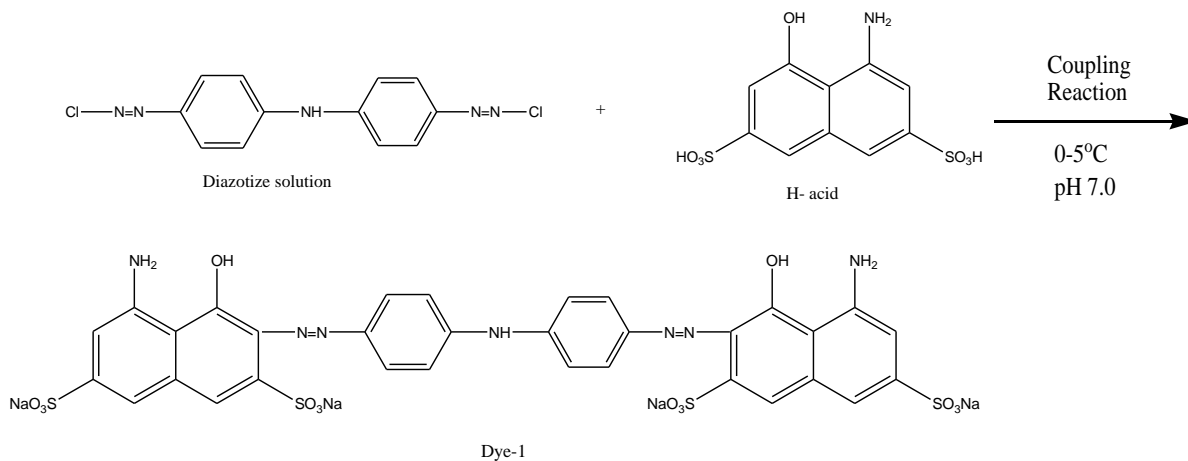
## Table-1: Characterization

| Dye No | Coupling Component | Molecular Formula | M.W. gm | Yield % | % C | | % H | | % N | | Rf Value |
|---|---|---|---|---|---|---|---|---|---|---|---|
| | | | | | Obt. | Req. | Obt. | Req. | Obt. | Req. | |
| $D_1$ | H-acid | $C_{32}H_{21}O_{14}N_7S_4Na_4$ | 947 | 85 | 40.52 | 40.54 | 2.20 | 2.21 | 10.33 | 10.34 | 0.48 |
| $D_2$ | K-acid | $C_{32}H_{21}O_{14}N_7S_4Na_4$ | 947 | 81 | 40.53 | 40.54 | 2.20 | 2.21 | 10.32 | 10.34 | 0.45 |
| $D_3$ | J-acid | $C_{32}H_{23}O_8N_7S_2Na_2$ | 743 | 88 | 51.66 | 51.68 | 3.07 | 3.09 | 13.17 | 13.18 | 0.61 |
| $D_4$ | T-acid | $C_{32}H_{19}O_{18}N_7S_6Na_6$ | 1119 | 85 | 34.30 | 34.31 | 1.67 | 1.69 | 8.74 | 8.75 | 0.46 |
| $D_5$ | R-acid | $C_{32}H_{23}O_{14}N_7S_4Na_4$ | 947 | 73 | 40.53 | 40.54 | 2.41 | 2.42 | 10.31 | 10.34 | 0.63 |
| $D_6$ | Gamma acid | $C_{32}H_{23}O_8N_7S_2Na_2$ | 743 | 81 | 51.67 | 51.68 | 3.08 | 3.09 | 13.16 | 13.18 | 0.55 |
| $D_7$ | N-phenyl J-acid | $C_{34}H_{27}O_8N_7S_2Na_2$ | 743 | 75 | 54.90 | 54.91 | 3.61 | 3.63 | 13.15 | 13.18 | 0.65 |
| $D_8$ | Tobias acid | $C_{32}H_{23}O_6N_7S_2Na_2$ | 711 | 78 | 53.98 | 54.00 | 3.21 | 3.23 | 13.77 | 13.78 | 0.51 |
| $D_9$ | Bronner's acid | $C_{32}H_{23}O_6N_7S_2Na_2$ | 711 | 77 | 53.99 | 54.00 | 3.22 | 3.23 | 13.76 | 13.78 | 0.64 |
| $D_{10}$ | Chicago acid | $C_{32}H_{23}O_8N_7S_2Na_2$ | 743 | 80 | 51.66 | 51.68 | 3.08 | 3.09 | 13.14 | 13.18 | 0.48 |
| $D_{11}$ | Laurent's acid | $C_{32}H_{23}O_6N_7S_2Na_2$ | 711 | 74 | 53.98 | 54.00 | 3.20 | 3.23 | 13.75 | 13.78 | 0.58 |
| $D_{12}$ | Peri acid | $C_{32}H_{23}O_6N_7S_2Na_2$ | 711 | 83 | 53.99 | 54.00 | 3.21 | 3.23 | 13.76 | 13.78 | 0.53 |
| $D_{13}$ | Sulfotobias acid | $C_{32}H_{23}O_6N_7S_2Na_2$ | 711 | 71 | 53.98 | 54.00 | 3.22 | 3.23 | 13.74 | 13.78 | 0.53 |
| $D_{14}$ | Schaeffer's acid | $C_{32}H_{21}O_6N_7S_2Na_2$ | 741 | 84 | 51.81 | 51.82 | 2.82 | 2.83 | 13.21 | 13.22 | 0.54 |
| $D_{15}$ | Cleve acid | $C_{32}H_{23}O_6N_7S_2Na_2$ | 711 | 82 | 53.98 | 54.00 | 3.21 | 3.23 | 13.77 | 13.78 | 0.59 |

**Table-2: Shade, Percentage, Exhaustion and Fixation of acid dyes on silk, wool and nylon fibres.**

| Dye No. | % Exhaustion | | | % Fixation | | |
|---------|------|------|-------|------|------|-------|
| | Silk | Wool | Nylon | Silk | Wool | Nylon |
| $D_1$ | 76.45 | 77.20 | 67.88 | 87.63 | 87.43 | 80.95 |
| $D_2$ | 68.35 | 74.95 | 66.75 | 79.80 | 83.52 | 84.76 |
| $D_3$ | 69.55 | 71.75 | 63.00 | 82.02 | 82.16 | 76.74 |
| $D_4$ | 72.55 | 68.75 | 62.35 | 84.83 | 80.58 | 96.74 |
| $D_5$ | 74.30 | 73.15 | 67.63 | 85.46 | 82.59 | 80.44 |
| $D_6$ | 68.85 | 75.10 | 68.25 | 80.90 | 83.95 | 73.99 |
| $D_7$ | 73.15 | 76.45 | 70.80 | 84.75 | 85.67 | 81.85 |
| $D_8$ | 69.95 | 71.00 | 70.25 | 82.41 | 80.98 | 81.70 |
| $D_9$ | 71.75 | 72.65 | 67.13 | 83.69 | 82.51 | 79.85 |
| $D_{10}$ | 75.30 | 67.00 | 69.85 | 86.32 | 78.05 | 80.95 |
| $D_{11}$ | 71.05 | 70.75 | 71.70 | 83.04 | 81.13 | 81.58 |
| $D_{12}$ | 67.78 | 68.10 | 65.70 | 79.08 | 79.88 | 78.69 |
| $D_{13}$ | 74.95 | 75.80 | 64.35 | 85.39 | 85.55 | 77.77 |
| $D_{14}$ | 72.25 | 74.05 | 66.50 | 83.73 | 83.11 | 79.32 |
| $D_{15}$ | 70.20 | 66.05 | 69.20 | 82.69 | 79.33 | 82.80 |

### Table-3: Fastness properties of acid dyes on silk, wool and nylon fibres.

| Dye No. | Light Fastness | | | Wash Fastness | | | Rubbing Fastness | | | | | |
|---------|---|---|---|---|---|---|---|---|---|---|---|---|
| | | | | | | | Dry | | | Wet | | |
| | S | W | N | S | W | N | S | W | C | S | W | N |
| $D_1$ | 5 | 3 | 6 | 4 | 3 | 5 | 3 | 3-4 | 4 | 3 | 3 | 4 |
| $D_2$ | 5-6 | 3-4 | 6 | 4-5 | 3-4 | 4-5 | 3-4 | 3 | 5 | 3-4 | 3-4 | 3-4 |
| $D_3$ | 4 | 4 | 5-6 | 4 | 4 | 4 | 4 | 3-4 | 5 | 3-4 | 3 | 3-4 |
| $D_4$ | 4-5 | 5 | 4-5 | 3 | 3-4 | 3-4 | 3 | 4 | 5 | 3 | 3-4 | 4 |
| $D_5$ | 5 | 4 | 5 | 3-4 | 4-5 | 4-5 | 3 | 3-4 | 4 | 3 | 3 | 3-4 |
| $D_6$ | 4-5 | 4-5 | 4-5 | 4 | 4 | 3-4 | 4-5 | 3 | 4 | 3-4 | 3 | 3-4 |
| $D_7$ | 6 | 5 | 5 | 5 | 3-4 | 4 | 3-4 | 3-4 | 3-4 | 3 | 4 | 4 |
| $D_8$ | 5 | 6 | 4 | 4-5 | 4 | 4 | 4 | 4 | 4-5 | 4 | 4 | 4 |
| $D_9$ | 5-6 | 4-5 | 5-6 | 3-4 | 4 | 5 | 4 | 4 | 5 | 3-4 | 3-4 | 3-4 |
| $D_{10}$ | 6 | 5-6 | 6 | 4 | 4 | 4 | 3-4 | 3-4 | 4 | 3 | 4 | 3 |
| $D_{11}$ | 5-6 | 4 | 5-6 | 3-4 | 3-4 | 4-5 | 3 | 4 | 3-4 | 3-4 | 4 | 3-4 |
| $D_{12}$ | 5 | 5 | 5 | 4 | 4-5 | 4-5 | 3-4 | 4-5 | 5 | 3 | 3-4 | 4 |
| $D_{13}$ | 4 | 4 | 4-5 | 4-5 | 4 | 4 | 3 | 5 | 4 | 3-4 | 4 | 3-4 |
| $D_{14}$ | 4 | 4 | 5 | 4 | 3-4 | 3-4 | 4 | 4-5 | 4-5 | 4 | 3-4 | 4 |
| $D_{15}$ | 4 | 4-5 | 5-6 | 4 | 4-5 | 4 | 3 | 5 | 5 | 4 | 5 | 5 |

S=Silk, W=Wool, N=Nylon

## References

[1] "Colour Index", Society of Dyes and Colourist, Bardford, 3$^{rd}$ Edn., Vol.1.

[2] "Ullmans Encyclopedia of Industrial Chemistry", 1996, 5$^{th}$ Edn., Vol. 3, 263-264.

[3] K. Peter, P. Jarmila, M. Jiri, Czech, 1991, 5, 269,163, Appl. 88/8, 254, Chem. Abstr. 1992, 116, 23753u.

[4] De Giorgi, M. Rita, "Jour. Soc. Dyer. Colo." 1993, 109, 121, 405, 10, Chem. Abstr. 1994,121, 23350y.

[5] Pual Wight (Zeneca Limited, UK); GBA PL. 1997, 97/26, 340-19, Chem. Abstr. 1999, 130, 253667u.

[6] J. F. Feeman; Ger. Offen., 2, 250, 865, "Jour. Soc. Dyer. Colo." 91, 316; Chem.  Abstr. 1973, 79, 106131q.

[7] J.F. Corbett, "Jour. Soc. Dyer. Colo." 1972, 88, 438.

[8] F. Ray Hunter, U.S. 4, 045, 425; Chem. Abstr. 1977, 87, 169245r.

[9] R.S. Patel, P.S. Patel, S.K. Patel and K.C. Patel; Oriental J. Of Chemistry, 2004, Vol. 20(2), 263-268.

[10] M.D. Koushic Uddin and H.M. Sonia, A Comparative Study on Silk Dyeing with Acid and Reactive Dye,   Int. J. Engr. and Tech., 2010, 10(6), 21-26.

[11] V.A. Shenai, Chemistry of Dyes and Principles of Dyeing; Sevak Publication, Bombay, 1973.

[12] A. Guesmi, N.B. Hamadi, N. Ladhari, F. Sakli, dyeing properties and colour fastness of wool dyed with   indicaxanthin natural dye, Industrial Crop and Products, 2012, 37, 493-499.

[13] Bernard Fried and Joseph Sharm, Thin Layer Chromatography Technique and Application, Marcel   Dekker, New York, Basel, 1982.

[14] N.B. Colthup, L.H. Daly and E.W. Stephen, Introduction of Infrared and Raman Spectroscopy, Academic  Press, New York, San Francisco, 1975.

# A COMPARATIVE STUDY ON PHOTOCATALYTIC ACTIVITY OF ZnO, ZnS AND THEIR COMPOSITE

BASANT K. MENARIYA, TARUNA DANGI, RAKSHIT AMETAAND  SURESH C. AMETA

Department of Chemistry, PAHER University, Udaipur- 313003 (Raj.) INDIA
E-mail: basant.menaria@gmail.com

## ABSTRACT

A composite of ZnO and ZnS was prepared by simple solid state mechanochemical technique and it was used as a semiconductor  for the photocatalytic degradation of Azure B. The effect of several parameters like  pH, Azure B concentration, amount of composite and  intensity of light was monitored.The optimum conditions obtained for this degradation were: Azure B $= 1.80 \times 10^{-5}$ M, pH $= 10.0$, amount of composite $= 0.10$ g and light intensity $= 60.0$ mWcm$^{-2}$. The photocatalytic efficiency of ZnO-ZnS composite was compared with pure ZnO and ZnS.. It was found that composite of  ZnO - ZnS shows better photocatalytic activity as compared with ZnO and ZnS alone for the degradation of Azure B in the presence of visible light.

**Key words:**ZnO , ZnS, Composite ,Photocatalytic activity, Azure B

## INTRODUCTION

Effluents from various industries like dyeing, textile, paper, pulp and printing industries contain pollutants such as, detergent, acids, soaps, pesticides, chemicals,  dye etc, which are the major sources of water pollution. Large scale production and extensive applications of synthetic dyes cause considerable environmental pollution. Dyes are difficult to decompose biologically and chemically.

Therefore, severaltechniques such as precipitation, flocculation, air stripping, adsorption, reverse osmosis, ultrafiltration, etc. are being used for removal of contaminants. Heterogeneous photocatalytic oxidation is an effective method to remove organic pollutant even at low concentrations. Here, semiconductor particles on excitation act as photocatalysts or short-circuited microelectrodes. Semiconductor generates electron-hole pair on excitation which may be used either for oxidation or reduction of the dye.

Photocatalysis has shown various promising applications. Vinodgopal andPrashant[1]studied degradation of azo dye by $SnO_2/TiO_2$ coupled semiconductor thin films. Preparation of $Bi_{12}TiO_{20}$ and use in photocatalytic degradation was studied by Xuet al.[2] Ungelenket al.[3]showed that nanoscale $\beta$-$Sn_{1-n}WO_4$·$n\alpha$-Sn is a highly efficient photocatalyst for degradation of organic dyes in day light and it was observed to be a real 'green' synthesis.

Kothari et al.[4] have carried out the photoreduction of malachite green using CdS as photocatalyst and ascorbic acid/EDTA as reductants. The photocatalytic degradation of crystal violet in aqueous solutions was investigated by Sahoo et al.[5] with $Ag^+$ doped $TiO_2$ under UV and simulated solar light. Kansal et al.[6] reported photocatalytic degradation of methyl orange and rhodamine 6G using several photocatalyst such as titanium dioxide, zinc oxide, stannic oxide, zinc sulphide and cadmium sulphide. A comparative photooxidative degradation of azure-B using sono-photo-Fenton and photo-Fenton reagents has been reported by Vaishnave et al.[7] and they concluded the photochemical decomposition rate of azure-B is markedly increased in the presence of ultrasound. Azure B was photocatalytically degraded by Sharma et al.[8] using NiS-ZnS composite in molar ratio 1:5. Claudia et al.[9] synthesized nanocrystals of ZnS (~3 to 5 nm diameter) with>50% product yield and reported the photocatalytic degradation of p-nitrophenol and acid orange 7. Visible light-driven degradation of methylene blue in the presence of semiconducting ZnS and CdS nanoparticles was reported by Soltani et al.[10]

Wenjiang et al.[11] prepared spherical ZnO/ZnS core/shell particles under the hydrothermal condition and studied the photocatalytic degradation of methyl orange as a probe reaction. Nuengmatcha et al.[12] studied visible light-induced photocatalytic degradation of rhodamine B and industrial dyes (texbrite BAC-L and texbrite NFW-L) in the presence of ZnO-graphene-$TiO_2$ composite. The novel zirconium oxide, nickel oxide and zinc oxide nanoparticles supported on activated carbons were successfully fabricated through microwave irradiation method by Suresh et al.[13] and used for photocatalytic degradation of textile dyeing wastewater. Lachheb et al.[14] studied photocatalytic degradation of anthraquinonic (alizarin S), azoic (crocein orange G, methyl red), Congo red, heteropolyaromatic (methylene blue) dyes in $TiO_2$/UV aqueous suspensions. Bhati et al.[15] synthesized $CeCr_2O_5$ nanoparticles by microwave method for the decolorization of yellowish orange and fast green dyes, common water effluents of textile industries. Gandhi et al.[16] degradated methylene blue using coprecipitated sulphide photocatalyst. This coprecipitated semiconductor CoS-ZnS (in 1 : 10 mole ratios) was prepared by coprecipitation and used for photodegradation of methylene blue. Daneshvar et al.[17] compared the degradation of acid red 14 in the presence and absence of UV light using photocatalyst ZnO and observed that the amount of $H_2O_2$ affect the photodegradation of dye. Devipriya and Yesodharan[18] have performed complete photocatalytic mineralization of pesticides to harmless products.

ZnO and ZnS composite was prepared using a simple mechanochemical method. The obtained nanoparticles were characterized by XRD, UV-Vis absorption spectroscopy, SEM and

EDX. The photocatalytic activity of as prepared composite was examined in the degradation of Azure B under visible light in air at room temperature and  the influence of different experimental parameters such as the ZnS-ZnS amount,  pH of the solution, dye concentration and light intensity on the rate of degradation was observed.

## EXPERIMENTAL

**Preparation of composite**

Composite of ZnO and ZnS was prepared by simple solid state mechanochemical method.Equal amount of ZnO and ZnS(1:1 ratio) was taken and then it was ground with the help of pestle and mortar. Then it was used for photocatalytic degradation of Azure B.

**Characterization of Composite**

X-rays diffraction pattern of the ZnO-ZnS composite is shown in Fig. 1. Average particle size of the crystalline composite was calculated by Debye-Scherrer's equation and it was found 87.03 nm.



**Fig. 1: XRD spectrum of composite**

The elemental composition and surface morphology were observed out by scanning electron microscope equipped with an energy dispersive X-ray spectrophotometer. The SEM image of ZnO-ZnS composite is given Fig. 2. It shows that the particles of composite have rough surface with irregular size.

Electron Image 1

EDX analysis was performed to analyze the elemental constituent of mixed ZnO – ZnSand it revealed that three elements are present in nanomaterial i.e. Zn, S and O (Fig. 3) .

**Table1: Elemental composition**

| Elements | Weight (%) | Atomic (%) |
|----------|-----------|------------|
| Zn | 67.63 | 46.41 |
| O | 16.39 | 34.40 |
| S | 15.97 | 19.18 |

**Photocatalytic degradation**

0.0305 g Azure B was dissolved in 100.0 mL of doubly distilled water so that the concentration of dye solution was $1.0 \times 10^{-3}$ M. It was used as a stock solutionand further diluted as and, when required. The absorbance of Azure B solution was observed with the help ofspectrophotometer( Systronic model 106 )  at $\lambda_{max}= 650$ nm.It was irradiated with a 200 W tungsten lamp (CEL, Model SM 201) Reaction solution was exposed to visible light.A water filter was used between light source and solution to cut off the thermal radiation.

The dye solution was divided into four beakers. These beakers were kept under four different experimental conditions and initial and final absorbances (A) were observed after 3 hrs for solution of each beaker.Control experiments were carried out, which proved that this reaction is photocatalytic in nature.

The photocatalytic degradation of Azure B dye was studied, after adding of 0.10 g of composite in 50 mL dye solution ($1.8 \times 10^{-5}$ M) at pH 10.0. A 200W tungsten lamp wasused for

irradiation (60.0 W cm$^{-2}$ light intensity). Irrdiationwas carried out in glass vessel.A solarimeter (Suryamapi CEL 201) was used for the measurement of light intensities. Water filter was usedto cut thermal effect. A digital pH meter was used to measure pH of the dye solutions.pH of the dye solutions was adjusted by addition of previously standardized 0.1 N sulphuric acid and 0.1N sodium hydroxide solution. UV-Visible spectrometer (Systronic Model 106) was used to measureabsorbance (A) of the dye solution at regular time intervals. A linear plot between plot of 1+ logA and timeshows that Azure Bdegradation follows pseudo-first order kinetics.

The rate constant was calculated with the help of given formula -

$$k = 2.303 \times slope$$

## RESULTS AND DISCUSSION

### Table 2: Atypical run

[Azure B ] = 1.80 x 10$^{-5}$ M        pH= 10.0

Amount of composite = 0.10 g     Light intensity = 60.0 mWcm$^{-2}$

| Time (min.) | Absorbance (A) | 1+log A (ZnO-ZnS) |
|---|---|---|
| 0 | 0.693 | 0.8407 |
| 5 | 0.591 | 0.7715 |
| 10 | 0.478 | 0.6794 |
| 15 | 0.391 | 0.5922 |
| 20 | 0.311 | 0.4927 |
| 25 | 0.269 | 0.4297 |
| 30 | 0.226 | 0.3541 |
| **Time (min.)** | **Absorbance (A)** | **1 + log A (ZnO-ZnS)** |
| 35 | 0.174 | 0.2405 |
| 40 | 0.152 | 0.1818 |
| 35 | 0.129 | 0.1106 |
| 50 | 0.108 | 0.0334 |

Rate constant ( k ) with ZnO = 4.72 x 10$^{-4}$ sec$^{-1}$

Rate constant ( k ) with ZnS = 4.38 x 10$^{-4}$ sec$^{-1}$

Rate constant ( k ) with ZnO-ZnS = 6.14 x 10$^{-4}$ sec$^{-1}$

**Effect of pH**

The effect of pH on photocatalytic degradation was monitored in the range 6.0- 11 and the results are tabulated in Table 3. It was observed that the rate of degradation of azure B increaseswith increase in pH and maximum efficiency was exhibited at pH 10.0. This result may beexplained on the basis that on increasing pH, there was greater probability for the formationof oxygen anion radical ($O_2^{\bullet-}$), which are produced from the reaction between $O_2$ moleculeand electron ($e^-$) of the semiconductor. When pH was increased above 10.0, the rate of thereaction was found to decrease, which may attributed  the fact that cationic form of azure B isconverted to its neutral form, which faces no attraction towards the negatively chargedsemiconductor surface due to the absorption of hydroxyl ions.

**Table 3: Effect of pH**

[Azure B ] = 1.80 x $10^{-5}$ M

Amount of composite = 0.10 g    Light intensity = 60 .0 mWcm$^{-2}$

| pH | Rate constant (k) $\times 10^4$(sec$^{-1}$) |
|---|---|
| 6.0 | 0.59 |
| 6.5 | 0.63 |
| 7.0 | 0.75 |
| 7.5 | 1.17 |
| 8.0 | 1.49 |
| 8.5 | 2.32 |
| 9.0 | 3.14 |
| 9.5 | 4.06 |
| **pH** | **Rate constant (k) $\times 10^4$ (sec$^{-1}$)** |
| **10.0** | **6.14** |
| 10.5 | 5.19 |
| 11.0 | 4.93 |

**Effect of dye concentration**

Effect of concentration of Azure B was studied by taking its different concentrations i.e. 1.0 x $10^{-5}$M-2.6 x $10^{-5}$M. The results are reported in Table 4. It was observed that the rate of photocatalytic degradation increased with increase in concentration of dye up to a certain concentration (1.8 x $10^{-5}$M). This may be attributed to the fact that as the concentration of dye was increased, more dye molecules were available for excitation and hence, there was an

increase in the rate. The rate of photocatalytic degradation was found to decrease with futher increase in the concentration of dye. This indicated that after certain concentration, the dye itself start acting as obstacle for the incident light and it does not allow the required light intensity to reach the semiconducting particles and thus, declining the rate of the photocatalytic degradation of dye.

**Table 4: Effect of dye concentration**

Amount of composite = 0.10 g     pH= 10.0

Light intensity = 60.0  mWcm$^{-2}$

| [ Azure B ] x $10^5$ | Rate constant (k) $\times 10^4$(sec$^{-1}$) |
|:---:|:---:|
| 1.0 | 4.03 |
| 1.2 | 4.46 |
| 1.4 | 5.03 |
| 1.6 | 5.57 |
| **1.8** | **6.14** |
| 2.0 | 5.57 |
| 2.2 | 5.32 |
| 2.4 | 5.03 |
| 2.6 | 4.53 |

**Effect of amount of semiconductor (ZnO-ZnS) composite**

The rate of photocatalytic degradation of Azure B increases with an increase in the amountof composite but finally, it becomesalmost constant after a certain amount, i.e. 0.10g. This may be attributed to the fact that as thequantity of composite was increased, theexposed surface area also increases, but aftera definite limit, if the quantity of compositewas further increased, then there will be noincrease in the exposed surface area of thephotocatalyst. It may be considered like asaturation point; above which, any increase inthe amount of semiconductor has insignificantor no effect on the rate of photocatalyticdegradation of Azure B, as any increasein the amount of composite after thissaturation point will only increase the thicknessof the film at the bottom of the reaction vessel.The saturation point shifts to upper rangefor bigger vessels, while reverse was true forsmaller vessels.

**Table 5: Effect of photocatalyst**

[Azure B ] = $1.80 \times 10^{-5}$ M        pH= 10.0

Light intensity = 60.0  mWcm$^{-2}$

| Amount of composite (g) | Rate constant (k) $\times 10^4$ (sec$^{-1}$) |
|---|---|
| 0.02 | 4.06 |
| 0.04 | 4.58 |
| 0.06 | 5.20 |
| 0.08 | 5.77 |
| **0.10** | **6.14** |
| 0.12 | 6.05 |
| 0.14 | 6.05 |

### Effect of light intensity

To observe the effect of intensity of light on the photocatalytic degradation of Azure B, the lightintensity was varied either by changing the wattage of lamp or the distance between lamp and semiconductor surface. The results obtained are tabulated in Table 6. The data shows that an increase in the light intensity increases the rate of photodegradation and the optimum value were found at 60.0 mWcm$^{-2}$. It may be explained on the basis that as the light intensity was increased, the number of photons striking per unit area also increased, resulting into a greater rate of degradation. Further increase in the light intensity decrease the rate of reaction. It may be possibly due to thermal side reactions

**Table 6: Effect of light intensity**

[Azure B ] = $1.80 \times 10^{-5}$ M        pH= 10.0

Amount of composite = 0.10 g

| Light intensity (mW cm$^{-2}$) | Rate constant (k) $\times 10^4$(sec$^{-1}$) |
|---|---|
| 20 | 2.76 |
| 30 | 3.38 |
| 40 | 3.69 |
| 50 | 4.92 |
| **60** | **6.14** |
| 70 | 5.23 |

**Mechanism** –

On the basis of these observations, a tentative mechanism for photocatalytic degradation of azure B (Dye) has been proposed as follows:

$$^1Dye_0 \xrightarrow{hv} {}^1Dye_1 \text{ (Singlet excited state)}$$

$$^1Dye_1 \xrightarrow{ISC} {}^3Dye_1 \text{ (Triplet excited state)}$$

$$SC \xrightarrow{hv} e^- (CB) + h^+ (VB)$$

$$e^- + O_2 \longrightarrow O_2^{\bullet-}$$

$$O_2^{\bullet-} + {}^3Dye_1 \longrightarrow \text{Leuco Dye}$$

$$\text{Leuco Dye} \longrightarrow \text{Products}$$

Azure B absorbs suitable wavelength and gives its first excited singlet state followed by intersystem crossing (ISC) to triplet state. On the other hand, the semiconducting composite ZnO-ZnS also uses the radiant energy to excite its electron from valence band to the conduction band; thus, leaving behind a hole. The dissolved oxygen accepts electron of composite and is converted into oxygen anion radical. In the next step, the dye molecule in triplet state donate an electron to oxygen anionradical and oxidized to its leuco form, which further degrades into harmless products. The hydroxyl radicals do not participate in the photodegradation of dye as the reaction rate was not appreciably retarded in presence of hydroxyl radical scavengers; isopropanol.

## CONCLUSION

A comparative study has been carried out between photocatalytic activity of pure ZnO and ZnSand their composite. Azure B dye was used as a model system to compare their photocatalytic activity. The rate constants for photocatalytic degradation of Azure B  using ZnO, ZnS and ZnO-ZnSwere $4.72 \times 10^{-4}$ sec$^{-1}$, $4.38 \times 10^{-4}$ sec$^{-1}$ and $6.14 \times 10^{-4}$ sec$^{-1}$, respectively. These results clearly indicates that the composite ZnO-ZnSshowed better results as compared to individual ZnO and ZnS. The observation of present work will explore the use of composites in enhancing photocatalytic performance of a photocatalyst.

## REFERENCES

1.  K. Vinodgopal, V. K.  Prashant. Sci. Tech., 1995, 29, 841.

2.  S. Xu , W. Shangguan, J.  Yuan, J. Shi, M. Chen, Sci. Tech. Adv. Mater., 2007, 8, 40.

3.  J.Ungelenkand,C. Feldmann, Appl.Catal. B: Environ., 2011, 102, 515.

4.  S. Kothari, A. Kumar, R. Vyas, R. Ameta, P. B. Punjabi, J. Braz. Chem. Soc., 2009, 20, 1821.

5.  C. Sahoo, A. K. Gupta, A. Pal, Dyes and Pigmen., 2005, 66, 189.

6.  S. K. Kansal, M. Singh, D. Sud, J. Hazard. Mater., 2007, 141, 581.

7.  P. Vaishnave, A. Kumar, R.  Ameta, P. B. Punjabi, S. C. Ameta, Arab. J. Chem.,2014, 7, 981.

8.  V. Sharma, N. Gandhi,  A. Khant R.C. Khandelwal, Int. J. Chem. Sci., 2010, 8, 1965.

9.  L. Claudia, T. Martinez, R. K. Mehra, J. Coll. Interf. Sci., 2001, 240, 525.

10. N. Soltani, E. Saion, M. Z. Hussein, M. Erfani, A.  Abedini , G. Bahmanrokh,  M. Navasery, P. Vaziri, Inter. J. Mol. Sci., 2012, 13, 12242.

11. L. Wenjiang, G. Song, F. Xie,   M. Chen, Y. Zhao,  Mater. Lett., 2013, 96, 221.

12. P. Nuengmatcha, S. Chanthai,  R. Mahachai, W. Chunoh, J. Environ. Chem. Eng., 2016, 4, 2170.

13. P. Suresh, J. Judithvijaya, L. Johnkennedy, Trans. Nonfer. Met. Soc. China, 2015, 25, 4216.

14. H. Lachheb, E. Puzenat, A. Houas, M. Ksibi, E. Elaloui, C. Guillard, J. M. Herrmann, Appl. Catal. B: Environ., 2002, 39, 75.

15. I. Bhati, J. Sharma, A. Ameta, S. C. Ameta, Int. J. Chem. Sci., 2011, 9, 1787.

16. N. Gandhi, V. Sharma, A. Khant,R. C. Khandelwal,  Int. J. Chem. Sci., 2010, 8, 1924.

17. N. Daneshvar, D. Salari, A. R. Khataee, J. Photochem. Photobiol. A: Chem., 2004, 162, 317.

18. S. Devipriya, S. Yesodharan, Sol. Energy Mater. Solar. Cells, 2005, 86, 309.

# Water Quality Study of Groundwater of Bhabhar Taluka (Banaskantha District, Gujarat State, India)

## Kiran V. Mehta

Department of Chemistry, R. R. Mehta College of Science and C. L. Parikh College of Commerce, PALANPUR-385001, Dist. – Banaskantha, State - Gujarat(India)

Email: kiranvmehta@ymail.com

**Abstract**

This research paper is about drinking water quality of groundwater on the basis of physicochemical evaluation. Groundwater samples were collected from the various places of rural areas of Bhabhar taluka of Gujarat state of India and their parameters like temperature, colour, odour, turbidity, electrical conductance (E.C.), pH, total dissolved solids (TDS), total alkalinity and concentrations of ions like fluoride, chloride, calcium, magnesium sodium and potassium were assessed. The results were compared with the drinking water guidelines suggested by Indian Council of Medical Research (ICMR). The study shows that water should be treated properly before its use as drinking water to avoid its probable adverse effects on health.

**Keywords -** Evaluation, quality, groundwater, awareness.

**Introduction**

In rural areas like Bhabhar Taluka of Banaskantha district of Gujarat state of India where rainfall is very low and water transportation is not greatly effective, local people use groundwater for irrigation as well as for drinking purpose. Owing to the increased strain on ground-water resources, it becomes valued to evaluate the groundwater quality: whether the water is suitable for drinking or not? With such a point of view, this work was carried out. This kind of research may generate awareness not only in local people but also in the other people about drinking water quality and its management.

## Materials and Methods

The present study is related to the groundwater quality of some places of the Bhabhar Taluka which is situated in Banaskantha district ($23.33^o$ to $24.25^o$ north latitude and $71.03^o$ to $73.02^o$ east longitude) of the Gujarat state of India. The district lies on the north-west side of the Gujarat State. The weather of Bhabhar taluka is dry and hot. Bhabhar is a main town of this taluka. This taluka is a rural area of the district and agriculture and dairy production are the majoreconomical activities. From this taluka, groundwater samples of bore/tube wells were collected in pre-cleaned one liter plastic containers during January-February, 2016. The samples were taken from the places like: (a) BhemBordi,(b) Chembuva, (c) Sanva, (d) Tetarva, (e) Vadpag and (f) Kuvala.

Temperature, colour and odour were noted after the collection of samples immediately. The samples were examined for physicochemical features by the standard titrimatric and instrumental procedures described in the literature [1- 5]. Physical parameters like pH, Electrical Conductivity (E. C.), turbidity and Total Dissolved Solids (TDS) were determined by pH meter, E.C. meter, turbidity meter and TDS meter respectively. Chemical parameters like concentration of calcium ($Ca^{2+}$) and magnesium ($Mg^{2+}$) were determined by standard EDTA titration. Carbonate ($CO_3^{2-}$) and bicarbonate ($HCO_3^{1-}$) were estimated by titrating with $H_2SO_4$. Chloride ($Cl^{1-}$) was determined by argentometric titration. Sodium ($Na^{1+}$) and potassium ($K^{1+}$) were measured by flame photometric method. Fluoride ($F^{1-}$) was measured by ion selective electrode.

## Results and Discussion

Values of different characteristics of water samples are shown in **Table 1**. Quality of samples is compared with the drinking water standards of Indian Council of Medical Research (ICMR) [6-7].

## Table-1: Values of physicochemical parameters of water samples

| Sr. No. of Para. | Parameter | a | b | c | d | e | f | Mean | S.D. |
| --- | --- | --- | --- | --- | --- | --- | --- | --- | --- |
| 1 | Temp.$^0$C | 24.2 | 24.5 | 24.4 | 24.2 | 24.5 | 24.4 | 24.37 | 0.13 |
| 2 | Colour | Cl | Cl | Cl | Cl | Cl | Cl | - | - |
| 3 | Odour | Ol | Ol | Ol | Ol | Ol | Ol | - | - |
| 4 | Tur. (NTU) | 2.50 | 2.00 | 2.10 | 2.50 | 2.75 | 1.75 | 2.27 | 0.38 |
| 5 | TDS (mg/l) | 1400 | 1560 | 1440 | 1380 | 1025 | 1130 | 1322.50 | 202.52 |
| 6 | pH | 8.10 | 8.15 | 7.90 | 8.40 | 8.50 | 7.80 | 8.14 | 0.27 |
| 7 | E.C. ($\mu$s cm$^{-1}$) | 1725 | 1800 | 1690 | 1500 | 1230 | 1450 | 1565.83 | 212.66 |
| 8 | T. A. (mg/l) | 331.40 | 330.10 | 315.70 | 280.10 | 400.60 | 350.20 | 334.68 | 39.89 |
| 9 | $F^{1-}$ (mg/l) | 1.90 | 0.80 | 1.20 | 1.30 | 0.90 | 0.80 | 1.15 | 0.42 |
| 10 | $Cl^{1-}$ (mg/l) | 150.15 | 210.40 | 166.40 | 170.90 | 140.55 | 110 | 156.07 | 33.62 |
| 11 | $Na^{1+}$ (mg/l) | 180 | 204.26 | 209.80 | 210.30 | 190.80 | 220.70 | 202.64 | 14.78 |
| 12 | $K^{1+}$ (mg/l) | 2.40 | 4.80 | 5.18 | 4.10 | 3.50 | 3.27 | 3.88 | 1.03 |
| 13 | $Ca^{2+}$ (mg/l) | 13.25 | 11.80 | 10.75 | 14.20 | 12.60 | 15.45 | 13.01 | 1.68 |
| 14 | $Mg^{2+}$ (mg/l) | 6.10 | 4.85 | 6.33 | 7.80 | 5.47 | 6.11 | 6.11 | 0.99 |

Para.: Parameter, S.D.: standard Deviation

All the samples were found colourless and clear. Direct inspection of the samples for odour was done and found that samples were odourless. Turbidity indicates dimness of water. Clear water contains low turbidity level while grubby water contains high turbidity level. For all the samples, turbidity was in the range of 1.75 to 2.75 NTU (Nephelometric Turbidity Unit).

TDS for the samples varied from 1025 to 1560 mg/l. For TDS, ICMR suggests 500 mg/l as the desirable limit while 1500-3000 mg/l as the maximum permissible limit. Here, all the samples (a tof) showed TDS values which were exceeding the desirable limit. High TDS reduces the quality and affects the taste of water.

pH values of samples were in the range of 7.80 to 8.50. All the samples were in the desired pH range (7.0 - 8.5) suggested by ICMR. High values of electrical conductivity (E. C.) exhibit large amount of salts dissolved in water. This kind of property is not desired as it makes water unsuitable for drinking. E. C. of the samples varied from 1230 to 1800$\mu$s cm$^{-1}$ having standard deviation of 212.66$\mu$s cm$^{-1}$.

Presence of large amount of fluoride (higher than 1.5 mg/l) is associated with dental and skeletal fluorosis, while inadequate amount of fluoride (less than1.0 mg/l) is associated with dental carries. The $F^{1-}$ concentration in samples was from 0.80 to 1.90 mg/l. Samples (a, c, d) were beyond the desirable limit (1.0 mg/l) indicated by ICMR.

$Cl^{1-}$ values of samples were in the range of 110 to 210.40.Sample(b) was violating the limit (200 mg/l) for $Cl^{1-}$ indicated by ICMR.

High level of $Na^{1+}$ is associated with excessive salinity in water. $Na^{1+}$ values of samples were in the range of 180 to 220.70.$K^{1+}$ values of samples were in the range of 2.40 to 5.18 having mean 3.88 and standard deviation 1.03.

Hardness of water is caused by multivalent cations and is largely due to $Ca^{2+}$ and $Mg^{2+}$ ions. $Ca^{2+}$ values of samples were in the range of 10.75 to 15.45.Thus, $Ca^{2+}$ in the samples was within the desirable limit (75 mg/l) indicated by ICMR. $Mg^{2+}$ values of samples were in the range of 4.75 to 7.80.

## Conclusions

The TDS values of samples suggest that this water is not suitable for drinking purpose.

The quality of water samples studied were acceptable from the some of the physicochemical parameters but as $Cl^{1-}$, $F^{1-}$ and $Na^{1+}$ values of few samples were violating the desirable limit suggested by ICMR, the water should be treated properly before its usage as drinking water to avoid probable unpleasant effects. Remedial measures should be taken. As a result, public should be made aware of drinking water quality. Active participation of people to keep the situation of groundwater under control is also of a great worth.

## References

[1] Trivedi R. K. and Goel P. K., 1986, Chemical and Biological Methods for Water Pollution Studies, Environmental Publication, Karad (India), 1-112.

[2] Food and Agriculture Organization (FAO), 1997, Chemical Analysis Manual for Food and Water, FAO, Rome, 20-26.

[3] Aghazadeh N. andMogaddam A. A.,2010, Assessment of Groundwater Quality and its Suitability for Drinking and Agricultural Uses in the Oshnavieh Area, Northwest of Iran, *Journal of Environmental Protection, 1,* 30-40.

[4] Ackah M., Agyemang O., Anim A. K., Osei J.,Bentil N. O., Kpattah L., Gyamfi E.T. and Hanson J.E.K., 2011, Assessment of groundwater quality for drinking and irrigation: the case study of Teiman-Oyarifa Community, Ga East Municipality, Ghana, *Proceedings of the International Academy of Ecology and Environmental Sciences,  1(3-4),* 186-194.

[5] Mohamed A. A. J., AbdulRahman I. and Lim L. H., 2014, Groundwater Quality Assessment in the Urban-West Region Of Zanzibar Island, *Environmental Monitoring and Assessment,186*, 6287–6300.

[6] Etim E.E., Odoh R., Itodo A.U., Umoh S. D. and Lawal U., 2013,Water Quality Index for the Assessment of Water Quality from Different Sources in the Niger Delta Region of Nigeria,*Frontiers in Science,3(3),* 89-95.

[7] Chatterjee P.R. and Raziuddin M., Studies on the Water Quality of a Water Body at Asansol Town, West Bengal,2007, *Nature Environment and Pollution Technology*, *6(2),* 289-292.

# NOVEL 1,3,4-OXADIAZOLE DERIVATIVES CONTAINING FURAN RING: SYNTHESIS, CHARACTERIZATION, ANTIMICROBIAL ASPECTS

**Name – Darshansinh Ajitsinh Raol,Dr.G.D.Acharya**

**Chemistry Department,**

**R.R.Mehta College of Science & C.L.Parikh College of Commerce, Palanpur**

**Email – govindvarde7@gmail.com**

## ABSTRACT

5-(naphtho[2,1-b] furan-2-yl)-1,3,4-oxadiazole-2(3H)-thione (1) is prepared by reaction between Ethyl naphtho[2,1-b]furan-2-carboxylate and hydrazine hydrate, followed by reaction with $CS_2$/KOH. The mannich reaction of 1,3,4-oxadiazole compound (1) followed by reaction with 4-chloro phenyl hydrazine yield different 4-(4-chlorophenylamino)-1-((disubstitutedamino)methyl)-3-(naphtho[2,1-b]furan-2-yl)-1H-1,2,4-triazole-5(4H)-thione (3a-e). The newly synthesized compounds (3a-e) were characterized using their physical properties, elemental analysis and spectral data. Also these compounds were evaluated for their antimicrobial activities against different bacterial and fungal strains.

## KEYWORDS

4-chlorophenylhydrazine, naphtho[2,1-b]furan, Mannich reaction, Spectral studies, antimicrobial activities.

## INTRODUCTION

Now a day, Mannich base reaction has increased interest due to their medicinal importance [1,2]. The presence of basic Mannich side chain has shown a noticeable increase in activities like antimalarial, anticancer, antitumor and anti-HIV activities [3-6]. The important molecule derived through the mannich base reaction named 1,3,4-Oxadiazoles are

important heterocyclic compounds in pharmaceutical field and several from them are the key compounds with potential biological activities such as anticancer, antitubercular, anti-inflammatory, antianlgesic,  [7-9]. Also derivatives of 1,3,4-oxadiazole have been the object of investigation due to their antibacterial and antifungal [10,11].

Naphtho[2,1-b]furan nucleus has been widely accepted as a unique substructure for the synthesis of biologically active molecules [12]. In addition, Naphtho[2,1-b]furan moiety present in many natural products were reported to possess biological activities [13,14].

In recent past the heterocycles containing Naphtho[2,1-b]furan were synthesized in our laboratory [15,16] have exhibited significant biological activities. Such a versatile biological activity of the both the molecules has encouraged further investigations in the biological field. Hence, the present communication comprises the synthesis, characterization and antimicrobial aspects of novel 1,3,4-oxadiazole derivatives containing furan ring. The general synthesis of novel 1,3,4-oxadiazole derivatives are shown in **Scheme-1**.

5-(naphtho[2,1-*b*]furan-2-yl)-1,3,4-oxadiazole-2(3*H*)-thione
(1)

CH$_2$O/NR$_1$R$_2$

3-((disubstitutedamino)methyl)-5-(naphtho[2,1-*b*]furan-2-yl)-1,3,4-oxadiazole-2(3*H*)-thione
(2a-e)

4-ClPhNHNH$_2$

4-(4-chlorophenylamino)-1-((disubstitutedamino)methyl)-3-(naphtho[2,1-*b*]furan-2-yl)-1*H*-1,2,4-triazole-5(4*H*)-thione (3a-e)
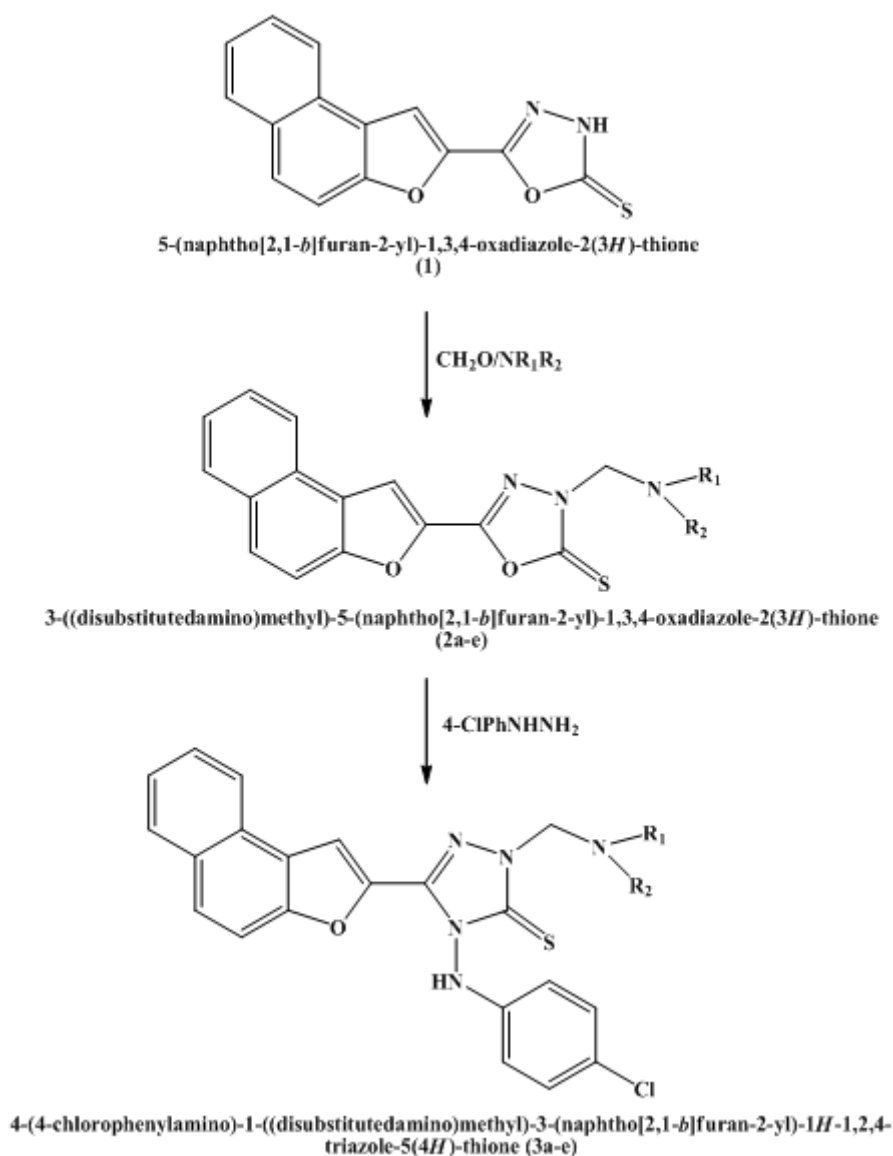
**Scheme-1 General synthesis of novel 1,3,4-oxadiazole derivatives**

## MATERIALS AND METHODS

All the necessary chemicals were purchased from local market while all solvents were of laboratory grade and used after further purification. 5-(naphtho[2,1-b]furan-2-yl)-1,3,4-oxadiazole-2(3H)-thione **(1)** was prepared according to reported method [15]. Melting points of all synthesized compounds were determined in open capillary tubes were uncorrected. The FTIR spectra were recorded using KBr pellets on a Nicolet 400D spectrometer and ^{1}H NMR

spectra were recorded in DMSO with TMS as internal standard on a Bruker spectrometer at 400 MHz.

## Preparation of 4-(4-chlorophenylamino)-1-((disubstitutedamino)methyl)-3-(naphtho[2,1-b]furan-2-yl)-1H-1,2,4-triazole-5(4H)-thione (3a-e):-

The compounds 3a-e were prepared according to following two step method:

In the first step equimolar mixture of  5-(naphtho[2,1-b]furan-2-yl)-1,3,4-oxadiazole-2(3H)-thione (1), formaldehyde and secondary amine **(a-e)**  in 20 ml ethyl alcohol was taken into round bottom flask and stirred for about 18-20 hrs. The solid product separated was filtered and wash with ethyl alcohol. The solid products obtained were 3-((disubstitutedamino)methyl)-5-(naphtho[2,1-b]furan-2-yl)-1,3,4-oxadiazole-2(3H)-thione and designated as **(2a-e)**.

In second step 3-((disubstitutedamino)methyl)-5-(naphtho[2,1-b]furan-2-yl)-1,3,4-oxadiazole-2(3H)-thione **(2a-e)**  was added to a solution of 4-cholorophenyl hydrazine hydrate (0.02 mole) in ethyl alcohol (40 ml) and refluxed on water bath for 8-9 hrs. The resultant mixture was poured into cold water, acidified with glacial CH₃COOH and recrystallization from Rectified spirit yield 4-(4-chlorophenylamino)-1-((disubstitutedamino)methyl)-3-(naphtho[2,1-b]furan-2-yl)-1H-1,2,4-triazole-5(4H)-thione **(3a-e)**. The yields, melting points and elemental analysis results of all compounds are given in **Table-1**.

**Table-1 Physical properties and elemental analysis of compounds (3a-e)**

| Compound | R₁ | R₂ | Yield | M.P. °C | Elemental Analysis | | | | | | | | | |
| --- | --- | --- | --- | --- | --- | --- | --- | --- | --- | --- | --- | --- | --- | --- |
| | | | | | %C | | %H | | %N | | %S | | | |
| | | | | | Found | Calcd. | Found | Calcd. | Found | Calcd. | Found | Calcd. | | |
| **3a** | $CH_3$ | $CH_3$ | 72 | 215 | 61.39 | 61.35 | 4.48 | 4.47 | 15.56 | 15.52 | 7.13 | 7.09 | | |
| **3b** | $CH_3$ | Et | 75 | 204 | 62.13 | 62.10 | 4.78 | 4.72 | 15.09 | 15.07 | 6.91 | 6.90 | | |
| **3c** | Et | Et | 70 | 207 | 62.82 | 62.79 | 5.06 | 5.03 | 14.65 | 14.62 | 6.71 | 6.68 | | |
| **3d** | Et | $C_6H_5$ | 66 | 201 | 66.21 | 66.18 | 4.60 | 4.57 | 13.31 | 13.25 | 6.10 | 6.08 | | |
| **3e** | $C_6H_5$ | $C_6H_5$ | 62 | 198 | 69.04 | 68.98 | 4.21 | 4.17 | 12.20 | 12.16 | 5.59 | 5.58 | | |

## ANTIMICROBIAL STUDY

### Antibacterial activities

The antibacterial activities of all compounds **(3a-e)** were studied against two gram-positive bacteria (*Bacillus subtilis and Staphylococcus aureus*) and two gram-negative bacteria (*Klebsiella Promioe and Escherichia Coli*) using agar cup plate method at a concentration of 50μg/ml. A methanol was used as control in this method while tetracycline was used as a standard drug for comparison purpose. The area of inhibition of zone measured in cm. The antibacterial activity results are tabulated in following **Table-2**.

**Table-2 Antibacterial Activity of Compounds (3a-e)**

| Compounds | Gram +Ve | | Gram -Ve | |
|---|---|---|---|---|
| | *B. Subtilis* | *S. aureus* | *K. Promioe* | *E. Coli* |
| **3a** | 64 | 55 | 70 | 66 |
| **3b** | 61 | 54 | 66 | 69 |
| **3c** | 59 | 51 | 65 | 72 |
| **3d** | 63 | 56 | 71 | 75 |
| **3e** | 68 | 58 | 73 | 71 |
| **Tetracycline** | 72 | 64 | 78 | 82 |

### Antifungal Activities

The Antifungal activity of all compounds **(3a-e)** was studied by agar cup method at 1000 ppm concentration. Fungal strains used in the present study are *Aspergillus niger, Nigrospora Sp, and Rhizopus nigricum*. The antifungal activities were measured on each of these fungal strains on a potato dextrose agar (PDA) medium. Such a PDA medium contained potato 200g, dextrose 20g, agar 20g and water 1c. Five days old cultures were employed for the study. The compounds to be tested were suspended (1000ppm) in a PDA medium and

autoclaved at $120^o$ C for 15 min. at 15atm. pressure. These media were poured into sterile Petri plates and the organisms were inoculated after cooling the Petri plates. The percentage inhibition for fungi was calculated after five days using the formula given below:

**Percentage of inhibition = 100(X-Y) / X**

Where,   X = Area of colony in control plate

Y = Area of colony in test plate

The antifungal activity results are display in following Table-3.

**Table- 3 Antifungal Activity of Compounds (3a-e)**

| Zone of Inhibition at 1000 ppm (%) | | | |
|---|---|---|---|
| Compound | *Aspergillus Niger* | *Nigrospora Sp.* | *Rhizopus Nigricum* |
| **3a** | 64 | 68 | 65 |
| **3b** | 57 | 66 | 63 |
| **3c** | 67 | 66 | 69 |
| **3d** | 69 | 74 | 72 |
| **3e** | 71 | 76 | 70 |

**RESULTS AND DISCUSSION**

It was observed that 3-((disubstitutedamino)methyl)-5-(naphtho[2,1-b]furan-2-yl)-1,3,4-oxadiazole-2(3H)-thione, on condensation with 4-chloro hydrazine hydrate yields 3-final compounds i.e. 4-(4-chlorophenylamino)-1-((disubstitutedamino)methyl)-3-(naphtho[2,1-b]furan-2-yl)-1H-1,2,4-triazole-5(4H)-thione **(3a-e)**.

The structures of (3a-e) were confirmed on the basis of their elemental analysis, FTIR spectrum and $^1$H NMR spectrum. The C, H, N analysis data of all compounds were well agreed with their predicted structures presented in Scheme-1.

The FTIR spectrum of all compound shows an important band at 3254 and 1175 cm$^{-1}$ due to NH stretching and C=S group, respectively. The another bands were found at their respective positions such as at 3035 cm$^{-1}$ (C-H of Ar), 1632 cm$^{-1}$ (C=N), 771 cm$^{-1}$ (C-O-C ring), 2953,1372 cm$^{-1}$ (-CH$_3$/3a and 3b).

The $^1$H NMR spectrum of compound 3a-e in DMSO indicates that the all compounds shows singlet of 1H at ~3.95 δ ppm due to NH group, singlet of 2H at ~4.52 δ ppm due to CH$_2$. Also all the aromatic protons are appeared in multiplicity at 7.05-8.72 δ. Also some important substituted protons for each compound is found as follows:

**3a**; 2.17 (s,6H,CH$_3$), **3b**; 2.20 (s,3H,CH$_3$), 1.15 (t,3H,CH$_3$), 2.57 (q,2H,CH$_2$), **3c**; 1.14 (t,6H,CH$_3$), 2.62 (q,4H, CH$_2$), **3d**;1.12 (t,3H,CH$_3$), 2.60 (q,2H,CH$_2$), 6.80–7.21 (m,5H,Ar-H), **3e**; 6.80–7.21 (m,10H,Ar-H). Thus the structures of compounds 3a-e are confirmed as shown in **Scheme-1**.

The elemental analysis results revealed that the CHNS content of all compounds are consistence with their predicted structure. The IR data also direct for assignment of the predicted structure. Compounds 3g and 3e were shows good antimicrobial activity.

**CONCLUSION**

In conclusion, in present we synthesized novel 1,3,4-oxadiazole derivatives containing furan ring says, 4-(4-chlorophenylamino)-1-((disubstitutedamino)methyl)-3-(naphtho[2,1-b]furan-2-yl)-1H-1,2,4-triazole-5(4H)-thione. All the synthesized compounds were studied for their antibacterial and antifungal activity which shows good to moderate activity against all employed antimicrobial strains. Compounds 3d and 3e was found more

toxic for microbes while other compounds found to be moderately active compared to standard drug tetracycline.

## REFERENCES

[1] S. Bala, N. Sharma, A. Kajal, S. Kamboj and V. Saini, *International Journal of Medicinal Chemistry*, **2014**, 2014, 1-15.

[2] G. Roman.  European *Journal of Medicinal Chemistry*, **2015**, 89, 743-816.

[3] D. Sharma, D. Chetia, and M. Rudrapal, *Asian Journal of Chemistry*, **2016**, 28, 782-788.

[4] G. Chen, *Letters in Drug Design & Discovery,* **2016**, 13, 395-400.

[5] S. Bondock, H. Gieman and A. El-Shafei. *Journal of Saudi Chemical Society,* **2016**, 20, 695-702.

[6] S. Li and J.-An Ma. *Chemical Society* Reviews, **2015**, 44, 7439-7448.

[7] S. Bajaj, *European Journal of Medicinal Chemistry,* **2015**, 97, 124-141.

[8] N. C. Desai, H. Somani, A. Trivedi, K. Bhatt, L. Nawale, V. M. Khedkar, P. C. Jha and D. Sarkar, *Bioorganic & Medicinal Chemistry Letters,* **2016**, 26, 1776-1783.

[9] S. N. Thore, S. V. Gupta and K. G. Baheti, *Journal of Saudi Chemical Society,* **2016**, 20, S46-S52.

[10] P. Li, Pei, L. Shi, M. N. Gao, X.Yang, W. Xue, L. H. Jin, D. Y. Hu and B. A. Song, *Bioorganic & medicinal chemistry letters,* **2015**, 25, 481-484.

[11] M. Y. Wani, A. Ahmad, R. A. Shiekh, K. J. Al-Ghamdi, and A. J. Sobral, *Bioorganic & Medicinal Chemistry*, **2015**, 23, 4172-4180.

[12] A. H. El-Wahab, Z. I. A. Al-Fifi, A. H. Bedair, F. M. Ali, A. H. Halawa and A. M. El Agrody, *Molecules*, **2011**, 16, 307-318.

[13] G. M. B. Bettolo, C. G. Cassinovi and C. Galeffi, *Tetrahedron Letters*, **1965**, 6, 4857-4864.

[14] J. Stochigt, U. Srocka and M. H. Zenk, *Phytochemistry*, **1973**, 12, 2389-2391.

[15] D. Raol *Journal of Chemical and Pharmaceutical Research*, **2015**, 7, 104-107.

[16] G. R. Varde and G. D. Aacharya, *Der Chemica Sinica*, **2015**, 6, 9-13.

# Study of Thermodynamic Parameters and Activation Energy from TGA of Synthesized New Ternary Transition Metal Complexes

**Dhara Patel, Anal patel**
Shri Sarvajanik Science College Mehsana
dr.dhara29@gmail.com

## Abstract
Ternary Transition Metal complexes of Co(II),Cu(II) and Ni(II) with Schiff base and metformin. have been synthesized . They were characterized by Elemental analysis, Infrared spectra, Electronic spectra and Thermo gravimetric analysis studies. Kinetic Parameters, such as energy of activation (Ea), enthalpy ($\Delta H\#$), entropy ($\Delta S\#$) and Gibbs energy ($\Delta G\#$), were computed from the TGA data. Based on the thermal studies, Thermal stability and kinetic parameters of these complexes were studied by employing Thermo gravimetric Analysis (TGA). The percentage of loss observed in all complexes above 300 $^{o}$C was higher, indicating the decomposition of complexes and formation of oxides. Activation energy for decomposition has been calculated using Broido method. Mathematical analysis of the data has allowed us to determine various parameters using integral method. The trend of the kinetic parameters was found to be different from that of the thermal stability order.

## Keyword
Ternary Transition Metal complexes, TGA, Enthalpy, Entropy, Gibbs energy

## Introduction
Metformin hydrochloride is a strongly basic bi substituted guanidine derivative with short side chains[1] The metabolic abnormalities of non-insulin dependent diabetes mellitus are generally acknowledged to result from a  combination of insulin resistance and impaired insulin secretion[2]. Schiff bases offer a versatile and flexible series of ligands capable to bind with various metal ions to give complexes with suitable properties for theoretical and/or practical Applications [3].. The metal complexes of Schiff bases derived from heterocyclic compounds have been the centre of attraction for many workers in recent years.[4,5]. The physico-chemical data suggested tetrahedral geometry for the Cu(II), Co(II) and Ni(II) complexes. Thermo kinetic and spectral studies of metal complexes some Schiff bases [6] TGA is commonly employed in research and testing to determine characteristics of materials such as polymers, In presence study The thermal behaviour (TGA) of the complexes was studied and kinetic parameters were determined by Broido method [7]. Very few systems have been reported [8] showing the relationship between thermal stability of metal chelates and structure of the chelating agents. Wendlandt and co-workers [9,11] and Hill and co-workers[12] studied the thermal properties of metal chelates with different types of complexing ligands. Structural studies on several metal chelates of 1-diketones and 2-hydroxycarbonyl compounds have been reviewed by Holm and O' Connor. The Broido method was used to evaluate the kinetic parameters from the TGA curves. Plots of ln(ln 1/y) versus 1000/T (where y is the fraction not yet decomposed) for different stage of the thermal degradation of the complexes and evaluation of kinetic parameters the integral method.

## Synthesis of Metal complexes
The complexes under investigation were prepared by three mixing  ethanolic solution of 0.01M Schiff base, 0.01M metal salt and 0.01M metformin. The obtained mixture was

refluxed with continues stirring for four hours. The resulted mixture was filtered, product was collected and then washed several times with hot ethanol until the filtrate became clear. The complexes were dried in desiccator over anhydrous CaCl2 under vacuum. The yield ranged from 60-75% and the melting points of all complexes was above 350ºC.



$X = 4H_2O \cdot Cl$

or

$X = Cl$

or

$X = 4H_2O \cdot Cl_2$
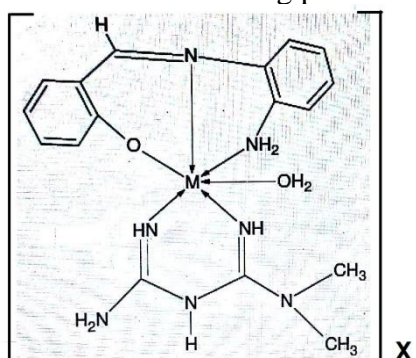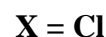
## Results and Discussion

The analytical data of the complexes is presented in Table - 1 indicates 1:1:1 stoichiometry. All synthesized complexes were Coloured and possess high decomposition points. All were amorphous and stable in air.

**Table-1: Analytical Data and Some Physical Properties of the Metal Complexes**

| Complex | Molecular Formula | Colour | Formula Weight | Yield % (g) | Analysis of elements (%) Found (Calculated) | | | | | | Molar Conductance $\Omega^{-1}$ cm$^2$ mol$^{-1}$ | D.P. ($^o$C) |
| --- | --- | --- | --- | --- | --- | --- | --- | --- | --- | --- | --- | --- |
| | | | | | M | C | H | O | N | Cl | | |
| [Ni·Sb·Met·H$_2$O] Cl$_2$ | NiC$_{17}$H$_{25}$N$_7$O$_2$Cl$_2$ | Cherry red | 489.087 | 68 (7.34) | 12.00 (11.89) | 41.75 (41.65) | 5.11 (5.02) | 6.54 (6.39) | 20.1 (19.90) | 14.49 (14.40) | 78.9 | >400 |
| [Co·Sb·Met·H$_2$O] 4H$_2$O ·Cl$_2$ | CoC$_{17}$H$_{33}$N$_7$O$_6$Cl$_2$ | Brown | 561.233 | 68 (8.42) | 10.50 (10.39) | 36.37 (35.98) | 5.88 (5.48) | 17.11 (16.99) | 17.46 (17.35) | 12.63 (12.49) | 73.7 | >350 |
| [Cu·Sb·Met·H$_2$O] 4H$_2$O· Cl$_2$ | Cu C$_{17}$H$_{33}$N$_7$O$_6$Cl$_2$ | Dark green | 565.846 | 65 (8.48) | 11.23 (11.10) | 36.1 (35.90) | 5.83 (5.69) | 16.96 (16.77) | 17.32 (17.26) | 12.53 (12.46) | 55.8 | >350 |

Sb = Schiff Base , D.P. = Decomposition point, Met = Metformin

## Analysis and Physical Measurements:

Elements like C, H, O and N were analyzed with a Perkin-Elmer 2400 series II elemental analyzer. The metal content was estimated with titrematry method using standardized EDTA solution after decomposing the complexes with aquaregia mixture. Magnetic susceptibilities were measured at room temperature on a Gouy[13] balance using Hg[Co(CNS)]4 as calibrate. The IR spectra were recorded on a Perkin-Elmer Lamda-983 spectrometer with samples prepared as KBr pellets and UVVisible reflectance spectra were obtained on a

Beckman DK-2A spectrophotometer using MgO as reference. Thermal measurements were carried out using perkin-Elmer TGA- 7DSC-PYRIS-1-DTA-7 thermal analyzer.

## Conductance Measurements:

All the synthesized metal complexes in DMF. The analytical data were summarized in [Table1] reveals a stoichiometry of 1:2, metal: ligand. The molar conductance values of $10^{-3}$ M solutions in DMF were in the range of (55.8-78.9) $ohm^{-1}cm^2$ $mol^{-1}$, indicating a intermediate-electrolytic behaviour of the complexes.

## Infrared Spectra & Electronic Spectra :

There is strong coupling among the IR bands of ternary complexes and hence quantitative interpretation of the bands in the IR spectra is not possible without normal coordinate analysis. Important IR frequencies of the complexes are listed in Table 2 along with their suggested assignments. The IR spectra of all of the complexes differed from those of the ligands. A strong band ascribed to the presence of υOH of Schiff base appears at 3009 cm-1 in spectrum. This band disappeared in spectra of all metal complexes which accounts for coordination of -OH. Similarly frequency appear at 3010 cm-1 to 3153 cm-1 in complexes, which gives indication for presence of water molecules. The spectra of schiff base showed υC=N- stretching band, thus band was observed at 1660 cm-1 related to schiff base but such band does not appear in the spectrum of metformin. [Table-2]. The complex of Ni(II) has shown electronic transitions at 4273cm-1 (υ1), 11627 cm-1 (υ2) and 15384 cm-1 (υ3) respectively. The complex of Co(II) has shown electronic transitions at 4255 cm-1 (υ1), 6450 cm-1 (υ2) and 14230 cm-1 (υ3).The complex of Cu(II) has shown electronic transitions bands between 14492 cm-1 - 5208 cm-1 broad band.above three complexes are suggested for octahedral geometry.data shown in [table 3].

### Table-2: Infrared Spectral data of the Metal Complexes (cm⁻¹)

| Complex | υ-NH Metformin | υ-C=NH Metformin | υ-N-CH3 Metformin | υ-C=N- Schiff base | υ –OH Schiff base | υ-C=C- Schiff base | υ-NH Schiff base | υ M-N | υ M-N=C | υ M-NH | υ M-OH2 |
| --- | --- | --- | --- | --- | --- | --- | --- | --- | --- | --- | --- |
| Metformin | 1580 sharp(s) | 3367 sharp(s) | 1381 sharp(m) | - | - | - | - | - | - | - | - |
| Schiff Base | - | - | - | 1660 sharp(s) | 3009 sharp(m) | 1612 sharp(s) 910 sharp(m) | 1361 sharp(m) | - | - | - | - |
| [Ni·Sb·Met·H₂O]Cl₂ | 1558 sharp(s) | 3053 sharp(m) | 1371 sharp(m) | 1641 sharp(s) | 3010 sharp(m) | 1610 sharp(s) 812 sharp(m) | 1260 sharp(m) | 580 sharp(m) | 812 sharp(m) | 472 sharp(m) | 848 sharp(m) |
| [Co·Sb·Met·H₂O]4H₂O·Cl₂ | 1529 sharp(s) | 3059 sharp(m) | 1357 sharp(m) | 1639 sharp(s) | 3050 sharp(m) | 1612 sharp(s) 758 sharp(m) | 1329 sharp(m) | 567 sharp(m) | 783 sharp(m) | 470 sharp(m) | 820 sharp(m) |

| $[Cu \cdot Sb \cdot Met \cdot H_2O]$ $4H_2O \cdot Cl_2$ | 1522 sharp(s) | 3020 sharp(m) | 1377 sharp(m) | 1644 sharp(s) | 3153 sharp(m) | 1595 sharp(s) 846 sharp(m) | 1289 sharp(m) | 580 sharp(m) | 802 sharp(m) | 480 sharp(m) | 856 sharp(m) |

Sb = Schiff Base, Met = Metformin, (s) = Strong,   (m) = Medium

**Table-3: Electronic Spectra and Magnetic Moment Data for the Complexes**

| Complex | Absorption region ($cm^{-1}$) | Band assignment | Magnetic moment $\mu_{eff}$ (B.M.) | Geometry |
| --- | --- | --- | --- | --- |
| $[Ni \cdot Sb \cdot Met \cdot H_2O]Cl_2$ | 4273 $cm^{-1}$ <br> 11627 $cm^{-1}$ <br> 15384 $cm^{-1}$ | $^3A_{2g} \rightarrow {}^3T_{2g}$ <br> $^3A_{2g} \rightarrow {}^3T_{1g}(F)$ <br> $^3A_{2g} \rightarrow {}^3T_1(P)$ | 2.83 | Octahedral |
| $[Co \cdot Sb \cdot Met \cdot H_2O]$ $4H_2O \cdot Cl_2$ | 4255 $cm^{-1}$ <br> 6450 $cm^{-1}$ <br> 14230 $cm^{-1}$ | $^4T_{1g} \rightarrow {}^4T_{2g}$ <br> $^4T_{1g} \rightarrow {}^2E_g$ <br> $^4T_{1g} \rightarrow {}^4A_{2g}$ | 3.87 | Octahedral |
| $[Cu \cdot Sb \cdot Met \cdot H_2O]$ $4H_2O \cdot Cl_2$ | 14492$cm^{-1}$---5208$cm^{-1}$ Broad band | $e_g \rightarrow t_{2g}$ <br> $x^2-y^2 \rightarrow z^2$ <br> $x^2-y^2 \rightarrow xy$ | 1.87 | Octahedral |

Sb = Schiff Base,  Met = Metformin

**Thermal studies**

The complexes lost weight gradually during every phase of the experiment, then the samples underwent an accelerated weight loss and finally in the temperature range of about 500-600$^o$C rate of weight loss became much more moderate. During the initial phase the gradual weight loss may be due to water of hydration which may be either crystal or coordinated water. The cumulative weight loses of metal complexes at 50C, 100°C, 150°C, 200°C and 250°C are presented in [Table 4]. Decomposition of all complexes starts above 300$^o$C. The rate of decomposition of metal complexes is lower than that of the ligand suggested that there may be weak intermolecular hydrogen bonding. Co(II) has five, Ni(II) has one and Cu(II) has five water molecules as part of their structure. All complexes lost hydration water 50°C and 150°C and then the co-ordinated water molecule was lost above ≥250°C. The decomposition was complete at >600°C for all complexes. Above three complexes are suggested one water molecule is coordinated.The TGA curves of all complexes were shown in [Figure 1].

## Table-4: Cumulative Weight Loss Data of Metal Complexes at $50^oC$ to $250^OC$

| Complex | Found | | | | | | | | | |
|---|---|---|---|---|---|---|---|---|---|---|
| | $50^oC$ | | $100^oC$ | | $150^oC$ | | $200^oC$ | | $250^oC$ | |
| | g | % | g | % | g | % | g | % | g | % |
| [Ni·Sb·Met·H$_2$O]Cl$_2$ | 0.48 | 0.1 | 0.48 | 0.1 | 0.97 | 0.2 | 7.34 | 1.5 | 8.80 | 1.8 |
| [Co·Sb·Met·H$_2$O] 4H$_2$O·Cl$_2$ | 5.61 | 1.0 | 11.22 | 2.0 | 14.03 | 2.5 | 75.76 | 13.5 | 95.41 | 17.0 |
| [Cu·Sb·Met·H$_2$O] 4H$_2$O·Cl$_2$ | 0.56 | 0.1 | 6.22 | 1.0 | 8.48 | 1.5 | 14.14 | 2.5 | 19.80 | 4.5 |

Sb = Schiff Base , Met = Metformin



| Cu(II) Complex | Co(II) Complex | Ni(II) Complex |
|---|---|---|
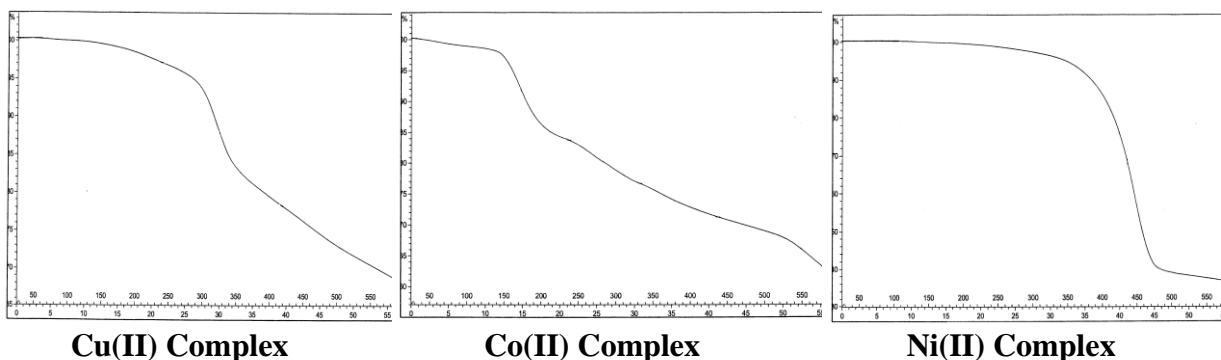
### Fig-1: TGA curves for metal complexes

**Activation Energy and Thermodynamic Parameters studies**

The Broido method was used to evaluate the kinetic parameters from the TGAcurves. Plots of ln(ln 1/y) versus 1000/T (where y is the fraction not yet decomposed) for three stage of the thermal degradation of the complexes are shown in [Figure2] .
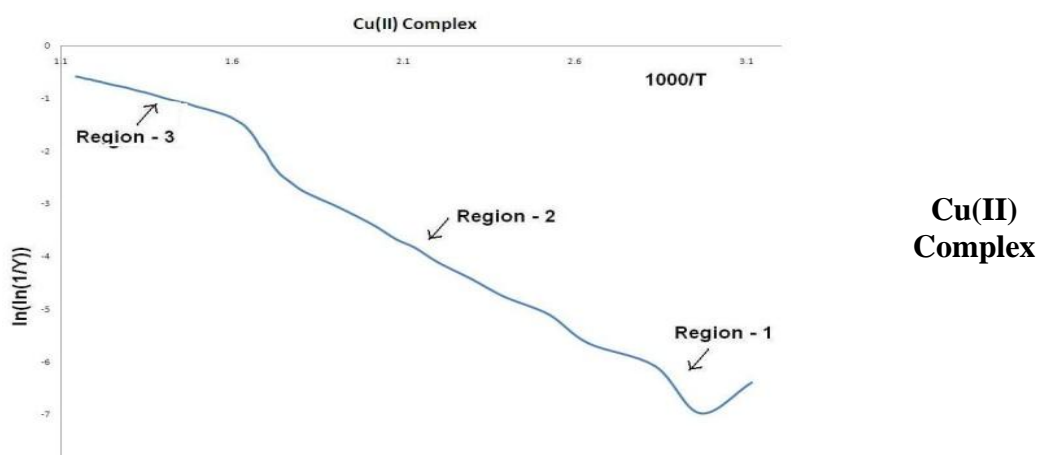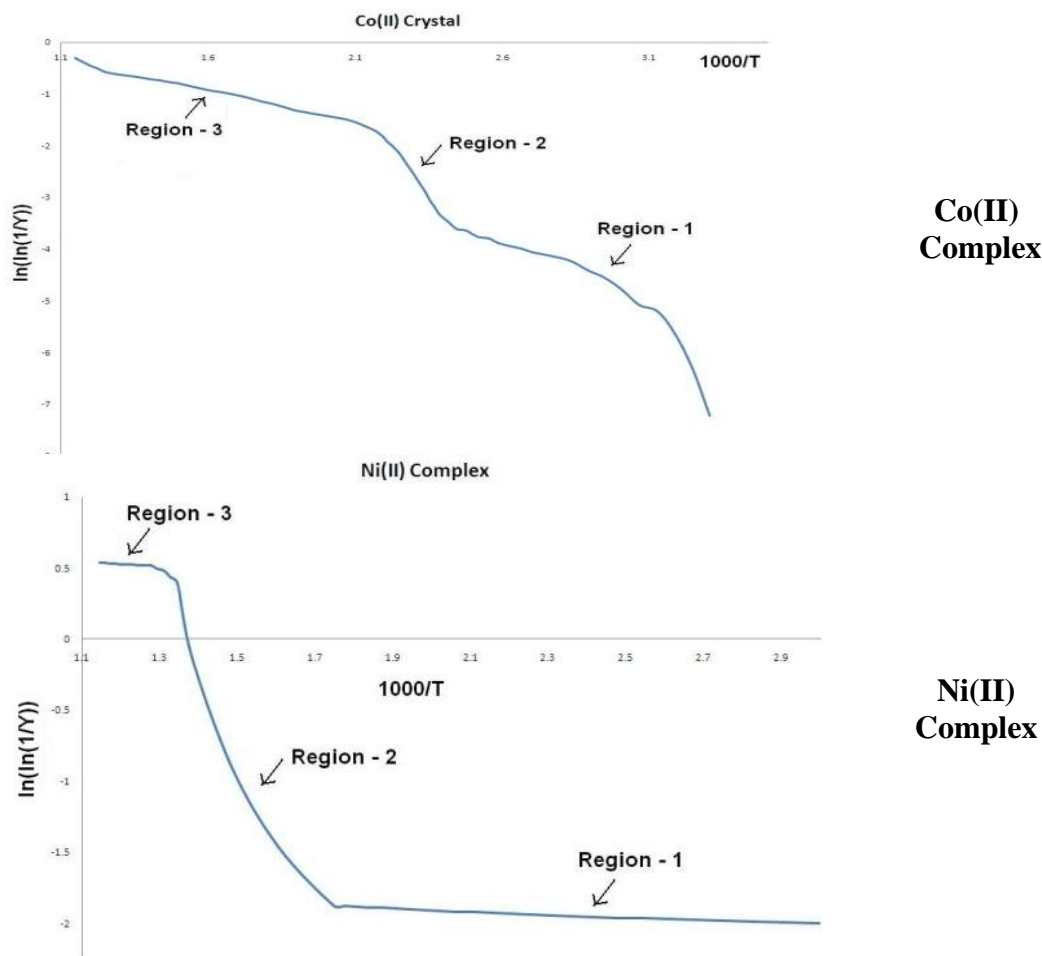


Cu(II) Complex

**Fig 2: Plot of ln[ln(1/y)] vs 1000/T for metal (II) Complexes**

The slope of the plot ln(ln 1/y) versus 1000/T is related to the energy of activation as

$$Ea = –2.303 \times R \times slope \qquad (1)$$
$$Where, R = gas\ constant.$$

The parameters, enthalpy (DH#), entropy (DS#) and Gibbs energy (DG#) of activation were calculated using the following standard equations

$$DH\# = Ea – R\ Td \qquad (2)$$
$$DS\# = DH\#/T – 4.576\ log\ T/K' – 47.22 \qquad (3)$$
$$where\ K' = –ln(ln\ 1/y)$$
$$DG\# = DH\# –DTS\# \qquad (4)$$

The activation energies of decomposition were the range (10.66-42.36), (10.34-29.09),and (8.25-16.56) kJ mol-1 in Cu(II), Co(II) and Ni(II) respectively. The high values of the activation energies reflect the thermal stability of the complexes[12-13]. The entropy of activation (DS#) and enthalpies of activation(DH#) values for three steps of all the complexes are negative and the negative values of the entropies of activation are compensated by the values of the enthalpies of activation leading to almost the same values

(27883-28739 kJ mol-1) for the free energies of activation(DG#). The data were summarized in [Table 5].

**Table -5 Activation energy and Thermodynamic parameters some metal complexes**

| Complex | Stage | Temp Range ºC | Ea kJ mol-1 | ($\Delta H$#) | ($\Delta S$#) | ($\Delta G$#) |
|---|---|---|---|---|---|---|
| [Ni· Sb·Met ·H$_2$O] Cl$_2$ | 1 | 60-290 | 16.56804 | -6659.57 | -42.0805 | 28731.21 |
| | 2 | 300-490 | 8.290411 | -6667.85 | -42.0926 | 28739.48 |
| | 3 | 500-600 | 8.257179 | -6667.88 | -42.0926 | 28739.51 |
| [Co· Sb·Met ·H$_2$O] 4H$_2$O·Cl$_2$ | 1 | 50-130 | 29.09889 | -6647.04 | -42.1357 | 27925.95 |
| | 2 | 130-180 | 22.38045 | -6653.76 | -42.1458 | 27932.66 |
| | 3 | 210-600 | 10.34211 | -6665.8 | -42.164 | 27944.68 |
| [Cu·Sb·Met·H$_2$O] 4H$_2$O·Cl$_2$ | 1 | 60-120 | 42.36379 | -5885.52 | -41.4452 | 27883.87 |
| | 2 | 120-500 | 22.86517 | -5905.02 | -41.4742 | 27903.34 |
| | 3 | 500-600 | 10.6681 | -5917.21 | -41.4923 | -22003.7 |

Sb = Schiff Base, Met = Metformin

The entropy of activation had negative values in all the complexes, which indicates that the decomposition reactions proceed with a lower rate than normal ones.The calculated values of the activation energy of the complexes are relatively low, indicating the autocatalytic effect of the metal ion on the thermal decomposition of the complex. The negative activation entropy value indicates that the activated complexes were more ordered than the reactant and that the reactions were slow.

**References**

1. Stepensky D., Friedman M., Srour W., Raz, I. and Hoffman A., *J. Control. Rel.,71*, 107 (2001).
2. Stumvoll M., Nurjahan N., Perriello G.,Dailey. G and Gerich J. E., *N Engl J Med.,33(9),* 550 (1995).
3. Ahmed A. A., BenGuzzi S. A. and ELHadiA. A., *J of Sci. and Its Appli*., *1(1),*79, (2007).
4. Raman, N., Dhaveethu Raju, J., Sakthivel, A.( 2007). Synthesis, spectral characterization of Schiff base transition metal complexes: DNA cleavage and antimicrobial activity studies. J. Chem. Sci., 119, 303.
5. Wang, D., Yang, Y., Zhao, T., Wu, X., Wang, S., Hou, Y., Chen, W. (2006), Synthesis and properties of a Pr(III) complex with 2-acetylbenzimidazoledehyde-glycine Schiff-base ligand. Chin. Sci. Bull., 51, 785.
6. Sanjiv, A., Sohan, L., Satish, K., Mahender, K., Comparative degradation kinetic studies of three biopolymers: Chitin, chitosan and cellulose. Archives of Applied Science Research, 3(2011), 3, pp. 188-201.
7. Broido, A. (1761). A simple, sensitive graphical method of treating thermogravimetric analysis data. J. Poly. Sci., 7A(2), 1761.

8.  Wendlandt, W. W. (1957). The thermal decomposition of the 5,7-dihalo-8-quinolinol rare earth metal chelates. Anal. Chim. Acta, 17, 428.

9.  Ascenzo, G D., Wendlandt, W. W. (1970). The thermal properties of some metal pyridinecarboxylates. Anal. Chim. Acta, 50, 79.

10. Chang, F. C., Wendlandt, W. W. (1971). Thermal reactions of coordination compounds: Part II.  Chlorobromobis(ethylenediamine)- and dibromobis(ethylenediamine)- cobalt (III) complexes. Thermochim Acta, 2(4) , 293.

11. Perry, D. L., Vaz, C. Wendlandt, W. W. (1974). The thermogravimetry and differential thermal analysis curves of some di-2- pyridyl ketone nickel(II) complexes. Thermochim Acta, 9, 76. |

12. Scency, C. G., Hill, J. O., Magee, R., J. (1975). Thermal analysis of copper dithiocarbamates. Thermochim Acta, 11, 301.

13. Pierce W. S., *Magneto Chemistry,* New York (USA): Interscience, 62 (1956).

# METHOD DEVELOPMENT AND VALIDATION OF MEBENDAZOLE BY RP HPLC TECHNIQUE

AMI PATEL[a], SMITKUMAR PATEL[b], VIPAL PATEL[c],
BHASKARRAV MAKWANA[d]

a.   amipatel1116@gmail.com
b.   smit.patel89@gmail.com
c.   vipalpatel87@gmail.com
d.   bhaskarrav_1985@yahoo.com

## ABSTRACT

A simple, selective, linear, precise and accurate RP-HPLC method was developed and validated for rapid assay of MEBENDAZOLE. Isocratic elution at a flow rate of 1.2 ml /min was employed on a symmetry C18 column at ambient temperature. The mobile phase consisted of Acetonitrile: 0.1M Acetic Acid 60:40 (v/v). The UV detection wavelength was at 210 nm. Linearity was observed in concentration range of 60-100 mg/ml. The retention time for MEBENDAZOLE was 3.0 min. The method was validated as per the ICH guidelines. The proposed method can be successfully applied for the estimation of MEBENDAZOLE.

**Key words:**  Mebendazole, Method Development, Validation, 210nm, 3.0min.

## INTRODUCTION TO MEBENDAZOLE

**Mebendazole** (**MBZ**) is a medication used to treat a number of parasitic worm infestations.[3] This includes ascariasis, pinworm disease, hookworm infections, guinea worm infections, hydatid disease, and giardia, among others.[3] It is taken by mouth.[3]

Mebendazoleis usually well tolerated.[3] Common side effects include headache, vomiting, and ringing in the ears.[3] If used at large doses it may cause bone marrow suppression.[3] It is unclear if it is safe in pregnancy.[3] Mebendazole is a broad-spectrum antihelminthic agent of the benzimidazole type.[3]

Mebendazole came into use in 1971, after it was developed in Belgium.[4] It is on the World Health Organization's List of Essential Medicines, the most effective and safe medicines needed in a health system.[5] Mebendazole is available as a generic medication.[6]

## Description

## DRUGS: Mebendazole

## STRUCTURE:

The structural formula of Mebendazole is shown below:
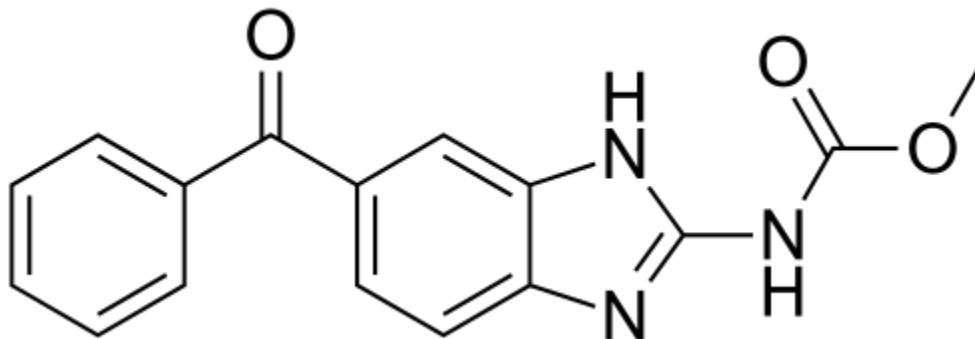


*Figure – 1 Molecular structure of Mebendazole*

**IUPAC NAME:** Methyl (5-benzoyl-1*H*-benzimidazol-2-yl)carbamate

**Molecular Formula:** $C_{16}H_{13}N_3O_3$
**Molecular Weight:** 295.293 g/mol

**Classification of Drugs** :Antiparasitic agent

## 1.1 Pharmacokinetic data

| Bioavailability : | 2–10% |
| --- | --- |
| Protein binding : | 95% |
| Metabolism : | Extensive liver |

| Biological half-life : | 3–6 hours |
| --- | --- |
| Excretion : | Faeces, urine (5–10%) |

## 2. EXPERIMENTAL

### 2.1 Materials

Mebendazole was providedby Arti drugs lab Ltd. as raw material. Analytical HPLC grade Acetonitrile was purchased from Merk Pvt. Ltd. HPLC grade Acetic Acid and Water were obtained from Finar laboratory.

### 2.2 Instrumentation

The chromatographic system used to perform development and validation of this assay method was comprised of a LC-20AT*vp* binary pump, a SPD-20Avp UV-VIS detector and a rheodyne manual injector model 7725i with 20µl loop (Shimadzu, Kyoto, Japan) connected to a multi-instrument data acquisition and data processing system (Class-VP 6.13 SP2, Shimadzu).

### 2.3 Mobile phase preparation

The mobile phase consisted of Acetonitrile – 0.1M Glacial Acetic Acid (60: 40, v/v). To prepare 0.1M Glacial Acetic Acid solution, 60 gram (5.7 ml) Glacial Acetic Acid were weighed and dissolve in 1000 ml HPLC grade Water. Mobile phase was filtered through a 0.45 μm nylon membrane (Millipore Pvt. Ltd. Bangalore, India) and degassed in an ultrasonic bath (Spincotech Pvt. Ltd., Mumbai).

### 2.4 Diluent Preparation

Mobile phase was used as diluent.

### 2.5 Standard Preparation

100mg of  Mebendazole was weighed and transferred (working standard) into a 100ml volumetric flask. The diluent methanol was added and sonicated to dissolve it completely and made up to the mark with the same solvent. Further 1ml

of the above stock solution was pipetted into a 10ml volumetric flask and diluted up to the mark with diluent. The contents were mixed well and filtered through 0.45 μm nylon membrane paper. The calibration curve was plotted with the concentrations of the 60 to 100 mg/ml working standard solutions. Calibration solutions wereprepared and analyzed immediately after preparation.

The formulation tablets of mebendazole were crushed to give finely powdered material. Powder  equivalent to 60 mg ofdrug was taken in 100 ml of volumetric flask containing 5 ml of mobile phase and was shaken to dissolve the drug and then filtered through 0.45 μm nylon membrane paper.

## 2.6 Chromatographic Conditions

Chromatographic analysis was performed on Luna hypersil C18 (250x4.6 mm, 5 μ) column. The mobile phase was consisted of Acetonitrile and 0.1M Glacial Acetic Acid (60: 40, v/v).  The flow rate of the mobile phase was adjusted to 1.2 mL/min and the injection volume was 20 μl. Detection was performed at 210 nm.

## 3. RESULT AND DISCUSSION

## 3.1Development and Optimization of the HPLC Method

Proper selection of the method depends upon the nature of the sample (ionic or ionisable or neutral molecule), its molecular weight and solubility. Mebendazole is dissolved in polar solvent hence RP-HPLC was selected to estimate them. To develop a rugged and suitable HPLC method for the quantitative determination of Mebendazole, the analytical conditions were selected after testing the different parameters such as diluents, buffer, buffer concentration, organic solvent for mobile phase and mobile phase composition and other chromatographic conditions. Our preliminary trials using different composition of mobile phases consisting of water with methanol or Acetonitrile, did not give good peak shape.

The mobile phase consisted of Acetonitrile – 0.1M Glacial Acetic Acid (60: 40, v/v). To prepare the buffer solution, 60 gm(5.7 ml) Glacial Acetic Acid was weighed and dissolves in 1000 ml HPLC grade water. Mobile phase was filtered through a 0.45 μmnylon membrane (Millipore Pvt. Ltd. Bangalore, India) and degassed in an ultrasonic bath (Spincotech Pvt. Ltd., Mumbai).

By using 0.1M Glacial Acetic Acid in 1000 ml of buffer and keeping mobile phase composition as Acetonitrile – 0.1M Glacial Acetic Acid (60: 40, v/v), best peak shape was obtained. For the selection of organic constituent of mobile phase, Acetonitrile was chosen to reduce the longer retention time and to attain good peak shape. Figure 2 represents wavelength selection. Figure 2 represent the chromatogram of standard respectively.
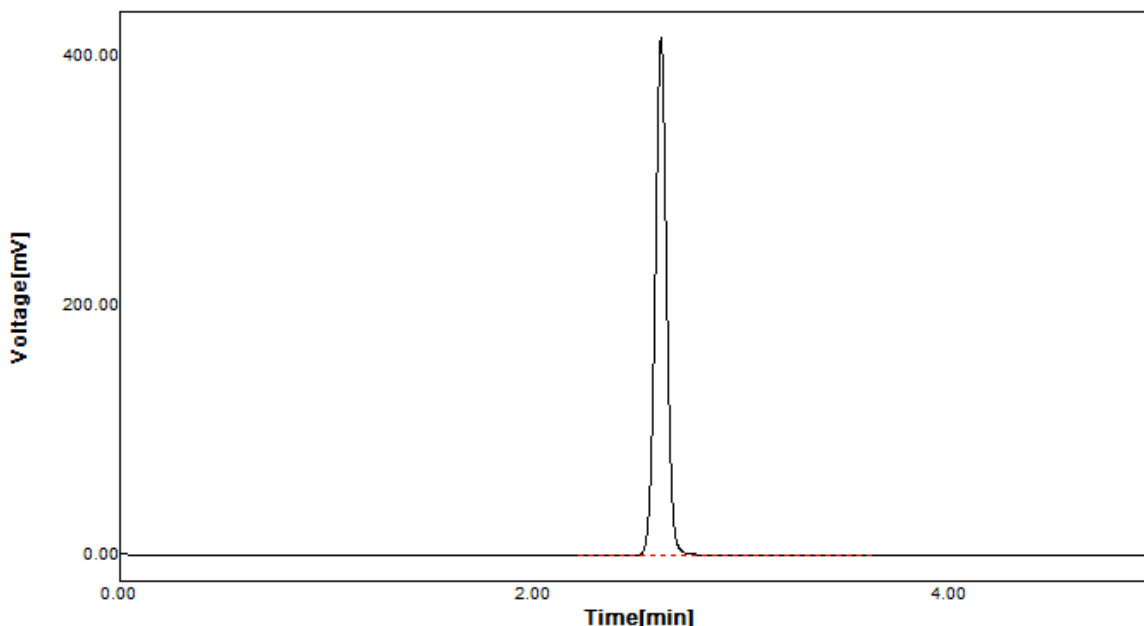


*Figure 2: Chromatogram of standard preparation*

## 3.2 Method Validation

### 3.2.1 Linearity

Five points calibration curve were obtained in a concentration range from 60-100 mg/ml for Mebendazole. The response of the drug was found to be linear in the investigation concentration range and the linear regression equation was $y = 499.994x - 25999.64$ with correlation coefficient 0.9958. (Figure 3)
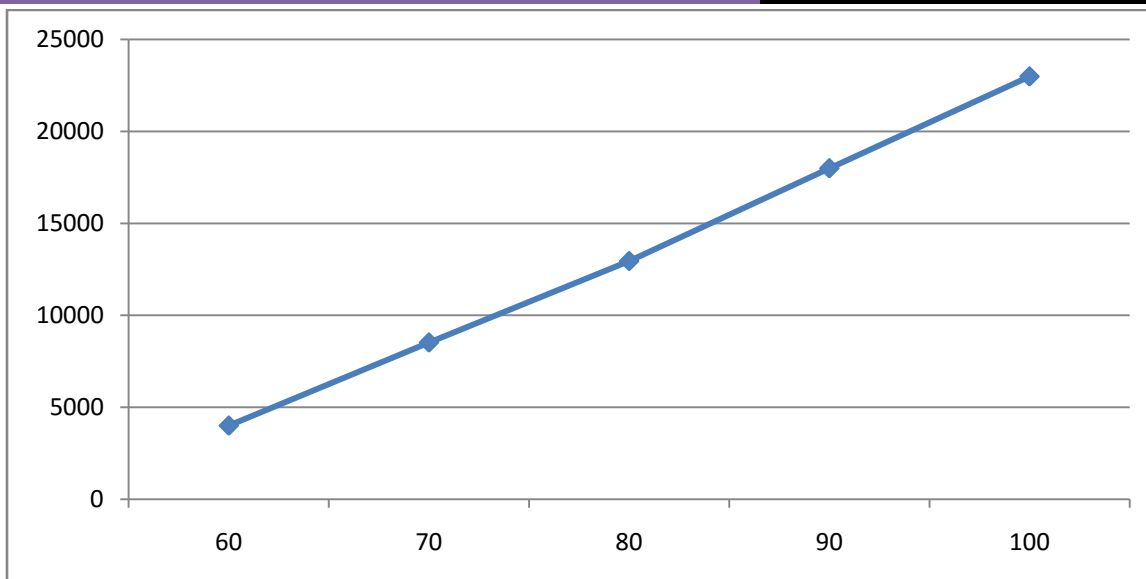
*Figure 3: Linearity curve for Mebendazole*

**Table No. 3.1** Linearity of  Mebendazole

| Set No | Concentration | Area |
|--------|---------------|------|
| 1 | 60 mg/ml | 4000.000 |
| 2 | 70 mg/ml | 8520.001 |
| 3 | 80 mg/ml | 12950.120 |
| 4 | 90  mg/ml | 17996.096 |
| 5 | 100 mg/ml | 22590.000 |

## 3.2.2 LOD and LOQ

The limit of detection and limit of quantification were evaluated by serial dilutions of Mebendazole stock solution in order to obtain signal to noise ratio of 3:1 for LOD and 10:1 for LOQ. The LOD value for Axitinib was found to be 1 mg/ml and the LOQ value 10 mg/ml.

## 3.2.3 Precision

Precision study was established by evaluating method precision and intermediate precision study. System precision was evaluated by analyzing the standard solution five times. Method precision of the analytical method was determined by analyzing six sets of sample preparation. Assay of all six replicate

sample preparations was determined and mean % assay value, standard deviation; % relative standard deviation was calculated. Intermediate precision of the analytical method was determined by performing method precision on another day by another analyst under same experimental condition. Assay of all six replicate sample preparations was determined and mean % assay value, standard deviation; % relative standard deviation was calculated.

Data obtain from precision experiments are given in Table 5.2 for intraday and interday precision study for Axitinib. The RSD values for intraday precision study and interday precision study was < 2.0% for Mebendazole, which confirm that the method was precise.

The result of repeatability and intermediate precision study are shown in Table 3.2. The developed method was found to be precise as the %RSD values for the repeatability and intermediate precision studies were 0.00019 % and 0.00006 %, respectively, which confirm that method was precise.

### Table 3.2: Evaluation data of precision study

| Set (80 mg/ml) | Intraday (n=6) | Interday (n=6) |
|:---:|:---:|:---:|
| 1 | 12950.120 | 12950.999 |
| 2 | 12950.124 | 12950.980 |
| 3 | 12950.078 | 12951.003 |
| 4 | 12950.137 | 12950.998 |
| 5 | 12950.114 | 12950.999 |
| 6 | 12950.078 | 12950.998 |
| *Mean* | 12950.100 | 12951.00 |
| *Standard Deviation* | 0.0248 | 0.0081 |
| *%RSD* | 0.00019 | 0.00006 |

### 3.2.4 Accuracy

The HPLC area responses for accuracy determination are depicted in Table 3.3. The result shown that best recoveries (99.00 - 100.00 %) of the spiked drug were obtained at each added concentration, indicating that the method was accurate. Chromatogram obtain during accuracy study were shown in Figure 13-15

**Table 3.3: Evaluation data of accuracy study**

| Concentration in mg/ml | Amount added concentration [a] (mg/ml) | Amount found Concentration[a] (mg/ml) | % Recovery | % RSD |
| --- | --- | --- | --- | --- |
| 80 | 0.1000 | 0.0990 | 99.00 | 0.012 |
| 90 | 0.1001 | 0.0999 | 99.99 | 0.015 |
| 100 | 0.1001 | 0.1000 | 100.00 | 0.018 |

[a] Each value corresponds to the mean of three determinations.

### 3.2.5 Robustness

The result of robustness study of the developed assay method was established in Table 5.4. The result shown that during all variance conditions, assay value of the test preparation solution was not affected and it was in accordance with that of actual. System suitability parameters were also found satisfactory; hence the analytical method would be concluded as robust.

### 3.2.6 System suitability

A system suitability test of the chromatographic system was performed before each validation run. Five replicate injections of standard preparation were injected and asymmetry, theoretical plate and % RSD of peak area were determined for same. Acceptance criteria for system suitability, asymmetry not more than 2.0, Theoretical plate not less then 5000 and % RSD of peak area not more then 2.0, were full fill during all validation parameter.

### 4. REFERANCE

1. www.google.com

2. www.wikipedia.com

3. "Mebendazole". *The American Society of Health-System Pharmacists.*Retrieved Aug 18, 2015.

*4. Mehlhorn, Heinz (2001). Encyclopedic reference of parasitology. 107 tables (2 ed.). Berlin [u.a.]: Springer. p. 259. ISBN 9783540668299.*

*5. "WHO Model List of Essential Medicines (19th List)" (PDF). World Health Organization. April 2015. Retrieved 8 December 2016.*

*6. Hamilton, Richard J. (2012). Tarascon pocket pharmacopoeia (13 ed.). Burlington, Mass.: Jones & Bartlett Learning. p. 33. ISBN 9781449624286*

*7. Durgeshparekh et al, "RP HPLC method development and validation for quantification of mebendazole  inapi and pharmaceutical formulation", PharmaTutor (Print-ISSN: 2394 - 6679; e-ISSN: 2347 - 7881) Volume 4, Issue 5 , page 46-51.*

*8. AnantAgrekar and et ai, " Simultaneous determination of mebendazole and pyrantelpamoate from tablets by RP HPLC", Article in Talanta 44 (11): 1959-69, December 1997 , DOI : 10.1016/S0039-9140(96)02118-2, source: Pubmed*

*9. Indian pharmacopeia*

*10.British Pharmacopeia*

# Comparison Study About Physico-Chemical Analysis of Ground Water Quality of Selected Two Talukas of Mehsana District. (North Gujarat).

## [1]Limbachiya M.C, [2]Joshi D. N, [3]Patel P. S, [4]Solanki M.R

[1, 2, 3, 4] **R.R.Mehta College of Science & G D Modi College of Commerce, Palanpur (North Gujarat), India.**

**Abstract:**
Irrigation water samples were analyzed for Electrical Conductivity (EC), pH, Total Dissolved Solids (TDS), cations ($Ca^{+2}$, $Mg^{+2}$, $Na^+$ and $K^+$) and anions ($CO_3^{-2}$, $HCO_3^{-1}$, $Cl^{-1}$, and $SO_4^{-2}$). Various indices *viz.,* Residual Sodium Carbonate (RSC), Sodium Adsorption Ratio (SAR) and Soluble Sodium Percentage (SSP) were calculated from the estimated cations and anions expressed in me / L.
In general, the well/tube well water samples of Mehsana district were slightly alkaline in reaction (pH values 7.02 to 8.21), TDS values range from 270 to 1970 ppm in study area. The maximum salt concentration was found in groundwater samples of Bechraji and Mehsana taluka .The minimum concentration of $CO_3^{-2}$ was found in ground water samples of Bechraji taluka. For $HCO_3^{-1}$ ions, the minimum concentration was found in ground water samples of in Bechraji taluka. The minimum concentration of sulphate ($SO_4^{-2}$) ion was found in ground water samples of Bechraji taluka. The overall RSC values were ranged from -22.71 to 8.2 with mean value of 0.8825 me/L.
As per RSC values, the result show that 90 percent ground water samples of Bechraji taluka fall under safe categories and only 10 percent ground water samples fall under unsafe categories.The highest value of $Na^{+1}/K^{+1}$ ratio was recorded in ground water samples of Bechraji taluka

**Keywords:** Ground Water, Residual Sodium Carbonate (RSC), Physico-Chemical.Sodium Adsorption Ratio (SAR).

**Introduction:**
In India most of the population in dependent on ground water as the only source of drinking water supply. The ground water is believed to be comparatively much clean and free form pollution then surface water. But prolonged discharge of the industrial effluents, domestic of the industrial effluents, domestic sewage and solid was dump caused the ground water to become polluted and created health problemes[1]. Water is never found pure in nature. Rain water is the nearest approach to chemically pure water, but it contains small account of organic matter and dissolved gases,principally O2and Co2 taken from the air. Much of the current concern with regards to environmental quality is focused on water because of its importance in maintaining the human health and health of the ecosystem. Fresh water is finite resource, essential for agriculture, industry and even human existence, without fresh water of adequate quantity and quality, sustainable development will not be possible[2].
71 % of the Earth's surface is covered by water. Earth's surface water is held in two different kinds of water bodies: Salt water bodies and Fresh water bodies.

Fresh water resource is becoming day-by-day at the faster rate of deterioration of the water quality is now a global problem[3].

**The study area:**
Mehsana district is situated in the northern part of the Gujarat state. Spreading over 4376.38 sq.km having ten talukas. This district is situated between $23^o$ 0' to $24^o$ 1' N latitude and $72^o$ 0' to $72^o$ 50' E longitude. It is bounded by Banaskantha district in North, Patan district in West, Sabarkantha district in East and Ahmedabad, Gandhinagar district in South. Almost all the areas of this district fall under arid and semi-arid climate. There is no any permanent river in this district.

The groundwater is also very deep and salty forest is very rare, in this district. In northern part of Mehsana district, single cropping is predominant cropping pattern double cropping is possible only where irrigation facilities are available.The mean annual temp of the area is $26^0$ C.The maximum temperature in may being $44^0$C.The average rain fall of the area is 25-303mm.[4]

**Material and Methods:**
The underground well/tube well water samples from representative area were collected, filtered and stored in the plastic bottle putting a layer of toluene and analyzed  for major ion chemistry employing the standard water quality procedure APHA.[5,6]  The methods used for analysis or different constituents of water are as under:

**Methods used for analysis of irrigation water:**
The underground well/tube well water samples from representative area were collected, filtered and stored in the plastic bottle putting a layer of toluene. The methods used for analysis or different constituents of water are as under:

| Characteristics | Methods used | Reference |
|---|---|---|
| pH | pH meter (Systronic India Ltd., Model type 322) | Richard (1954) |
| EC | Electric Conductivity meter (Systronic India Ltd., Model No. 303) | Richard (1954) |
| $CO_3^{-2} + HCO_3^{-1}$ | Neutralization method (Titrating against sulphuric acid) | Richard (1954) |
| $Cl^-$ | $AgNO_3$ Titration (Precipitation method) | Richard (1954) |
| $SO_4^{-2}$ | Titration against standard Barium chloride solution | Vogel, A.I. (1948) |
| $Na^+$ | Flame photometrically (Mediflame 127, Systronic India Ltd., Sr. No. 2913) | Richard (1954) |
| $K^+$ | Flame photometrically  (Mediflame 127, Systronic India Ltd., Sr. No. 2913) | Richard (1954) |
| $Ca^{+2}$ | Versenate method (Titration against EDTA solution) | Richard (1954) |
| $Mg^{+2}$ | Versenate method (Titration against standard EDTA solution) | Richard (1954) |

The following water quality indices were calculated by standard formulas for categorization purpose.

**Soluble Sodium Percentage (SSP)**

| Soluble Sodium Percentage | = | $\dfrac{Na^+}{Ca^{+2} + Mg^{+2} + Na^+ + K^+}$ | X | 100 |
|---|---|---|---|---|

(Concentration of all cations are in me/L)

**Sodium adsorption ratio (SAR):**

Sodium adsorption ratio is calculated using the formula:

$$SAR = \frac{Na^+}{\sqrt{\dfrac{Ca^{+2} + Mg^{+2}}{2}}}$$

(Concentration of all cations are in me/L)

**Residual Sodium Carbonate (RSC)**

The residual sodium carbonate may be calculated simply by substracting the quantity of Ca + Mg from the sum total of carbonates and bi-carbonates determined separately in a given sample and expressed in me/L.

Thus,

$$RSC = (CO_3^{-2} + HCO_3^{-1}) - (Ca^{+2} + Mg^{+2})$$

(All ionic concentrations are in me/L)

**Table - 1 Range and Average value of chemical constituents of underground well waters of Becharaji taluka.**
**(Sample No. 1 to 20)**

| Sr. No. | Characteristics | Values | | | |
|---|---|---|---|---|---|
| | | Minimum | Maximum | Average | |
| 1. | EC dSm$^{-1}$ at 25$^o$C | 0.4 | 6.15 | 3.22 | |
| 2. | pH | 7.02 | 8.08 | 7.78 | |
| 3. | TDS | 270 | 1970 | 1276.5 | |
| 4. | SSP | 49.53 | 83.18 | 67.38 | |
| 5. | SAR | 2.33 | 21.69 | 9.76 | |
| 6. | RSC | -9.1 | 3.1 | -3.08 | |
| | Cations, me/L | | | | |
| 7. | Ca$^{+2}$ + Mg$^{+2}$ | 2.8 | 17.1 | 9.79 | |
| 8. | Na$^{+1}$ | 2.75 | 47.5 | 21.9 | |
| 9. | K$^{+1}$ | 0.0007 | 0.0179 | 0.005765 | |

| | Anions, me/L | | | |
|---|---|---|---|---|
| 10. | $CO_3^{-2}$ | 0.00 | 0.8 | 0.28 |
| 11. | $HCO_3^{-1}$ | 3.4 | 9.7 | 6.43 |
| 12. | $Cl^{-1}$ | 10 | 44 | 23.5 |

**Table – 2 Range and Average value of chemical constituents of underground Well waters of Mehsana taluka**
**(Sample No. 21 to 42).**

| Sr. No. | Characteristics | | Values | |
|---|---|---|---|---|
| | | Minimum | Maximum | Average |
| 1. | EC dSm$^{-1}$ at 25$^o$C | 0.85 | 7.7 | 2.8 |
| 2. | pH | 7.23 | 8.01 | 7.69 |
| 3. | TDS | 570 | 1830 | 1110.46 |
| 4. | SSP | 52.27 | 75.82 | 66.21 |
| 5. | SAR | 3.95 | 14.95 | 9.28 |
| 6. | RSC | -22.2 | 3.7 | -2.46 |

| | Cations, me/L | | | | |
|---|---|---|---|---|---|
| 7. | $Ca^{+2} + Mg^{+2}$ | 4.5 | 30.5 | 10.5 | |
| 8. | $Na^{+1}$ | 7 | 49 | 21.69 | |
| 9. | $K^{+1}$ | 0.0025 | 0.0083 | 0.0059 | |

| | Anions,me/L | | | |
|---|---|---|---|---|
| 10. | $CO_3^{-2}$ | 0 | 1.2 | 0.5 |
| 11. | $HCO_3^{-1}$ | 5.6 | 9.9 | 7.56 |
| 12. | $Cl^{-1}$ | 6 | 70 | 20.48 |

**Table II and III** give information about the quality of water in relation to their sodium absorption ratio (SAR)    and RSC Value.

**Table – 3 Cationic and anionic percentage of the total ions Taluka –Bechraji**
**Sample No. 1 to 20**

| Sr. No. | Ions (me/L) | Values | | |
|---|---|---|---|---|
| | | Minimum | Maximum | Average |
| 1. | $Ca^{+2} + Mg^{+2}$ | 2.8 | 17.1 | 9.79 |
| 2. | $Na^{+1}$ | 2.75 | 47.5 | 21.9 |
| 3. | $K^{+1}$ | 0.0007 | 0.0179 | 0.005765 |
| 4. | $CO_3^{-2}$ | 0.00 | 0.8 | 0.28 |
| 5. | $HCO_3^{-1}$ | 3.4 | 9.7 | 6.43 |
| 6. | $Cl^{-1}$ | 10 | 44 | 23.5 |

## Table – 4 Taluka- Mehsana
### Sample No. 21 to 42

| Sr. No. | Ions (me/L) | Values | | |
| --- | --- | --- | --- | --- |
| | | Minimum | Maximum | Average |
| 1. | $Ca^{+2} + Mg^{+2}$ | 4.5 | 30.5 | 10.5 |
| 2. | $Na^{+1}$ | 7 | 49 | 21.69 |
| 3. | $K^{+1}$ | 0.0025 | 0.0083 | 0.0059 |
| 4. | $CO_3^{-2}$ | 0 | 1.2 | 0.5 |
| 5. | $HCO_3^{-1}$ | 5.6 | 9.9 | 7.56 |
| 6. | $Cl^{-1}$ | 6 | 70 | 20.48 |

Mean cation composition in different EC classes are given in Table III. The result shows     that $Na^+$ and $Ca^{+2} + Mg^{+2}$, ions increased with the salinity, but $K^+$ ion decreased in C4 class of EC in Bechraji taluka.

The concentration of $Na^+$, $Ca^{+2} + Mg^{+2}$ ions regularly increased with salinity but and $K^+$  ion decreased in $C_4$ class of EC  in ground water samples of Vijapur taluka of Mehsana district. Such observations were also recorded by Timbadiya and Paliwal *et al.* (1975) and Patel *et al.* (1993) in ground water samples of three talukas of Mehsana district.

### Mean cation composition in different EC classes Taluka Bechraji
### Sample No: 1 to 20

| Sr. No. | Cations (me/L) | EC in $dSm^{-1}$ | | | |
| --- | --- | --- | --- | --- | --- |
| | | 0.0-0.25 (C$_1$) | 0.25-0.75 (C$_2$) | 0.75-2.25 (C$_3$) | 2.25-5.0 (C$_4$) |
| 1. | $Na^{+1}$ | - | 2.75 | 11.6875 | 25.89 |
| 2. | $K^{+1}$ | - | 0.0025 | 0.007 | 0.0057 |
| 3. | $Ca^{+2} + Mg^{+2}$ | - | 2.8 | 4.575 | 11.64 |

### Taluka- Mehsana
### Sample No. 21 to 42

| Sr. No. | Cations (me/L) | EC in $dSm^{-1}$ | | | |
| --- | --- | --- | --- | --- | --- |
| | | 0.0-0.25 (C$_1$) | 0.25-0.75 (C$_2$) | 0.75-2.25 (C$_3$) | 2.25-5.0 (C$_4$) |
| 1. | $Na^{+1}$ | - | - | 21.125 | 22.66 |
| 2. | $K^{+1}$ | - | - | 0.0058 | 0.0061 |
| 3. | $Ca^{+2} + Mg^{+2}$ | - | - | 10.62 | 10.29 |

In bechraji taluka, the concentration of $CO_3^{-2}$, $HCO_3^{-1}$ and $Cl^{-1}$ varied from 0.0 to 0.8, 3.4 to 9.7 and 10.0 to 44.0 me/L with the mean values of 0.28, 6.43 and 23.5 me/L, respectively (Table 4.5).In Mehsana taluka, the concentration of these anions varied from 0.0 to12, 5.6 to 9.9 and 6 to 70 me/L with the mean value of 0.5 and 7.56 and 20.48 me/L respectively

### Results and Discussion:
As per experimental data, the water of Bechraji taluka of Mehsana District has high to very high salinity (EC of 0.4 to 4.15) and low sodium hazard (2.33 to 21.69 SAR Value) and probably safe to unsafe limits of RSC (-9.1 to 3.1).Only 9.09% as doubt to unsafe (unsuitable) for irrigation

.Unsuitable irrigation water not only reduces the crop growth but also affects the chemical characteristics of the soil in which the crop is growing.

Out of twenty two samples of Mehsana taluka, about Foutteen samples fall under $C_3$ class, eight samples fall under $C_4$ class and as per USSL classification. None of sample falls under $C_1$ class in Mehsana taluka.  As per Kanwar's and Ramamoorthy's classification, 2 9 and 11 samples fall under $C_5$, $C_4$ and $C_3$ classes, respectively.

From the above results, it can be concluded that most of the ground water samples fall under $C_3$class in Mehsana taluka. About 61 percent samples fall under $C_3$ class in Bechraji, Mehsana taluka. and 6 percent ground water samples fall under $C_2$ class in Bechraji,Mehsana,taluka. The ground water of Bechraji and Mehsana taluka is more salineThe ground water of Bechraji taluka had very high salinity maximum number of ground water samples in high to very high salinity ($C_3$ and $C_4$ class). A very high proportion of sodium in these water samples is also reflected in the Eton's (1935) classification. Based on Soluble Sodium Percentage (SSP) classification, maximum numbers of ground water samples *i.e.,* about 5 percent samples fall under SSP class I (0.0 – 50.0) in Bechraji taluka. In ground water samples of Mehsana taluka 13 samples fall under class III. As per value of RSC, ground water of Bechraji and Mehsana taluka was mostly found free from RSC hazards and maximum quantity of underground water of Kadi taluka of Mehsana district was found unsafe for irrigation purpose.

## References:

1. Raja R E, Lydia Sharmila, J.Princy Merlin, Chritopher G, (2002) Physico-Chemical Analysis of some Ground water samples of KotputliTown Jaipur,Rajasthan, *Indian J Environ Prot*., **22(2)**, 137.
2. Kumar N, (1997) A View on Freshwater environment, *Ecol. Env & Cons*. **3**, **(3-4)**.
3. Mahananda H.B, Mahananda M.R, and. Mohanty B.P, (2005). Studies on the Physico-chemical and Biological Parameters of a Fresh Water Pond Ecosystem as an Indicator of Water Pollution.  *Ecol. Env & Cons*.**11 (3-4)**, pp 537-541.
4. Limbachiya M.C.,Patel K.C.Nimavat K.S., and Vyas K.B.,Study on quality of irrigation water of vijapur talukas of mehsana disrtrict.Gujarat India.Elixir Appl.Chem.40(2011):5471-5473.
5. Standard method for examination of water and waste water ,"American public health Association",Washington DC.,18$^{th}$ edition.,1962:p.1134
6. Standard method for examination of water and waste water ,"American public health Association",Washington DC.,18$^{th}$ edition .,1995:2-4,29-179.

# SYNTHESIS, CHARACTERIZATION AND BIOLOGICAL EVALUATION OF SOME AZETIDINONES DERIVATIVES CONTAINING HYDRAZIDE MOEITIES

Milankumar Arjunbhai Sharda, Dr.G.D.Acharya

Department of chemistry,

RR.Mehta College of Science & C.L.Parikh College of Commerce, Palanpur

E-mail - govindvarde7@gmail.com

## ABSTRACT

N-arylidene derivatives**(3a-h)** was synthesized using Naphtho[2,1-b]furan-2-carbohydrazide **(1)** react with aromatic aldehydes **(2a-h)**. Further cyclocondensation reaction between compounds **(3a-h)** with chloroacetyl chloride yields desired compoundsViz N-(3-chloro-2-oxo-4-phenylazetidin-1-yl)naphtho[2,1-b]furan-2-carboxamide**4(a-h).** The characterization of these compounds was carried outby using analytical and spectral analysis. Also synthesized compounds were examined for their antimicrobial activities. The results show good to moderate antimicrobial activity for all compounds.

**KEY WORDS:**Naphtho[2,1-b]furan-2-carbohydrazide, Azetidinones, Arylidine derivatives, Antimicrobial activity, Spectral Studies.

## INTRODUCTION

Heterocyclic compounds extensivelyfound in nature and also synthesized were studiedfor their wide variety of biological activities [1-3]. Many naturally occurring and synthetic compounds contain hydrazide as a basic moiety, which posses interesting pharmaceutical, agricultural and industrial properties [4-6]. Hydrazide and its derivative are well known for their extensive biological activities such as antibacterial, antifungal, antitubercular, anti-cancer, anti-inflammatory anti-consuvalentactivity [7-10].

Since the first discovery of the β-lactams by Staudinger, the interest continued for these derivatives because of the pharmalogical significance of β-lactam antibiotics along with finding of

naturally occurring β-lactams. A vast research has been carried out over the years for the chemistry of azetidinones which continues as an emerging field [11,12]. As a result many of azetidinone derivatives found diverse therapeutic applications such as antibacterial, antifungal, antitubercular, anti-cancer, anti-inflammatory, and antihypertensive [13-17].

In search of biological active compounds merge both of azetidinone and hydrazide moieties which may enhance the biological activity of compounds. Hence the present communication comprises the synthesis and characterization of new azetidinone derivatives based on N-arylidine derivatives. Also the antimicrobial evaluation were carried out for all compounds against different bacterial and fungal strains. The general procedure for targeted compounds is shown in **Scheme-1**.

**Scheme-1**

## MATERIALS AND METHODS

Melting points were determined in open capillary tubes and were uncorrected. The IR spectra were recorded in KBr pellets on a Nicolet 400D spectrometer and ^{1}H NMR spectra were recorded in DMSO with TMS as internal standard on a Bruker spectrometer at 400 MHz. LC-MS of selected samples taken on LC-MSD-Trap-SL-01046.

All the chemicals were laboratory grade and purchased from local market. naphtho[2,1-b]furan-2-carbohydrazide was prepared by reported method [18],While the synthesis of N-arylidene derivatives were carried out according to our previous report [19]. The yields, melting points and elemental analysis data of arylidene derivatives are given in **Table -1**.

### PreparationN-(3-chloro-2-oxo-4-phenylazetidin-1-yl)naphtho[2,1-b]furan-2-carboxamide (4a-h):

A mixture of arylidine derivatives (3a-h) and triethyl amine (TEA) was dissolved in 1,4-dioxane and stirred well at 0-5 °C. To this well-stirred cooled solution drop wise addition of chloroacetyl chloride was carried. The mixture was then allowed stirring for 3-4 hours and further left at room temperature for 24 hours. The resultant mixture was concentrated, cooled, poured into ice-cold water, and then air-dried. Further the products were recrystallized using ether and n-hexane. The final products **(4a-h)** were obtained in good yield. The physical and elemental results of compounds (4a-e) are displayed in **Table -2**.

**Table: 1Physical and Elemental Analysis of Compounds (3a-h)**

| Compd. | Molecular formula (Mol.wt.) | LC-MS Data | Yield | M.P.* °C | Elemental Analysis | | | | | |
| | | | | | %C | | % H | | %N | |
| | | | | | Found | Calcd. | Found | Calcd. | Found | Calcd. |
|---|---|---|---|---|---|---|---|---|---|---|
| 3a | $C_{20}H_{14}N_2O_2$ (314) | 315 | 66 | 178-180 | 76.40 | 76.4 | 4.47 | 4.4 | 8.89 | 8.9 |
| 3b | $C_{21}H_{16}N_2O_2$ (328) | 324 | 64 | 175-176 | 76.79 | 76.8 | 4.90 | 4.9 | 8.51 | 8.5 |
| 3c | $C_{21}H_{16}N_2O_2$ (328) | 327 | 63 | 181-183 | 76.80 | 76.8 | 4.88 | 4.9 | 8.51 | 8.5 |
| 3d | $C_{20}H_{14}N_2O_3$ (330) | 333 | 65 | 176-178 | 72.69 | 72.7 | 4.25 | 4.2 | 8.46 | 8.4 |
| 3e | $C_{20}H_{14}N_2O_3$ (330) | 336 | 67 | 182-184 | 72.71 | 72.7 | 4.26 | 4.2 | 8.47 | 8.4 |
| 3f | $C_{21}H_{16}N_2O_3$ (344) | 341 | 65 | 167-168 | 73.22 | 73.2 | 4.66 | 4.6 | 8.10 | 8.1 |
| 3g | $C_{21}H_{16}N_2O_3$ (344) | 348 | 63 | 173-174 | 73.22 | 73.2 | 4.67 | 4.6 | 8.12 | 8.1 |
| 3h | $C_{20}H_{13}N_2O_2Cl$ (348.5) | 353 | 63 | 180-182 | 68.86 | 68.8 | 3.74 | 3.7 | 8.01 | 8.0 |

* Uncorrected

**Table:2 Physical and Elemental Analysis of Compounds (4a-h)**

| Compd. | Molecular formula (Mol.wt.) | Yield | M.P.* °C | Elemental Analysis | | | | | |
|---|---|---|---|---|---|---|---|---|---|
| | | | | %C | | %H | | %N | |
| | | | | Found | Calcd. | Found | Calcd. | Found | Calcd. |
| 4a | $C_{22}H_{15}ClN_2O_3$ (390) | 65 | 225-226 | 67.61 | 67.5 | 3.87 | 3.8 | 7.17 | 7.1 |
| 4b | $C_{23}H_{17}ClN_2O_3$ (404) | 62 | 210-212 | 68.23 | 68.2 | 4.23 | 4.2 | 6.92 | 6.9 |
| 4c | $C_{23}H_{17}ClN_2O_3$ (404) | 61 | 205-206 | 68.23 | 68.2 | 4.23 | 4.2 | 6.92 | 6.9 |
| 4d | $C_{22}H_{15}ClN_2O_4$ (406) | 67 | 220-221 | 64.95 | 64.9 | 3.72 | 3.7 | 6.89 | 6.8 |
| 4e | $C_{22}H_{15}ClN_2O_4$ (406) | 64 | 202-203 | 64.95 | 64.9 | 3.72 | 3.7 | 6.89 | 6.8 |
| 4f | $C_{23}H_{17}ClN_2O_4$ (420) | 65 | 199-201 | 65.64 | 65.6 | 4.07 | 4.0 | 6.66 | 6.6 |
| 4g | $C_{23}H_{17}ClN_2O_4$ (420) | 68 | 195-197 | 65.64 | 65.6 | 4.07 | 4.0 | 6.66 | 6.6 |
| 4h | $C_{22}H_{14}Cl_2N_2O_3$ (425) | 55 | 211-212 | 62.13 | 62.1 | 3.32 | 3.3 | 6.59 | 6.6 |

*Uncorrected

**BIOLOGICAL SCREENING**

**Antibacterial activities**

The antibacterial activities of all the compounds were studied against gram-positive bacteria and gram-negative bacteria at a concentration of 50μg/ML by agar cup plate method. A methanol system was used as control in this method. Similar conditions using tetracycline as a control was used standard for comparison. The area of inhibition of zone measured in mm. Some compounds were found more toxic for *Bacillus subtilis* and *E.coli* bacterial strains, while for other bacterial strains the compounds shows moderate activity compare to standard drug used **(Table -3)**.

**Table: 3 Antibacterial Activities of Compounds (4a-h)**

| Compounds | Gram +Ve | | Gram -Ve | |
| --- | --- | --- | --- | --- |
| | *Staphylococcus aureus* | *Bacillus subtilis* | *E.coli* | *Klebsiella promioe* |
| **4a** | 44 | 64 | 63 | 62 |
| **4b** | 40 | 61 | 59 | 57 |
| **4c** | 42 | 65 | 57 | 50 |
| **4d** | 44 | 72 | 70 | 61 |
| **4e** | 46 | 74 | 71 | 65 |
| **4f** | 41 | 69 | 67 | 68 |
| **4g** | 43 | 70 | 69 | 70 |
| **4h** | 40 | 57 | 62 | 63 |
| **Tetracycline** | 57 | 76 | 74 | 84 |

**Antifungal Activities**

The fungicidal activity of all the compounds was studied at 1000 ppm concentration in vitro. Plant pathogenic organisms used were*Botrydepladia thiobromine, Nigrospora Sp, Aspergillus niger and*

*Rhizopus nigricum*. The antifungal activities of all the compounds (4a-h) were measured on each of these plant pathogenic strains on a potato dextrose agar (PDA) medium. Such a PDA medium contained potato 200g, dextrose 20g, agar 20g and water 1c. Five days old cultures were employed. The compounds to be tested were suspended (1000ppm) in a PDA medium and autoclaved at $120^{o}$ C for 15 min. at 15atm. pressure. These media were poured into sterile Petri plates and the organisms were inoculated after cooling the Petri plates. The percentage inhibition for fungi was calculated after five days using the formula given below:

**Percentage of inhibition = 100(X-Y) / X**

Where,   X = Area of colony in control plate

Y = Area of colony in test plate

The fungicidal activity displayed by various compounds **(4a-h)** is shown in **Table-4**.

**Table: 4 Antifungal Activities of Compounds (4a-h)**

| Zone of Inhibition at 1000 ppm (%) | | | | |
|:---:|:---:|:---:|:---:|:---:|
| **Compounds** | **Nigrospora Sp.** | **Aspergillus Niger** | **Botrydepladia Thiobromine** | **Rhizopus Nigricum** |
| **4a** | 74 | 77 | 64 | 69 |
| **4b** | 68 | 70 | 62 | 64 |
| **4c** | 69 | 72 | 60 | 62 |
| **4d** | 70 | 73 | 61 | 65 |
| **4e** | 70 | 76 | 63 | 67 |
| **4f** | 68 | 74 | 60 | 64 |
| **4g** | 66 | 72 | 57 | 61 |
| **4h** | 65 | 70 | 55 | 60 |

**RESULTS AND DISCUSSION**

Condensation reaction between Naphtho[2,1-b]furan-2-carbohydrazide **(1)** react with aromatic aldehydes **(2a-h)** resulted into the different N-arylidine derivatives **(3a-h)**. Further reaction of these N-arylidine derivatives **(3a-h)** withchloroacetyl chloride in presence of 1,4-dioxane gives targeted compounds in good yields i.e. N-(3-chloro-2-oxo-4-phenylazetidin-1-yl)naphtho[2,1-b]furan-2-carboxamide **(4a-h)**. IR spectra showing an essential absorption band at 3435 cm$^{-1}$(N-H),1240 cm$^{-1}$(C-O), 3030-3080cm$^{-1}$ (C-H of Ar.),1690cm$^{-1}$(CONH),2815-2850cm$^{-1}$(-OCH$_3$),2950,1370cm$^{-1}$(-CH$_3$).**$^1$H NMR:**7.53-8.56(12H,m,Ar-H),11.6-11.9(1H,s,CONH),8.4-8.6(1H,s,N=CH),3b;2.28(3H,s,CH$_3$),3c;2.32(3H,s,CH$_3$),     3d; 5.10(1H,s,-OH),3e; 5.23(1H,s,-OH),3f; 3.84(3H,s,-OCH$_3$), 3g; 3.85(3H,s,-OCH$_3$).The C, H, N analysis data of all compounds are presented in **Table -1**.

The experimental C,H,N data of newly prepared **(4a-h)(Table-2)** were in very good agreement with predicted structure **(Scheme-1)**were further supported by the IR spectra showing an absorption bands at1735-1750 cm$^{-1}$ (C=O of β-lactam), 3030-3080 cm$^{-1}$(C-H, of Ar.), 1725,1675 cm$^{-1}$ (-CO,CONH),3410-3425(N-H),1240-1250 (C-O), 2815-2850 cm$^{-1}$ (-OCH$_3$), 2950,1370 cm$^{-1}$ (-CH$_3$)for (4a-h) compound.

**$^1$H NMR:**5.3, 5.8 (2H, s, β-lactam of azitidinone), 11.2-11.4 (1H, s,-CONH),4b; 2.29 (3H,s,-CH$_3$), 4c; 2.35 (3H,s,CH$_3$), 4d; 5.21 (1H,s,-OH), 4e; 5.27 (1H,s,-OH),4f; 3.94 (3H,s,-OCH$_3$), 4g; 3.91 (3H,s,-OCH$_3$). The C, H, N, S analysis data of all compounds are presented in **Table-2**.

**CONCLUSION**

The final products were prepared by using condensation of N-arylidine derivatives with chloroacetyl chloride and further characterization carried out by using elemental, IR and NMR analysis. The elemental analyses are well matched with the predicted structure as shown in **scheme-1** while the IR analyses shows essential peaks to support the probable structure of synthesized compounds.The antimicrobial activity possess good to moderate activity against employed strains.

## ACKNOWLEDGEMENT

## REFERENCES

[1].M.S. Saini, A. Kumar, J. Dwivedi and R. Singh, Inter. J. Pharm. Sci. Res., **4**, 66 (2013).

[2]. S. V. Hote and S. P. Bhoyar, IOSR J. Appl. Chem., **1**, 43 (2014).

[3]. R. Dua, S. Shrivastava, S. K. Sonwane and S. K. Srivastava, Adv. Biol. Res. **5,** 120 (2011).

[4]. R. A. Rane, N. K. Sahu, C. P. Shah and N. K. Shah. J. Enzyme Inhib. Med. Chem., **29**, 401 (2013).

[5]. R. M. Mohare, D. H. Fleit and O. K. Sakk. Mol., **16**, 16 (2010).

[6]. M. N. Koopaei, M. J. Assarzadeh, A. Almasirad, S. F. Ghasemi-Niri, M. Amini, A. Kebriaeezadeh, N. N. Koopaei, M. Ghadimi and A. Tabe, Iran. J. Pharm. Res., **12**, 721  (2013).

[7]. N. Kumar and L. Singh, Int. J. Cli. Pharm. Res., **7**, 154 (2015).

[8]. R. Narang, B. Narasimhan and S. Sharma, Curr. Med. Chem., **19**, 569 (2012).

[9]. T. Nasr, S. Bondoc and M. Youns, Euro. J. Med. Chem., **76**, 539 (2014).

[10].M. Kim, S. Lee, E. B. Park, K. J. Kim, H. H. Lee, J. S. Shin, K. Fischer, A. Koeberle, O. Werzd, K. T. Lee and J. Y. Lee, Bioorg. Med. Chem. Lett., **1**, 94 (2016).

[11]. H. Staudinger, Commun. Liebigs Ann. Chem., **51**, 356 (1907).

[12]. D. S. Salunkhe and P.B. Piste, Int. J. Pharm. Sci. Res., **4**, 666 (2014).

[13]. A. Deep, P. Kumar, B. Narasimhan, S. M. Lim, K. Ramasamy, R. K. Mishra and V. Mani, Acta Poloniae Pharm. Drug Res., **73**, 65 (2016).

[14]. S. D. Joshi, U. A. More, D. Parkale, T. M. Aminabhavi, A. K. Gadad, M. N. Nadagouda and R. Jawarkar, Med. Chem. Res., **24**, 3892 (2015).

[15]. M. W. Majewski, K. D. Watson, S. Cho, P. A. Miller, S. G. Franzblau and M. J.

Miller, Med. Chem. Commu., **7**, 141 (2016).

[16]. S. K. Gupta, A. Mishra, Anti-inflammatory & Anti-allergy Agents in Med. Chem., **15**,

DOI: 10.2174/1871523015666160210124545, (2015).

[17]. N. Singh, R. C. Agarwal and C. P. Singh, J. Chem. Pharm. Res., **4**, 5185 (2012).

[18]. P.J. Shah, H.S. Patel and B.P.Patel, J.  Saudi. Chem. Soc.,**17**, 307 (2013).

[19]. First paper reference

# A Study of Salinity of ground water in some semi-arid tracts in Kheralu Taluka of Gujarat

## M.R.Solanki[1], M.C.Limbachiya

*Department of Chemistry, R. R. Mehta College of Science and C. L. Parikh*
*College of Commerce, Palanpur, Gujarat.*

**Abstract**

Because of the insufficiency of water resources and serious environment, it becomes much more mergence to develop the water saving agricultureThe northern part of Gujarat state may be classified as a semi-arid region because most of the area receiving low rainfall. About fiftysamples of ground water were collected from different tracts in Kheralu regions during pre-monsoon2015,post-monsoon 2015 and pre-monsoon 2016 and tested for their EC and $P^H$values. These water samples were further tested for cations and anions. The data obtainwere used for classification of water into different categories on the basis of EC (ElectricalConductivity).In general it was found that there was no area having EC within 250 micromhos/cm in ground water during year 2015-16. Thus, the water quality has improved duringpre-monsoon 2016, as compared to pre-monsoon 2015 due to the recharging of ground waterby high rainfall in year 2015.

**Key words**: Water Analysis, Salinity, Electrical Conductivity.

## Introduction

Soil salinization and soil water pollution were great concerned with fast development in Northern part of Gujarat.Water is an elixir part of our lifeit is a universal solvent. [1] and it dissolves the minerals from the rock in which, it isstored and thus chemical and physical parameters of a particular area will be changed. Tillsome time ago, the quality of ground water was considered to be relatively very good incomparison to surface water[2-3]. Handa[4]has carried out ground water contamination studies invarious parts of the country. Study on ground water quality with respect to drinking,irrigation, and industrial purposes have been carried out in different part of India [5-7]Underground water in North Gujarat have diversity of quality problems. Ground water whichis always in motion interacts with the subsurface environment during this movement. Itdissolves transports and deposits mineral matter. The health and economic prosperity ofcommunity rest on the supply of clean water to individual. In our Nation, it is estimated thatabout 75 million work days are lost every year due to water related diseases. The quality of ground water varies from place to place.

In the arid and semi-arid region, majority of ground water are of poor quality. i.e. eithersaline or alkali. Soil degradation through salination has seriously affected the productivity ofover 1.214 Mha of land in Gujarat state out of which 55 percent of the area comes undermoderately to highly saline which is unsuitable for cultivation of the crops. The remaining 45percent area has low to moderately salinating problems. The problems related with waterquality are more servers in North Gujarat.

Quality of irrigation water is one of the main factors to be understood in irrigated agriculture. Injudicious irrigations even with good quality water turn much agriculturally good soil in toSaline or alkali condition. Quality of water is an important consideration in any appraisal ofsalinity or alkali conditions in an irrigated area. Generally all irrigation water that have beenused for successfully for a long period have a conductivity value less than 2250 micromhos/cm. Water of higher conductivity may be used with suitable amendments

andprecautions, but under normal conditions they are harmful to the soil structure and theircontinuous use will result in salinity hazard, with ultimate effect on plant growth. Salinityhazards affect the plant through the effects of excessive salts and osmotic pressure of soilsolution which restricts the water and nutrient absorption. The first effect of salinity underfield situation is the reduction in germination. The salt concentration are measure in terms of
micro mhos/cm (or dsm-1), mg /L (ppm) and meq/L.

## Materials and Methods

### Experimental

The northern part of Gujarat state may be classified as a semi arid region. The mean annualtemperature of the area is 27.0ºc. The maximum temperature in May being 43ºc. Theaverage annual rainfall of the area is 26-32″there being fairly wide variation from year toyear. There is no any permanent river in this region. The ground water is also very deep

There is under study some areain Kheralu taluka in Mehsana district of North Gujarat.The area is a semi arid region. The major water resources of the area are wells and tube wells.

During the year 2015-2016, about 42 ground water samples were collected during pre-monsoon2015, 48 samples during post monsoon 2015, and about fifty (50) samples duringpre-monsoon 2016. The samples collected from the wells were analyzed for major ionchemistry, employing the standard water quality procedures APHA [8-9]. pH and electricconductance were measured usingpH and EC meter. Total dissolved solids were computed bymultiplying the EC by conversion factor 0.65 as suggested by Hem [10]. Total hardness asCaCO₃ was measured by using standard EDTA solution. Mg was calculated taking thedifference of TH and ca. Chloride was determined volumetric method using standard AgNO₃solution. Sulphate was estimated through turbidimetric method. Table-1 presents the resultsof some typical ground water samples. The data obtained were used for classification ofwater into different categories on the basis of electrical conductivity(EC).

**Table-1 : Chemical properties of ground water in some semi-arid tracts of North Gujarat during year 2015-16.**

| SR No. | EC. Dsm$^{-1}$ at 25°c | TDS (ppm) | P$^H$ | mg / L. | | | | | | | |
| :--- | :--- | :--- | :--- | :--- | :--- | :--- | :--- | :--- | :--- | :--- | :--- |
| | | | | Ca$^{+2}$ | Mg$^{+2}$ | Na$^{+1}$ | K$^{+1}$ | CO$_3^{-2}$ | HCO$_3^{-1}$ | Cl$^{-1}$ | SO$_4^{-2}$ |
| 1 | 2.02 | 989 | 8.20 | 2.5 | 3.2 | 11.5 | 0.06 | 1.8 | 4.5 | 9.1 | 1.8 |
| 2 | **0.80** | 721 | 8.46 | 1.2 | 1.0 | 14.2 | 0.05 | 0.4 | 7.8 | 8.9 | 4.6 |
| 3 | 1.82 | 772 | 8.06 | 1.0 | 1.3 | 15.3 | 0.03 | 1.0 | 6.4 | 7.7 | 9.2 |
| 4 | 1.75 | 784 | 8.01 | 1.7 | 0.9 | 12.5 | 0.01 | 0.8 | 10.2 | 11.3 | 7.5 |
| 5 | 2.39 | 875 | 8.87 | 1.9 | 2.1 | 6.7 | 0.03 | 0.4 | 7.3 | 8.7 | 4.6 |
| 6 | 2.47 | 947 | 8.11 | 1.9 | 2.0 | 10.3 | 0.01 | 0.6 | 7.6 | 8.9 | 1.8 |
| 7 | 4.24 | 1049 | 7.09 | 2.9 | 2.6 | 5.3 | 0.06 | 1.6 | 9.2 | 21.4 | 1.7 |
| 8 | 4.46 | 1200 | 8.49 | 3.4 | 3.3 | 16.7 | 0.05 | 1.2 | 4.6 | 23.1 | 11.1 |
| 9 | 3.31 | 689 | 8.22 | 1.5 | 1.4 | 14.6 | 0.04 | 0.5 | 3.8 | 7.4 | 4.9 |
| 10 | 4.04 | 931 | 7.08 | 3.1 | 1.9 | 8.8 | 0.01 | 2.1 | 9.38 | 11.8 | 6.7 |

**Table-2to Table-4 gives an information about the distribution of samples under variousranges of salinity in the ground water during the pre-monsoon 2015, post monsoon 2015 and pre- monsoon 2016[10-15]**

**Table-2 : Distribution of ground water samples , under various ranges of salinity During the Pre-monsoon 2015**

| Sr. No | Electrical Conductivity In m mhos/cm. | Pre-monsoon 2015 | |
|---|---|---|---|
| | | Number of samples | % of samples |
| 1 | 0-250 | Nil | Nil |
| 2 | 250-750 | 01 | 2.35 |
| 3 | 750-2250 | 21 | 50.64 |
| 4 | 2250-5000 | 16 | 37.46 |
| 5 | >5000 | 04 | 9.55 |

**Table-3 : Distribution of ground water samples , under various ranges of salinity During the Post-monsoon 2015**

| Sr. No | Electrical Conductivity In m mhos/cm. | Post-monsoon 2015 | |
|---|---|---|---|
| | | Number of samples | % of samples |
| 1 | 0-250 | Nil | Nil |
| 2 | 250-750 | 01 | 2.11 |
| 3 | 750-2250 | 29 | 61.20 |
| 4 | 2250-5000 | 15 | 30.24 |
| 5 | >5000 | 03 | 6.45 |

**Table 4: Distribution of ground water samples, under various ranges of salinity. During the Pre-monsoon 2016**

| Sr. No | Electrical Conductivity In m mhos/cm. | Pre-monsoon 2016 | |
|---|---|---|---|
| | | Number of samples | % of samples |
| 1 | 0-250 | Nil | Nil |
| 2 | 250-750 | 01 | 2.0 |
| 3 | 750-2250 | 28 | 55 |
| 4 | 2250-5000 | 17 | 35 |
| 5 | >5000 | 04 | 8 |

**Results and Discussion**

The quality of water is influenced by the nature of rock minerals through which it passes. Itmay undergo changes due to ion exchange, dissolution of salts, and hydrolysis of materials ofthe rocks, as well as the surface soils. The total concentration of soluble salts as measured byelectrical conductivity. The categories of water on the basis of their electrical conductivity areas follows: (Table-5)

**Table-5 : Classification of water**

| Sr. No | Electrical Conductivity In m mhos/cm. at $25^0$C | Category |
| --- | --- | --- |
| 1 | 0-250 | Excellent |
| 2 | 250-750 | Good |
| 3 | 750-2250 | Permissible |
| 4 | 2250-5000 | Doubtful |
| 5 | >5000 | Unsafe |

It can be seen from the above tables that there was no sample having EC within 250 micromhos/cm in ground water during year 2015-16. During pre-monsoon 2015, 2.35 percentwater samples had EC values between 250 to 750 micro mhos/cm which was slightly decreased to 2.11percent during post monsoon 2015 and it was again slightly decreased to2.0 percent during pre-monsoon 2016. There was 50.64 percent samples having EC Between750 to 2250 micro mhos/cm during pre monsoon 2015 it was increased to 61.20 percentduring post-monsoon 2015and it was again decreased to 55.0 percent during pre monsoon2016. There was 50.64 percent samples having EC Between 2250-5000 micro mhos/cmduring pre monsoon 2015. It was decreased to 30.24percent during post monsoon 2015. Andit was increased to 35.0 percent during pre monsoon 2016. There was 9.55 percent watersamples having EC more than 5000 micro mhos/cm during pre monsoon 2015. It wasdecreased to 6.45percent during post monsoon 2015 and again it was increased to 8.0 percentduring pre-monsoon 2016

**Conclusion**

The water quality has improved during pre monsoon 2016, as compared to pre monsoon 2015in North Gujarat due to the recharging of ground water by high rainfall in year 2015.

**References**

[1] Chiew, F. H. S., and T. A. McMahon. 1991. Groundwater recharge from rainfall and irrigation in the Campaspe River Basin. Australian Journal of Soil Research 29:651–70.
[2] So, H. B., and L. A. G. Aylmore. 1993. How do sodic soils behave? The effect of sodicity on soil physical behavior. Australian Journal of Soil Research 31:761–77.
[3] Bhat D. M., and Hegde G. R., *IJEH,* **1997,** 39, 61.
[4] Handa B. K., Ground Water Contamination in India Key Paper Regional Workshop on Environmental Aspects of Ground Water Development, Kurrukshetra**1994,** Oct. 17-19.
[5]Kitamura Y., Tomohisa Y., Toshimasa H., et al.. Agricultural Water Management, 2006, 85:1-14.
[6] Majmudar D. and Gupta N., *IJEH,* **2002,** 42, 28.
[7] Kurshid S. H., Hussain H. and Zabeerudein, *Indian J. Appl. Hydrology,* **2002,** V(XV), 30.
[8] APHA, Standard methods for the examination of water and waste water; Washington USA, (1995).
[9] Standard Method for Examination of Water and Waste Water American Public Health

Association, Washington DC, 18th Edition, **1992**, pp. 1134.

[10] Hem J.D., Study and interpretation of the Chemical Characteristics of Natural Waters 2254, Scientific Publisher, Jodhpur, **1991**.

[11] Abbasi S.A., A method manual by Water Quality 'sampling and Analysis: Discovery publishing house New Delhi, **1998**.

[12] Annual Reports: Soil Survey Division, Govt. of Gujarat, Gandhinagar.

[13] Durga Prasad N. K. and Sankarapitchaiah. P, . Inland water Resources: India. Discovery Publishing House. New Delhi.

[14] Water and Salinity Balances for Irrigated Agriculture in Pakistan. Jacob W. Kijne, 1996.

[15]Cheng-Shin Jang A, Shih-Kai Chen B, Yi-Ming Kuo , "Establishing An Irrigation Management Plan of Sustainable Groundwater Based On Spatial Variability of Water Quality and Quantity" *Journal of Hydrology* (Elsevier) 414–415, 201–210 (2012)

# PHOTOCATALYTIC DEGRADATION OF FAST GREEN DYE OVER CuO/Al$_2$O$_3$ COMPOSITE

## DEEPIKA PALIWAL[a*], RAKSHIT AMETA[a] and BINDU KATARIA[b]

[a]Department of Chemistry, PAHER University, UDAIPUR – 313003 (Raj.) INDIA

[b]Department of Chemistry,S. M. B. Govt. P.G. College, NATHDWARA – 313301 (Raj.)

INDIA

Email: deepikapaliwal666@gmail.com

## ABSTRACT

Fast green dye is generally used in artificial food coloring, which is harmful for human health. The photocatalytic degradation of fast green was monitored by spectrophotometrically in presence of CuO/Al$_2$O$_3$. The effect of some parameters affecting the rate of reaction, such as pH, dye concentration, amount of composite, light intensity, etc. has been studied. Optimum parameters were found as pH =8.0, concentration = $1.20\times10^{-5}$M; amount of semiconductor = 0.12g and intensity of light = 60.0 mWcm$^{-2}$. It was observed that composite was having better photocatalytic activity, then individual components.

## INTRODUCTION

Various industries use dyes in order to colour their products and throw a lot of coloured wastewater in the form of effluent. The discharge of dye-bearing wastewater into natural streams and rivers from the textile, paper, carpet, leather, distillery and printing industries make severe problems. The cleaning of wastewater is one of the most serious environmental problems of the present day. Discharge of dyeing industry wastewater into natural water bodies is not desirable as the colour prevents re-oxygenation in receiving water by cutting off penetration of sunlight. It also increases the BOD, and cause lack of dissolved oxygen to sustain aquatic life. Nowadays, research is focused on reactive and other anionic dyes because a large fraction of these dyes are remain in wastewater due to low removal efficiency of the conventional wastewater treatment plants. Fast green dye has been widely used in histology and cytology. It has been found to have tumorigenic effects in experimental animals, as well as mutagenic effects in both; experimental animals and humans. Furthermore, in its undiluted form, it poses risks of irritation of eyes, skin, digestive tract, and respiratory tract.

A number of studies have been made on the degradation of toxic organic compounds in wastewater by photocatalytic process using various semiconductors.Akpan and

Hameed[1]presented a review of the effects of operating parameters on the photocatalytic degradation of textile dyes using $TiO_2$-based photocatalysts. The findings revealed that different parameters, such as the initial pH of the solution, oxidizing agents, temperature of calcination, dopant(s) content and catalyst loading exert their individual influence on the photocatalytic degradation of any dye in wastewaters.Sharma et al.[2]degraded fast green FCF by Fe-pillared bentonite clay in presence of light. Bhatiet al.[3]preparedthe nano-sized bimetal ternary oxide($CeCrO_3$)using microwave treatment and used itfor photocatalytic degradation of fast green dye. Rochkind et al.[4] treated effluents stream containing hazardous dyes. They are of the opinion that dyes are inappropriate as model compound for the evaluation of photocatalytic activity of noval photocatalysts claimed to operate under visible light.Ntsendwana et al.[5] prepared a photo anode of exfoliated graphite-ZnO nanocomposite. They studied degradation of eosin yellow dye arefound that degradation efficiency of eosin yellow was 93%.Gupta et al.[6] used barium chromate powder as a photocatalyst for the degradation of eosin yellow.

Byberg at al.[7] studied the photocatalytic degradation of six acid dyes, i.e. direct red 80, direct red 81, direct red 23, direct violet 51, direct yellow 27 and direct yellow 50. All these dyes were compared in term of their mineralization, toxicity and removal of colour. $TiO_2$ was used as a semiconductor for this purpose. Hassan et al.[8]modified CN-$TiO_2$ with cryptomelane octahedral molecular sieves(OMS-2) by sol-gel method based self-assembly technique to enhance its photocatalytic activity under the daylight irradiation. ljubas et al.[9] used $TiO_2$ nanoparticles as semiconductor photocatalysts for the degradation ofcongo red (CR) and methyl orange (MO) dyes in an aqueous solution. Since $TiO_2$ particles become photocatalytically active on exposure to UV radiation, two sources of UV-A radiation were used – natural solar radiations, which contains 3–5% UV-A and artificial, solar-like radiation, created by using a lamp.

Mohabansiet al.[10]degraded aqueous solution of methylene blue dye in presence of a photocatalyst and UV light. Titanium dioxide and zinc oxide were used as photocatalyst for the study.The rate of decolorisation was estimated spectrophotometrically from residual concentration. Shrivastava et al.[11]reportedthat removal of dye methylene blue and Cr (VI) by considering influent concentration, loading of photocatalyst, pH and contact time as operating variables. The percentage removal of dye and Cr(VI) increases with increasing contact time. Tayade et al.[12] degraded methylene blue selecting it as a model compound. They used

ultraviolet light emitting diodes (UV-LED) as an alternate source. The photocatalytic activity of P-25 Degussa $TiO_2$ was evaluated using UV-LED reactor. Kottam et al.[13] preparednano-sized ZnO powder and photocatalytic degradation of rhodamine B dye was carried out usingthis ZnO nanopowder.

## EXPERIMENTAL

$1.0 \times 10^{-3}$ M stock solution was prepared by dissolving 0.0808 g of fast green in 100.0 mL of doubly distilled water. The absorbance of fast green was determined with the help of spectrophotometer at $\lambda_{max} = 624$nm. The structure of the dye is shown in Fig. 1.
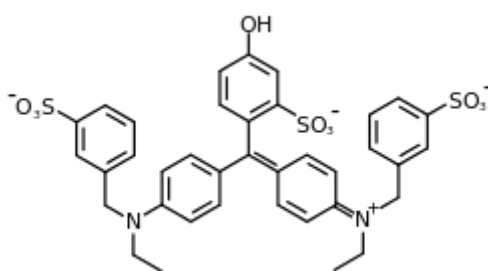


**Figure 1: Chemical Structure of fast green**

The dye solution was placed in equal amounts in three beakers.

- The first beaker containing fast green solution was kept with by CuO (copper oxide).
- The second beaker containing fast green solution was kept with by using $Al_2O_3$ (aluminium oxide)
- The third beaker containing fast green solution was kept with $CuO/Al_2O_3$ composite.

$1.0 \times 10^{-5}$M Fast green solution was prepared using doubly distilled water and 0.12 g of $CuO/Al_2O_3$ composite was added to it and pH was kept 8.0.Then this solution was exposed to a 200 W tungsten lamp at 60.0 mWcm$^{-2}$. A decrease in absorbance of fast green solution was observed with increasing time of exposure and it was faster in case of composite than individual components. A plot of $1 + \log A$ against time was found to be linear, which indicates that the photocatalytic degradation of fast green follows pseudo-first order kinetics (Fig. 2). The rate constant was measured with the help of expression $k = 2.303 \times$ slope. A typical run is presented in Table1.

## Table 1: A typical run

pH = 8.0, [Fast green] = $1.20 \times 10^{-5}$M, Amount of $CuO/Al_2O_3$ = 0.12g, Light intensity

$= 60.0 \text{ mWcm}^{-2}$

| Time (min.) | CuO | | Al$_2$O$_3$ | | CuO/Al$_2$O$_3$ | |
|---|---|---|---|---|---|---|
| | A | 1 + logA | A | 1 + logA | A | 1 + logA |
| 0 | 0.589 | 0.7701 | 0.589 | 0.7701 | 0.589 | 0.7701 |
| 10 | 0.569 | 0.7551 | 0.582 | 0.7649 | 0.549 | 0.7396 |
| 20 | 0.550 | 0.7404 | 0.573 | 0.7582 | 0.533 | 0.7267 |
| 30 | 0.526 | 0.7210 | 0.568 | 0.7543 | 0.501 | 0.6998 |
| 40 | 0.524 | 0.7193 | 0.549 | 0.7396 | 0.473 | 0.6749 |
| 50 | 0.501 | 0.6998 | 0.543 | 0.7348 | 0.457 | 0.6599 |
| 60 | 0.490 | 0.6902 | 0.537 | 0.7299 | 0.437 | 0.6405 |
| 70 | 0.473 | 0.6749 | 0.531 | 0.7251 | 0.412 | 0.6149 |
| 80 | 0.452 | 0.6551 | 0.525 | 0.7202 | 0.398 | 0.5998 |
| 90 | 0.441 | 0.6444 | 0.519 | 0.7152 | 0.376 | 0.5752 |

Rate constant (k) for CuO $= 5.36 \times 10^{-5} \text{sec}^{-1}$

Rate constant (k) for Al$_2$O$_3 = 2.34 \times 10^{-5} \text{sec}^{-1}$

Rate constant (k) for CuO/Al$_2$O$_3 = 8.30 \times 10^{-5} \text{sec}^{-1}$
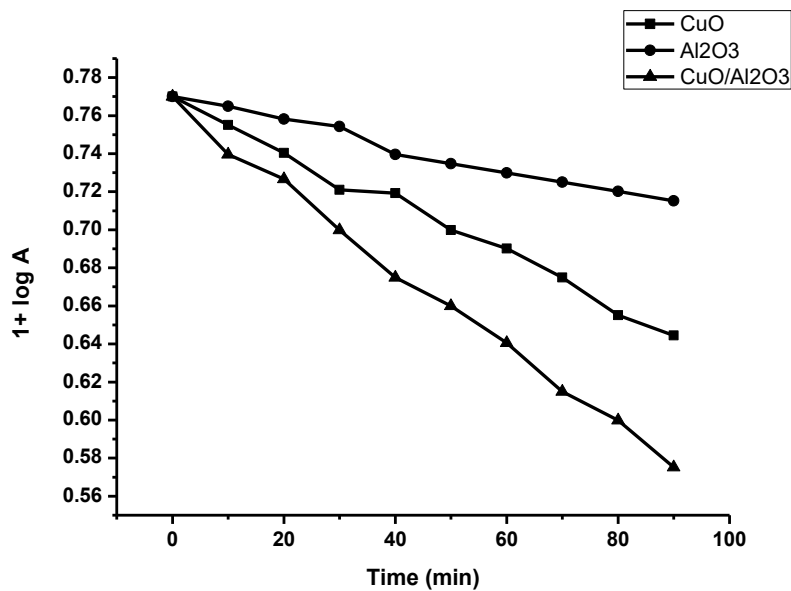


**Figure 2: Typical run**

## RESULTS AND DISCUSSION

### Effect of pH

The rate of degradation of fast green was investigated in the pH range 5.0 to 10.0. The results are given in Table 2. It was observed that the rate of degradation of fast green increases as pH was increased and optimum value found at pH=8.0.On further increasing pH, beyond 8.0, the rate of the reaction was decreased. This may be explained on the basis that at lower pH, the dye molecules present in neutral form have less attraction towards $H^+$ ions, but as the pH of the dye solution was increased, attraction between anionic dye molecules and $H^+$ ion increases, but after optimum value at 8.0, anionic dye molecules face repulsion with $^-$OHions and therefore the rate is retarded.

### Table 2: Effect of pH

[Fast green] = $1.20 \times 10^{-5}$ M, CuO/Al$_2$O$_3$ = 0.12 g, Light intensity = 60.0 mWcm$^{-2}$

| pH | Rate constant (k) $\times 10^5$(sec$^{-1}$) |
| --- | --- |
| 5.0 | 4.54 |
| 5.5 | 5.26 |
| 6.0 | 6.10 |
| 6.5 | 6.14 |
| 7.0 | 7.35 |
| 7.5 | 8.12 |
| **8.0** | **8.30** |
| 8.5 | 6.88 |
| 9.0 | 6.19 |
| 9.5 | 5.55 |

### Effect of fast green concentration

The effect of fast green concentration was studied on degradation rate of dye by taking its different concentrations.

The results are tabulated in Table 3.

### Table 3: Effect of fast green concentration

pH = 8.0, CuO/Al$_2$O$_3$ = 0.12 g, Light intensity = 60.0 mWcm$^{-2}$

| [Fast green] $\times 10^5$ M | Rate constant (k) $\times 10^5$ (sec$^{-1}$) |
| --- | --- |
| 0.20 | 5.70 |
| 0.40 | 6.64 |
| 0.60 | 7.14 |
| 0.80 | 7.66 |
| 1.00 | 8.06 |
| **1.20** | **8.30** |
| 1.40 | 7.20 |
| 1.60 | 6.93 |

As concentration of fast green was increased rate of reaction was also increased. It reaches a maximum at $1.20 \times 10^{-5}$M concentration but thereafter, rate of reaction decreases on increasing the dye concentration further. As the concentration of dye was increased, number of dye molecules also increased resulting in higher rate of degradations but above this particular limit, it acts as an internal filler and proper light intensity does not reach to semiconductor surface at on the bottom of the vessel and as a result degradation rate decreases.

**Effect of amount of CuO/Al$_2$O$_3$**

The amount of composite is also likely to affect the degradation of dye and hence, different amounts of CuO/Al$_2$O$_3$ composite were used. Results are tabulated in Table 4.

**Table 4: Effect of amount of CuO/Al$_2$O$_3$ composite**

pH = 8.0, [Fast green] = $1.20 \times 10^{-5}$ M, Light intensity = 60.0 mWcm$^{-2}$

| Amount of CuO/Al$_2$O$_3$ | Rate constant (k) $\times 10^5$sec$^{-1}$ |
| --- | --- |
| 0.02 | 5.15 |
| 0.04 | 6.01 |
| 0.06 | 6.59 |
| 0.08 | 7.11 |
| 0.10 | 7.98 |
| **0.12** | **8.30** |
| 0.14 | 7.67 |
| 0.16 | 6.92 |

The rate of degradation of dye was increased on increasing the amount of composite up to 0.12 g; but as the amount of composite was increased further. The rate of degradation decreases. This may be explained on the basis that after a particular value, it forms multilayer permitting close contact between particles; thus, $e^- - h^+$ recombination takes place resulting in a decrease in rate of reaction.

**Effect of light intensity**

The distance between the light source and exposed surface area of photocatalyst was varied to find out the effect of light intensity. As the intensity of light was increased, rate of degradation also increases. It is because of the fact that when light intensity was increased, the number of photons striking per unit area of semiconductor powder per unit time also increases. On further increasing the intensity of lightabove 60.0 mWcm$^{-2}$, rate of reaction decreases may be due to some side reactions.

**Table 5: Effect of light intensity**

pH = 8.0, CuO/Al$_2$O$_3$ = 0.12 g, [Fast green] = $1.20 \times 10^{-5}$ M

| Light intensity (mWcm$^{-2}$) | Rate constant (k) $\times 10^5$(sec$^{-1}$) |
|---|---|
| 20.0 | 5.26 |
| 30.0 | 5.39 |
| 40.0 | 5.85 |
| 50.0 | 6.80 |
| **60.0** | **8.30** |
| 70.0 | 6.72 |

**Mechanism**

According to observations, mechanism for photocatalytic degradationof fast green (FG)has been proposed as follows:

$$^1FG_0 \xrightarrow{h\nu} {}^1FG_1 \qquad \ldots(1)$$

$$^1FG_1 \xrightarrow{ISC} {}^3FG_1 \qquad \ldots(2)$$

$$SC \xrightarrow{h\nu} e^-(CB) + h^+(VB) \qquad \ldots(3)$$

$$e^- + O_2 \longrightarrow O_2^{\bullet-} \qquad \ldots(4)$$

$$O_2^{\bullet-} + {}^3FG_1 \longrightarrow \text{Leuco FG} \qquad \ldots(5)$$

$$\text{Leuco FG} \longrightarrow \text{Products} \qquad \ldots(6)$$
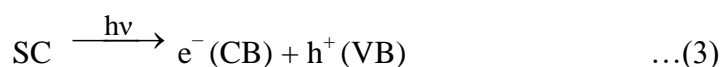
Fast green absorbs light and excited to its singlet excited state from ground state. Singlet state is then converted to its corresponding triplet state through inter system crossing.Composite is also excited by absorbing light and an electron is promoted to its conduction band leaving a $h^+$ (hole) in valence band. This electron combines with oxygen (dissolved oxygen) and form oxyanion radical. These oxyanion oxidizes the triplet state of fast green into its leuco form, which finally degrades to colourless product. The hydroxyl radical does not participates as an active oxidizing species as the rate of degradation remains unaffected even ion the presence of hydroxyl radical scavenger i.e. 2-propanol.

After complete degradation of dye,some physico-parameters were analyzed for treated and untreated dye solution and the results weregiven in Table 6.

**Table 6: Comparison of physico-chemical parameters**

| Quality parameter | Before degradation | After degradation |
|---|---|---|
| DO | 7.6ppm | 9.15ppm |
| Hardness | 465ppm | 280ppm |
| pH | 8.0 | 7.0 |
| Conductance | 10.3 mS | 62.2 mS |
| TDS | 407ppm | 513ppm |

**Dissolved Oxygen**

Dissolved oxygen refers to the level of free, non-compound oxygen present in water or other liquids. It is an important parameter in assessing water quality because of its influence on the organisms living within a body of water. The dissolved oxygen is 5ppm in normal potable water. Value of fast green dye was increased from 7.6ppm to 9.15ppm.

**Hardness**

Hardness is the amount of dissolved calcium and magnesium in the water. Hard water is high in dissolved minerals; both, calcium and magnesium. General guidelines for classification of waters are: 0 to 60 mg/L (milligrams per liter) as calcium carbonate is

classified as soft; 61 to 120 mg/L as moderately hard; 121 to 180 mg/L as hard; and more than 180 mg/L as very hard.Fast green hardness decreases from 465ppm to 280ppm.

## pH

Catalytic advanced oxidationreactions developed for the discoloration of the dye wastewater result in very effective oxidative degradation of a variety of dyes from food and textile industry effluents. pH value decreases from 8.0 to 7.0 after degradation of fast green.

## Conductance

Conductivity is directly proportional to dissolved minerals in the solution. Conductometer was used for measuring ion concentration of solution. Fast green dye solution shows conductance 10.3 mS before degradation, but after degradation, it increased up to62.2 mS.

## Total dissolved solid (TDS)

In general, the total dissolved solids concentration is the sum of the cations (positively charged) and anions (negatively charged) ions in the water. Therefore, the total dissolved solids test provides a qualitative measure of the amount of dissolved ions but does not tell us the nature or ion relationships. TDS value of fast green increased from 407 to 513ppm due to mineralization of dye.

## CONCLUSION

In the present investigation, it was found that the degradation rate of fast green dye was higher when we have used composite of $CuO/Al_2O_3$in compare to $CuO$ and $Al_2O_3$. The optimum conditions for dye degradation were achieved. The comparison of physico-chemical parameters of fast green dye solutions (before and after treatment) were analyzed, which supported that the dye solution after treatment may be reused in cleaning and irrigation purpose.

## REFERENCES

1. U. G. Akpan and B. H. Hameed, J. Hazard. Mater., 2009, 520–529, 170.
2. G. Sharma, D.Sonia, S.Benjamin, R.Ameta and S.Sharma, Sci. Revs. Chem. Commun., 2014,138-145, 4(4).

3.   I. Bhati, P. B. Punjabi and S. C. Ameta, Macedon. J. Chem. Chem.Eng.,2010,195–202, 29(2).

4.   M. Rochkind, S. Pasternak and Y. Paz, Molecules, 2015,88-110, 20.

5.   B. Ntsendwana, S. Sampath, B.B. Mamba, O.S. Oluwafemi and O.A. arotiba,  J. Mater. Sci. Electro.,2016, 592-598, 27(1).

6.   S. Gupta, D. Soni, R. Ameta and S. Benjamin, Chem. Sci. Tran., 2015, 851-857, 4(3).

7.   R. Byberg, J. Cobb, L. D. Martin, R. W. Thompson, T. A. Camesano, O. Zahraa and M. N. Pons, Environ. Sci. Pollut. Res. Int., 2013,3570-3581, 20(6).

8.   M. E. Hassan, J. Chen, G. Liu, D. Zhu and J. Cai, Materials, 2014,8024-8036, 7.

9.   D. ljubas, G. Smoljanic and H. Juretic,J. Env. Manage., 2015, 83–91, 161.

10.   N.P.Mohabansi, V. B. Patil and N.Yenkie,Rasayan J. Chem., 2011, 814-819, 4(4).

11.   V. S. Shrivastava, Arch. App. Sci. Res.,2012, 1244-1254, 4 (3).

12.   R. J. Tayade, T. S. Natarajan and H. C. Bajaj,Ind. Eng. Chem. Res., 2009 10262–10267, 48 (23).

13.   N. Kottam,C.R. Girija and B.M. Nagabhushana,Powder Technology,2012, 91-97, 215.

# STUDIES ON CHANGES OF PROTEIN IN LIVER OF TWO SPECIES OF FISHES OFF JODIA COAST IN GULF OF KUTCH.

Y.M.Kadiyani, D.N.Joshi*
Department of Biology, Bhavan's College, Dakor-388225
Department of Chemistry,
*R.R.Mehtacollege of science and
C.L.Parikh College of commerce Palanpur 385001

## Abstract

In case of *E.tetradactylum* protein content in the liver shows an increased level during pre-spawning and spawning period and the level decreases during post-spawning period, and normally same trend is observed in *L.tade* during active spawning period. It is worth noting that when compared to liver, the red muscles have more protein, as compared to the white muscles. This may be treated as the indication of nutritive value of both the species the fish muscles.

## Introduction

The liver in fishes perform may function as liver of higher vertebrates. It is generally believed to be main site for production and distribution of intermediary metabolites (Popper and Schaffner, 1957). A relative increase in liver size and maturity in fish has been reported and a steady increase in liver weight of female fish along with gonadal maturation has been recorded. Marked variations in liver, glycogen, lipids, amino acids, inorganic ions, in liver of fishes in relation to sexual maturity have been presented by many workers (Love, 1970; a review). The liver in *L. tade* is of dark red colour whereas *E. tetradactylum*is of yellow brown colour and it has occupied the largest protein viscera.

It is obvious that when the main sites of metabolic processes in *E. tetradactylum* and *L. tade* the liver is studied biochemically to investigate the variations in glycogen, lipids, cholesterol, protein, sodium, potassium, calcium, magnesium, phosphorus and iron. An attempt to throw some lights on various facets of metabolism of *E. tetradactylum* and *L. tade* would be fruitful.

However, very few investigations on variations in protein content, of fishes have been undertaken suggesting transit of protein from organs like liver to ovary, at various maturing stages of ovary, was reported by Philips, et al. (1964); Yamashita (1967).A decrease in protein in the organs other than ovaries at late maturing stages in the fishes have also been reported (Love, 1970).

Varghese (1976) has estimated monthly percentage of protein in white muscles and red muscles of male and female of *Pampus argenteus* and *Parastromateus niger* and found a rise in protein value from stage I to III of maturity and that declined at stages IV and V of maturity in *P. argenteus* female and in both female and male of *P. niger.*

**Material and Methods**

Samples of liver were taken from fifteen to twenty live fish, *E. tetradactylum* and *L. tade* every month. The samples were then dried in an oven at $48^0$C for 3 to 5 days. The dried homogenous powders were prepared. Total nitrogen was determined by Kjeldhal's method (A.O.A.O. 1965) with distillate collected in 4% boric acid solution. Now protein nitrogen (NPN) was estimated as that protein of the total nitrogen (TN) soluble in trichloroacetic acid as per the method of Jacobs (1951).

Protein nitrogen (PN) was calculated by deducting the value from total nitrogen (TN) value and Protein content by multiplying the protein nitrogen (PN) value with 6.25 the protein factor was calculated as per formula (Nimi 1972).

...... X 6.25 = Protein factor

## Results and Discussion

The protein content in liver increases in May to July and shows fluctuating level from July to December in *E. tetradactylum.* Comparing the protein content in liver with sexual maturity it is revealed that amount of protein increase during pre-spawning and spawning and the level starts to decrease during the late period of spawning and post spawning period i.e. from February to April.

In case of *L. tade* it gradually increases in pre-spawning period (July to October) and show higher level during late period of spawning and after spawning. Varghese (1976) has reported the rise in liver protein during early stage of maturity and in late stage of sexual maturity. The fall in proteins value at stages V and VI of the fishes possibly caused by depletion was also recorded by Varghese (1976). Similarly, decrease of protein content in organs other than ovaries at late maturity stages have been reported by several workers (Love, 1970). The protein content in liver of *E. tetradactylum* and *L. tade* shows higher level during pre-spawning, love level during late period spawning and after spawning agree with results of Love, (1970) and Varghese, (1976).

It is worth noting that when compared to liver, the red muscles have more protein, as compared to the white muscles. This may be treated as the indication of nutritive value of both the species the fish muscles.

## Table-1 Showing the Month wise Protein Content in Liver mg/gm

| Month | *E. tetradactylum* | *L. tade* |
|---|---|---|
| January | 47.27±0.03 | 51.20±0.05 |
| February | 45.95±0.06 | 38.90±0.03 |
| March | 40.25±0.03 | 36.30±0.01 |
| April | 36.30±0.03 | 32.40±0.00 |
| May | 33.65±0.00 | 27.15±0.06 |
| June | 44.65±0.08 | 30.20±0.06 |
| July | 52.10±0.03 | 32.80±0.06 |
| August | 46.65±0.05 | 35.85±0.03 |
| September | 49.00±0.00 | 38.50±0.00 |
| October | 45.10±0.03 | 44.20±0.03 |
| November | 52.92±0.06 | 42.95±0.01 |
| December | 51.90±0.03 | 47.70±0.02 |



Fig.-1 Protein Content in Liver
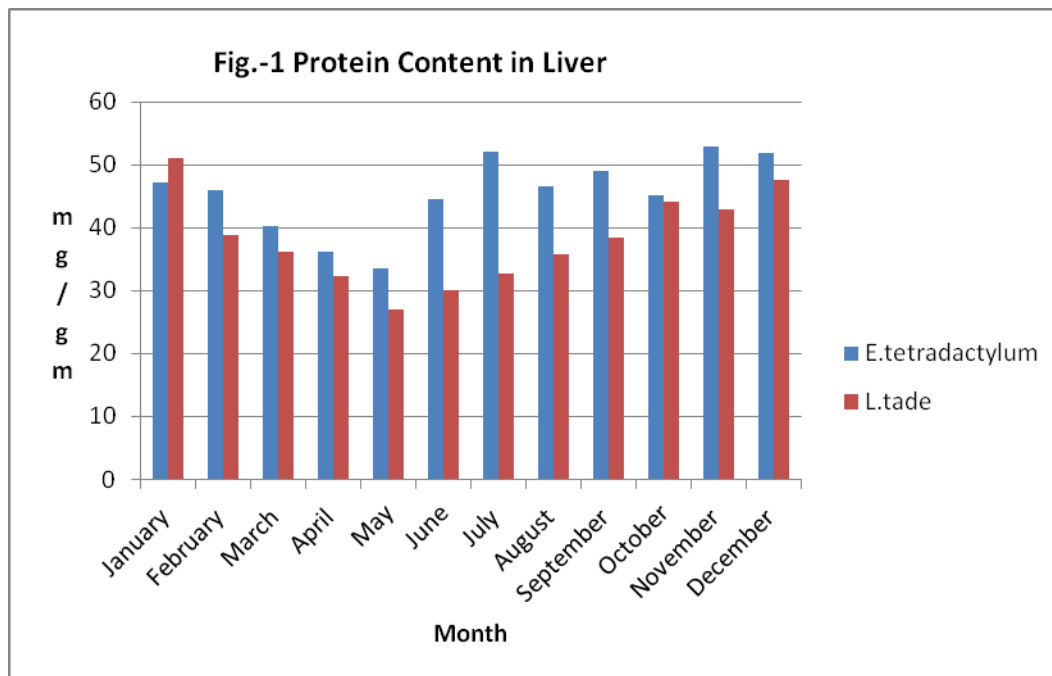
**Reference**

[1] Airan, J .W. (1950). J .W. (1950). Studies on Kolhapur Fresh Water fishes I. Water extractable proteins and minerals contents. Indian J.Med. Research 38, 169-172.

[2] Arevalo, A. (1948). Study of the variation in the chemical composition of the *Trachurus trachurus*L. Botn. Inst.esp.Occanogr.no.8 – 13.

[3] Atwater., (1892).The chemical composition and nutritive value of food fishes. Ann.Rept.Comm.Fish and Fisheries for 1888.Washington, 697.

[4] Bano, Yagna. (1977).Seasonal variations in the biochemical composition of *Clarius batyachius*. L.Proc Indian Acad.Sci. Vol. 85(B) (3): 147 – 155.

[5] Dawson, A.S. & Grimm A.S. (1980), quantitative seasonal change in the Protein and energy content of the carcass, ovaries and liver of adult female Place, *Pleuronecle platessa* L. Fish Biol.16, 493 – 504.

[6] Dela Hunty, G. & De vlaming, V.L. (1980).Seasonal relationships of ovary Weight, liver weight and fat Stores with body weight in the gold fish, *Carassiusauratus* L.J.Fish Biol 16:5-13.

[7] Geiger, E. and Borgstrom, G. (1962).Fish protein – nutritive aspects. IN "Fish as Food" (G.Borgastrm.ed.).Vol.II Chapter 2, pp.29-114 Academic Press, Landon and New York.

[8] Gerking, S.D. (1955) Induence of rato of feeding on body composition and Protein metabolism of blue gill sunfish.Physiol.Zool.28, 26 – 282.

[9] Hamior, G. (1955). Fish Proteins. IN "Advance in Protein chemistry", Vol.X. Edited by M.L.Anson, Bailey, and J.T. Edsall.Academic Press, NewYork.PP. 227 - 288.

[10] Ilder, D.P. and Bitnersm I. (1960).Biochemical studies on *Sockey salmoon* During spawning migration.IX.Fat, Protein and water in the major internal Organs and Cholesterol in the liver and gonads of the standard fish.J.Fish. Res.Bd.Can.17, 113-122.

[11] Jeeja Tharakan and N.D.Inasu 2009 Variations in the Protein content of Muscle, Liver and Ovary during Reproductive Cycle in *Puntius Parrah.* Millennium Zoology Vol.10 (1),2009:30-33

[12] Krivobok M.N. (1964). On the role of the liver in the maturation of the Ovaries of the Baltic herring,*Clupea harengus membress* L.Vop.Ikhtiol. 4,483-494.

[13] Medford B.A.and Mackay W.C.1978 Protein and lipid content of gonads, Liver and muscles of northern pike *Esoxhiclus* in relation to Gonad growth. J.ish.Research Board of Canada 35:213-219

[14] Varghese, T. P. (1976). Studies on muscles, gonads and liver of pomfrets, *Pamus argenteus* and *Parastormatesus niger*of Saurashtra coast. Ph. D. Thesis.

# SYNTHESIS AND ANTIMICROBIAL ACTIVITY OF 3-ARYL-5-(4' N, N-DIMETHYL AMINO PHENYL)-1-PHENYL PYRAZOLINES

## DIGANT N.JOSHI*, M.C.LIMBACHIYA, P.S.PATEL, Y.M.KADIYANI

*R.R.MEHTA COLLEGE OF SCIENCE & C.L.PARIKH COLLEGE OF COMMERCE

PALANPUR385001(GUJARAT)

Department of Biology, Bhavan'sCollege,Dakor 388225GUJARAT

4 N,N-Dimethyl amino phenyl Benzaldehyde1 on treatment with different acetophenones yielded 1 Aryl-3-(4'N,N-dimethylamino Phenyl)-2- Propenone (2a-e) which on cyclisation with phenyl hydrazine hydrate gives 3 Aryl-5-(4' N,N-dimethyl aminophenyl)-1-Phenyl pyrazolines (3a-e). The structures of the compounds 2a-e,3a-e were confirmed by elemental analysis, IR,NMR &MASS spectral data. All the products were evaluated for their in vitro growth inhibitory activity against several microbes.

## INTRODUCION

Among a wide variety of heterocycles that have been explored for developing pharmaceutically important molecules like pyrazolines[1-4]have played an important role in medicinal chemistry. In the light of these interesting biological activities, it appeared of interest to synthesize some new pyrazoline derivatives bearing 4- N,N' dimethylaminophenyl benzaldehyde moiety and asses their biopotential.

The starting compound 4- N,N' dimethylaminophenyl benzaldehyde4- N,N' dimethylaminophenyl benzaldehyde on reaction with aromatic acetophenones yielded corrospopnding 1-Aryl-3-(4'N,N-dimethyl amino phenyl)[2] propenone(2a-e). Compound(2a-e) on treatment with hydrazine hydrate in ethanol and in glacial acetic acid afforded corresponding 3-Aryl-5-(4'N,N-dimethyl amino phenyl)-1-Phenyl pyrazolines. (3a-e)[5] (scheme 1)

The structures of the compounds synthesized were assigned on the basis of elemental analysis IR,NMR &MASS spectral data. The compounds were evaluated for their antimicrobial screening.

## ANTIMICROBIAL ACTIVITY

The antimicrobial activity was determined using cup-plate agar diffusion method. The plates were incubated at $37^0$ C FOR 24 hrs. in case of  antimicrobial activity and at $30^0$ C for48 hrs. in case of antifungal activity. The control was also maintained with 0.1 ml of DMF in similar manner. The zones of inhibition of the growth were measured in mm. All the compounds were screened invitro for their antimicrobial activity against a variety of bacterial strains like Bacillus megaterium and Bacillus subtilis Gram positive and Escherichia coli and Aerobactoraerogen Gram negative bacteria and fungaiAspergillusawamori .Known antibiotics like Ampicillin,

Amoxicillin, Chloramphenicol, Norfloxacin, Gresiofulvin Showed a zone of inhibition at 25-30 mm.and greseofulvin at 25 mm. against various strains at bacteria and fungi.

## CONCLUSION
 Most of the compounds displayed moderate antimicrobial activity.

##  EXPERIMENTAL SECTION

 All the melting points were determined in open capillary tubes and are uncorrected. IR spectra were recorded on SHIMADZU-FT-IR-8400 Spectrophotometer 4000-400 cm$^{-1}$ KBr disc.PMR spectra on BRUKER Spectrometer(300 MHz) Mass spectra were recorded at C.D.R.I. Lucknow.

### 1 Aryl-3-(4' N,N dimethyl aminophenyl) -2- propenone.

        To an afficiently stirred solution of 4 N,N-dimethyl amino phenyl benzaldehyde 1 (0.01 mole  1.49 gm.) and 4- ethoxy acetophenone (0.01 mole 1.64 gm) in ethanole(25 ml) added 40% NaOH (3ml). The reaction mixture was heated for 10 min. and kept on stirrer for 24 hrs. The mixture was poured into ice water and acidified and crystallized from ethanole to give  (2e). Yield 50%,m.p.88$^0$C Calcd. For $C_{19}H_{21}NO_2$; C,77.28;H,7.11; N,4.74%; Found; C77.25; H, 7.08; N,4.72%

        Similarly other members were prepared and their physical data recorded in Table-1.

### 3-4-Ethoxy-5-(4'N,N-dimethyl amino phenyl)-1-Phenyl pyrazoline (2e)

 A mixture of  1,4-Ethoxyphenyl-3-(4'-N,N-dimethylaminophenyl)-propenone  (0.01  mole2.95 gm) and phenyl hydrazine (1.08g, 0.01M) in ethanole (25 ml)  was refluxed on a boiling water bath for 8 hrs.The reaction mixture was poured over crushed ice and acidified with acetic acid. The product was isolated and crystallized from ethanol to give 3e. Yield 59%, m.p. 79$^o$C, calcd.for;$C_{25}H_{27}N_3O$;  C,77.92; H,7.01; N,10.90 %     C,77.88; H,7.88; N,10.85%

    Similarly other 3-Aryl-5-(4'-N,N-dimethylaminophenyl)-1-phenyl pyrazolines were prepared. The physical data recorded in Table 1

## SPECTRAL DATA

When R=4-ethoxyphenyl

**IR (KBr) Values in cm$^{-1}$**

Compd. (2e) C=O1641cm$^{-1}$;C-O-C 1255cm$^{-}$1;HC=CH 3000cm$^{-1}$;CH$_3$ 2904cm$^{-1}$
Compd. (3e) C=N 1606cm$^{-1}$;N-H 3423 cm$^{-1}$; C-O-C 1251,1043 cm$^{-1}$; CH$_3$ 2970 cm$^{-1}$
Compd. (4e) C=O1650 cm$^{-1}$ C=N 1606 cm$^{-1}$;C-O-C 1250, 1050 cm$^{-1}$  CH$_3$ 2990 cm$^{-1}$

**PMR TMS CDCl$_3$  Value in Dppm**

Compd.(2e) 3.00 (s,6H,N(CH$_3$)$_2$); 6.96 (d,1H,HC=C-CO); 6.69(d,1H,C=CH-CO); 4.10 (q,2H, Ar-O-CH$_2$).
Compd.(3e) 3.02(s,6H,N(CH$_3$)$_2$); 8.59 (s,1H,NH-Ar) ;4.50(q,2H,OCH$_2$); 1.25 (t,3H,CH$_3$-C)
Compd.(4e) 2.89 (s,6H,N(CH$_3$)$_2$ ;2.38 (s,3H, CO-CH$_3$) ;4.12 (q,2H,O-CH$_2$); 1.39(t,3H,CH$_3$-C)

## MASS DATA

We have observed molecular ion peak at in compd. 2e at 296, 3e at 310, and 4e at 351.

## REFERENCES

1. Fahmay A.M., Hassan Kh. M., Khalaf A.A. & Ahmed R.A.,(Fac sci. AssiutEgypt) Rev Chim, 1988(Eng.); ChemAbstr. 111(1989) 77898.
2. Das &Mittra A.S., Indian J.Chem. 16 B (1978) 638.
3.Cremlyn R.J., Swinbourne F.J., &Mookerjee E. (Sch. Nat.Sci.Hatfieldpolytech,HalfieldHetrtford Shire Uk), Indian J. Chem 25 B(1986) 562; Chem. Absr. 105 (1986) 16428.
4. Lapm&Philip G (Dupont de Nemours, EI and Co.) Eur Pat Appl EP 300,692 (Cl  CO7D 231/05) 25 Jan 1989, U S Appl(1987 74, 795, 48, pp. CHEM Abstr. 111(1989) 7397.
5. Murthy A.K. RaoN.v., Indian J Chem. 10 (1972) 38, Chem. Abstr. 77 (1972) 29615.

| | R | Molecular formula | M.W. | M.P. $^0$C | Yield % | % of Nitrogen | |
|---|---|---|---|---|---|---|---|
| | | | | | | Calcd. | Found |
| 2a | Phenyl | $C_{17}H_{17}NO$ | 251 | 65 | 60 | 5.57 | 5.53 |
| 2b | 4-Bromo phenyl | $C_{17}H_{16}NOBr$ | 330 | 107 | 70 | 4.24 | 4.19 |
| 2c | 4-Chloro phenyl | $C_{17}H_{16}NOCl$ | 288.5 | 115 | 68 | 4.90 | 4.80 |
| 2d | 2,4-dihydroxy phenyl | $C_{17}H_{17}NO_3$ | 283 | 80 | 59 | 4.94 | 4.91 |
| 2e | 4-ethoxy phenyl | $C_{19}H_{21}NO_2$ | 295 | 85 | 50 | 4.74 | 4.68 |
| 2f | 2-Hydroxy phenyl | $C_{17}H_{17}NO_2$ | 267 | 155 | 44 | 5.24 | 5.19 |
| 2g | 4-Hydroxy phenyl | $C_{18}H_{19}NO_2$ | 267 | 83 | 40 | 5.24 | 5.16 |
| 2h | 4-Methoxy phenyl | $C_{17}H_{18}N_3Cl$ | 281 | 90 | 63 | 4.98 | 4.94 |
| 2i | 2-Methyl phenyl | $C_{18}H_{19}NO$ | 265 | 80 | 71 | 5.28 | 5.25 |
| 2j | 4-Nitro phenyl | $C_{18}H_{16}N_2O3$ | 308 | 190 | 56 | 9.09 | 9.07 |
| 3a | Phenyl | $C_{23}H_{23}N_3$ | 318 | 69 | 60 | 13.20 | 13.19 |
| 3b | 4-Bromo phenyl | $C_{23}H_{22}N_3Br$ | 397 | 110 | 65 | 10.57 | 10.54 |
| 3c | 4-Chloro phenyl | $C_{23}H_{22}N_3Cl$ | 352.5 | 98 | 67 | 11.91 | 11.86 |
| 3d | 2,4-dihydroxy phenyl | $C_{23}H_{23}N_3O_2$ | 350 | 180 | 53 | 12.00 | 11.95 |
| 3e | 4-ethoxy phenyl | $C_{25}H_{27}N_3O$ | 385 | 79 | 59 | 10.90 | 10.82 |
| 3f | 2-Hydroxy phenyl | $C_{23}H_{23}N_3O$ | 357 | 115 | 47 | 11.76 | 11.72 |
| 3g | 4-Hydroxy phenyl | $C_{23}H_{23}N_3O$ | 357 | 149 | 45 | 11.76 | 11.74 |
| 3h | 4-Methoxy phenyl | $C_{24}H_{25}\,N_3O$ | 371 | 90 | 61 | 11.32 | 11.31 |
| 3i | 2-Methyl phenyl | $C_{24}H_{25}\,N_3$ | 355 | 133 | 56 | 11.83 | 11.80 |
| 3j | 4-Nitro phenyl | $C_{23}H_{22}N_4O_2$ | 386 | 75 | 60 | 14.50 | 14.48 |

**TABLE No. 2A. BIOLOGICAL ACTIVITY OF STANDARD DRUGS TOWARDS STRAINS OF BACTERIA AND FUNGI**

| Sr. No. | Drugs | B.mega | B.subtilis | E.coli | A.aerogens | A.awamori |
|---------|-------|--------|-----------|--------|-----------|-----------|
| 1 | Amoxicillin | 25 | 16 | 23 | 24 | 0 |
| 2 | Ampicillin | 23 | 18 | 27 | 25 | 0 |
| 3 | Chloramphenicol | 24 | 19 | 26 | 25 | 0 |
| 4 | Norfloxacin | 24 | 19 | 30 | 30 | 0 |
| 5 | Griseofulvin | - | - | - | - | 25 |
| 6 | D.M.F. | 10 | 10 | 12 | 11 | 10 |

(Zones of inhibition in m.m)

**TABLE No. 2B. ANTIMICROBIAL ACTIVITY OF 2a-j, 3a-j.TOWARDSDIFFERENT STRAINS OF BACTERIA AND FUNGI**

| No | R | Antimicrobial activity Zone of inhibition in m.m | | | | Antifungal Activity |
|----|---|--------|-----------|--------|----------|---------------------|
| | | B.mega | B. subtilis | E.coli | A.aerogen | A.awamori |
| 2a | **Phenyl** | 13 | 15 | 12 | 15 | 16 |
| 2b | **4-Bromo phenyl** | 18 | 16 | 15 | 18 | 14 |
| 2c | **4-Chloro phenyl** | 19 | 21 | 17 | 19 | 19 |
| 2d | **2,4-dihydroxy phenyl** | 13 | 15 | 16 | 14 | 14 |
| 2e | **4-ethoxy phenyl** | 15 | 18 | 12 | 16 | 14 |
| 2f | **2-Hydroxy phenyl** | 16 | 17 | 15 | 14 | 16 |
| 2g | **4-Hydroxy phenyl** | 14 | 15 | 13 | 16 | 14 |
| 2h | **4-Methoxy phenyl** | 21 | 19 | 20 | 17 | 20 |
| 2i | **2-Methyl phenyl** | 19 | 20 | 17 | 18 | 21 |
| 2j | **4-Nitro phenyl** | 18 | 16 | 16 | 17 | 22 |
| 3a | **Phenyl** | 15 | 16 | 18 | 14 | 20 |
| 3b | **4-Bromo phenyl** | 14 | 13 | 17 | 15 | 18 |
| 3c | **4-Chloro phenyl** | 13 | 18 | 15 | 16 | 19 |
| 3d | **2,4-dihydroxy phenyl** | 17 | 19 | 16 | 18 | 14 |
| 3e | **4-ethoxy phenyl** | 15 | 18 | 21 | 18 | 15 |
| 3f | **2-Hydroxy phenyl** | 18 | 16 | 17 | 14 | 20 |
| 3g | **4-Hydroxy phenyl** | 16 | 17 | 19 | 15 | 15 |
| 3h | **4-Methoxy phenyl** | 15 | 20 | 17 | 18 | 18 |
| 3i | **2-Methyl phenyl** | 17 | 14 | 20 | 17 | 18 |
| 3j | **4-Nitro phenyl** | 19 | 16 | 18 | 20 | 17 |

# Removal of Coloured Substance by Agricultural Product through Adsorption

Kiran V. Mehta

Department of Chemistry,

R. R. Mehta College of Science and C. L. Parikh College of Commerce,

**PALANPUR**-385001, Dist.-Banaskantha, State-Gujarat(India)

**kiranvmehta@ymail.com**

## Abstract

Coloured substances which are generated as wastage by factories may create environmental issues. Complex aromatic coloured substances do not easily degrade and remain in the environment. Coloured water may be made harmless by physical or chemical processes. Adsorption is a good processbut use of activated carbon as an adsorbent is costly. It gives chance for other low cost adsorbents. Agricultural product- wheat straw can be used as a low cost adsorbent for the removal of coloured substances. Wheat straw was used for the present study for the removal of a coloured  substance: 3,4-dihydroxy-9,10-dioxoanthracene-2-sulfonic acid from the solution. Effect of initial dye concentration and effect of adsorbent amount with respect to time were studied. The study indicates that wheat straw powder can be used as a low cost adsorbent.

**Key words :** adsorption, coloured substance, removal.

## Introduction

The demand for colourants has experienced extraordinary increase in the past some years. Industries like textile, rubber, food, drug, paper, cosmetics,beverages and plastic use colourants. These colourants are water

pollutants. They are present in variousextentsin industrial waste water. Coloured industrial waste water expulsion is done into land area or water area(lake, river or sea). However, most of the colourants are hard to degrade because they are stable to light and oxidizing agents. Thus, they tend to persist in the environment. It creates public health problems[1-6]. This contaminated water affects the flora and fauna of the related region. As a result, the environmental issues about the removal of these pollutants are gaining much more attention in recent years.

Conventional technologies employed for eliminating dye from industrial effluents include coagulation, chemical oxidation and biological treatment. Generally, coloured water is treated with either by physical, biological or chemical processes. However, these processes are very pricey. The dyes from aqueous medium can be efficiently removed by adsorption process which is a surface phenomenon. A well known adsorbent, activated carbon can be prepared from carbonaceous material. As activated carbon is highly porous, it is a superb adsorbent but is very expensive[1,2]. This has led to further research for the cheaper replacement of adsorbent material.

General skills applied for the removal of colourants are: chemical oxidation, coagulation and biological treatment. These processes are costly. Colourants from aqueous solution can be eliminated by adsorption. Activated carbon is a good adsorbent but it is pricey[3,4]. Hence, research for the cheaper adsorbent material becomes important and interesting.These materials include ginger waste, jute fibers, coconut shell, sugarcane bagasse, castor seed shell, rice husk, almond shell, saw dust, spent tea leaves, plum kernel, jack fruit leaves, palm fruit bunch, orange peel, etc.[5-11]. These materials are low-priced and natural.

Discovering competent and environment friendly adsorbents for the abstraction of colourants from aqueous medium is an important work for reducing the black side of industrial development.  In the present research

paper, dry wheat straw powder(WSP) was applied for the elimination of colouring matter (3,4-dihydroxy-9,10-dioxoanthracene-2-sulfonic acid) (DDSA) from its aqueous solution.

## Materials and Methods:

### Adsorbate :
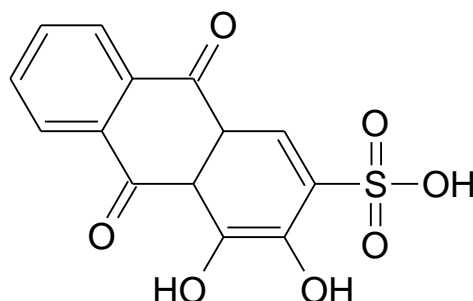


**General name:** 3,4-dihydroxy-9.10 dioxoanthracene--2-sulfonic acid

**IUPAC name :**
3,4-dihydroxy-9,10-dioxo-4a,9,9a,10-tetrahydroanthracene-2-sulfonic acid

**Fig.-1:Structure of DDSA**

Sodium salt of 3,4-dihydroxy-9,10-dioxoanthracene-2-sulfonic acid**(DDSA)**, a colourant, was used as adsorbate for the present study. The structure of this colourant is shown in **Figure-1**.

## Adsorbent:

India is a country producing a huge amount of wheat. So, dry straws are easily obtainable as an agricultural byproduct. Dry straws of wheat plants used for the present work were collected from the local farms. They were washed four times with distilled water to remove dust and water soluble impurities. Straws were dried till they became brittle. Then it was sieved in the range of 45-50 mesh(US). Straws were further washed with distilled water till the washings were free from turbidity. The powdered material

obtained was dried at $105^{\circ}$C for 4-5 hours and placed in a desiccator. Then, Wheat Straw Powder(WSP) was used as the adsorbent.

## Adsorption Experiments:

Adsorption of DDSA on powder of dry wheat straw powder (WSP) was carried out and effect of initial concentration of adsorbate and effect of amount of adsorbent with respect to contact time were studied. Simultaneously, all experiments were conducted with no adsorbent to ensure that adsorption was by wheat straw powder and not by the other factors. The process of adsorption was studied by analyzing adsorption elimination of the colourant from the solution. The experimental mixture was stirred on a rotary orbit shaker at 180 rpm. The study was performed according to the methods described in the literature[13-21].

## Results and Discussion:

For the determining effect of the initial dye concentration, the study was performed at fixed adsorbent amount(0.4 g/100 ml) at room temperature $(33\pm1)^{0}$C for 120 minutes at various initial concentrations of DDSA. The DDSA removal was determined at 20, 40, 60, 80, 100 and120 minutes. The results are shown in **Table - 1**.

## Table – 1:  Effect of initial concentration of DDSA on adsorption using WSP

Amount of adsorbent (WSP): 0.4 g/100ml, time:  120 min.

| Initial DDSA concentration (mg/l) | % of DDSA removal with time(min.) | | | | | |
|---|---|---|---|---|---|---|
| | 20 | 40 | 60 | 80 | 100 | 120 |
| 25 | 9.50 | 15.80 | 26.40 | 62.80 | 65.25 | 60.51 |
| 50 | 11.25 | 21.30 | 30.12 | 73.10 | 75.51 | 77.52 |
| 75 | 28.40 | 32.25 | 31.58 | 77.45 | 68.84 | 79.11 |
| 100 | 29.00 | 33.15 | 34.10 | 68.50 | 70.30 | 79.62 |
| 125 | 30.11 | 38.20 | 45.28 | 79.25 | 75.63 | 81.14 |
| 150 | 32.24 | 40.55 | 42.65 | 80.10 | 82.19 | 80.11 |
| 175 | 10.50 | 12.35 | 33.40 | 59.85 | 64.57 | 70.15 |

The adsorption of DDSA on WSP was studied by changing the amount of adsorbent for 120 minutes. During this, DDSA concentration was kept 100 mg/l. The results are shown in **Table - 2.** The results indicate that the percentage of adsorption increases with the increase in the amount of adsorbent.

## Table – 2 : Effect of amount of adsorbent on DDSA removal

DDSAconcentration: 100 mg/l, time :  120 min.

| Adsorbent (WSP) dose (g/100ml) | % of DDSA removal with time(min.) | | | | | |
|---|---|---|---|---|---|---|
| | 20 | 40 | 60 | 80 | 100 | 120 |
| 0.2 | 14.27 | 18.89 | 20.12 | 22.03 | 31.50 | 30.14 |
| 0.4 | 17.33 | 20.02 | 23.05 | 30.87 | 36.24 | 35.07 |
| 0.6 | 28.55 | 37.09 | 45.06 | 47.01 | 58.04 | 69.01 |
| 0.8 | 30.46 | 40.15 | 46.01 | 48.09 | 59.90 | 78.65 |
| 1.0 | 22.52 | 42.23 | 44.16 | 44.70 | 51.92 | 47.84 |

## Conclusion:

The present study shows that the dry wheat straw powder can be used as a good, low cost adsorbent for the removal of the DDSA from aqueous solution. The amount of DDSA adsorbed was found to alter with time, adsorbent dosage and initial concentration of DDSA.

# References:

[1]   Perkowski J., Kos L., DecolourizationOf Model Dye House Wastewater With Advanced Oxidation Processes, *Fibres And Textiles In Eastern Europe,***2003,** 11, 67-71.

[2]   Oclay T., Isik K., Gulen E., Derin O.,  Colour Removal From Textile Wastewaters, *Water Science And Technology,***1996,** 34, 9-11.

[3]   Karaca S., Gurses A., Aclkyldlz M., Ejder M., Adsorption Of Cationic Dye From Aqueous Solutions By Activated Carbon, *Microporous And Mesoporous Materials,***2008,** Vol. 115, Issue-3, 376-382.

[4]   Kannan N., Sundram M. M., Kinetic And Mechanism Of Removal Of Methylene Blue By Adsorption On Various Carbons-A Comparative Study, *Dyes And Pigments,* **2001,** 1, 25-40.

[5]   Ahmad R., Kumar R., Adsorption Study Of Patent Blue Vf Using Ginger Waste Material, *Journal Of The Iranian Chemical Research,***2008,** Vol. 1, 85-94.

[6]   Memon G. Z., Bhanger M.I., Akhtar M., Peach-Nut Shells-An Effective And Low Cost Adsorbent For The Removal Of Endosulfan From Aqueous Solutions, *Pakistan Journal Of Analytical Environmental Chemistry,* **2009**, Vol. 10, No. 1-2, 14-18.

[7] Ozer A., Dursun G., Removal Of Methylene Blue From Aqueous Solution By Dehydrated Wheat Bran Carbon, *Journal Of Hazardous Materials,***2007,** Vol. 146, Issue: 1-2, 262-269.

[8] Bat Zias F. A., Sindiras D. K., Dye Adsorption By Calcium Chloride Treated Beech Sawdust In Batch And Fixed Bed Systems, *Journal Of Hazardous Materials,***2004,** Vol. 114, Issue: 1-3, 167-174.

[9] Lo Stuart T., William R. R., Michael A. C., Removal Of Dissolved Textile Dyes From Wastewater By A Compost Sorbent, *Coloration Technology,***2003,**119, 14-18.

[10] Annadurai G., Juang R. S., Lee D. J., Use Of Cellulose Based Wastes For Adsorption Of Dyes From Aqueous Solutions, *Journal Of Hazardous Materials,***2002,** B-92, 263-274.

[11] Nassar M. M., The Kinetics Of Basic Dye Removal Using Palm-Fruit Bunch, *Adsorption Science Technology,***1997,** 15, 609-617.

[12] Dae-Hee, Won–Seok, Tai-Il Y, Dyestuff Wastewater Treatment Using Chemical Oxidation, Physical Adsorption And Fixed Bed Biofilm Process, *Process Biochemistry,***1999,** 34, 429-439.

[13] Safarik I., Namburska K., Safarikova M., Adsorption Of Water Soluble Organic Dyes On Magnetic Charcoal, *Journal Of Chemical Technology And Biotechnology,***1997,** 69, 1-4.

[14] Noroozi, B., Sorial, G. A., Bahrami, H., Arami, M., Equilibrium And Kinetic Adsorption Study Of A Cationic Dye By A Natural Adsorbent-Silkworm Pupa, *Journal Of Hazardous Materials,***2007**, B139, 167–174.

[15] Ola A., Ahmed E. N., Amany E. S., Azza K., Use Of Rice Husk For Adsorption Of Direct Dyes From Aqueous Solution: A Case Study Of Direct F. Scarlet, *Egyptian Journal Of Aquatic Research*, **2005,** 31(1), 1–11.

[16] Mckay G., Equilibrium Studies For The Adsorption Of Dyestuffs From Aqueous Solutions By Low Cost Materials, *Water, Air And Soil Pollution,***1986,** 29, 273-283.

[17] Inthorn D., Singhtho S., Thiravetyan P., Khan E., Decolorization of Basic, Direct And Reactive Dyes By Pre-Treated Narrow-Leaved Cattail(Typhaangustifolia Linn.), *Bioresource Technology*, **2004,** 94, 299–306.

[18] Renmin, G. Yi. D., Mei L., Chao Y., Huijun L., Yingzhi S., Utilization Of Powdered Peanut Hull As Biosorbent For Removal Of Anionic Dyes From Aqueous Solution, *Dyes And Pigments*, **2005,** 64, 187–192.

[19] Changwei H., Jian Long L., Yin Zhou, Mei Li, Feng X., Huiming Li, Enhanced Removal Of Methylene Blue From Aqueous Solution By Pummelo Peel Pretreated With Sodium Hydroxide, *Journal Of  Health Science,***2009,** 55(4), 619-624.

[20] Rasheedkhan A., Tahir H., Uddin F., Hameed U., Adsorption Of Methylene Blue From Aqueous Solution On The Surface Of Wool Fiber And Cotton Fiber, *Journal Of Applied Science And Environmental Management,***2005,**9(2), 29-35.

[21] Perineau F., Molinier J., Gaset A., Adsorption Of Ionic Dyes Onto Charred Plant Material,*Journal Of Chemical Technology and Biotechnology,***1982,** 32, 749-755.

# Formation of some novel Acid azo dyes : synthesis, characterisation and Application properties :III

## Dr.D.G.Patel  and Dr.R.T.Patel, Dr.M.K.Thkor, Dr.B.K.Patel

*Department of Chemistry, Municipal arts and Urban bank science college,*

*Mehsana-384001, Gujarat, India.*

*Email : drdgpatel11@gmail.com*

## Abstract

Novel acid azo dyes have been prepared by the coupling of diazo solution of 4 –methoxy Aniline with 1-(4-*N*-acetyl amino) 2-methyl phenyl , 2-chloro ethanone. The resultant product were hydrolysis  by refluxing with  ethanol containing for 4-5 hours .The coupling compound  of various  aromatic acid $R_1$-$R_6$  with above  diazonium  salt soln.The resultant  dyes were characterized by spectral techniques, *i.e*., elemental analysis, IR, UV—visible spectroscopy. The dyeing performance of all the dyes was evaluated on wool and nylon fabrics and studies their light and washing  fastness properties.

*Keywords:* acid azo dye, UV—visible spectroscopy , light fastness, washing  fastness.

## Introduction:

Out of different classes of dyes, azo dyes constitute the largest group of colorants used in industry [1]. Azo dyes do not occur in nature and are produced only through chemical synthesis[2]. The emergence of diverse classes of synthetic dyes including azo-dye occurred due to constant effort to find specific dye or a particular class of dye for application on diverse materials of industrial importance mainly textile fibres, aluminium sheet, leather, electro optical devices,ink –jet printers etc. [3]

While phenols are well established intermediates for the synthesis of various commercial dyes [4-8], they are marketed in the form of azo-acid dyes *etc*. All of these dyes having phenolic motif, containing hydroxyl group as an auxochrome group. Such auxochromic(-OH) and chromophoric (>C=O) group containing compound The area in which the acid azo dyes formation based on this compound may yield the dyes with good hue properties. Hence, in continuation of our earlier work [9-10], it was thought interesting to explore the field of acid azo dyes based on 1-(4-*N*-acetyl amino) 2-methoxy phenyl 2-chloro ethanone. The proposed synthetic route is shown in Scheme 1.

## Materials and Methods :

All the chemicals used were of analytical reagent grade and were used without further purification, All the product were synthesized and characterized by their spectral analysis, All Chemicals and solvents like acetone, ethanol, $NaNO_2$, NaOH, sodium acetate were purchased from S.D.fine chemicals (india).

Melting points were taken by open capillary tube and are uncorrected.. The UV-Visible spectra were recorded in DMF using Shimadzu A-200 Spectrophotometer and C,H,N of all disperse dyes were estimated by the means of a carlo Erba elemental analyzer (Italy) The characteristic data of different molecules were studied their light, wash fastness properties and further study applied on wool fibers and nylon fibers.

## Experimental :

## Synthesis of acid azo dyes :

First 4-methoxy aniline was dissolve in a mixture of anhydrous actetone And pyridine in 250ml flask then added dropwise to a mixture of 1-(4-N-acetyl amino) 2-methyl phenyl 2-chloro ethanone and sodiumbicarbonate as an accepter.The reaction mixture is set aside over night. Then resultant product were hydrolysis by refluxing with ethanol containing HCl for 4-5 hours . The cool solution was dilute with water and was mass just alkaline with

conc.NH$_3$ solution (d= 0.880) to give yield 1-(4-$N$-acetyl amino) - 2-($N$-methyl phenyl amino) ethanone. Diazotization of various aromatic acid was performed by a reported method [11-13] .The yield was dissolved in HCl with stirring and the solution cooled to 0-5°C in an ice-bath . A solution of sodium nitrite (0.01 mole) in 5ml water cooled to 0°C then was added .The excess nitrous acid was neutralized with sulfamic acid/urea (1.0 gm) and the mixture was filtered to get the clear diazonium salt solution. R$_1$-R$_6$ coupling component was dissolved in NaOH (15 ml) and then solution cooled 0-5˙c To this well stirred solution the above diazonium salt solution was added slowly so that temperature did not rise above 0-5˙c while maintaining the pH 4-5 by the action of sodium acetate solution (10% w/v) the mixture was stirred for 3 hrs. at 0-5°C.After completion of the reaction the solid material was filtered, washed and dried it. So R$_1$-R$_6$ acid azo dyes were prepared.

## Results and Discussion :

The acid azo dyes obtained from this compounds are shown in Scheme-I The observed bands in the IR spectra for each dye are shown in Table-I,

IR spectra of all seven series of acid azo dyes contain aromatic nuclei, azo group and hydroxyl group. The band appeared from 1030 to 1350 cm$^{-1}$ due to primary –OH group, The strong band at 1610 to 1640 cm$^{-1}$ appeared in the spectra are considered for the presence of azo (-N=N-) group. The bands around of 6505 to 1050 cm$^{-1}$ are attributed to the presence of –SO$_3$OH group. In the spectra of dyes obtained from aniline derivatives side chain attached to the tertiary nitrogen The broad band around 3445-3540 comprises to primary stretching. The weak bands observed 2890-and 2950 cm$^{-1}$ which is attributed to the -CH$_2$ stretching vibration.

The IR spectra of all dyes comprise the important bands due to initial diazo component. The bends due to –CH$_3$ stretching 2905-2930 and 1320-1475 cm$^{-1}$ and -CO of -COCH$_2$ aniline (-CH$_3$) . The other bands due to presence of coupling component are their respective positions. The elemental of C,H,N confirmed by Table: II.

The visible absorption spectroscopic properties of the all dyes were recorded in DMF. Absorption maximum (λmax), Intensities' ( log ε), dyeing assessment of acid azo dyes on

Wool and Nylon fabrics are shown in Table-III, The absorption maximum ($\lambda$max) of all the dyes falls in the range 471-527 nm in DMF. The values of the logarithm of molar extinction coefficient ( log $\varepsilon$) of all the dyes were in the range of 3.910-4.921 , consistent with their medium absorption intensity The disperse azo dyes were applied at a 2% dye bath on nylon and wool fabrics and gave various shade implied in Table-III.

## Conclusion :

The azo disperse dyes have been prepared using based on 1-(4-N-acetyl amino) - 2-(N-methoxy phenyl amino) ethanone. The present study prepared acid azo dyes showed wide range of shades like Desert sandy, Rose like, Sandy, Pink, Crimson, Violet. They showed good dyeing performance on wool and nylon fiber and The light fastness values of the acid azo dyes are more consistent. The dyeing showed an fair and good fastness to light, R-$_6$ acid azo dyes was excellent fastness to washing and other dyes were with good to very good fastness to washing.

**Conclusion**

Two brilliant azo dyes were successfully synthesized by standard methods of diazotization and coupling using little variation of pH maintenance and methods of crystallization. Brilliant crystals of 4-methoxybenzeneazo-2'-naphthol and 2-nitrobenzeneazo-2'-naphthol were isolated and characterized by a number of spectroscopic methods. The results on the elemental analysis and spectral studies of each dye were consistent and hence confirm the predicted structure. The synthesized dyes showed excellent fastness to light, washing with good fastness to rubbing. They also showed remarkable levelness after washing. The nature of the substituents in the coupling components also showed little influence on the visible absorption and the shade of the dyeing. The results showed that both the dyes exhibited very slow rate of oxidation and also inhibited bacterial growth but the rate of oxidation of dye 2 was comparatively lower than dye 1 and hence resulted more antibacterial effect.

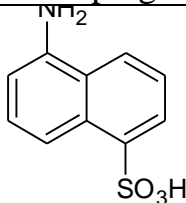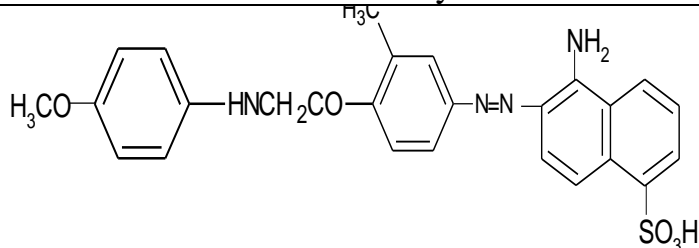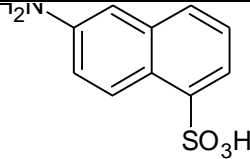## Table : I   Structure of the Coulping component and corresponding of  novel azo dyes :
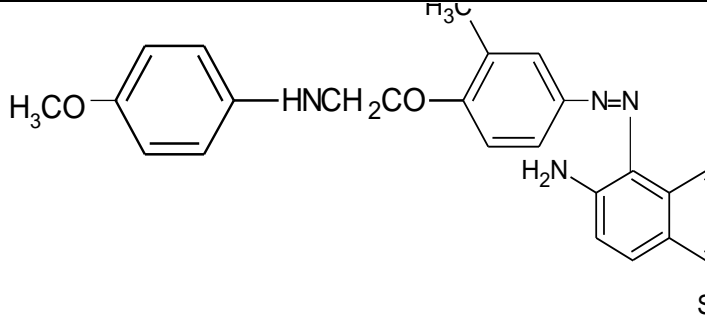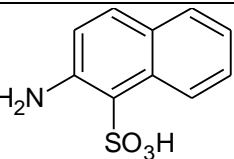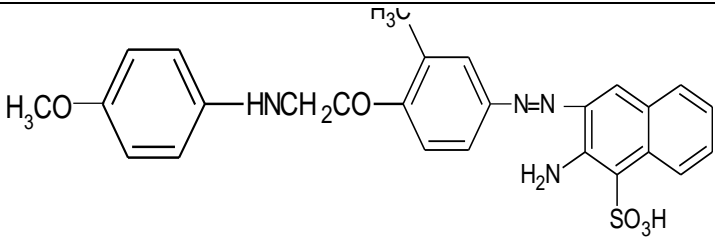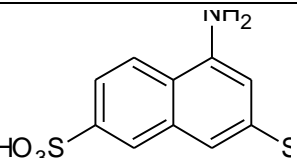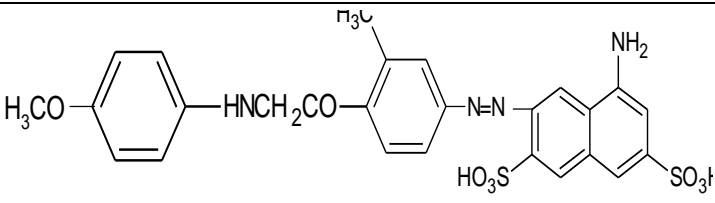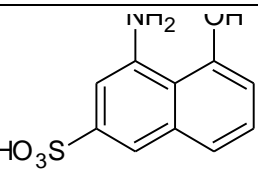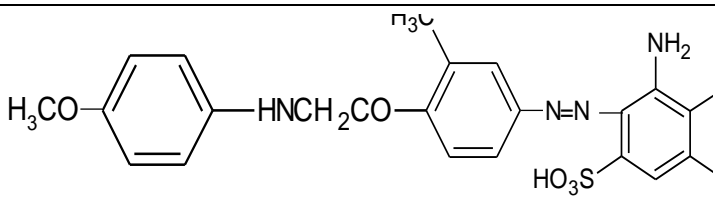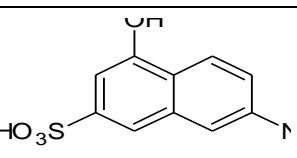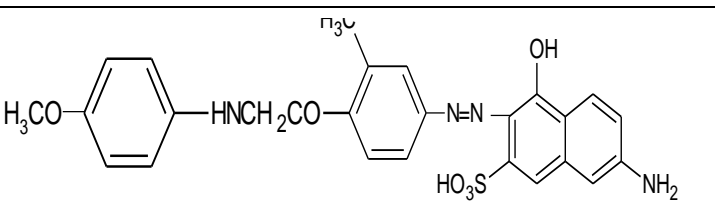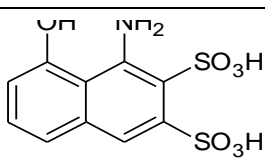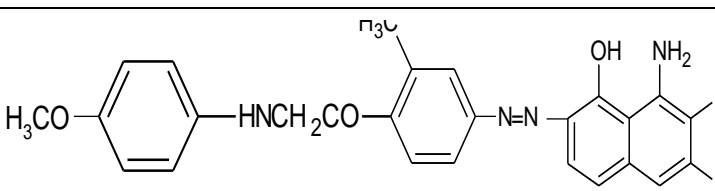
| Dye No | Coulping component | Acid azo Dyes |
|--------|--------------------|---------------|
| R-1 |  |  |
| R-2 |  |  |
| R-3 |  |  |
| R-4 |  |  |
| R-5 |  |  |
| R-6 |  |  |
| R-7 |  |  |

## Table: I  Position selected Bands in IR Spectra of Aid azo dyes :

| Dye No | Primary amine cm$^{-1}$ | C-H Stretching aromatic cm$^{-1}$ | N=N Stretching aromatic cm$^{-1}$ | Napthelene Substituted cm$^{-1}$ | 1,4-di Substituted cm$^{-1}$ | Primary Alcohol cm$^{-1}$ | Tertiary Amine cm$^{-1}$ | S=O Stretching vibration of Sulfonic acid cm$^{-1}$ |
|---|---|---|---|---|---|---|---|---|
| R-1 | 3540 | 2930 1615,1470 | 1630 | 1570 | 1575,1180 1035 | 1030 1275 | 1145 | 1150,1035 655 |
| R-2 | 3450 | 2950,2985 1615,1425 | 1640 | 1565 | 1565 1155 | 1030 1260 | 1155 | 1150,1035 675 |
| R-3 | 3445 | 2935,1615 1475,1450 | 1620 | 1580 | 1575,1160 1025 | 1030 1240,1250 | 1165 | 1150 655 |
| R-4 | 3445 | 2905,2950 1515,1615 | 1610 | 1545 | 1540,1145 1055 | 1030 1240 | 1145 | 1150,1065 655 |
| R-5 | 3455 | 2945 1630,1615 | 1610 1620 | 1580 | 1575,1150 1050 | 1030 1050,1350 | 1155 | 1195,1055 655 |
| R-6 | 3455 | 2910,1580 1525 | 1620 | 1525 | 1520,3010 1185,1055 | 1050 1300 | 1145 | 1185,1055 655 |
| R-7 | 3450 | 2915,1570 1515 | 1620 | 1625 | 1620,1210 1075 | 1050, 1275 | 1185 | 1160,1050 655 |

All thes spectra comparised the bands around 2890 and 2950 cm$^{-1}$ presented of -CH$_2$ of -COCH$_2$ group

**Table : II  Characterization of novel Acid azo dyes :**

| Dye No | Molecular Formula | Mol.Wt (gm/mole) | Melting Point °C | % C Found | % C Cal | % H Found | % H Cal | % N Found | % N Cal |
| --- | --- | --- | --- | --- | --- | --- | --- | --- | --- |
| R-1 | $C_{26}H_{22}N_4O_5S$ | 504 | 217 | 61.90 | 61.93 | 4.36 | 4.46 | 11.11 | 11.12 |
| R-2 | $C_{26}H_{22}N_4O_5S$ | 504 | 220 | 61.90 | 61.93 | 4.36 | 4.46 | 11.11 | 11.12 |
| R-3 | $C_{26}H_{22}N_4O_5S$ | 504 | 212 | 61.90 | 61.93 | 4.60 | 4.46 | 11.11 | 11.12 |
| R-4 | $C_{26}H_{22}N_4O_8S_2$ | 600 | 232 | 52.00 | 52.10 | 3.66 | 3.70 | 9.33 | 9.40 |
| R-5 | $C_{26}H_{22}N_4O_6S$ | 520 | 235 | 60.0 | 60.1. | 4.23 | 4.25 | 10.76 | 10.80 |
| R-6 | $C_{26}H_{22}N_4O_6S$ | 520 | 230 | 60.0 | 60.1. | 4.23 | 4.25 | 10.76 | 10.80 |
| R-7 | $C_{26}H_{22}N_4OS_2$ | 600 | 244 | 52.00 | 52.10 | 3.66 | 3.70 | 9.33 | 9.40 |

**Table :III  Absorption maximam (λmax), Intensites ( log ε), Acid azo dyes on Wool and Nylon fabrics :**
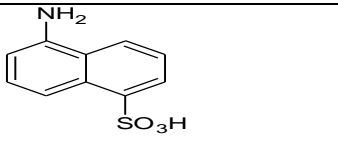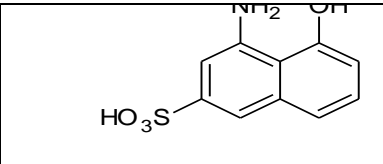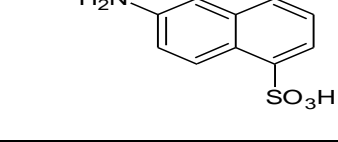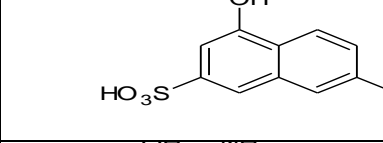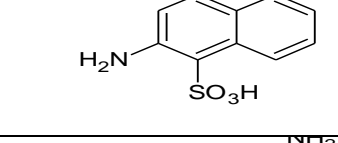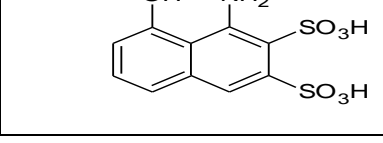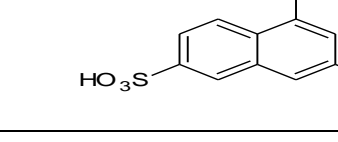
| Dye | λmax (nm) | Log ε | Shade | Dyeing properties Dyeing on wool L | W | Dyeing on nylon L | W |
| --- | --- | --- | --- | --- | --- | --- | --- |
| R-1 | 478.0 | 4.216 | Desert Sandy | 5 | 4 | 5 | 4 |
| R-2 | 485.0 | 4.678 | Rose like | 5 | 3 | 5 | 3 |
| R-3 | 471.0 | 4.395 | Sandy | 4-5 | 4 | 4-5 | 4 |
| R-4 | 527.0 | 3.910 | Pink | 4-5 | 4 | 4-5 | 4 |
| R-5 | 526.0 | 4.445 | Pink | 4 | 3 | 4 | 3 |
| R-6 | 513.0 | 4.841 | Crimson | 5 | 5 | 5 | 5 |
| R-7 | 518.0 | 4.921 | Violet | 5 | 4 | 5 | 4 |

Light fastness: 1-poor, 2-slight, 3-moderate, 4-fair, 5-good, 6-very good.
Wash fastness: 1-poor, 2-fair, 3-good, 4-very good, 5-excellent.

## Reaction scheme-I



1-(4-acetyl amino-2-methyl phenyl)-2-(N-4-methoxy phenyl amino) ethanone
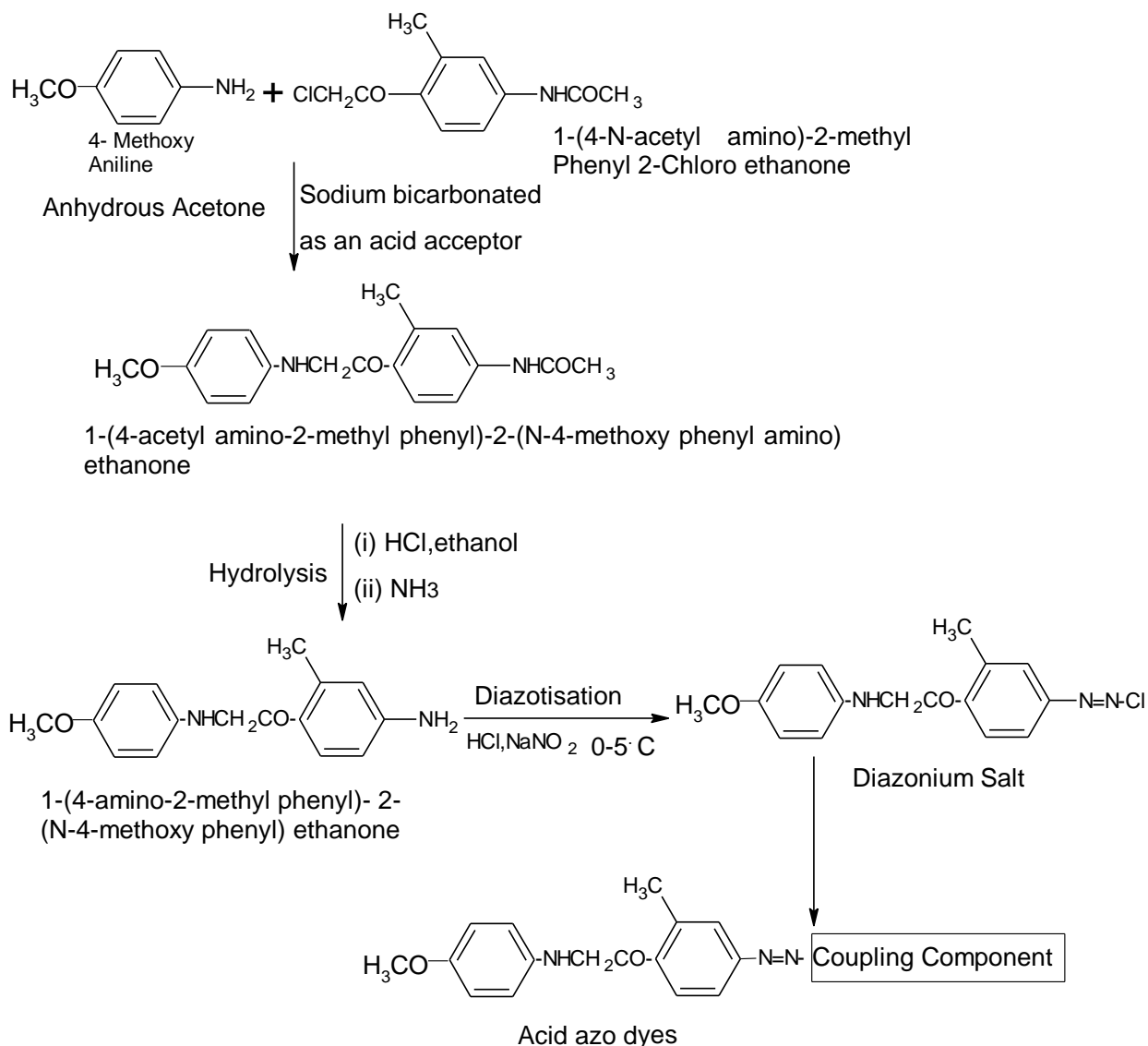
| R-1 | Laurent's acid |  | R-5 | Gamma acid |  |
|-----|----------------|---------------------|-----|------------|---------------------|
| R-2 | Bronner's acid |  | R-6 | J-acid |  |
| R-3 | Tobias acid |  | R-7 | Chicago acid |  |
| R-4 | H-acid |  | | | |

## References :

1. Zollinger, H.,. *Color Chemistry-Synthesis, Properties and Application of Organic Dyes and Pigments,* VCH publishers, New York, 1987, 92-102.

2. Maynard, C. W., *Riegel's Handbook of Industrial Chemistry*, 3rd ed. Van Nostard Reinhold,New York, 1983, 809-861

3. catino S. C and Farris, R. E., *Concise Encyclopedia of Chemical Technology,* M. Grayson Ed., John Wiley & sons, New York, 1985,142.

4. Cumming W M and Howie G, *J Chem Soc*., 1933, 133.

5. Peters A T and Walker D, *J Chem Soc*., 1956, 429.

7. Gordon P F and Gregory P, *Organic Chemistry in Colour*, 1st Ed., Springer-Verlag Berlin Heidelberg: New York, 1983, 60.

8. Mohamed S K, Nour A M and El-Din, *J Chem Res*.,(s) 1999, 8, 508.

9. Naik R D, Desai C K and Desai K R, *Oriental J Chem*., 2000, 16, 159.

10 B.C.Dixit,H.M.Patel,D.J.Desai,R.B.Dixit,E-J. chem..2009,6(2), 315.

11      Vogel A I, A Textbook of Practical Organic Chemistry, 3rd Ed.,  Longman:London, 1961, p.620.

12      M.szymczyk,A.E.shafei,H.S.Freeman,Dye pign.2007,8,72.

13.     H.E.Frirz-David,L.Blengy,Fundamental process of dye chemistry,3rd edition, wiley, Newyork,1949,p.241.

# A Preliminary investigation of cytotoxic and genotoxic effect of nicotine on human cells

Sandeep Chovatiya*, Sharthak Zaveri and Dipika Patel

Ashok & Rita Patel Institute of Integrated Study and Research in Biotechnology and Allied Science, New Vallabh Vidhyanagar – 388 120, Gujarat.

*Corresponding author email Id: sandeepchovatiya@aribas.edu.in

**Abstract:**

The objective of the present study was to investigate the potential of nicotine to induce micronucleated polymorphism in tobacco chewing individuals; as well as geneotoxic effect of nicotine on chromosomes. *In vivo* and *in vitro* cytological studies carried out in control and tobacco chewing individuals clearly indicated marked differences. In tobacco chewing individuals, micronuclei (MN) formation was significantly higher along with an increase the size of the nucleus. No significant cell mortality was observed in 10% and 20% nicotine treatment to the leucocytes by MTT assay. The results show that nicotine causes significant genotoxic effect on leukocytes by comate assay and chromosome abbreviation.

**Key words:** Nicotine, Chewing tobacco, Micronuclei, Cell viability

## 1. Introduction:

Nicotine is found in a wide variety of plants. However, the principal source of nicotine exposure is through the use of tobacco and nicotine-replacement therapies such as transdermal nicotine patches and nicotine-containing gum [1]. Nicotine is known to have various toxic effects on humans. Also, nicotine is shown to have genotoxic effect on human lymphocytes and tonsillar tissue [2]. Moreover the deaths caused by nicotine are highest in comparison to deaths caused by other factors or diseases as shown in figure-1. The exact effect of nicotine on human cells and DNA is still unknown and so a lot of research still needs to be done in this field.
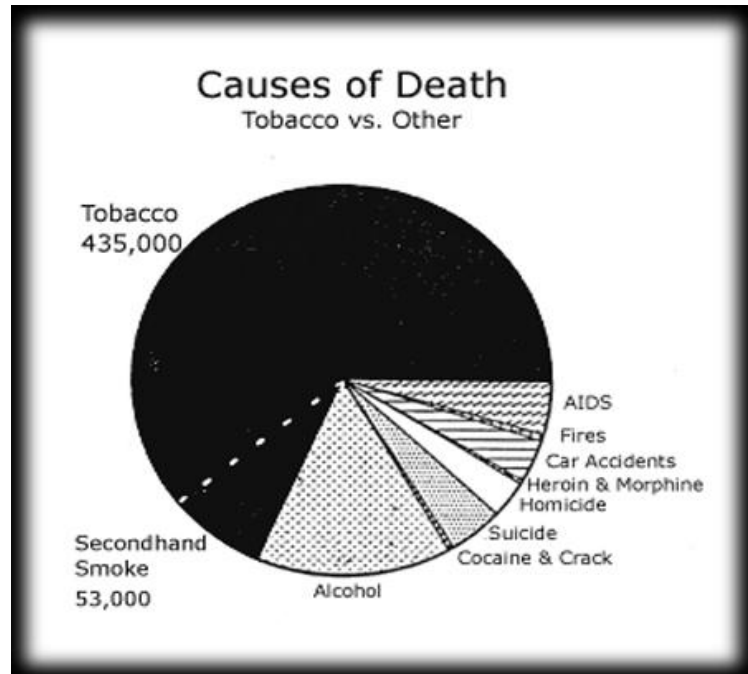
*Figure 1: Causes of Death in World Population (The Source is taken from a survey carried out in USA and conducted by WHO).*

Barbour *et al.* [3] showed a connection between smoking and Breast Cancer. Tobacco smoke is highly addictive and has been linked to 20 percent of all deaths in the United States.  It contains many cancer causing chemicals such as nicotine, and almost one third of all cancer deaths are related to tobacco use. Tobacco smoking has generally been considered to have little or no association with breast cancer risk.  Newer studies have challenged this conclusion and suggested a connection between smoking and an increased risk of breast cancer, but more investigation is needed to resolve this issue.

Kleinsasser *et al*. [2] showed that Nicotine demonstrates genotoxicity in human tonsillar tissue and lymphocytes. To assess the genotoxicity of nicotine, the DNA damaging effect on human lymphocytes and target cells from lymphatic tissue of the palatine tonsils from 10 healthy patients was tested with the alkaline single-cell microgel electrophoresis (Comet) assay. The degree of DNA migration, a measure of possible DNA single strand breaks, alkali labile sites, and incomplete excision repair sites, was expressed as the Olive tail moment, the percentage of DNA in the tail, and the tail length. One hour exposure to nicotine at 0.125, 0.25, 0.5, 1, 2,

and 4 mM induced a statistically significant dose-dependent increase of DNA migration up to 3.8-fold and 3.2-fold in tonsillar cells and lymphocytes, respectively.

It is estimated that one in three people in the world will develop cancer at some stage in their lives and that one in four will die from the disease. Smoking is the biggest risk factor for and largest single cause of cancer and approximately one third of all cancer deaths are attributable to smoking.  Globally, one in five cancer deaths are caused by tobacco. In October 2009, scientists from 10 countries met at the International Agency for Research on Cancer (IARC) to reassess the carcinogenicity of several compounds, including tobacco. The review, published by The Lancet Oncology, concludes that there is sufficient evidence to confirm that smoking is a cause of 15 types of cancer namely: cancer of the bladder, bone marrow (myeloid leukemia, cervix, colorectal (large bowel), kidney, larynx (voice box), liver, lung, mouth (including lip and tongue), nose, esophagus (gullet), ovaries, pancreas, pharynx (throat) and stomach. The report also states that there is some evidence to suggest that smoking is a cause of breast cancer [4, 5].

About 92% of human cancers are derived from external and internal epithelium. No effective techniques are available for making direct chromosome preparation from epithelium tissues. Casartelli *et al.* [6] observed MN frequencies in exfoliated buccal cells in normal mucosa, precancerous lesions and squamous cell carcinoma. They suggested a link of this bio-marker with neoplastic progressions. The induction in vivo by carcinogens and mutagens is a sign of the genotoxic effect of such substances. The MN assay in exfoliated cells is an innovative genotoxicity technique and holds promise for the study of epithelial carcinogens. It is considered to be a sensitive method for monitoring genetic damage [7].

Direct genotoxic effects of nicotine have been shown in human gingival fibroblasts [8] and spermatozoa [9]. Furthermore, nicotine may also stimulate tumor development by non-genotoxic mechanisms such as angioneogenesis [10, 11], growth stimulation [12], and receptor-regulated cellular growth [13].

The present study reports the cytotoxic and genotoxic effects of chewing tobacco in ex-foliated cells through MN assay; and on lymphocyte through MTT test, cellular apoptosis, COMET assay and chromosomal aberrations through Metaphase plate preparation under in vitro conditions.

## 2. Materials and Methods

### 2.1. EXTRACTION OF NICOTINE BY SOXHLET ASSEMBLY:

Tobacco leaves were taken directly from fields. They were then dried and grinded to fine powder and then placed in a thimble made of thick filter paper. The thimble was placed in a soxhlet extractor which was placed onto a flask containing the extraction solvent. The Soxhlet was then equipped with a condenser. The solvent i.e. distilled water was heated to reflux. The cycle was repeated over and over for 6 hours to get a high concentration of the sample in the solvent. Same process was repeated for tobacco obtained commercially (Budhalal, Budhalal & Co. (Tobacco Merchant), Ahmedabad).

### 2.2. STUDY OF CYTOTOXIC EFFECTS OF CHEWING TOBACCO IN IN-VIVO CONDITIONS:

**2.2.1. How the subjects were chosen:** The sample was collected from subjects who were known to chew tobacco from last 5-8 years.

**2.2.2. Oral smears were obtained from the subjects as follows:** The subjects were asked to rinse their mouth thoroughly with water.  A pre moistened wooden spatula/toothpick was used to collect the cells from the oral    mucosa.  The spatula was applied to a pre-cleaned slide to prepare the smear [7].

**2.2.3. Staining of cheek cells with Giemsa for identification of Micronulei:** Smears were air dried fixed in 80% methanol and stained with Giemsa solution. Cheek cells were observed under 10X and 40X compound microscope for observation of micronuclei [7].

### 2.3. VIABILITY ASSAY:

The blood cells were cultured in falcon tubes as in leukocyte culturing. After 24 hours of incubation, cells were treated with sample of 10% and 20% nicotine and again incubated for 48 hours. After that cell suspension was taken and 1:1:1 dilution of the suspension was prepared using cells with media, 0.4% trypan blue solution and doubled distilled water. The suspension was loaded on a hematocytometer and immediately observing under microscope.

## 2.4. MTT TEST:

The MTT assay was used to determine the effect of nicotine on cell growth / proliferation. A 96-well plate was seeded with 100 µl hematocytes along with the media incubated for 24 hours in incubator at 37 $^\circ$C. After completion of incubation the cells were treated with 10% and 20% nicotine, while control well was exempted from addition of sample and the plate was again incubated at 37 $^\circ$C for 48 hours. After incubation, plate was removed from incubator and 20 µl MTT reagent solution (1mg/ml; prepared in 1X PBS) was added. The plate was then incubated for 3 hours. After that the 100 µl stop solution i.e. DMSO was added and precipitates were allowed to dissolve for 1 hour followed by spectrophotometric analysis at 490 nm. The results were expressed as percentage of untreated control in RPMI 1640 culture medium.

## 2.5. DETERMINATION OF CELLULAR APOPTOSIS:

To evaluate whether nicotine induce apoptosis or not, the blood cells were cultured in falcon tubes and sample added and incubated as seen in cell viability assay. After incubation, cells were washed with $NH_4Cl$ at 1500 rpm for 10 minutes until white pellet was obtained. The obtained pellet was suspended in 200 µl saline solution (1X PBS). 100 µl of Hoechst 33342 (1 µg/ml) was added, mixed by inverting 3-4 times and kept in incubator at 37 $^\circ$C for 40-45 minutes. Then suspension was centrifuged at 1500 rpm for 10 minutes and pellet resuspended in 50 µl of 1X PBS. A drop of the prepared suspension was placed on clean slide, covered by a coverslip and observed under fluorescent microscope.

## 2.6. COMET ASSAY:

The alkaline version of comet assay was performed according to Singh *et al.* [14] with a slight modification. The culture was prepared and sample added as shown in leukocyte culturing and then incubated for 48 hours. Harvesting was done using 10 ml mixture of 0.85% ammonium chloride ($NH_4Cl$), 0.1% SDS and a pinch of EDTA (for lyses of RBCs) and centrifuged at 1500 rpm for 10 minutes. Centrifugation was repeated until white pellet was obtained. The white pellet obtained was suspended in 100 µl PBS. Meanwhile, a thin layer of normal melting agarose (1%) was prepared on clean, grease free slides was allowed to solidify. Now on the solidified NMA slides, 20 µl of the obtained white pellet (suspended in PBS) was

added at the centre followed by addition of 5 µl of sample (10% and 20% nicotine). The mixture was properly mixed using a micropipette. Now ~40 µl of low melting agarose (0.5%) was added over the mixture and allowed to solidify. The prepared slides were kept in lysing solution (Stock: 14.6 gm-NaCl, 3.72 gm-EDTA, 0.12-gm Tris HCl, 0.8 gm-NaOH in 100 ml distilled water, pH 10. Working (freshly prepared): 36 ml Stock solution, 4 ml DMSO, 0.4 ml Triton X-100) for 2 hours. After 2 hours the slides were removed from the lysing solution and kept in an electrophoretic unit filled with electrophoresis buffer (3 gm-NaOH, 0.075 gm EDTA in 250 ml D/W, pH >13). The slides were allowed to run for 20 minutes at 50V/300 mA. Immediately the slides were transferred in a neutralizing buffer (4.85 gm-tris buffer in 1000 ml D/W, pH 7.5) for 10 minutes. The slides were lastly stained with 80 µl EtBr (0.1 mg/ml) and left for 5 minutes. Slides were washed with PBS to remove excess stain and observed under florescence microscope.

## 2.7. LEUKOCYTE CULTURING:

For leukocyte culture, blood was collected from the healthy donor in heparinized tubes. Cultures containing RPMI 1640 (0.8 ml), Blood (0.4ml) 15 % fetal calf serum (1.5ml), PHA (0.1ml), and antibiotics were incubated at 37 °C for 72 h. Then 75 µl of 10% and 20% prepared solution of tobacco extract was added in 4 experimental tubes (2 each respectively) after completion of 24 hours of incubation. Control culture tubes were incubated without tobacco extract. Two hours prior to harvesting, 20 µl EtBr (1 mg/ml) was added to all culture tubes. After that 75 µl colchicine (0.2 mg/ml) was added to culture tubes 1 hour prior to harvesting. For harvesting of cells, the culture was first centrifuged at 1000 rpm for 5 minutes and 8 ml hypotonic solution (560 mg KCl/100 ml) was added to the pellet followed by incubation in water bath at 37 $^0$C for 35 minutes. After that, 1 ml of chilled fixative (Methanol and Glacial Acetic Acid in 3:1 ratio) was added followed by centrifugation at 1000 rpm for 5 minutes. Supernatant was discarded and again 6-7 ml of chilled fixative was added and centrifuged. This step was repeated twice until white pellet was obtained. The obtained white pellet was suspended in 1 ml of fixative, and slides were prepared by putting few drops of solution on wet slide and were dried followed by staining with 8% Giemsa for 20 minutes [15].

## 3. RESULTS AND DISCUSSION:

### 3.1. STUDY OF CYTOTOXIC EFFECTS OF CHEWING TOBACCO IN IN-VIVO CONDITIONS BY OBSERVING THE FORMATION OF MICRONUCLEI:

The results of micronucleus (MN) analysis of oral epithelial cells from person chewing tobacco and, those not chewing tobacco are shown in *figure-2*. All the experimental samples were found to chew different types of tobacco, 4-6 times a day, consuming approximately 2-5 gms of tobacco/day. All of them seem to be taking tobacco since last 5-8 years. Apart from tobacco chewing habit, subjects in experimental samples seem to be not taking any other cytotoxic agents like alcohol, tobacco in smoking form, drug etc.
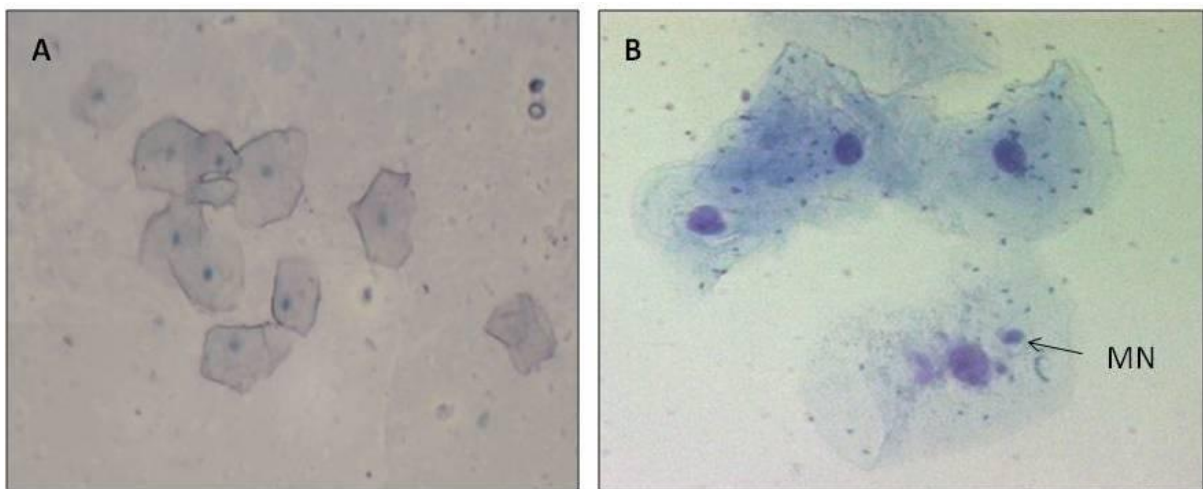


*Figure 2: Smear of oral exfoliated cells. Arrow indicates the presence of micronuclei. (A) Control (B) Subject.*

Results suggest that controls do not show any micronuclei and so were not taking any cytotoxic agents. Micronucleus assays was performed on oral exfoliated cells of subjects chewing tobacco and not chewing tobacco, using conventional giemsa staining. The experimental subjects showed a significantly higher micronucleus frequency than the control.

Tobacco is a primary cause of cancer. Cigarette smoke is identified as a factor involved in the early stages of tumorogenesis, especially lung cancer and may also be involved in other organs example, Mouth, Pharynx and Bladder [16]. MN methods have been used for diffracting genotoxic effects in human lymphocytes and in oral mucosa cell as well. Halder et al [7] suggested the role of MN frequency as a marker of epithelial carcinogenic progression. According to MN assay is reliable and technically easy to perform and is an efficient alternative to the metaphase analysis. It can also be used as marker of epithelial carcinogenic progression. MN is considered to be the result of chromosome fragments or whole chromosome lagging behind the genome at the cell division. They arise from fragments

produced by chromosome breaks, by certain types of chromatid interchanges and from whole chromosomes. At telophase, they form a small nucleus near the main one from which they are derived.

## 3.2. CELL VIABILITY:

The viability of cells can be analyzed by staining cells with trypan blue. Live cell exclude dye from entering because of intact cell-membrane and thus remained colourless while the dead cells were stained blue. The result showed that there was no significant effect on cell viability and most of the cells treated with different concentration of sample remained viable. The viability of cell in control was almost 100 %, while it was 99% and 95% in cells treated with 10% and 20% nicotine respectively. There was no observable change in cell morphology.

Kleinsasser *et al.* [2] showed that nicotine did not exert cytotoxic effects in any of the experiments based on the trypan blue test. Cell viability was well above 75% in both cell types before and after exposure to nicotine. In another experiment to study effect of nicotine on cell viability and morphology of human fibroblasts, the test results revealed that more unviable cells were found in the groups exposed to nicotine, in comparison with the control group. Moreover, with increasing doses of nicotine there was a directly proportional increase in the number of unviable cells [17]. It was also shown that Cigarette smoke condensate at 50 lg/mL induced a moderate increase in cell viability, whereas the corresponding nicotine concentration (3.2 lg/mL) did not produce this response. Cigarette smoke condensate at 250 lg/mL, but not nicotine at 16 lg/mL (the corresponding nicotine concentration) induced cell death [18]. To understand the effects of nicotine in human retinal pigment epithelial (ARPE-19), human microvascular endothelial cells (HMVEC) and rat neurosensory retinal (R28) cells, ARPE-19, HMVEC and R28 cell cultures were treated with $10^{-2}$ and $10^{-4}$ nicotine for 24 h. Trypan blue dye exclusion assay was performed. With $10^{-2}$ M nicotine treatment, R28 cell cultures and HMVEC cultures showed decreased cell viability, while ARPE-19 cells showed no change in cell viability [19].

## *3.3. MTT ASSAY:*

The cytotoxic effect of nicotine on cell proliferation of hematocytes was evaluated by using MTT assay. The graph obtained is shown below:

**% Viability of cells at different nicotine concentration**
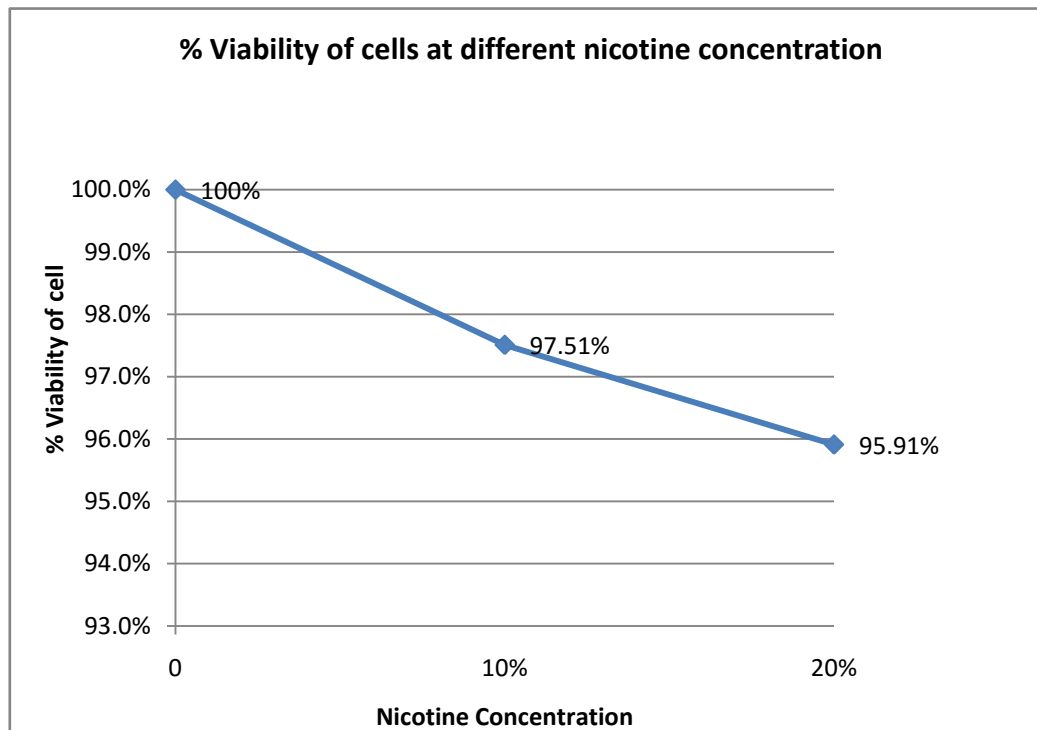
*Figure 3: Cell viability at 10% and 20% nicotine concentration by MTT test*

The results showed that upon incubation with nicotine for 48 hour, there was a dose-dependent increase in mitochondrial dysfunction within cells. There was a statistically countable difference in cell viability by various concentration of nicotine, compared to the untreated control. Though there was notable decrease in mitochondrial dysfunction in treated cell, the overall viability of cell remain >95%. Nicotine inhibited the proliferation of immortalized and malignant keratinocytes in dose- and time-dependent manners as determined by MTT assay [20]. The significant decrease of MTT reduction and increase of lipid peroxidation in PC12 cells were only observed at treatments with high concentrations of nicotine (1 and 10 mM) [21].

### 3.4. CELL APOPTOSIS:

The nuclear chromatin of cells was stained with Hoechst 33342 fluorochrome, followed by observation under a fluorescence microscope. Apoptotic cells were distinguished from viable cells by observing the condensed chromatin which was of bright blue colour, while viable cells showed light blue colour. Nicotine showed dose dependent apoptotic effects on lymphocyte cells, compared with untreated cells.
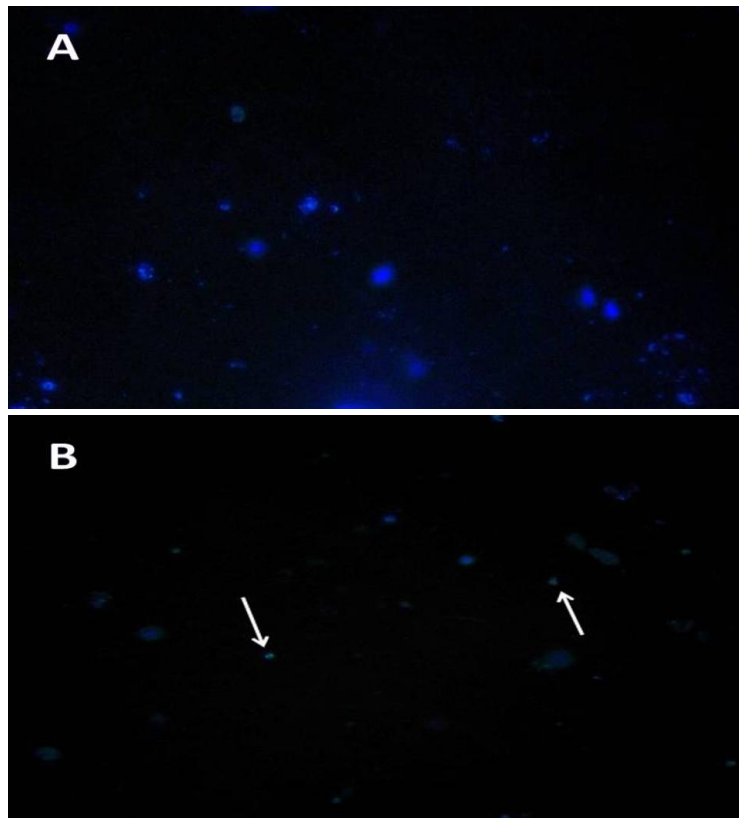
*Figure 4: Fluorescent photograph of lymphocyte cells stained with Hoechst 33342. (A)Control (B) 20% nicotine. The arrow indicates the brightly blue stained chromatin of dead cells.*

The results indicate that as nicotine concentration increases there is a gradual increase in the no. of apoptotic cells (Figure 4). Control as well as culture with 10% nicotine did not show any apoptotic cell while culture with 20% nicotine showed very few (~1-2) apoptotic cell/s.

Hoechst 33342 is a popular cell-permeant nuclear stain that emits blue fluorescence when bound to dsDNA [22]. Hoechst 33342 induce apoptosis in the HL-60 cells in a time- and dose-dependent manner [23].  Nicotine induces paradoxical effects that might alternatively enforce survival or trigger apoptosis. Nicotine acts as an inducer of apoptosis in normal or transformed lymphocytes, and possibly other non-neuronal cells [24]. When the rats were pretreated by nicotine, neuronal degeneration was attenuated. This observation was confirmed by Hoechst 33342 staining which allowed identifying of cells with condensed, fragmented nuclei, which has been proposed to be a vital sign of apoptosis [25].

### 3.5. COMET ASSAY:

DNA level damage at every individual cell level can be measured by the comet assay.
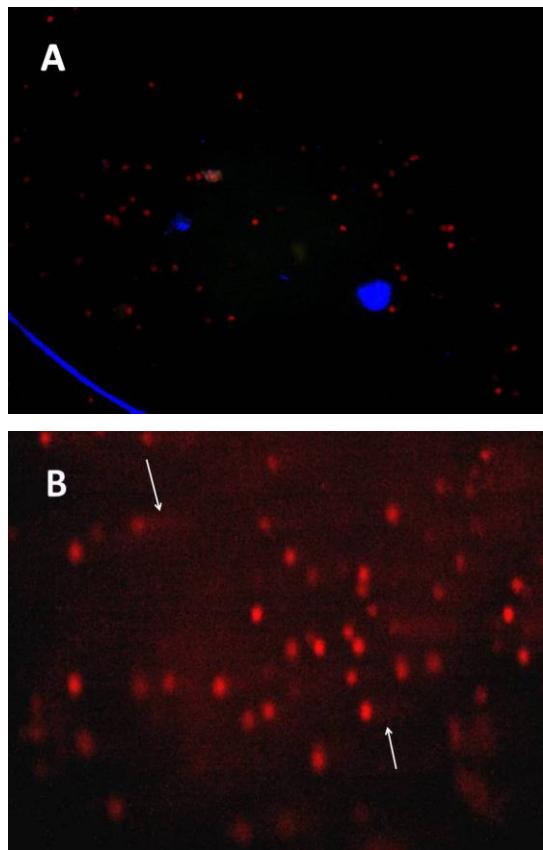


*Figure 5: Effect of nicotine and formation of comet tail (A) Control-20X (B) Cells treated with 20% nicotine-45X*

The results show that nicotine causes significant genotoxic effect on leukocytes. The DNA damage can be visualized as the length of comet tail formed (*Figure 5*). The alkaline single-cell microgel electrophoresis (Comet) assay is a sensitive tool for detection of DNA single strand breaks, as well as foralkali labile and incomplete excision repair sites [26]. Lymphocytes and mucosal cells as human target cells have been analyzed by this method [27]. Kleinsasser *et al*., [2] showed that 1 hr of incubation with nicotine induced a significant concentration-dependent increase in DNA migration in the Comet assay in tonsillar cells as well as in peripheral lymphocytes from the same donors. When highly pure nicotine from two different commercial sources was used, the significant concentration dependent DNA damage by nicotine was confirmed for both tonsillar cells and peripheral lymphocytes. There was no difference in DNA migration as far as the source of nicotine was concerned. A similar effect was shown previously for myosmine, a minor tobacco alkaloid that also occurs in a variety of foods, e.g., cereals, nuts, cocoa, and dairy products [2, 28]. Nicotine was equally genotoxic to lymphocytes and tonsillar cells. This finding is in contrast to results obtained for other

genotoxic compounds such as vanadium and, to a lesser extent, phthalates and myosmine, which were more genotoxic to lymphocytes than to mucosal cells [2]. An analysis of a possible influence of smoking status on DNA migration in the negative controls showed no significant differences. This finding is in line with results of Hoffmann and Speit [29], showing no differences in peripheral blood cells from heavy smokers and nonsmokers, in the comet assay. A significant increase was observed in Olive tail moment and tail length was obtained when dose of nicotine was increased. Higher dose of nicotine showed significant DNA damage while at lower conc. no damage was detected by comet assay [30].

### 3.6. LEUKOCYTE CULTURING:

Leukocyte culture in the presence of nicotin has exhibited different chromosomal aberrations like ring chromosome, chromosome breaks and with total change in chromosomal organization. *Figure-6* shows that different chromosomal aberrations are observed. The results found in tubes with 20% nicotine sample added to it, shows the formation of ring chromosome as shown in *Figure 6 (B),* while chromosome condensation was observed *Figure 6 (C)* in another culture.
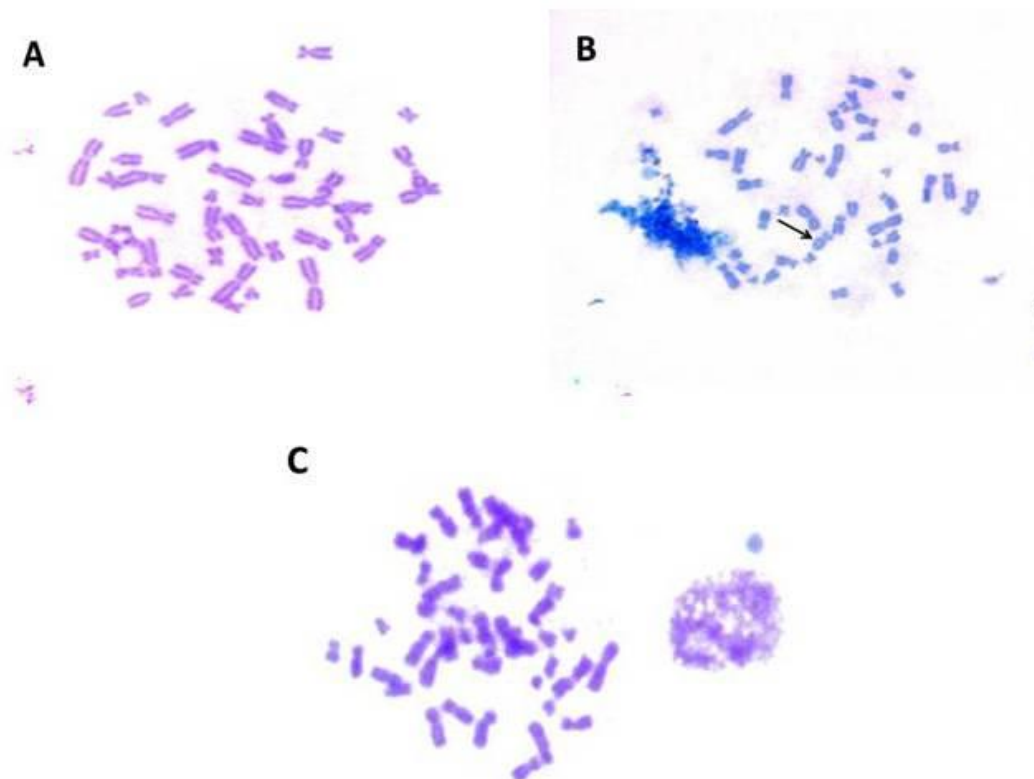
*Figure 6: Metaphase plate showing chromosomes.(A) Control (B) & (C) Effect on chromosome by treatment with 20% nicotine. (B) Ring Chromosome - Arrow shows the occurance of ring chromosome (C) Completely Condensed Chromosome*

Development of chromosomal aberrations in cultured leukocytes in the presence of nicotine confirms the genotoxic effect of nicotine most probably by forming DNA adducts. Though we could only check the effects of nicotine at the concentration of 10% & 20% only, the effects of nicotine with different concentrations should further be studied for the proper evaluation of genotoxic effect. When leukocytes were cultured with tobacco extract, chromosomal aberrations like chromatid break, dicentric chromosomes, chromosome ring formation and complete change in the organization could be observed. In a similar observation, elevated chromosomal aberration frequencies in smokers have been reported [31, 32]. The review, published by The Lancet Oncology, concludes that there is sufficient evidence to confirm that smoking is a cause of 15 types of cancer [5]. Tobacco metabolites formed in the form of carcinogens form DNA adducts, usually with adenine or guanine. DNA adducts which escape cellular repair could persist and may lead to miscoding and mutation [33].

## 4. CONCLUSION:

The findings suggest that micronuclei assay of oral epithelial cells can be used as simple markers for understanding genotoxic damage caused by chewing tobacco products by people and they can be warned for possible development of cancer later in life. We could also confirm the genotoxic effects of tobacco in *in-vitro* conditions on cultured leukocytes by studying chromosomal aberrations and by performing comet assay. The formation of comet tail on cultured leukocytes indicates the DNA damage done by nicotine. Though there is no significant change in cell viability or cell apoptosis we could conclude that nicotine causes a dose-dependent damage on human hematocytes. As the concentration of nicotine increases there is a gradual decrease in viable cells and an increase in apoptotic cells. The exact genotoxic and cytotoxic effect of nicotine is still not known and thus a further research needs to be focused in this field.

## 5. ACKNOWLEDGEMENTS

## 6. REFERENCES:

[1] Heisheman, S.C., Taylor, R.C. and Henningfield, J.E. Nicotine and smoking: a review of effects on human performance, Exp. Clin. Pharmacol. (1994), 2: 345–395.

[2] Kleinsasser NH *et al.* - Toxicological Sciences, (2005), 86(2), 309–317.

[3] Barbour S. Warren et al. - Cornell University Program on Breast Cancer and Environmental Risk Factors in New York State (BCERF) (2002).

[4] Peto R et al. Mortality from smoking in developed countries 1950-2000 (2nd edition) Oxford University Press (2004).

[5] Straif Kurt et al. The Lancet Oncology, (2009), 10 (11), 1033 – 1034.

[6] Casartelli G, Bonatti S, De Ferrari M, Scala M, Mereu P, Margarino G, Abbondandolo A. Micronucleus frequencies in exfoliated buccal cells in normal mucosa, precancerous lesions and squamous cell carcinoma. Anal Quant Cytol Histol. (2000), 22(6):486-92.

[7] Halder A., T. Chakraborty, K. Mandal, P. K. Gure, S. Das, R. Raychowdhury and A. K. Ghosh Comparative Study of Exfoliated Oral Mucosal Cell Micronuclei frequency in Normal, Precancerous and Malignant Epithelium. Int J Hum Genet, (2004), 4(4), 257-260.

[8] Argentin, G., and Cicchetti, R. Genotoxic and antiapoptotic effect of nicotine on human gingival fibroblasts. Toxicol. Sci. (2004), 79, 75–81.

[9] Arabi, M. Nicotinic infertility: assessing DNA and plasma membrane integrity of human spermatozoa. Andrologia, (2004), 36, 305–310.

[10] Heeschen, C., Jang, J. J., Weis, M., Pathak, A., Kaji, S., Hu, R. S., Tsao, P. S., Johnson, F. L., and Cooke, J. P. Nicotine stimulates angiogenesis and promotes tumor growth and atherosclerosis. Nat. Med. (2001), 7, 835–841.

[11] Cooke, J. P., and Bitterman, H. Nicotine and angiogenesis: A new paradigm for tobacco-related diseases. Ann. Med. (2004), 36, 33–40.

[12] Shin, V. Y.,Wu,W. K. K., Ye, Y.-N., So,W. H. L., Koo, M.W. L., Liu, E. S. L., Luo, J.-C., and Cho, C.-H. Nicotine promotes gastric tumor growth and neovascularization by

activating extracellular signal-regulated kinase and cyclooxygenase-2. Carcinogenesis, (2004), 25, 2487–2495.

[13] Schuller, H. M., Plummer, H. K., and Jull, B. A. Receptor-mediated effects of nicotine and its nitrosated derivative NNK on pulmonary neuroendocrine cells. Anat. Rec., (2003), 270A, 51–58.

[14] Singh NP, McCoy MT, Tice RR, Schneider EL. A simple technique for quantitation of low levels of DNA damage in individual cells. Experimental Cell Research. (1988) 175(1):184–191.

[15] Patel R. K., Radhakrishna U. and Khoda V. K.. A modified technique of GTG banding in Cattle and buffaloes. The Nucleus. (1995), 38: 37-39.

[16] Rowland RE, Harding KM. Increased sister chromatid exchange in the peripheral blood lymphocytes of young women who smoke cigarettes. Hereditas, (1999), 131(2):143-6.

[17] Martinez AE, Silverio KG, Rossa C Jr. - Effect of nicotine on the viability and morphology of fibroblasts: in vitro study. Brazilian Oral Research. (2002), 16(3):234-8.

[18] Silva D, Cáceres M, Arancibia R, Martínez C, Martínez J, Smith PC. Effects of cigarette smoke and nicotine on cell viability, migration and myofibroblastic differentiation. Journal of Periodontal Res. (2012), 47(5):599-607.

[19] Patil AJ, Gramajo AL, Sharma A, Seigel GM, Kuppermann BD, Kenney MC. Differential effects of nicotine on retinal and vascular cells in vitro. Toxicology. (2009), 259(1-2):69-76.

[20] Lee HJ, Guo HY, Lee SK, Jeon BH, Jun CD, Lee SK, Park MH, Kim EC. Effects of nicotine on proliferation, cell cycle, and differentiation in immortalized and malignant oral keratinocytes. Journal of Oral Pathology and Medicine, (2005), 34(7): 436-43.

[21] Guan ZZ, Wen-Feng Yu, Agneta Nordberg (2003) - Dual effects of nicotine on oxidative stress and neuroprotection in PC12 cells. Neurochemistry international. Volume 43, Issue 3, August 2003, Pages 243–249.

[22] Oriowo OM, Cullen AP, Sivak JG. Impairment of eye lens cell physiology and optics by broadband ultraviolet A-ultraviolet B radiation. Photochem Photobiol. (2002), 76:361–7.

[23] Zhang X, Chen J, Davis B, Kiechle F. Hoechst 33342 induces apoptosis in HL-60 cells and inhibits topoisomerase I in vivo. Arch Pathol Lab Med. (1999), 123(10):921-7.

[24] Oloris SC, Ashley A. Frazer-Abel, Cristan M. Jubala, Susan P. Fosmire, Karen M. Helm, Sally R. Robinson, Derek M. Korpela, Megan M. Duckett, Shairaz Baksh and Jaime F. Modiano. Nicotine-Mediated Signals Modulate Cell Death And Survival Of T Lymphocytes. Toxicology and Applied Pharmacology. (2010), 242(3):299-309.

[25] Riljak V., M. Milotová, K. Jandová, J. Pokorný, M. Langmeier. Morphological changes in the Hippocampus following nicotine and kainic acid administration. Physiol. Res. (2007), 56: 641-649.

[26] Lee E., Lee J., Sul D., and Lee J. Use of the tail moment of the lymphocytes to evaluate DNA damage in human biomonitoring studies. Toxicol. Sci. (2004), 81, 121–132.

[27] Harrus U., Schmezer P., Kuchenmeister F. and Maier H. Genotoxic effect on human mucous membrane biopsies of the upper aerodigestive tract. Laryngorhinootologie, (1999), 78, 176–181.

[28] Tyroller S., Zwickenpflug W., and Richter E. New sources of dietary myosmine uptake from cereals, fruits, vegetables and milk. J. Agric. Food. Chem. (2002), 50, 4909–4915.

[29] Hoffmann H., and Speit G. Assessment of DNA damage in peripheral blood of heavy smokers with the Comet assay and the micronucleus test. Mutat. Res., (2005), 581, 105–114.

[30] Sobkowiak R, Lesicki A. Genotoxicity of nicotine in cell culture of Caenorhabditis elegans evaluated by the comet assay. Drug Chem Toxicol. (2009), 32(3):252-7.

[31] Obe G., Herha, J. Chromosomal aberrations in heavy smokers, Hum. Genet. (1987), 41, 259-263.

[31] Vijayalaxmi, H. J. Evans.  In vivo and in vitro effects of sister chromatid exchanges in human peripheral blood lymphocytes, Mutat. Res. 92 (1982) 321-332.

[33] Kuper H, Adami HO, Boffetta P. Tobacco use, cancer causation and public health impact. J Intern Med. (2002), 251(6):455-66.

# Synthesis, Characterization and Glass reinforced composites based on Arylhydrazino- Epoxy resin system

Dr.S.V.Patel [1] and Dr.J.N.Patel [2]

Chemistry Department, Sir P.T.Science College, Modasa. Gujarat (India)

[1]Corresponding author, Email: [1]svp2938@gmail.com , [2]Jay_gullu@yahoo.co.in

## ABSTRACT

Arylhydrazino-bismaleimide (AHBM) were prepared by Michael addition reaction between phenyl hydrazine derivatives with N,N'-(4-4'-biphenylene) bismaleimide (BBM). These AHBM were used for curing of commercial epoxy resin. The curing behaviour of commercial epoxy resin with this AHBM compounds have been monitored on differential scanning calorimetry (DSC) using 2- methyl imidazole as a catalyst. Glass reinforced composites of epoxy-AHBM system have been also prepared and characterized by mechanically and chemically.

**Keywords :** Bismaleimide, Michael addition reaction, Phenyl hydrazine, epoxy resin

## INTODUCTION

Epoxy resins are extensively used in a number of applications like molding, adhesives, paints, powder coatings etc.[1] Epoxy resins in their pre-cured state they are either in form of colorless to yellowish brown viscous liquid. The viscous state of epoxy resins are quite stable and do not affect by whether at room temperature. The cure state of such epoxy resins can be exhibited by adding curing agents in to them. Numbers of curing agents are reported and some of them received commercial value. The diamines, anhydrides, thiols etc. are well known epoxy curing agents i.e. hardeners.[1] The area in which the epoxy hardener containing hydrazine group have received patentable reports.[2] Only hydrazine derivatives of carboxylic acid have been reported as epoxy curing agents.[3-6] If the hydrazine derivatives of bismeleimide tried for hardening epoxy resin which may alter the properties of end products up to some extent. It is also well known that imide containing polymers say, polyimides have high performance properties.[7-11] Hence with a view of merging of epoxy resin as soft segment and bismaleimied as a hard segment, in to cured network, the present paper comprises curing study of epoxy resin by arylhydrazine derivatives of bismaleimide (AHBM) and composite fabrication study.

## EXPERIMENTAL

### Materials

Commercial epoxy resin i.e. Novolac was obtained from sympol products Pvt.Ltd. Ahmadabad, India. The specification of this epoxy resin is as indicating under.

**Epoxy equivalent:** 171-183, **Viscosity:** 1.10-1.70 Poise, **Density:** 1.21-1.23 gm/cm$^3$

Aryl hydrazine derivatives were obtained from Chiti Chem. Baroda, India, and used as received. N-N′ (4, 4′ - biphyenylene) bismaleimide (BBM) was prepared by the method reported in literature[8]. Other chemicals used were of laboratory grade.

### Synthesis of arylhydrazino-N-N′ biphenylene) bismaleimide (AHBBM)

All the arylhydrazino –N-N′ (4, 4′- biphenylene) bismaleimide (AHBBM) derivatives (shown in scheme – I) were prepared according to our earlier communication[9].

### Synthesis of unreinforced epoxy resin – AHBBM systems

The unreinforced epoxy resin – AHBBM products were by mixing epoxy resin (1 mol) and AHBBM derivatives (0.25 mol)[12]. (As used for DSC study) and heated for 2 hrs at curing temperature (i.e. Tp obtained from DSC experiment) shown in Table -1. The products were crushed, washed by hot water and them air dried. The thermal properties of these products are presented in Table-2.

### Composite Fabrication

The glass fiber reinforced composites (GRC) based on epoxy resin – AHBBM system were prepared by mixing stochiometric ratio of epoxy resin and AHBBM (40%wt. of total glass cloth) in THF[12-14].The resulting mixture was mixed well for 10 min .The suspension was then applied with a brush on to a 150 mm X 150 mm epoxy compatible fiber glass cloth, and the solvent was allowed to evaporate. Once dried the ten prepregs were stacked one on top of another, press between steel plates coated with a Teflon film release and compressed in flat platen under about 0.5 Mpa pressure. The prepregs were cured by heating the press at 170-180 °C for 12 hrs in an air circulated oven. The laminated so obtained was cooled at room temperature before the pressure was released. Test specimens were made by cutting the laminates and machining them to final dimension.

## MEASUREMENT

FTIR spectral analysis was carried on Perkin Elmer- 983 spectrophotometer. Curing of a epoxy resin with AHBBM compounds were monitored by differential scanning calorimetry using a Dupont 900 DSC. The instrument was calibrated using standard material known heated of fusion. Curing was carried out using a single heating rate of 10 Kelvin/min.

The sample for this investigation was in the range of 4 to 5 mg and an empty cell was used as a reference. The thermo gravimetric analysis (TGA) of all AHBBM epoxy cured and their uncured products was carried out on a DuPont thermo balance in air at a heating rate of 10 Kelvin/min. All the mechanical and chemical properties were determined according to ASTM or ISO methods.

## RESULTS AND DISCUSSION

In our earlier communication [11] we have reported the synthesis of hydrazine-bismaleimides. The synthesis was based on Michel-addition of phenyl hydrazine and bismaleimides. Further study of few of these derivatives for epoxy curing presented here.

The DSC study of epoxy – AHBBM was adopted to establish the curing temperature for bulk curing. Examination of all the DSC scan of epoxy –AHBBM system, a broad curing exotherm was observed in the temperature range of 120-250°C. The exotherm was characterized by noting Tp-temperature obtained by drawing a tangent to the steepest position of the start of the exotherm, Tp- the peak exotherm temperature, $T_f$ - the final exotherm temperature and ΔH – the heat of curing obtained from the area under exotherm. The result of DSC scans for the curing of all the AHBBM resins by AHBBM in the presence of catalyst are summarized in Table-1. All the samples have a Tp in the range of 100-170°C and depending upon the nature of the system. The heat of curing is fast as indicating reaction was completed in the presence of catalyst.

The unreinforced AHBBM epoxy resin system have also been prepared and characterized. Observation of the IR spectra (not shown here) of all the AHBBM – epoxy unreinforced system revels that all the spectra comprise the spectral feature of aromatic ring (3030, 1500, 1600 cm$^{-1}$). Only the discernible difference is observed between cured product and parent compounds. The band due to epoxy ring at 910 cm$^{-1}$ in the spectra of resin is almost vanished in the spectra of all the epoxy- AHBBM cured products. This indicates that the curing of epoxy ring exhibited through epoxy group and – NHNH- group of AHBBM compounds.    The TGA data of all cured products are given in Table-2. The cured products start their decomposition at around 250 °C. The rate of decomposition increase between 300 °C and 500 °C. The results of TGA show that the cured products lose almost 90% of their mass at 600 °C. The results of TGA show that the cured products have quit good thermal stability.

The glass reinforced composites of epoxy-AHBBM resins have density of in the range of 1.8 to 2.0 gm/cm$^3$. Examination of chemical resistance test reveals that all composites have

remarkable resistance to organic solvents and concentrated HCL. However treatment with concentrated NaOH changes their thickness is small amount and weight by about 1.3%. Examination of the results of mechanical properties of all composites reveals that all the composites have good mechanical strength. All the mechanical properties and chemical resistance data furnished in Table-3.

**Table-1 : DSC Curing study of AHBBM-epoxy resin System.**

| Sample | Cure Onset temperature Ti (°C) | Peak temperature Tp (°C) | Final temperature $T_f$ (°C) | Activation energy (Ea) K.cal/mol |
| --- | --- | --- | --- | --- |
| AHBBM$_1$ + NE | 135 | 165 | 175 | 34.10 |
| AHBBM$_2$ + NE | 115 | 149 | 166 | 30.90 |
| AHBBM$_3$ + NE | 106 | 118 | 168 | 32.10 |
| AHBBM$_4$ + NE | 95 | 110 | 160 | 34.10 |
| AHBBM$_5$ + NE | 126 | 169 | 190 | 35.30 |
| **Stoichiometric proportion of AHBBM – epoxy resin was used.** | | | | |

**Table-2: TGA of AHBBM – epoxy resin system.**

| Sample | % Weight loss at various temperature (°C) | | | | |
| --- | --- | --- | --- | --- | --- |
| | 250 | 300 | 400 | 500 | 600 |
| AHBBM$_1$ + NE | 4 | 12 | 35 | 68 | 91 |
| AHBBM$_2$ + NE | 6 | 15 | 37 | 67 | 92 |
| AHBBM$_3$ + NE | 5 | 14 | 37 | 69 | 93 |
| AHBBM$_4$ + NE | 6 | 14 | 38 | 65 | 90 |
| AHBBM$_5$ + NE | 5 | 13 | 36 | 66 | 91 |
| **Where, NE  = Novolac Epoxy Resin** | | | | | |

**Table - 3: Mechanical and electrical properties of glass reinforced composites based on AHBBM- epoxy ( equivalent ratio ) system.**

| Sample | Chemical Resistance % change in | | Density gm/cm$^3$ | Flexural Strength ( MPa) (ASTM D-790) | Compressive Strength (MPa) (ISO Method) | Impact Strength (MPa) (ASTM) D-790 | Hardness (R) (ASTM D- 790) |
| --- | --- | --- | --- | --- | --- | --- | --- |
| | Thick ness | Weight | | | | | |
| AHBBM$_1$ + NE | 0.8 | 1.2 | 1.85 | 195 | 189 | 215 | 133 |
| AHBBM$_2$ + NE | 0.9 | 1.0 | 1.95 | 197 | 213 | 240 | 134 |
| AHBBM$_3$ + NE | 1.0 | 1.1 | 1.92 | 192 | 209 | 230 | 137 |
| AHBBM$_4$ + NE | 0.9 | 1.0 | 1.95 | 202 | 214 | 230 | 140 |
| AHBBM$_5$ + NE | 0.8 | 1.1 | 1.97 | 207 | 198 | 270 | 133 |

## Scheme -I

Ar  = 1.  Phenyl
2. 4- Chloro phenyl
3. 4- Bromo phenyl
4. 4- Methyl phenyl
5. 4- Methoxy phenyl

## ACKNOWLEDGEMENTS

## REFERENCES

1. Lee H and Naville K., Hand Book of Epoxy Resin, McGraw Hill, New York. (1978).
2. Young Glenda, C., US Patent: 4,816,531, Chem. Abstr, 111, 196058c. (1989).
3. Baraban, O.P., Ryskina A.E. and Efimenco L.V.
   (i)  Sintezi, SvoistavZhidk, Unglevodorod Kauchakovnaikh Osnove M (1979), 121.
   (ii) Zh. KhimAbstr. No. 24T, (1979), 600.
4. Kochetov, D.P., Gritsenko F.R., Grishchenko V.K. and Yu.L.Spirin, VysokomolSoedin (A) 21, (1979), 2171.
5. Aelony , D., J. Appli. Polym.Sci.13 (1969), 227.
6. Levine, H.H. US Petent: 3 (1959) 3, 014,009.
7. Adrora, N.A. "Polyimides" Academy of science of USSR (1968).
8. Crivelio, J.V., J.Poly. Sci., Polym.Chem. Ed., (1976) 14,159.
9. Patel, H.S. ; Patel , B.K. Interacting blends of acrylated poly(ester- amide) resins  with methyl methacrylate monomer Part 2 . J. Rein. Plast. Comp. 29, 1359 – 1365 (2010).
10. Patel, H.S. ; Patel , B.K. ; Morekar, M.M. ; Dixit,B.C. Synthesis, characterization and glass reinforcement of urea-formaldehyde-phenol resins . Int. J. Poly. Mater. 2009, 58, 604 – 611.
11. Patel, S.V. and Daraji, J.M. Oriental J.Org.Chem.(India) Vol.17(2),(2001),299-302.
12. Patel, S.V. and Daraji, J.M. Ultra Sc.of.Phy.Sci.(India) Vol.14(1),(2002).
13. O Al-Qabandi, Anjali De Silva, Salah Al-Enezi,M Bassyouni, Journal of Reinforced Plastics and Composites. Volume: 33 issues: 24, page(s): 2287-2299, (2014).
14. Bhavdeep K. Patel , Hasmukh S. Patel & Manish M. Morekar. Jor.of Poly.Plastics Technology and Engineering.  Volume 52, Issue 4, Pages 332-336., (2013).

# Synthesis of a series of novel 1,3,4oxadiazole containing semicarbazide (SC) and thiosemicarbazide (TSC) as potential antimicrobial agents

Vikram N. Panchal[1*], Hiran H. Variya[1], G.R.Patel[1] , Manoj A Vora[2]

[1]Department of Chemistry, Sheth M. N. Science College, NGES campus, Patan - 384265, India
[2]Department of Chemistry, School of science, Gujarat university, Ahmedabad, Gujarat, India
E-mail:Vikrampanchal1988@gmail.com

**Abstract**

The newly synthesized two series namely: (E)-2-benzylidene-N-(2-((5-phenyl-1,3,4-oxadiazol-2-yl)thio)acetyl)hydrazinecarboxamide/(E)-2-benzylidene-N-(2-((5-phenyl-1,3,4-oxadiazol-2-yl)thio)ethanethioyl)hydrazinecarboxamide **(3a-3r)** were prepared. These compounds synthesized from 5-phenyl-1,3,4-oxadiazole-2-thiol, Thiosemicarbazide (TSC) and Semicarbazide (SC) were vital functionalities containing the wide range of Pharmacological activities and have a wide range of therapeutic properties. The structure of the synthesized compounds was confirmed by spectral data and evaluated for their in vitro antibacterial and antifungal activities against fungi, Gram-positive and Gram-negative bacteria.

**Keywords:** 1,3,4 oxadiazole, Thiosemicarbazide, Semicarbazide, Antimicrobial.

**Introduction**

Drug discovery is considered a complex and activity. Therefore, researcher trying to developed Heterocyclic new entities containing N,O,S, and P having broad range of microbial activities against a number of bacteria and fungi and become most important field of research in Phrama industry due to their many wide applications. It follows from the literature that depending on the type of substituent, the analogues of 1,3,4-oxadaizoles have high potential for a wide range of biological activities such as antimicrobial[1,2], anti-inflammatory[3], analgesic[4] , anticancer[5], anti-malarial[6], antihypertensive[7] and antiviral[8]. 1,3,4-oxadaizole based compounds are plenty. Schiff bases have also gained important in the field of medicine due to their wide range of biological

activities such as antimicrobial[9-11], anti-tubular[12], anti-HIV[13], anticancer[13], antitumor[14], anti-inflammatory[15], analgesic[15] and anticonvulsant[16,17]. In the medicinal applications, many heterocyclic nuclei, 1,3,4-oxadaizle and Schiff bases have been considerable interest due to their important biological properties.

Data from NMR, FTIR, mass and elemental analysis were used to characterize the compounds. The antibacterial activities potency of these Schiff base bearing 1,3,4-oxadiazoles compounds were evaluated against certain standard strains. The antibacterial activities of compounds were compared to standards.

With these criteria and literature data considering the importance of 1,3,4-oxadaizole moiety in medicinal chemistry, here two series containing 1,3,4-oxadaizole and TSC, SC were designed and synthesized for their antimicrobial activities against Gram-positive and Gram-negative bacteria.

## RESULT AND DISCUSSION

### *Chemistry*

The title compounds were prepared according to the synthetic strategy described in Scheme-1. The key moiety in the present work Schiff base **1a-1r** were synthesized from using various benzaldehyde and thiosemicarbazide (TSC) or Semicarbazide (SC) in the presence of acetic acid in ethanol, Further, we planned to extended our studies by using chloroacetylchloride (CAC) with TEA in presence of DMF to yielded **2a-2r** which treated with 5-phenyl-1,3,4-oxadiazole-2-thiol,  to afford different substituent's of title compounds **3a-3r** which confirmed by spectral data.

**Scheme -1** Synthesis of targeted compound **3a-3r**

**Table 1.** The substituent of the compounds for derivatives of **3a-3r.**

| Compounds | R | X | Molecular Formula | Yield (%) | Melting Point°C |
|---|---|---|---|---|---|
| **3a** | Ph | O | $C_{18}H_{15}N_5O_3$ | 80 | 165-168 |
| **3b** | p-F Ph | O | $C_{18}H_{14}FN_5O_3S$ | 76 | 161-165 |
| **3c** | p-Cl Ph | O | $C_{18}H_{14}ClN_5O_3S$ | 77 | 165-169 |
| **3d** | p-Br Ph | O | $C_{18}H_{14}BrN_5O_3S$ | 70 | 161-165 |
| **3e** | p-OCH$_3$ Ph | O | $C_{19}H_{17}N_5O_4S$ | 78 | 161-165 |
| **3f** | p-CH$_3$ Ph | O | $C_{19}H_{17}N_5O_3S$ | 75 | 165-168 |
| **3g** | m-NO$_2$ Ph | O | $C_{18}H_{14}N_6O_5S$ | 76 | 161-165 |
| **3h** | p-OH Ph | O | $C_{18}H_5N_5O_4S$ | 73 | 162-165 |
| **3i** | 2,4- (Cl)$_2$ Ph | O | $C_{18}H_{13}Cl_2N_5O_3S$ | 72 | 167-170 |
| **3j** | Ph | S | $C_{18}H_{15}N_5O_2S_2$ | 78 | 164-167 |

| **3k** | p-F Ph | S | $C_{18}H_{14}FN_5O_2S_2$ | 77 | 165-168 |
| --- | --- | --- | --- | --- | --- |
| **3l** | p-Cl Ph | S | $C_{18}H_{14}ClN_5O_2S_2$ | 75 | 161-165 |
| **3m** | p-Br Ph | S | $C_{18}H_{14}BrN_5O_2S_2$ | 78 | 161-165 |
| **3n** | p-OCH$_3$ Ph | S | $C_{19}H_{17}N_5O_3S_2$ | 72 | 165-168 |
| **3o** | p-CH$_3$ Ph | S | $C_{19}H_{17}N_5O_2S_2$ | 71 | 161-165 |
| **3p** | m-NO$_2$ Ph | S | $C_{18}H_{14}N_6O_4S_2$ | 70 | 162-165 |
| **3q** | p-OH Ph | S | $C_{18}H_{15}N_5O_3S_2$ | 74 | 168-171 |
| **3r** | 2,4- (Cl)$_2$ Ph | S | $C_{18}H_{13}Cl_2N_5O_2S_2$ | 73 | 170-173 |

## Antimicrobial activity

The Synthesized Series of **3a-3r** compounds were screened for their antimicrobial activity. Agar well diffusion technique was used for the activity. The microorganisms like gram negative The newly synthesized compounds **3a-3r** were screened in vitro for antibacterial activity against Gram positive *Micrococcus luteus* (MTCC No. 11948), *Bacillus Cereus* (MTCC No. 8558) and Gram negative *Enterobacter aerogens* (MTCC No. 8558), *Escherichia coli* (MTCC No. 1610). The standard inoculums (110 CFU/mL) were distributed on the surface of sterile nutrient agar plates by a sterile glass spreader. *Candida albicans* and *Aspergillus fumigatus* was used for the antifungal activity. A loopful of a particular fungal strain was used for the antifungal assay. Fungal strain was transferred to a 3.0 mL saline to achieve a suspension of related species. 0.1 mL of the spore suspension was spread on the surface of sterile sabouraud dextrose agar plates. A 6 mm diameter well punched in the agar media and packed with 100 μL of (500 μg/mL in DMSO) the tested chemical compounds previously sterilized through 0.45 sterile membranes filter. The plates kept at RT for 1 hrs then incubated at 24 hrs for bacteria and 5 days for fungi. The activities were evaluated by measuring the inhibition zone diameters. Antimicrobial activities of compounds are shown in table 2.

**Table 2:  Antimicrobial activity of compounds 3a to 3r.**

| Compound | Inhibition Zone Diameter (mm) | | | | | |
| --- | --- | --- | --- | --- | --- | --- |
| | *Enterobacter aerogens* *MTCC No. 8558* | *Escherichia coli* *MTCC No. 1610* | *Micrococcus luteus* *MTCC No. 11948* | *Bacillus cereus* *MTCC No. 8558* | Penicillium marneffei | Collectotrichum capsici |
| **3a** | 20 | 22 | 26 | 23 | 12 | 15 |
| **3b** | 21 | 20 | 19 | 20 | 11 | 14 |
| **3c** | 25 | 26 | 21 | 22 | Negative | 15 |
| **3d** | 20 | 19 | 23 | 20 | Negative | Negative |
| **3e** | 22 | 21 | 21 | 19 | 12 | 17 |
| **3f** | 19 | 23 | 22 | 21 | Negative | 17 |
| **3g** | 21 | 21 | 25 | 23 | 11 | 15 |
| **3h** | 20 | 22 | 22 | 19 | Negative | Negative |
| **3i** | 24 | 25 | 20 | 21 | 10 | 12 |
| **3j** | 22 | 22 | 21 | 21 | 14 | Negative |
| **3k** | 22 | 20 | 21 | 23 | Negative | 15 |
| **3l** | 20 | 21 | 24 | 20 | Negative | 16 |
| **3m** | 21 | 24 | 19 | 19 | 12 | Negative |
| **3n** | 18 | 19 | 21 | 21 | Negative | 13 |
| **3o** | 22 | 21 | 21 | 22 | 11 | 14 |
| **3p** | 20 | 19 | 19 | 19 | Negative | 13 |
| **3q** | 21 | 21 | 23 | 22 | Negative | Negative |
| **3r** | 18 | 22 | 24 | 23 | 11 | 15 |
| **Tetracycline** | 25 | 23 | 25 | 25 | - | - |
| **Flucanazole** | - | - | - | - | 22 | 25 |

**Minimum inhibitory Concentration (MIC)**

Broth dilution technique was used for determination of MIC. The nutrient broth and yeast extract broth media and it contain 1mL of different concentrations of Compounds (5,10,15,20 μg/mL).

Spectrophotometer was used for the moniter of growth. The microbial screening data revealed that compounds **3i** and **3c** have highest inhibition zone diameter while **3q,3d** and **3h** have no antifungal effect. Compounds **3c,3d,3f,3h,3k,3l,3n,3p** and **3q** were completely inactive against *Aspergillus fumigates*.MIC results of compounds are shown in table 3.

**Table 3: MIC (µg/mL) results of compounds 3a to 3r**

| Compound | MIC values (µg/mL) | | | | | |
| | *Enterobacter aerogens* *MTCC No. 8558* | *Escherichia coli* *MTCC No. 1610* | *Micrococcus luteus* *MTCC No. 11948* | *Bacillus cereus* *MTCC No. 8558* | Aspergillus fumigatus | Candida albicans |
|---|---|---|---|---|---|---|
| 3a | 10 | 5 | 10 | 10 | 15 | 10 |
| 3b | 10 | 10 | 15 | 15 | 20 | 10 |
| 3c | 15 | 15 | 5 | 10 | 10 | 10 |
| 3d | 5 | 10 | 10 | 10 | 10 | 15 |
| 3e | 10 | 20 | 15 | 15 | 10 | 5 |
| 3f | 15 | 10 | 5 | 5 | 15 | 10 |
| 3g | 10 | 15 | 10 | 10 | 5 | 15 |
| 3h | 20 | 5 | 15 | 15 | 10 | 10 |
| 3i | 10 | 10 | 10 | 10 | 15 | 15 |
| 3j | 15 | 15 | 20 | 20 | 10 | 5 |
| 3k | 5 | 10 | 10 | 5 | 20 | 10 |
| 3l | 10 | 20 | 15 | 10 | 10 | 15 |
| 3m | 15 | 5 | 5 | 15 | 10 | 10 |
| 3n | 5 | 10 | 10 | 10 | 10 | 20 |
| 3o | 10 | 15 | 15 | 20 | 15 | 10 |
| 3p | 15 | 10 | 10 | 10 | 5 | 5 |
| 3q | 10 | 20 | 20 | 15 | 10 | 10 |
| 3r | 20 | 10 | 10 | 5 | 15 | 10 |

**EXPERIMENTAL SECTION**

*General*

All starting materials and other reagents were purchased from commercially supplier. All the melting points were determined in open capillary and uncorrected by using a Melt-Tempt instrument, The absorbance spectra IR were recorded on Perkin-Elmer 377 spectrophotometer, ^{1}H NMR spectra were recorded on Bruckner at 400MHz, In DMSO solution. The elemental analysis were analyzer for C,H,N,O, and S were estimated on PerkinElmer, series II, 2400 CHNS analyzer (CSIR Bhavnagar, INDIA)  Mass spectra were recorded at Advion Expression CMS, USA

**General Procedure for the (E)-2-benzylidenehydrazinecarboxamide / (E)-2-benzylidene hydrazinecarbothioamide derivatives. (1a-1r)**

The aqueous Solution of Semicarbazide/thiosemicarbazide (0.01 mol) and benzaldehyde derivatives (0.01 mol) in 1:1 molar ratio taken in an RBF. The reaction mixture was kept over a magnetic stirrer and stirred well at a room temperature for 2 h. the solid was formed, filtered and washed with petroleum ether. Obtained solid was dried and checked by TLC.

**General procedure for the (E)-2-benzylidene-N-(2-chloroacetyl)hydrazinecarboxamide / (E)-2-benzylidene-N-(2-chloroacetyl)hydrazinecarboxamide derivatives. (2a-2r)**

A mixture of compound 1(0.01 mol) with Chloroacetyl chloride (0.015 mol) and 4-5 drops of TEA(triethylamine) in 25 ml DMF as the solvent in RBF. The reaction mixture was stirred for 4 hr at Room temperature. The Completion of the reaction was checked by TLC using toluene: Acetone (30%). The solution poured in to ice water. Obtained solid was filtered by vacuum pump and crystalline it in Ethanol.

**General procedure for the (E)-2-benzylidene-N-(2-((5-phenyl-1,3,4-oxadiazol-2-yl)thio)acetyl)hydrazinecarboxamide / (E)-N-(2-benzylidenehydrazinecarbonothioyl)-2-((5-phenyl-1,3,4-oxadiazol-2-yl)thio)acetamide derivatives (3a-3r)**

Above synthesized derivatives (0.01 mol) was reacted with 5-phenyl-1,3,4-oxadiazole-2-thiol (0.01 mol) in presence of potassium carbonate (0.02 mol) and acetone. The reaction was stirred

at room Temperature for 5 hr. The Completion of the reaction was checked by TLC using toluene: Acetone (20%). The product was poured into water and stirred for 1 hr. The obtained solid was collected and dried. Crystallize into ethanol.

*(E)-2-benzylidene-N-(2-((5-phenyl-1,3,4-oxadiazol-2-yl)thio)acetyl)hydrazinecarboxamide* **3a**
I.R (KBr) (υmax, cm-1): 3195 (N-H), 3088, 2964 (C-H), 1666 (C=O), 1587, 1542, 1512, 1457,1284 (C=N, C=C), 1159, 1002, 920, 746, 685 3456 cm$^{-1}$; $^1$H NMR (400 MHz, DMSO) δ 11.08 (s, 2H, NH), 4.27 (s, 2H, CH2), 7.00-7.82 (m, 10H, ArH), 6.4 (s, 1H HC=N) $^{13}$C-NMR δ 38.6, 147.6, 172.5, 123-154.8 (14 aromatic carbons),  MS (m/z) 380.89 (M$^+$); Elemental Analysis C, 56.68; H, 3.96; N, 18.36; O, 12.58; S, 8.41, Found: C 56.6, H 3.92, N 18.16, O 12.53, S 8.18%.

*(E)-2-(4-fluorobenzylidene)-N-(2-((5-phenyl-1,3,4-oxadiazol-2-yl)thio)acetyl)hydrazinecarbox amide* **3b** I.R (KBr) (υmax, cm-1): 3197 (N-H), 3088, 2965 (C-H), 1668 (C=O), 1585, 1541, 1522, 1455,1284 (C=N, C=C), 1159, 1004, 925, 742, 685 3456 cm$^{-1}$; $^1$H NMR (400 MHz, DMSO) δ 11.10 (s, 2H, NH), 4.32 (s, 2H, CH2), 7.05-7.92 (m, 9H, ArH), 6.6 (s, 1H HC=N) $^{13}$C-NMR δ 38.5 (CH2), 147.8 (N-CH-Ar), 172.2 (C=O), 123-154.8 (14 aromatic carbons), MS (m/z) 398.92 (M$^+$); Elemental Analysis C, 54.13; H, 3.53; F, 4.76; N, 17.53; O, 12.02; S, 8.03% Found: C 53.7, H 3.32, N 17.16, O 12.22 S 8.58 %.

*(E)-2-(4-chlorobenzylidene)-N-(2-((5-phenyl-1,3,4-oxadiazol-2-yl)thio)acetyl)hydrazinecarbox amide* **3c** I.R (KBr) (υmax, cm-1): 3196 (N-H), 3086, 2966 (C-H), 1665 (C=O), 1584, 1542, 1512, 1448,1294 (C=N, C=C), 1159, 1004, 925, 742, 685 3456 cm$^{-1}$; $^1$H NMR (400 MHz, DMSO) δ 11.02 (s, 2H, NH), 4.12 (s, 2H, CH2), 7.05-8.42 (m, 9H, ArH), 6.6 (s, 1H HC=N) $^{13}$C-NMR δ 39.5 (CH2), 145.8 (N-CH-Ar), 170.2 (C=O), 123-154.8 (14 aromatic carbons), 167.7 (S-C-N benz thio), MS (m/z) 414.97 (M$^+$); Elemental Analysis: C, 51.99; H, 3.39; Cl, 8.53; N, 16.84; O, 11.54; S, 7.71; Found: C 50.7, H 3.22, N 16.06,O 11.88 S 7.58 %.

*(E)-2-(4-bromobenzylidene)-N-(2-((5-phenyl-1,3,4-oxadiazol-2-yl)thio)acetyl)hydrazinecarbox amide* **3d** I.R (KBr) (υmax, cm-1): 3192 (N-H), 3080, 2956 (C-H), 1662 (C=O), 1581, 1539, 1522, 1448,1294 (C=N, C=C), 1149, 1004, 921, 742, 684 3455 cm$^{-1}$; $^1$H NMR (400 MHz,

DMSO) δ 11.11 (s, 2H, NH), 4.15 (s, 2H, CH2), 7.05-7.48 (m, 4H, ArH), 7.5-8.5, (m, 9H, thiazole ArH),6.6 (s, 1H HC=N) $^{13}$C-NMR δ 39.5 (CH2), 145.8 (N-CH-Ar), 171.2 (C=O), 123-154.8 (14 aromatic carbons), 166.7 (S-C-N benz thio), MS (m/z) 460.91 (M$^{+}$); Elemental Analysis: C, 46.97; H, 3.07; Br, 17.36; N, 15.21; O, 10.43; S, 6.97; Found: C 45.7, H 2.82, N 15.46,O 10.18 S 6.58 %.

*(E)-2-(4-methoxybenzylidene)-N-(2-((5-phenyl-1,3,4-oxadiazol-2-yl)thio)acetyl)hydrazinecarbox \amide* **3e** I.R (KBr) (υmax, cm-1): 3192 (N-H), 3082, 2955 (C-H), 1662 (C=O), 1570, 1534, 1522, 1458,1296 (C=N, C=C), 1154, 1006, 924, 740, 684 3454 cm$^{-1}$; $^{1}$H NMR (400 MHz, DMSO) δ 3.71 (s,3H Ar-OCH$_3$) 11.03 (s, 2H, NH), 4.16 (s, 2H, CH2), 7.05-8.45 (m, 9H, ArH), 6.6 (s, 1H HC=N) $^{13}$C-NMR δ 39.5 (CH2), 145.8 (N-CH-Ar), 171.2 (C=O), 123-154.8 (14 aromatic carbons), 55.4 (OCH$_3$), MS (m/z) 411.01 (M$^{+}$); Anal. Elemental Analysis: C, 55.47; H, 4.16; N, 17.02; O, 15.55; S, 7.79: Found: C 53.7, H 4.99, N 17.96,O 14.98 S 7.8 %.

*(E)-2-(4-methylbenzylidene)-N-(2-((5-phenyl-1,3,4-oxadiazol-2-yl)thio)acetyl)hydrazinecarbox amide* **3f** I.R (KBr) (υmax, cm-1): 3190 (N-H), 3082, 2955 (C-H), 1662 (C=O), 1570, 1534, 1522, 1458,1296 (C=N, C=C), 1154, 1006, 924, 740, 684 3454 cm$^{-1}$; $^{1}$H NMR (400 MHz, DMSO) δ 2.51 (s,3H Ar-CH$_3$) 11.05 (s, 2H, NH), 4.15 (s, 2H, CH2), 7.05-8.55 (m, 9H, ArH), 6.6 (s, 1H HC=N) $^{13}$C-NMR δ 39.4 (CH2), 145.6 (N-CH-Ar), 171.2 (C=O), 124-154.4 (14 aromatic carbons), 54.4 (CH$_3$), MS (m/z) 394.02 (M$^{+}$); Elemental Analysis: C, 57.71; H, 4.33; N, 17.71; O, 12.14; S, 8.11% Found: C 56.7, H 4.19, N 17.56,O 11.98 S 8.58 %.

*(E)-2-(3-nitrobenzylidene)-N-(2-((5-phenyl-1,3,4-oxadiazol-2-yl)thio)acetyl)hydrazinecarbox amide* **3g** I.R (KBr) (υmax, cm-1): 3192 (N-H), 3080, 2956 (C-H), 1662 (C=O), 1581, 1539, 1522, 1448,1294 (C=N, C=C), 1149, 1004, 921, 742, 684 3455 cm$^{-1}$; $^{1}$H NMR (400 MHz, DMSO) δ 11.11 (s, 2H, NH), 4.15 (s, 2H, CH2), 7.05-8.48 (m, 9H, ArH), 6.6 (s, 1H HC=N) $^{13}$C-NMR δ 39.5 (CH2), 145.8 (N-CH-Ar), 171.2 (C=O), 123-154.8 (14 aromatic carbons), MS (m/z) 425.97 (M$^{+}$); Elemental Analysis: C, 50.70; H, 3.31; N, 19.71; O, 18.76; S, 7.52 % Found: C 49.2, H 3.12, N 18.76,O 18.38 S 7.48 %.

*(E)-2-(4-hydroxybenzylidene)-N-(2-((5-phenyl-1,3,4-oxadiazol-2-yl)thio)acetyl)hydrazinecarbox amide* **3h** I.R (KBr) (υmax, cm-1): 3198 (N-H), 3088, 2965 (C-H), 1668 (C=O), 1585, 1541, 1522, 1455,1284 (C=N, C=C), 1159, 1004, 925, 742, 685 3456 cm$^{-1}$; $^1$H NMR (400 MHz, DMSO) δ   11.02 (s, 2H, NH), 11.59 (s, 1H, OH), 4.32 (s, 2H, CH2), 7.05-8.38 (m, 9H, ArH), 6.6 (s, 1H HC=N) $^{13}$C-NMR δ 38.5 (CH2), 147.8 (N-CH-Ar), 172.2 (C=O), 123-154.8 (14 aromatic carbons), MS (m/z) 396.99 (M$^+$); Elemental Analysis: C, 54.40; H, 3.80; N, 17.62; O, 16.10; S, 8.07% Found: C 52.7, H 3.62, N 16.51, O 15.42 S 8.58 %

*(E)-2-(2,4-dichlorobenzylidene)-N-(2-((5-phenyl-1,3,4-oxadiazol-2-yl)thio)acetyl)hydrazine carboxamide* **3i** I.R (KBr) (υmax, cm-1): 3192 (N-H), 3088, 2965 (C-H), 1668 (C=O), 1585, 1541, 1522, 1455,1284 (C=N, C=C), 1159, 1004, 925, 742, 685 3456 cm$^{-1}$; $^1$H NMR (400 MHz, DMSO) δ   11.08 (s, 2H, NH), 4.32 (s, 2H, CH2), 7.05-8.28 (m, 8H, ArH), 6.6 (s, 1H HC=N) $^{13}$C-NMR δ 38.7 (CH2), 147.8 (N-CH-Ar), 172.4 (C=O), 123-155.8 (14 aromatic carbons), MS (m/z) 448.88 (M$^+$); Elemental Analysis: C, 48.01; H, 2.91; Cl, 15.75; N, 15.55; O, 10.66; S, 7.12% Found: C 46.5, H 2.32, N 15.76, O 10.22 S 7.58 %

*(E)-N-(2-benzylidenehydrazinecarbonothioyl)-2-((5-phenyl-1,3,4-oxadiazol-2-yl)thio)  acetamide* **3j** I.R (KBr) (υmax, cm-1): 3190 (N-H), 3088, 2964 (C-H), 1666 (C=O), 1220 (C=S), 1587, 1542, 1512, 1456,1284 (C=N, C=C), 1155, 1002, 920, 746, 685 3456 cm$^{-1}$; $^1$H NMR (400 MHz, DMSO) δ 11.04 (s, 2H, NH), 4.26 (s, 2H, CH2), 7.00-8.32 (m, 9H, ArH), 6.4 (s, 1H HC=N) $^{13}$C-NMR δ 38.6 (CH2), 147.4 (N-CH-Ar), 172.4 (C=O), 182.4 (C=S), 123-154.8 (14 aromatic carbons), MS (m/z) 397.01 (M$^+$); Elemental Analysis: C, 54.39; H, 3.80; N, 17.62; O, 8.05; S, 16.13 % Found: C 52.80, H 3.72, N 17.56, O 8.13.4 S 16.88%.

*(E)-N-(2-(4-fluorobenzylidene)hydrazinecarbonothioyl)-2-((5-phenyl-1,3,4-oxadiazol-2-l)thio) acetamide* **3k** I.R (KBr) (υmax, cm-1): 3192 (N-H), 3088, 2965 (C-H), 1668 (C=O), 1222 (C=S), 1585, 1541, 1522, 1455,1284 (C=N, C=C), 1159, 1004, 925, 742, 685 3456 cm$^{-1}$; $^1$H NMR (400 MHz, DMSO) δ 11.10 (s, 2H, NH), 4.32 (s, 2H, CH2), 7.05-8.38 (m, 9H, ArH), ,6.6 (s, 1H HC=N) $^{13}$C-NMR δ 38.5 (CH2), 147.8 (N-CH-Ar), 172.2 (C=O), 181.4 (C=S), 123-154.8 (14 aromatic carbons), MS (m/z) 415.02 (M$^+$); Elemental Analysis: C, 52.04; H, 3.40; F, 4.57; N, 16.86; O, 7.70; S, 15.44% Found: C 53.7, H 3.32, N 16.16, O 8.22 S 15.58 %.

*(E)-N-(2-(4-chlorobenzylidene)hydrazinecarbonothioyl)-2-((5-phenyl-1,3,4-oxadiazol-2yl)thio) acetamide* **3l** I.R (KBr) ($\upsilon$max, cm-1): 3196 (N-H), 3086, 2966 (C-H), 1665 (C=O), 1584, 1542, 1512, 1448,1294 (C=N, C=C), 1159, 1004, 925, 742, 685 3456 cm$^{-1}$; $^{1}$H NMR (400 MHz, DMSO) $\delta$ 11.02 (s, 2H, NH), 4.12 (s, 2H, CH2), 7.05-8.42 (m, 9H, ArH), 6.6 (s, 1H HC=N) $^{13}$C-NMR $\delta$ 39.5 (CH2), 145.8 (N-CH-Ar), 170.2 (C=O), 180.4 (C=S), 123-154.8 (14 aromatic carbons), MS (m/z) 430.98 (M$^{+}$); Elemental Analysis: C, 50.05; H, 3.27; Cl, 8.21; N, 16.21; O, 7.41; S, 14.85% Found: C 48.7, H 3.12, N 16.36,O 7.88 S 14.88 %.

*(E)-N-(2-(4-bromobenzylidene)hydrazinecarbonothioyl)-2-((5-phenyl-1,3,4-oxadiazol-2-yl)thio) acetamide* **3m** I.R (KBr) ($\upsilon$max, cm-1): 3194 (N-H), 3080, 2956 (C-H), 1665 (C=O), 1215 (C=S),1581, 1539, 1522, 1448,1294 (C=N, C=C), 1149, 1004, 921, 742, 684 3455 cm$^{-1}$; $^{1}$H NMR (400 MHz, DMSO) $\delta$ 11.09 (s, 2H, NH), 4.17 (s, 2H, CH2), 7.05-7.48 (m, 9H, ArH), 6.6 (s, 1H HC=N) $^{13}$C-NMR $\delta$ 39.5 (CH2), 145.9 (N-CH-Ar), 171.2 (C=O), 181.4 (C=S), 123-154.8 (14 aromatic carbons), MS (m/z) 476.78 (M$^{+}$); Elemental Analysis: C, 45.38; H, 2.96; Br, 16.77; N, 14.70; O, 6.72; S, 13.46% Found: C 43.7, H 2.82, N 14.46,O 6.48 S 13.68 %.

*(E)-N-(2-(4-methoxybenzylidene)hydrazinecarbonothioyl)-2-((5-phenyl-1,3,4-oxadiazol-2-yl)thio) acetamide* **3n** I.R (KBr) ($\upsilon$max, cm-1): 3192 (N-H), 3082, 2955 (C-H), 1662 (C=O), 1222 (C=S), 1570, 1534, 1522, 1458,1296 (C=N, C=C), 1154, 1006, 924, 740, 684 3454 cm$^{-1}$; $^{1}$H NMR (400 MHz, DMSO) $\delta$ 3.71 (s,3H Ar-OCH$_3$) 11.03 (s, 2H, NH), 4.16 (s, 2H, CH2), 7.05-8.45 (m, 9H, ArH), 6.6 (s, 1H HC=N) $^{13}$C-NMR $\delta$ 39.5 (CH2), 145.8 (N-CH-Ar), 171.2 (C=O), 181.4 (C=S), 123-154.8 (14 aromatic carbons), 55.4 (OCH$_3$), MS (m/z) 427.01 (M$^{+}$); Elemental Analysis: C, 53.38; H, 4.01; N, 16.38; O, 11.23; S, 15.00% Found: C 53.7, H 4.09, N 16.96,O 10.98 S 15.08 %.

*(E)-N-(2-(4-methylbenzylidene)hydrazinecarbonothioyl)-2-((5-phenyl-1,3,4-oxadiazol-2-yl)thio )acetamide* **3o** I.R (KBr) ($\upsilon$max, cm-1): 3198 (N-H), 3082, 2955 (C-H), 1664 (C=O), 1220 (C=S), 1570, 1534, 1522, 1458,1296 (C=N, C=C), 1154, 1006, 924, 740, 684 3454 cm$^{-1}$; $^{1}$H NMR (400 MHz, DMSO) $\delta$ 2.51 (s,3H Ar-CH$_3$) 11.05 (s, 2H, NH), 4.15 (s, 2H, CH2), 7.05-8.65 (m, 4H, ArH),6.6 (s, 1H HC=N) $^{13}$C-NMR $\delta$ 39.4 (CH2), 145.6 (N-CH-Ar), 171.2 (C=O), 180.2 (C=S), 124-154.4 (14 aromatic carbons), 54.4 (CH$_3$), MS (m/z) 411.04 (M$^{+}$); Elemental

Analysis: C, 55.46; H, 4.16; N, 17.02; O, 7.78; S, 15.58% Found: C 53.7, H 4.09, N 17.01,O 7.98 S 14.08 %.

*(E)-N-(2-(4-nitrobenzylidene)hydrazinecarbonothioyl)-2-((5-phenyl-1,3,4-oxadiazol-2-yl)thio)*
*acetamide* **3p**I.R (KBr) (υmax, cm-1): 3192 (N-H), 3080, 2956 (C-H), 1662 (C=O), 1224 (C=S), 1581, 1539, 1522, 1448,1294 (C=N, C=C), 1149, 1004, 921, 742, 684 3455 cm$^{-1}$; $^1$H NMR (400 MHz, DMSO) δ 11.11 (s, 2H, NH), 4.15 (s, 2H, CH2), 7.05-8.48 (m, 9H, ArH), 6.6 (s, 1H HC=N) $^{13}$C-NMR δ 39.5 (CH2), 145.8 (N-CH-Ar), 171.2 (C=O), 181.5 (C=S), 123-154.8 (14 aromatic carbons), MS (m/z) 442.03 (M$^+$); Elemental Analysis: C, 48.86; H, 3.19; N, 18.99; O, 14.46; S, 14.49 % Found: C 47.2, H 3.12, N 18.26,O 14.18 S 14.28 %.

*(E)-N-(2-(4-hydroxybenzylidene)hydrazinecarbonothioyl)-2-((5-phenyl-1,3,4-oxadiazol-2-yl)thio)*
*acetamide* **3q** I.R (KBr) (υmax, cm-1): 3198 (N-H), 3088, 2965 (C-H), 1668 (C=O), 1221 (C=S), 1585, 1541, 1522, 1455,1284 (C=N, C=C), 1159, 1004, 925, 742, 685 3456 cm$^{-1}$; $^1$H NMR (400 MHz, DMSO) δ 11.02 (s, 2H, NH), 11.59 (s, 1H, OH), 4.32 (s, 2H, CH2), 7.05-8.38 (m, 9H, ArH), 6.6 (s, 1H HC=N) $^{13}$C-NMR δ 38.5 (CH2), 147.8 (N-CH-Ar), 172.2 (C=O), 180.5 (C=S), 123-154.8 (14 aromatic carbons), MS (m/z) 413.05 (M$^+$); Elemental Analysis: C, 52.29; H, 3.66; N, 16.94; O, 11.61; S, 15.51 % Found: C 50.7, H 3.62, N 16.01, O 10.92 S 15.98 %

*(E)-N-(2-(3,5-dichlorobenzylidene)hydrazinecarbonothioyl)-2-((5-phenyl-1,3,4-oxadiazol-2-yl)*
*thio)acetamide* **3r** I.R (KBr) (υmax, cm-1): 3192 (N-H), 3088, 2965 (C-H), 1668 (C=O), 1210 (C=S), 1585, 1541, 1522, 1455,1284 (C=N, C=C), 1159, 1004, 925, 742, 685 3456 cm$^{-1}$; $^1$H NMR (400 MHz, DMSO) δ 11.08 (s, 2H, NH), 4.32 (s, 2H, CH2), 7.05-8.28 (m, 8H, ArH), 6.6 (s, 1H HC=N) $^{13}$C-NMR δ 38.7 (CH2), 147.8 (N-CH-Ar), 172.4 (C=O), 180.1 (C=S), 123-155.8 (14 aromatic carbons), MS (m/z) 464.90 (M$^+$); Elemental Analysis: C, 46.36; H, 2.81; Cl, 15.20; N, 15.02; O, 6.86 ; S, 13.75 % Found: C 44.81, H 2.62, N 15.36, O 6.52 S 13.18 %

**Conclusion**

In this study, analogues of 5-phenyl-1,3,4-oxadiazole-2-thiol bearing Thiosemicarbazide and 5-phenyl-1,3,4-oxadiazole-2-thiol bearing Semicarbazide have been designed , synthesized and

characterized. All the compounds evaluated for their antimicrobial study against gram positive, gram negative bacteria and fungi. The microbial screening data revealed that compounds **3i** and **3c** have highest inhibition zone diameter while **3q, 3d** and **3h** have no antifungal effect. Compounds **3c, 3d, 3f, 3h, 3k, 3l, 3n, 3p** and **3q** were completely inactive against *Aspergillus fumigates*.

## Acknowledgement

## References

[1]. M. Afroz, M. S. Yar, S. G. Abdel-hamid, S. I. Al, and A. Samad, "European Journal of Medicinal Chemistry Molecular properties prediction , synthesis and antimicrobial activity of some newer oxadiazole derivatives," *Eur. J. Med. Chem.*, vol. 45, no. 12, pp. 5862–5869, 2010.

[2]. S. Ningaiah, U. K. Bhadraiah, S. D. Doddaramappa, S. Keshavamurthy, and C. Javarasetty, "Novel pyrazole integrated 1,3,4-oxadiazoles: Synthesis, characterization and antimicrobial evaluation," *Bioorg. Med. Chem. Lett.*, 2013.

[3]. M. Farooqui, R. Bora, and C. R. Patil, "Synthesis , analgesic and anti-inflammatory activities of novel," *Eur. J. Med. Chem.*, vol. 44, no. 2, pp. 794–799, 2009.

[4]. S. Yavuz *et al.*, "Synthesis and Pharmacological Evaluation of Some Novel Thebaine Derivatives: N-(Tetrazol-1H-5-yl)-6, 14-endoethenotetrahydrothebaine Incorporating the 1, 3, 4-Oxadiazole or the 1, 3, 4-Thiadiazole Moiety," *Arch. Pharm. (Weinheim).*, vol. 346, no. 6, pp. 455–462, 2013.

[5]. S. Valente *et al.*, "1,3,4-Oxadiazole-Containing Histone Deacetylase Inhibitors: Anticancer Activities in Cancer Cells," pp. 1–7, 2014.

[6]. M. Zareef *et al.*, "Synthesis and antimalarial activity of novel chiral and achiral benzenesulfonamides bearing 1, 3, 4-oxadiazole moieties," *J. Enzyme Inhib. Med. Chem.*, vol. 22, no. 3, pp. 301–308, 2007.

**[7].** K. A. Ali, E. A. Ragab, T. A. Farghaly, and M. M. Abdalla, "Synthesis of new functionalized 3 subsitituted [1, 2, 4] triazolo [4, 3-a] pyrimidine dreivatives: Potential antihypertensive agents," *Acta Pol. Pharm*, vol. 68, no. 2, pp. 237–247, 2011.

**[8].** T. Kampmann *et al.*, "In silico screening of small molecule libraries using the dengue virus envelope E protein has identified compounds with antiviral activity against multiple flaviviruses," *Antiviral Res.*, vol. 84, no. 3, pp. 234–241, 2009.

**[9].** Shi L, Ge H, Tan S, et al. Synthesis and antimicrobial activities of Schiff bases derived from 5-chloro-salicylaldehyde. Eur J Med Chem. 2007;42:558–564

**[10].** Sinha D, Tiwari A, Singh S, et al. Synthesis, characterization and biological activity of Schiff base analogues of indole-3-carboxaldehyde. Eur J Med Chem. 2008;43:160–165

**[11].** Karthikeyan MS, Prasad DJ, Poojary B, Bhat KS, Holla BS, Kumari NS. Synthesis and biological activity of Schiff and Mannich bases bearing 2,4-dichloro-5-fluorophenyl moiety. Bioorg Med Chem. 2006;14:7482–7489

**[12].** Patole J, Shingnapurkar D, Padhyea S, Ratledge C. Schiff base conjugates of paminosalicylic acid as antimycobacterial agents. Bioorg Med Chem Lett. 2006;16:15 14–1517

**[13].** Vicini P, Geronikaki A, Incerti M, et al. Synthesis and biological evaluation of benzo[d]isothiazole, benzothiazole and thiazole Schiff bases. Bioorg Med Chem. 2003;11:4785–4789

**[14].** Ren S, Wang R, Komatsu K, et al. Synthesis, biological evaluation and quantitative structure-activity relationship analysis of new Schiff Bases of hydroxysemicarbazide as potential antitumor agents. J Med Chem. 2002;45:410–419.

**[15].** Bhandari SV, Bothara KG, Raut MK, Patil AA, Sarkate AP, Mokale VJ. Design, synthesis and evaluation of antiinflammatory, analgesic and ulcerogenicity studies of novel S-substituted phenacyl-1,3,4-oxadiazole-2-thiol and Schiff bases of diclofenac acid as nonulcerogenic derivatives. Bioorg Med Chem. 2008;16:1822–1831

**[16].** Sridhar SK, Pandeya SN, Stables JP, Ramesh A. Anticonvulsant activity of hydrazones, Schiff and Mannich bases of isatin derivatives. Eur J Pharm Sci. 2002;16:129–132.

**[17].** Kaplan JP, Raizon BM. New anticonvulsants: Schiff Bases of g-aminobutyric acid and g-aminobutyramide. J Med Chem. 1980;23:702–704.

# Silicon Oxide Based InterfaceLayer Coating on Carbon Fibers by Dip Coating Process for Carbon Fiber Reinforced Silicon Carbide Composites

## Harsh Vyas[a,b], C. Jariwala[a*]

a Institute for Plasma Research, GIDC Electronics Estate, Sector-25, Gandhinagar, INDIA

b Department of Metallurgical and Material Engineering, Government Engineering College, Sector-28, Gandhinagar,  INDIA.

* *Corresponding author e-mail*: chetan@ipr.res.in&chetanjari@yahoo.com

**Abstract**

Carbon fibres-reinforced ceramic matrix composites are promising candidate materials for high-temperatureapplications in many technological challenging areas such as aerospace and nuclear reactor industries. In oxidizing environments at temperatures above 400°C, however, carbon fibres are rapidly oxidized. Therefore, a need to coat carbon fibres is essential for carbon fibre-reinforced composite in order to protect it against oxidation [1-3]. In this present work, we investigated an effect of Silicon Oxide ($SiO_2$) interface layer coating on Carbon fibers deposited by dip coating method. Prior to dip coating, Carbon fiberswere thoroughly cleaned for removal of surface contamination and sizing. Carbon fiberswere dipped into coating precursor solution prepared from tetraethyl orthosilicate [$Si(OC_2H_5)_4$] for different dipping cycles & dipping time duration, followed by standard heat-treatment. Scanning Electron Microscopic surface analysis confirmed uniformity & consistency of $SiO_2$ coating on carbon fibers surface. Energy Dispersive X-ray spectrum obtained for $SiO_2$ dip coated layer on carbon fibers shows the presence of Si element in the form of $SiO_2$ in dip-coated carbon fibers, whereas tensile testing prove the enhancement of tensile strength of $SiO_2$ coated carbon fibers as compared to un-coated carbon fibers.

**IndexTerms —$C_f$/SiC composites, $SiO_2$ Interface layer coating, Dip Coating process, Scanning Electron Microscopy (SEM), Energy Dispersive X-ray (EDX) Analysis, Tensile Testing.**

## Introduction

Carbon fibers ($C_f$) reinforced silicon carbide (SiC) matrix ($C_f$/SiC) composites consisting of reinforcing $C_f$ embedded in a SiC matrix are widely used in high temperature applications due to their outstanding properties such as high thermal and mechanical strength, low density, radiation tolerance, chemical stability and stiffness compared to the conventional materials like metals and alloys[3-6]. At high temperature, the interface between $C_f$andSiC matrix degrades and starts oxidizing exposed $C_f$surface [2-5]. Hence, the role of the interface layer coating is to allow de-bonding between $C_f$and SiC matrix during deformation and to increase fracture toughness, and also to prevent oxidation of $C_f$[7-11]. Here, interface layer permits the adjustment of the difference in thermo-mechanical properties between the fibers and matrix. Without an interface, $C_f$/SiC composites behave as brittle materials in the same manner as monolithic ceramics [12-15].

In this present work, we investigated an effect of $SiO_2$ interface layer coating by dip coating method on $C_f$. Prior to dip coating, $C_f$were thoroughly cleaned in an acetone for removal of dust particles, other surface contaminations and sizing. $C_f$were dipped into coating precursor solution for different dipping cycles & dipping time duration, followed by drying up to 200˚C after each dipping cycle & then finally heat-treated at 500˚C temperature. The detail characterization of dip coated $C_f$ were performed using SEM, EDX and tensile testing for surface analysis, composition analysis and strength measurement, respectively.

## EXPERIMENTAL

The detail procedure for $SiO_2$ coating on $C_f$ and their characterization are mention in flow chart as shown in fig.1. The coating solution was prepared by dissolving tetraethyl orthosilicate into 2-propanol. The home-made dip coating system is shown schematic in fig.2 used for preset study. The de-sized & cleaned $C_f$ -tows of 60mm (long) sizes were gripped into the stain-less steel fiber holder for dip coating. $C_f$ along with stain less steel holder were dipped into the coating solution for $SiO_2$ coating on $C_f$. The $C_{f\_}$ tows were dipped into the coating precursor for 3, 5, 7, 9, 11, 13 &15 (no.) dipping cycles & for 5minutes (constant) dipping time duration. Each dipping cycles were include the step of dipping of carbon fibers into the coating precursor, pull-out of carbon fibers from the coating precursor, drying of fibers using IR-heater and also cooling of the carbon fibers at room temperature for few minutes.  The fibers were dipped and pull out at fixed rate of 3cm.m$^{-1}$ from the coating precursor. Carbon fibers were dried up to 200°C after pull out from the

coating solution using IR-heater and finally heat-treated/sintered at 500˚C in an inert atmosphere for 60 minutes for densification & strong bonding of $SiO_2$ coating with carbon fibers in vacuum furnace. The detail dip coating parameters were mentioned in table-1. The surface morphology analyses of coated-Cf were performed using SEM (440i, LEO make, UK) and EDX were used for chemical composition investigation. The Instron Tensile Tester (Model 4411) was used to measure tensile strength of $SiO_2$ coated –$C_f$ with different process parameters.
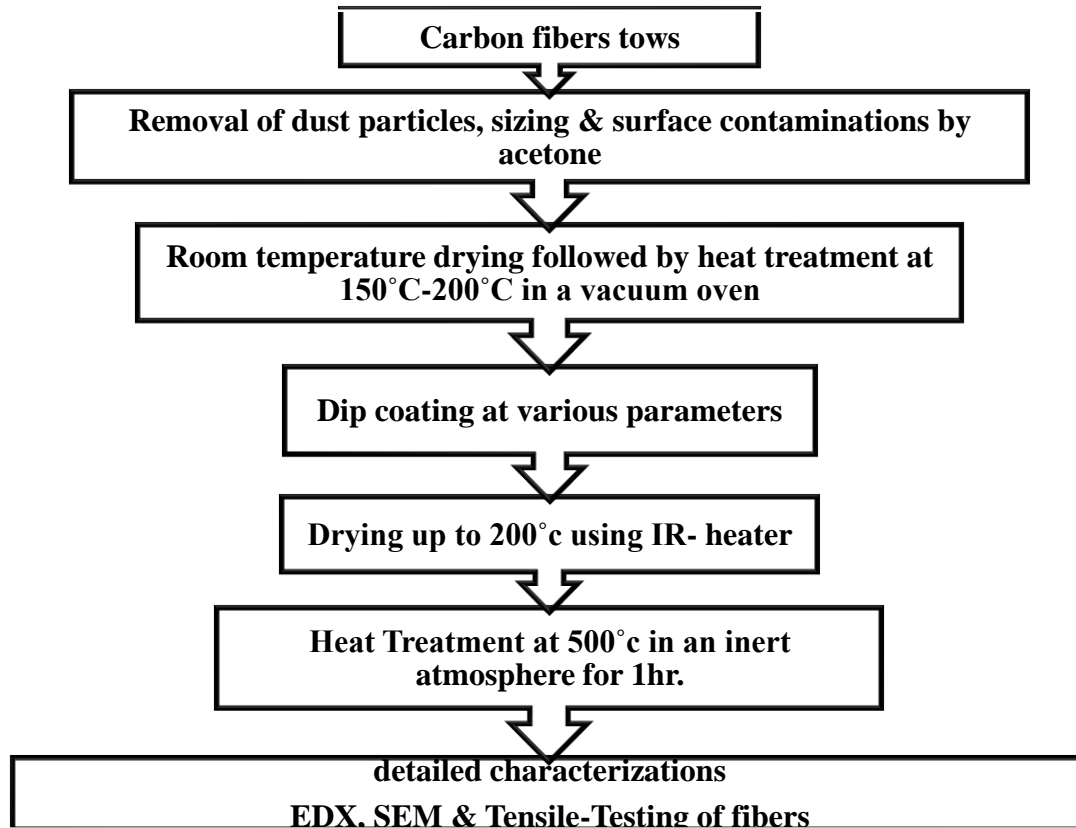


*Fig.1: Process flow chart for dip coating process*

**TABLE I**

| Table: Process parameters for dip coating | |
| --- | --- |
| **Temperature of the-bath during dip-coating** | **Room-temperature(25-30˚c)** |
| **Pull out rate** | **3 cm.m$^{-1}$** |
| **Dipping time** | **5 minutes.** |
| **Dipping cycles (no.)** | **3, 5, 7, 9, 11, 13 & 15 dipping cycles** |

| Drying temperature for carbon fibers after pull-out from the coating solution | 100-200°c |
| --- | --- |
| Drying time | 2-5 minutes |
| Sintering/heat-treatment- temp. | 500°c ( in an inert atmosphere) |
| Sintering/heat-treatment time | 1hr. |



*Fig. 2: Homemade Dip Coating Assembly*

## Results & Discussion

### I. Energy Dispersive X-ray (EDX) analysis:

In order to determine the chemical composition of $SiO_2$ dip-coated $C_f$, EDX analysis of all dip-coated carbon fibers were carried out by using EDX analyzer connected to SEM.
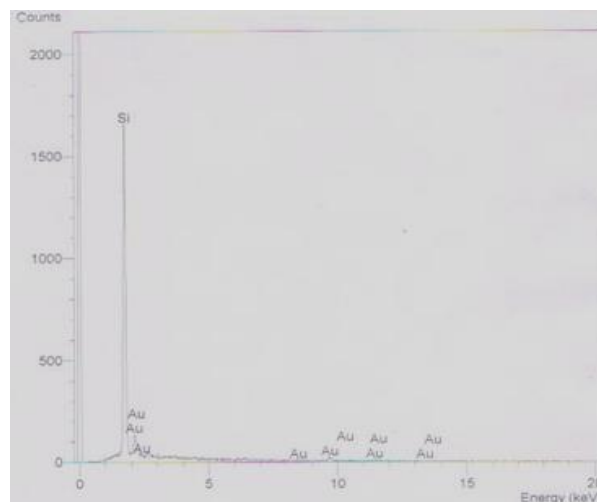


*Fig. 3: EDX spectrum of SiO₂ dip coated film on un-treated carbon fibers*

A typical EDX spectrum obtained for 5 (no.) dipping cycles coated $SiO_2$ dip coated film on untreated carbon fibers is shown in figure 3, confirms the presence & consistency of Si element in the form of $SiO_2$ in all dip-coated carbon fibers.

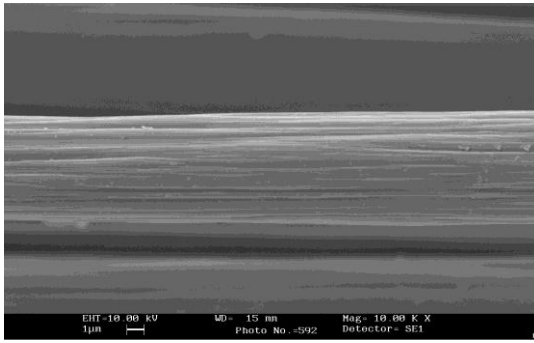## II.    Scanning Electron Microscopy (SEM) – Analysis:



Fig. 4 Typical SEM monograph at 10KX shows the surface morphology of Carbon fiber single filament, which confirms the presence of ridges on surface of the $C_f$.
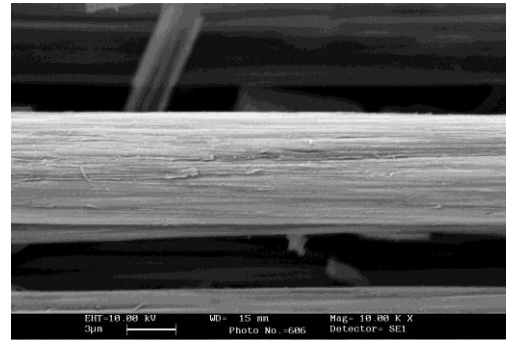
Fig. 5 Typical monograph of SEM at 10KX shows the surface morphology of 3dipping cycles coated Carbon fiber single filament



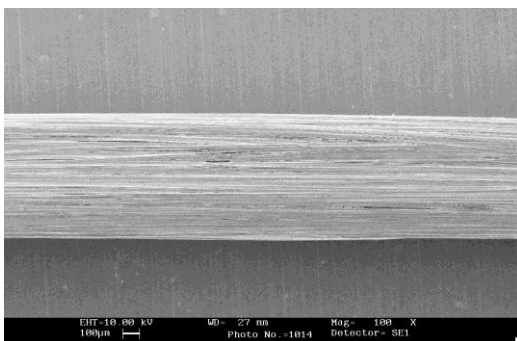Fig. 6  Typical monograph of SEM at 100X shows the surface morphology of 3 dipping cycles coated Carbon fiber tow (similar SEM monographs were obtained for 3, 5, 7 & 9 dipping cycles coated carbon fibers)
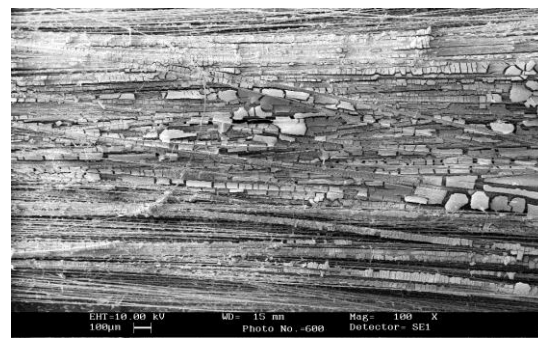
Fig. 7 Typical monograph of SEM at 100X shows the surface morphology of 11 dipping cycles coated Carbon fiber tow (A similar monograph of SEM obtained for 11, 13 & 15 dipping cycles coated carbon fibers).

The SEM-image of as received carbon fiber-single filament (after de-sizing & cleaning) at 10KX shows the carbon fiber's surface has parallel aligned grooves and ridges along the fiber axis (fig.4). Whereas, the SEM-image of 3 (no.)-dipping cycles coated carbon fiber at 10KX shows the consistency & uniformity of the coating on to the surface of the carbon fiber-single filament (fig. 5).

The SEM-monograph for 3, 5, 7 & 9 (no.) dipping cycles coated carbon fibers-tows shows the consistency & uniformity of the coating on to the surfaces of the carbon fibers-tows (Fig. 6). Whereas The SEM-monograph of   11, 13 & 15 (no.) dipping cycles coated carbon fibers-tows shows the pilling off of the coating from the surfaces of the carbon fibers-tows (Fig.7). Here, during the pilling off of the coating from the surfaces of the carbon fibers-tows, some bunch of the carbon fiber-filaments could also peel out with the coating. So, the weight of the 11, 13 & 15 (no.) dipping cycles coated (untreated) carbon fibers-tows was suddenly decreased as compared to the weight of as received carbon fibers-tow.

## III.    Tensile – Testing:

Tensile-Testing of all coated & uncoated carbon fibers was carried out by using Instron Tensile-Tester (Model 4411) for determining the tensile properties of coated & uncoated carbon fibers. Table -2 shows the typical tensile testing parameters used for measurement of tensile strength of coated $C_f$.

*Table: 2*

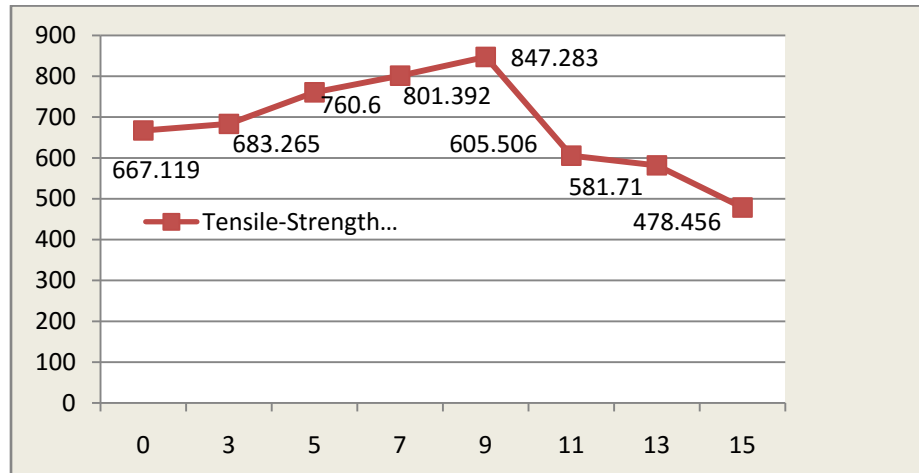| Table: Tensile Testing parameters | |
|---|---|
| General: Method description | ASTM D 2256 |
| Dimension: Final Length | 25.00mm |
| Dimension: Final Width | 50.00mm |
| Dimension: Geometry | Rectangular |
| Test: Control mode 1 | Extension |
| Speed | 2mm/min |

*Fig.8 Tensile-Strength (N/mm$^2$) Vs Dipping Cycles (number) for C$_f$coated with SiO₂ by Dip Coating Process*

Fig.8 shows the Tensile Strength vs. Dipping Cycles graph. Here, the coating improves the strength of the Carbon fibers up to 9 no. of dipping cycles. The tensile strength of Carbon Fiber with 3, 5, 7 & 9 no. of dipping cycles coating increases from 667.119N/mm$^2$ to 847.283N/mm$^2$ which confirms the enhancement of Tensile-Strength in respect to dipping cycles (Fig.7). Whereas, tensile strength of 11, 13 & 15 dipping cycles coated carbon fibers decreases from 847.283N/mm$^2$ to 478.456N/mm$^2$ due to the pilling off of the coating from surfaces of the coated carbon fiber tows (Fig.7).

**Conclusion:**

In present study, Silicon Oxide (SiO₂) interface layer coating on Carbon fibers deposited by dip coating method. The effects of dipping cycles with fixed dipping time have been attempted in detail for interface layer application on carbon fibers.  EDX spectrum obtained for SiO₂ dip coated film on carbon fibers confirms the presence of Si element in the form of SiO₂ in dip-coated carbon fibers. SEM monographs obtained for 3, 5, 7 & 9 no. of dipping cycles coated carbon fibers confirms the uniformity & consistency of coating on surface of the C$_f$. Whereas, SEM images obtained for 11, 13 & 15 no. of dipping cycles coated carbon fibers shows the pilling off of coating on surface of the carbon fiber tow. Tensile Strength of as received C$_f$, 3, 5, 7 & 9 dipping cycles coated Carbon fibers increases from 667.119N/mm$^2$ to 847.283N/mm$^2$ which confirms the enhancement of Tensile-Strength with respect to dipping cycles whereas, tensile strength of 11, 13 & 15 dipping cycles coated carbon fibers decreases from

847.283N/mm$^2$ to 478.456N/mm$^2$ due to the pilling off of the coating on surface of the coated carbon fibers tows as seen by SEM analysis.

**References:**

[1] Bin Li, Yi Feng, Gang Quian, Jingcheng Zhang, ZhongZhuang, &Xianping Wang, "The effect of gamma ray irradiation on PAN-based intermediate modulus carbon fibers", Journal of nuclear materials 443 (2013) 26-31.

[2] P. C. Kang, G. Q. Chen, B. Zhang, G. H. Wu, S. Mula, & C. C. Koch, "Oxidation protection of carbon fibers by a reaction sintered nanostructured SiC coating", Surface & coating technology 206 (2011) 305-311.

[3] Yunzhou Zhu, Zhengren Huang, Shaoming Dong, Ming Yuan &Dongliang Jiang, "Manufacturing 2D carbon-fiber-reinforced SiC matrix composites by slurry infiltration & PIP process", Ceramics International 34 (2008), pp1201-1205.

[4] S. P. Lee, K. S. Cho, H. U. Lee, J. K. Lee, D. S. Bae, & J.H. Byun, "Microsture& Mechanical property of SiC/SiC&C$_f$ / SiC composites", IOP Conf. Series: Materials science & engineering 18 (2011) 162017.

[5] W. Krenkel&F. Berndt, "C/SiC composites for space applications and advanced friction systems", Materials Science and Engineering A 412, July 2005, pp 177–181.

[6] Laifei Cheng, YongdongXu, Litong Zhang, &Xiaowei Yin, "Oxidation behavior of three dimensional C/SiC composites in air and combustion gas environments", Carbon 38 2000, pp 2103–2108.

[7] Jeanne Petko, J. Douglas. Kisser, Terry. McCue & Michael Verrilli, "Characterizations of C/SiC ceramic matrix composites with novel fiber coatings", 26th annual conference on composites, materials, & structures cape Canaveral, Jan 28-31, 2002.

[8] N. Igawa, T. Taguchi, R. Yamada, Y. Ishii, S. Jitsukawa, "Mechanical properties of SiC/SiC composite with magnesium-silicon oxide interphase", Journal of nuclear materials (J. Nucl. Mater.), 367-370 (2007) 725-729.

[9] N. Igawa, T. Taguchi, R. Yamada, Y. Ishii, S. Jitsukawa, "Preperation of silicon-based oxide layer on high-crystalline SiC fiber as an interphase in SiC/SiC composites", of nuclear materials (J. Nucl. Mater.), 329-333 (2004) 554-557.

[10] T. Taguchi, N. Igawa, R. Yamada, M. Futakawa, S. Jitsukawa, Ceram. Eng. Sci. Proc. 22A (2000) 533.

[11] T. Taguchi, T. Nozawa, N. Igawa, Y. Katoh, S. Jitsukawa, A. Kohyama, T. Hinoki, L. L. Snead, J. Nucl. Mater.329-333(2004)572.

[12] H. Y. Zhu, Y. C. Zhang, H. Y. Wu, Y. P. Qui," Nano effect of oxygen-plasma Treatment nano-SiO2 sol-gel coating T-300 carbon-fiber", Materials Science Forum, 2009,  pp.706-713.

[13] F. Lamouroux, S. Bertrand, R. Pailler, R. Naslain, M. Cataldi, "Oxidation-resistant carbon-fiber-reinforced ceramic-matrix composites", Composites science and technology 59 (1999) 1073-1085

[14] L. Liu, Y. J. Song, H. J. Fu, Z. X. Jiang, X. Z. Zhang, L. N. Wu, Y. D. Huang, "The effect of interphase modification on carbon fiber/polyarylacetylene resin composites", Applied surface science 254 (2008) 5342-5347.

[15] R. M. Rocha, C. A. A. Cairo, M. L. A. Graca (2006). "Formation of carbon fiber-reinforced ceramic matrix composites with ploysiloxane/silicon derived matrix". Materials Science and Engineering, Part A 437, 2006, pp 268–273.

# Formulation and characterization of lipid nanoparticles: appraise its anti-inflammatory property with therapeutic drugs

Vaishwik J. Patel[1*], Niket S. Powar[1], Vikram N. Panchal[1•]

[1]School of Engineering and Applied Science1: Ahmedabad University, GICT Building, Central Campus,Navrangapura Ahmedabad, 380009, Gujarat, India.
[1•]Sheth M.N. Science College, HNGU, Patan, Gujarat, India.

1* Correspondence: Vaishwik Patel, Email: vaishwiksmile@gmail.com

**Abstract:**

Inflammation is one of the defensive responses of the body that reduce initial cause of injury. Chronic inflammation, type of the inflammation which in uncontrolled manner leads to hay fever, periodontitis, atherosclerosis, rheumatoid arthritis, and cancer. Study is an orchestrated attempt to formulate and characterized lipid based drugs delivery vehicle, liposomes designed for sustained and controlled delivery of methotrexate (MTX) and aceclofeanc (Ace). Inflammation was induced in breast cancer cells by LPS treatment for *in-vitro* estimation was characterized by pro-inflammatory cytokines such as TNF-α, IL-6 and IL-1β[8][11]. Anti-inflammatory drugs including MTX and Ace have great efficiency towards inflammation but also have limitations such as, shorter half-life, lack of target specificity, bio-distribution in kidney, liver and other organs and toxicity rendered to healthy cells to refrain their use. Liposomes have been invented due to lower toxicity, bio-compatibility and capability to deliver both hydrophilic and lipophilic drug. This study was aimed at formulation of drug entrapped liposome by thin film hydration method and characterized formulated liposomes by various methods. MTT assay were performed to calculate IC50. The levels of pro-inflammatory cytokines were estimated to observe sustained and controlled release of MTX and Ace via liposomes and open new vistas to address inflammatory diseases.

**Introduction:**

Inflammation is one of the defensive responses of the body that involvesvarious molecules or mediators to fight against pathogens. It is characterized by five prime signs, namely redness, swelling, heat, pain and loss of function [22].The protective inflammatory responses are normally induced and remain for short duration; however, during the pathogenic attack inflammatory responses last-longer to activate the defense system [18]. Inflammation is categorized as; 1) Acute inflammation, 2) Chronic inflammation. The acute inflammation initiated by infection or tissue injury, transport of blood components (plasma and leukocytes) to the site of infection or injury[1]. Infection is firstly recognized by tissue resident macrophages and mast cells, which involves in production of various inflammatory mediators[1][13][14]. The neutrophils kill the invaders by

releasing the toxic contents which are specific enough to differentiate microbial and host molecules [13]. The immunological balance between pro-and anti- inflammatory molecule is crucial for the resolution of inflammation and thereby infection [17]. The inability of macrophages to engulf and destroy pathogens or foreign bodies may initiate the synthesis of granulomas [12], full of lysosomes. Prolonged synthesis of reactive molecules, injured healthy cells and activated immune cells lead to various cytokine production reduce the normal tissue function [5], resulting into various pathologies. Whereas chronic inflammation mostly leads to the autoimmune diseases like rheumatoid arthritis, psoriasis, pernicious anemia, vitiligo, scleroderma, inflammatory bowel disease, type-2 diabetes etc.have been reportedly established. Higher production pro-inflammatory cytokines play an instrumental role in pathogenesis of disease [15].
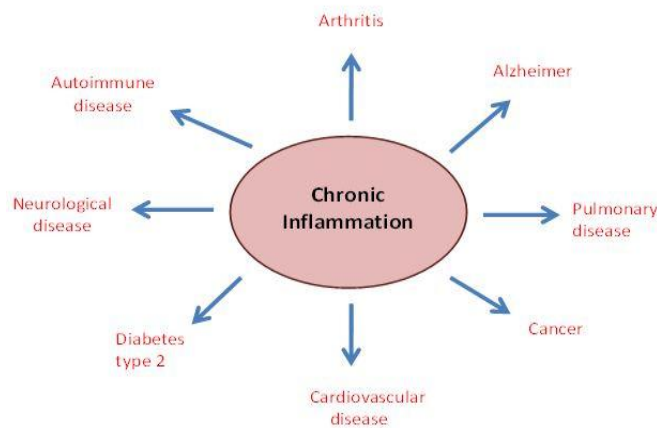


**Figure I** Schema of chronic inflammation & associated diseases

Pro-inflammatory cytokines are secreted by various immune cells including synovial macrophages, B cells, fibrocytes, synoviocytes, CD4 and CD8 positive T cells present at inflammation sites and can be detected by synoviumimmunohistochemistry[10].



**Figure II:** Pro-inflammatory cytokines involved in inflammatory diseases

Various types of Non-Steroidal Anti-Inflammatory Drugs (NSAIDs), corticosteroids, and Disease Modifying Anti-Rheumatic Drugs DMARDs) have been used for treatment of chronic

inflammation associated diseases[16]. NSAIDs areused only to provide symptomatic relief by inhibiting cyclooxygenase (COX) enzymes. The inhibition of COX activity by NSAID leads to the reduction in pain and inflammation[19].
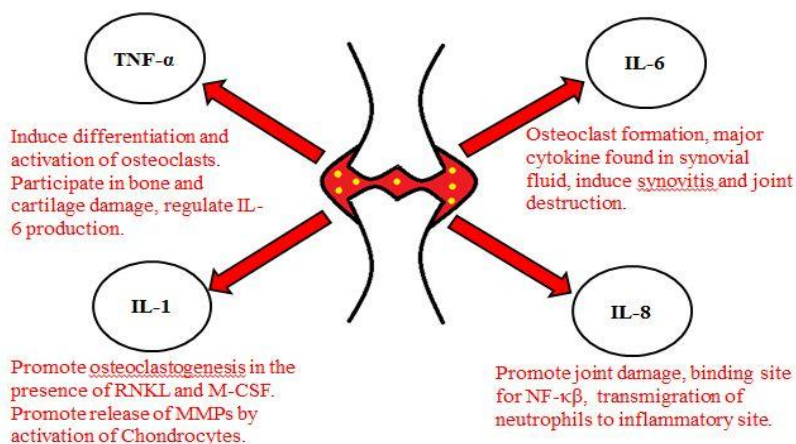
Aceclofenac and its metabolic product (4`-hydroxydiclofenac) reduces IL-1&TNF-alpha by penetrates monocytes/macrophages to suppress inflammation but it cause gastrointestinal complications, dyspepsia, heartburn, anorexia, abdominal pain, nausea, flatulence, diarrhea, and peptic ulcers at higher doses [9].
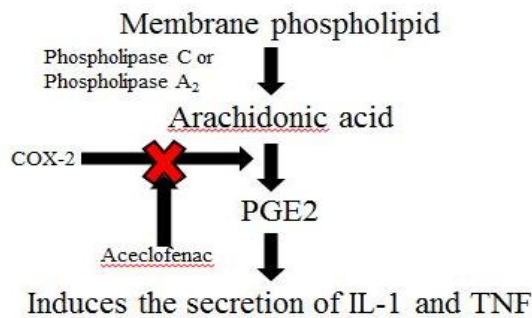


**Figure III**: Mechanism of action of aceclofenac

Like NSAIDs, DMARDs like methotrexate (MTX) are widely used for the treatment inflammatory diseases. Methotrexate (MTX) majorly used DMRDs, inhibits dihydrofolatereductase involved in de novo synthetic pathway of purine and pyrimidine, intermediates of DNA and RNA. Tetrahydrofolate plays a crucial role in methylation of DNA, RNA proteins.
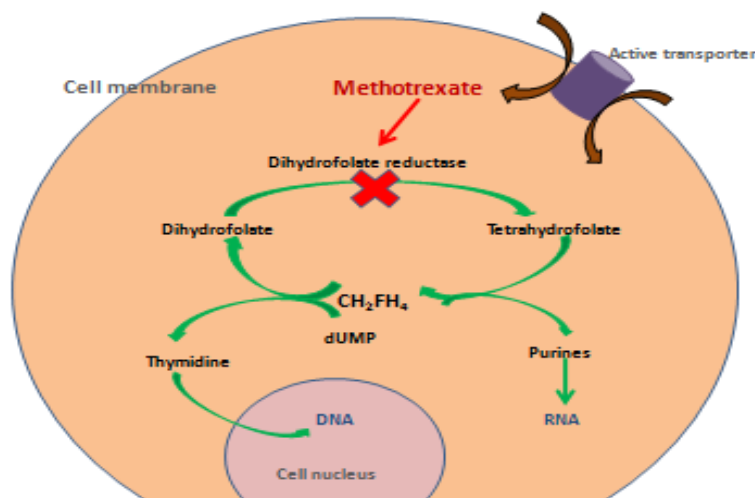


**Figure IV:** Mechanism of action of Methotrexate

MTX at lower concentration act as anti-inflammatory drug than anti-proliferative (immunosuppressive) drug[2][4]. MTX are reported to be effective against RA but oftentimes doses of DMARDs are associated with diseases such as digestive organ dysfunction such as liver, kidney, stomatitis, depilation and myelo-suppression [9].Eventhough the half-lifeof MTX and Aceis short, 0.7-5.8 hour and 4 hoursrespectively.Hence need of drug delivery vehicle is necessary for the targeted and sustained release of drug.Various drug delivery carriers are introduced such as lipid and polymer based nanocarriers, micelles, liposomes, nanoparticles, neosome etc.

Liposomes are attributable to bio-compatible, less immunogenic; moreover the potential to deliver lipophilic and hydrophilic drugs for sustained drug release and rendering less toxicity to healthy cells as compare with other nanocarriers [21][3].Various types of liposome are used for delivery of therapeutic drugs such as conventional liposomes, pH-sensitive liposomes, cationic liposomes, immune-liposomes and long-circulating liposomes [5].Conventional liposome for the delivery of MTX and Ace is formulated with varying concentration of soya-phosphatidyl choline (soya PC) and Cholesterol (chol) and maintains the same drug concentration.Breast cancer cell line MDA-MB 468 was used to assess the *in-vitro* analysis of anti-infammatory effect of plain drug and drug loaded liposomes. For mimic inflammation in cell line, Lipopolysaccharide (LPS) isolated from bacterial cell wall was given to cell line for *in-vitro* estimation of inflammation. Inflammation was characterized by pro-inflammatory cytokines like interleukin-6 (IL-6) and tumor necrosis factor-$\alpha$ (TNF-$\alpha$). Elisa assay for determination of pro-inflammatory cytokines by kit-based method was for the comparison between naked and liposomal drug delivery. The target specificity and sustained delivery of drug(s) is the prominent issue and should be objectively addressed to develop therapeutic interventions against various inflammatory diseases.

## Synthesis of liposomes

**Materials:** Methotrexate and aceclofenac, Cholesterol, Methanol and Soya phosphatidyl choline were purchased from sigma-aldrich. Chloroform was purchased from Merk,Phosphate-bufferedsaline(PBS),3-(4,5-dimethylthiazol-2-yl)-2,5-diphenyltetrazolium bromide (MTT) and DMEM high glucose media purchased from Hi-media, 96- well flat bottom plate, Rotevarotary evaporator, Branson probe-sonicator, Malvern Zetasizer (nano ZS), UV spectrometer (Perkin Elmer, Lambda 365), TEM (JEOL 1400).

## Method:

Three Different concentration of lipids and cholesterol were dissolved in organic solvent, organic phase removed by rotary evaporator. Obtained film was hydrated by the PBS. The Liposomal suspension was sonicated (Probe sonicator) to get unilamelar vesicles from multilamelar vesicles.Liposomal suspension was then determined using zetasizer for size, zeta potential and polydispersity whereas TEM analysis was also done for its size and shapes. For TEM analysis liposome suspension was dropped on carbon coated copper grid and placed overnight for drying.Drug entrapment efficiency was calculated by the centrifugation of liposome suspension at 17000rpm for 1 hr[7]. The supernatant wastransferred in another tube and pallet containing the liposome is disintegrated using triton-X. The absorbance of supernatant and pelletwere measured using UV spectrophotometer at 275nm for aceclofenac and 300nm for methotrexate.MDA-MB-

468, triple negative breast cancer cell line was cultivated in DMEM high glucose medium. IC50 assay was performed for determining of inhibitory concentration of MTX and Ace drug. For in-vitro analysis of anti-inflammatory activity cell-line was inflamed by using lipopolysaccharide after 24 hours cell were treated with plain and drug loaded liposomes anti-inflammatory activity was checked after 24 hours post treatment by cytokine ELISA kit.

**Results & Discussion:**
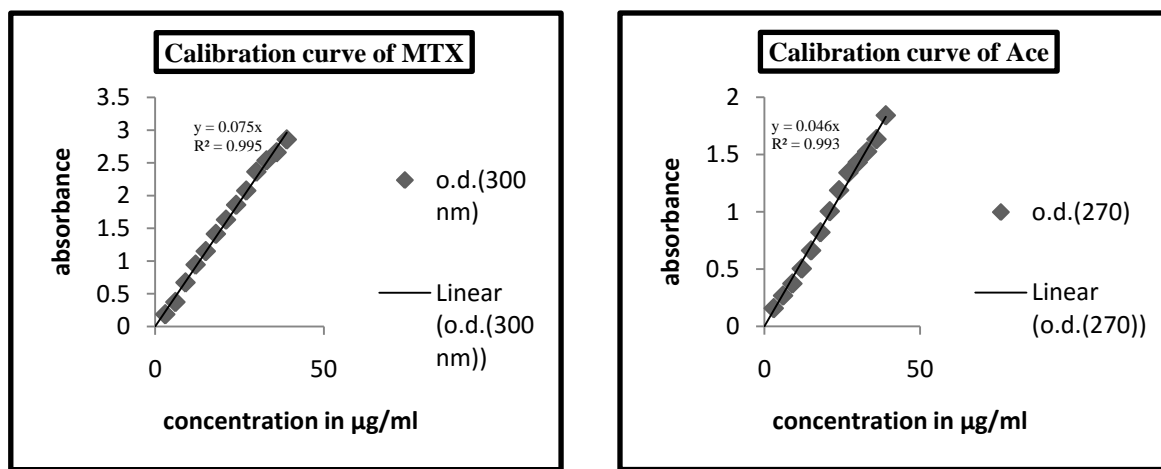


**Figure V:**(a) Standard calibration curve of MTX at 300nm.(b) Standard calibration curve of Ace at 270nm.

**The drug loading efficiency was calculated by the formula given below:**

$$\frac{(\text{Weight of Total drug} - \text{weight of free drug})}{(\text{Weight of lipid polymer})} \times 100$$

The drug loading efficiencies were calculated for three different formulations of both the drug. The drug loading efficiency has been always estimated to be lesser than 30%.

| Formulations of Methotrexate | Loading efficiency |
|---|---|
| Formulation 1 | 10.73% |

| | |
| --- | --- |
| Formulation 2 | 10.7% |
| Formulation 3 | 10.4% |

**Table I**: Percentage drug loading efficiency of Methotrexate

| Formulations of Aceclofenac | Loading efficiency |
| --- | --- |
| Formulation1 | 10.7% |
| Formulation2 | 10.5% |
| Formulation3 | 10.5% |

**Table II**: Percentage drug loading efficiency of Aceclofenac

Formulation1 was seen to have better loading efficiency than rest of the two other formulations. Hence, we decided to carry-out the characterization using formulation1 with both MTX and Ace.
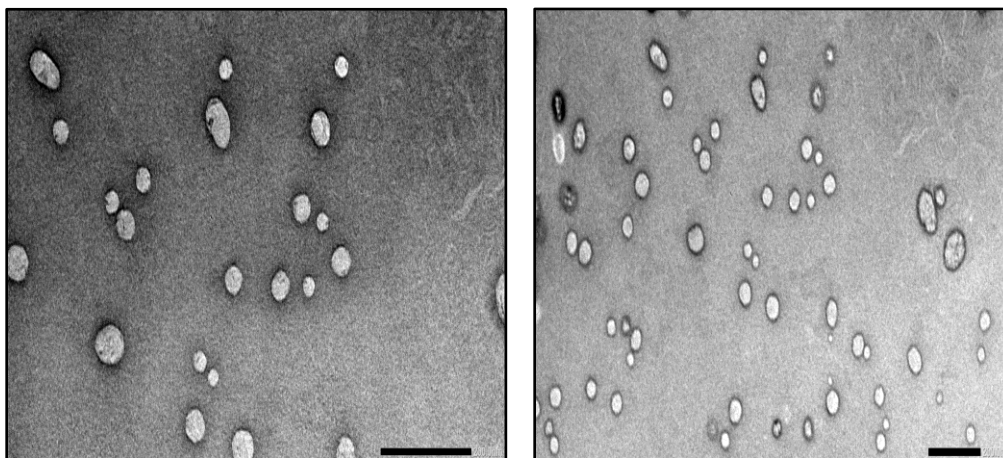


**Figure VI:** TEM image of drug loaded (a) and unloaded liposomes (b) range of 500

The zeta-potential, particle size and polydispersity index (PDI) of formulation1 with both drugs was analyzed using Zeta-sizer (Malvern, Nano zs). Subsequently the zeta-potential of MTX and Ace was obtained -13.4 and -27.4mv. The average size of aceclofenac was obtained to be 289nm whereas for MTX, it was 200nm. PDI of MTX and Ace was 0.372 & 0.272, respectively. The zeta-potential indicates that repulsion between, similarly charged particles in dispersion. So, the particles with higher potential have higher stability. Particle size is difficult to regulate, it is one of the important parameters as it helps to escape the immune system especially the wandering macrophages at the size of ≤200nm[6].

## MTT Assay for determination of IC50
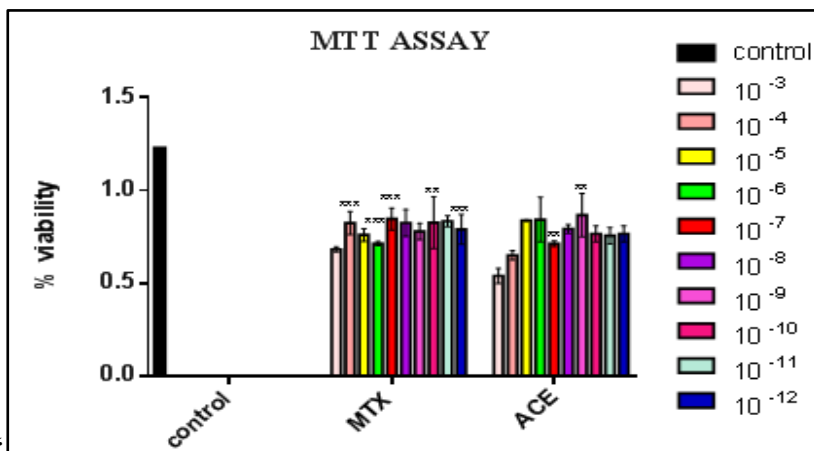


**Figure VII:** IC50 determination of MTX and Ace by MTT

Ten different concentrations [$10^{-4}$M to $10^{-12}$ M] of MTX and Ace were selected.A graph was plotted between percentage cell viability Vs. concentration of drug (M). IC50 for MTX and Ace was estimated to be 0.45μg/ml and 0.035μg/mlat $10^{-6}$M and $10^{-7}$ respectively.The IC50 estimation with both drugs paved the way for *in-vitro* analysis of drug entrapped in liposomes.

### *In-vitro* analysis of cytokines (IL-6 and TNF-α)
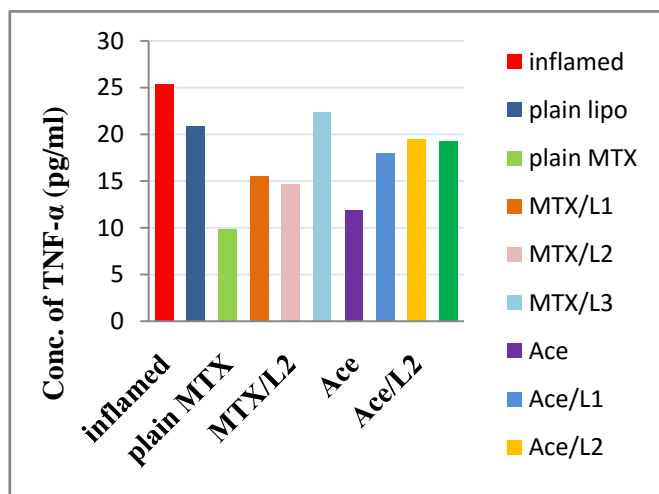


**Figure VIII:**Concentration of TNF-α at 48hr post treatment.
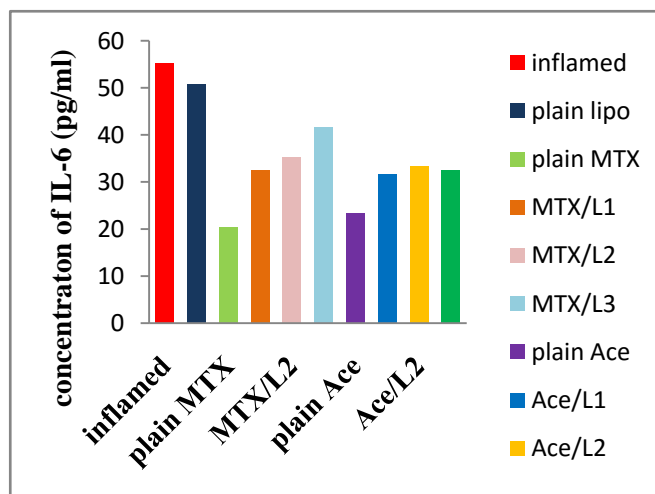


**Figure IX:**Concentration of IL-6 at 48hr post treatment.

Pro-inflammatory cytokines estimation was carried out by ELISA kit [20].We demostratedthat concentration of IL-6 saw a steep decrease with free drug due to burst release, but the drug

loaded liposomes are seen to release their content (MTX) in a sustained manner and therefore inhibition of inflammatory cytokines (IL-6) lasted-longer.

**Conclusion:**

The comparative analysis of free drug and drug(s) loaded liposome shows that drug loaded onto liposome showed low bio-degradability, and sustained release in reducing the inflammation induced by the LPS treatment even with smaller concentrations used. Liposomal formulation used in *in-vitro* delivery have capability to form nano-dimmers for approximately 199.3±0.3nm and 285.6±0.2nm size and loading efficiencies are approximately 10.7% and 10.5%for MTX and Ace loaded liposome, respectively. The level of pro-inflammatory cytokines in experimentally induced inflammation in breast cancer cells before and after therapeutic treatment with liposomally entrapped drug is suggestive of the relevance of the present study in surfacing the sustained and controlled release attributes of liposomes. Liposomal formulation and its engineered versions might be used to deliver MTX and Ace to subside inflammation in a specific and in regulated manner with reduced toxicity and minimal adverse.The nearby delivery vehicle opens new avenues to study systemic inflammatory diseases such as Rheumatoid Arthritis, brain cancer etc, and needs to be further exploredboth *in vitro* as well as in experimentally induced animal models.

**References**

1.  Barton, Gregory M., The Journal of clinical investigation 118, no. 2, 2008, 413.

2.  Laouini, Abdallah, Chiraz Jaafar-Maalej, Imen Limayem-Blouza, S. Sfar, Catherine Charcosset, and Hatem Fessi., Journal of colloid Science and Biotechnology 1, no. 2, 2012, 147-168.

3.  Çağdaş, Melis, Ali Demir Sezer, and Seyda Bucak., In Application of Nanotechnology in Drug Delivery. InTech, 2014., 1-50.

4.  Cutolo, M., A. Sulli, C. Pizzorni, Bm Seriolo, and R. H. Straub., Annals of the rheumatic diseases 60, no. 8, 2001, 729-735.

5.  Franceschi, Claudio, and Judith Campisi., Journals of Gerontology Series A: Biomedical Sciences and Medical Sciences 69, no. 1, 2014, S4-S9.

6.  Garg, Neeraj K., Priya Dwivedi, Christopher Campbell, and Rajeev K. Tyagi., European Journal of Pharmaceutical Sciences 47, no. 5, 2012, 1006-1014.

7.  Mohamed, j. Muthu, P. Bharathidasan, and M. Mohamed Raffick., International Journal of Pharma and Bio Sciences 3, no. 4, 2012, 419–432.

8.  Lan Li, Fadi S. Braiteh., Pharmaceutical and Nano Sciences 4, no .3, 2015, 162–174.

9.  Kapoor, Bhupinder, Sachin Kumar Singh, Monica Gulati, Reena Gupta, and Yogyata Vaidya., The Scientific World Journal 2014.

10. Konigsberg, Paula J., J. Eric Debrick, Tomasz J. Pawlowski, and Uwe D. Staerz., Biochimica et Biophysica Acta (BBA)-Biomembranes 1421, no. 1, 1999, 149-162.

11. Makene, Vedastus W., and Edmund J. Pool., Water and Environment Journal 29, no. 3 2015, 353-359.

12. Medzhitov, Ruslan., Nature 454, no. 7203, 2008, 428.

13. Nathan, Carl., Nature reviews. Immunology 6, no. 3, 2006, 173.

14. Pober, Jordan S., and William C. Sessa., Nature reviews,  Immunology 7, no. 10, 2007

15. Russell, Anthony, Boulos Haraoui, Edward Keystone, and Alice Klinkhoff., Clinical therapeutics 23, no. 11, 2001, 1824-1838.

16. Sanka, Krishna, Rajeswara Rao Pragada, and Prabhakar Reddy Veerareddy., Journal of microencapsulation 32, no. 8, 2015, 794-803.

17. Serhan, Charles N., and John Savill., Nature immunology 6, no. 12, 2005, 1191-1197.

18. Valeyev, Najl V., Christian Hundhausen, Yoshinori Umezawa, Nikolay V. Kotov, Gareth Williams, Alex Clop, Crysanthi Ainali, Christos Ouzounis, Sophia Tsoka, and Frank O. Nestle., PLoS computational biology 6, no. 12, 2010.

19. Yuan, Fang, Ling-dong Quan, Liao Cui, Steven R. Goldring, and Dong Wang., Advanced drug delivery reviews 64, no. 12, 2012, 1205-1219.

20. Williams, A. S., S. G. Jones, R. M. Goodfellow, N. Amos, and B. D. Williams., British journal of pharmacology 128,  no. 1, 1999, 234-240.

21. Bangham, Alec D., and R. W. Horne., Journal of molecular biology 8, no. 5, 1964,  660-668.

**Book**

22. Hurley, John Victor. Acute inflammation. Churchill Livingstone, 1972.

# A COMPARATIVE STUDY ON PHOTOCATALYTIC ACTIVITY OF ZnO, ZnS AND THEIR COMPOSITE

## BASANT K. MENARIYA, TARUNA DANGI, RAKSHIT AMETA, SURESH C. AMETA

### Department of Chemistry, PAHER University, Udaipur- 313003 (Raj.) INDIA
### E-mail: basant.menaria@gmail.com

## ABSTRACT

A composite of ZnO and ZnS was prepared by simple solid state mechanochemical technique and it was used as a semiconductor for thephotocatalytic degradation of Azure B. The effect of several parameters like pH, Azure B concentration, amount of composite and intensity of light was monitored.The optimum conditions obtained for this degradation were: Azure B = $1.80 \times 10^{-5}$ M, pH = 10.0, amount of composite = 0.10 g and light intensity = 60.0 mWcm$^{-2}$. The photocatalyticefficiency of ZnO-ZnS composite was compared with pure ZnO and ZnS.It was found that composite of ZnO-ZnS shows betterphotocatalytic activity as compared with ZnO and ZnS alone for the degradation of Azure B in the presence of visible light.

**Key words:**ZnO ,ZnS, Composite ,Photocatalytic activity, Azure B

## INTRODUCTION

Effluents from various industries like dyeing, textile, paper, pulp and printing industries contain pollutants such as, detergent, acids, soaps, pesticides, chemicals, dye etc, which are the major sources of water pollution. Large scale production and extensive applications of synthetic dyes cause considerable environmental pollution. Dyes are difficult to decompose biologically and chemically.

Therefore, severaltechniques such as precipitation, flocculation, air stripping, adsorption, reverse osmosis, ultrafiltration, etc. are being used for removal of contaminants. Heterogeneous photocatalytic oxidation is an effective method to remove organic pollutant even at low concentrations. Here, semiconductor particles on excitation act as photocatalysts or short-circuited microelectrodes. Semiconductor generates electron-hole pair on excitation which may be used either for oxidation or reduction of the dye.

Photocatalysis has shown various promising applications.Vinodgopal andPrashant[1]studied degradation of azo dye by $SnO_2/TiO_2$ coupled semiconductor thin films. Preparation of $Bi_{12}TiO_{20}$ and use inphotocatalytic degradation was studied by Xuet al.[2]Ungelenket al.[3] showed that

nanoscale $\beta$-$Sn_{1-n}WO_4 \cdot n\alpha$-Sn is a highly efficient photocatalystfor degradation of organic dyes in day light and it was observed to be a real 'green' synthesis. Kothari et al.[4] have carried out the photoreduction of malachite green usingCdS as photocatalyst and ascorbic acid/EDTA as reductants. Thephotocatalytic degradation of crystal violet in aqueous solutions was investigated by Sahooet al.[5] with $Ag^+$ doped $TiO_2$ under UV and simulated solar light.Kansalet al.[6] reported photocatalytic degradation of methyl orange and rhodamine 6G using several photocatalyst such as titanium dioxide, zinc oxide, stannic oxide, zinc sulphide and cadmium sulphide. A comparative photooxidative degradation of azure-B using sono-photo-Fenton and photo-Fenton reagents has been reported by Vaishnaveet al.[7] and they concluded the photochemical decomposition rate of azure-B is markedly increased in the presence of ultrasound. Azure B was photocatalytically degraded by Sharmaet al.[8] using NiS-ZnS composite in molar ratio 1:5. Claudia et al.[9] synthesized nanocrystals of ZnS ($\sim$3 to 5 nm diameter) with>50% product yield and reported the photocatalytic degradation of p-nitrophenol and acid orange 7. Visible light-driven degradation of methylene blue in the presence of semiconductingZnS and CdS nanoparticles was reported by Soltaniet al.[10]

Wenjianget al.[11] prepared spherical ZnO/ZnS core/shell particles under the hydrothermal condition and studied the photocatalytic degradation of methyl orange as a probe reaction. Nuengmatchaet al.[12] studied visible light-inducedphotocatalytic degradation of rhodamine B and industrial dyes (texbrite BAC-L and texbrite NFW-L) in the presence of ZnO-graphene-$TiO_2$ composite. The novel zirconium oxide, nickel oxide and zinc oxide nanoparticles supported on activated carbons were successfully fabricated through microwave irradiation method by Suresh et al.[13] and used for photocatalytic degradation of textile dyeing wastewater. Lachhebet al.[14] studied photocatalytic degradation of anthraquinonic (alizarin S), azoic (crocein orange G, methyl red), Congo red, heteropolyaromatic (methylene blue) dyes in $TiO_2$/UV aqueous suspensions. Bhati et al.[15] synthesized $CeCr_2O_5$ nanoparticles by microwave method for the decolorization of yellowish orange and fast green dyes, common water effluents of textile industries. Gandhi et al.[16]degradated methylene blue using coprecipitatedsulphidephotocatalyst. This coprecipitated semiconductor CoS-ZnS (in 1 : 10 mole ratios) was prepared by coprecipitation and used for photodegradation of methylene blue.Daneshvar et al.[17] compared the degradation of acid red 14 in the presence and absence of UV light using photocatalystZnO and observed that the amount of $H_2O_2$affect the photodegradation of dye. Devipriya and Yesodharan[18] have performed complete photocatalytic mineralization of pesticides to harmless products.

ZnO and ZnS compositewas preparedusing a simple mechanochemicalmethod. The obtained nanoparticles were characterized by XRD, UV-Vis absorption spectroscopy, SEM and EDX. The photocatalytic activity of as prepared composite was examined in the degradation of Azure B under visible light in air at room temperature and the influence of different experimental parameters such as the ZnS-ZnS amount, pH of the solution, dye concentration and light intensity on the rate of degradation was observed.

## EXPERIMENTAL

### Preparation of composite

Composite of ZnO and ZnS was prepared by simple solid state mechanochemical method.Equal amount of ZnO and ZnS(1:1 ratio) was taken and then it was ground with the help of pestle and mortar. Then it was used for photocatalytic degradation of Azure B.

### Characterization of Composite

X-rays diffraction pattern of theZnO-ZnS composite is shown in Fig. 1. Average particle size of the crystalline composite was calculated by Debye-Scherrer's equation and it was found 87.03 nm.



**Fig. 1: XRD spectrum of composite**

The elemental composition and surface morphology were observed out by scanning electron microscope equipped with an energy dispersive X-ray spectrophotometer. The SEM

image of ZnO-ZnS composite is given Fig. 2. It shows that the particles of composite have rough surface with irregular si



**Fig. 2: SEM Image of composite**

EDX analysis was performed to analyze the elemental constituent of mixed ZnO –ZnSand it revealed that three elements are present in nanomaterial i.e. Zn, S and O (Fig. 3) .

**Table1: Elemental composition**

| Elements | Weight (%) | Atomic (%) |
|----------|-----------|-----------|
| Zn | 67.63 | 46.41 |
| O | 16.39 | 34.40 |
| S | 15.97 | 19.18 |

**Photocatalytic degradation**

0.0305 g Azure B was dissolved in 100.0 mL of doubly distilled water so that the concentration of dye solution was $1.0 \times 10^{-3}$ M. It was used as a stock solutionand further diluted as and, when required. The absorbance of Azure B solution was observed with the help ofspectrophotometer( Systronic model 106 ) at $\lambda_{max}$= 650 nm.It was irradiated with a 200 W tungsten lamp (CEL, Model SM 201) Reaction solution was exposed to visible light.A water filter was used between light source and solution to cut off the thermal radiation.

The dye solution was divided into four beakers. These beakers were kept under four different experimental conditions and initial and final absorbances (A) were observed after 3 hrs for solution of each beaker. Control experiments were carried out, which proved that this reaction is photocatalytic in nature.

The photocatalytic degradation of Azure B dye was studied, after adding of 0.10 g of composite in 50 mL dye solution ($1.8 \times 10^{-5}$ M) at pH 10.0. A 200W tungsten lamp wasused for irradiation (60.0 W cm$^{-2}$ light intensity). Irrdiationwas carried out in glass vessel.A solarimeter (Suryamapi CEL 201) was used for the measurement of light intensities. Water filter was usedto cut thermal effect. A digital pH meter was used to measure pH of the dye solutions.pH of the dye solutions was adjusted by addition of previously standardized 0.1 N sulphuric acid and 0.1N sodium hydroxide solution. UV-Visible spectrometer (Systronic Model 106) was used to measureabsorbance (A) of the dye solution at regular time intervals. A linear plot between plot of 1+ logA and timeshows that Azure Bdegradation follows pseudo-first order kinetics.
The rate constant was calculated with the help of given formula -

$$k = 2.303 \times \text{slope}$$

## RESULTS AND DISCUSSION

**Table 2: Atypical run**

| [Azure B ] = 1.80 x $10^{-5}$ M | | pH= 10.0 |
| --- | --- | --- |
| Amount of composite = 0.10 g | Light intensity = 60.0 mWcm$^{-2}$ | |

| Time (min.) | Absorbance (A) | 1+log A (ZnO-ZnS) |
| --- | --- | --- |
| 0 | 0.693 | 0.8407 |
| 5 | 0.591 | 0.7715 |
| 10 | 0.478 | 0.6794 |
| 15 | 0.391 | 0.5922 |
| 20 | 0.311 | 0.4927 |
| 25 | 0.269 | 0.4297 |
| 30 | 0.226 | 0.3541 |
| 35 | 0.174 | 0.2405 |

| Time (min.) | Absorbance (A) | 1 + log A (ZnO-ZnS) |
| --- | --- | --- |
| 40 | 0.152 | 0.1818 |
| 35 | 0.129 | 0.1106 |
| 50 | 0.108 | 0.0334 |

Rate constant ( k ) with ZnO = 4.72 x $10^{-4}$ $sec^{-1}$

Rate constant ( k ) with ZnS = 4.38 x $10^{-4}$ $sec^{-1}$

Rate constant ( k ) with ZnO-ZnS = 6.14 x $10^{-4}$ $sec^{-1}$

## Effect of pH

The effect of pH on photocatalytic degradation was monitored in the range 6.0- 11 and the results are tabulated in Table 3. It was observed that the rate of degradation of azure B increaseswith increase in pH and maximum efficiency was exhibited at pH 10.0. This result may beexplained on the basis that on increasing pH, there was greater probability for the formationof oxygen anion radical ($O_2^{\bullet-}$), which are produced from the reaction between $O_2$ moleculeand electron ($e^-$) of the semiconductor. When pH was increased above 10.0, the rate of thereaction was found to decrease, which may attributed the fact that cationic form of azure B isconverted to its neutral form, which faces no attraction towards the negatively chargedsemiconductor surface due to the absorption of hydroxyl ions.

## Table 3: Effect of pH

[Azure B ] = 1.80 x $10^{-5}$ M

Amount of composite = 0.10 g     Light intensity = 60 .0 mWcm$^{-2}$

| pH | Rate constant (k) × $10^4$ ($sec^{-1}$) |
|---|---|
| 6.0 | 0.59 |
| 6.5 | 0.63 |
| 7.0 | 0.75 |
| 7.5 | 1.17 |
| 8.0 | 1.49 |
| 8.5 | 2.32 |
| 9.0 | 3.14 |
| 9.5 | 4.06 |
| **pH** | **Rate constant (k) × $10^4$ ($sec^{-1}$)** |
| **10.0** | **6.14** |
| 10.5 | 5.19 |
| 11.0 | 4.93 |

### Effect of dye concentration

Effect of concentration of Azure B was studied by taking its different concentrations i.e. $1.0 \times 10^{-5}M$-$2.6 \times 10^{-5}M$. The results are reported in Table 4. It was observed that the rate of photocatalytic degradation increased with increase in concentration of dye up to a certain concentration ($1.8 \times 10^{-5}M$). This may be attributed to the fact that as the concentration of dye was increased, more dye molecules were available for excitation and hence, there was an increase in the rate. The rate of photocatalytic degradation was found to decrease with futher increase in the concentration of dye. This indicated that after certain concentration, the dye itself start acting as obstacle for the incident light and it does not allow the required light intensity to reach the semiconducting particles and thus, declining the rate of the photocatalytic degradation of dye.

### Table 4: Effect of dye concentration

| Amount of composite = 0.10 g | pH= 10.0 |
|---|---|
| Light intensity = 60.0 mWcm$^{-2}$ | |

| [ Azure B ] x $10^5$ | Rate constant (k) $\times 10^4$(sec$^{-1}$) |
|---|---|
| 1.0 | 4.03 |
| 1.2 | 4.46 |
| 1.4 | 5.03 |
| 1.6 | 5.57 |
| **1.8** | **6.14** |
| 2.0 | 5.57 |
| 2.2 | 5.32 |
| 2.4 | 5.03 |
| 2.6 | 4.53 |

### Effect of amount of semiconductor (ZnO-ZnS) composite

The rate of photocatalyticdegradation of Azure B increases with an increase in the amountof composite but finally, it becomesalmost constant after a certain amount, i.e. 0.10g. This may be attributed to the fact that as thequantity of composite was increased, theexposed surface area also increases, but aftera definite limit, if the quantity of compositewas further increased, then there will be noincrease in the exposed surface area of thephotocatalyst. It may be considered like asaturation point; above which, any increase inthe amount of semiconductor has insignificantor no effect on the rate of photocatalyticdegradation of Azure B, as any increasein the amount of composite after thissaturation point will only increase the thicknessof the film at the

bottom of the reaction vessel.The saturation point shifts to upper rangefor bigger vessels, while reverse was true forsmaller vessels.

**Table 5: Effect of photocatalyst**

[Azure B ] = 1.80 x $10^{-5}$ M            pH= 10.0

Light intensity = 60.0 mWcm$^{-2}$

| Amount of composite (g) | Rate constant (k) $\times 10^4$ (sec$^{-1}$) |
|---|---|
| 0.02 | 4.06 |
| 0.04 | 4.58 |
| 0.06 | 5.20 |
| 0.08 | 5.77 |
| **0.10** | **6.14** |
| 0.12 | 6.05 |
| 0.14 | 6.05 |

**Effect of light intensity**

To observe the effect of intensity of light on the photocatalytic degradation of Azure B, the lightintensity was varied either by changing the wattage of lamp or the distance between lamp and semiconductor surface. The results obtained are tabulated in Table 6. The data shows that an increase in the light intensity increases the rate of photodegradation and the optimum value were found at 60.0 mWcm$^{-2}$. It may be explained on the basis that as the light intensity was increased, the number of photons striking per unit area also increased, resulting into a greater rate of degradation. Further increase in the light intensity decrease the rate of reaction. It may be possibly due to thermal side reactions

**Table 6: Effect of light intensity**

[Azure B ] = 1.80 x $10^{-5}$ M            pH= 10.0

Amount of composite = 0.10 g

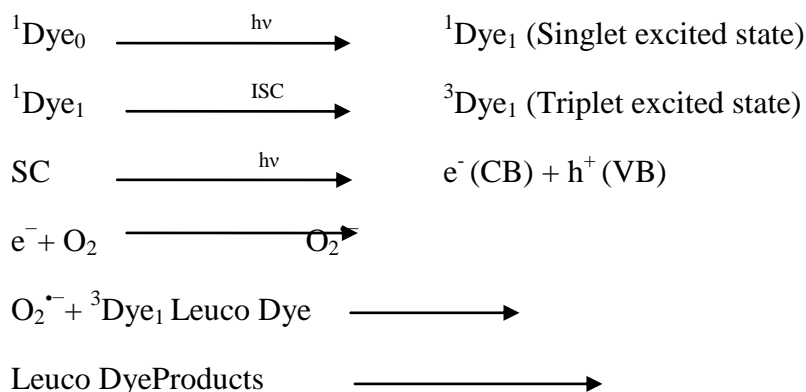| Light intensity (mW cm$^{-2}$) | Rate constant (k) $\times 10^4$(sec$^{-1}$) |
|---|---|
| 20 | 2.76 |
| 30 | 3.38 |
| 40 | 3.69 |
| 50 | 4.92 |

| | |
| --- | --- |
| **60** | **6.14** |
| 70 | 5.23 |

**Mechanism** –

On the basis of these observations, a tentative mechanism for photocatalytic degradation of azure B (Dye) has been proposed as follows:

$$^{1}Dye_0 \xrightarrow{\quad h\nu \quad} {}^{1}Dye_1 \text{ (Singlet excited state)}$$

$$^{1}Dye_1 \xrightarrow{\quad ISC \quad} {}^{3}Dye_1 \text{ (Triplet excited state)}$$

$$SC \xrightarrow{\quad h\nu \quad} e^{-} (CB) + h^{+} (VB)$$

$$e^{-} + O_2 \xrightarrow{\quad\quad} O_2^{\bullet -}$$

$$O_2^{\bullet -} + {}^{3}Dye_1 \text{ Leuco Dye} \xrightarrow{\quad\quad}$$

$$\text{Leuco Dye Products} \xrightarrow{\quad\quad}$$

Azure B absorbs suitable wavelength and gives its first excited singlet state followed by intersystem crossing (ISC) to triplet state. On the other hand, the semiconducting composite ZnO-ZnS also uses the radiant energy to excite its electron from valence band to the conduction band; thus, leaving behind a hole. The dissolved oxygen accepts electron of composite and is converted into oxygen anion radical. In the next step, the dye molecule in triplet state donate an electron to oxygen anionradical and oxidized to its leuco form, which further degrades into harmless products. The hydroxyl radicals do not participate in the photodegradation of dye as the reaction rate was not appreciably retarded in presence of hydroxyl radical scavengers; isopropanol.

## CONCLUSION

A comparative study has been carried out between photocatalytic activity of pure ZnO and ZnSand their composite. Azure B dye was used as a model system to compare their photocatalytic activity. The rate constants for photocatalytic degradation of Azure B usingZnO, ZnS and ZnO-ZnSwere $4.72 \times 10^{-4}$ sec$^{-1}$, $4.38 \times 10^{-4}$ sec$^{-1}$ and $6.14 \times 10^{-4}$ sec$^{-1}$, respectively. These results clearly indicates that the composite ZnO-ZnSshowed better results as compared to individual ZnO and ZnS. The observation of present work will explore the use of composites in enhancing photocatalytic performance of a photocatalyst.

## ACKNOWLEDGEMENTS

## REFERENCES

1.  K. Vinodgopal, V. K.Prashant. Sci. Tech., 1995, 29, 841.

2.  S. Xu , W.Shangguan, J. Yuan, J. Shi, M. Chen, Sci. Tech. Adv. Mater., 2007, 8, 40.

3.  J.Ungelenkand,C. Feldmann, Appl.Catal. B: Environ., 2011, 102, 515.

4.  S. Kothari, A. Kumar, R. Vyas, R. Ameta, P. B. Punjabi, J. Braz. Chem. Soc., 2009, 20, 1821.

5.  C. Sahoo, A. K. Gupta, A. Pal, Dyes and Pigmen., 2005, 66, 189.

6.  S. K. Kansal, M. Singh, D. Sud, J. Hazard. Mater., 2007, 141, 581.

7.  P. Vaishnave, A. Kumar, R.Ameta, P. B. Punjabi, S. C. Ameta, Arab. J. Chem.,2014, 7, 981.

8.  V. Sharma, N. Gandhi, A. Khant R.C. Khandelwal, Int. J. Chem. Sci., 2010, 8, 1965.

9.  L. Claudia, T. Martinez, R. K. Mehra, J. Coll. Interf. Sci., 2001, 240, 525.

10. N. Soltani, E. Saion, M. Z. Hussein, M. Erfani, A.Abedini , G. Bahmanrokh, M. Navasery, P. Vaziri, Inter. J. Mol. Sci., 2012, 13, 12242.

11. L. Wenjiang, G. Song, F. Xie, M. Chen, Y. Zhao, Mater. Lett., 2013, 96, 221.

12. P. Nuengmatcha, S. Chanthai, R. Mahachai, W. Chunoh, J. Environ. Chem. Eng., 2016, 4, 2170.

13. P. Suresh, J. Judithvijaya, L. Johnkennedy, Trans. Nonfer. Met. Soc. China, 2015, 25, 4216.

14. H. Lachheb, E. Puzenat, A. Houas, M. Ksibi, E. Elaloui, C. Guillard, J. M. Herrmann, Appl. Catal. B: Environ., 2002, 39, 75.

15. I. Bhati, J. Sharma, A. Ameta, S. C. Ameta, Int. J. Chem. Sci., 2011, 9, 1787.

16. N. Gandhi, V. Sharma, A. Khant,R. C. Khandelwal, Int. J. Chem. Sci., 2010, 8, 1924.

17. N. Daneshvar, D. Salari, A. R. Khataee, J. Photochem. Photobiol. A: Chem., 2004, 162, 317.

18. S. Devipriya, S. Yesodharan, Sol. Energy Mater. Solar. Cells, 2005, 86, 309.

# Quality of Underground water of Some Saline Tracts in Banaskantha District

Nidhi k. patel, Arpita Paramar, kinjal k. Patel and K.C. Patel

Department of Chemistry, R.R. Mehta College of Science & C.L.Parikh College of Commerce, PALANPUR-385001[Gujarat]

## Abstract

About twenty samples of water from various sources in the northern and eastern part of Banaskantha district were examined for their chemical characteristics. The data obtained were used for classification of water into different categories on the basis of electrical conductivity, sodium absorption ratio (SAR),Residual sodium carbonate value(RSC) and soluble sodium percentage(SSP).

In general, it is found that about 95 percent tubewell waters have very high EC value. So, it is doubtful quality for irrigation purpose. As per SAR value, 35 percent samples fall under law SAR value and 15 percent samples fall under high SAR value. As per SSP value, it is found that only 25 percent samples falls under permissible limit, 50 percent tube-well water samples fall under doubtful quality and 25 percent samples fall under unsuitable water for irrigation purpose.

Key words : SSP, SAR, RSC, etc.

## Introduction:

The northern, central and southwest parts of Gujarat state may be classified as a semi-arid region. Banaskantha District of Gujarat state is situated on the bank of river "Banas". The mean annual temperature of the district is about $30^0$ to $35^0$ C. The maximum temperature of the district in May be about $42^0$ C. The average annual rainfall of the area is 25"- 30". There being fairly wide variation from year to year. Most of the rain is confined to the months June to September.

Although irrigation is useful and practiced even in areas of heavy precipitation it becomes an indispensable requirement in the arid regions of the world. The quantity of water available assumes paramount importance in arid regions. However, the quality of ground water supplied becomes a move critical factor with the increasing need for additional water for irrigation in semiarid and arid areas. Hence the classification of ground water resources in any arid region becomes of primary importance from the point of view of irrigation and agriculture.

## Material and methods:

The principal ground water resources of the Banaskantha district are wells and tube-wells. In all about twenty samples of ground water were collected from various parts of the district and analyses for some cat ions and anions, $P^H$ and electrical conductivity (EC) of water samples were also determined. The data obtained from chemical analysis of the samples are presented in Table. No: I

## Table No:-I

| Sr. No. | Electrical Conductivity dsm$^{-1}$ | P$^H$ | TDS ppm |
|---|---|---|---|
| 1 | 7110 | 7.12 | 4080 |
| 2 | 6290 | 7.34 | 3620 |
| 3 | 2420 | 7.89 | 1460 |
| 4 | 7010 | 8.31 | 4030 |
| 5 | 5190 | 7.64 | 2990 |
| 6 | 4420 | 7.78 | 2590 |
| 7 | 7670 | 8.38 | 4490 |
| 8 | 4010 | 8.19 | 2460 |
| 9 | 3240 | 8.76 | 2040 |
| 10 | 3590 | 8.20 | 2150 |
| 11 | 9080 | 7.56 | 5150 |
| 12 | 4980 | 7.96 | 2900 |
| 13 | 2520 | 8.75 | 1560 |
| 14 | 4690 | 7.60 | 2760 |
| 15 | 7480 | 8.21 | 4410 |
| 16 | 5580 | 8.28 | 3300 |
| 17 | 3790 | 7.82 | 2300 |
| 18 | 2040 | 8.84 | 1390 |
| 19 | 2810 | 8.38 | 1770 |
| 20 | 2570 | 8.08 | 1680 |

# Table No:-II (All results are in ppm)

| Sample No. | $Ca^{+2}$ | $Mg^{+2}$ | $Na^+$ | $K^+$ | $CO_3^{-2}$ | $HCO_3^{-1}$ | $SO_4^{-2}$ | $Cl^-$ | $F^-$ |
|---|---|---|---|---|---|---|---|---|---|
| 1 | 265 | 231 | 881 | 11 | nil | 329 | 125 | 2240 | 0.71 |
| 2 | 295 | 198 | 723 | 9 | nil | 232 | 240 | 1920 | 0.73 |
| 3 | 60 | 78 | 336 | 4 | nil | 220 | 123 | 640 | 0.79 |
| 4 | 245 | 204 | 934 | 10 | 12 | 256 | 170 | 2200 | 0.83 |
| 5 | 185 | 183 | 625 | 08 | nil | 281 | 107 | 1600 | 0.76 |
| 6 | 115 | 126 | 639 | 6 | nil | 207 | 174 | 1320 | 0.78 |
| 7 | 275 | 168 | 1119 | 12 | 12 | 195 | 426 | 2280 | 0.84 |
| 8 | 50 | 30 | 804 | 06 | 12 | 207 | 228 | 1120 | 0.82 |
| 9 | 30 | 18 | 673 | 05 | 24 | 244 | 243 | 800 | 0.88 |
| 10 | 85 | 69 | 592 | 06 | 12 | 220 | 125 | 1040 | 0.82 |
| 11 | 445 | 297 | 999 | 14 | nil | 220 | 291 | 2280 | 0.76 |
| 12 | 165 | 102 | 755 | 08 | nil | 134 | 176 | 1560 | 0.80 |
| 13 | 25 | 27 | 497 | 04 | 24 | 220 | 101 | 664 | 0.88 |
| 14 | 150 | 93 | 724 | 07 | nil | 171 | 170 | 1440 | 0.76 |
| 15 | 150 | 126 | 1300 | 11 | 12 | 220 | 315 | 2280 | 0.82 |
| 16 | 140 | 87 | 951 | 08 | 12 | 207 | 170 | 1720 | 0.83 |
| 17 | 80 | 30 | 719 | 06 | nil | 183 | 161 | 1120 | 0.78 |
| 18 | 30 | 12 | 410 | 03 | 24 | 476 | 58 | 376 | 0.91 |
| 19 | 60 | 51 | 477 | 05 | 12 | 354 | 121 | 688 | 0.85 |
| 20 | 55 | 51 | 428 | 04 | nil | 488 | 103 | 552 | 0.82 |

## Table No:-III

| Sample No. | Sodium Absorption Ratio. (SAR) | Residual Sodium Carbonate. (RSC) | Soluble Sodium Percentage (SSP) |
|---|---|---|---|
| 1 | 9.50 | nil | 53.88 |
| 2 | 7.96 | nil | 49.96 |
| 3 | 6.70 | nil | 60.35 |
| 4 | 10.63 | nil | 57.92 |
| 5 | 7.76 | nil | 52.37 |
| 6 | 9.75 | nil | 62.88 |
| 7 | 13.08 | nil | 63.42 |
| 8 | 22.13 | nil | 87.16 |
| 9 | 23.98 | 1.8 | 90.34 |
| 10 | 11.49 | nil | 71.72 |
| 11 | 8.95 | nil | 47.84 |
| 12 | 11.36 | nil | 65.94 |
| 13 | 16.37 | 0.90 | 85.72 |
| 14 | 11.41 | nil | 66.11 |
| 15 | 18.84 | nil | 75.56 |
| 16 | 15.49 | nil | 74.09 |
| 17 | 17.37 | nil | 82.46 |
| 18 | 15.82 | 6.10 | 87.36 |
| 19 | 10.92 | nil | 73.76 |
| 20 | 9.95 | 1.00 | 72.38 |

## Results and Discussion:

The quality of irrigation water is judged not only by the total but also by the kind of salts it contains and the individual ions involved. Most of the classification of irrigation water (USSL 1954, Wilcox 1955) supplies the total dissolved solids. (TDS)(Salinity hazard) and concentration of sodium (Alkali hazard) the sodium adsorption Ratio.(SAR) recommended by Richard (1954) has been computed for all the samples for the assessment of alkali hazard in this study.

The various categories take into account both the electrical conductivity (EC) as well as the soluble sodium percentage (SSP) The following table represents the basis of classification (Millar and Turk," Fundamental of soil science" 1952 P.450)

### Table No:-IV

### Classification of Ground Water

| Sr. No. | Class | Electrical Conductivity $(EC \times 10^6)$ at $25^0 C$ | Soluble Sodium Percentage (SSP) |
|---|---|---|---|
| 1 | Excellent | < 250 | < 20 |
| 2 | Good | 250 to 750 | 20 to 40 |
| 3 | Permissible | 750 to 2000 | 40 to 60 |
| 4 | Doubtful | 2000 to 3000 | 60 to 80 |
| 5 | Unsuitable | > 3000 | > 80 |

The sodium absorption Ratio (SAR) suggests the fate of a soil in equilibrium with the water under use the high SAR is likely to make the soil alkaline, on long continued use. The high chloride to bicarbonate Ratio indicates intrusion of a ground water resource with a brackish salty stream.

It can be seen from the above results 95% of the samples have EC value higher than 2250 micromhos per cm.at $25^0$C. Only one samples have EC value between 750-2250 micromhos /cm.Thus there are a large number of water resource which fall out of question for irrigation practices in the according the present method of classification suggested by U.S.D.A. U.S.Salinity laboratory suggests that the water having electrical conductivity above 2250 micromhos /cm. are generally unsuitable for irrigation purpose. There are however in use irrigation water with salt concentrations large enough to have conductivity value much greater than those mentioned above in arid and semi arid regions.

The analytical data indicate that about 35 percent samples have low SAR value (between 0 to 10) and 50 percent samples have SAR value between 10 to 18. and only 15 percent water sample under high SAR value.(between 18 to 26)

Taking the region as a whole of the twenty samples of ground water's examined about 15 percent water samples fall under Doubtful unsuitable categories .Only 25 percent samples fall under permissible limit as per SSP Value.

# EFFECT OF SOUND TREATMENT ON GERMINATION AND GROWTH OF PLANT SEEDS

**Rajiv D. Vaidya[1], Kaushik R. Patel[2], Mehul S. Dave[3] and Devendra B. Vanol[4]**

**[1]Biogas Research Center, Gujarat Vidyapith, SADRA**

**[2]Sheth P. T. Arts and Science College, GODHRA**

**[3]N. V. Patel College of Pure and Applied Sciences, V. V. Nagar**

**[4]ARIBAS, New Vallabh Vidyanagar**

**rajivdvaidya@gmail.com**

## ABSTRACT

An attempt has been made to understand the effect of sound treatment on the germination rate and growth of various plant seeds viz., Choli (*Vigna unguiculata*), Methi (*Trigonella foenum graceum*), Damro (*Ocimum basilicum L.*) and Guar or Cluster Bean (*Cyamopsis tetragonoloba*) seeds. The seeds have been subjected to rhythmic classical music. The genetically uniform seeds were exposed to classical sound for one hour daily up to one week period using normal mobile instrument. Out of these species, Guar or Cluster Bean (*Cyamopsis tetragonoloba*) was treated with different types of sound (music-rhythmic classical, rhythmic rock and non rhythmic traffic noise) with varying frequency (low- 50 to 100 Hz and High- 1500 to 2000 Hz) for distances (near – 25 cm and far- 550 cm) using laptop attached with loudspeaker.

The seeds with no sound treatment were considered as control. Both treated and non-treated seeds were kept in similar environment and conditions. The germination rate was monitored for a week and then growth of Guar plants for the period of 45 days. The results shows that sound have a significant positive effect on plant germination rate. Plant seeds under the influence of sound treatment had a higher germination rate compare to control. No adverse effects of sound treatment on germination rate were noticed.

## KEY WORDS

Sound treatment, germination rate, growth, plant seeds, frequency of sound

## INTRODUCTION

The use of music and sound to improve health is not a novel idea. Both harmful and beneficial effects of music have been recognized by the ancient Greeks and Romans, including Pythagoras, Democritus, Aristotle, Galenand Celsus [1]. Music is used in treatment of illnesses since for a long time past in China, India and Turkey. The effects of music treatment are better in neuropathies and depressions [2]. Many experiments have been done to see the effects of music on growing plants. In the 1950's, Indian botanist T. C. Singh made first recorded studies about effects of music on plants [3]. Studies about the effects of music were continued with Purple Passion vine plants [3] Paddy [4], wheat [5], Arabidopsis [6], Mimosa pudica [7], Groovy plants [8], corn [9]. The effect of influence of different ecological factors and physiological attributes of plants have been explored extensively [10]. Seed germination and seedling growth behavior influences by different pretreatments has been studied for different plants [11]. Sound wave can accelerate growth of plants and the stimulation of sound wave has an obvious effect on growth and development of plants [12].

The aim of the present study is to investigate the effect of sound treatment on germination rate of plant seeds and growth of plants. The primary experiments were done on Choli (*Vigna unguiculata*), Methi (*Trigonella foenum graceum*), Damro (*Ocimum basilicum L.*) and Guar or Cluster Bean (*Cyamopsis tetragonoloba*) seeds as they have applications for human consumption, medicinal purpose, crop and soil improvement, cattle feed and various industrial applications.

## MATERIALS AND METHODS

Genetically uniform seeds of Choli (*Vigna unguiculata*), Methi (*Trigonella foenum graceum*), Damro (*Ocimum basilicum L.*) and Guar or Cluster Bean (*Cyamopsis tetragonoloba*) were collected from Anand Agriculture University (AAU), Anand , Gujarat ,India . The Seeds were soaked in a tape water for overnight to make their skin softer; then after fungicides (bavastine) treatment was given for five minute and seeds were washed repeatedly by tap water. Seeds were distributed into three sets of petri plates (5 seeds / petri plates) with blotting paper in it and then given sound treatment (Classical Music) using mobile instrument for one hour daily to grow these seeds at room temperature. The petri plates were kept at a distance of 2 cm from the mobile instrument and classical music was played to the set labeled treatment using it. The control was not given any external sound exposure. The volume of the selected sound pieces and the piece of music played was uniform throughout the exposure period. The regular observations of number of seeds

germinated and other physical parameters were recorded and compared with control. Out of these species, Guar or Cluster Bean (*Cyamopsis tetragonoloba*) was treated with different types of sound (music-rhythmic classical, rhythmic rock and non rhythmic traffic noise) and with varying frequency (low- 50 to 100 Hz and High- 1500 to 2000 Hz) for distances (near – 25 cm and far- 550 cm) using laptop attached with loudspeaker. Three replications were taken for comparison. Each set was kept in the same environmental conditions and were received the same external sound.

## RESULTS AND DISCUSSION

Seed germination recorded everyday till germinated all seeds in petridish. Figure 1 shows Petri dish experiment with mobile instrument for First day for T1: Choli (*Vigna unguiculata*), T2: Methi (*Trigonella foenum graceum*) and T3: Damro (*Ocimum basilicum L.*). Figure 2 indicated the Petri dish experiment with treated seeds on Third day. Whereas Petri dish experiment with control seeds on Fifth day is shown in Figure 3.



Figure 1: Petri dish experiment with mobile instrument. (First day)
T1: Choli (*Vigna unguiculata*), T2: Methi (*Trigonella foenum graceum*)
and T3: Damro (*Ocimum basilicum L.*)

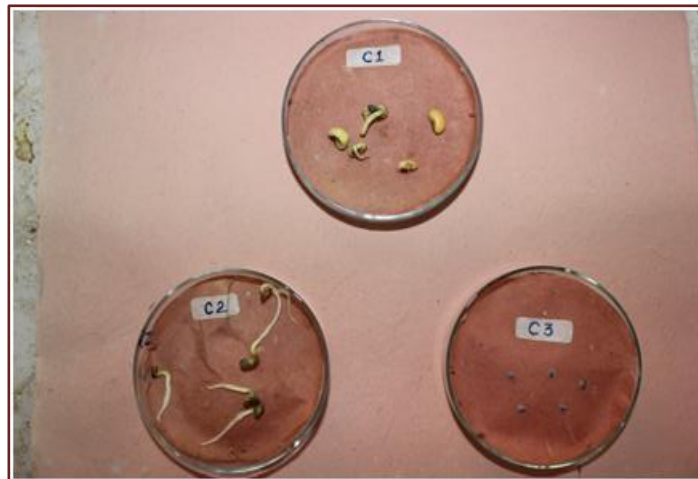Figure 2: Petri dish experiment with treated seeds. (Third day)



Figure 3: Petri dish experiment with control seeds.  (Fifth day)

The difference in germination of seeds were maximum for the plants exposed to at near (25cm) at low(50-100)  and high(1500-2000) frequency in silent classical music in 4ᵗʰ day and also maximum for the plants exposed to at near (25cm) and far(550cm)  at high(1500-2000)  frequency in silent classical music in 7ᵗʰ day, followed by the plants exposed to rhythmic rock music maximum germination rate observed in near(25cm) ;far(550cm) at low(50-100) frequency; and near(25cm) at high(1500-2000) frequency in 4ᵗʰ day and also maximum for the plants exposed  to both near (25cm) and far(550cm) at low(50-100)   and  high(1500-2000) frequency  in rhythmic rock music   in 7ᵗʰ day and when non rhythmic traffic noise exposed to plants seed germination rate would be maximum in near(25cm) at high(1500-2000)  frequency and same for the plants exposed to at near (25cm) and far(550cm) low (50-100)  and  high(1500-2000)   frequency in traffic noise  in 7ᵗʰ day.  Variation in Height (Growth) of  Guar Plant with different types of music up to  13 days observations is shown in Figure 4.
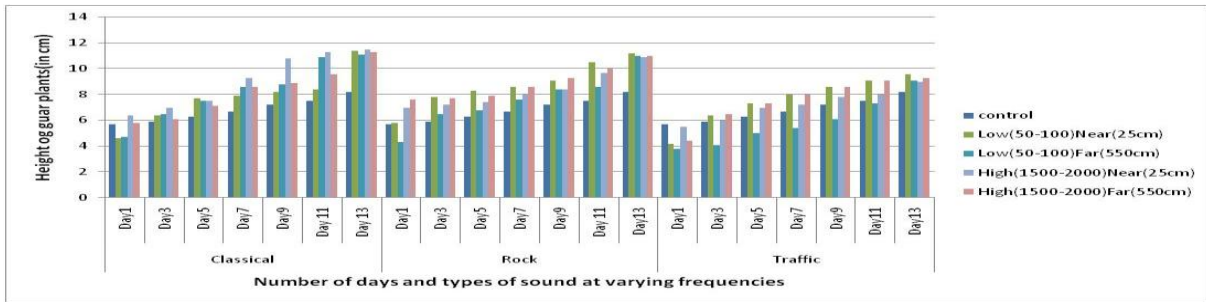
Figure 4: Variation in Height (Growth) of Guar Plant with different types of music up to 13 days observations.

The control set showed the minimum difference compare to other frequencies and types of sound. That means that musical sound with high(1500-2000) frequency has definitely helped in better growth of the plant and same effect in traffic noise in case of seed germination in petridishplates. Therefore, the plants with no external sound or untreated control being played showed slower growth.

Further, Figure 5 indicates number of leaves (Growth) of Guar Plant with different types of music up to 13 days observations. Figure 6 is about the Size of leaves for Guar Plant. Total Chlorophyll concentration in Guar Plant for classical sound treatment was observed and shown here in Figure 7.
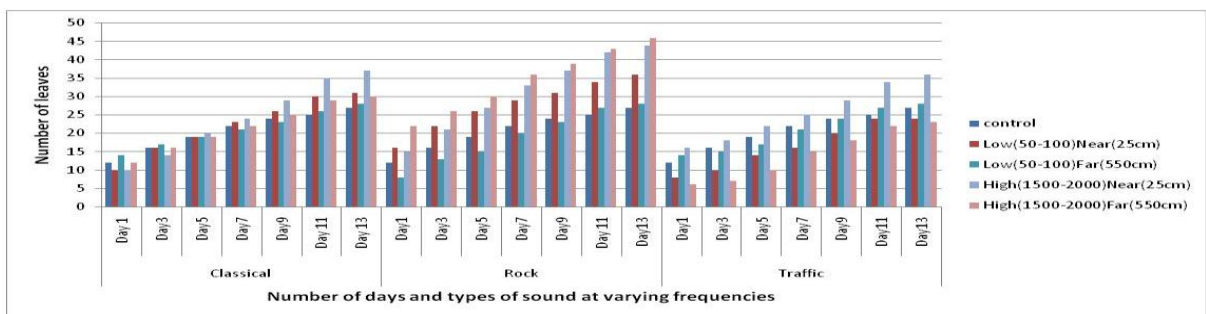


Figure 5: Number of leaves (Growth) of Guar Plant with different types of music up to 13 days observations.
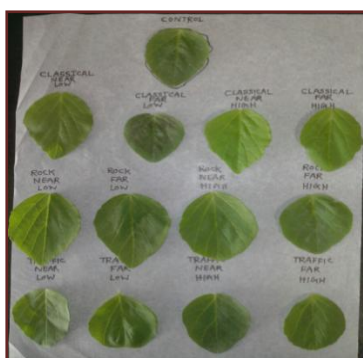




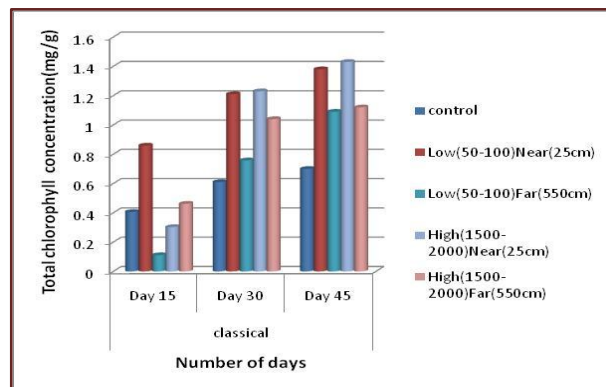Figure 6: Size of leaves In Guar Plant.

Figure 7: Total Chlorophyll concentration in Guar Plant for classical sound treatment.

The tremendous scope in the field of agriculture to be bio-simulation with sound of different frequency and exposure period to increase the germination as well as growth rate and yield of the various plants. It has also been observed and reported that such treatment are not harmful to plants as well as to environment. The environmental friendly techniques can be utilized for the same purpose. The farmers can take best advantage in terms of quantity and quality of crops by giving sound treatment. It is possible to establish a small working business in pilot scale primarily for providing effective and improved eco-friendly technique for better agricultural product that may also be useful for further research.

## CONCLUSIONS

(1) The considerable improvement in germination rate was observed as compare to control due to sound treatment.

(2) The plots for difference in number of seeds germination; height and in number of leaves clearly show that there is positive effect of silent classical musical sound compare to rhythmic rock musical sound on the growth of the plants. Both silent classical music and rhythmic rock music have given better results than the control.

(3) Higher frequency (1500-2000 Hz) have given better results than lower frequency (50-100 Hz).

(4) Near (25cm) distant plants shows positive effect compare to far (550cm) distant plants.

(5) The plant is able to differentiate between "some sound" and "no sound"; "music" and "noise" and also between higher frequency (1500-2000 Hz) and lower frequency (50-100 Hz); near(25cm) and far(550cm) in particular.

## ACKNOWLEDGEMENT

## REFERENCES

[1] Rooke A, Sunrise Magazine, Theosophical University Press, 1985.

[2] Wicke, 2005

[3] Tompkins P and C Bird, Harper Collins, 1989.

[4] Subramanian S et al., Madras Agric. J., 56: 510-516, 1969.

[5] Weinberger P and M Measures, Can. J. Bot., 57: 1036-1039, 1979.

[6]Braam J and Davis RW, Cell, 60: 357-364, 1990.

[7] Jones D, Green Music Naure, 351: 104, 1991.

[8] Davis R and P Scott, J. Exp. Bot., 51: 73, 2000.

[9] Talos, ASPB News, 286:8-9, 2001.

[10] Abd El-Naby, Zeinab M, Sakr H O, Asian Journal of Plant Sciences and Research, 2 (4): 388-395, 2012.

[11] Asha R, Pawan K, Asian Journal of Plant Sciences and Research, 2 (4): 409-413, 2012.

[12] Collin M and Foreman J, Canadian Acoustics, 29, 2001.

# Chemical Bath Deposition and Characterization of ZnO Rod-Array Films

Anjana Kothari* and T K Chaudhuri[§]

Dr. K C Patel Research and Development Centre (KRADLE),

Charotar University of Science and Technology (CHARUSAT),

CHARUSAT Campus, Changa 388 421, Anand, Gujarat, India

[§]Former Head, KRADLE, CHARUSAT, Changa

*E-mail:anjanakothari12@gmail.com

**Abstract:**

Chemical bath deposition (CBD) is asimple, low-costtechnique used to deposit various nanostructures of ZnO. In this paper, we report CBD of ZnO rod-array filmsdeposited on large area substrates. The films have been deposited on the side walls of thegrowth assembly which forms a chemical bath. The side walls are the bare glass plates which act as substrate for the deposition of ZnO rod-arrays films. Deposition of the film has been carried out at 85 $^{o}$C using an aqueous bath of tetra ammonium zinc complex prepared from RO water (drinking water). X-ray diffraction study shows that the as-deposited films are uniaxially out-of-plane textured along the c-axis. Scanning Electron Microscopy reveals the films consist of rod-arrays of dia. ~ 150 – 200 nm and length ~ 4.5 μm. Optical study such as diffuse reflectance has been carried out.

**Keywords:** ZnO rod-arrays, Chemical Bath Deposition, X-ray Diffraction, Scanning Electron Microscopy, Diffuse Reflectance.

**Introduction:**

Industrial production of zinc oxide had begun in around 1840. However, its use for industrial application was first reported by P. Puscher in 1869, 148 years back [1-4]. ZnO has been used in rubber industry since a long time by providing an invisible support. It is also used in various applications such as ceramics, food, agriculture, and cosmetics. Nowadays, ZnO finds place in various optoelectronic applications depending on their nano-/microstructures. These applications range from solar cells to transistors to sensors [5-9]. All these applications require a simple, low-cost, energy efficient and environment friendly deposition routes which can be scale-up at

industrial level. Since the device applications always require a film, we put our efforts to deposit the ZnO films on large area substrate by using a simple deposition technique, Chemical Bath Deposition (CBD).This manuscript describes the deposition of ZnO rod-array films on large area substrate at relatively low deposition temperature. The films were deposited from the RO water which we use as drinking water.

## Materials and Methods:

ZnO rod-array films were deposited from aqueous solution of tetra ammonium zinc complex, $Zn(NH_3)_4^{2+}$ at $85^oC$ [10]. This typical deposition procedure requires 85ml (pH:10)of $Zn(CH_3COO)_2 \cdot 2H_2O$ (3.6583 g/l) and $NH_4OH$ (5N) solutions prepared from Reverse Osmosis (RO) water (drinking water). To depositthe films we had prepared a growth assembly by using bare glass plates as shown in Fig. I. These bare glass plates act as substrate. The precursor solution (PS) waspoured into this chemical bath, and thenthe whole assemblywas introducedintothe waterbath which waskeptat $90^oC$. The assembly was taken outafter45 min. All the four sides of the assembly were coated with the white film of ZnO. These films were washedinrunningwatertoremoveany non-adherentpowder and finally driedinanovenat$60^oC$.The detailed procedure of the film deposition is given in our earlier reports [10]. The chemicals used were ofanalytical grade supplied by Merck Ltd., Mumbai, India. The typical dimension of the glass plates are 75 mm x 75 mm x 1.5 mm. Before making the square shaped growth assembly, the substrates were ultrasonically cleaned in chromic acid, distilled water, acetone, methanoland dried in warm air.The compositionandtextureoftheproductsweredetermined from X-raydiffraction(XRD)plots($\theta$–2$\theta$) recordedwithaPhilips (X'Pert) X-raydiffractometer(XRD) (usingNi-filteredCuK$_\alpha$ radiation) from $20^o$ to $80^o$. Themorphologyandstructureoftheproducts wasstudiedbyaJeol(JSM-5610LV)scanningelectronmicroscope (SEM). The diffuse reflectance($R_D$) spectra of the films were measured from 300 to 1200 nm with aPerkin Elmer (Lambda 19) spectrophotometer.

## Results and Discussion:

Adhesive, uniformand white ZnO rod-array films were deposited on the bare glass plates of the chemical bath. The bottom of this bath doesn't show any deposition of ZnO particles. It proves the films get deposited at preferred sites only. Hence, only heterogeneous nucleation prevailed.
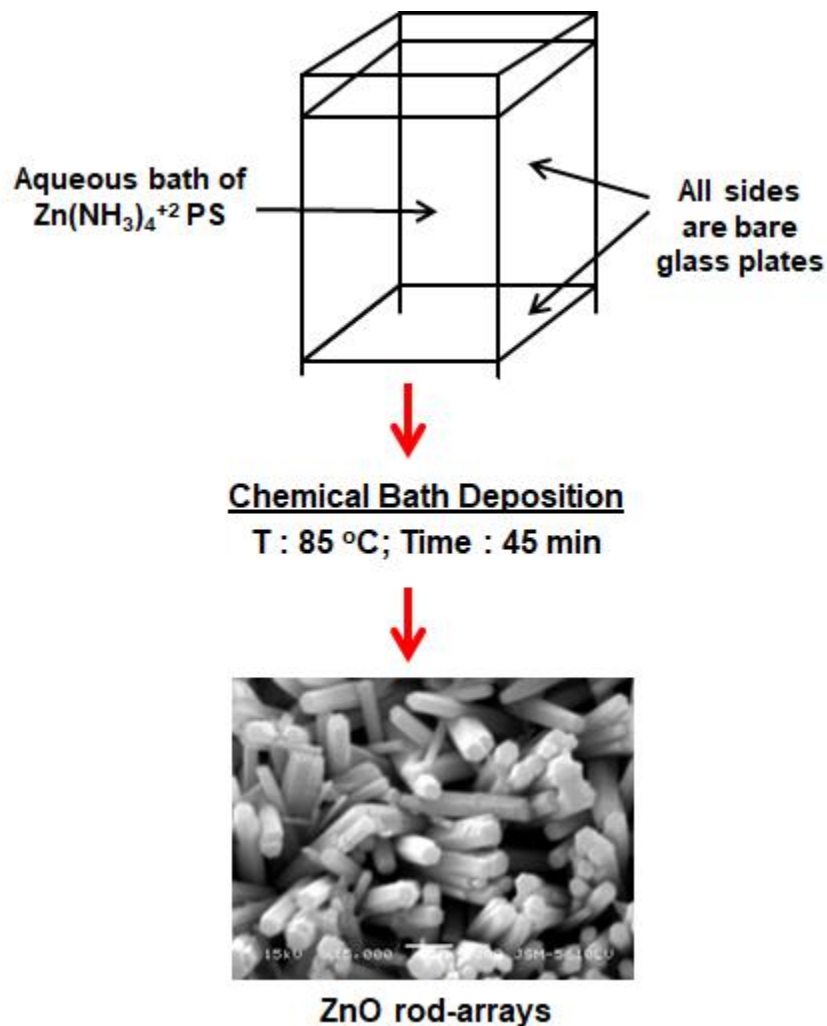
**Fig. I  Schematicof growth assembly-a chemical bath, used to deposit ZnO rod-array films**

Figure Irepresents schematic of growth assembly used as chemical bath to deposit ZnO rod-array films on large area substrate. The films have been deposited on the side walls of the growth assembly. All these walls are at 90° angle (vertical) to each other. The scanning electron microphotograph (Fig. I) reveals the deposition of ZnO rod –arrays of diameter ~ 150- 200 nm and length ~ 3.5 - 4 μm.

An XRD plot of ZnO rod-array film deposited at 85 $^{o}$C is depicted in Fig. II. The graph consists of peaks at 31.595°, 34.205°, 36.065°, 47.315°, 56.405°, 62.645°, 67.775° and 72.335°. These diffraction lines match well with standard XRD lines of hexagonal ZnO (JCPDS: 36-1451) and are due to reflections from (100), (002), (101), (102), (110) (103), (201)and (004) planes,

respectively. The film shows prominently strong line of (002) along with fairly strong lines of (100) and (101) suggests the films are preferentially oriented along the c-axis. The texture coefficient [11] $T_c(002) \sim 2.49$ indicates that the film has strong uniaxially out-of-plane texturing along c-axis.
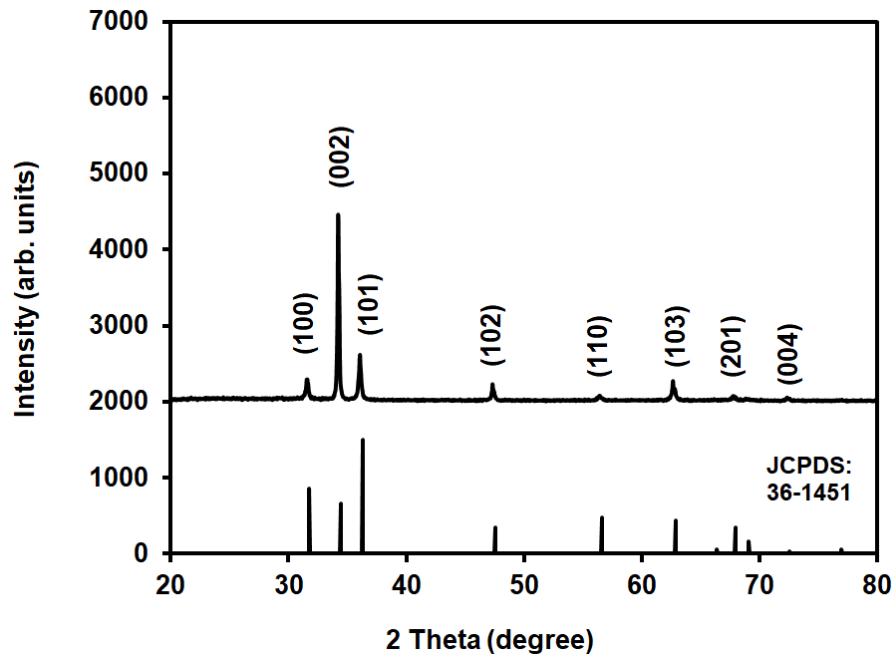


**Fig. II X-ray Diffractogram of ZnO rod-array film deposited on bare glass plates of the growth assembly**

Scanning Electron Microphotograph of ZnO rod-array film deposited on the sides of the growth assembly is presented in Fig. III. The inset image shows the top-view of the film. These films consist of an array of rods which are aligned normal to the bare glass substrate. Some of the rods are agglomerated and very few rods are aligned parallel to the plane of the substrate.
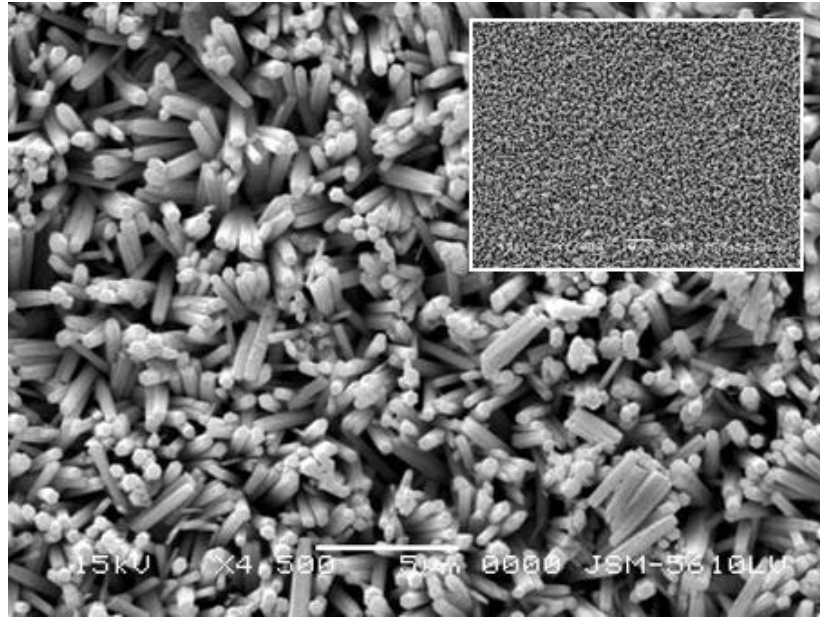
**Fig. IIIScanning Electron Microphotograph of ZnO rod-array deposited on the sides of the growth assembly; Inset shows the top view of the film**

Figure IV represents the ZnO rod-arrays deposited on the bare (seedless) glass substrate at 85°C in 45 min. The enlarged view of the selected growth region shows the filmconsists of rod-arrays of dia. ~ 200 nm and length ~ 3 μm. As revealed in the micrograph some of the rods are agglomerated (big red circle on the RHS) whereas some are twinned (Red colour square). The circled region (black circle) shows the formation of steps in the single, well-grown ZnO rod. This proves the rodswere grown via step growth mechanism.The ZnO rod-array films also show some non-uniformity in the deposition as depicted in Fig. V. As shown in the enlarged view of the Fig. V, a rod deposited parallel to the substrate acts as an origin, and from this origin the secondary and tertiary rods are growing out which forms flower-like structure.Few rods have emerged from the bigger size rod and are grown to the length of ~ 1 μm to 4 μm. Micrograph also reveals twinning of the rods as well as splitting of the tips.
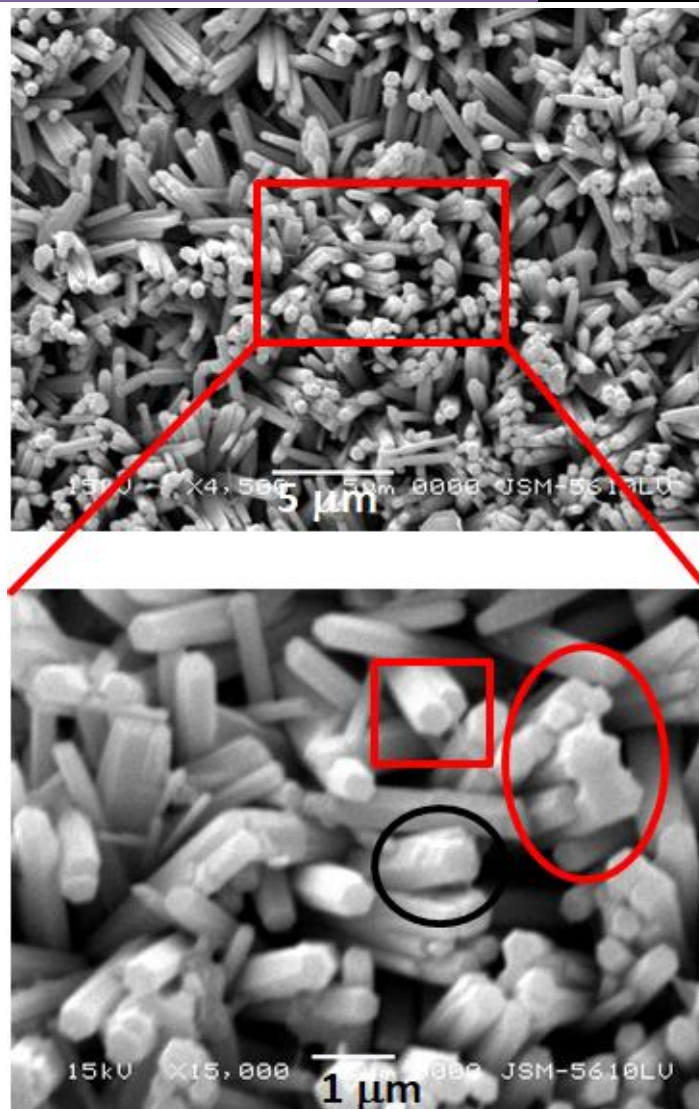
**Fig. IVScanning Electron Microphotograph of twinned ZnO rod-arrays deposited on the sides of the growth assembly**
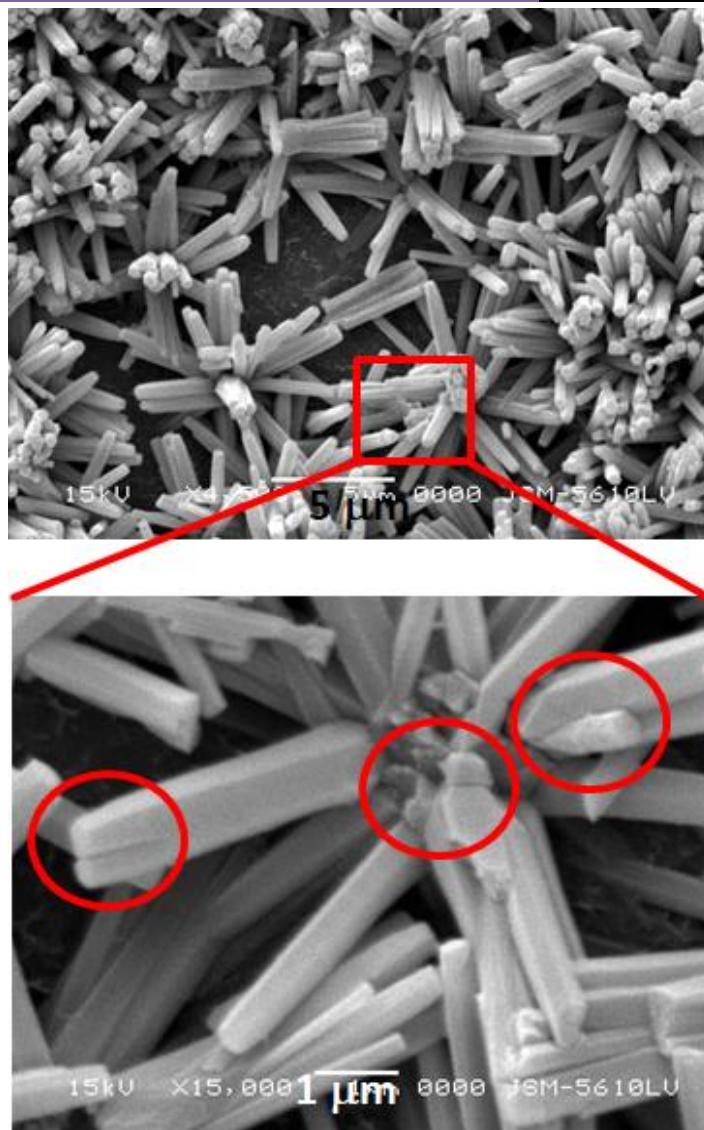
**Fig.V   Scanning Electron Microphotograph ofZnO rod-array film deposited on the sides of the chemical bath**

Diffuse reflectance ($R_D$) spectrum of ZnO rod-array film on seedless glass is shown in Fig. VI. As shown in the Fig., R increases from ~ 28 % to 36 % from the wavelength 1200 nm to 450 nm. Thehigher diffusereflectance is because of granular structure of the films which leads to scattering of incident beam of light. Figure 6 shows a plot of wavelength (nm) versus $(\alpha h v)^2$ obtained by using Kubelka-Munk function [12]. The energy band gap value is calculated from this plot by extrapolating the band edge. The energy band gap value derived for the ZnO rod-

array films is 3.22 eV (Fig. VII). The shift in the band gap, from 3.37 eV to 3.22 eV, may be due to the presence of defects in these rods.
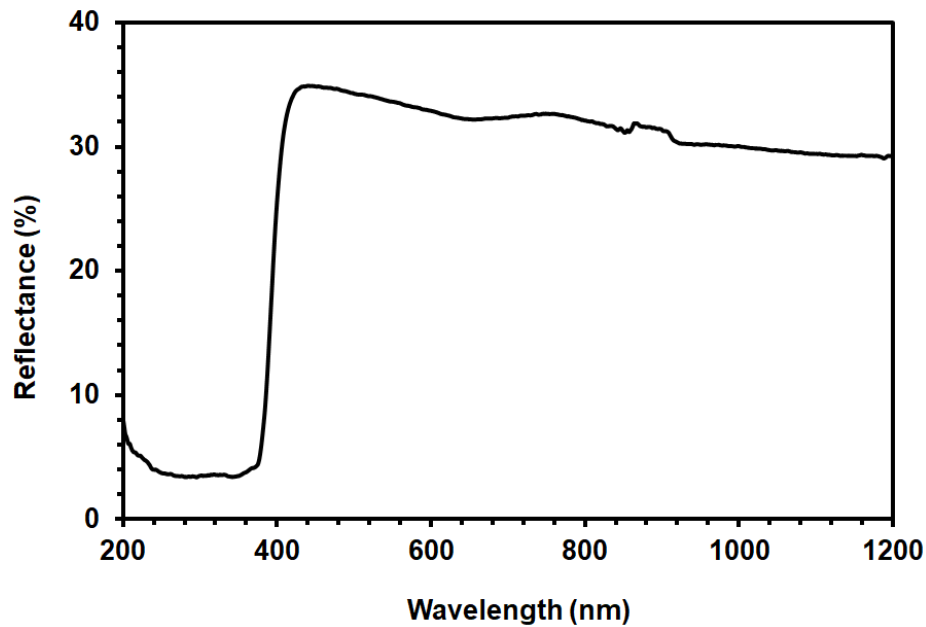


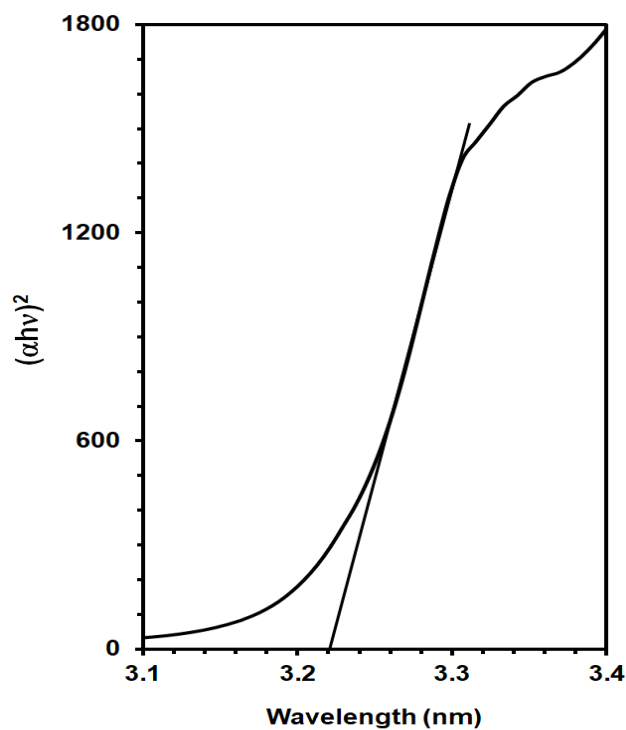**Fig. VI          Diffuse reflectance spectrum of ZnO rod-array film deposited on bare glass substrate**



*Fig. VII*          **Plot of wavelengthvs Kubelka-Munk function for ZnO rod-array films**

**Conclusion:**

A simple growth assembly has been developedtodeposit ZnO rod-array films on seedless large area substrateat 85$^{\circ}$C within 1 h. The films have been deposited from a chemical bath of $Zn(NH_3)_4^{2+}$prepared from drinking water. Thedepositionmethodholdspromiseforindustrialproductionofvariousnano-/microstructuresofZnO.

**Acknowledgements:**

**References**

[1]     Zinc Oxide Producers Association (ZOPA) – A Sector Group of The European Chemical Industry Council [2013, 2017]. Available: ⟨http://www.zopa.org/⟩.

[2]     C. Puscher, Polytechn. J., 1869, 190, 421.

[3]     G. Hodes, Phys. Chem. Chem. Phys., 2007, 9, 2181–2196.

[4]     M. R. De Guire, L. P. Bauermann, H. Parikh, J. Bill, Chemical     Bath Deposition, (Chapter 1), Springer DOI:10.1007/978-3-211-99311-8_14

[5]     Y. E. Romanyuk, H. Hagendorfer, P. Stücheli, P. Fuchs, A. R. Uhl, C. M. Sutter-Fella, M. Werner, S. Haass, J. Stückelberger , C. Broussillou, P-P. Grand, V. Bermudez, A. N. Tiwari, Adv. Funct. Mater, 2014, 1-16 (DOI: 10.1002/adfm.201402288).

[6]     H. Wang, T.  Kubo, J. Nakazaki, H. Segawa, Phys. Stat Solidi RRL Solar, 2014, 1–5 / DOI 10.1002/pssr.201409461.

[7]     J. Roh, H. Kim, M. Park, J. Kwak, C. Lee, Appl. Surf Sci, 2017, 420, 100 – 104.

[8]     Z. Fan and J.G. Lu, Internat. J. High Speed Electr. Syst., 2006, 16, 883 – 896.

[9]     Y. H.Navale, S.T.Navale, N.S.Ramgir, F.J.Stadler, S.K.Gupta, D. K.Aswal, V.B.Patil, Sens. Actuators B, 2017, 251, 551 – 563.

[10]    A. Kothari, T K. Chaudhuri, Mater.Lett., 2014, 137, 366 – 368.

[11]    M. Wang,C-H.Ye, Y. Zhang, H-X.Wang, X-Y. Zeng, L-D Zhang, J. Mater. Sci.: Mater.Electron.,2008, 19, 211–216.

[12]    Kubelka andMunk, Zeit. FürTekn. Physik, 1931,12, 593.

# HETERO-MOLECULAR INTERACTIONS IN BINARY MIXTURES USING DIELECTRIC DATA

## A. N. Prajapati

Department of Applied Physics,

Faculty of Technology and Engineering,

The M. S. University of Baroda,Vadodara.

Email:anprajapati-apphy@msubaroda.ac.in

**Abstract**:

Studies on Physico-chemical properties of binary liquid mixtures provide information on the nature of interactions between the constituent of the binaries. Literature provides extensive data on the static dielectric constant ($\varepsilon_0$) and refractive index (n) of liquids, but the combined study of all is quite scarce.In the present report, static dielectric constant ($\varepsilon_0$)and refractive index (n)have beenexperimentally determined for binary liquid mixture of 1-Butanol (1-BuOH) with N, N Dimethylformamide (DMF)over varying concentration of both mixture composition in the range (0.0 →1.0) at constant temperature303 K.Static dielectric constant ($\varepsilon_0$) and refractive index (n) for the binary mixture have beenmeasured using high precision LCR meter (0.2 MHz) and Abbe's refractometer respectively. Various dielectric parameters namely Kirkwood correlation parameter (g), Kirkwood effective correlation parameter ($g^{eff}$), Kirkwood angular correlation parameter ($g_F$) and Bruggeman parameter ($f_B$) are determined for the binary mixtures. Variations of these parameters against the concentration of constituents are discussed in terms of molecular interaction between the constituent species. Excess of static dielectric constant ($\varepsilon_0$)$^E$ and refractive index (n)$^E$ are determined and fitted with Redlich-Kister polynomial equation to derive the binary coefficients and standard deviations. These data have great significance in applied areas of research. They are needful for design processes in chemical, pharmaceutical, petrochemical and to develop models.

## 1. Keywords

1-Butanol, Bruggeman factor, Binary mixtures, DMF, Kirkwood parameters, Molecular interactions, Refractive index, Static dielectric constant.

## 2. Introduction

Dielectric constant is an intrinsic property of the bulk material, which plays an important role in the solution properties. In recent years, measurements of static dielectric constant, refractive index and density have been adequately employed in understanding the nature of

molecular interactions and physico-chemical behaviour in liquid mixtures. The nonrectilinear behaviour of above mentioned properties of liquid mixtures with changing mole or volume fractions is attributed to the difference in size of the molecules and strength of interactions. Dielectric studies on binary mixtures are important for understanding the heterogeneous and homogeneous interactions (dipole–dipole interaction and hydrogen bonding) in the mixture. [1-10]. The broad classifications of the methods to study H-bonding are chemical, crystallographic, spectroscopic and theoretical. The chemical methods are mainly concerned with the thermodynamic properties like enthalpy, entropy, heat of mixing, etc. The crystallographic studies are mostly related to the conformation of the structure in H-bonded systems by X-ray diffraction, neutron diffraction and electron diffraction methods [11]. The spectroscopic effects consider the physical aspects of H-bonding like molecular potentials, barrier to internal rotation, the vibrational energies of the bonds which are modified by the potential field, etc. Dielectric studies have often proved to be a powerful tool to give insights into the mechanisms of association and reorientational dynamics of dipolar liquids [2–4]. Amides have high polarity and strong solvating power; which makes them important solvents in chemical industry. N, N-Dimethylformamide (DMF) has been chosen for the present study because its properties have been the subject of considerable interest due to its relationship to peptides and proteins [2-4,8,11]. Further it is an important solvent that finds applications in polymer science and pharmaceutical industry too. DMF is highly aprotic polar solvent with a large dipole moment and a relatively high dielectric constant. In the pure state, it shows self-association through dipole-dipole interactions. Therefore, the solution chemistry of these compounds can be strongly influenced by inter and intra molecular H-bonding interactions, which consequently plays an important role in determining the physiochemical properties of these molecules. 1-Butanol (1-BuOH) is used as an ingredient in perfumes and as a solvent for the extraction of essential oils, also used as an extractant in the manufacture of antibiotics, hormones, and vitamins. It is a solvent for paints, coatings, natural resins, gums, synthetic resins, dyes, alkaloids, and camphor. 1-BuOH is used as a swelling agent in textiles, as a component of hydraulic brake fluids, cleaning formulations, degreasers, repellents and as a component of ore floation agents [12-14].

## 3. Materials and Methods

1-Butanol (1-BuOH) of AR Grade was procured from Sd-finechem, India. AR grade N, N Dimethylformamide (DMF) was supplied by LobaChemie Pvt Ltd, (India). Binary mixtures were prepared in hermetically sealed glass vials at 11 volume concentrations (0.0 →1.0) over

the entire mixing range at 303 K. The mole fractions of the mixture constituents were determined using the formula

$$X_1 = \frac{(\rho_1 \cdot \emptyset_1/M_1)}{(\rho_1 \cdot \emptyset_1/M_1)+(\rho_2 \cdot \emptyset_2/M_2)} \qquad (1)$$

where $\phi$ is the volume fraction, $\rho$ is the density, M is molecular weight, suffix 1 and 2 are the components 1-BuOH and DMF of the binary mixtures, respectively.

## 3.1. Dielectric measurement

The static dielectric constant values ($\varepsilon_0$) of DMF, 1-BuOH and their binary mixtures are determined using the capacitive measurement method at 0.2 MHz using high precision LCR meter (Hameg HM8118) with help of cylindrical test fixture designed at lab for the electrical capacitance measurements. Electrical capacitance of the cell without and with the sample are measured. The Electrical capacitance of the cell was stable and reproducible.

## 3.2. Refractive index measurement

The refractive index of each of the solution is determined at a wavelength of 589 nm using an Abbe Refractometer. The refractometer is initially calibrated by a standard liquid (HPLC grade) and then used to perform refractive index measurement at constant temperatures. The temperature of the refractometer was controlled by circulation of water in the sample compartment. The optical dielectric constant ($\varepsilon_\infty$) of DMF, 1-BuOH and their binary are taken as the square of the refractive index (n).

All measurements were carried out at constant temperature (303 K). The temperature was controlled thermostatically using constant temperature water bath. The maximum measurement error in the values of ($\varepsilon_0$) and n are 0.9 % and 0.02 % respectively.

Table 1. Comparison of static dielectric constant ($\varepsilon_0$) and refractive index (n) with the literature values.

| Compound Name | Static dielectric constant ($\varepsilon_0$) | | Refractive index (n) | |
| --- | --- | --- | --- | --- |
| | Experimental | Literature | Experimental | Literature |
| 1-BuOH | 16.67 | 16.91 [a] | 1.3994 | 1.3983 [b] |
| DMF | 38.77 | 36.55 [d] | 1.4293 | 1.4163 [c] |

[a]Ref- 14,[b]Ref- 15, [c]Ref- 16,[d]Ref- 17

## 4. Results and Discussion

The experimental values of static dielectric constant ($\varepsilon_0$) and refractive index (n) of pure organic liquids used in the present study along with their literature values are presented in Table 1. It is seen that the experimental values obtained in the present study are in good agreement with the literature values. Variation of static dielectric constant ($\varepsilon_0$) and refractive index (n) against mole fraction of 1-BuOH are shown in Figure 1.
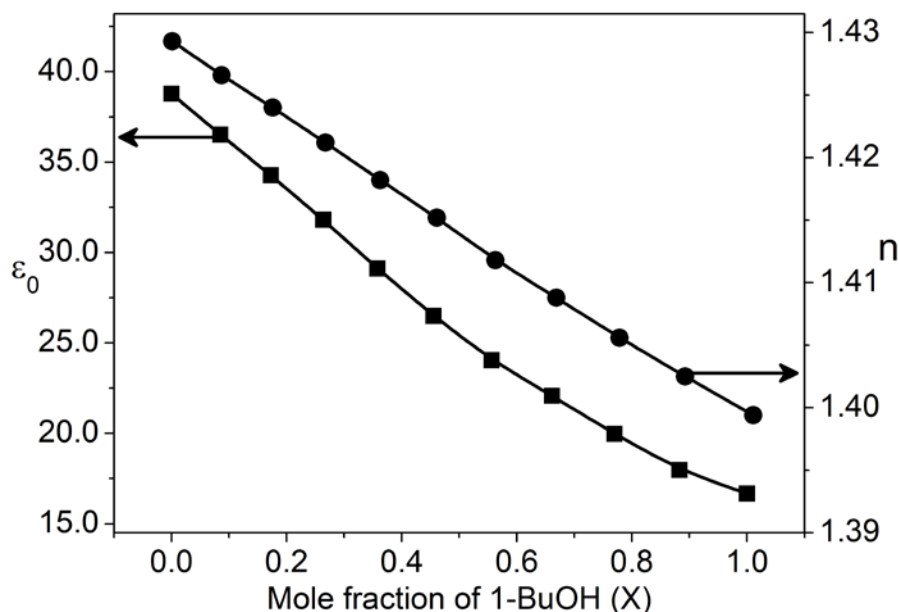


Figure1. Variation of static dielectric constant and refractive index against mole fraction of 1-BuOH in the binary mixtures of (DMF+1-BuOH) at 303 K.

The nonlinear variation of static dielectric constant ($\varepsilon_0$) against mole fraction of 1-BuOH suggests molecular interaction between the molecular constituents. In the liquid binary mixtures, there is a wide range of possible molecular interactions between the constituents such as hydrogen bonding, dipole-dipole and induced dipole-dipole interactions. As a result of these interactions deviations occur from ideal dielectric behaviour with the variation in concentration of mixture constituents [2-4,18,19]. There is a considerable difference between dipole moment values ($\mu_{DMF}$ = 3.82 D and $\mu_{1\text{-}BuOH}$ = 1.68 D) of the constituent molecules. Therefore, the internal field in the pure state would be very different from the internal field in the mixed state. The excess static dielectric constant ($\varepsilon_0$)$^E$ and excess refractive index (n)$^E$ are calculated from the experimental data [4,7,10,18],

$$(\varepsilon_0)^E = (\varepsilon_{0m} - \varepsilon_{\infty m}) - \left((\varepsilon_{01} - \varepsilon_{\infty 1}) \cdot x_1 + (\varepsilon_{02} - \varepsilon_{\infty 2}) \cdot x_2\right) \qquad (2)$$

$$(n)^E = n_m - (n_1 \cdot x_1 + n_2 \cdot x_2) \qquad (3)$$

where suffix 'm', '1' and '2' have their usual meaning mixture, component 1 (i.e. 1-BuOH) component 2 (i.e. DMF) respectively. These excess parameters are fitted in Redlich-Kister polynomial equation [16,19]

$$(A)^E = x_1 \cdot x_1 \sum_i^n a_i \cdot (x_2 - x_1)^i \qquad (4)$$

To obtain the parameters $a_i$, $X_1$ and $X_2$ are the mole fractions of 1-BuOH and DMF, 'n' is the degree of polynomial. The linear least-squares fitting procedure was used to fit the polynomials to the data. The adjustable parameters $a_i$, with standard errors is listed in Table 2.

Table 2. Redlich-Kister parameters $a_i$ (i = 0 to 3) with correlation parameter for binary mixtures.

| Parameter | $a_0$ | $a_1$ | $a_2$ | $a_3$ | $\sigma$ |
|---|---|---|---|---|---|
| $(\varepsilon_0)^E$ | -8.92085 | -3.60637 | 2.23260 | -2.21551 | 0.99319 |
| $(n)^E$ | -0.002582 | -0.003693 | 0.0001918 | 0.003706 | 0.98137 |

The variations of excess function $((\varepsilon_0)^E$ and $(n)^E)$ are shown in figure 2 (Geometrical shapes and smooth line shows expt. data points and R-K fitted respectively). The character changes of the static dielectric constant are very clear as the function of composition of mixtures in the case of excess values of $\varepsilon_0$. The $(\varepsilon_0)^E$ values of binary mixtures of 1-BuOH+DMF are non zero and shows $((\varepsilon_0)^E < 0)$ negative deviation . This indicates that both molecular species interact so as to reduce the total effective dipoles due to orientation of some of the neighbouring dipoles in opposite direction in these systems. Hence there is a decrease in the values of the static dielectric constants of the binary mixture from their ideal mixing values. These suggest that the molecular species may form multimers leading to less effective dipoles. The different strength of H-bond interactions and net dipolar alignments is responsible for the divergent magnitude of $(\varepsilon_0)^E$ values in these mixtures. Whereas the negative deviation of $(n)^E$ suggests mixtures have slightly lower values of the optical permittvity than the ideal case at Na-D line wavelength.
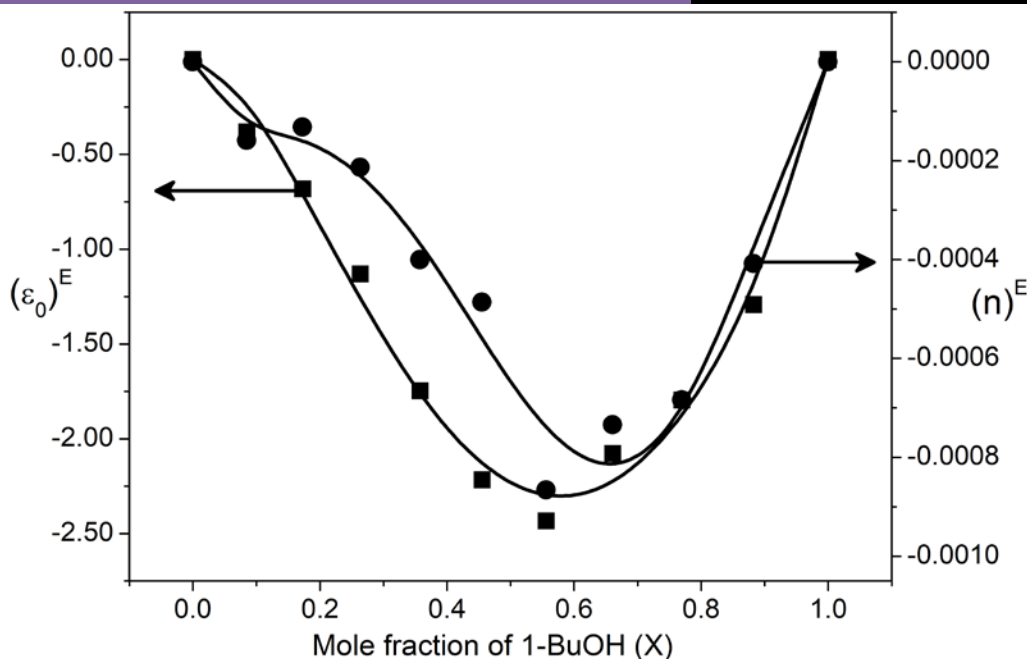
Figure 2. Variation of excess static dielectric constant $((\varepsilon_0)^E)$ and excess refractive index $(n)^E$) against mole fraction of 1-BuOH in the binary mixtures of (DMF+1-BuOH) at 303 K.

The Kirkwood correlation factor (g) provides a more clear and detailed information on dipole-dipole correlation in associating polar liquids and the information regarding orientation of electric dipoles in polar liquids [18-19]. The expression for g

$$\frac{4\pi N}{9kT}\frac{\rho}{M}g\mu^2 = \frac{(\varepsilon_0-\varepsilon_\infty)(2\varepsilon_0+\varepsilon_\infty)}{\varepsilon_0(\varepsilon_\infty+2)^2}$$  (5)

Where $\mu$ is the dipole moment, $\rho$ is the density of liquid at temperature T, M is the molecular weight, k is the Boltzmann constant, N is the Avogadro's number. For a liquid in which molecules tend to orient themselves with the parallel dipole alignments in the same direction results the 'g' value greater than unity. When the polar liquid molecules prefer an ordering with anti-parallel dipoles, the 'g' value comes smaller than unity, and for non-associating molecules, the 'g' value is nearly unity. The departure of 'g' value from unity is a measure of degree of short range dipolar ordering due to H-bond interactions. 'g' value 1-BuOH greater than unity (g = 3.24), which confirms the existence of H-bonded molecular multimers with parallel dipole alignments. The value of 'g' for DMF is near to unity (g = 1.21) and thus confirms its weakly-associative behaviour. For the mixtures of two polar

liquids, the effective Kirkwood correlation factor ($g^{eff}$) of two different molecules is evaluated from the modified Kirkwood equation. The Modified Kirkwood equation for the binary mixture is expressed as

$$\frac{4\pi N}{9kT}\left(\frac{\rho_1}{M_1}\mu_1^2\emptyset_1 + \frac{\rho_2}{M_2}\mu_2^2\emptyset_2\right)g^{eff} = \frac{(\varepsilon_{0m}-\varepsilon_{\infty m})(2\varepsilon_{0m}+\varepsilon_{\infty m})}{\varepsilon_{0m}(\varepsilon_{\infty m}+2)^2} \qquad (6)$$

The corrective Kirkwood correlation factor ($g_F$) equally affecting the Kirkwood correlation factors of pure substances 1 and 2

$$\frac{4\pi N}{9kT}\left(\frac{\rho_1}{M_1}\mu_1^2\emptyset_1 g_1 + \frac{\rho_2}{M_2}\mu_2^2\emptyset_2 g_2\right)g_F = \frac{(\varepsilon_{0m}-\varepsilon_{\infty m})(2\varepsilon_{0m}+\varepsilon_{\infty m})}{\varepsilon_{0m}(\varepsilon_{\infty m}+2)^2} \qquad (7)$$
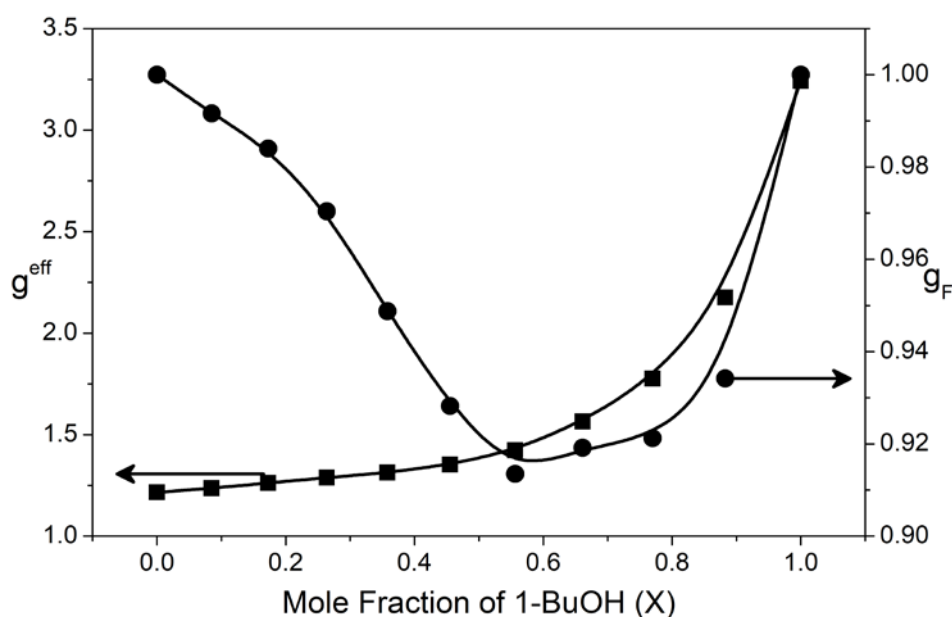


Figure 3. Variation of $g^{eff}$ and $g_F$ against mole fraction of 1-BuOH in the binary mixtures of (DMF+1-BuOH) at 303 K.

The evaluated $g^{eff}$ and $g_F$ values of the binary mixtures are plotted against the volume fraction of 1-BuOH in Fig. 3. The $g^{eff}$ values of binary mixtures have shown deviation from ideality, which confirms the net change in dipolar ordering of the mixture constituents due to H-bond complexation. It is observed that for the studied binary mixture system shows negative deviation from ideality. The deviation of $g_F$ values from unity confirms that the H-bonded structures of mixture constituents changes significantly. The extent of departure of $g_f$ from unity represents the degree of interaction in binary mixture constituents. In the present

study, the magnitude of deviation of $g_F$ values from unity is maximum at 0.55 mole fraction of 1-BuOH. This suggests that strong molecular interaction is taking place at this concentration. Another important dielectric parameter is the Bruggeman parameter ($f_B$) which give information about the interaction between components in the mixture [19-21]. If there is no interaction between the components in the mixture then the Bruggeman parameter ($f_B$) varies linearly with the volume fraction $\Phi_B$, but if there is interaction between the molecular species then $f_B$ varies nonlinearly with $\Phi_B$. The Bruggeman parameter $f_B$ is given by

$$f_B = \left(\frac{\varepsilon_{0m} - \varepsilon_{02}}{\varepsilon_{01} - \varepsilon_{02}}\right)\left(\frac{\varepsilon_{01}}{\varepsilon_{0m}}\right)^{\frac{1}{3}} = 1 - \emptyset_2 \qquad (8)$$

Here, $\Phi_B$ is the volume fraction of component B, whereas $\varepsilon_{oA}$, $\varepsilon_{oB}$ and $\varepsilon_{om}$ are the static dielectric constants of component A, component B and binary mixture respectively. According to Eq. 8, a linear relationship is expected which should give a straight line when $f_B$ is plotted against $\Phi_B$. However, from the Fig. 4, it is observed that for the studied binary system experimental values of $f_B$ are found to deviate from the linear relationship.

$$f_B = \left(\frac{\varepsilon_{0m} - \varepsilon_{02}}{\varepsilon_{01} - \varepsilon_{02}}\right)\left(\frac{\varepsilon_{01}}{\varepsilon_{0m}}\right)^{\frac{1}{3}} = 1 - (a - (a - 1)\emptyset_2)\emptyset_2 \qquad (9)$$

where '*a*' is a numerical fitting parameter. Here, it is assumed that the volume fraction of the solute in the mixture is modified by a factor of [*a*–(*a*–1)$\Phi_B$]. This modification of volume fraction is may be due to structural rearrangement of the solute molecules in the mixture. which signify the change in the orientation of the constituent molecules and thus measures the extent of the dipole interaction of the constituent polar liquids of the binary mixture in terms of size of molecules and their occupation of volume. For the studied system, the observed value of numerical fitting parameter (a = 1.15) indicating hetero molecular interaction between the molecular species. Further it also suggests that the effective volume of the DMF molecules decrease as 1-BuOH added in the mixture.
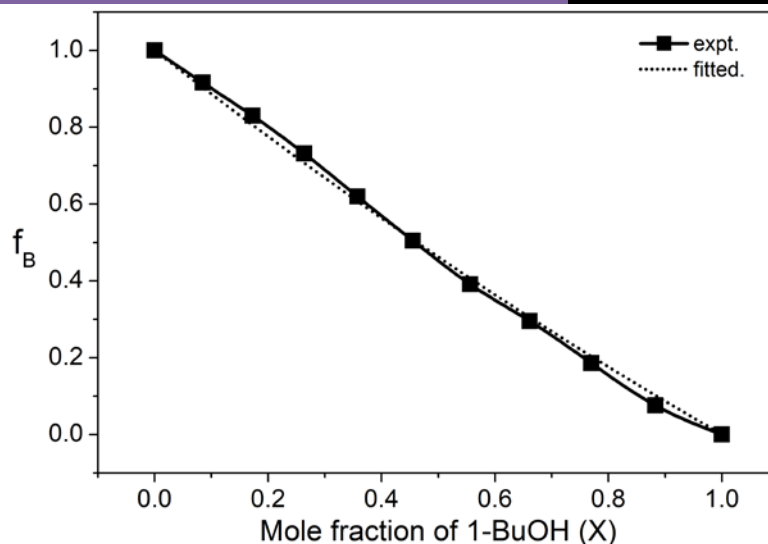
Figure 4. Variation of $f_B$ against mole fraction of 1-BuOH in the binary mixtures of (DMF+1-BuOH) at 303 K.

## 5 Conclusions

The static dielectric constant ($\varepsilon_0$) and refractive index (n) of 1-BuOH, DMF and their binary mixtures are determined. Excess static dielectric constant ($\varepsilon_0$)$^E$, excess refractive index (n)$^E$ Kirkwood parameters ($g^{eff}$ and $g_F$) and Bruggeman parameter ($f_B$) are evaluated and discussed in terms of hetero molecular interaction between molecular species. The results obtained from the present investigation indicate that the molecules of studied binary mixtures may be joined, by a network of interactions such as dipolar and hydrogen bonds, to form stable intermolecular complexes between the molecular species.

## 6 Acknowledgement

## References

[1]    A. Gilani, H. Gilani, M. Ansari, N. Ojani, J. Chem. Thermodynamics, 2012, 44, 44.

[2]    R. Sengwa, V. Khatri, S. Sankhla, J Mol. Liqs., 2009, 144, 89.

[3]    R. Sengwa, V. Khatri, S. Sankhla, Indian J. Chem. A, 2009, 48, 512.

[4]    R. Sengwa, S. Sankhla, N. Shinyashiki, J Sol. Chem., 2008, 37, 137.

[5]    A. Prajapati, A. Vyas, V. Rana, S. Bhatnagar, J. Mol. Liq., 2010, 151, 12.

[6]    A. Rodriguez, J. Canosa, J. Tojo, J. Chem. Eng. Data., 2001, 46, 1506.

[7]    A. Prajapati, V. Rana, A. Vyas, D. Gadani, J. Int.  Acad. Phys. Sci., 2012, 16, 387.

[8]    A. Prajapati, V. Rana, A. Vyas, D. Gadani, Advanced Materials Research., 2013, 665, 317.

[9] A. Prajapati, Advanced Materials Research., 2016, 1141, 125.

[10] A. Prajapati, V. Rana, A. Vyas, Ind. J. Pure & Appl. Phys., 2017, 55, 297.

[11] T. Thenappan, U. Sankar, J Mol. Liqs., 2006, 126, 38.

[12] I. Mellan, Industrial Solvents, Van Nostrand Reinhold, New York, 1950, 482.

[13] A. Doolittle, The Technology of Solvents and Plasticizers, Wiley, New York, 1954, 644.

[14] C. Dorota, B. Adam, R. Sengwa, J Mol. Liqs., 2013, 179, 72.

[15] F. Dossoki, J Chin. Chem. Soc., 2007, 54, 1129.

[16] M. Andrea, P. Carlo, T. Mara, T. Lorenzo, T. Giuseppe, J Chem. Eng. Data, 1991, 36, 365.

[17] R. Sengwa, V. Khatri, S. Sankhla, J Sol. Chem., 2009, 38, 763.

[18] T. Madhumohan, T. Vijayalaxmi, Phys. Chem. Liq., 2013, 51, 480.

[19] A. Prajapati, V. Rana, A. Vyas, S. Bhatnagar, Ind. J. Pure & Appl. Phys., 2011, 49, 478.

[20] A. Prajapati, V. Rana, A. Vyas, Ind. J. Pure & Appl. Phys., 2013, 51, 104.

[21] S. Puranik, A. Kumbharkhane, S. Mehrotra, Bruggeman model, J. Mol. Liqs., 1994, 94, 173.

# E.P.R. Study of Pure and Doped Calcium Tartrate Single Crystals

**S. R. Suthar and M. J. Joshi**

Physics Department, Municipal Arts & Urban Bank Science College,

Mehsana , Gujarat, 384002 .

Crystal Growth Laboratory, Department of Physics, Saurashtra University, Rajkot 360005.

**E-Mail : srsuthar96@gmail.com**

.

**Abstract:**

Calcium dextro and levo tartrate single crystals with different amounts of doping of $Mn^{2+}$ have been grown by single diffusion gel growth technique in silica hydrogel.The powder XRD pattern suggested that the crystals were found to be of single phase and no significant variations in the values of cell parameters were observed due to the doping of $Mn.^{2+}$ The {110} faces of single crystalline $Mn.^{2+}$ doped calcium dextro and levo-tartrate crystals were investigated by EPR(Electron Paramagnetic Resonance) spectroscopy in perpendicular as well as parallel directions to this face. From the spectra two different phases of $Mn^{2+}$ were observed.The values of EPR parameters were found to be nearly the same for calcium dextro tartrate and calcium levo-tartrate crystals with different amounts of $Mn^{2+}$ doping within the experimental limits.

## 1. Introduction:

The electron paramagnetic resonance technique has attracted the attention of not only chemists but also the material scientists and solid state physicists to study various materials. Materials may be monocrystalline, microcrystalline or glassy and give spectra according to their nature, which may be rich and well resolved -or poorly resolved. The EPR technique has been employed for spin identification, spin counting spin mapping, spin motion and spin imaging of a variety of advanced materials, transition metals, rare- earth and actinide cmpounds, organic charge transfer complexes,etc. This technique has proved to be specific, sensitive up to ppm level of composition, phase and texture, accurate as a quantitative and non distructive tool[1-4], which has been reviewed by Sunanda.[1]

Calcium tartrate crystals are found to be exhibiting ferroelectric and non linear optical properties[5-9]. The ferroelectricity in gel grown calcium tartrate was reported by Gon[8]. Suryanarayana et al.[9] have studied optical and structural properties of strontium doped calcium tartrate crystals. In the present investigation, calcium dextro tartrate (CDT) and, calcium levo tartrate (CLT) crystals have been grown by the gel technique by doping them with $Mn^{2+}$ in different amounts. An attempt is made by the present authors to investigate these doped crystals by EPR spectroscopy to find out the effect of optically sensitive dextro and levo tartrate radicals on the growth of crystals as well as the effect of doping.

## 2. Experimental Techniques:--

Single crystals of calcium tartrate were grown in silica hydro-gel by incorporating single diffusion reaction technique. The gel was set by mixing the aqueous solutions of sodium metasilicate of 1.06

specific gravity with 1.0 M tartaric acid, either dextro or levo as the case may be so that the pH of mixture could be set at 3.8.This mixture was transferred in to glass test tubes of 2.5 cm diameter and 15 cm length. After setting the gel supernatant solutions were poured in different test tubes without disturbing the gel. After a few days, nucleation started in the gel and good quality, prismatic, transparent crystals grew. The crystals of pure calcium tartrate crystal were colorless and transparent. Whereas the $Mn^{2+}$ doped crystals were light yellowish in colour.

The samples were analyzed by the powder X-ray diffraction technique using PHILIPS x' PERT MPD system at C.S.M.C.R.I.,Bhavnagar.The sample were analyzed by powder X computer software and the crystal structure was determined for different samples.

The field was applied perpendicular and parallel to {110} face of the crystals. The EPR spectra were recorded in X-band (8.5 to 9.5GHz) at room temperature at RSIC, I.I.T., Mumbai. The crystals were rotated and the spectra were recorded perpendicular and parallel to the {110} face with the help of a suitable goniometer using TCNE as a marker.

### 3 Results and discussion:

There has been considerable interest in the study of the EPR spectra of single crystals either by irradiating with X-Rays or gamma-rays or doping by transition or rare earth elements.[2-3] The ESR study of $Mn^{2+}$ in $Co_2M(SO_4)_26H_2O$(M=Zn,Mg,Co,Ni) single crystals[10] and $Mn^{2+}$ in $Nd_2Zn_3(NO_3)_{12}.24H_2O$ single crystals[11] have been reported. Pure and vanadyl doped single crystals of strontium tartrate tetra hydrate have been characterized by EPR spectroscopic technique. The angular variation has shown that $Vo^{2+}$ ion has a fixed orientation in the lattice. The **g** and **A** tensors and their direction cosines were evaluated from the EPR analysis. The EPR and electronics spectral results have shown that the $Vo^{2+}$ ions occupy the interstitial sites in the lattice (tetragonal) having $C_{4v}$ symmetry. Suzuki et al [12] reported the ESR spectra of $Cu^{2+}$ doped sodium ammonium tartrate.

In the present investigation, $MnCl_2$ solution of different concentrations of were added along with 1.0M $CaCl_2$ solutions in order to achieve appropriate doping of $Mn^{2+}$ in the calcium tartrate lattice. Calcium tartrate crystals were grown by diffusion of $Ca^{2+}$ and tartrate ions in gel media and the reaction between them forming nucleation centers, subsequently, the growth of crystals occurs on such nucleation centers. Doping of $Mn^{2+}$ is expected substitute $Ca^{2+}$ in calcium tartrate lattice during the growth of the crystals, which is not expected to change the crystal structure and the cell dimensions of calcium tartrate crystals. This has been verified by powder X-Ray diffraction (XRD) patterns and no extra phase appears in the XRD patterns due to doping of $Mn^{2+}$. The crystal structure and cell parameters are found to be same within the experimental variations. Table (1) shows the cell parameters obtained for $Mn^{2+}$ doped calcium tartrate crystals. These values are matching with the standard values of cell parameters reported by Amady[13] for calcium tartrate crystals as follows.

a = 9.24 $\pm$ 0.02 Å , b = 10.63 $\pm$ 0.02 Å and  c = 9.66 $\pm$ 0.02 Å

**Table 1** Powder XRD data of pure and doped CT crystals

| Sample | Cell parameters | | |
|---|---|---|---|
| | a | b | c |
| Pure $CaC_4H_4O_6$ | 9.2134 | 10.5841 | 9.6253 |
| 0.001M $Mn^{2+}$ doped CLT crystals | 9.2053 | 10.6018 | 9.6117 |
| 0.01M $Mn^{2+}$ doped CLT crystals | 9.21 | 10.5763 | 9.615 |
| 0.1M $Mn^{2+}$ doped CLT crystals | 9.2168 | 10.5677 | 9.6147 |
| 0.001M $Mn^{2+}$ doped CDT crystals | 9.2084 | 10.5964 | 9.6276 |
| 0.01M $Mn^{2+}$ doped CDT crystals | 9.216 | 10.59 | 9.621 |
| 0.1M $Mn^{2+}$ doped CDT crystals | 9.2979 | 10.5766 | 9.6488 |

The EPR spectra of $Mn^{2+}$ doped calcium tartrate single crystals exhibit hyperfine splitting in form of five regions of each block containing six lines. The EPR -spectra of 0.01% $Mn^{2+}$ doped calcium tartrate crystals recorded perpendicular and parallel to{110} face are shown in Figure (1)and Figure (2), respectively. The EPR parameter s $g_\parallel$ $g_\perp$, $A_\parallel$, $A_\perp$, $D_\parallel$, $D_\perp$ are calculated from the spectra and listed in Table (2)
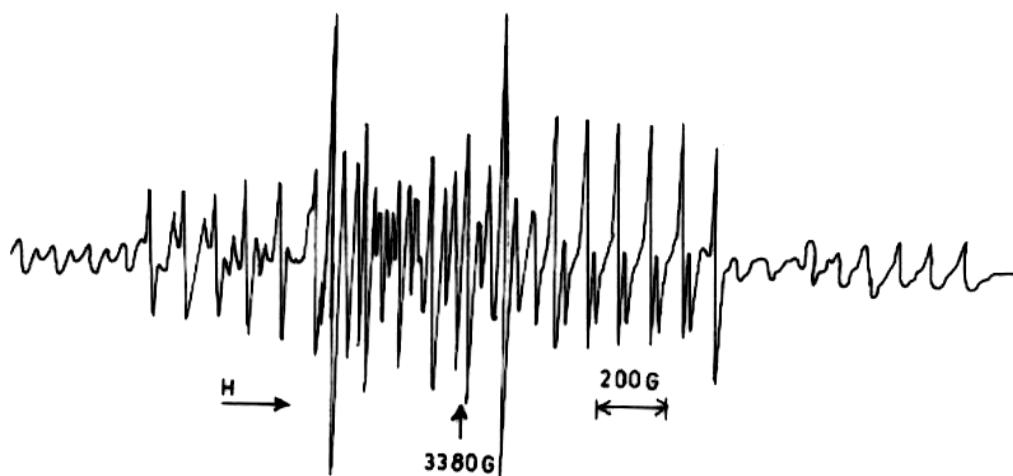


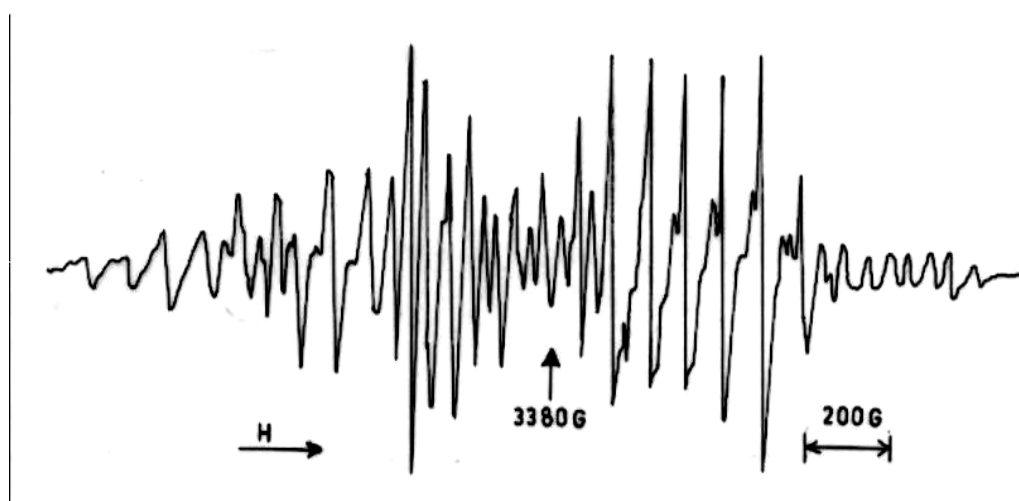**Figure (1) EPR of 0.01% $Mn^{2+}$ doped ⊥ to {110} face CLT crystal**



**Figure (2) EPR of 0.01% $Mn^{2+}$ doped ∥ to {110} face CLT crystal**

$Mn^{2+}$ is a $d^5$ ion having a total electron spin S = 5/2 in its ground state as required by the Hund's rule of maximum multiplicity. The ground term of this ion is $^6S_{5/2}$. This term split up, due to zero filed, into three Kramer's doublets e.g., ±5/2, ±3/2, ±1/2. This degeneracy is lifted as used in EPR experiment giving six energy levels with spin –5/2, -3/2, -1/2, +1/2, +3/2, +5/2 in increasing order. Each of these energy levels is further split into six equally spaced levels by the interaction of these spins with the nuclear spin, which for $Mn^{+2}$ is I=5/2 and hence the number of levels (2I+1) gives six lines. Therefore, the energy level diagram with total thirty levels is obtained in the presence of an applied magnetic field and for microwave absorption signals to be observed two selection rules are obeyed Viz., ΔS= ±1, and $\Delta M_I$ = o. These results in five regions of spectral absorption each block containing six lines.

**Table 2 EPR Parameters of $Mn^{2+}$ doped CLTT crystals**

| Samples | $A_\perp$ | $A_\parallel$ | $g_\perp$ | $g_\parallel$ | $D_\perp$ | $D_\parallel$ |
|---|---|---|---|---|---|---|
| 0.001M $Mn^{2+}$ doped CDT crystals | 96 | 97.5 | 2.029357 | 1.97331 | 201.25 | 301.25 |
| 0.01M $Mn^{2+}$ doped CDT crystals | 94 | 90 | 2.044639 | 1.98776 | 167.5 | 270.625 |
| 0.1M $Mn^{2+}$ doped CDT crystals | 98.12 | 91 | 2.085278 | 1.96759 | 294 | 190.62 |
| 0.001M $Mn^{2+}$ doped CLT crystals | 96.25 | 94.99 | 1.9779 | 2.044639 | 300.62 | 207.5 |
| 0.01M $Mn^{2+}$ doped CLT crystals | 92.5 | 95.66 | 2.03057 | 1.98195 | 203.12 | 295 |
| 0.1M $Mn^{2+}$ doped CLT crystals | 95.33 | 92 | 2.057307 | 1.9977 | 285.25 | 151.875 |

From the spectra of Figure (1) and Figure (2), it is found that there are two different phases of $Mn^{+2}$ tartrate complexes present in the crystal. This corresponds to the results of Jain and Venkateswaralu [11]. The EPR spectra of phase one is well spread out while that of the other is found to be located in close signals with a small spread in the middle of the spectra. Different parameters for $Mn^{+2}$ doped calcium tartrate crystals are comprised in Table (2), which suggest that no marked deference either due to level of $Mn^{+2}$ doping or the type of parent compound i.e., dextro or levo tartrate is observed.

## 4  CONCLUSION

Calcium tartrate crystals were grown with different amount of $Mn^{+2}$ doping did not change the cell parameters of grown calcium tartrate crystals and produced the single phase crystals. $Mn^{++}$ doped calcium CT crystals are characterized by EPR spectroscopy in X-band at room temperature. Single crystalline samples of $Mn^{++}$ doped CLTT crystals are analyzed parallel and perpendicular to {110} face. Various EPR parameters are observed as the concentration of $Mn^{++}$ increases in the crystals. From the two types of spreads in the EPR spectra it is conjectured that two types of different environments of $Mn^{++}$ exist in the crystals. $Mn^{++}$ is expected to occupy the interstitial positions in CLTT crystals.

## ACKNOWLEDGEMENTS

## References

(1)    Sunandana S., *Bull. Mater Sci. 21* (1998)1.

(2)    Ayscough P. B., *"Electron Spin Resonance in Chemistry", Methuen & Co., London* (1967)

(3)    Carrington A. McLachlan A.D, " *Introdution to Magnetic Resonance" Harper  Int., New York*,(1967)

(4)    Drago R. S., *"Physical Methods in Chemistry" Saunders College ,NewYork*  (1977)

(5)    Medrano C. Gunter P. and Arend H, *phys. Status Solid.* 14B (1987) 749

(6)    Brehat F. and Wyncke B. *J.Phys. B.: At Mol.Opt. Phys.* 22 (1989) 1981

(7)    Nakatani N. *Jpn. J. Appl. Phys.* 30 (1991) 1961

(8)    Gon H B *J. Cryst. Growth*.102 (1990) 501

(9)    Suryanarayana K.Dharmaprakash SM and Sooryanarayana K *Bull. Mate. Sci.*  21(1998)87

(10)   Jain V K, Kapor V, Prakash V; *Solid State Commun*.,97(1996) 425

(11)   Jain V K and Venkateswaralu, *Indian J. of pure and Appl. Phys. 16* (1978) 841

(12)   Suzuki I, Maeda M, Abe R*; J.Phys. Soc. Japan*, 33 (1972) 860

(13)   Ambady G K, *Acta cryst*. B24(1968) 1548

# Magnetic Nanostructure, Nano optics and its Applications

Paresh V Modh[1] Kalpesh C Mevada[2]

R R Mehta College of Science

C L Parikh College Commerce, Palanpur[1]

Municipal Arts & Urban Bank Science College, Mahesana[2]

Email:Paresh.modh_rediffmail.com

**Abstract:** The present paper reports the study of modulation in intensity of light transmitted through the thin films of nanostructured. The form of the created features ranges from craters and ditches to hillocks. The process has been demonstrated on gold substrates by utilization of uranium, carbon, and cesium tips. Nanoparticles are now being used in the manufacture of scratchproof eyeglasses, crack- resistant paints, and anti-graffiti coatings for walls, transparent sunscreens, stain-repellent fabrics, self-cleaning windows and ceramic coatings for solar cells. Nanotechnology is a part of science and technology about the control of matter on the atomic and molecular scale - this means things that are about 1000 nanometers or smaller. Nanotechnology includes making products such as magnetic devices, analysts, sensors, etc. Nanotechnology is being studied for both the magnetic and electric. Magnetic Nanotechnology in medicine involves applications of nanoparticles currently under development, as well as longer ranges research that involves the use of manufactured Nano-robots to make repairs at the cellular level. Nanotechnology eases the water cleansing process because inserting nanoparticles into underground water sources is cheaper and more efficient than pumping water for treatment. The primary objective of this magnetoscopy is to apply Nano tools in biological systems to overcome the current problems in medical/biological world. Magnetic devices are proposed use of 100 pm diameter magnetic particles, with and without a carrier fluid.

**Keywords**: Magnetoscopy, Nano motor, AC and DC Magnetic field, rotating magnetic power generator

**Introduction:** In this work, we present on some extent to experimental and theoretical study on the small angle scattering. Theoretical study of small angle scattering is explained more effectively. When the radiation is incident on the specimen, it deviates from its path is known as small angle scattering. Nanostructure is very important technique to obtain detail information of bulk sample. In the Nanostructure, partially crystalline or amorphous solids, liquids or gases are used as target. Moreover electrons, gamma rays, X-rays, are incident and target should be point object. But I consider only X-ray, so it is known as small angle scattering. The improvement in the Nanostructure instrumentation has recently enabled to get easy collection of datas. Distortion due to the X- ray detection system can be removed. The transverse dimension **t** of the coherence volume is also defined and discussed, as coherence volume is important to analyze datas. Out of three aspects like shape, Nanostructure and packing, two properties must be known in order to explain rest of above properties. Characteristics of nanoparticles like gold can be known, if TEM method is included with the SAXS method, we will get best performance like information on morphological features ranging from micro structure to macro structure. Explanation of pin-hole collimated instruments, Bose- Hart instruments, slit collimated instruments are very popular due to their flexibility                                                                multi-

phase system to explain scattering. There is also drawback of SAXS related to scattering intensity will be explained in paper.

**Nano Structure:** Magnetic Nano structure indicates that space time emerges in the low energy sector of a fundamental condensate. Small angle scattering is very important method for the Nano structural particles. SAS is developing at a high step over the past two decades. All the theoretical datas pass under this method so that improvements in data correction steps are corrected. Mathematical descriptions are also given where it is necessary. An introduction is also explained here for Nano optics.

Irradiate a sample with a well collimated beam of some type of radiation measure the resulting intensity as a function of angle between the incoming beam and scattered beam, and then determine the structure that caused the observed pattern. Scattering patterns are caused by the interference of the secondary waves that are emitted from various structures when irradiated. Scattering of X-Ray is caused by difference in electron density, scattering of neutrons is caused by difference in scattering power of different nuclei and scattering of light is caused by difference in refractive index.

If at any instant there are n particles in a beam with a velocity v, the flux of the beam is nv and if N be the number of nuclei exposed to the beam at any instant of time, then the rate of react or scattering is expressed as proportional to nv and N.

In 19 th centuries, Rontgen discovered radiation with wavelength much smaller than that of visible light. Rontgen named this high energy radiation Nano optics because of their unknown nature. Soon after this discovery, Von Laue and his associate discovered that scatter X-ray in distinct pattern. It was quickly recognized that these patterns give direct insight into the structure of the materials that caused the scattering. Since these early discoveries, many technical advances made Nano optics scattering one of the most powerful characterization tools available for both homogeneous and heterogeneous materials.

Irradiate a sample with a well- collimated beam of some type of radiation measure the resulting intensity as a function of angle between the incoming beam and scattered beam, and then determine the structure that caused the observed pattern. Scattering patterns are caused by the interference of secondary waves that are emitted from various structures (electron for X-rays and light, nuclei for neutrons) when irradiated. Scattering of X-ray is caused by differences in electron density, scattering of neutrons is caused by differences in scattering power of different nuclei and scattering of light is caused by difference in refractive index. Since the larger the diffraction angle the smaller the length scale probed, wide angle X-ray scattering is used to determine crystal structure on the atomic length scale while small angle X-ray scattering or small angle scattering is used to explore microstructure on colloidal length scale.

Nano optics has many drawbacks but still this method has much important information, for example, experiment of gold nanoparticles, krypton bubbles in copper, coated silica particles, zerolite precursor particles are exactly agreement between Nano optics and Nano crystal analysis. Small angle X-Ray scattering requires combined techniques of TEM and AP. When two main contrasting phases are involved in these methods, we get best performance of the sample. When someone uses these two conditions are coincide, hence we will get information on morphological features ranging from sub nanometer region to several micron. This information is valid for the entire range of radiation.

**Nano Optics:** One more drawback of Nano optics, even it is more used in the phase system, Nano optics measures only the scattering intensity is collected. This method cannot measure phase of photons. And critical information of the originals structure is also lost. According to latest research, distribution of electron density is responsible for the scattering. This means many solutions may be equally valid for a particular set of collected intensities which may only be resolved by obtaining structural information from other technique such as transmission electron microscope. This is unexpected correction.

Nano optics, which is virtually nonexistence at small angles, refers to scattered waves that have changed phase and wavelength. The coherent scattering of Nano optics by a single fixed particle is explained. The increasing availability of intense short pulse Nano optics sources allows a measurement of a type not possible before, namely angular fluctuations of intensity about mean values on rings of constant q from snapshots of a relatively small number of identical particles differing only in random positions and random orientations. In an optical instrument a monochromatic beam of Nano optics is brought to a sample from which some of the X-rays scatter, while most simply go through the sample with interacting with it. The scattered X-ray from a scattering pattern which is then detected at a detector which is typically a three dimensional flat Nano optics detector situated behind the sample perpendicular to the direction of the primary beam that initially hit the sample. The purpose here is not to familiarize the reader with all these methods but rather to describe the most commonly used approaches. An important is that Monte-Carlo methods can be used to calculate entire scattering patterns.

The signal from each molecule will be its vibrational average and signal amplification is provided by the addition of such vibrational averages from all illuminated atoms, as given by the Nano optics. Nowadays, there are many instruments like SAXS, and variety of flavors and colors. There are three parts (1) pin hole collimate instruments (2) slit collimated instruments (3) Boson-Hart instruments. Pinhole collimated instrument is very popular due to their flexibility in terms of samples and easy availability in the market. This part of instrument is very useful and also dominates the SAXS field and for neutron sources.

Slit collimated instrument is much more compact than the pin hole collimated systems. Slit collimated instrument is less expensive and illuminates a larger amount of sample to collect more scattering. SAXS is capable of delivering structural information of macro molecules between 10 to 35 nm of repeat distance in partially ordered systems of up to 160nm. SAXS instruments can be divided into two main groups point collimation and line collimation instruments. Point –collection instruments have pin holes that shape the X-ray beam to a small circular spot that illuminates the sample. Due to the small illuminated sample volume and the waste fullness of collimation process- only those photons are allowed to pass that happens to fly in the right direction. Moreover the scattered intensity is small and therefore the measurement time is in the order of hours or days in case of very weak scatterers. And second type of instrument is much larger compared to point collimation. Line collimation is of great benefit for any isotropic nanostructured materials like proteins and particle dispersion.

Nanostructure method is a technique to solve a complex problem by the observation of a random process whose parameters are based on the complex problem. Consider the task of choosing points in space to simulate a sphere with a radius equal to 5 cm. The points in space, once chosen, will then be used as scattering points. However, there are problems with the shell and grid method, the problem is that the discrete shells cause artifacts in the scattering pattern. Also it is very difficult to get a constant point

density with this method. So the t of choosing random points to simulate the sphere is by far the most appropriate choice.

**Applications:** In order to reduce scattering, more focusing and mono chromatization crystals, high intensities Optics sources and total reflective mirrors, three collimators are used. These types of inventions led to adoption of all of these elements in, subsequent instruments to improve the flux and signal to noise ratio. Due to X-ray sources we can increase brightness, increase in photon flux $10^7$ photons per second, photons are generated from micro source tubes. Nano optics topology experiment, $10^{11}$ -$10^{13}$ photons per second are necessary. This is only happening when synchrotron based instruments are used.

"Nikon" camera is suitable for ultra-small angle scattering purposes which are used for high angular selectivity of crystalline reflections to single out a very narrow band of cattering angles for observations.

Actually, there are three important parameters to know a structure properties (1) polydisperity (2) shape (3) packing. Out of these three, two properties must be known for the structural properties. With the help of particle size distribution and shape, we know an arrangement of particles in the space. A unique particle size distribution can be obtained by making a low density packing assumption and from particle shape. Particle shape is determined by TEM method. This essay investigates what could be meant by this claim.

In the case of Nano optics application, the materials can be solid or liquid and they can contain solid, liquid or gaseous domains of the same or another material in any combination. Not only particles, but also the structure of ordered systems likes lamellae, and fractal- like materials can be studied. The most important outcome of this part of the research is in learning how to properly perform these simulations. The existence of analytical solutions allowed me to pinpoint error in the code, allowed for the determination of simulation times required, and also aided in the choice of a random number generator.

**Conclusion:** The ultimate goal of this research to develop a Nano Optics and its application method that is able to fit real experimental data. For the simplest systems, i.e. identical single particles that are infinitely symmetric or identical single particles with perfect alignment, this goal could currently be reached if a suitable least square routine are developed. The former could probably be cooled and run on a fast PC, while the latter is obviously more time consuming because an entire two dimensional pattern is necessary.

**References:**

(1) Glatter O, Kratky O, ed.(1982). Small Angle X-ray Scattering
(2) J. Doumerc, A. Ammar, A. Wichainchai, M. Pouchard and P. Hagenmuller, "Sur Quelques Nouveaux Composes de Structure de Type Delafossite," Journal of physical chemistry of Solids.

(3) J.E. Maslar, W.S. Hurst, T.A. Vanderah and I. Levin," The Raman Spectra of X- ray" Journal of Raman Spectrograph"

(4)E.V.Lavor, F. Bornnert and J. Weber," Dominant Hydrogen-Oxygen Complex in Hydrothermally Grown ZnO"

(5)W.A Schutte, "Production of Organic Molecules in Interstellar Ices," Advances in Space Research.

(6) A.Wada,N. Mochizuki and K. Hiraoka, "Methaanol Formation from Electron-Irradiated Mixed$H_2O$/$CH_4$ Ice at 10K."